ASME
SETTING THE STANDARD
1880 2005

Transactions of the ASME, Journal of Fluids Engineering (ISSN 0098-2202) is published bimonthly (Jan., Mar., May, July, Sept., Nov.) by The American Society of Mechanical Engineers, Three Park Avenue, New York, NY 10016. Periodicals postage paid at New York, NY and additional mailing offices.
POSTMASTER: Send address changes to Transactions of the ASME, Journal of Fluids Engineering, c/o THE AMERICAN SOCIETY OF MECHANICAL ENGINEERS, 22 Law Drive, Box 2300, Fairfield, NJ 07007-2300.
CHANGES OF ADDRESS must be received at Society headquarters seven weeks before they are to be effective. Please send old label and new address.
STATEMENT from By-Laws. The Society shall not be responsible for statements or opinions advanced in papers or ... printed in its publications (B7.1, Par. 3).

Journal of Fluids Engineering

Published Bimonthly by ASME

VOLUME 128 • NUMBER 1 • JANUARY 2006

EDITORIAL

SPECIAL SECTION ON THE FLUID MECHANICS AND RHEOLOGY OF NONLINEAR MATERIALS AT THE MACRO, MICRO AND NANO SCALE

(Contents continued on inside back cover)

This journal is printed on acid-free paper, which exceeds the ANSI Z39.48-1992 specification for permanence of paper and library materials. ♾™
♻ 85% recycled content, including 10% post-consumer fibers.

(Contents continued)

TECHNICAL PAPERS

TECHNICAL BRIEFS

MEMORIAM

ERRATA

(Contents continued on facing page)

The ASME Journal of Fluids Engineering is abstracted and indexed in the following:

Applied Science & Technology Index, Chemical Abstracts, Chemical Engineering and Biotechnology Abstracts (Electronic equivalent of Process and Chemical Engineering), Civil Engineering Abstracts, Computer & Information Systems Abstracts, Corrosion Abstracts, Current Contents, Ei EncompassLit, Electronics & Communications Abstracts, Engineered Materials Abstracts, Engineering Index, Environmental Engineering Abstracts, Environmental Science and Pollution Management, Excerpta Medica, Fluidex, Index to Scientific Reviews, INSPEC, International Building Services Abstracts, Mechanical & Transportation Engineering Abstracts, Mechanical Engineering Abstracts, METADEX (The electronic equivalent of Metals Abstracts and Alloys Index), Petroleum Abstracts, Process and Chemical Engineering, Referativnyi Zhurnal, Science Citation Index, SciSearch (The electronic equivalent of Science Citation Index), Shock and Vibration Digest, Solid State and Superconductivity Abstracts, Theoretical Chemical Engineering

Journal of Fluids Engineering

Editorial

Special Section on the Fluid Mechanics and Rheology of Nonlinear Materials at the Macro, Micro, and Nano Scale

This collection of selected papers are drawn from those presented at the IMECE 2004 in Anaheim, California at the Symposia "Rheology & Fluid Mechanics of Non-linear Materials," "Advances in Processing Science," and "Electric and Magnetic Phenomena in Micro and Nano-Scale Systems" sponsored by the Fluids Engineering Division and the Materials Division, as well as the Symposium on "Flows in Manufacturing Processes" held at the 4th JSME-FED (Japanese Society of Mechanical Engineers–Fluids Engineering Division of the ASME) joint meeting in Hawaii in July 2003. They represent excellent examples of cutting-edge multidisciplinary research.

This editorial is accompanied by an addendum, "Current Unanswered Questions and Future Directions." I asked the authors in this special section to contribute their thoughts on yet unexplored issues they view as important in their respective areas, and they kindly obliged. I am grateful to those who decided to contribute. I learned the usefulness of the platform from my friend, the late Professor Lloyd Trefethen, who put together several very well received unanswered questions sessions during the meetings of the FED.

The symposia series centered on the theme of complex fluids developed as an interdivisional effort in the early nineties, and has been sustained primarily by the FED, the Materials Division and, in the early years, the Applied Mechanics Division, with organizing committees led by Dennis Siginer. Symposia focused on Electroheological Fluids, non-Newtonian and viscoelastic fluids, and industrial applications were held at every annual winter meeting of the ASME. A wider scope and a more encompassing recurring theme were embraced in the mid-nineties, and symposia on the "Rheology & Fluid Mechanics of Non-linear Materials" have been held every year since then without interruption. A second symposia series sponsored by the FED and the Materials Division addressing issues on "Electric and Magnetic Phenomena in Micro and Nano-Scale Systems," of great interest to emerging technologies and to homeland security, was initiated early in this decade by Dennis Siginer and Boris Khusid. Two complementary symposia of interest to industry in materials processing and manufacturing, "Advances in Materials Processing Science" and "Flows in Manufacturing Processes," have also been organized regularly for several years, the former held during IMECE and the latter during Summer Meetings of the FED.

This collection of papers opens with three contributions related to micro and nano scale problems. The first two are concerned with micro fabrication for the manipulation of nanoparticles using dielectrophoresis, and the third looks into optical finishing using magnetorheological jet polishing technology for a peak-to-valley surface accuracy of the order of 30 nm.

Riegelman et al. describe their research on the positioning of carbon nanotubes at predetermined locations with the use of dielectric forces and a fabrication technique to construct carbon nanotube based multiwalled fluidic devices. The technique combines dielectrophoretic trapping with photolithography.

James et al. present a novel separation device based on "dielectrophoretic gating" to discriminate between biological and non-biological analytes captured in air samples. A technique for batch fabrication of self-sealed, surface micro-machined micro-channels equipped with dielectrophoretic gates is described. Setting the gates to a moderate voltage in the MHz-frequency range removes bacteria cells from a mixture containing non-biological particles.

Kordonski et al. present research on a new polishing technology, magnetorheological finishing (MRF). MRF can produce nanometer order surface accuracy and roughness and does not damage the material at the subsurface level, a major disadvantage of conventional "contact" polishing. However, high precision finishing requires a stable, relatively high-speed, low viscosity fluid jet which remains collimated and coherent before it impinges the surface to be polished.

The next group of papers is concerned with flow stability problems. The stability of the flow in the co-extrusion of multilayered sheets from a die is a major concern for product quality. Multilayered sheets are composite materials with specific physical properties. Any interfacial instability during the extrusion process will result in undesirable effects. The behavior of non-Newtonian fluids in curved pipes of non-circular shape is of great interest and has not received as yet the attention it deserves, in particular the Dean instability. Aspects of the Taylor-Couette flow fall in the same category. Although the elastic instability in Taylor-Couette flow has received a lot of attention recently, the important symmetry breaking effect of an obstruction on the flow relevant to horizontal oil drilling operations has not.

Rousset et al. study the influence of an interphase on the stability of the plane Poiseuille flow of two compatible polymers during the co-extrusion process. Each layer of these composite materials provides a specific end-use characteristic, such as optical, mechanical, or barrier properties. The authors successfully explain why stratified flows of compatible polymers are generally more stable than those of incompatible polymers.

Fellouah et al. investigate numerically the Dean instability of Newtonian, power-law, and yield stress fluids in curved ducts of rectangular cross-section with various aspect and curvature ratios. Curved channels are commonly encountered in turbomachinery and heat exchangers for heating or cooling systems because of the extended laminar flow regime and enhanced transverse mixing. The influence of the aspect ratio and the curvature ratio on Dean instability is investigated as well as the effect of the power law index and the Bingham number.

Loureiro et al. investigate the flow inside a horizontal annulus due to the inner cylinder rotation when the bottom of the annular space is partially blocked by a plate parallel to the axis of rotation, as is encountered in the drilling process of horizontal oil and gas wells. A major problem in this drilling technique is the efficient removal of the cuttings that settle and accumulate at the lower part of the annular gap. The objective of the research presented in the paper is to determine the influence of the partial obstruction on the flow structure in the gap for low rotational Reynolds numbers, both for Newtonian and power-law liquids.

Numerical computations with viscoelastic fluids suffer from the curse of high Weissenberg number limit. Numerical algorithms for

the solution of flow problems break down for reasons which are not yet well understood at values of the Weissenberg number larger than one depending on the type of flow. The source of the instability does not necessarily stem from the algorithm and/or may not be grid dependent, although that is a clear possibility, but it is rather related quite often to the constitutive structure. Hadamard-type instabilities as well as dissipative instabilities are the major deficiencies most constitutive equation formulations at the macro as well as micro level suffer. Over the years considerable progress has been made and the Weissenberg limit has been moved higher, but the problem is far from being completely solved and is still a burning issue in rheological fluid mechanics. Similar problems exist in numerical computation of dry granular flows and dispersed particle flows. The next two papers investigate computational issues with polymeric fluids and granular flows.

Feigl and Senaratne develop a micro-macro simulation algorithm capable of resolving multiple levels of description to calculate the flow of polymeric fluids. The calculation of the velocity and pressure fields is performed using standard finite element techniques, while the polymer stress is calculated from a microscopic-based rheological model using stochastic simulations.

The capability of the Lagrangian Molecular Dynamics simulation to track individual particles in dispersed particle and dry granular flows is limited by the computational expense. Continuum models remove this difficulty, but constitutive relations for fluid drag and solid drag are needed in the momentum equations of each particle phase to close the field equations. Gao et al. focus on particle-particle momentum transfer in a dry bidisperse granular mixture and perform molecular dynamics simulations of the mixture to characterize the solid drag.

The thread which connects the following five papers is the study of the effect of surfactants used as additives on the flow structure in various settings. Although surfactant solutions exhibit viscoelasticity, their behavior shows anomalous features and quite often deviates from the pattern of a closely associated class of fluids to that of dilute polymeric solutions. A class of motions which has attracted attention recently is the swirling flow of viscoelastic fluids driven from the bottom in cylindrical containers with either free surface or confined, in particular because of the vortex breakdown characteristics shaped by the elasticity of the solution and/or the use of the free surface shape to determine the constitutive constants of the fluid and characterize the fluid. Because surfactants do not degrade in shear as polymeric solutions do due to the stretching of long chains, it has long been advocated that they can be used in large-scale heating/cooling systems to save pumping energy through the considerable drag reduction they induce. Various aspects of these issues are explored in the next five papers.

In two complimentary papers on the swirling flow of viscoelastic fluids with free surface in cylindrical containers driven from the bottom, Wei et al. present a detailed experimental investigation of the structure of the flow and a numerical study. The motivation for these studies lies with the significant drag reducing ability in turbulent flow of very dilute surfactant solutions of the order of 70–80% with mass concentrations of only 30 and 75 ppm. In Part I the high Reynolds number swirling flow of water and a surfactant solution is experimentally investigated using a double-pulsed particle image velocimetry system. In Part II flow simulations in laminar regime are presented for both Newtonian and viscoelastic solutions. The numerical simulations are run for laminar flow as viscoelastic large-eddy simulation (LES) turbulence models have not yet been developed for viscoelastic solutions. The tested Marker-and-Cell (MAC) method for Newtonian flow is extended to viscoelastic flow to track the free surface.

In a related paper Itoh et al. investigate the steady confined swirling flow of viscoelastic fluids in cylindrical containers using laser Doppler velocimetry. Prominent among the findings in the paper is the decrease in the azimuthal velocity with increasing Weissenberg number at any aspect ratio tested. Experimental data is compared to the numerical predictions based on the Giesekus and power-law models, both of which can fairly well describe the retardation in the azimuthal velocity in the range of small Weissenberg numbers.

Watanabe et al. use the laser-induced fluorescence (LIF) technique for visualization of the formation of Taylor vortices in the gap between two coaxial cylinders. The nonlinear test fluids are drag-reducing polymeric solutions in various concentrations and surfactant solutions. Experimental observations show that Taylor cells form in polymer solutions but not in surfactant solutions with viscoelastic properties, a puzzle which needs further investigation.

Munekata et al. experimentally investigate by two-dimensional laser Doppler anemometry the effect of drag-reducing surfactants in swirling pipe flow. The considerable drag-reducing ability of surfactants when used as additives to a Newtonian fluid is well known in straight, non-swirling pipe flow, but in most industrial applications pipes are not straight. Swirl decay, vortex type, and turbulence intensity are discussed and compared with the swirling flow of water.

The last two papers in this collection cover industrially important flows in the blow molding film manufacturing process, the rimming flow on the inside of a horizontal cylinder which presents a rich variety of fluid mechanics phenomena and flow between coaxial cylinders driven by an axial pressure gradient as well as the rotation of the inner cylinder.

Fomin and Hashida present an asymptotic analysis of the coating of shear-thinning non-Newtonian fluids on the inner surface of a hollow rotating horizontal cylinder, and derive the runoff condition. The solution for the film thickness is continuous if the runoff condition is satisfied with subcritical, critical, and supercritical flow regimes.

Woo et al. present an experimental study of the fully developed laminar and transitional vortex flow, and in particular of the skin friction coefficient of Newtonian and shear-thinning fluids in a concentric annulus driven by the rotating inner cylinder and the axial pressure gradient. The study is motivated by the importance in engineering applications of flows in annular passages with a rotating inner wall such as bearings, rotating-tube exchangers and, especially, mud flow in the case of slim hole drilling of oil wells.

In closing I would like to express my deepest appreciation to the Editor of JFE, Professor Joe Katz, for his leadership and for the opportunity to include this special section among the pages of this Journal. I would like to again thank the numerous anonymous reviewers and the authors who made this special section possible.

Dennis Siginer
Associate Editor
e-mail: dennis.siginer@wichita.edu

Unraveling the Behavior of Liquids at the Nanoscale

H. H. Bau
Department of Mechanical Engineering and Applied Mechanics, University of Pennsylvania, Philadelphia, PA
e-mail: bau@seas.upenn.edu

Y. Gogotsi
Department of Material Science and Engineering, Drexel University, Philadelphia, PA

C. M. Megaridis
Department of Mechanical and Industrial Engineering, University of Illinois at Chicago

J.-C. Bradley
Department of Chemistry, Drexel University, Philadelphia, PA

The behavior of liquids under extreme confinement is of interest from both the scientific and the technological points of view. Advances in nanotechnology have facilitated the fabrication of devices in which conduits and pores have hydraulic diameters as small as a few nanometers. Conduits and pores with nanoscale dimensions are also ubiquitous in nature. Since the dimensions of these flow conduits are much smaller than those commonly encountered in many engineering applications and the conduits are characterized by very large surface area to volume ratios (on the order of 10^8 m^2/m^3), one wonders whether highly confined liquids behave differently than their macroscopic counterparts. Some of the relevant questions are: (1) At what length scale does the continuum approximation break down? (2) Is the nonslip boundary condition applicable at very small scales? How do fluid/solid molecular interactions affect slip? (3) Are surface phenomena that are typically ignored in larger conduits important in their small-size counterparts? (4) How are fluid phase change equilibrium and dynamics affected by the presence of surfaces and interfaces at ultrafine length scales? To answer some of these questions, our research group is conducting fluid flow experiments in conduits consisting of carbon nanotubes. Carbon nanotubes are a convenient material with which to work for several reasons. First, carbon nanotubes can be fabricated with diameters ranging from a fraction of a nanometer to several hundred nanometers, allowing one to conduct experiments with various tube sizes. Second, the tube's surface properties can be modified with heat and/or chemical treatments to facilitate behaviors ranging from hydrophilic to hydrophobic, allowing one to probe the effect of surface properties on the liquids' behaviors. Indeed, there is growing experimental evidence that liquids flowing on hydrophobic surfaces exhibit slip. See Ref. [1] for a recent review. Third, the tubes' walls are sufficiently thin to be transparent to light [2] and electrons [3–6]. Moreover, the tubes can contain high-pressure fluids for an extended time even in the vacuum environment of the electron microscope [3,4].

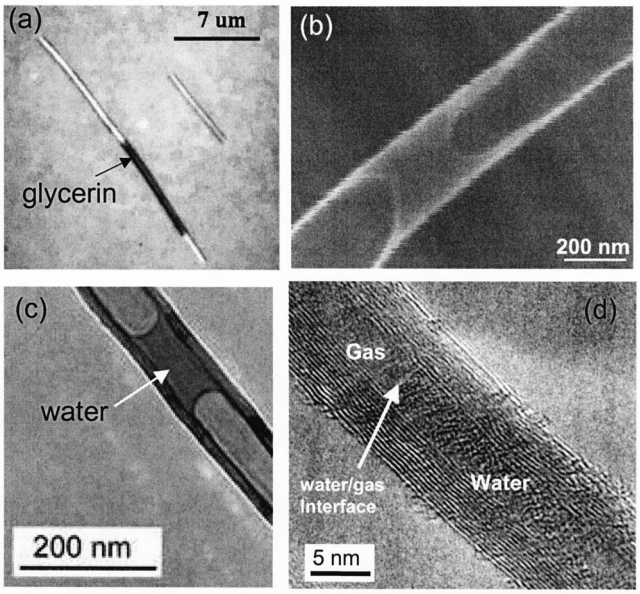

Fig. 1 Micrographs showing glycerin (*a*) and water (*b*)–(*d*) inside carbon nanotubes. The tubes shown in (*a*) and (*b*) were fabricated with chemical vapor deposition in alumina templates. The tubes in (*c*) and (*d*) were hydrothermally produced. (*a*) Optical micrograph of glycerin inside an open CVD-grown nanotube. (*b*) Environmental SEM image of water inside a nanotube similar to the one shown in (*a*). (*c*) TEM image of water inside a hydrothermally-produced, sealed carbon nanotube. (*d*) TEM micrographs of a fluid inside a multi-wall, hydorthermally-produced, sealed carbon nanotube.

One of the obstacles encountered when studying nanoscale phenomena is the limited resolution of visible light. Fortunately, given the relatively small wavelengths of electrons, scanning and/or transmission electron microscopy allows one to visualize phenomena at sub-nanometer length scales. Hence, electron microscopy holds great promise for the study of liquid behavior at the nanoscale. Unfortunately, however, conventional electron microscopy requires vacuum conditions, and, in the past this has precluded its use for the study of volatile fluids. With present day technology, at best, one can operate with environmental chambers that allow the introduction of humid gases. This shortcoming of electron microscopes can be alleviated by fully encapsulating the fluids in sufficiently small containers that facilitate electron transmission through them. Indeed, our group has demonstrated the feasibility of observing and thermally actuating liquids confined in nanotubes with both transmission and scanning electron microscopy [3–7] (see Fig. 1). To make additional progress and enable controlled experiments with well-characterized fluids in an electron microscope, it is necessary to construct nanotube-based devices that allow for the deliberate introduction and removal of well-characterized liquids in the vacuum environment of the electron microscope's chamber. The construction of and preliminary experiments with such a device, made utilizing hybrid fabrication technology, are described in this issue [8]. This hybrid technology utilizes dielectrophoresis, a phenomenon that involves interesting fluid mechanics all by itself, for the controlled positioning of nanotubes at predetermined locations, and photolithography and microfabrication for the construction of functional devices.

Although the use of electron microscopy to study the behavior of liquids at the nanoscale appears to be promising, there are also potential hurdles. Through ionization, radiolysis, and heating, the electron beam may alter the liquid and the tube's surface properties [5,6]. Additionally, the electron microscope data may require sophisticated interpretation. To partially address some of these issues, we are comparing optical and electron microscope images

of liquid flow in tubes of diameters in the range that allows both optical and electron imaging (Figs. 1(*a*) and 1(*b*).

References

[1] Bau, H. H., Sinha, S., Kim, B., and Riegelman, M., 2004, "The Fabrication of Nanofluidic Devices and the Study of Fluid Transport Through Them, Transport Phenomena in Micro and Nanodevices," to appear in *Nanofabrication: Technologies, Devices, and Applications*, Conference Proceedings 5592, SPIE, Optics East, Philadelphia, Oct. 25–28.

[2] Kim, B. M., Sinha, S., and Bau, H. H., 2004, "Optical Microscope Study of Liquid Transport in Carbon Nanotubes," Nano Lett., **4**(11), pp. 2203–2208.

[3] Gogotsi, Y., Libera, J. A., Güvenç-Yazicioglu, A., and Megaridis, C. M., 2001, "In-situ Multi-Phase Fluid Experiments in Hydrothermal Carbon Nanotubes," Appl. Phys. Lett., **79**, pp. 1021–1023.

[4] Megaridis, C. M., Güvenç-Yazicioglu, A., Libera, J. A., and Gogotsi, Y., 2002, "Attoliter Fluid Experiments in Individual Closed-end Carbon Nanotubes: Liquid Film and Fluid Interface Dynamics," Phys. Fluids, **14**, pp. L5–L8.

[5] Rossi, M. P., Ye, H., Gogotsi, Y., Babu, S., Ndungu, P., and Bradley, J. C., 2004, "Environmental Scanning Electron Microscope Study of Water in Carbon Nanopipes," Nano Lett., **4**(5), pp. 989–993.

[6] Naguib, N., Ye, H., Gogotsi, Y., Yazicioglu, A. G., Megaridis, C. M., and Yoshimura, M., 2004, "Observation of Water Confined in Nanometer Channels of Closed Carbon Nanotubes," Nano Lett., **4**(11), pp. 2237–2243.

[7] Yarin, A. L., Yazicioglu, A. G., and Megaridis, C. M., 2005, "Thermal Stimulation of Aqueous Volumes Contained in Carbon Nanotubes: Experiment and Modeling," Appl. Phys. Lett., **86**, p. 013109.

[8] Riegelman, M., Liu, H., and Bau, H. H., 2006, "Controlled Nanoassembly and Construction of Nanofluidic Devices," ASME J. Fluids Eng., **128**, pp. 6–13.

Modeling and Computational Simulation of Viscoelastic Flows

Kathleen Feigl
Michigan Technological University, Houghton, MI
e-mail: feigl@mtu.edu

An important goal in viscoelastic fluid mechanics is to understand the relationship between a flow process, the flow-induced microstructure of the fluid, and the rheology of the fluid. Achieving this goal requires theoretical modeling, computational simulations, and experiments. On the modeling side, the development of accurate stress-strain models for rheologically complex fluids remains a challenge. Advances in this area require the development and investigation of models which incorporate structural information on the fluid. For polymer solutions and melts, this translates into molecular-based modeling involving, for example, reptation theory and/or network theory. It is vital to continue these efforts. It is equally important to investigate other suitable modeling approaches for these fluids and for emulsions and polymer blends. In particular, more attention should be given to the GENERIC thermodynamical approach which allows the derivation of a complete set of evolution equations for a defined set of state variables, including structural variables. A second challenge is the development and implementation of accurate, efficient, stable, and robust numerical algorithms for solving flow problems involving these models in engineering applications. Micro-macro simulations of polymeric flow involve the coupling of the conservation equations from continuum mechanics with a molecular-based rheological model. While perhaps out of its infancy, this multiscale simulation approach needs much more development and theoretical analysis. Efficient numerical algorithms are also needed for solving the very large, coupled, nonlinear systems of equations which the GENERIC modeling approach typically produces in inhomogeneous flows. Furthermore, it is important to increase the use of these simulations as a model validation tool, including the comparison of simulation results, e.g., velocity and stress fields, with experimental data.

Research in Rimming Flows

Sergei Fomin
California State University, Chico
e-mail: sfomin@csuchico.edu

The problem of rotational flow on the inner wall (rimming flow) and on the outer wall (coating flow) of a hollow horizontal cylinder is of interest due to its wide range of applications in industry. Both coating and rimming flows are shaped by the same forces, exhibit similar hydrodynamic effects, and are described by the same governing equations. In both configurations flow exhibits a surprisingly rich variety of phenomena, including various instabilities and pattern formations. Due to the complexity of the problem previous investigations were focused only on the analysis of the isothermal flows of Newtonian fluids with constant physical properties. However, real polymeric solutes used in rotational molding and coating technology are chemically very complex strongly nonlinear substances and, therefore, are non-Newtonian (shear-thinning and shear-thickening, viscoplastic and viscoelastic) and heterogeneous (multi-component) reactive fluids. Thermophysical properties of these fluids are strongly temperature-dependent. To the best of our knowledge, the impact of important factors such as chemical reactions and temperature variation on the flow regime has not been discussed in the literature related to rimming flows.

Elimination of instabilities and determination of a criterion for flow stability of reacting nonlinear polymeric solute to obtain a continuous and smooth coating film on the wall of the cylinder are of major concern for the engineer-practitioner. Therefore, there is a need in the near future for attention to be focused on the following issues: (i) assessment of the effect of the nonlinear properties of the liquid polymer on the flow regime and flow instabilities; (ii) derivation of the stability criteria for non-Newtonian fluids; (iii) analysis of the effect of chemical reactions, temperature, and concentration variations in the solute on the stability of the rimming flow.

A Puzzling Pattern in Taylor-Couette Flow

Keizo Watanabe
Tokyo Metropolitan University and Tokyo University of Agriculture and Technology, Tokyo, Japan
e-mail: keizo@ecomp.metro-u.ac.jp; mot1z019@cc.tuat.ac.jp

The flow pattern for a Newtonian fluid between two coaxial cylinders changes to Taylor-Couette flow from rotational Couette flow with increasing rotational speed of the inner cylinder. This flow field is ideal for research into the transition process from laminar to turbulent flow because it is slower than other flow systems and the instabilities are well understood. Thus, much theoretical and experimental research on the transition process using this flow field has been carried out for Newtonian fluids since Taylor's work. However, there are comparatively few studies on the flow of non-Newtonian fluids.

Flow visualization results for polymer solutions show that Görtler vortices of half the number of Taylor cells occur in the gap between coaxial cylinders when Taylor vortex flow in the primary mode is formed [1]. However, for 50 and 100 ppm surfactant solutions Taylor vortices are not apparent and Görtler vortices collapse. Thus, the following questions naturally arise: Why is it that surfactant solutions do not form Taylor cells in the stale Taylor-Couette flow, whereas dilute polymer solutions do so, even though both are viscoelastic? What is the crucial difference between polymeric and surfactant solutions in constitutive formulation and physical properties to result in this behavior? What are the consequences concerning the Weissenberg assumption for the shear flow of surfactant solutions?

References

[1] Watanabe, K., Takayama, T., and Ogata, S., 2004, "Instability of Surfactant Solution Flow in a Taylor Cell," J. Visualization, **7**(4), pp. 273–280.

Research in Optical Finishing Technology

William Kordonsky
e-mail: kordonski@qedmrf.com

Aric B. Shorey
e-mail: shorey@qedmrf.com

QED Technologies, Rochester, NY

Conformal (or freeform) and steep concave optics are important classes of optics that are difficult to finish using conventional techniques due to mechanical interferences and steep local slopes. It has been demonstrated that impingement of a magnetically stabilized, collimated jet of MR fluid provides an ideal tool for finishing such challenging shapes. Existing theoretical work is focused on the modeling of the flow in the impingement zone. In numerous experiments with different process parameters (jet velocities, nozzle diameters, and fluid viscosity) it was shown that material removal in the polishing spot closely correlates with the computed rate of work done at the surface by the fluid. Future optimization of the technology requires theoretical considerations to model the mechanism of jet stabilization.

Controlled Nanoassembly and Construction of Nanofluidic Devices

M. Riegelman

H. Liu

H. H. Bau[1]
e-mail: bau@seas.upenn.edu
Department of Mechanical Engineering and Applied Mechanics,
University of Pennsylvania,
Philadelphia, PA 19104

This paper describes the combined use of controlled nanoassembly and microfabrication (photolithography) to construct multi-walled, carbon, nanotube-based fluidic devices. The nanoassembly technique utilizes dielectrophoresis to position individual nanotubes across the gap between two electrodes patterned on a wafer. The dielectrophoretic migration process was studied theoretically and experimentally. Once a tube had been trapped between a pair of electrodes, photoresist was spun over the wafer and developed to form microfluidic interfaces. Liquid condensation in and evaporation from the nanotubes were observed with optical microscopy. The nanotube-based fluidic devices can be used for studies of fluid transport under extreme confinement and as sensitive sensors. [DOI: 10.1115/1.2136932]

1 Introduction

Recent advances in the synthesis of nanotubes offer opportunities for fundamental studies of transport and interactions in highly confined systems and for the development of novel, sensitive devices and measurement techniques [1–3]. Due to their small size, nanotubes are difficult to manipulate. Dielectrophoresis provides a convenient and attractive means for positioning the nanotubes at predetermined locations.

The term dielectrophoresis was coined by Pohl [4], and it describes the migration of suspended particles in a nonuniform electric field. The particles need not be charged. Briefly [5], the nonuniform electric field polarizes the particles and induces a dipole moment. Since the dipole's poles are subjected to different electric field intensities, a net force results that stretches the particle and causes it to migrate in the electric field. In addition to translational forces, the particle is subjected to torque that typically tends to align it with the electric field. Dielectrophoresis allows one to apply noncontact forces to suspended particles. The phenomenon should not be confused with electrophoresis, which pertains to the motion of charged particles in an (not necessarily nonuniform) electric field. While dielectrophoresis occurs in both ac and dc electric fields, ac fields are often preferred to minimize the adverse effects of the electrodes' electrochemistry, to suppress migration due to the particle's charge, and to affect the particle's dielectric properties (through their dependence on electric field frequency). Depending on the dielectric properties of the particle and the suspending medium, the dielectric force may be directed either towards the location of maximum electric field intensity (positive dielectrophoresis) or away from the maximum field intensity (negative dielectrophoresis).

The dielectrophoretic forces are quite small, and traditionally they have been used to manipulate particles with characteristic lengths on the order of a few micrometers such as cells. Microfabrication technology allows one, however, to fabricate electrodes with very small gaps between them. The very high electric fields produced—on the order of 10^7 V/m—allow one to manipulate nanotubes and large macromolecules such as DNA, actin filaments, and microtubules.

Various groups have demonstrated the use of dielectrophoresis to position single-wall nanotubes, nanowires, DNA, and microtubules across the gap between adjacent electrodes. Yamamoto et al. [6] demonstrated that when ac field was applied to an isopropyl alcohol suspension of multi-walled nanotubes placed on top of electrodes patterned on a glass substrate, the multi-walled tubes accumulated on the electrodes' surfaces. More recently, Chung et al. [7] applied a similar technique and described the need for the combined use of dc and ac electric fields to successfully trap multi-walled nanotubes across the gap between two electrodes. In the presence of an ac field alone, successful trapping was not achieved [7]. In contrast, in our work, we employed solely ac fields to trap single nanotubes across the gap between electrodes with good reproducible results.

The nanotubes' migration was visualized directly with optical microscopy and modeled theoretically. When the solution was dilute and the electric field was applied for a relatively short amount of time, single tubes were assembled across the gap between adjacent electrodes. When the solution was less dilute or the electric field was applied for an extended period of time, we observed the formation of chains of nanotubes. Once a tube had been positioned in a desired location, we were able to use photolithographic techniques to construct fluidic interconnects and fabricate a nanotube-based fluidic device.

The nanotubes used in our study were synthesized by chemical vapor deposition of carbon in pores etched in alumina membranes [8]. These carbon nanotubes had sufficiently thin walls to allow direct observations with optical microscopy of liquid motion through the tubes. The tubes filled readily when brought into contact with a liquid drop. We also observed condensation and evaporation inside the tube. Consistent with Rossi et al. [9], who studied with an environmental scanning microscope condensation and evaporation in the same type of tubes, we found that the alumina-grown tubes were hydrophilic.

The paper is organized as follows. In Sec. 2, we describe the unique fabrication process that combines dielectrophoretic positioning of individual nanotubes and photolithography. Section 3 provides experimental observations of the nanotube dielectrophoretic migration process and the fascinating phenomenon of chain formation. In Sec. 4, we carry out a few theoretical calculations of particle migration and compare the theoretical predictions with experimental observations. Section 5 concludes.

2 Nanoassembly and Construction of a Nanotube-Based Device

Gold electrodes with a NiCr adhesion layer were patterned on SiO_2-coated silicon wafers and on glass microscope slides. The

[1]All correspondence should be directed to this author.

Contributed by the Fluids Engineering Division of ASME for publication in the JOURNAL OF FLUIDS ENGINEERING. Manuscript received July 9, 2004; final manuscript received April 11, 2005. Review conducted by Dennis Siginer.

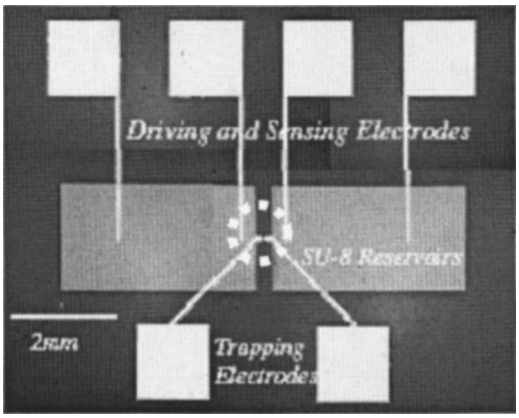

Fig. 1 Top view of a nanotube-based fluidic device. The trapping electrodes are enclosed with a dashed circle. The gap between the trapping electrodes is 8 μm. The image was taken with an optical microscope. The photographs also show electrodes for the induction of electrophoretic flow and for the measurement of ionic currents.

glass slides had the advantage of allowing us to carry out observations from both sides of the device. Various electrode configurations were fabricated and tested with respect to their dielectrophoretic trapping effectiveness. Figure 1 depicts an image of one electrode layout. Six gold electrodes were patterned using standard photolithographic techniques and the liftoff process. The circled pair of electrodes in Fig. 1 was used for nanotube trapping. The gap between the trapping electrodes was 8 μm. The other electrodes were deposited for driving and sensing the flow through the tube. The sensing and driving electrodes are not discussed in this paper. Figure 2 depicts schematically yet another electrode configuration with the relevant dimensions that were used in many of our experiments. For additional information on the various electrode configurations that we tested and their relative advantages and disadvantages, see [2].

The carbon nanotubes that we used in our experiments were synthesized by chemical vapor deposition of carbon in a commercially available alumina membrane template with pore diameters of ~250 nm. Subsequent to the deposition process, the nanotubes were released by dissolving the alumina in a 1 M NaOH solution [8]. These particular tubes were selected because they are typically open ended, straight, relatively smooth, and possess uniform bore geometry (outer diameter of approximately 250 nm, wall thickness of 15 nm, and lengths of up to 50 μm). Because of their thin wall thickness, the tubes are transparent in a scanning electron microscope (SEM) as well as to visible wavelengths. SEM and transmission electron microscope (TEM) images of these tubes are available in [9]. The fabrication technique that we describe below can be applied to any type of nanotubes.

The tubes were suspended in an isopropanol solution to a concentration of approximately 0.1 mg/mL and sonicated to break aggregates and separate the tubes. Unfortunately, the tubes were quite fragile and tended to disintegrate during prolonged sonication. Repeated experiments suggested that five repetitions of 5 s sonication followed with 1 min of manual shaking yielded useful tubes with an average length of about 10 μm.

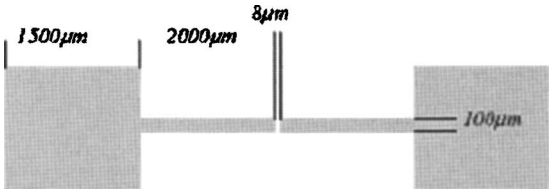

Fig. 2 A schematic depiction of another layout of trapping electrodes. The dimensions of the electrodes are shown in the figure.

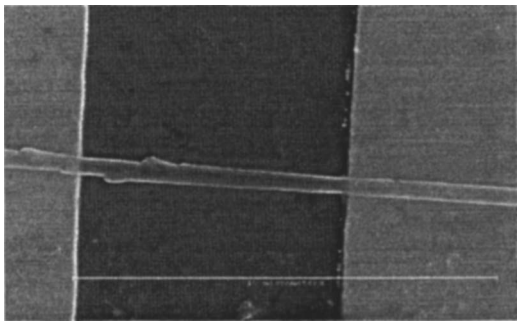

Fig. 3 A SEM image of a trapped nanotube. The gap between the electrodes is 8 μm.

A drop of approximately 20 μL isopropanol solution laden with nanotubes was placed with a pipette on top of the trapping electrodes. A function generator (Tektronix CF6250) was connected to the electrodes' pads with micromanipulators (Micromanipulator Inc., model 110). A potential difference of 12 V peak to peak at 2 MHz frequency was applied across the electrodes. Concurrently, the electrical signal was viewed with an oscilloscope. The experiments were carried out on a microscope stage (Olympus BX-51), and the tube migration was viewed with 400× magnification. The nanotube migration was photographed with a CCD camera (Nikon coolpix 995) mounted on the microscope. The experiment was terminated upon nanotube capture. Typically, the nanotube solution was exposed to the electric field for about 30 s. No significant change in the voltage signal was detected upon trapping nor did the electrodes shorten. This is perhaps due to the relatively high contact resistance between the trapped nanotube and the electrodes. Once a nanotube had been captured, the power supply was turned off and the isopropanol drop was left to dry. The drop evaporated within about 2 min.

Figure 3 is a SEM image of a nanotube trapped between two electrodes. Witness that a single nanotube is resting across the gap between the electrodes. The nanotube is nearly perpendicular to the electrodes' edges, and both ends of the tube are resting on the opposite electrodes with a significant overlap between the tube and the electrodes.

Subsequently, the chip was cleaned. The chip with the captured nanotube was washed with buffered HF solution for 20 s to remove the thin oxide layer. This was followed by a 1 min rinse in deionized (DI) water. The chip was then sprayed with acetone followed by IPA to further clean the surface, and then washed again with DI water for 1 min. The wafers were then spun dry and baked on a hot plate for 5 min at 200°C to remove any residual moisture. The adhesion forces between the nanotubes and the gold electrodes were sufficiently strong to leave most of the nanotubes intact during the washing process. The presence of the nanotube was confirmed with visual observation through a microscope.

Once the chip was cooled to room temperature, it was mounted on a spinner and a drop of SU-8 (Microchem 2050) negative photoresist was placed on the chip. The chip with the drop was spun at 500 rpm for 5 s and at 3000 rpm for 30 s. The wafer was soft baked for 4 min at 65°C. Subsequently, the temperature was ramped to 100°C, and the wafer was held at 100°C for 9 min. The wafer was then cooled to room temperature.

The lithographic mask was aligned with the SU-8 coated wafer and exposed to a 375 W, 365 nm UV light source. The wafer was postexposure baked using a protocol similar to the one used for the soft bake. The wafer was then allowed to cool to room temperature. Next, the pattern was developed by immersing the wafer

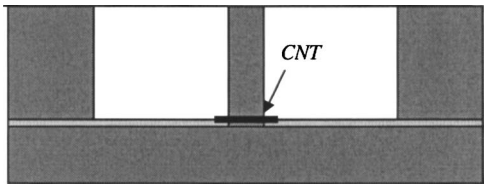

Fig. 4 A schematic depiction of a cross section of the nanofluidic device

in SU-8 developer (Microchem) for 6 min under manual agitation. The patterned SU-8 was then sprayed with IPA and spun dry.

Figure 4 depicts schematically the cross-section of the device obtained at the conclusion of the process. The device consists of two wells separated with a thin layer of SU-8 and interconnected with a nanotube. Figure 5 is a SEM image of the same nanofluidic device (top view). The insert (top left) is a magnified view of the region next to the SU-8 barrier that separates the two wells. Observe the end of the nanotube that emerges from under the barrier.

An important question is whether the nanotube can be filled with liquid. To answer this question, we submerged nanotubes in drops of various liquids such as water and ethylene glycol. The liquid drops were then evaporated with a stream of dry air. The nanotube was observed with an inverted microscope (Olympus IX71). The presence of liquid inside the nanotube was evidenced by the dark appearance of the nanotube. The liquid vapor interface was clearly visible. We also were able to observe the evaporation of the liquid from the tube's interior. Figure 6 provides a sequence of images depicting the receding meniscus (liquid-air interface) in a nanotube filled with ethylene glycol. In some cases, the meniscus receded on both sides of the liquid slug. In other cases such as the one in Fig. 6, the meniscus receded only on one side of the liquid slug. We speculate that the tube was slightly tapered. As liquid evaporated at the lower end of the tube, capillary forces drew the slug towards that end and assured that as long as liquid was present in the tube, the lower end of the tube was filled with liquid. The observations depicted in Fig. 6 were repeated numerous times with excellent reproducibility. For quantitative measurements of the tube filling by capillary forces and by condensation and the evaporation of a liquid slug confined in the tube, see [10]. Our experimental observations are consistent with the observations of Rossi et al. [9] in an environmental scanning electron microscope. It is speculated that the tubes are hydrophilic because the synthesis of the tubes in the hydrocarbon environment causes the graphene sheets to be hydrogen terminated.

The devices depicted in Figs. 4 and 5 allow us to carry out controlled experiments involving flow through nanotubes driven by various forces such as capillary action, pressure, and electroosmosis. These experiments, however, will not be described in this paper. If desired, the device also can be capped to form closed wells.

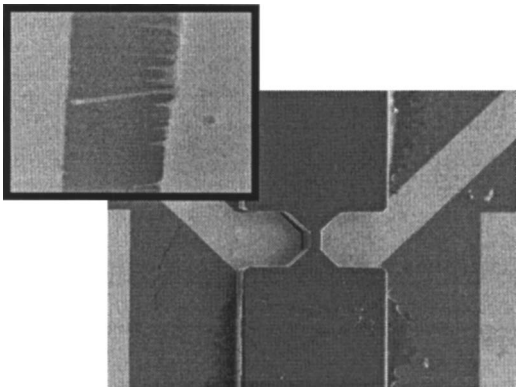

Fig. 5 A SEM image of the nanofluidic device (top view). The insert (top left) is a magnified view of the region next to the barrier between the two wells, showing the end of the nanotube under the barrier.

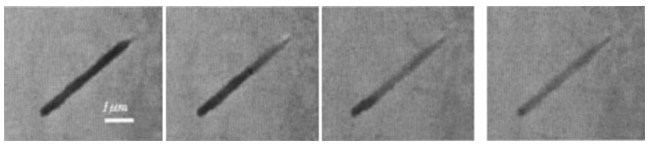

Fig. 6 Various stages of evaporation of ethylene glycol from the interior of a nanotube. The tube on the left is nearly full; the nanotube on the right is nearly empty.

3 Experimental Observations of the Nanoassembly Process

The migration of the nanotubes during the trapping experiments was captured with a video camera. Our experimental setup allowed us to obtain only the top view of the particle's trajectory. Figures 7(*a*)–7(*c*) depict, respectively, the positions of the nanotube at times 0, 0.2, and 0.28 s during the trapping process. For better visibility, the tracked nanotube was encircled with an ellipse.

Observations indicate that when the particle was far from the trap, it moved at nearly level height with nearly uniform speed towards the gap, while rotating to align itself with the electric field. Once arriving in close vicinity of the gap, the particle's trajectory underwent an abrupt turn, and the particle accelerated towards the gap.

Figure 8 depicts the horizontal velocity and horizontal projection of the nanotube's inclination angle as functions of its horizontal distance from the gap's center during the migration process. The horizontal distance is defined as the projection of the distance between the center of the tube and the center of the gap on a line parallel to the electrodes' long edge. The inclination angle is defined in Fig. 7(*c*). When the nanotube was about 100 μm horizontal distance from the gap's center, its velocity was about 200 μm/s. This velocity stayed nearly constant until the nanotube arrived at the gap's location. When the nanotube was about 10 μm away from the gap's center, its velocity started to increase rapidly. Because of the low frame speed of our camera, we were not able to obtain data for distances shorter than 10 μm. The data point at $x=10$ μm is an underestimate of the actual velocity since the actual moment of the tube's landing occurred between successive frames. Witness that as the nanotube migrated towards the gap, the dielectrophoretic torque aligned the tube with the electric field lines. In a later section, we will compare the observations of Fig. 8 with theoretical predictions.

In most cases, we were careful to carry out the experiment for a relatively short amount of time to avoid the trapping of multiple nanotubes. In some experiments, however, we left the electric field active for prolonged times to observe the interesting phenomenon of chain formation. In the presence of an electric field, the nanotubes get polarized and tend to attract each other and form aggregates. Additionally, tubes that were attracted to and trapped at the edges of the electrodes served as nanoelectrodes and attracted additional nanotubes. Although the chain formation and nanotube aggregation were undesired in our particular application, we found the phenomenon to be sufficiently fascinating to warrant brief description.

Figures 9 and 10 show, respectively, SEM images of early and advanced stages of the chain formation process. In Fig. 9, a few nanotubes were trapped at the high electric field intensity at the edge of the electrode. These tubes got polarized and served as nanoelectrodes that attracted additional nanotubes. When this process was allowed to continue over an extended time-period, fractal patterns resembling trees formed (Fig. 10). Since the dielectrophoretic force is proportional to the particle's volume, larger par-

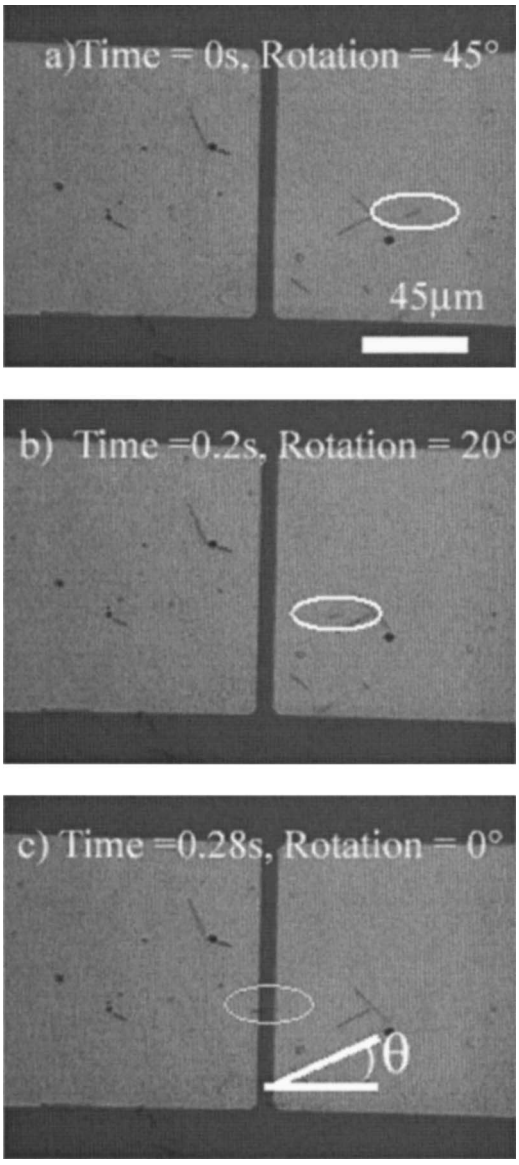

Fig. 7 Images of the nanotube during various stages of the trapping process: 0 s (*a*), 0.2 s (*b*), and 0.28 s (*c*). The nanotube is encircled with an ellipse for better visibility.

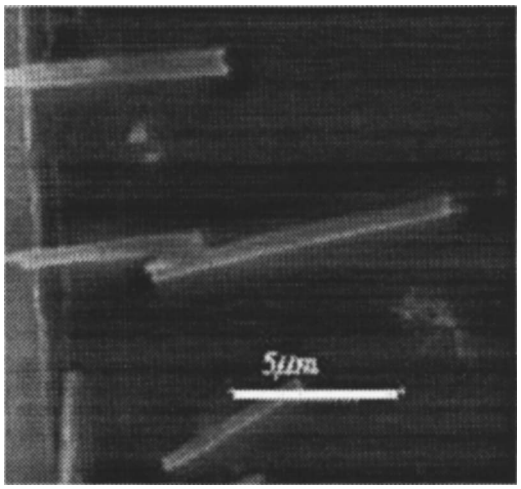

Fig. 9 Early stages of the nanotube chain formation process

ticles or nanotube aggregates arrived first at the electrode's edge to form "tree" trunks. As the trees developed, the size of the branches typically decreased. In some cases (Fig. 10, left), nanotubes were aligned back to back to form long, continuous composite tubes.

4 Dielectrophoretic Trapping—Theoretical Considerations

In this section, we provide an approximate model to describe the nanotubes' migration towards the electrodes in the presence of the electric field. The model is depicted schematically in Fig. 11. The domain consists of a semi-infinite medium of perfectly dielectric, isotropic liquid of relative dielectric permittivity ϵ_m. The liquid is bounded from below by a flat substrate. Two electrodes having a gap of length G between them are patterned on the substrate. The right and left electrodes are maintained, respectively, at uniform, constant potentials ΔV and $-\Delta V$. The electrodes induce an electric field $\mathbf{E}$ in the liquid. We adopt the convention that bold letters represent vectors. The Cartesian coordinates x and y are aligned, respectively, parallel and normal to the substrate. The origin of the coordinate system is located at the gap's center.

We will assume a two-dimensional electric field. We justify this approximation by the fact that the electrodes are wide (into the plane of the figure) compared to the gap's length and the particle's size and that we will be focusing mostly on particle migration at relatively small heights and close to the electrodes' mid-width. The use of a semi-infinite medium is justified on the ground that

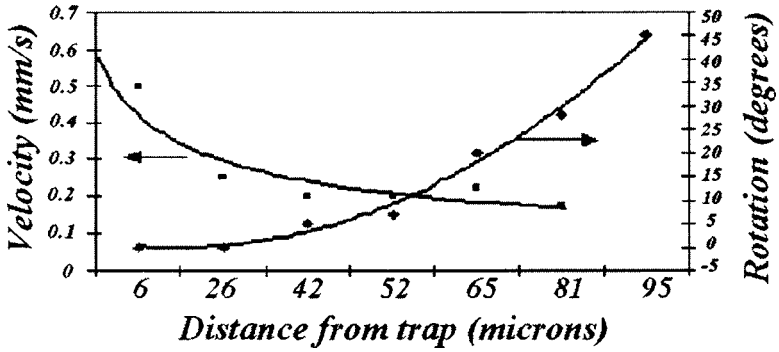

Fig. 8 The nanotube's velocity and inclination angle as functions of the horizontal distance from the tube's center to the gap's center. The inclination angle is defined in Fig. 7(*c*).

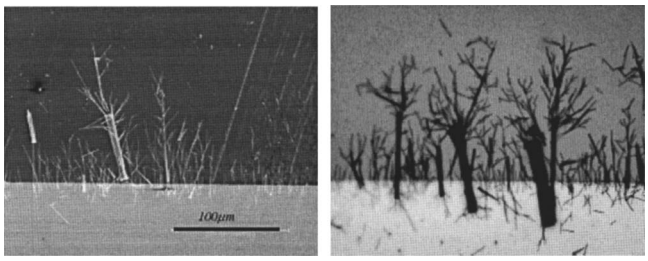

Fig. 10 A nanotube forest

the radius of the liquid drop positioned over the electrodes is two to three orders of magnitude larger than the gap's length.

To obtain an approximate expression for the electric field, it is convenient to use elliptic coordinates. The transformation between the Cartesian and elliptic coordinates is [11]

$$\zeta + i\theta = \cosh^{-1}\left(\frac{2}{G}(x+iy)\right), \tag{1}$$

where the ζ curves are confocal ellipses and the θ curves are hyperbolas, all with foci at $x=\pm G/2$. In the elliptic coordinate system, the potential is represented with the relatively simple expression:

$$\phi = \Delta V\left(1-\frac{2}{\pi}\theta\right), \tag{2}$$

where $\theta=\cos^{-1}\{[\sqrt{(x+G/2)^2+y^2}-\sqrt{(x-G/2)^2+y^2}]/G\}$. Constant potential contour lines are depicted in Fig. 12. The gap's dimensions in Fig. 12 are consistent with our experimental setup. Witness that the electrodes' surfaces form constant potential lines and that the potential contours are perpendicular to the insulated gap between the electrodes. The electric field is $\mathbf{E}_0=-\nabla\phi$. The subscript zero indicates that this is the electric field in the absence of the particle. The electric field can be readily calculated from expression (2). Since the corresponding formulas for the electric field components are somewhat lengthy, we do not reproduce them here.

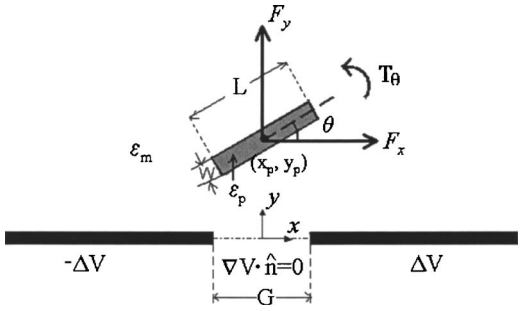

Fig. 11 A schematic description of the model used to calculate the dielectrophoretic and viscous forces acting on the particle and to predict the particle's trajectory

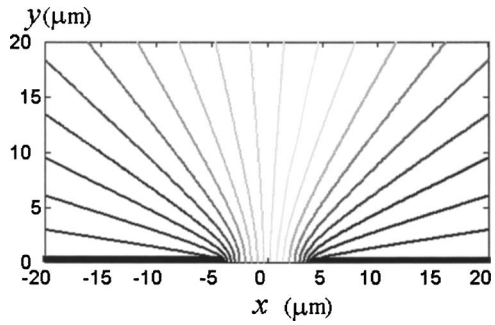

Fig. 12 The electric potential (contour lines) in the gap's vicinity

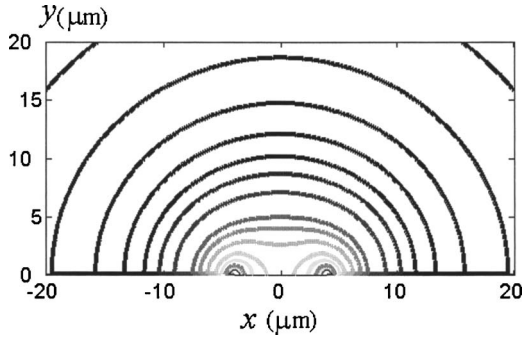

Fig. 13 Contours of electric field intensity $|\mathbf{E}_0|$

Figure 13 depicts contours of the electric field intensity $|\mathbf{E}_0|$. Not surprisingly, the maximum field intensity occurs at the edges of the electrodes. In fact, the electric field is singular at the electrodes' edges. This singularity will not present a problem here since we will focus our attention on events occurring not too close to the electrodes' edges. The theory that we use below is not applicable in very close proximity to the electrodes' edges.

It is instructive to depict the electric field intensity as a function of x at various elevations above the electrodes' surface. Figure 14 depicts $|\mathbf{E}_0|$ as a function of x at $y=0.2$, 2, 4, and 10 μm. As y increases, the field intensity decreases. Witness that immediately above the electrodes' surface, there are two peaks at the edges of the electrodes ($y<10$ μm). As y increases, the two peaks eventually merge into a single peak located above the center of the gap ($x=0$).

Next, we will evaluate the forces that act on the nanotube when it is suspended in a perfectly dielectric fluid and subjected to the electric field depicted in Figs. 13 and 14. We focus on a cylindrical particle of length $2a_1$, radius a_2, and volume V_p, having an isotropic dielectric constant ϵ_p and an electric conductivity σ. The complex dielectric constant of the tube is [5] $\epsilon_p^*=\epsilon_p+\sigma/(j\omega)$, where ω is the frequency of the electric field and $j=\sqrt{-1}$. We estimated $\sigma\sim 1.6\times 10^4$ S/m from electric conductivity measurements [2]. Since the electric conductivity of the tube material is much higher than the electric conductivity of the suspending fluid (isopropanol), positive dielectrophoresis of the carbon nanotubes is expected and, indeed, observed. The nanotube's center is located at $\{x_p, y_p\}$ and the nanotube's axis forms angle θ with the x axis. We assume that the nanotube is not charged. This assumption

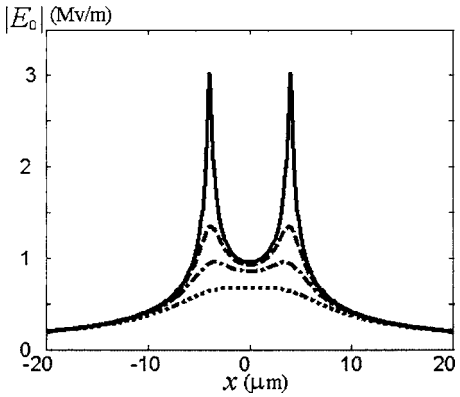

Fig. 14 The electric field intensity $|\mathbf{E}_0|$ as a function of x at $y=0.2$ (solid line), 2 (dashed line), 4 (dashed-dot line), and 10 μm (dotted line)

of electric neutrality is not critical since, in the experiments, we used ac fields and any migration due to the tube's charge will be nearly nullified.

The electric field **E** polarizes the nanotube and induces a dipole moment **P** in the tube. Roughly, the tube can be imagined as acquiring an electric charge at one end and an opposite sign charge of equal magnitude at the other end. The interaction of the induced charges with the electric field **E** results in electrostatic forces. When the particle is small compared to the length scale of the nonuniformities associated with the externally imposed electric field, the force (**F**) and torque (**T**) acting on the tube may be approximated as [5]

$$\mathbf{F} = (\mathbf{P} \bullet \nabla)\mathbf{E}_0 \tag{3}$$

and

$$\mathbf{T} = \mathbf{P} \times \mathbf{E}_0. \tag{4}$$

In the above, $\mathbf{E}_0$ is the electric field at the location of the particle's center in the particle's absence. When an ac field is applied, $\mathbf{E}_0$ represents the rms of the field. Equations (3) and (4) are known as the dipole moment approximation. For the range of validity of this approximation, see [12].

The effective dipole moment is:

$$\mathbf{P} \sim \epsilon_0 \epsilon_m V_p \mathrm{Re}(f_{CM})\mathbf{E}_0, \tag{5}$$

where ϵ_0 is the dielectric constant of free space; V_p is the particle's volume; and $\mathrm{Re}(f_{CM})$ is the real part of the Clausius-Mossotti factor. f_{CM} depends on the particle's geometry and dielectric properties.

When the particle is an ellipsoid with semi-axes a_1, a_2, and a_3, the Clausius-Mossotti factor in the direction of the a_i axis is [13]

$$f_{CM,i} = \frac{\epsilon_p^* - \epsilon_m^*}{\epsilon_m^* + (\epsilon_p^* - \epsilon_m^*)L_i}, \tag{6}$$

where $L_i = a_1 a_2 a_3 / 2\int_0^\infty ds/[(s+a_i^2)R_s] > 0$ is the depolarization factor, $V_p = 4\pi a_1 a_2 a_3/3$ is the ellipsoid's volume, and $R_s = \sqrt{(s+a_1^2)(s+a_2^2)(s+a_3^2)}$. In the above, we use the superscript $(^*)$ to indicate that, in general, the dielectric constants may be complex quantities. When $a_1 = a_2 = a_3$, we obtain the well-known result for the spherical particle with $L_i = 1/3$.

When the particle is a prolate ellipsoid ($a_1 \gg a_2 = a_3$), the depolarization factors L_1 and L_2 can be calculated in closed forms:

$$L_1 = S^2\left(\frac{1}{S^2-1} - \frac{\mathrm{Sec}^{-1}(S)}{(S^2-1)^{3/2}}\right) \tag{7}$$

and

$$L_2 = \frac{1}{2}\left[\frac{1}{(1-S^2)} + \frac{S^2}{(S^2-1)^{3/2}}\left(\frac{\pi}{2} - \mathrm{Csc}^{-1}(S)\right)\right], \tag{8}$$

where $S = a_2/a_1$ is the slenderness factor. When $S \ll 1$, Eqs. (7) and (8) can be further simplified with the aid of Taylor series expansions:

$$L_1 \sim S^2\left[\ln\left(\frac{2}{S}\right) - 1\right] + O(S^4) \tag{9}$$

and

$$L_2 \sim \frac{1}{2} + \frac{1}{2}(1 - \ln 2 + \ln S)S^2 + O(S^4). \tag{10}$$

When $\epsilon_p > \epsilon_m$, the particles will be attracted to the regions of maximum field intensity (positive dielectrophoresis). When $\epsilon_p < \epsilon_m$, the particles will be attracted to the regions of minimum field intensity (negative dielectrophoresis). In our case, the nanotube's effective permittivity is significantly larger than that of the surrounding medium because the tube's conductivity is significantly higher than that of the liquid. We therefore expect migration toward the location of maximum field intensity.

The migration of the nanotubes is mitigated by viscous drag. Unfortunately, exact expressions for the drag acting on a cylinder translating next to a plane surface are not available. Instead, we will use the slender body approximation for a cylindrical object translating at a distance H from and parallel to a plane in the Stokes flow regime. Due to the very small size of the nanotubes, we are justified in assuming creeping flow. The drag coefficients D_x and D_y [14,15] in the x and y directions are, respectively,

$$D_x = \frac{F_x}{2\pi\mu U_x a_1} = -2\chi - \chi^2(-0.614 + W_I) + O\left(\chi^3, \frac{\chi^2 a_2}{H}\right) \tag{11}$$

and

$$D_y = \frac{F_y}{2\pi\mu U_y a_1} = -4\chi - 2\chi^2(-1.386 + W_{II}) + O\left(\chi^3, \frac{\chi^2 a_2}{H}\right). \tag{12}$$

In the above, F_x and F_y are, respectively, the viscous forces in the x and y directions. U_x and U_y are the velocity components in the x and y directions. μ is the fluid's viscosity. $\chi = [\ln(2/S)]^{-1}$,

$$W_I = 2\sinh^{-1}(a_1/H) - 3\sqrt{1 + \frac{H^2}{a_1^2}} + \frac{7H}{2a_1} - \frac{H^2}{2a_1^2\sqrt{1 + H^2/a_1^2}}$$

and

$$W_{II} = 2\sinh^{-1}(a_1/H) + \frac{1}{\sqrt{1 + H^2/a_1^2}}.$$

By equating the viscous and electrostatic forces, we obtain the velocity components of the nanotube. Figures 15 and 16 depict the horizontal and vertical velocities of a cylindrical particle as functions of the x coordinate. Figure 15(a) depicts the horizontal velocity when $H=1$ (solid line) and 2 μm (dashed line). Figures 15(b) and 16 depict, respectively, the horizontal and vertical velocities when $H=4$ (solid line), 6 (dashed line), and 10 μm (dotted line). The velocities are expressed in mm/s and the distances in μm. The inserts in the figure provide a magnified view of the velocity distribution some distance from the gap. Since general expressions for drag forces of a tube as a function of the inclination angle are not available, we focus only on tubes that are parallel to the surface. In our calculations, the nanotube has half-length $a_1=6$ μm and radius $a_2=125$ nm. The medium has a relative permittivity of 20 and a viscosity of 2×10^{-3} kg/m-s.

The theory predicts that when the tube is relatively far from the gap, both the horizontal and vertical velocities are relatively small—on the order of a fraction of mm per second (Fig. 15). As the tube approaches the gap, its velocity increases rapidly and attains a maximum in the vicinity of the electrodes' edges. The maximum velocity is on the order of centimeters per second. These predictions are in qualitative agreement with our experimental observations (Fig. 8).

When the tube is close to the surface [Fig. 15(a)], the tube senses the presence of the two electric field maxima at the electrodes' edges and the horizontal velocity is directed towards the electrodes' edges. In other words, the velocity is positive on the left-hand side of the edge and negative on the right-hand side. When the tube is sufficiently far from the gap [Fig. 15(b)], the horizontal velocity is directed towards the center of the gap. Due to symmetry, the horizontal velocity vanishes at the gap's center ($x=0$). These observations are consistent with Fig. 14 which depicts the presence of two peaks in the electric field in the electrode's vicinity and the merging of these two peaks into a single peak some distance above the electrodes' surface. In other words, a particle cruising well above the surface will be attracted (horizontally) to $x=0$. Particles close to the surface will be attracted to the electrodes' edges.

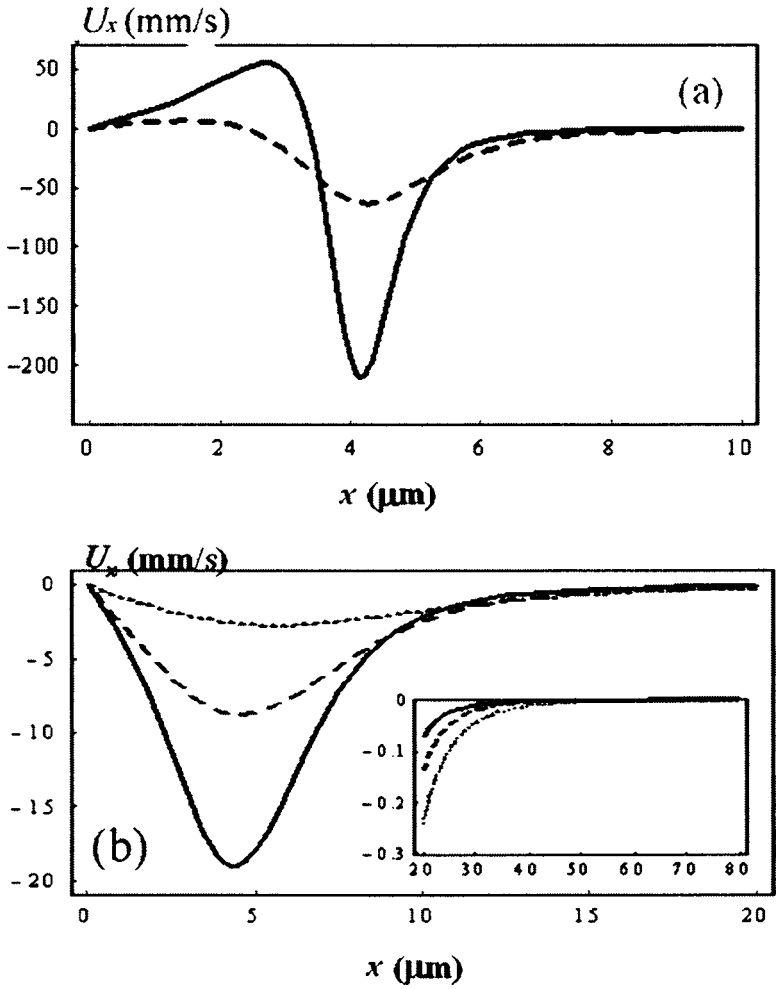

Fig. 15 The horizontal velocity U_x as a function of x at (a) y=1 (solid line) and 2 μm (dashed line) and (b) y=4 (solid line), 6 (dashed line), and 10 μm (dotted line) is depicted as a function of x. The insert depicts a magnified view of the velocity far from the gap.

The vertical velocity (Fig. 16) exhibits somewhat similar trends to the ones depicted in Fig. 15. Unexpectedly, at relatively large x values, the vertical velocity is directed upwards. The magnitude of this vertical velocity is very small, and the tube would appear to be cruising at a nearly constant elevation. Indeed, in the experiments, we observed that tubes migrated at nearly level height when approaching the gap. To verify that this positive velocity is not an artifact of the dipole moment approximation, we carried out finite element simulations to calculate the forces acting on the tube. The numerical simulation results were consistent with the above predictions.

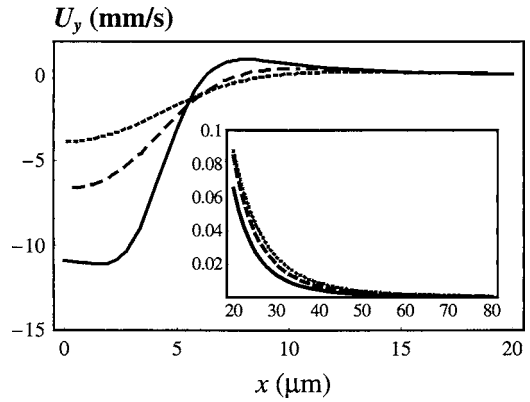

Fig. 16 The vertical velocity U_y at y=4 (solid line), 6 (dashed line), and 10 μm (dotted line) is depicted as a function of x. The insert depicts a magnified view of the velocity far from the gap.

Recall that the dipole moment approximation is valid only when the length scale associated with the electric field is large compared to the particle's size. This is no longer true when the particle is close to the gap. To obtain more accurate estimates of the forces acting in the gap's vicinity, one would need to calculate the electric field ($\mathbf{E}$) in the presence of the particle and obtain the forces by integrating the surface force density,

$$\mathbf{f} = \epsilon_0 \epsilon_m \left(\mathbf{E}(\mathbf{E} \cdot \hat{n}) - \frac{1}{2}(\mathbf{E} \cdot \mathbf{E})\hat{n} \right), \tag{13}$$

around the particle's surface. In the above, $\hat{n}$ is the outer unit vector normal to the particle's surface. This type of calculation as well as accurate estimates of the viscous drag for a particle translating close to a wall would require, however, the use of numerical simulations which we do not address in this paper. Liu and Bau [12] compared the forces predicted using the dipole moment approximation with predictions based on the Maxwell stress tensor [Eq. (13)] for the cases of spherical and cylindrical (two-dimensional) particles. They found that when a spherical particle

is located at a distance larger than three radii from the electrode's edge, the predictions of the dipole moment approximation were in good agreement with the predictions of the exact theory. Unfortunately, similar results are not available for the case studied here. Nevertheless, the good qualitative agreement between the theoretical predictions and the experimental observations suggests that the dipole moment based theory is capable of providing an adequate qualitative description of the tube's migration.

We do expect quantitative differences between theory and experiment. The experimental velocity and rotation measurements are based on a two-dimensional top view of the tube. We were unable to experimentally determine the velocity in the vertical direction. Moreover, in the experiments, there may have been flow in the drop that assisted in bringing tubes to the trap's vicinity. The circulation in the drop might have resulted from polarization effects along the drop's surfaces, from Marangoni convection resulting from thermal and electric field effects, and from drop evaporation. All these factors were not accounted for in the simple theory that we presented here.

5 Conclusions

The paper describes the positioning of carbon nanotubes at predetermined locations with the use of dielectric forces. The migrations of the carbon nanotubes in the electric field were observed and their velocities were estimated with a simple mathematical model. Dielectrophoresis is a versatile and convenient tool for the manipulation and assembly of nanoparticles, and we have extended its use to the positioning and manipulation of individual macromolecules (not reported here).

The paper also describes a new, practical means of constructing nanotube-based fluidic devices. The fabrication technique combines dielectrophoretic trapping with photolithography. Once the nanotube has been positioned at a predetermined position, one can bring to bear the tools of photolithography to fabricate fluidic conduits that will allow one to transmit various fluids, macromolecules, and nanoparticles through the tube. Such devices can be used for fundamental studies of the behavior of simple and complex fluids under extreme confinement. Moreover, these devices can be used as highly sensitive biological and chemical sensors. The fabrication technique can be readily scaled down to allow one to trap single-walled nanotubes. Moreover, the process is consistent with mass production. Numerous devices can be fabricated in parallel.

Consistent with other researchers, we have demonstrated that the nanotubes readily fill with various liquids and that the tubes' thin walls allow direct observation of a liquid's presence with the use of optical microscopy. The motion of the liquid/vapor interface during the evaporation of the liquid inside the tube was clearly visible.

Acknowledgment

The research was supported by the NSF NIRT Grant No. CTS 0210579, the Pennsylvania State Nano Technology Institute (NTI), and DARPA SIMBIOSYS Program No. N66001-01-C-8056. M. Riegelman also acknowledges support from a GAANN fellowship. We are grateful to Professor Evoy for introducing us to the dielectrophoretic nanoassembly technique.

References

[1] Riegelman, M., Liu, H., Evoy, S., and Bau, H. H., 2004, "Nanofabrication of Carbon Nanotube (CNT) Based Fluidic Device," *Proceedings of NATO-ASI Nanoengineered Nanofibrous Materials*, S. Guceri, V. Kutznetsov, and Y. Gogotsi, Eds., Kluwer, The Netherlands, pp. 407–414.

[2] Riegelman, M., 2004, "Dielectrophoretic Assembly and Integration of Nanofluidic Devices," M.S. thesis, The University of Pennsylvania.

[3] Evoy, S., DiLello, N., Deshpande, V., Narayanan, A., Liu, H., Riegelman, M., Martin, R. R., Hailer, B., Bradley, J. -C., Weiss, W., Mayer, T. S., Gogotsi, Y., Bau, H. H., Mallouk, T. E., and Raman, S., 2004, "Dielectrophoretic Assembly and Integration of Nanowire Devices with Functional CMOS Operating Circuitry," Microelectron. Eng., **75**(1), pp. 31–42.

[4] Pohl, H. A., 1978, *Dielectrophoresis: The Behavior of Neutral Matter in Nonuniform Electric Fields*, Cambridge University Press, New York.

[5] Jones, T. B., 1995, *Electromechanics of Particles*, Cambridge University Press, New York.

[6] Yamamoto, K., Akita, S., and Nakayama, Y., 1998, "Orientation and Purification of Carbon Nanotubes Using AC Electrophoresis," J. Phys. D, **31**, pp. L34–L36.

[7] Chung, J., Lee, K. -H., Lee, J., and Ruoff, R. S., 2004, "Toward Large-Scale Integration of Carbon Nanotubes," Langmuir, **20**, pp. 3011–3017.

[8] Bradley, J. -C., Babu, S., Ndungu, S., Nikitin, P., and Gogotsi, Y., 2004, "Nanotube Synthesis Using Alumina Template," SMIRP Bradley Research Lab Knowledge Product 10975_0004.

[9] Rossi, M. P., Ye, H., Gogotsi, Y., Babu, S., Ndungu, P., and Bradley, J. -C., 2004, "Environmental Scanning Electron Microscopy Study of Water in Carbon Nanopipes," Nano Lett., **4**(5), pp. 989–993.

[10] Kim, B. M., Sinha, S., and Bau, H. H., 2004, "Optical Microscope Study of Liquid Transport in Carbon Nanotubes," Nano Lett., **4**(11), pp. 2203–2208.

[11] Morse, P. M., and Feshbach, H., 1953, *Methods of Theoretical Physics*, McGraw-Hill, New York.

[12] Liu, H., and Bau, H. H., 2004, "Dielectrophoresis of Cylindrical and Spherical Particles Submerged in Shells and in Semi-Infinite Media," Phys. Fluids, **16**(5), pp. 1217–1228.

[13] Stratton, J. A., 1941, *Electromagnetic Theory*, McGraw-Hill, New York.

[14] Blake, J. R., 1974, "Singularities of Viscous Flow," J. Eng. Math., **8**, pp. 113–124.

[15] De Mestre, N. J., and Russel, W. B., 1975, "Low Reynolds Number Translation of a Slender Cylinder Near a Plane Wall," J. Eng. Math., **9**, pp. 81–91.

Conrad D. James
e-mail: cdjame@sandia.gov

Murat Okandan
e-mail: mokanda@sandia.gov

Paul Galambos
e-mail: pcgalam@sandia.gov

Seethambal S. Mani
e-mail: ssmani@sandia.gov

Sandia National Laboratories,
P.O. Box 5800,
Albuquerque, NM 87185

Dawn Bennett
e-mail: dawnb@umbc.edu
The University of Maryland,
Baltimore County,
1000 Hilltop Circle,
Baltimore, MD 21250

Boris Khusid
e-mail: khusid@adm.njit.edu
New Jersey Institute of Technology,
University Heights,
Newark, NJ 07102

Andreas Acrivos
e-mail: acrivos@scisun.sci.ccny.cuny.edu
The Levich Institute,
The City College of New York,
140th Street & Convent Avenue,
New York, NY 10031

Surface Micromachined Dielectrophoretic Gates for the Front-End Device of a Biodetection System

We present a novel separation device for the front-end of a biodetection system to discriminate between biological and non-biological analytes captured in air samples. By combining AC dielectrophoresis along the flow streamlines and a field-induced phase-separation, the device utilizes "dielectrophoretic gating" to separate analytes suspended in a flowing fluid based on their intrinsic polarizability properties. The gates are integrated into batch fabricated self-sealed surface-micromachined fluid channels. We demonstrate that setting the gate to a moderate voltage in the radio frequency range removed bacteria cells from a mixture containing non-biological particles without the need for fluorescent labeling or antibody-antigen hybridization, and also validate experimentally basic relations for estimating the gate performance. [DOI: 10.1115/1.2136924]

Introduction

There is an increasing demand for novel systems to enable the rapid detection of biological materials in the field or their continuous monitoring in a hospital setting. The first step in the operation of such a system consists of concentrating and separating the analytes of interest from the background matrix and positioning them into selected locations for analysis. The next step is to provide a "trigger/cue" that signals the detection of a biological substance. Many biological detection systems use a trigger/cue based on ultraviolet laser-induced fluorescence (UV-LIF), which can detect biosignatures specific to living organisms, such as amino acids and coenzymes [1,2]. UV-LIF and other optical techniques are the gold standards for biological detection in the laboratory setting, but they suffer from several drawbacks. For instance, specificity is a major concern in that contaminants, such as engine exhaust particles, will also fluoresce under UV excitation, triggering high rates of false positives [2]. In addition, UV-LIF technology is difficult to miniaturize, a process that would reduce cost, increase portability, and facilitate the rapid detection in nonlaboratory settings. Optical systems require fragile components and delicate alignment of sources, samples, and detectors, making such systems more difficult to implement in small portable devices where vibrations and accelerations can compromise detector function. Gas phase lasers are commonly used as UV sources in such systems [3], but these lasers are bulky, draw large amounts of power, and lack the robustness necessary for typical field applications. Also, the high initial and lifetime maintenance cost of UV-LIF laser sources limits overall system affordability. Currently, solid-state lasers, which are compact, rugged, and use less power, are now being employed [4] and have been successfully demonstrated in the field [5], but specificity and sensitivity problems remain.

For these and other reasons, many researchers are pursuing nonoptical methods, such as dielectric spectroscopy and impedance monitoring, for biological characterization and detection [6,7]. The focus of the present work is a related technique, dielectrophoretic separation, which is being examined as a detection/separation method [8–10]. Compared to other available methods, AC dielectrophoresis (DEP) is particularly well suited for collecting and separating particles because the application of a high-frequency (megahertz) AC field suppresses undesirable electrode polarization, electrolytic effects, and electroconvection in the liquid. Also, the polarization forces exerted on analytes are insensitive to the particle charge, a property of analytes that is difficult to control. A hypothetical front-end of a biological detection system using "dielectrophoretic gates" [11] is shown in Fig. 1. After an air sampler collects a sample, the captured analytes are suspended

Contributed by the Fluids Engineering Division of ASME for publication in the JOURNAL OF FLUIDS ENGINEERING. Manuscript received July 20, 2004; final manuscript received April 21, 2005. Assoc. Editor: Dennis Siginer.

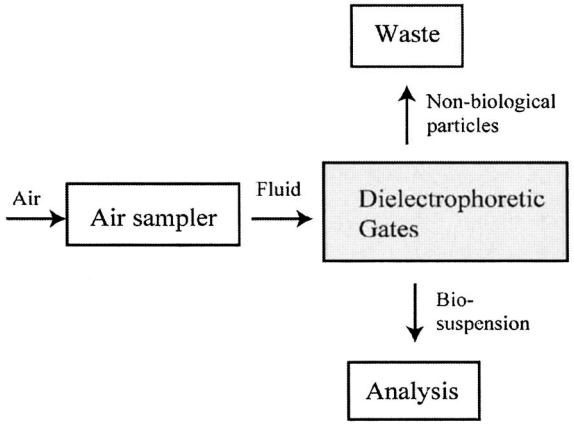

Fig. 1 Proposed biodetection system that uses dielectrophoretic gates as a trigger/cue to signal the detection of an unknown biological analyte, and to separate biological from non-biological materials

in a carrier fluid for transport to the dielectrophoretic gates. The gates are essentially sources of high-frequency AC voltage that will impart electrokinetic forces on the flowing analytes. The gate will separate biological (cellular) from nonbiological analytes using the frequency dependence of the analytes' complex dielectric permittivity, an intrinsic property of all substances. We showed [11] that, in addition to the dielectrophoretic force imparted by the gate along the flow streamlines, long-range electrical and hydrodynamic forces due to interparticle interactions lead to an accompanying phase separation of constituents, thus enhancing separation. After the cellular material is collected, the contaminants can be flushed as waste, and the remaining cellular material can be transported to the detector for identification. Specifically, we demonstrated the dielectrophoretic and field-induced phase separation of heat-killed bacteria and latex microspheres in a surface micromachined fluidic device [11].

The purpose of this paper is: (i) to describe a technique for the fabrication of a microchannel equipped with the dielectrophoretic gate and the experimental setup and procedures for studying the gate performance not included in Ref. [11] due to page constraints, (ii) to present new experimental data on the motion and separation of biological and nonbiological particles, and (iii) to validate a simplified method for evaluating the particle velocity flowing through the gate.

Dielectrophoretic Gate Theory

A new concept for the electroseparation of bioparticles from nonbiological materials, termed "dielectrophoretic gating," combines the field-induced DEP along the flow streamlines and phase transition for manipulating particles in microfluidics [11]. Figure 2(*a*) depicts the gate, which consists of a pair of microelectrodes that span a fluid channel, perpendicular to the direction of fluid flow. When an AC voltage is applied to the microelectrodes, an electric field is generated within the fluid channel. When exposed to such a spatially nonuniform electric field, a particle flowing through the channel will polarize and acquire a dipole moment that will interact with the electric field, generating a time-averaged dielectrophoretic force $\mathbf{F}_{\mathrm{DEP}}$, given by [12]

$$\mathbf{F}_{\mathrm{DEP}} = \tfrac{3}{2}\varepsilon_0\varepsilon_f V_p \,\mathrm{Re}[\beta^*(\omega)]\,\nabla\,\mathbf{E}^2_{\mathrm{rms}} \tag{1}$$

where ε_0 and ε_f are the vacuum and fluid permittivity, respectively, V_p is the particle volume, $\mathrm{Re}[\beta^*(\omega)]$ is the real component of the relative particle polarization $\beta^*(\omega)$ at the field frequency ω, and $\nabla\mathbf{E}^2_{\mathrm{rms}}$ is the gradient of the squared root-mean-square electric field. Under this force, the particle is either attracted toward

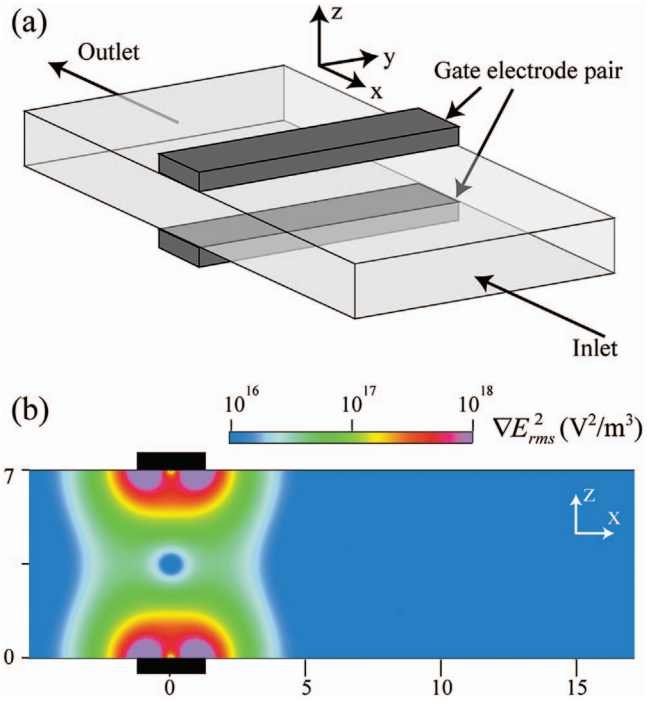

Fig. 2 (*a*) Schematic of a dielectrophoretic gate consisting of two electrodes arranged perpendicular to the fluid flow. (*b*) Log plot of the simulated $\nabla\mathbf{E}^2_{\mathrm{rms}}(x,z)$ for the two-electrode dielectrophoretic gate. Electrodes (black rectangles) are added for clarity. Dimensions are in μm.

[$\mathrm{Re}(\beta^*)>0$, positive DEP (pDEP)] or repelled from [$\mathrm{Re}(\beta^*)<0$, negative DEP (nDEP)] regions of large $\nabla\mathbf{E}^2_{\mathrm{rms}}$, depending on whether the particle is more or less polarizable than the liquid, respectively. We previously demonstrated for pDEP [13,14] and nDEP [15] that the predictions of a single-particle model, which considers the combined effect of $\mathbf{F}_{\mathrm{DEP}}$, the Stokes drag force, and the gravity force acting on a single particle are quantitatively consistent with experimental data on the particle motion. These predictions were made for suspensions with ~0.1% (v/v) polarized particles under the action of strong electric fields, even though $\beta^*(\omega)$ was measured at low fields (approximately, volts per millimeter). In the radio frequency range, the relative polarizability of a particle immersed in water is mainly influenced by the ratio of the capacitances of the particle and of the water, so that a reasonable estimate of $\mathrm{Re}(\beta^*)$ is given by

$$\mathrm{Re}(\beta^*) \approx \frac{\varepsilon_p - \varepsilon_f}{\varepsilon_p + 2\varepsilon_f} \tag{2}$$

where ε_p is the particle permittivity. The dielectric constant of water at radio frequencies is about 78. In contrast, the dielectric constants of soil components and common industrial and natural materials (for example, resins, plastics, carbon black, soot, ash, and gravel), when dry, fall in the range 1.5–15. Since the particle polarization in the radio frequency range is mainly specified by its bulk dielectric constant, these materials, when dispersed, in water will exhibit strong negative dielectrophoresis. In contrast, biological particles, such as cells, have polarizabilities typically close to or greater than that of water. Thus, we employ an AC field in the radio frequency range (0.1–30 MHz) to separate biological from nonbiological particles in our device. Another essential advantage of operating in this frequency range is that undesirable electric effects in water, such as electrolysis and other irreversible chemical reactions, electroosmosis, and electroconvection are suppressed, making this scheme particularly well suited for microfluidic applications. Since electrophoretic effects also vanish at

megahertz frequencies, this separation technique relies on the bulk polarization properties of a particle, given by $\mathrm{Re}(\beta^*)$, that are insensitive to the particle surface properties which may vary randomly due to environmental effects or intentionally due to the method of aerosolization.

The range of $\mathbf{F}_{\mathrm{DEP}}$ operating along the flow streamlines was extended throughout the height (z-axis) of the channel by placing an electrode on the top and bottom surfaces of the channel. This helps to increase the gating efficiency in that particles suspended in a fluid flowing at any position in the yz plane will be subjected to $\mathbf{F}_{\mathrm{DEP}}$. Figure 2($b$) shows a two-dimensional simulation of the dielectrophoretic gate (CFD-ACE+ Version 2003.0.136). The grid density was 10 points per micrometer, and the electrodes were set to 10 V. In this simulation, the height of the channel was 7 μm, and the electrode surfaces were 2 μm wide. The topography at the electrode edges was neglected, and all other surfaces were set to the boundary condition of zero-normal current. The field gradient is largest at close distances to the microelectrodes, and in this example, $\nabla\mathbf{E}^2_{\mathrm{rms}}$ maintains a value of $\sim 10^{17}\ \mathrm{V}^2/\mathrm{m}^3$ or greater throughout the z-axis near the gate. Upon injecting a solution of analytes that are more polarizable than the suspending fluid, the analytes will accelerate under pDEP toward the regions of highest $\nabla\mathbf{E}^2_{\mathrm{rms}}$, which is near the microelectrodes. Solving the equation of motion for a particle by taking into account $\mathbf{F}_{\mathrm{DEP}}$ and the drag force while neglecting the interparticle interactions and the gravity force, the velocity of a small spherical particle of radius a traveling in a flowing fluid is given by [13,16]

$$\mathbf{u} = \mathbf{v} + \frac{\mathbf{F}_{\mathrm{DEP}}}{6\pi\eta a}, \tag{3}$$

where η and $\mathbf{v}$ are the fluid viscosity and velocity, respectively. For large $\nabla\mathbf{E}^2_{\mathrm{rms}}$, $\mathbf{F}_{\mathrm{DEP}}$ will attract highly polarizable analytes to the microelectrodes where they will come to rest. In contrast, for analytes that are less polarizable than the fluid, $\mathbf{F}_{\mathrm{DEP}}$ will act as a repulsive force as the analytes seek to migrate toward regions of low $\nabla\mathbf{E}^2_{\mathrm{rms}}$. Thus, if the particles injected into the channel have low polarizability, they will be carried with the fluid flow until the value of $\nabla\mathbf{E}^2_{\mathrm{rms}}$ reaches the point at which the particles start being subjected to nDEP. This nDEP force will then decelerate the particles, producing a drag force as the particle motion begins to oppose the fluid motion, and at some location upstream from the gate, the particles will come to rest at the point where $\mathbf{F}_{\mathrm{DEP}}$ equals the drag force. A larger fluid velocity will push the particles closer to the gate, whereas a smaller fluid velocity will allow the particles to be repelled at greater distances from the gate. Upon injection of a mixture of low- and high-polarizability particles, the opposing nDEP and pDEP forces will separate the particles rapidly.

After coming to rest, the particles interact with one another due to their polarization. As the distance between the particles decreases, the polarization force increases, greatly exceeding the magnitude given by the dipole approximation for the interparticle separation smaller that the particle radius. When the local concentration of the accumulated particles exceeds a threshold value so that the average interparticle separation becomes sufficiently small, the polarization forces cause the particles to undergo a phase transition (referred to as the electrorheological effect [17]) and to form a distinct front between the regions enriched with and depleted of particles [11]. The evolution of the particle patterns formation is well described by a proposed electrohydrodynamic model [11,18], which does not require any fitting parameters. This three-dimensional model encompasses the quasi-steady electrodynamic equations coupled with the momentum and continuity balance equations of the "mixture" model for a suspension. Now we shall demonstrate that the simulation of the electric field configuration and Eqs. (1) and (3) provides a simplified method for estimating the particle velocity and the front location, which are needed for the design and optimization of the gate performance.

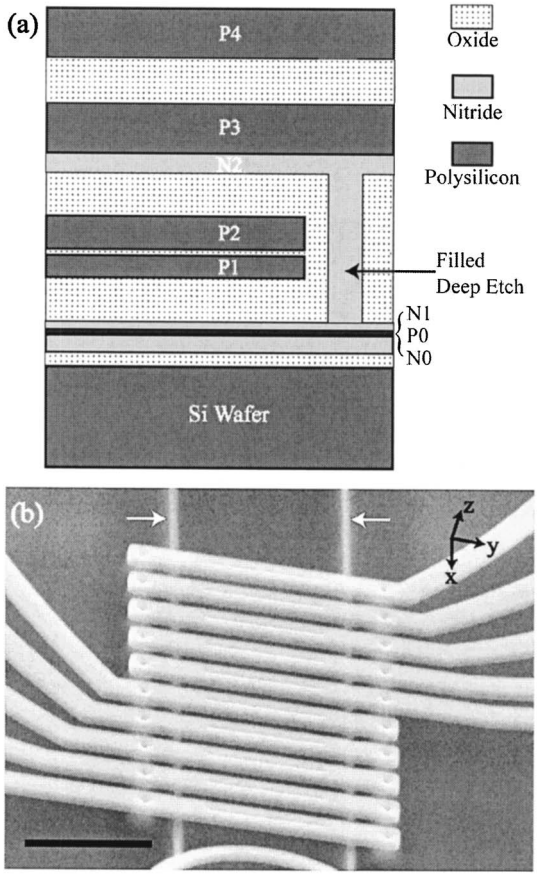

Fig. 3 (*a*) SwIFT™ film stack with five polysilicon, three silicon nitride, and four sacrificial silicon oxide layers. (*b*) Scanning electron micrograph of a series of dielectrophoretic gates. The fluid channel sidewalls are denoted by the white arrows. Scale bar=30 μm.

Device Fabrication

The devices were fabricated at the Sandia National Laboratories Microelectronics Development Laboratory. The dielectrophoretic gate we present here was fabricated using a previously described process termed SwIFT™ (surface micromachining with integrated fluidic technology) [19]. SwIFT is a sacrificial layer method that uses multiple layers of structural materials (polysilicon and silicon nitride) and sacrificial materials (silicon oxide) to build devices. The SwIFT process begins with a 6 in. bare (100) n-type wafer with 2–20 Ω cm resistivity (Fig. 3(a)). Next, the bulk silicon is isolated from the devices with a 0.6 μm layer of thermally grown silicon oxide followed by a 0.8 μm layer of nonstoichiometric (silicon-rich) low-stress silicon nitride (N0). Up to five layers of fine-grained doped polysilicon (P0–P4) are deposited from silane in a low-pressure chemical vapor-deposition furnace. These layers are used for making electrical connections and microelectrodes in order to impart electric fields into microfluidic compartments. Polysilicon layers are on the order of 1–2 μm thick, with the exception of P0, which is 0.3 μm. The sacrificial oxide layers are deposited using both low pressure chemical vapor deposition and plasma enhanced chemical vapor deposition. Chemical-mechanical polishing is used to reduce the topography in the final two sacrificial oxide layers. The structural layers of silicon nitride (N1: 0.3 μm, N2: 0.8 μm thick) provide optically transparent and electrically insulating surfaces that serve as barriers for the fluidic components. Figure 3(a) indicates a deep etch through several sacrificial oxide films down to N1. This trench is then filled with

N2, forming sidewalls and ceiling covers for fluidic channel components. The total film thickness is 16 μm, and the distance between N1 and N2 is $\sim$7 μm. The channels are fabricated in a fully encapsulated state, obviating the need for substrate bonding, a process that slows the device production and reduces reproducibility.

After completing the surface micromachining, access ports to the fluidic devices are fabricated using deep reactive ion etching [20]. The sacrificial oxide layers in devices are then removed in an HF-based etchant at 20°C for 100–200 min depending on the length of the fluidic channel. The devices are then rinsed in deionized (DI) water and dried in supercritical CO_2. Figure 3(*b*) shows a completed fluidic device with integrated dielectrophoretic gates. The N2 channel sidewalls are visible, along with the P3 electrode traces perpendicular to the fluid channel axis. P4 was not utilized in this particular device. The circular depressions are vias that connect the P3 microelectrodes to the P0 microelectrodes (not visible), allowing them to be held at the same potential. The long depressions in the center of the P3 traces are due to etches in N2 that allow the P3 microelectrode to be in direct contact with the fluid flowing through the channel. Similar etches are made in N1 to allow P0 to contact the fluid.

Experimental Methods

Following [11], experiments were performed on aqueous mixtures of latex beads (1 μm dia, Duke Scientific) chosen to be representative on non-biological particles and heat-killed Staphylococcus aureus bacteria (Molecular Probes) chosen as sample biological particles. Latex beads and bacteria were suspended at 0.01% (v/v) in DI water. An equal mixture of bacteria and beads in DI water was prepared immediately before the separation experiments to minimize aggregation. The conductivity of the DI water was measured to be 1 μS/cm. The latex particle polarizability, $\beta \cong -0.45-0.27i$ for 10–30 MHz, was calculated from the low-field measurements [11].

For testing devices, glass capillaries (285 μm outer diameter) were placed into the counterbores and epoxied in place. The capillary connections were then sealed with polydimethylsiloxane (GE RTV615A) to prevent leaking. Teflon tubing (30 gage) was run from the capillaries to a syringe and the fluid suspensions were injected manually. The dielectrophoretic gates were energized with a sinusoidal wave, 10 V peak-to-peak (pp) and 0.1–30 MHz, using a function generator. The experiments were recorded onto a videotape, and later digitized for analysis. The fluid velocities were estimated by calculating particle velocities on the videotape, either with the gates inactivated or when the particles were at large distances ($x > 50$ μm) from the activated gates.

Experimental Results

Figure 4(*a*) shows the separation of a mixture of 1 μm latex particles from dead Staphylococcus aureus bacteria. The gate was set to 10 v peak-to-peak at 15 MHz. It is evident that the positively polarized bacteria accumulate at the gate microelectrode, while the negatively polarized latex particles are repelled from the gate region. Upon injection of the mixture, the fluid velocity was measured to be 5–10 μm/s, and at this velocity, the latex particles formed a distinct front $\sim$40 μm upstream from the gate. In contrast, the bacteria accumulate at the gate, and, as the polarization interactions occur, long pearl chains of bacteria form that exceed the bounds of the gate. Three individual bacteria had their distance-dependent velocities, $u(x)$, tracked from their entrance into the channel until they came to rest at the tips of pearl chains 5 μm upstream from the gate (Fig. 4(*b*)). The fluid velocity was kept low (5–10 μm/s), which was much smaller than the DEP-induced particle velocity. The large DEP-induced particle velocities made it difficult to track bacteria within 20 μm of the gates, hence the velocity data were fitted to an exponential curve [$u = 1330e^{-0.122x}$ μm/s, x in micrometer, with $r^2 = 0.92$] to provide an estimate of the particle velocities generated near the gate. Thus, it was found that the bacteria were accelerated to velocities up to $\sim$700 μm/s before coming to rest adjacent to the gate. Using Eq. (3), the maximum estimated forces exerted on individual bacteria are on the order of 5 pN. Figure 4(*b*) also shows the velocity data of four latex particles that were tracked while undergoing nDEP. In addition, the fluid velocity was increased in order to examine the strength of the repulsive force. It was found that, after the latex particles were injected at velocities of 75–100 μm/s, the DEP force started to exert an observable deceleration of particles at $x \sim 30$ μm from the gate, with full repulsion bringing particles to a halt $\sim$12 μm upstream from the gate.

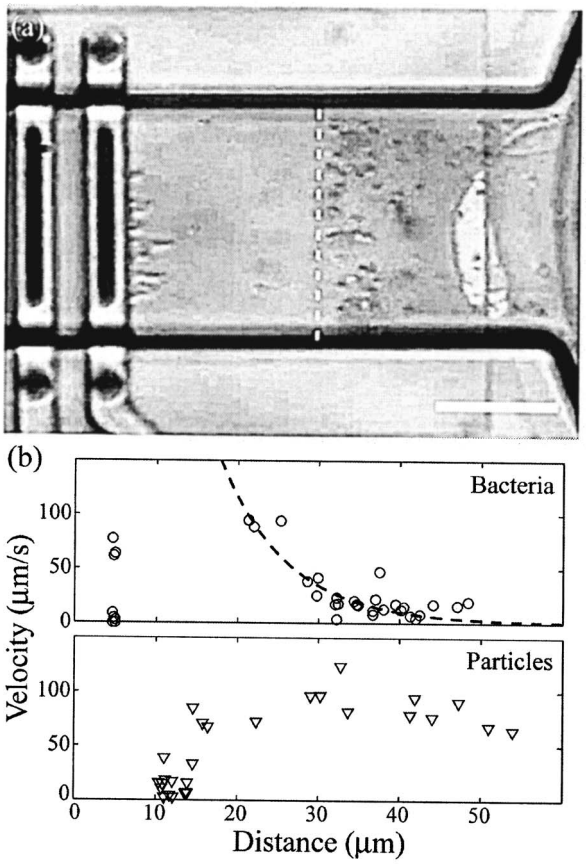

Fig. 4 (*a*) At 10 V pp, 15 MHz, bacteria adhere to the gate, while latex particles are repulsed and form a front (dashed line). Fluid velocity, 5–10 μm/s. Scale bar=20 μm. (*b*) DEP-induced velocity of bacteria (n=3) and latex particles (n=4) at 15 MHz as a function of distance from the center of the gate.

At higher fluid velocities, the latex particles formed fronts closer to the gate and the interparticle interactions became more apparent. In particular, at a fluid velocity of $\sim$45 μm/s (the flow rate $\sim$6 pL/s) the repelled latex particles aggregated at $x \sim 25$ μm upstream from the center of the gate with the average particle concentration in the aggregate running as high as 40–50% (v/v) (estimated from the images on the assumption that aggregates span the channel height) [11]. The particle aggregate oscillated between forming one bolus being located in the center of the channel and two rotating boluses being located at the channel sidewalls. Figure 5 documents that switching the gate frequency from 15 MHz to 100 kHz causes the particle aggregates adjacent to the channel sidewalls to traverse the gate, while the bacteria remain trapped, and in the presence of an estimated fluid velocity of 45 μm/s, all the accumulated latex particles escape the gate

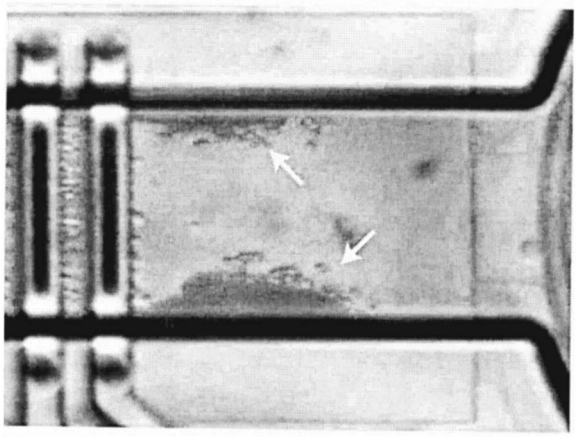

Fig. 5 Approximately 0.5 s after the frequency is switched from 15 MHz to 100 kHz, latex particles are traversing the gate along the sidewalls, while bacteria remain trapped. All accumulated latex particles escape the gate within 5 s following the frequency shift.

within ~5 s following this frequency shift. However, the pDEP force on the bacteria at this frequency is still strong enough to withstand the fluid flow. This release of the latex particles may be related to the reduction of their relative polarizability, $\mathrm{Re}(\beta^*)$, with decreasing field frequency, as was observed in [21] under similar conditions, or with an AC generated electroosmotic fluid flow caused by the action of the field along the double layer at the channel sidewalls [22]. Further analysis of the gate operation at submegahertz frequencies is in progress and will constitute the subject of future publication.

Discussion

Simulations of the profile of $\nabla \mathbf{E}^2_{\mathrm{rms}}$ provide a rough estimate for the DEP-induced velocity of individual bacteria and latex particles using Eq. (3). In particular, with $\nabla \mathbf{E}^2_{\mathrm{rms}} \sim 7 \times 10^{15}\ \mathrm{V}^2/\mathrm{m}^3$ at a distance of 20 μm from the center of the gate, the DEP-induced velocity of a single bacteria at this distance is estimated to be ~94–188 μm/s (estimating $\mathrm{Re}(\beta^*)$ to be in the range from 0.2 to 0.4), whereas the exponential fit of the experimental velocity data yields 108 μm/s. Measurements of $\mathrm{Re}(\beta^*)$ for the bacteria will be conducted in the future. The predictions of the DEP-induced velocity of the latex particles also agree with our observations in that, at a fluid velocity of 10 μm/s, a 0.5 μm radius latex particle should experience a drag force of ~0.08 pN if brought to rest by an opposing DEP force. Using our simulations for $\nabla \mathbf{E}^2_{\mathrm{rms}}$ and Eq. (1), $\mathbf{F}_{\mathrm{DEP}}$ should first reach 0.08 pN ~45 μm from the gate, which agrees reasonably with our observations of the formation of a particle front at 40 μm from the gate. At a fluid velocity of 45 μm/s, our simulations predict that the latex particles should be brought to rest at $x \sim 33$ μm upstream from the microelectrodes, while we observed the formation of a front at $x \sim 25$ μm from the gate. These estimates agree reasonably well with our observations. Several factors that have been neglected in these estimates are likely responsible for any discrepancies, for instance, interparticle interactions and additional hydrodynamic forces caused by the formation of particle aggregates in the channel.

The separation efficiency of the dielectrophoretic gate is optimal at relatively low fluid velocities and long separation times. No bacteria or particles were observed to escape the trap during its activation at 10 V, 15 MHz and at fluid velocities up to ~600 μm/s. Our simulations indicate that the gates should be able to repel particles traveling up to ~1000 μm/s. Latex particles were observed to traverse the gate only when the amount of collected particles began to fill the entire yz cross section of the channel in which case particles near the sidewalls, the weakest point of the $\mathbf{F}_{\mathrm{DEP}}$, were found to escape the gate.

Another phenomenon was observed in several instances when a bacterial cell adhered to a single latex particle thereby creating a bacteria-particle complex susceptible to pDEP which, therefore, was trapped at the gate. In such cases, within 5–10 s of the complex coming to rest, the latex particle was observed to break away from the bacteria and to accelerate toward the rest of the repelled particle aggregate upstream of the gate. Thus, longer separation times may be required to reduce the effect of this phenomenon, which could possibly contaminate the analysis and identification procedures conducted on the biosuspension.

Conclusions

We have described a surface-micromachined dielectrophoretic gate for separating micrometer-sized analytes based on their intrinsic polarizability properties and validated experimentally basic relations for estimating the gate performance. The separation technique uses AC dielectrophoresis along the flow streamlines accompanied by the field-induced phase separation through electrical and hydrodynamic interparticle interactions. The self-sealed microfluidic devices were fabricated using a surface- and bulk-micromachining technology, which is amendable to mass production. Setting the device to a moderate voltage in the radio frequency range selectively removed bacteria cells from a mixture containing nonbiological particles. The low aspect ratio of the device permitted a high-efficiency separation because the range of the dielectrophoretic force extended throughout the cross section of the fluid channel. This reduces the number of particles that escape the trap, producing highly concentrated (by factor over 500 the initial concentration) and spatially separated aggregates of negatively and positively polarizable analytes. We see a potential use for the proposed technology for discriminating between biological and nonbiological analytes that are captured in air samples. Future work is aimed at the optimization of the gating technique and the development of integrated biodetection systems.

Acknowledgment

The authors would like to thank Randy Shul and Peggy Clews of Sandia National Laboratories for their aid in the development of the DRIE counterbore microfluidic interconnect, and the development of the device release chemistry, respectively. We would also like to thank Larry Gilbert of Lockheed Martin for valuable discussions on biodetection. This work was supported, in part, by grants from the National Aeronautics and Space Administration, No. NAG3-2698 (B.K. and A.A.), the Defense Advanced Research Projects Agency (DARPA) through the Bioflips/Simbiosys Program, Mission Research Corporation/DARPA Contract No. DAAH01-02-C-R083 (B.K.), National Science Foundation, NSF-CTS-030799 (B.K. and A.A.), and the joint NSF/Sandia program (B.K.). D.B. thanks Sandia's MESA Institute and the NSF MAGNET/SEM program for support. Sandia is a multiprogram laboratory operated by Sandia Corporation, a Lockheed Martin Company, for the United States Department of Energy under Contract No. DE-ACO4-94-AL85000.

References

[1] (IOM) Institute of Medicine of the National Academies, Board on Health Sciences Policy, 1999, "Chemical and Biological Terrorism: Research and Development to Improve Civilian Medical Response," National Academy Press, Washington, DC, Chap. 6.

[2] TENG Solutions, 2002, "Protective Measures to Mitigate Chemical and Biological Threats for GSA Federal Buildings—Region 4," http://www.coa.gatech.edu/bc/research/, Georgia Institute of Technology, Atlanta GA.

[3] Chiem, N. H., and Harrison, D. J., 1998, "Microchip Systems for Immunoassay: An Integrated Immunoreactor With Electrophoretic Separation for Serum Theophylline Determination," Clin. Chem., **44**, pp. 591–598.

[4] Jiang, G., Attiya, S., Ocvirk, G., Lee, W. E., and Harrison, D. J., 2000, "Red Diode Laser Induced Fluorescence Detection With a Confocal Microscope on

a Microchip of Capillary Electrophoresis," Biosens. Bioelectron., **14**, pp. 861–869.
[5] Narang, U., Gauger, P. R., and Ligler, F. S., 1997, "A Displacement Flow Immunosensor for Explosive Detection Using Microcapillaries," Anal. Chem., **69**, pp. 2779–2785.
[6] Asami, K., 2002, "Characterization of Biological Cells by Dielectric Spectroscopy," J. Non-Cryst. Solids, **305**, pp. 268–277.
[7] Yang, L., Ruan, C., and Li, Y., 2003, "Detection of Viable *Salmonella Typhimurium* by Impedance Measurement of Electrode Capacitance and Medium Resistance," Biosens. Bioelectron., **19**, pp. 495–502.
[8] Gascoyne, P. R. C., Wang, X., Huang, Y., and Becker, F. F., 1997, "Dielectrophoretic Separation of Cancer Cells From Blood," IEEE Trans. Ind. Appl., **33**, pp. 670–678.
[9] Gascoyne, P. R. C., Satayavivad, J., and Ruchirawat, M., 2004, "Microfluidic Approaches to Malaria Detection," Acta Trop., **89**, pp. 357–369.
[10] Lapizco-Encinas, B. H., Simmons, B. A., Cummings, E. B., and Fintschenko, Y., 2004, "Insulator-Based Dielectrophoresis for the Selective Concentration and Separation of Live Bacteria in Water," Electrophoresis, **25**, pp. 1695–1704.
[11] Bennett, D. J., Khusid, B., Galambos, P. C., James, C. D., Okandan, M., Jacqmin, D., and Acrivos, A., 2003, "Field-Induced Dielectrophoresis and Phase Separation for Manipulating Particles in Microfluidics," Appl. Phys. Lett., **83**, pp. 4866–4868.
[12] Gascoyne, P. R. C., and Vykouval, J., 2002, "Particle Separation by Dielectrophoresis," Electrophoresis, **23**, pp. 1973–1983.
[13] Markarian, N., Yeksel, M., Khusid, B., Farmer, K., and Acrivos, A., 2003, "Particle Motions and Segregation in Dielectrophoretic Micro-Fluidics," J. Appl. Phys., **94**, pp. 4160–4169.
[14] Qiu, Z., Markarian, N., Khusid, B., and Acrivos, A., 2002, "Positive Dielectrophoresis and Heterogeneous Aggregation in High-Gradient AC Electric Fields," J. Appl. Phys., **92**, pp. 2829–2843.
[15] Dussaud, A. D., Khusid, B., and Acrivos, A., 2002, "Particle Segregation in Suspensions Subject to High-Gradient AC Electric Fields," J. Appl. Phys., **88**, pp. 5463–5473.
[16] Castellanos, A., Ramos, A., Gonzalez, A., Green, N. G., and Morgan, H., 2003, "Electrohydrodynamics and Dielectrophoresis in Microsystems: Scaling Laws," J. Phys. D, **36**, pp. 2584–2597.
[17] Halsey, T. C., 1992, "Electrorheological Fluids," Science, **258**, pp. 761–766.
[18] Kumar, A., Qiu, Z., Acrivos, A., Khusid, B., and Jacqmin, D., 2004, "Combined Negative Dielectrophoresis and Phase Separation in Nondilute Suspensions Subject to a High-Gradient AC Electric Field," Phys. Rev. E, **69**, 021402.
[19] Okandan, M., Galambos, P. C., Mani, S., and Jakubczak, J., 2001, "Development of Surface Micromachining Technologies for Microfluidics and BioMEMS," Proc. SPIE, **4560**, pp. 133–139.
[20] Laermer, F., and Schilp, A., 1996, "Method of Anisotropically Etching Silicon," U.S. Patent No. 5,501,893.
[21] Cui, L., Holmes, D., and Morgan, H., 2001, "The Dielectrophoretic Levitation and Separation of Latex Beads in Microchips," Electrophoresis, **22**, pp. 3893–3901.
[22] Ramos, A., Morgam, H., Green, N. G., and Castellanos, A., 1999, "AC Electric-Field-Induced Fluid Flow in Microelectrodes," J. Colloid Interface Sci., **217**, pp. 420–422.

Magnetorheological Jet (MR Jet™) Finishing Technology

William I. Kordonski
e-mail: kordonski@qedmrf.com

Aric B. Shorey

Marc Tricard

QED Technologies®, Inc.,
1040 University Avenue,
Rochester, NY 14607

Conformal (or freeform) and steep concave optics are important classes of optics that are difficult to finish using conventional techniques due to mechanical interferences and steep local slopes. One suitable way to polish these classes of optics is by using a jet of abrasive/fluid mixture. The energy required for polishing may be supplied by the radial spread of a liquid jet, which impinges a surface to be polished. Such fluid flow may generate sufficient surface shear stress to provide material removal in the regime of chemical mechanical polishing. Once translated into a polishing technique, this unique tool may resolve a challenging problem of finishing steep concave surfaces and cavities. A fundamental property of a fluid jet is that it begins to lose its coherence as the jet exits a nozzle. This is due to a combination of abruptly imposed longitudinal and lateral pressure gradients, surface tension forces, and aerodynamic disturbance. This results in instability of the flow over the impact zone and consequently polishing spot instability. To be utilized in deterministic high precision finishing of remote objects, a stable, relatively high-speed, low viscosity fluid jet, which remains collimated and coherent before it impinges the surface to be polished, is required. A method of jet stabilization has been proposed, developed, and demonstrated whereby the round jet of magnetorheological fluid is magnetized by an axial magnetic field when it flows out of the nozzle. It has been experimentally shown that a magnetically stabilized round jet of magnetorheological (MR) polishing fluid generates a reproducible material removal function (polishing spot) at a distance of several tens of centimeters from the nozzle. The interferometrically derived distribution of material removal for an axisymmetric MR Jet™ , which impinges normal to a plane glass surface, coincides well with the radial distribution of rate of work calculated using computational fluid dynamics (CFD) modeling. Polishing results support the assertion that the MR Jet finishing process may produce high precision surfaces on glass and single crystals. The technology is most attractive for the finishing of complex shapes like freeform optics, steep concaves, and cavities.
[DOI: 10.1115/1.2140802]

Keywords: optical, finishing, jet, magnetorheological (MR), polishing, sub-aperture

1 Introduction

In traditional polishing, particularly in chemo-mechanical polishing (CMP), material removal results from the polishing slurry particles' mechanical interaction with a chemically reacting workpiece surface, resulting in material removal on the atomic or molecular level [1]. For example, in glass polishing, the chemical activity of water lowers the energy needed to break the silicon-oxide bonds, whereas the mechanically activated abrasive particles perform work in removing the silica glass basic unit (silica tetrahedron), and transporting the debris away from the workpiece surface. Further, in this particular case, the rate of the bond-rupture reaction depends not only on chemical environment, but also on the magnitude of the applied mechanical stress [2]. Different methods are used to supply mechanical energy to the workpiece surface, thus providing a mechanical interaction between polishing particles and the workpiece surface to be polished [3]. Considerable recent attention has been focused on the techniques where such energy is supplied by fluid flow, which may generate sufficient surface stresses to provide material removal in the regime of CMP. The advantage of this approach lies in the fact that, in contrast to conventional "contact" polishing, the surface normal stress and the surface indentation are not dominant in the process of material removal. This results in the absence of a subsurface damaged layer.

In magnetorheological finishing (MRF®), the mechanical energy required for material removal over a portion of the workpiece surface is generated by the magnetically controlled hydrodynamic flow of a magnetorheological polishing fluid. A fundamental advantage of MRF over existing technologies is that this sub-aperture polishing tool conforms to the local surface shape and does not "wear" since the state of the recirculated fluid is continuously monitored and maintained, heat is removed, and polishing is done inside a stable magnetic field. MRF can produce surface accuracy on the order of 30 nm peak-to-valley (p-v) and surface micro-roughness less than 1 nm root mean square (rms) [4,5].

A method called "Hydroplane Polishing" is based on the phenomenon of hydrodynamic lubrication [6]. In this process, material removal is achieved by way of hydrodynamic flow of abrasive particle/fluid mixture. Multiple inclined surfaces are formed in a circumferential direction on a circular plate, which then rotates in fluid. Hydrodynamic pressure that is generated through the fluid wedge balances the normal load. The workpiece floats above the plate surface and is polished by the abrasive particles, which pass through the converging gap with the fluid.

A hydrodynamic principle is also used to provide high precision polishing in "Elastic Emission Machining" [7]. In this technique, a loaded elastic polyurethane ball polishes the workpiece as it scans over the part surface. The ball is rotated rapidly in a polishing fluid and, due to hydrodynamic forces, floats above the workpiece surface. The floating gap, which is created by an elasto-hydrodynamic lubrication state, is much larger than the diameter of the abrasive particles, but is still very small. The mechanism proposed for this process is an elastic bombardment of the surface by the polishing particles.

Previous work has shown that water jets can be used to polish materials such as glass, diamond, ceramics, stainless steel, and

Contributed by the Fluids Engineering Division of ASME for publication in the JOURNAL OF FLUIDS ENGINEERING. Manuscript received May 5, 2004; final manuscript received April 17, 2005. Assoc. Editor: Dennis Siginer.

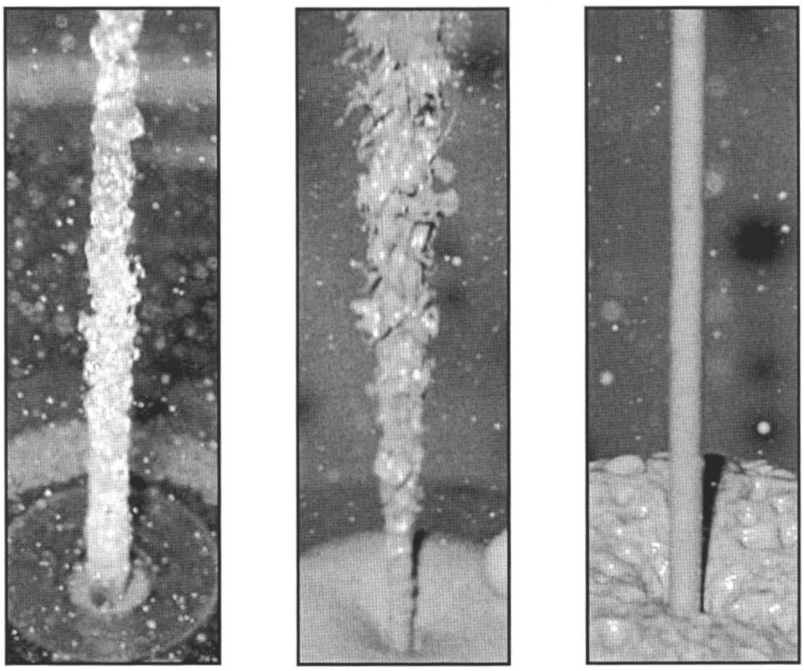

Fig. 1 Jet snapshot images (velocity=30 m/s, nozzle diameter=2 mm)

alloys [8]. The surface quality strongly depends on the size and impact angle of the abrasive grains. Surface roughness of Ra ~130 nm on glass has been achieved after processing. An appropriate adjustment of process parameters, such as jet velocity, abrasive size, and concentration makes reduction of surface roughness on glass to Ra=1.2 nm possible [9].

A fundamental property of a fluid jet is that it begins to lose its coherence as the jet exits a nozzle, due to a combination of abruptly imposed longitudinal and lateral pressure gradients, surface tension forces, and aerodynamic disturbances. The destabilizing aerodynamic disturbances are dramatically increased with jet velocity. This causes the high-speed liquid jet, which is the prime interest for finishing, to break into droplets and progressively spread out. For this reason, the diameter of a water jet used for cutting, for example, is very small to provide precision machining and high unit pressure. Also, a nozzle is situated as close to the work piece to be cut as is practically possible. Typically, such cutting jets contain abrasive particles with a high enough kinetic energy capable of sputtering (chipping) material away from the surface in the impact zone. Although a flow regime, where the jet can polish rather than cut, requires lower jet velocity, the problem of jet stability still persists. As this takes place, the jet irregularity increases progressively with the distance from the nozzle. That results in instability of the flow over the impact zone and consequently polishing spot instability, which is unacceptable for deterministic, high precision finishing. A reduction of jet velocity in order to obtain a coherent jet is impractical because it results in low impact energy, and therefore, low material removal rate. Increasing jet stability with fluid viscosity proportionally increases the resistance to fluid flow in the delivery system, and consequently, the pumping power required to deliver the fluid to the nozzle. It makes a high speed, high-viscosity jet impractical for polishing.

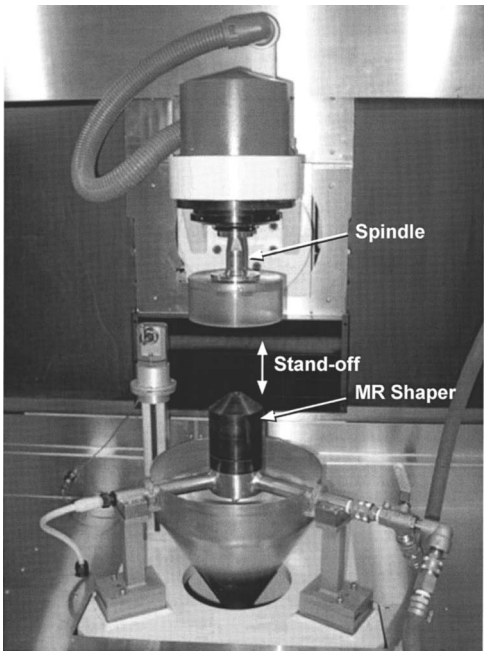

Fig. 2 Experimental setup

To be utilized in deterministic high precision finishing, a stable, relatively high-speed, low-viscosity fluid jet, which remains collimated and coherent before it impinges the surface, is required. Such a unique tool may also resolve a challenging problem of high precision finishing of steep concave surfaces and cavities.

2 Magnetorheological Jet (MR Jet^{TM}) Polishing

2.1 Jet Stabilization. In contrast to known jet polishing methods [8,9] where material removal relies on the kinetic energy of impacting abrasive particles, the technique discussed in this paper is based on an assumption that the energy required for the abrasive to provide polishing may be supplied by the radial spread of an abrasive liquid jet when it impinges upon the surface to be polished [10]. Such shear flow of abrasive slurry may result in material removal, which is characteristic to polishing. As was mentioned above, the liquid jet breaks down at a very short dis-

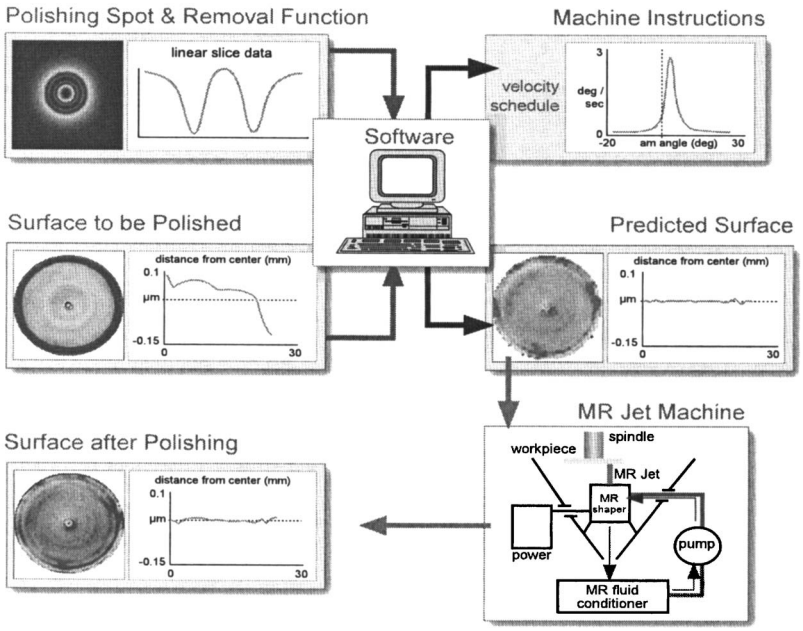

Fig. 3 MR Jet process flow diagram

tance from the nozzle (a few nozzle diameters) resulting in instability of the impinging flow, which in this case, is highly sensitive to the nozzle offset distance. As applied to polishing, this limits configurations where the removal function is stable resulting in significant restrictions on finishing of complex shapes.

A method of jet stabilization has been proposed, developed, and demonstrated, whereby the round jet of magnetorheological fluid, containing abrasive particles, is magnetized by an axial magnetic field when it flows out of the nozzle [10–12]. A local magnetic field induces longitudinal fibrillation and high apparent viscosity within the MR fluid [5]. In doing so, the application of the magnetic field adjacent to the nozzle results in suppression of all of the most dangerous initial disturbances. As a result, the MR fluid ejected from the nozzle defines a highly collimated, coherent jet. The stabilizing structure induced by the magnetic field within the jet gradually begins to decay while the jet passes beyond the field. However, remnant structure still suppresses disturbances and, thus, consequent stabilization of the MR Jet can persist for a sufficient time such that the jet may travel up to several meters (depending on the jet diameter) without significant spreading and loss of structure.

In the case of water, the jet remains stable only for ~2 nozzle diameters (transparent section of the jet at the outlet). MR fluid

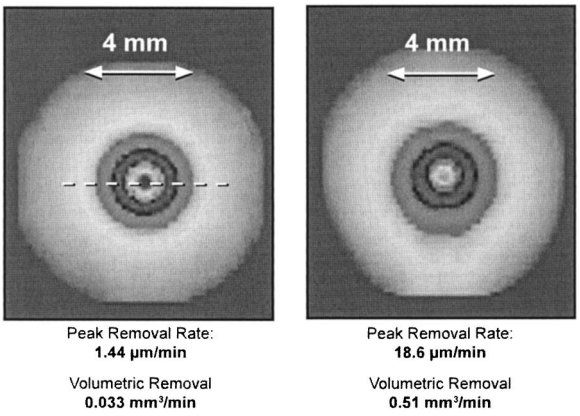

Fig. 4 Example of spots taken on fused silica glass at different jet velocities. The dashed white line gives the orientation of the profile shown in Fig. 5.

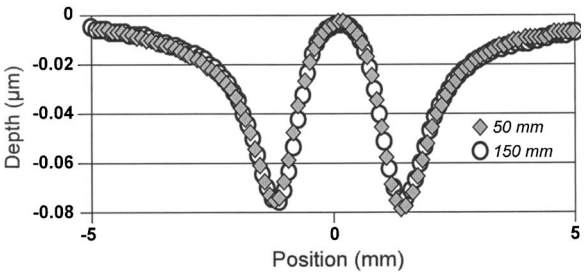

Fig. 5 MR Jet spot profiles of spots taken with a stand-off distance of 50 mm (filled makers) and 150 mm (open markers)

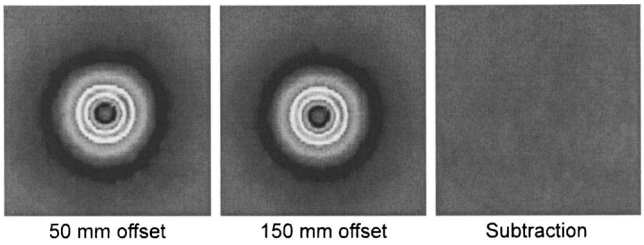

Fig. 6 Subtraction of the full material removal maps (spots) from Fig. 5 showing insensitivity to stand-off distances

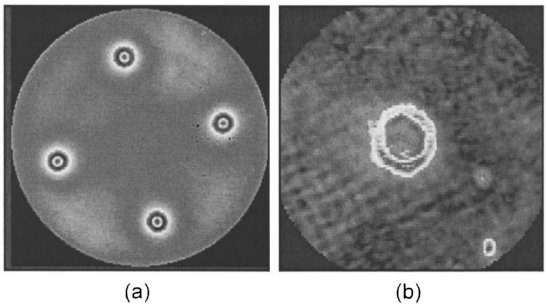

Fig. 7 (*a*) Image showing four 100 nm deep spots taken in succession; (*b*) standard deviation map of the four spots with a peak-to-valley of 4.2 nm

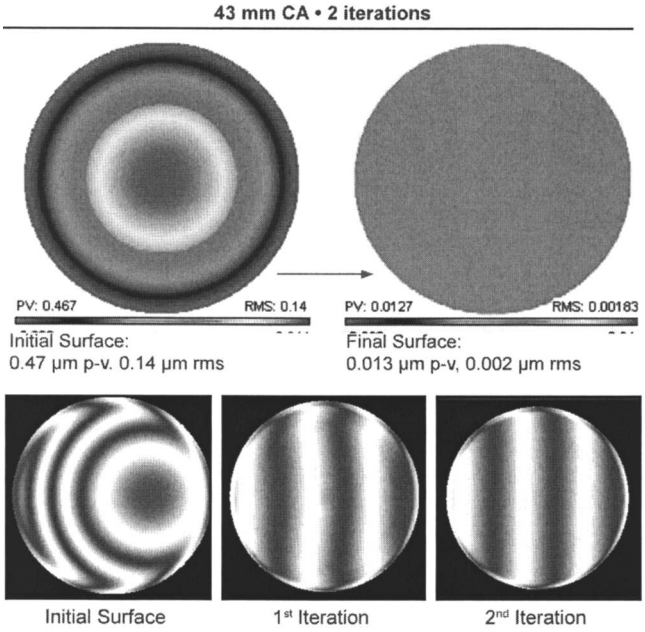

Fig. 8 Demonstration of ability to correct figure to extremely high precision with good convergence rate using MR Jet

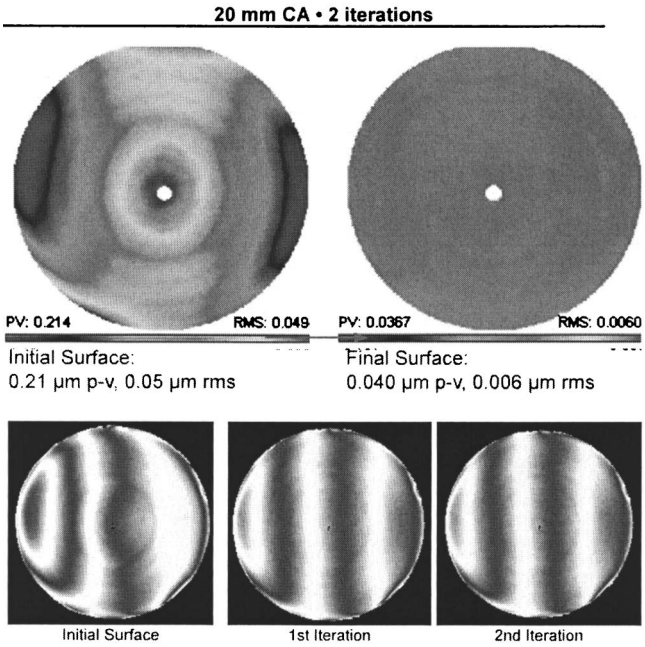

Fig. 11 Polishing results using the MR Jet system for the ogive shown in Fig. 9. Before MR Jet polishing, the p-v was 210 nm and the rms was 50 nm; after, the p-v was reduced by 5× and the rms by 8× to 44 nm and 6 nm, respectively.

has higher viscosity and therefore the coherent portion of the jet extends on ~7–8 diameters (see Fig. 1). Initial disturbances (visible in the form of ripples on the surface of the coherent part of the jet) eventually result in the jet breakdown and rapid spreading. Magnetized at the outlet, the jet of MR fluid remains coherent for more than 200 diameters. The MR fluid jets shown in Fig. 1 have the same fluid viscosity and jet velocity. This means that with the magnet off, the viscosity is too low and the velocity is too high to provide a stable jet of fluid. With the magnet on, the same low-viscosity, high-velocity jet of MR fluid is stabilized by the application of the magnetic field.

2.2 Experimental Setup. An MR Jet polishing system, a portion of which is shown in Fig. 2, has been constructed using a 5-axis CNC platform and polishing control software developed by

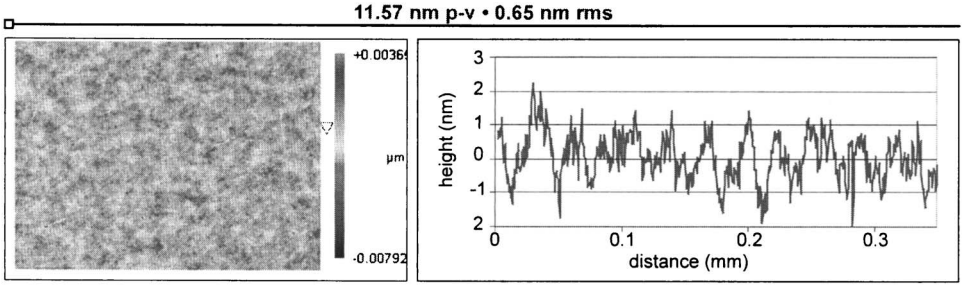

Fig. 9 Roughness map of a fused silica surface polished with MR Jet (NewView 5000 White Light Interferometer, 20× magnification)

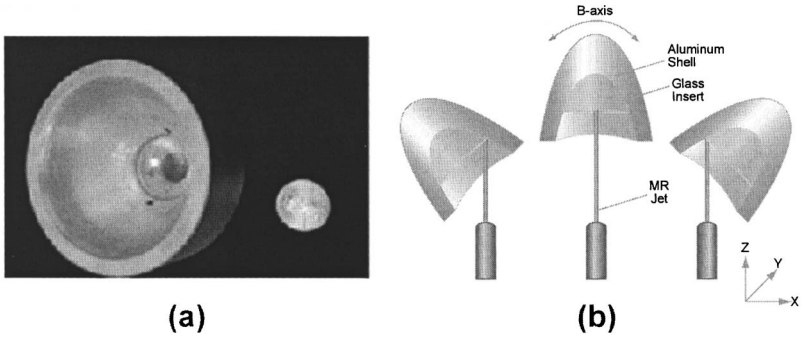

Fig. 10 (*a*) Photograph of a concave ogive, showing the glass insert at the center of an aluminum body, and (*b*) schematic of the ogive during polishing—the internal surface is kept normal to the impinging jet. The diameter of the aluminum shell is 58 mm and the total sag of the ogive surface is 39 mm.

QED Technologies®. The finishing process flow diagram is shown in Fig. 3. A computer code generates the machine control programs for polishing. Inputs to this code are the material removal spot (Fig. 4) and the initial surface figure. Outputs are the machine program (instructions in the form of velocity schedule) and a prediction of the final surface figure. The PC based software uses a series of complex algorithms, and convolves the removal function with the error function to derive an operating program for the CNC machine. The code specifies angles and velocities (dwell time) for the controller, the number of sweeps required between positive and negative angles, and the total estimated processing time. The CNC platform then carries out these motion instructions and executes the dwell schedule prescribed by the software as the workpiece is moved through the polishing zone.

The machine delivery system is comprised of a mixing vessel to disperse the solids in the MR fluid, a pump, means to maintain temperature and viscosity of the fluid, as well as pressure and flow sensors to monitor the system conditions. A MR shaper that uses the properties of the MR fluid and a magnetic field to stabilize the MR Jet is located beneath the spindle of the CNC platform. With the magnet activated, a collimated jet is directed vertically upwards to the part held by the spindle. Finally, means have been implemented to contain, collect, and recirculate the MR fluid after it impinges upon the part surface.

2.3 Removal Function. Typical MR Jet removal functions (or polishing "spots") are shown in Fig. 4. These two spots were taken at different jet velocities by dwelling the 1.5 mm diameter jet upon the stationary flat fused silica surface for a prescribed period of time. The distance between the nozzle exit and the part surface (the stand-off distance) was 50 mm for both. The spot on the left had a moderate fluid jet velocity giving a peak removal rate of 1.44 m/min and volumetric removal rate of 0.033 mm^3/min. The spot on the right was created with an identical setup; only a more aggressive jet velocity was used giving a peak removal rate of 18.6 m/min and volumetric removal rate of 0.51 mm^3/min. This demonstrates the ability to adjust material removal rate by more than an order of magnitude using the same setup. It is possible to vary removal rate further with appropriate system adjustments. The dashed white line in Fig. 4 shows the orientation of the profile shown in Fig. 5. Notice from this figure that there is no removal in the center of the spot. This is because the material removal is due to shear flow, which is zero at the center. This will be discussed in greater detail in later sections.

The stability of the removal function is demonstrated in Figs. 5 and 6. Figure 5 shows removal function profiles (the scan along the spot diameter) typical for MR Jet polishing spots. The two spot profiles given in this figure were taken with two different stand-off distances (the distance between the part surface and the nozzle exit, as shown in Fig. 2). The two distances were 50 mm (filled markers) and 150 mm (open markers) resulting in the same spot profile as shown in the figure. This is further emphasized in Fig. 6, where the maps of the material removal distribution are subtracted. The maximum variation in these removal maps is only 6.5%, even though the separation between the part and the nozzle changes by 100 mm. This quality is particularly important when considering precision finishing of steep concave (or freeform) optics.

Polishing spot stability is the most important characteristic required for high precision deterministic finishing. Evaluation of MR Jet polishing spot stability was performed as follows. Four spots were taken in succession at different locations on the same premeasured part (see Fig. 7(*a*)). The variance between the four spots (the standard deviation) is shown in Fig. 7(*b*). The error in this map is only 4.2 nm p-v and 0.54 nm rms, for 100 nm deep spots. These results demonstrate an exceptional MR Jet removal function, stability, and versatility, making it a valuable tool for high precision finishing of complex surfaces.

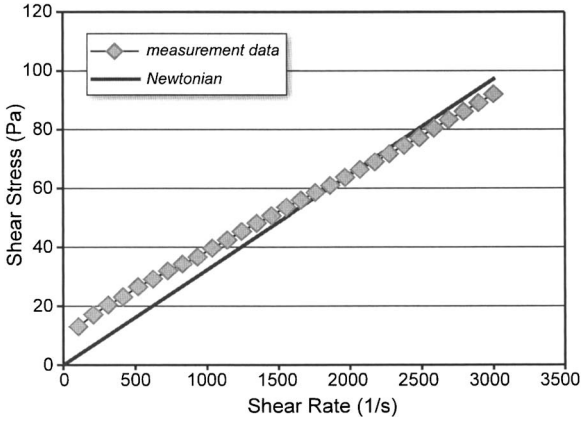

Fig. 12 Flow curve of an MR fluid outside of the magnetic field

2.4 Polishing Performance.

2.4.1 Flats. Given the stable spot, QED control software, and CNC control, MR Jet can be used to accurately correct surface figures. Figure 8 shows the results of polishing a flat fused silica part with 470 nm p-v of primarily power error. The error was reduced to 32 nm p-v in a single iteration, and as low as 13 nm p-v after the second iteration. Furthermore, the MR Jet process has regularly demonstrated the ability to achieve roughness values much better than 1 nm rms. Figure 9 shows an example of one of these roughness maps of fused silica glass and an accompanying profile plot.

2.4.2 Conformal Optics. The unique qualities of the MR Jet process enable the manufacture of conformal optics. This important class of optics is made up of designs, such as domes and other steep concaves, where the shape of the optic is driven by such considerations as the aerodynamic requirements instead of the optical requirements. Since the optics have to work in transmission, the internal concave surface must be polished as well as the external surface. This is a challenging problem for most polishing processes because of the deep sag of these surfaces. MR Jet offers a solution to reach into the center and correct this internal surface figure, as demonstrated above by the insensitivity to stand-off distance.

A small concave glass insert was placed inside an aluminum shell that approximates a missile nose cone ogive (Fig. 10(*a*)). The radius of the concave surface was 20 mm and the diameter was 23 mm. The part was polished in a rotational mode, rotating on axis and sweeping around its center of curvature to keep the jet normal to the optical surface (Fig. 10(*b*)). Excellent polishing results were obtained. Figure 11 shows the figure error of the concave surface before and after MR Jet. Both the symmetric and

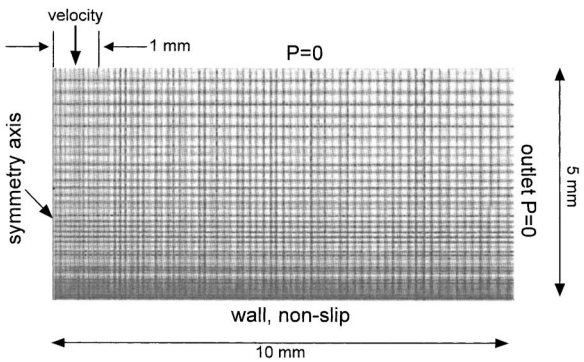

Fig. 13 Theoretical and experimental removal rate and rate of work profiles

asymmetric errors were corrected, leaving a peak-to-valley error of less than 50 nm (a 5× improvement from the initial conditions). In addition, the rms error was improved by more than 8× (0.05 mm to 0.006 mm).

3 Model Validation

3.1 Theoretical Considerations. The proposed model of jet polishing assumes that the energy for abrasive particles/surface mechanical interaction is provided by the radial laminar flow, which occurs as a result of impingement of the coherent liquid column with the surface. Also, the process of material removal is considered in the context of the fundamental Preston's statement that "the rate of polishing of the glass (that is, the rate at which material is removed) is proportional to the rate at which work is done on each unit area of the glass" [13].

To put it another way,

$$\dot{R} \sim \dot{W} \tag{1}$$

where $\dot{R}$ is the material removal rate and $\dot{W}$ is the rate of work done at the surface.

Generally, the rate of work done by the fluid at the control surface is [14]

$$\dot{W} = -\int_S \vec{F} \cdot \vec{V} dA \tag{2}$$

where $\vec{F}$ is the vector fluid stress applied to the element dA of the control surface and $\vec{V}$ is the vector fluid velocity. The fluid stress can be divided into components perpendicular to dA and in the plane of dA,

$$\vec{F} = \vec{s}_n + \vec{\tau}_x \tag{3}$$

where $\vec{s}_n$ is the normal stress and $\vec{\tau}_x$ is the shear stress. These considerations imply that $\dot{W}$ can be expanded as follows:

$$\dot{W} = -\int_S \vec{\tau}_x \cdot \vec{V} dA - \int_S \vec{s}_n \cdot \vec{V} dA \tag{4}$$

The fluid shear stress can arise only from viscosity, whereas the normal stress can result from both pressure and viscosity. However, in the case under consideration when there is no normal fluid velocity component at the surface, $\vec{s}_n$ will be dominated by the compressive stress of fluid pressure:

$$\vec{s}_n = -p\hat{n}, \quad \text{but} \quad \vec{s}_n \cdot \vec{V} = 0 \tag{5}$$

where p is the fluid hydrostatic pressure and $\hat{n}$ is the normal to the surface. The rate of work at the surface then becomes

$$\dot{W} = -\int_S \vec{\tau}_x \cdot \vec{V} dA \tag{6}$$

For the one-dimensional radial flow, which takes place in the case under consideration, the local rate of the work done at the surface will be

$$\dot{W}_r = \tau_r V_r \tag{7}$$

where τ_r is local shear stress and V_r is local fluid velocity.

From Eqs. (1) and (7), it follows that the local removal rate is proportional to the local shear stress times local fluid velocity

$$\dot{R}_r \sim \tau_r V_r \tag{8}$$

As expected, the same qualitative result follows from Preston's classical expression:

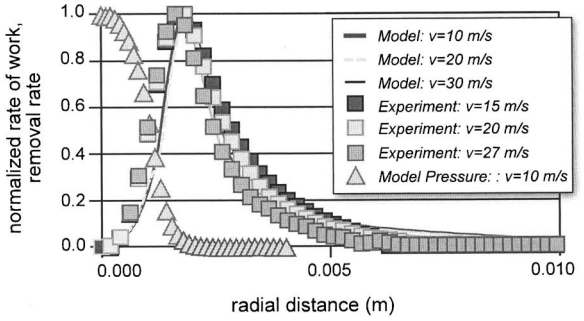

Fig. 14 Theoretical and experimental removal rate and rate of work profiles; *v*=jet velocity

$$\dot{R} = kPU = k\frac{L}{S}U = k\frac{F}{\mu S}U = k\frac{\tau U}{\mu} = k\frac{\dot{W}}{\mu} \tag{9}$$

where L is the normal load, S is the surface area on which wear occurs, F is the frictional force between the glass and the polishing lap, μ is the coefficient of friction, τ is the surface shear stress, $\dot{W}$ is the rate of work done per unit area (the power input) and k is the Preston coefficient, which is process-dependent and combines surface chemistry, abrasion effects, and specifics of part-polisher interaction.

3.2 Model Verification. An effort was made to find the correlation between the experimental removal function and the theoretical model described above. A normalized experimental radial removal rate profile was compared with the normalized radial distribution of the rate of work done at the surface calculated using a commercially available CFD package [15]. Due to the fact that the MR fluid is not affected by the magnetic field at the impingement zone, an assumption is made that it can be modeled as a Newtonian fluid. This assumption is validated by Fig. 12, which shows the flow curve of an MR fluid in the absence of the magnetic field. The small deviation from Newtonian behavior at low shear rate can be ignored for the flow regime considered in this model.

The two-dimensional solution was found using the free surface volume of fluid (VOF) method and laminar flow was assumed (the Reynold's number of the jet varies from 1500 to 9000, and that of the radial flow varied from 500 to 3000). In addition, some considerations were given to the time step and mesh size so that an accurate and stable solution could be achieved in a reasonable amount of time. That is, there needs to be sufficient elements across the boundary layer to calculate the flow, and the time step must be adjusted as the mesh is refined so that the calculation remains stable. However, the time step cannot be so small that it is cost prohibitive with respect to calculation time. The model setup used is shown in Fig. 13. Important parameters used for the calculation are as follows:

- The jet radius=0.8–1.2 mm
- Mesh area=5 mm high (parallel to jet), 10 mm wide (parallel to workpiece surface)
- Vertical mesh size: ratio of 1.05, cell height=41 μm at wall, to 280 μm at "top" (at the inlet)
- Horizontal mesh size: inside jet=100 μm uniform width, outside jet: ratio=1.0075, minimum cell width =120 μm, maximum cell width=185 μm.

The evaluation of accuracy was based on the magnitude of the velocity at the stagnation point, where it should be equal to zero. An error of less than 1% was achieved.

Results of the flow modeling are shown in Fig. 14. Experimental data for removal rate (square markers) were taken at three jet velocities (15, 20, and 27 m/s) with a jet diameter of 2.4 mm. The

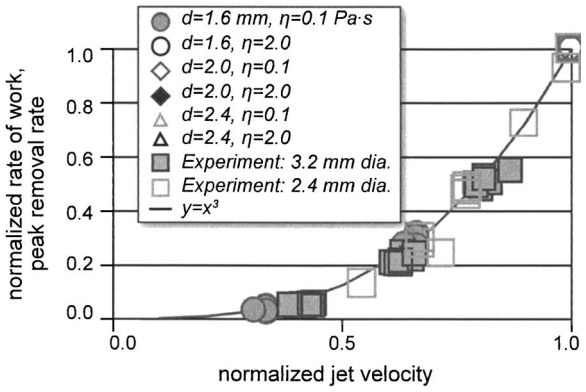

Fig. 15 Peak material removal rate versus jet velocity; *d* =diameter (mm), η=dynamic viscosity (Pa·s)

lines in Fig. 14 represent the radial distribution of the computed rate of the work done at the surface under similar conditions. The triangles show the calculated pressure profile. Note that this plot represents half of the removal profile shown in Fig. 5. Good correlation is observed between the removal rate profile and distribution of the rate of work done at the surface providing strong support for the model presented above. It is also worth noting that the position of the peak removal rate corresponds to the position of minimum pressure, whereas no removal occurs at maximum pressure. It means that the normal stress does not contribute in material removal as the model suggests. This gives strong support to our assertion that the shear mode is indeed responsible for material removal. In Fig. 15, the normalized experimental peak of removal rate (squares) and calculated normalized local rate of work at the position of peak removal are plotted against the jet velocity. The experiments were done with a viscosity of 0.05 Pa·s, and two different nozzle diameters. Again, there is a good correlation between the predicted and experimental results, in spite of the fact that calculations were done for different nozzle diameters and fluid viscosities. According to Fig. 15, the cubic dependence of removal rate on jet velocity prevails (solid line).

4 Summary

It has been demonstrated that impingement of a magnetically stabilized, collimated jet of MR fluid induces radial surface flow, which results in generation of the polishing spot. In numerous experiments with different process parameters (jet velocities, nozzle diameters, and fluid viscosity) it was shown that material removal in the polishing spot closely correlates with the computed rate of work done at the surface by the fluid. This agrees with the fundamental basis of Preston's model. It was also established that MR Jet finishing can produce high precision surfaces on the order of tens of nanometers p-v with roughness <1 nm rms. Due to insensitivity to the offset distance, this technique may be valuable in finishing complex shapes, especially those with steep concaves and parts with a variety of cavities.

Acknowledgment

The authors appreciate support from Don Golini, Arpad Sekeres, and other colleagues at QED Technologies. In addition, the authors acknowledge the contributions of Professor Sheryl Gracewski from University of Rochester's Department of Mechanical Engineering and Center for Optics Manufacturing. Portions of the research reported in this presentation were performed in connection with Contract/instrument No. DAAD17-03-C-0055 with the U.S. Army Research Laboratory. The views and conclusions contained in this document/presentation are those of the authors and should not be interpreted as presenting the official policies or position, either expressed or implied, of the U.S. Army Research Laboratory or the U.S. Government unless so designated by other authorized documents.

References

[1] Cook, L. M., 1990, "Chemical Processes in Glass Polishing," J. Non-Cryst. Solids, **120**, pp. 152–171.
[2] Agarwal, A., Tomozawa, M., and Lanford, W. A., 1994, "Effect of Stress on Water Diffusion in Silica Glass at Various Temperatures," J. Non-Cryst. Solids, **167**, pp. 139–148.
[3] Evans, C. J., Paul, E., Dornfield, D., Lucca, D. A., Byrne, G., Tricard, M., Klocke, F., Dambon, O., and Mullany, B. A., 2003, "Material Removal Mechanisms in Lapping and Polishing," CIRP Ann., **52**(2), pp. 611–633.
[4] Golini, D., Jacobs, S., Kordonski, W., and Dumas, P., 1997, "Precision Optics Fabrication Using Magnetorheological Finishing," *Advanced Materials for Optics and Precision Structures*, SPIE Proc., CR67-16, pp. 251–273.
[5] Golini, D., Jacobs, S., Kordonski, W., and Dumas, P., "Precision Optics Finishing Using Magnetorheological Finishing," *Optical Manufacturing and Testing Conference II*, SPIE Proc., SPIE Annual Meeting, San Diego, CA.
[6] Gormley, J., Manfra, M., and Calawa, A., 1991, "Hydroplane Polishing of Semiconductor Crystals," Rev. Sci. Instrum., **52**(8), pp. 1256–1259.
[7] Mori, Y., Yamauchi, K., and Endo, K., 1988, "Mechanism of Atomic Removal in Elastic Emission Machining," Stud. Cerc. Mat., **10**(1), pp. 24–28.
[8] Momber, A., and Kovacevic, R., 1998, *Principles of Abrasive Water Jet Machining*, Springer, New York, Chap. 9.6.
[9] Booij, S., Hedser van Brug, B. J., and Fahnle, O., 2002, "Nanometer Deep Shaping With Fluid Jet Polishing," Opt. Eng., **41**(8), pp. 1926–1931.
[10] Kordonski, W., Shorey, A., and Sekeres, A., 2004, "New Magnetically Assisted: Material Removal With Magnetorheological Fluid Jet," Proc. SPIE, **5180**, 107–114.
[11] Kordonski, W., Golini, D., Hogan, S., and Sekeres, A., 1999, "System for Abrasive Jet Shaping and Polishing of Surface Using Magnetorheological Fluid," U.S. Patent No. 5,971,835.
[12] Kordonski, W., 1984, "Apparatus and Method for Abrasive Jet Finishing of Deeply Concave Surfaces Using Magnetorheological Fluid," U.S. Patent No. 6,561,874.
[13] Preston, F. W., 1927, "The Theory and Design of Plate Glass Polishing Machines," J. Soc. Glass Technol., **11**, pp. 214–256.
[14] Blevins, R. D., 1984, *Applied Fluid Dynamics Handbook*, Van Nostrand Reinhold Co., Inc., New York.
[15] Fluent, Flow Modeling Software, Version 6, Fluent Inc., Lebanon, NH.

Plane Poiseuille Flow of Two Compatible Polymers: Influence of the Interphase on the Flow Stability

François Rousset

Patrick Bourgin

Liviu-Iulian Palade

Laboratoire de Recherche
Pluridisciplinaire en Plasturgie,
Site de Plasturgie de l'INSA de Lyon,
BP 807-01108 Oyonnax Cedex, France

This paper deals with coextrusion flows of two compatible polymers which are known to be generally more stable than the same flows of incompatible systems. We show that the weak response to disturbance of such flows can be predicted by considering an interphase of nonzero thickness (corresponding to an interdiffusion zone) instead of a purely geometrical interface between the two layers. As a first step we try to explain the weak sensibility to disturbance of compatible systems by the sole presence of this intermediate layer. For that purpose we study the linear stability response to very long waves of a three-layer phase Poiseuille flow with an inner thin layer which represents the interphase. Although this fact is an approximation, it nevertheless takes into account the diffusion phenomena which are generated in the interphase. This first approach (corresponding to a reduction in the effective viscosity ratio) is shown to explain the diminished growth rates but not the reduction in the size of the unstable region. As a second step, we formulate an energetic approach of the problem. We evaluate the energy dissipated during the interdiffusion process and the variation of kinetic energy of the global system. A modified growth rate is then determined by taking into account the energy dissipated by the interdiffusion process. This lower growth rate enables us to explain the increase of the stable domain in the case of compatible polymeric systems. [DOI: 10.1115/1.2136931]

1 Introduction

Coextrusion is an industrial process used to form multilayered sheets or films. Each layer of these composite materials provides a specific end-use characteristic, such as optical, mechanical, and barrier properties. Final products suit a large range of applications from food packaging to reflective polarizers. It has been found that under certain operating conditions, wavy interfaces are observed that originate inside the die. This interfacial instability is detrimental to the quality of the final product.

Yih [1] first studied the stability of Poiseuille flows of two Newtonian fluids submitted to very long waves. Using linear stability theory he showed that a viscosity difference could lead to instability, even for low Reynolds numbers. His analysis was extended by numerous authors to other shearing flows. Indeed, many studies have been devoted to this topic. Therefore it is not possible to give an exhaustive survey of the existing literature. We shall quickly list some works of close relevance to the present paper. For example let us mention the asymptotic methods developed by Hooper [2], Hooper and Boyd [3], or Yiantsios and Higgins [4]. Numerical solutions were proposed by Anturkar et al. [5,6]. A global overview of theoretical results is proposed by Joseph and Renardy [7]. Several authors carried out stability experiments mainly on polymeric liquids: Han [8], Khan and Han [9], Karagiannis [10], and White et al. [11]. All these investigations show that the interfacial stability of multilayer flows is determined by a number of factors including thickness, viscosity, density, elasticity ratios, and interfacial tensions. One notes that all these works have in common to consider flows of immiscible fluids.

Very comprehensive experiments have been carried out by Wilson and Khomami on both miscible and immiscible fluids [12–14]. Their facility made use of a system for introducing temporally regular disturbances with a controllable amplitude and frequency. The authors first investigated flows of immiscible fluids. They found that theoretically predicted growth rates agree with their experimental data. Then, they considered a superposed plane Poiseuille flow of a compatible polymer system. In such a system, there is a null interfacial tension and polymer chains diffuse across the original interface, forming a diffuse interface (i.e., an interphase). In this case growth rates have been found to be much lower than those obtained for incompatible systems and for classical theoretical studies. The authors proposed two mechanisms to explain this weak sensibility to disturbances. According to them, the "oscillatory flow in the vicinity of the interface enhances the mixing and diffusion process near the interface which in turn reduces the effective viscosity ratio and removes energy from the growing interfacial wave. It is this reduction in the effective viscosity ratio and the removal of wave energy which are responsible for the diminished growth rates and the reduction in the size of the unstable region."

The aim of this paper is to examine the contribution of the mechanisms proposed by Wilson and Khomami. As a first step we study the influence of the reduction in the effective viscosity ratio. For so doing, we consider the linear stability of a three-layer plane Poiseuille flow with an inner thin layer in which viscosity is intermediate between the ones of the two outer layers. As a second step, we examine the consequences of the removal of wave energy due to the interdiffusion process. In this section, energetic aspects of the formation of the interphase are taken into account in the stability analysis.

2 Mechanical Approach

2.1 Governing Equations. In this section we want to determine whether the sole presence of an inner thin layer is able to influence the stability of the flow of a compatible polymeric system. For so doing, we consider a three-layer Poiseuille flow (in which layers 1, 2, and 3 are occupied respectively by polymer A, the interphase, and polymer B) through an infinite parallel plate

Contributed by the Fluids Engineering Division of ASME for publication in the JOURNAL OF FLUIDS ENGINEERING. Manuscript received July 8, 2004; final manuscript received September 21, 2005. Assoc. Editor: Dennis Siginer.

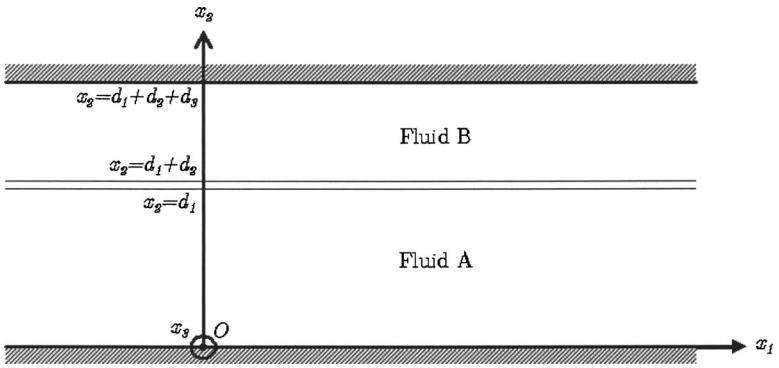

Fig. 1 Definition sketch

channel geometry, as shown in Fig. 1.

Each fluid is supposed to be incompressible and Newtonian. Thus, in each layer $k(k=1,2,3)$, the governing equations are the incompressibility and the Navier-Stokes equations. Let us note that in this model, the viscosity μ_2 and the thickness d_2 of the interphase are neither a function of time nor of space variables. In this section we consider indeed that the interphase is already formed. Moreover, the density is assumed to be the same in each layer as the effect of gravity is not studied. Thus, the equations of the problem are in each layer

$$\begin{aligned} \underline{\nabla} \cdot \underline{u}_k &= 0 \\ \rho \frac{D\underline{u}_k}{Dt} &= -\underline{\nabla} p + \mu_k \Delta \underline{u}_k \end{aligned} \tag{1}$$

where p is the pressure, ρ is the density, and the material derivative is defined by

$$D/Dt = \partial/\partial t + (\underline{u} \cdot \underline{\nabla})$$

This system is completed by the no-slip boundary condition and the continuity conditions at the interfaces on velocity and stress tensor (written here in the case of a null surface tension between the layers):

$$\begin{aligned} &\forall x_1 \in \mathbf{R}, \quad \underline{u}_1|_{x_2=0} = \underline{u}_2|_{x_2=d_1+d_2+d_3} = \underline{0} \\ &[\underline{u}]_{1,2} = \underline{0} \\ &[\underline{\sigma} \cdot \underline{n}]_{1,2} = \underline{0} \end{aligned} \tag{2}$$

Dimensionless equations are then written by using the following dimensionless variables for space, velocity, time, pressure and stress:

$$\hat{x}_j = \frac{x_j}{d_{tot}}, \quad \hat{\underline{u}}_k = \frac{\underline{u}_k}{V}, \quad \hat{t} = \frac{tV}{d_{tot}}, \quad \hat{p} = \frac{p}{\rho V^2}, \quad \hat{\underline{\sigma}} = \frac{1}{\rho V^2}\underline{\sigma}$$

where circumflex accents over variables denote dimensionless variables. Moreover, d_{tot} is defined as the total height of the flow and V (given in Appendix A) as an average velocity:

$$\begin{aligned} d_{tot} &= d_1 + d_2 + d_3 \\ V &= \frac{1}{d_{tot}} \int_{l_k} u_{l,k} dx_2 \end{aligned} \tag{3}$$

in which l_k is the thickness of the domain occupied by fluid k. Thickness ratios, viscosity ratios and Reynolds number are scaled with respect to layer 1:

$$\varepsilon_k = \frac{d_k}{d_1}, \quad m_k = \frac{\mu_k}{\mu_1}, \quad \mathrm{Re} = \frac{\rho V d_{tot}}{\mu_1}$$

Finally, the dimensionless equations in fluid k read as follows:

$$\begin{aligned} \hat{\underline{\nabla}} \cdot \hat{\underline{u}}_k &= 0 \\ \frac{\hat{D}\hat{\underline{u}}_k}{\hat{D}\hat{t}} &= -\hat{\underline{\nabla}} \hat{p} + \frac{m_k}{\mathrm{Re}} \hat{\Delta} \hat{\underline{u}}_k \end{aligned} \tag{4}$$

where new operators are defined with dimensionless variables. The boundary conditions are

$$\begin{aligned} &\forall \hat{x}_1 \in \mathbf{R}, \quad \hat{\underline{u}}_1|_{\hat{x}_2=0} = \hat{\underline{u}}_2|_{\hat{x}_2=1} = \underline{0} \\ &[\hat{\underline{u}}]_{1,2} = \underline{0}, \quad [\hat{\underline{\sigma}} \cdot n]_{1,2} = \underline{0} \end{aligned} \tag{5}$$

In the following, we shall omit accents over dimensionless variables.

2.2 Primary Flow. The undisturbed flow (or primary flow) is a channel flow with parabolic velocity profiles:

$$\bar{u}_{l,k} = A_{0k} + A_{1k} x_2 + A_{2k} x_2^2 \tag{6}$$

where bars over variables correspond to undisturbed variables. The constants A_{jk} (given in Appendix A) involve viscosity and thickness ratios.

2.3 Perturbation Flow. An infinitesimal disturbance is applied to the primary flow to study the stability of the interphase. The motion is resolved into the primary motion and the perturbation motion:

$$\begin{aligned} u_{j,k} &= \bar{u}_{j,k} + \tilde{u}_{j,k} \\ p &= \bar{p} + \tilde{p} \end{aligned} \tag{7}$$

where tildes over variables correspond to disturbed variables. In our stability analysis we assume the validity of Squire's theorem [15] (see also [16]), namely the two-dimensional disturbances are more unstable than three-dimensional ones, and therefore we consider two-dimensional disturbances. The customary representation of the velocity components (expressed in terms of a stream function) and the disturbed pressures in the linear stability analysis has an exponential form:

$$\begin{aligned} \hat{\psi}_k(x_1,x_2,t) &= \phi_k(x_2) e^{i\alpha(x_1-ct)} \\ \tilde{p}(x_1,x_2,t) &= f(x_2) e^{i\alpha(x_1-ct)} \end{aligned} \tag{8}$$

where α is the (real) wave number and c is the complex velocity of the disturbance. By substituting the perturbed variables into the motion equations, one obtains the Orr-Sommerfeld equations for each layer k:

$$\phi_k^{IV} - 2\alpha^2\phi_k'' + \alpha^4\phi = i\alpha\frac{\mathrm{Re}}{m_k}[(\phi_k'' - \alpha^2\phi_k)(\bar{u}_{1,k} - c) - \bar{u}_{1,k}''\phi_k] \quad (9)$$

where the derivatives with respect to x_2 are denoted by primes. The interfacial boundary conditions need to be evaluated at the disturbed locations of the interfaces. These interfacial conditions about the steady-state interfacial positions are then expressed through Taylor series. The latter and the no-slip conditions at the walls give rise to the following set of boundary conditions: *No slip at the walls*

$$\phi_1(0) = \phi_1'(0) = 0$$
$$\phi_3(1) = \phi_3'(1) = 0 \quad (10)$$

Continuity of $u_{1,k}$ at the interfaces (evaluated at $x_2 = d_1$ and d_2 for $k = 1$ and 2)

$$\phi_k' - \phi_{k+1}' = \frac{\phi_k}{c - \bar{u}_{1,k}}(A_{1,k} - A_{1,k+1}) \quad (11)$$

Continuity of $u_{2,k}$ at the interfaces

$$\phi_k = \phi_{k+1} \quad (12)$$

Continuity of shear stress at the interfaces

$$\left(\frac{d^2}{dx_2^2} + \alpha^2\right)(m_k\phi_k - m_{k+1}\phi_{k+1}) = 0 \quad (13)$$

Continuity of normal stress at the interfaces

$$\left(\frac{d^3}{dx_2^3} - 3\alpha^2\frac{d}{dx_2}\right)(m_k\phi_k - m_{k+1}\phi_{k+1}) = 0 \quad (14)$$

The Orr-Sommerfeld equations, the boundary conditions, and the interfacial conditions form an eigenvalue problem, which may admit several eigenvalues c and the corresponding eigenfunctions ϕ_k. Such a problem can be solved numerically (as it is the case for example in [6]). However, in the present work we obtain an analytical solution as a first step by using a nonsingular perturbation for α in the vicinity of 0. This corresponds to the case of very long waves, which is relevant for particle applications. Hence, the eigenfunctions and the eigenvalues are expanded as a regular perturbation series of α as follows:

$$\phi_k = \phi_{k,0} + \alpha\phi_{k,1} + O(\alpha^2)$$
$$c = c_0 + \alpha c_1 + O(\alpha^2) \quad (15)$$

The calculation leads to two zeroth-order eigenvalues, $c_{0,a}$ and $c_{0,b}$ (given in appendix B), which are found to be real and correspond to the amplification factors of waves. These two-phase velocities give two possible modes of wave motion. We must then determine the first-order solutions, as the stability of the flow is determined by the sign of the imaginary part of c (the flow is respectively stable, unstable, or neutrally stable according to whether c_i is negative, positive, or zero). We obtain two first-order eigenvalues which are purely imaginary. Therefore, the stability conditions are determined by the signs of $c_{1,a}$ and $c_{1,b}$. We now have to take into account the fact that d_2 (i.e., thickness of the inner layer) is negligible as compared to d_1 and d_3. Thus the two eigenvalues are expanded and approximated by the following Taylor series:

$$c_{1,a} = i\,\mathrm{Re}\,J_{1,a} + O(d_2)$$
$$c_{1,b} = i\,\mathrm{Re}\,J_{1,b}(d_2^2) + O(d_2^3) \quad (16)$$

where $J_{1,a}$ and $J_{1,b}$ are functions of thickness and viscosity ratios which result from straightforward but cumbersome calculations. For full details, we refer the reader to Appendix B. Our results are similar to those of Scotto [17], who considered the inner layer as a tie layer between two polymers having different properties needing to be stuck together. The function $J_{1,a}$ depends only on m_3 and ε_3. As a matter of fact, $c_{1,a}$ is independent of the inner layer and is shown to be identical to the eigenvalue of the two-fluid flow made of the two outer fluids (i.e., fluids A and B). As for the eigenvalue $c_{1,b}$, it represents the effect of the inner layer. Scotto showed that

$$\mathrm{sign}(J_{1,b}) = \mathrm{sign}(J_{1,a}) \times (\eta_3 - \eta_2)(\eta_2 - \eta_1) \quad (17)$$

As the inner layer is supposed to represent an interphase, we can assume that its viscosity is intermediate between that of the two outer layers. Thus, $J_{1,a}$ and $J_{1,b}$ are always of the same sign. As a consequence, the signs of $c_{1,a}$ and $c_{1,b}$ are always the same as the one of the eigenvalues of the two-fluid flow made of the two outer fluids. The stability criteria of the two-layer Poiseuille flow composed by the two outer layers are similar to those proposed by Yiantsios and Higgins [4] as

$$\mathrm{sign}(c_{1,a}) = \mathrm{sign}[(m_3 - 1)(m_3 - \varepsilon_3^2)] \quad (18)$$

It means that the less viscous fluid has to be in the thinner layer in order for the flow to be stable.

As the stability criteria for the three-layer flow are similar to the ones for the two-layer flow, we can say that the reduction in the effective viscosity ratio does not affect the stability criteria of the flow. It means that if the two-layer flow is unstable, the three-layer flow will remain unstable. The same conclusion holds for the opposite: if the two-layer flow is stable, the three-layer flow will remain stable. As a conclusion, the reduction in the effective viscosity ratio enables us to explain the diminished growth rates observed for flows of compatible fluids but not the reduction in the size of the unstable region. For that purpose, we need a complementary approach in which energetic aspects of the formation of the interphase are taken into account in the stability analysis.

3 Energetic Approach

3.1 General Formulation. This section devoted to the energetic approach falls into three parts. As a first step we evaluate the energy balance of the system in the ideal case of two incompatible fluids. Then we estimate the energy dissipated by the interdiffusion process, which corresponds to the removal of wave energy. We finally determine the energy available for the growth of the wave in the case of two compatible polymers.

As a first step, the disturbance of two incompatible fluids is considered from the energy point of view. For so doing we multiply the Navier-Stokes equations by the velocity disturbance and integrate over the thickness of each layer and over one wavelength as done by Albert and Charru [18]. This calculus enables us to determine numerically $\dot{E}_k$—which is the rate of change of the kinetic energy of the disturbance in layer $k(k = 1, 3)$—by

$$\dot{E}_k = \frac{d_k}{2}\frac{D}{Dt}\int_{\Omega_k}(u_{1,k}^2 + u_{2,k}^2)dx_1dx_2 \quad (19)$$

where Ω_k is the domain occupied by the fluid k (whose boundaries are a function of time and x_1 as the interface is submitted to a perturbation wave). Finally, we determine the mechanical energy of the global flow $\dot{E}_{tot}$ (which is the sum of $\dot{E}_1$ and $\dot{E}_3$) and normalize it so that

$$\dot{E}_{tot} = \alpha\,\mathrm{Im}(c) \quad (20)$$

In a second step the rate of dissipated energy by the interdiffusion process $\dot{E}_i$ is determined. A way to evaluate $\dot{E}_i$ is to examine the adhesive bond strength of the final product. Thus, the fracture energy G is the energy needed to pull out the interpenetrating chains per unit area. One should keep in mind that the orientation of polymer chains in a shear flow field profoundly influences the rate of the interdiffusion process and consequently the fracture energy. The latter has to be determined under shear flow conditions. We have chosen to follow the approach of Kim and Han

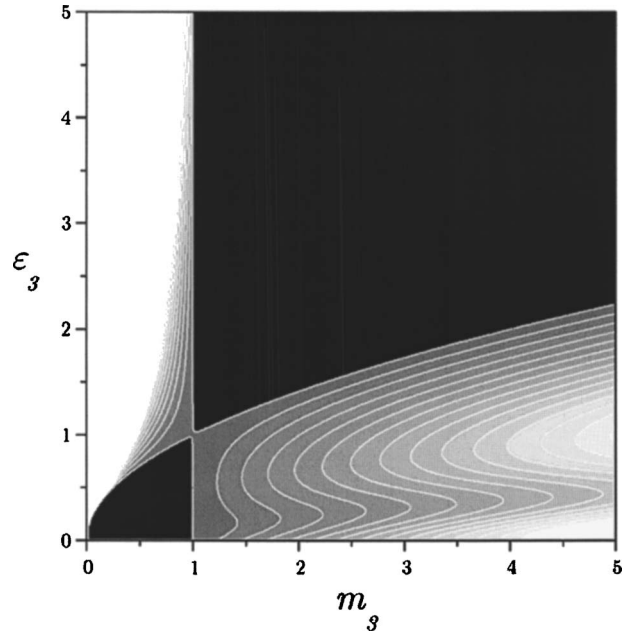

Fig. 2 Stability map in the case $\chi=0$. Black zones correspond to stable regions and gray zones to unstable regions.

[19] who proposed the following expression to evaluate G under a shear flow field (considering a Fickean one-dimensional diffusion):

$$G \propto (t\alpha_{avg}|\chi|)^{1/4} \tag{21}$$

where χ is the interaction parameter and t is the diffusion time (expressed in Appendix C as a function of the Reynolds number). The average orientation factor α_{avg} is defined by

$$\alpha_{avg} = \sqrt{\alpha_A \alpha_B} \tag{22}$$

where α_A and α_B are respectively the orientation factors for polymers A and B in steady shear flow. These factors depend on the steady-state shear compliance of the polymers and on shear stress at the interface. The formula that gives the orientation factor as a function of the Reynolds number may be found in Appendix C. Then, the energy dissipated by the interdiffusion process is $\dot{E}_i$ normalized so that at rest (i.e., for $\sigma_{int}=0$)

$$\dot{E}_i = G = n\varepsilon d \tag{23}$$

where, according to Wu et al. [20], "n is the number of chains bridging the original interface per unit area, ε the attractive energy per unit length of interpenetrating chain, and d the root-mean-square interpenetration depth (i.e., the interfacial thickness)."

As a last step, we determine $\dot{E}_c$, the energy rate available for the growth of the wave in the case of two compatible polymers. To obtain it we hypothesized that the total energy rate $\dot{E}_{tot}$ is made up of two terms: the energy rate required to create the interphase $\dot{E}_i$ and the energy rate available for the wave growth $\dot{E}_c$. We therefore assume that

$$\dot{E}_e = \dot{E}_{tot} - \dot{E}_i \tag{24}$$

The results obtained through the energetic approach will now be illustrated by a few examples.

3.2 Illustrative Examples

3.2.1 Incompatible Polymers. Let us first consider a plane Poiseuille flow of two incompatible polymers ($\chi=0$) submitted to very long waves. The stability criterion of the flow is given by the sign of the imaginary part of the complex velocity of the disturbance c. With the previous notations, the flow is stable if $J_{1,a}(\varepsilon_3, m_3) < 0$ [and unstable if $J_{1,a}(\varepsilon_3, m_3) > 0$]. For sake of clarity, we recall here that $J_{1,a}$ is defined by Eq. (16). The complete expression is given by Eqs. (B4) and (B5). In Fig. 2 are represented the zones where parameter $J_{1,a}$ is either positive or negative in the plane (ε_3, m_3). Black zones correspond to stable regions and gray zones to unstable regions. As expected, the stability map does not depend on the Reynolds number and is only governed by the viscosity and thickness ratios.

3.2.2 Compatible Polymers. The influence of the diffusion at the interface is now quantified by means of an energy concept. In the case of incompatible polymers, the energy available for the growth of the wave is given by

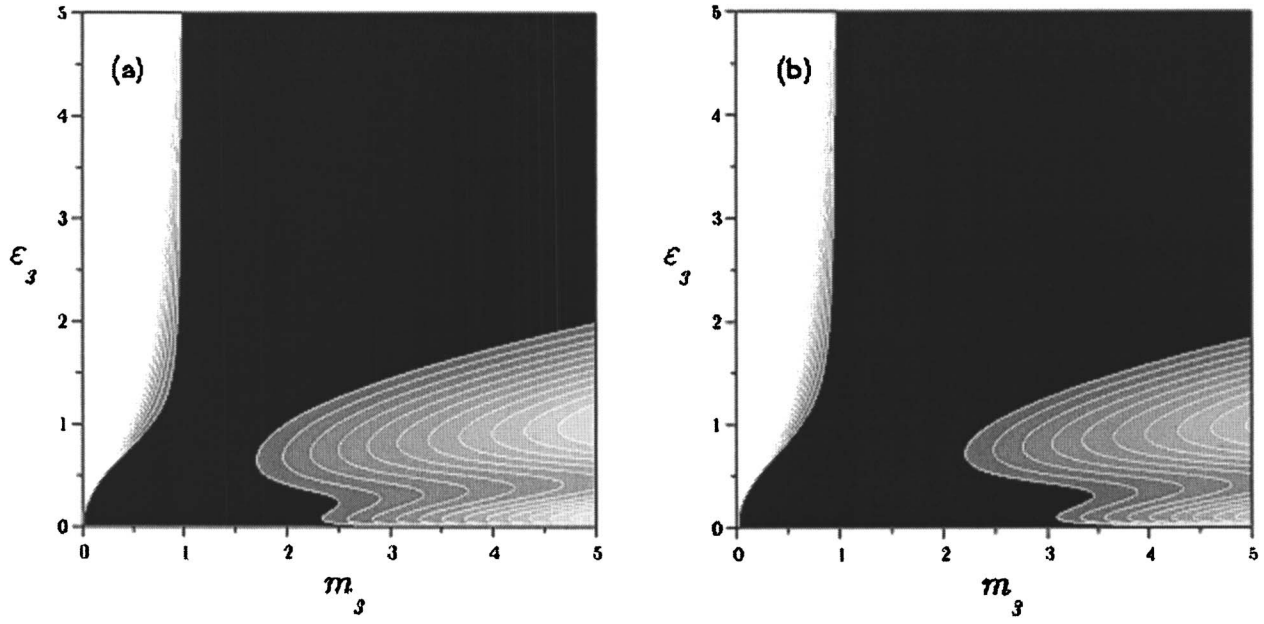

Fig. 3 Stability maps for Re=10^{-5}. (*a*) $\chi=-0.1$ and (*b*) $\chi=-0.7$.

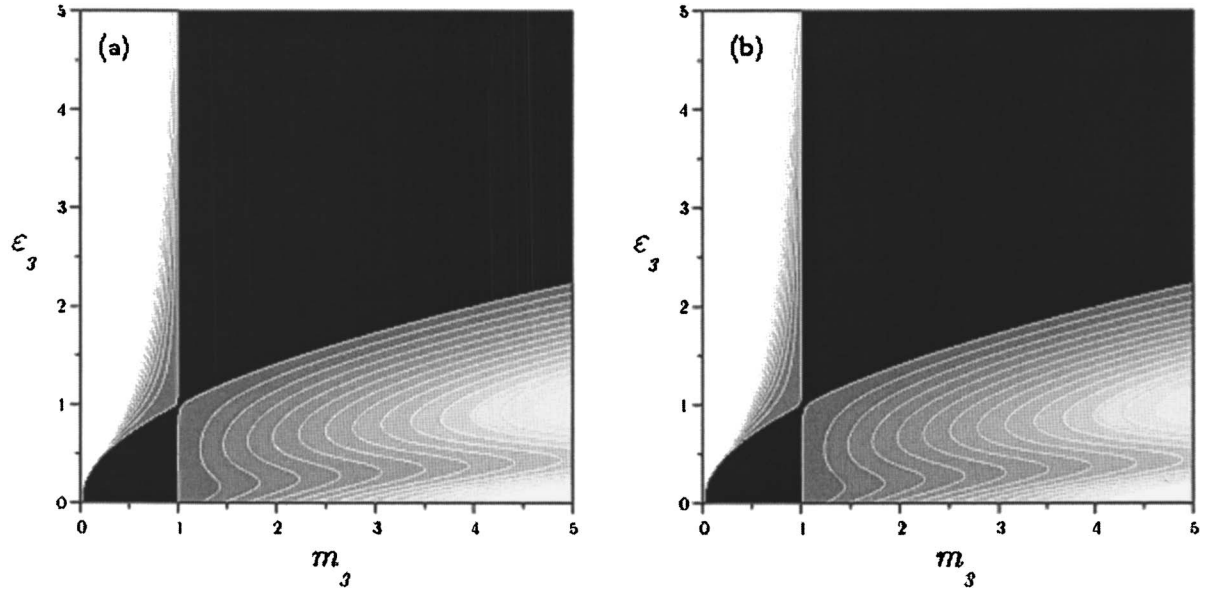

Fig. 4 Stability maps for Re=5.10^{-4}. (*a*) χ=−0.1 and (*b*) χ=−0.7.

$$\dot{E}_{tot} = \alpha \cdot \mathrm{Im}(c) = \alpha \cdot \mathrm{Re} \cdot J_{l,a}(\varepsilon_3, m_3) \tag{25}$$

It means that the stability of the flow is only determined by ε_3 and m_3 whereas the energy available for the growth is also a function of the Reynolds number.

Let us now consider that some interdiffusion process takes place between the two polymers. The energy rate dissipated by interdiffusion $\dot{E}_i$ is not only a function of ε_3 and m_3 but also of the Reynolds number and the interaction parameter. The energy available for the growth of the wave can be expressed by

$$\dot{E}_c = \dot{E}_{tot} - \dot{E}_i = \alpha \cdot \mathrm{Re} \cdot J_{l,a}(\varepsilon_3, m_3) - \dot{E}_1(\varepsilon_3, m_3, \mathrm{Re}, \chi) \tag{26}$$

We can then determine a modified growth rate by taking into account the energy dissipated by the interdiffusion process:

$$\mathrm{Im}(c_c) = \dot{E}_c / \alpha \tag{27}$$

In the following figures (Figs. 3 and 4) we shall represent $\mathrm{Im}(c_c)/\mathrm{Re}$ in the plane (ε_3, m_3) for several values of Re and χ. The reference is given by Fig. 2 which corresponds to the case χ=0.

Let us consider an extrusion die with the following dimensions: height $H=10^{-3}$ m and length $L=10^{-2}$ m. We also assume that each polymer presents a density of 10^3 kg/m^3 and a steady-state shear compliance of 10^{-5} Pa^{-1}. The viscosity of layer 1 is set to be 10^4 Pa s and the wave number of the disturbance α is set to be equal to 10. We first examine the case of a very weak, but realistic, Reynolds number (Re=10^{-5}).

Figures 3(*a*) and 3(*b*) correspond respectively to the cases χ

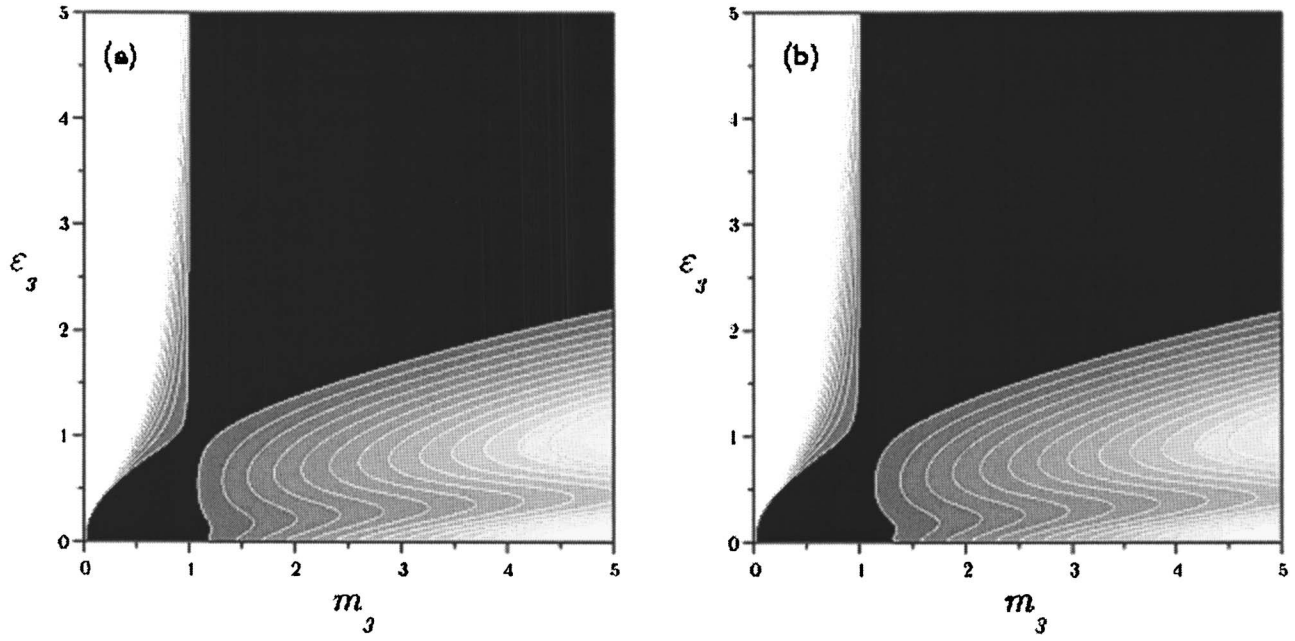

Fig. 5 Stability maps for Re=5.10^{-3}. (*a*) χ=−0.1 and (*b*) χ=−0.7.

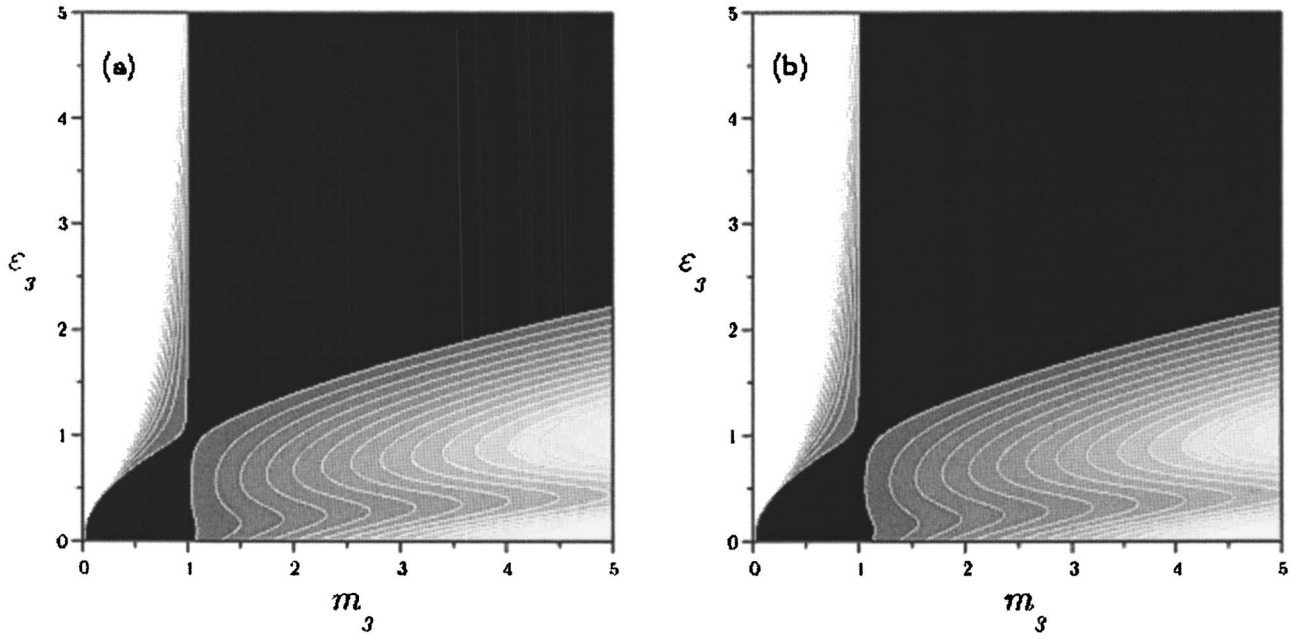

Fig. 6 Stability maps for Re=10^{-4}. (*a*) $\chi=-0.1$ and (*b*) $\chi=-0.7$.

$=-0.1$ and $\chi=-0.7$, the latter characterizing a very strong chemical affinity. We see that taking into account the interdiffusion process enlarges the stable domains. This model enables us to explain Wilson and Khomami's observation of a reduction in the size of the unstable region [14]. However, it should be noted that the interaction parameter weakly affects the stability.

Let us now consider a larger value for the Reynolds number, say $\mathrm{Re}=10^{-3}$. Figures 4(*a*) and 4(*b*) correspond respectively to the cases $\chi=-0.1$ and $\chi=-0.7$. For this value of the Reynolds number, taking into account interdiffusion phenomena has no significant effect on the stability maps. Indeed, at higher Reynolds numbers, more energy is available for the growth of the rate (as $\dot{E} \propto \mathrm{Re}$) and less energy is dissipated by interdiffusion (as $\dot{E}_i \propto 1/\mathrm{Re}$). Note that plots corresponding to intermediate cases ($\mathrm{Re}=5.10^{-5}$ and $\mathrm{Re}=10^{-4}$) can be found in Appendix D.

Our energetic approach of the problem enables us to explain the reduction in the size of the unstable regions at low Reynolds numbers. However, it seems to underestimate the role of chemical affinity on energy dissipation.

4 Conclusion

In this study we proposed a way to explain why stratified flows of compatible polymers are generally more stable than the same flows of incompatible polymers. To do so, we began by stating the existence of a third intermediary layer (which has not been previously done) as a result of polymer diffusion through the inner boundary between the two polymers. Next, we showed that taking into account an interphase between the polymers (i.e., considering the reduction in the effective viscosity ratio) enables us to explain the diminished growth rates observed but not the reduction of the unstable region. We then investigated the reduction of available energy due to mixing and diffusion processes. This second approach enables us to explain the reduction of the unstable regions at low Reynolds numbers. However, one must keep in mind that the two phenomena (reduction in the effective viscosity ratio and removal of wave energy) take place simultaneously and both tend to damp down the waves initially imposed to the flow. Further investigations will be dedicated to moderate wavelengths and to a viscoelastic model for the fluid. A way to evaluate the energy dissipated by the diffusion process through statistical considerations is also in progress.

Acknowledgment

This research was supported by the Ministère de l'Éducation Nationale, de la Recherche et de la Technologie (MENRT, France). A doctoral grant was awarded by the MENRT to F.R. We acknowledge the reviewers for valuable remarks. We also acknowledge Maël Moguedet for computer assistance.

Nomenclature

α = wave number of the disturbance
c = complex velocity of the disturbance ($=c_r+ic_i$)
d_k = thickness of layer k
e_j = unit vector
ε_k = thickness ratio d_k/d_l
$[g]_k$ = jump in g at the interface between layers k and $k+l$
$J^0_{b,i}$ = steady-state shear compliance of polymer i
m_k = viscosity ratio μ_k/μ_l
n = unit vector normal to the interface
μ_k = viscosity of layer k
Re = Reynolds number
$\underline{\underline{\sigma}}$ = stress tensor
σ_{int} = shear stress at the interface
u_k = velocity field in layer k
$u_{j,k}$ = projection of u_k on e_j
ψ_k = stream function of layer k

Appendix A: Primary Flow

$$V=\frac{1}{2}\left(-\frac{dp}{dx_1}\right)\frac{d_1^2}{\mu_1}\frac{h_3(1+\varepsilon_2+\varepsilon_3)}{(m_2m_3+m_3\varepsilon_2+m_2\varepsilon_3)} \tag{A1}$$

$$A_{01}=0 \quad A_{02}=\frac{1}{h_3}\frac{(m_2-1)[(m_2\varepsilon_3+m_2\varepsilon_3^2)+(m_3+2m_2\varepsilon_3)\varepsilon_2+m_3\varepsilon_2^2]}{m_2(1+\varepsilon_2+\varepsilon_3)} \tag{A2}$$

$$A_{03} = \frac{1}{h_3 m_3}[(m_2 m_3 \varepsilon_3 - m_2 \varepsilon_3) + (m_2 m_3 - m_3 + m_3 \varepsilon_3 - m_2 \varepsilon_3)\varepsilon_2] \tag{A3}$$

$$A_{21} = \frac{-1}{h_3}(1 + \varepsilon_2 + \varepsilon_3)[m_2(m_3 + \varepsilon_3) + m_3 \varepsilon_2], \quad A_{22} = \frac{A_{21}}{m_2}, \tag{A4}$$

$$A_{23} = \frac{A_{21}}{m_3}$$

$$A_{11} = \frac{1}{h_3}[m_2(m_3 + 2\varepsilon_3 + \varepsilon_3^2) + (2m_3 + 2m_2\varepsilon_3)\varepsilon_2 + m_3 \varepsilon_2^2] \tag{A5}$$

$$A_{12} = \frac{A_{11}}{m_2}, \quad A_{13} = \frac{A_{11}}{m_3} \tag{A6}$$

with

$$h_3 = \frac{1}{6(1 + \varepsilon_2 + \varepsilon_3)^2}\left(m_2\left(m_3 + 4\varepsilon_3 + 6\varepsilon_3^2 + 4\varepsilon_3^3 + \frac{\varepsilon_3^4}{m_3}\right) + (4m_3 + 12m_2\varepsilon_3 + 12m_2\varepsilon_3^2 + 4\varepsilon_3^3)\varepsilon_2 + (6m_3 + 12m_2\varepsilon_3 + 6\varepsilon_3^2)\varepsilon_2^2 + (4m_3 + 4\varepsilon_3)\varepsilon_2^3 + \frac{m_3}{m_2}\varepsilon_2^4\right) \tag{A7}$$

Appendix B: Perturbation Flow

$$c_{0,a} = c_{0,a}^0 + O(d_2)$$

$$c_{0,b} = c_{0,b}^0 + O(d_2) \tag{B1}$$

$$c_{0,a}^0 = \frac{6\varepsilon_3(1 + \varepsilon_3)^2(m_3 + 2m_3\varepsilon_3 + 6\varepsilon_3^2 + (2 + 2/m_3)\varepsilon_3^3 + \varepsilon_3^4/m_3)}{(m_3 + 4\varepsilon_3 + 6\varepsilon_3^2 + 4\varepsilon_3^3 + \varepsilon_3^4/m_3)^2} \tag{B2}$$

$$c_{0,b}^0 = \frac{6\varepsilon_3(1 + \varepsilon_3)^2}{(m_3 + 4\varepsilon_3 + 6\varepsilon_3^2 + 4\varepsilon_3^3 + \varepsilon_3^4/m_3)} \tag{B3}$$

$$J_{1,a} = (m_3 - \varepsilon_3^2)(m_3 - 1) f_{1,a}(\varepsilon_3, m_3) \tag{B4}$$

with

$$f_{1,a}(\varepsilon_3, m_3) = [(6\varepsilon_3 + 1)m_3^7 + (-2\varepsilon_3 - 9\varepsilon_3^2 - 120\varepsilon_3^3 - 88\varepsilon_3^4)m_3^6 + (32\varepsilon_3^2 + 344\varepsilon_3^3 + 821\varepsilon_3^4 + 1426\varepsilon_3^5 + 1096\varepsilon_3^6 + 224\varepsilon_3^7)m_3^5 + (408\varepsilon_3^4 + 1642\varepsilon_3^5 + 3667\varepsilon_3^6 + 3424\varepsilon_3^7 + 1240\varepsilon_3^8 + 224\varepsilon_3^9)m_3^4 + (224\varepsilon_3^5 + 1240\varepsilon_3^6 + 3424\varepsilon_3^7 + 3667\varepsilon_3^8 + 1642\varepsilon_3^9 + 408\varepsilon_3^{10})m_3^3 + (224\varepsilon_3^7 + 1096\varepsilon_3^8 + 1426\varepsilon_3^9 + 821\varepsilon_3^{10} + 344\varepsilon_3^{11} + 32\varepsilon_3^{12})m_3^2 + (-88\varepsilon_3^{10} - 120\varepsilon_3^{11} - 9\varepsilon_3^{12} - 2\varepsilon_3^{13})m_3 + \varepsilon_3^{14} + 6\varepsilon_3^{13}]/\left[420m_3^5(\varepsilon_3 + 1)^2\left(m_3 + 4\varepsilon_3 + 6\varepsilon_3^2 + 4\varepsilon_3^3 + \frac{\varepsilon_3^4}{m_3}\right)^3\right] \tag{B5}$$

Appendix C: Energy Dissipation

$$\alpha_i = \frac{\cos((\pi/4) + \tan^{-1}(J_{b,i}^0 \sigma_{int})/2)}{\cos(\pi/4)} \quad (i = A, B) \tag{C1}$$

$$t = \frac{L}{V} = \frac{LH\rho}{\mu_1}\frac{g_3}{\varepsilon_3}\frac{1}{\mathrm{Re}} \tag{C2}$$

$$\sigma_{int} = \mu_1 \left.\frac{\partial u_{1,1}}{\partial x_2}\right|_{x_2 = d_1} = \frac{\mu_1^2}{\rho H^3}\frac{\varepsilon_3^2 - m_3}{g_3} \times \mathrm{Re} \tag{C3}$$

with

$$g_3 = \frac{1}{6(1 + \varepsilon_3)^2}\left(m_5 + 4\varepsilon_3 + 6\varepsilon_3^2 + 4\varepsilon_3^3 + \frac{\varepsilon_3^4}{\varepsilon_3}\right) \tag{C4}$$

Appendix D: Additional Plots

See Figs. 5 and 6.

References

[1] Yih, C.-S., 1967, "Instability Due to Viscosity Stratification," J. Fluid Mech., **27**(2), pp. 337–352.

[2] Hooper, A. P., 1985, "Long-Wave Instability at the Interface Between Two Viscous Fluids: Thin Layer Effect," Phys. Fluids, **28**, pp. 1613–1619.

[3] Hooper, A. P., and Boyd, W. G. C., 1983, "Shear-Flow Instability at the Interface Between Two Viscous Fluids," J. Fluid Mech., **128**, pp. 507–528.

[4] Yantsios, S. G., and Higgins, B. G., 1988, "Linear Stability of Plane Poiseuille Flow of Two Superposed Fluids," Phys. Fluids, **31**(11), pp. 3225–3238.

[5] Anturkar, N. R., Papanastasiou, T. C., and Wilkes, J. O., 1990, "Stability of Multilayer Extrusion of Viscoelastic Liquids," AIChE J., **35**(5), pp. 710–724.

[6] Anturkar, N. R., Papanastasiou, T. C., and Wilkes, J. O., 1990, "Linear Stability of Multilayer Plane Poiseuille Flow," Phys. Fluids A, **2**(4), pp. 530–541.

[7] Joseph, D. D., and Renardy, Y. Y., 1992, *Fundamentals of Two-Fluid Dynamics, Part I: Mathematical Theory and Applications*, Springer-Verlag, New York.

[8] Han, C. D., 1973, "A Study of Bicomponent Coextrusion of Molten Polymers," J. Appl. Polym. Sci., **17**, pp. 1289–1303.

[9] Khan, A. A., and Han, C. D., 1976, "On the Interface Deformation in the Stratified Two-Phase Flow of Viscoelastic Fluids," Trans. Soc. Rheol., **20**(4), pp. 595–621.

[10] Karagiannis, A., Mavridis, H., Hrymak, A. N., and Vlachopoulos, J., 1988, "Interface Determination in Bicomponent Extrusion," Polym. Eng. Sci., **28**(15), pp. 982–988.

[11] White, J. L., Ufford, R. C., Dharod, K. R., and Price, R. L., 1972, "Experimental and Theoretical Study of the Extrusion of Two-Phase Molten Polymer Systems," J. Appl. Polym. Sci., **16**, pp. 1313–1330.

[12] Wilson, G. M., and Khomami, B., 1992, "An Experimental Investigation of Interfacial Instabilities in Multilayer Flow of Viscoelastic Fluids. Part I. Incompatible Polymer Systems," J. Non-Newtonian Fluid Mech., **45**, pp. 355–384.

[13] Wilson, G. M., and Khomami, B., 1993, "An Experimental Investigation of Interfacial Instabilities in Multilayer Flow of Viscoelastic Fluids. Part II. Elastic and Nonlinear Effects in Compatible Polymer Systems," J. Rheol., **37**(2), pp. 315–339.

[14] Wilson, G. M., and Khomami, B., 1993, "An Experimental Investigation of Interfacial Instabilities in Multilayer Flow of Viscoelastic Fluids. Part III. Compatible Polymer Systems," J. Rheol., **37**(2), pp. 341–354.

[15] Squire, H. B., 1933, "On the Stability of Three-Dimensional Disturbances of Viscous Flow Between Parallel Walls," Proc. R. Soc. London, Ser. A, **142**, p. 621.

[16] Hesla, T. I., Pranckh, F. R., and Preziosi, L., 1986, "Squire's Theorem for Two Stratified Fluids," Phys. Fluids, **29**, pp. 2808–2811.

[17] Scotto, S., 1998, "Etude de Stabilité Des Écoulements, Multicouches de Fluides Non Newtoniens," Ph.D. thesis, Université de Nice—Sophia Antipolis.

[18] Albert, F., and Charru, F., 2000, "Small Reynolds Number Instabilities in Two-Layer Couette Flow," Eur. J. Mech. B/Fluids, **19**, pp. 229–252.

[19] Kim, J. K., and Han, C. D., 1991, "Polymer-Polymer Interdiffusion During Coextrusion," Polym. Eng. Sci., **31**(4), pp. 258–269.

[20] Wu, S., Chuang, H. K., and Han, C. D., 1986, "Diffuse Interface Between Polymers: Structure and Kinetics," J. Polym. Sci., Polym. Phys. Ed., **24**, pp. 143–159.

A Numerical Study of Dean Instability in Non-Newtonian Fluids

H. Fellouah

C. Castelain

A. Ould El Moctar

H. Peerhossaini

e-mail: hassan.peerhossaini@univ-nantes.fr

Thermofluids, Complex Flows and Energy,
Laboratoire de Thermocinétique,
UMR CNRS 6607,
Ecole Polytechnique de l'Université de Nantes,
La Chantrerie, BP 50609,
F-44306, Nantes, France

We present a numerical study of Dean instability for non-Newtonian fluids in a laminar 180 deg *curved-channel flow of rectangular cross section. A methodology based on the Papanastasiou model (Papanastasiou, T. C., 1987, J. Rheol., **31**(5), pp. 385–404) was developed to take into account the Bingham-type rheological behavior. After validation of the numerical methodology, simulations were carried out (using FLUENT CFD code) for Newtonian and non-Newtonian fluids in curved channels of square or rectangular cross section and for a large aspect and curvature ratios. A criterion based on the axial velocity gradient was defined to detect the instability threshold. This criterion was used to optimize the grid geometry. The effects of curvature and aspect ratio on the Dean instability are studied for all fluids, Newtonian and non-Newtonian. In particular, we show that the critical value of the Dean number decreases with increasing curvature ratio. The variation of the critical Dean number with aspect ratio is less regular. The results are compared to those for Newtonian fluids to emphasize the effect of the power-law index and the Bingham number. The onset of Dean instability is delayed with increasing power-law index. The same delay is observed in Bingham fluids when the Bingham number is increased.* [DOI: 10.1115/1.2136926]

Keywords: Dean instability, curved channel, Newtonian fluids, non-Newtonian fluids, numerical study

1 Introduction

Curved channels are widely used in engineering applications, such as turbomachinery and heat exchangers for heating or cooling systems, because they provide, in addition to compactness, high heat and mass-transfer rates, transverse mixing, and an extended laminar flow regime.

In laminar flow through ducts, the effect of even very slight curvature is not negligible. Streamline curvature instigates a secondary flow that consists of a pair of counter-rotating roll-cells when viewed in the duct cross section. These are called Dean roll-cells after W. R. Dean [1], who developed a theory of this secondary flow phenomenon. We thus call the flow of a fluid in a curved duct *Dean flow* and the corresponding control parameter the *Dean number*, defined as

$$\mathrm{Dn} = \frac{UmD_h}{\nu}\sqrt{\frac{D_h}{R_c}} \tag{1}$$

Here Um is the mean velocity, ν the kinematic viscosity, D_h the hydraulic diameter and R_c the mean curvature radius. The plane separating two Dean roll-cells (the symmetry plane) is parallel to the curvature plane of the bend. Beyond a certain critical flow conditions, another pair of counter-rotating vortices appears on the concave wall of the duct; these are due to the Dean instability and are called *Dean vortices*.

The first solution for curved circular flow for Newtonian fluids was suggested by Dean [1]. He proved the existence of secondary flow found experimentally by Eustice [2] by injecting ink into water flowing through a coiled pipe. Early works on Newtonian curved flows of circular cross section is presented in the review article by Berger et al. [3].

Cheng and Akiyama [4] presented a numerical solution for steady fully developed laminar flow and convective heat transfer in curved rectangular channels with aspect ratios $b/a=0.2$, 0.5, 1, 2, and 5. Cheng et al. [5] reported an experimental study using flow visualization techniques of a fully developed laminar flow in a curved rectangular duct for aspect ratios $b/a=1$, 2, 3, 4, 5, 6, 8, 10, and 12 with $a/R_c=0.2$, and aspect ratio $b/a=12$ with $a/R_c=0.025$. They showed that further secondary flow vortices are set up in addition to the main secondary flow vortices, and that the number of additional vortex pairs depends on the aspect ratio and the Dean number. The evolution of the critical Dean number with aspect ratio was described.

Sugiyama et al. [6] reported an experimental investigation of a fully developed laminar flow in 20 mm wide curved rectangular channels of aspect ratios ranging from 0.5 to 2.5 and curvature ratios ranging from 5 to 8. They showed the development of the secondary flow vortices with Dean number. The critical Dean number takes minimum and maximum values at aspect ratios of about 1 and 2, respectively.

Recently, Chandratilleke and Nursubyakto [7] presented a numerical simulation of the secondary flow characteristics through curved rectangular ducts. They varied the aspect ratios from 1 to 8 and the Dean numbers from 20 to 500. Chandratilleke and Nursubyakto [7] reported also that the number of additional-Dean vortices formed in the flow is strongly influenced by the duct aspect ratio.

Because of its importance in polymer, biomedical/pharmaceutical, petroleum, and food processing, the flow behavior of non-Newtonian fluids in straight or curved circular or non-circular channels has received much attention. In straight tubes, we refer to Cho and Hartnett [8] for power-law fluids; Chen et al. [9] and Varadis et al. [10] for Bingham-plastic fluids. Fewer studies have been devoted to the flow of power law fluids in curved circular tubes, see Agrawal et al. [11], Hsu and Patanker [12], and Shanthini and Nandakumar [13]. These three works showed that the secondary flow becomes weak as the power-law index decreases, but that its dependence on Dean number is similar to that of Newtonian fluids and the axial velocity profile tends to flatten as the power-law index decreases. The Dean vortices are clear in

Contributed by the Fluids Engineering Division of ASME for publication in the JOURNAL OF FLUIDS ENGINEERING. Manuscript received August 2, 2004; final manuscript received May 17, 2005. Assoc. Editor: Dennis Siginer.

the study of Kumar et al. [14] for the power-law fluid flow in curved square duct. The results demonstrate the existence of dual solutions for a certain range of Dean number and power-law index. Little attention has been given to the flow of non-Newtonian fluids in curved rectangular channels.

The purpose of the present work is to characterize non-Newtonian laminar flow and Dean instability in curved channels of rectangular section with various aspect and curvature ratios. First, we describe and validate the methodology. Second, we study the Dean instability in Newtonian fluids. The influence of the aspect ratio and the curvature ratio is particularly emphasized. Finally, we study the Dean instability in non-Newtonian fluids. We focus on the effect of the power-law index and the Bingham number.

2 Methodology and Validation

2.1 Description of the General Numerical Methodology. In the numerical study, we used FLUENT CFD code to solve the stationary three-dimensional equations characterizing the flow in curved rectangular cross sections. Fluent proposes many algorithms to solve these equations. We choose an algorithm with the segregated solver (the solution algorithm in which the governing equations are solved sequentially) to iterate the nonlinear partial differential equations. The segregated solver is more adapted to a large grid, as in our case. To calculate pressure at the nodes, we chose the body-force-weighted scheme, which works well when inertia forces are not negligible. FLUENT uses the equation of continuity to deduce the pressure necessary to resolve the equations of motion. To obtain the pressure in the continuity equation, we choose the SIMPLEC algorithm for the pressure-velocity coupling. For the momentum equation, we used the QUICK scheme because it is recommended when there are rotating flows inside the flow.

GAMBIT is the program used to generate the grid or mesh for the FLUENT CFD solver. Because of our geometry's symmetry, we chose to impose a symmetry condition in order to decrease the required calculation capacity for the large geometries ($b/a>8$) and thus to limit our geometry to a half section. Calculations are carried out in a length upstream of the study section. At the entry of the straight length, a constant velocity equal to the mean velocity is imposed. At the exit of this length, the flow is hydrodynamically developed and reaches the study section. Convergence is controlled by following the evolution of residual for the velocity components and the continuity equation. For the velocity components, the residues represent the sum on all grid cells of the difference between the value of a variable calculated in one cell and that calculated by applying the conservation equation to the cells close to the first. For the continuity equation, the residues represent the ratio of the mass flow rate in a given iteration to the mass flow rate maximum of the first five iterations. In the convergence, the residual evolution must converge toward small (in any case $<10^{-6}$) and stable quantities. Figure 1 shows the coordinate system used for the laminar flow in a 180 deg curved rectangular channel. The cross section of the channel is a rectangle of width a and height b.

2.2 Non-Newtonian Fluid Behavior: Formulation. For non-Newtonian fluids, the generalized Reynolds number is established so that the relation between the friction factor and the Reynolds number for isothermal laminar flow of Newtonian fluids is the same as for non-Newtonian fluids [15].

The relation between the friction factor and the Reynolds number for isothermal laminar flow of Newtonian fluids in ducts is given by

$$\frac{C_f}{2}=\frac{2\tau_w}{\rho Um^2}=\frac{2}{\rho Um^2}\frac{D_h\Delta P}{4L}=\frac{\xi}{\mathrm{Re}} \tag{2}$$

where C_f is the friction factor, ΔP is the pressure loss, L is the length of the channel, τ_w the wall shear stress, Um is the mean flow velocity, and ξ is a dimensionless geometrical parameter

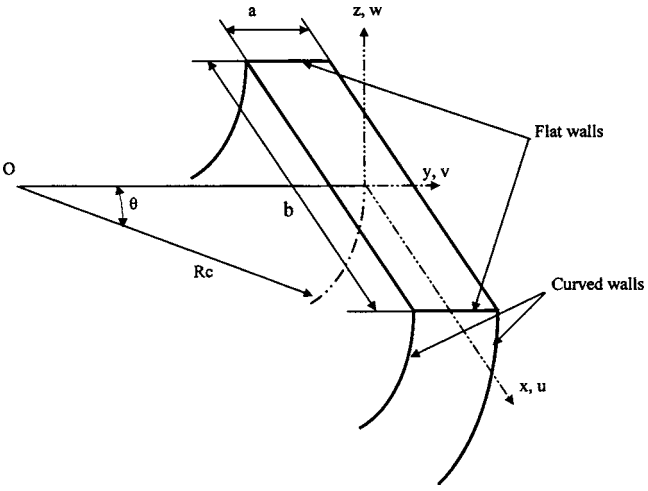

Fig. 1 Coordinate system

whose values for different ducts are given by Shah and London [16]. The Dean number for non-Newtonian fluids is defined as

$$\mathrm{Dn}=\mathrm{Re}_g\sqrt{\frac{D_h}{R_c}} \tag{3}$$

The result is given in Table 1. For Bingham fluids, the dimensionless radius of the plug-flow region ξ_0 (where $\xi_0=\tau_c/\tau_w$, τ_c is the yield stress) is initialized to start calculations for a given Dean number because the Dean number depends on this parameter. At the end of this calculation, we derive the pressure loss (ΔP) on the straight channel. Knowing the relation between the pressure loss and the wall shear stress τ_w, we determine the wall shear stress τ_w. Since we know the yield shear stress τ_c, we can calculate the exact value of ξ_0 and correct the Dean number.

The FLUENT CFD code does not include in its data library the rheological behavior of yield-stress fluids, so a subroutine that takes this behavior into account was developed. To handle the discontinuity in yield-stress fluids between the sheared and unsheared zone, the subroutine added to FLUENT is based on a model that is valid for both sheared and unsheared areas. Different models were tested

The Papanastasiou model [17]

$$\tau=\tau_c(1-e^{-m\dot\gamma})+k\dot\gamma^n \tag{4}$$

where m is the stress growth exponent; τ and $\dot\gamma$ are, respectively, the stress and the shear tensors. For low shear rates, this model transforms the plug region (in which the velocity is constant) into a region of high viscosity. It was shown by Papanastasiou [17] that this equation closely mimics an ideal Bingham plastic fluid for $m>1000$

The Bercovier and Engelman model [18]

$$\tau=\left(\frac{\tau_c}{\dot\gamma+\delta}+k\dot\gamma^{n-1}\right)\dot\gamma \tag{5}$$

where δ is the model parameter.

The biviscosity model [19]

$$\begin{cases}\tau=\mu_s\dot\gamma & si\ \dot\gamma\leqslant\dot\gamma_c\\ \tau=\left(k\dot\gamma^{n-1}+\dfrac{\tau_c}{\dot\gamma}\right)\dot\gamma & si\ \dot\gamma>\dot\gamma_c\end{cases} \tag{6}$$

where μ_s is the solid viscosity and $\dot\gamma_c$ the critical shear.

In order to validate the subroutine, we studied the laminar flow of Newtonian and non-Newtonian fluids in a cylindrical tube. In each case, the parameters of the different models were adjusted to represent the rheological model of the fluid studied, as given in

Table 1 Rheological models of fluids used in this work

Fluid	Constitutive equation	Circular channel: Generalized Reynolds number	Circular channel: Fully developed velocity profile	Rectangular channel: Generalized Reynolds number
Newtonian	$\tau=\mu\dot{\gamma}$	$\mathrm{Re}=\dfrac{UmD}{\nu}$	$\dfrac{u(r)}{Um}=2\left[1-\left(\dfrac{r}{R}\right)^2\right]$	$\mathrm{Re}=\dfrac{UmD_h}{\nu}$
Power law	$\tau=k\dot{\gamma}^n$	$\mathrm{Re}_g=8^{1-n}\left(\dfrac{4n}{3n+1}\right)^n\dfrac{\rho Um^{2-n}D^n}{k}$	$\dfrac{u(r)}{Um}=\dfrac{3n+1}{n+1}\left[1-\left(\dfrac{r}{R}\right)^{(n+1)/n}\right]$	$\mathrm{Re}_g=\dfrac{\rho Um^{2-n}D_h^n}{k\left[\dfrac{24n+\xi}{(24+\xi)n}\right]\xi^{n-1}}$
Bingham	$\tau=\tau_c+\mu_w\dot{\gamma}$ if $\tau>\tau_c$ $\dot{\gamma}=0$ if $\tau\leqslant\tau_c$	$\mathrm{Re}_g=\mathrm{Re}_w\psi_{cc}$ $\mathrm{Re}_w=\dfrac{\rho UmD_h}{\mu_w}$ $\psi_{cc}=\left[1-\dfrac{4\xi_0}{3}+\dfrac{\xi_0^4}{3}\right]$	$\begin{cases}\dfrac{u(r)}{Um}=\dfrac{Bm}{r}\dfrac{\tau_w}{\tau_c}\left[1-\left(\dfrac{r}{R}\right)^2-2\dfrac{\tau_c}{\tau_w}\left(1-\dfrac{r}{R}\right)\right] & \text{if } \tau>\tau_c\\ u(r)=C^{de}=Uc & \text{if } \tau\leqslant\tau_c\end{cases}$	$\mathrm{Re}_g=\mathrm{Re}_w\psi_{pp}$ $\mathrm{Re}_w=\dfrac{\rho UmD^h}{\mu_w}k$ $\psi_{pp}=(1-\xi_0)\left[1-\dfrac{\xi_0}{2}-\dfrac{\xi_0^2}{2}\right]^n$

Table 1.

The methodology is validated for a straight tube two meters long. To preserve the accuracy of the velocity profile near the wall, the mesh was made finer close to the wall. The exit velocity profiles obtained using the model are compared to the well-known analytical expressions given in Table 1. Calculations are carried out for a flat velocity profile at the tube entrance.

Figure 2 compares the velocity profiles of a Newtonian fluid and a pseudoplastic fluid of 0.5 power-law index and consistency of 2.7 for a generalized Reynolds number of 200. The distribution of Newtonian velocity across the tube has a parabolic profile. For the pseudoplastic fluid, the decrease of the power-law index flattens the velocity profile; i.e., the velocity gradient is increased in the tube-wall region and decreased near the tube center. The two velocity profiles show a high-velocity gradient near the wall and a central core where the velocity gradient is zero (the plastic region).

In order to choose the model used in our study of a yield-stress fluid, we compared the three models to the analytical profile and an experimental profile [20]. The calculations were made in a circular straight tube and for the same generalized Reynolds number ($\mathrm{Re}_g=14$). The profiles are presented in Fig. 3; we note that the three models give satisfactory results.

Figure 4 presents the difference between the analytically and numerically determined velocity profiles obtained with each model. It is noted that the Papanastatiou model [17] gives the smallest errors, and we retain this model hereafter.

For yield-stress fluids, we have compared the velocity profiles for two Bingham fluids ($\mathrm{Bm}=\tau_cD/Um\mu_w$, where μ_w the fluid viscosity at the wall) equal to 8.5 and 21 of the same viscosity and for a generalized Reynolds number of 200. The results are given in Fig. 5. Figure 5 shows that an increase in the Bingham number leads to an increase in the unsheared zone and to a reduction of the velocity maximum.

Figures 2 and 5 show good agreement between the analytical and numerical velocity profiles. The influence of the power-law index and the Bingham number on the flow described here is the same as that reported in the literature. This validates the model and lets us use it with confidence in what follows.

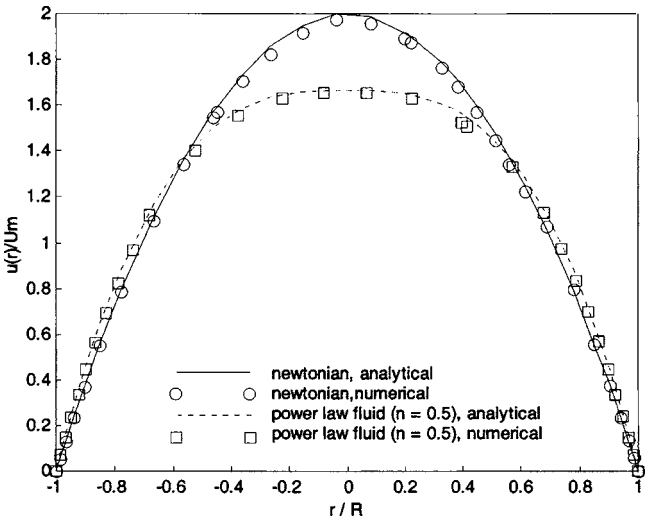

Fig. 2 Dimensionless velocity profiles for Newtonian fluid ($n=1$) and pseudoplastic fluid ($n=0.5$)

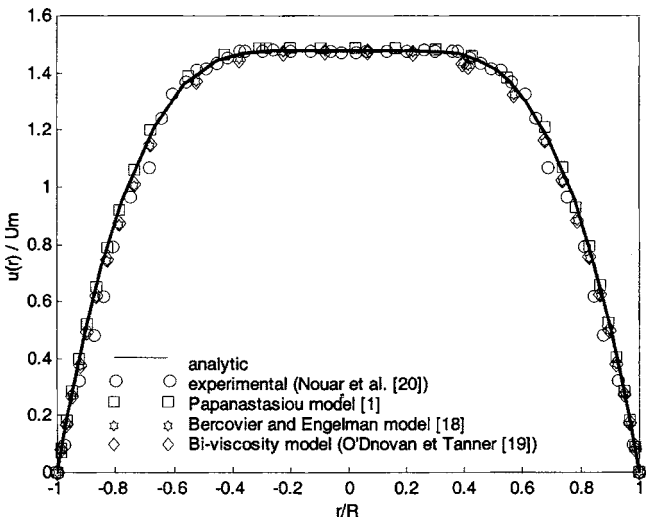

Fig. 3 Dimensionless velocity profiles for Bingham fluids ($\mathrm{Re}_g=14$)

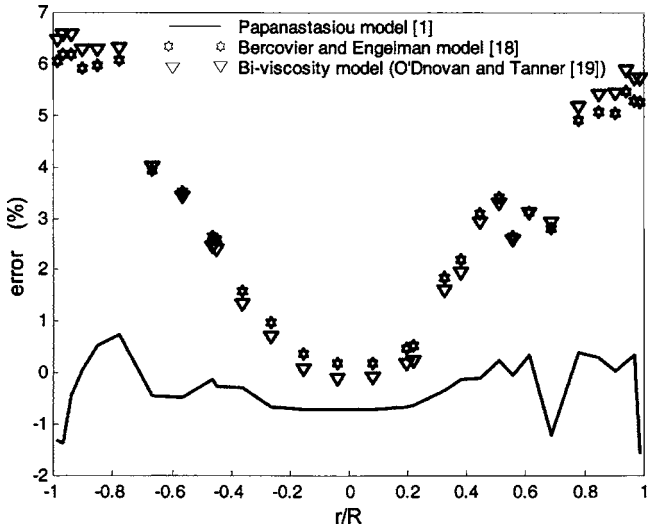

Fig. 4 Relative differences between analytical and calculated velocity profile for different regularization models

2.3 Criterion for Detection of Dean Instability. We must now define an accurate and reliable criterion for detection of Dean instability. The secondary flow in a curved duct consists of a pair of counter-rotating symmetrical vortices called Dean cells. Beyond a critical Dean number, another pair of counter-rotating vortices appears on the concave duct wall (Fig. 6). The question is how to calculate the critical Dean number or, equivalently, how to detect the passage from two to four cells.

In the literature, the criterion for the onset of instability is visual, i.e., the visualization of the Dean vortices. However, visualization remains a qualitative criterion. Here, we instead first locate the center of the Dean vortices for a supercritical Dean number (Fig. 6(*b*)) and then decrease the Dean number until the Dean vortices disappear (Fig. 6(*a*)). Line AA in Fig. 6(*b*) shows the junction between the centers of the Dean vortices.

Figure 7, which plots the axial velocity gradient (dw/dy) along the line AA in Fig. 6(*b*), shows that for a square duct the axial velocity gradient has a double peak at low Dean numbers and three peaks at high Dean numbers. The passage from two to three peaks is chosen as the criterion for the instability threshold. To facilitate the detection of this passage, we calculate the slope of the velocity gradient along the x coordinate: for low Dean numbers the slope is canceled three times, whereas for high Dean numbers it is canceled five times.

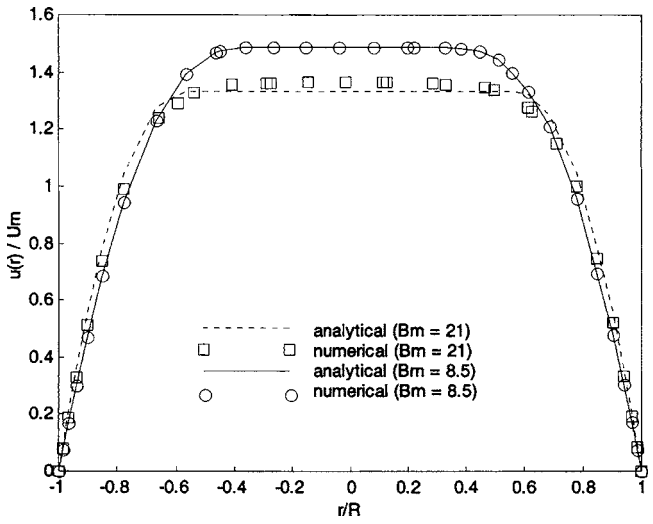

Fig. 5 Dimensionless velocity profiles for Bingham fluids

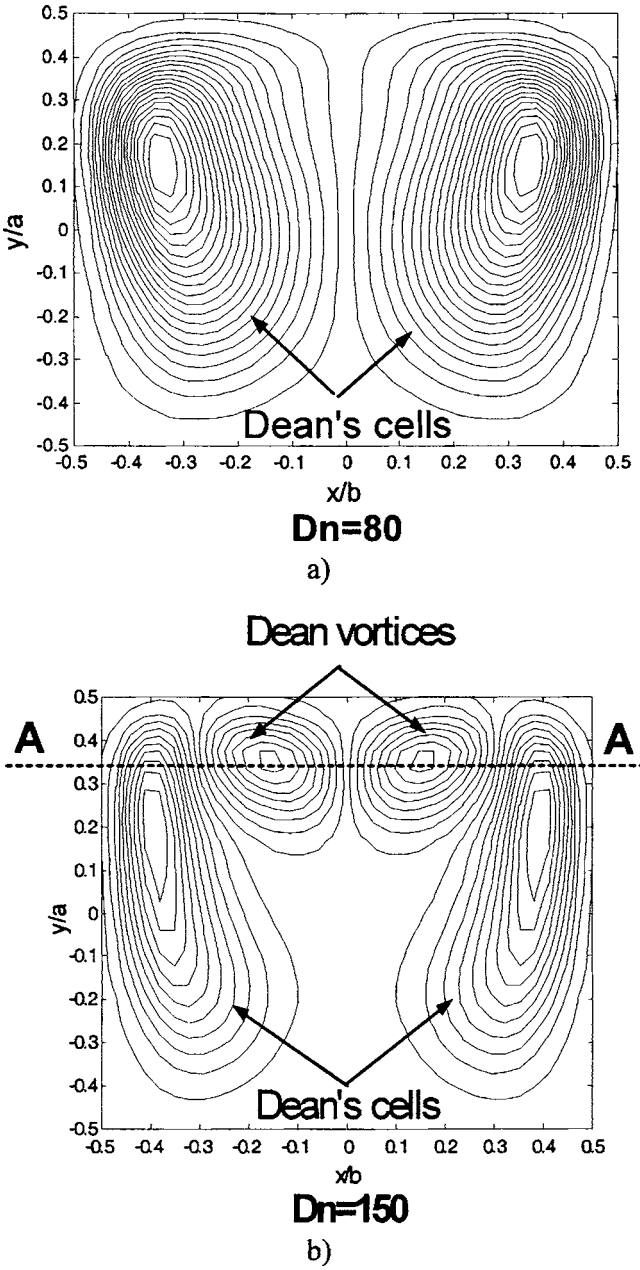

Fig. 6 Contour plots of helicity in square duct section: (*a*) flow without instability and (*b*) flow with instability

2.4 Optimization of the Mesh Grid. To optimize the mesh grid for a curved square duct (generated with GAMBIT), we tested several grids that increased from 20 to 38 nodes on the flat and curved walls and from 5 to 10 mm between two successive grid surfaces. The axial velocity gradient at the center of the Dean vortices (along line AA of Fig. 6) was plotted for various grids. All calculations are made for Dean number 110. The number of flat wall nodes is optimized by fixing the number of nodes on the curved walls, and the number of curved wall nodes is optimized by fixing the number of flat wall nodes. Finally, the distance between two successive grid surfaces is optimized. It appears reasonable to use 24 nodes on the flat and curved walls, which corresponds to square meshes of 0.83×0.83 mm^2 on the surface and

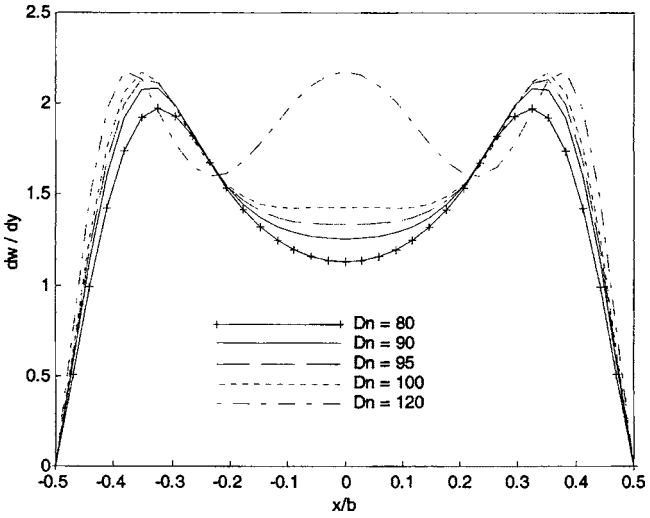

Fig. 7 Axial velocity gradient along line AA of Fig. 6

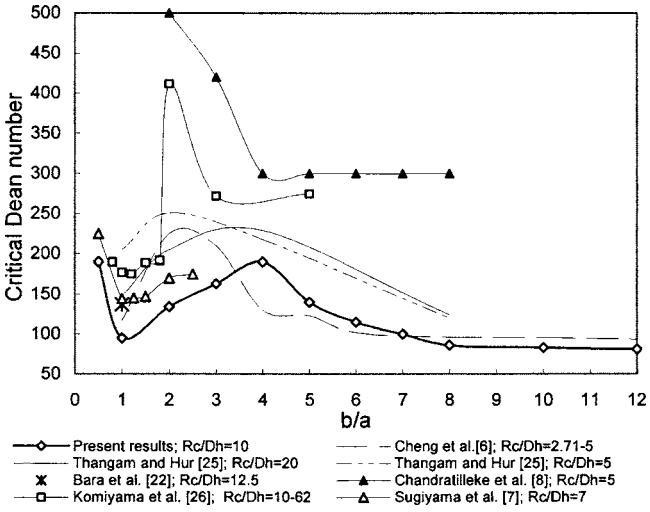

Fig. 9 Effect of aspect ratio on Dean instability

10 mm between two successive grid surfaces. For the curved duct of rectangular cross section, we have retained the same meshes along the duct.

3 Dean Instability in Newtonian Fluids

3.1 Effect of the Curvature Ratio. For curved ducts of circular cross section, most analyses [2,21] indicate that the Dean number is the primary parameter and that the effect of curvature is completely contained in this parameter. Many authors have tried to detect the critical Dean number for ducts of square cross section; Bara et al. [22], Ghia and Sokhey [23], Hille et al. [24], using visualization techniques, give critical Dean numbers, respectively, equal to 137, 143, and 150. This discrepancy is due to the fact that the Dean number is not the only parameter influencing the flow in curved ducts.

Figure 8 shows the influence of the curvature ratio on the onset of Dean instability for various aspect ratios, together with the available numerical and experimental results. Figure 8 shows that when the curvature ratio increases up to 10 for aspect ratio 8, the critical Dean number decreases quickly, and therefore the onset of instability is advanced; after a curvature ratio of 10, the critical Dean number reduction is weak. For the square section, the reduction in the critical Dean number is weak, and the onset of instability is independent of the curvature ratio.

Thangam and Hur [25] showed that the secondary flow intensity decreases when the curvature ratio increases. Ghia and Sokhey [23] and Kumar et al. [14] showed that when the Dean number is held constant, a change in curvature ratio induces a small variation in the axial velocity profiles. It can be concluded that the instability appears because of the decrease of the axial curved length when the curvature ratio decreases. To form Dean vortices in small axial curved lengths, a high centrifugal force is necessary.

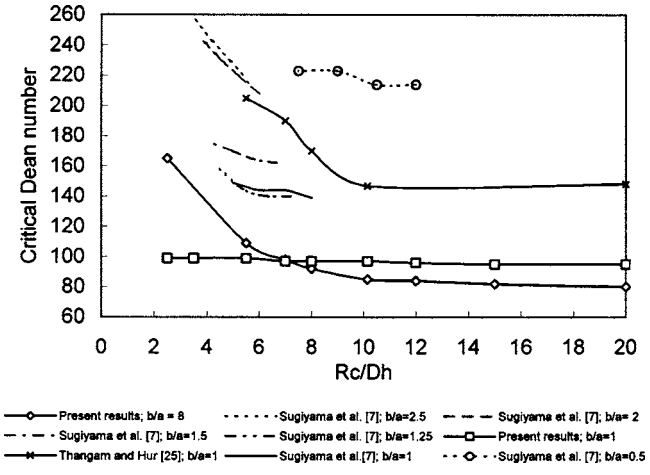

Fig. 8 Effect of curvature ratio in Dean instability

3.2 Effect of the Aspect Ratio. The effect of the aspect ratio variation on the onset of Dean instability is shown in Fig. 9. Here the curvature ratio is held constant and equal to 10. This figure compares our results with those of previous studies. The shape of our curve and the level of the critical Dean numbers are globally in a good agreement with the literature results, especially those of Cheng et al. [5] and Sugiyama et al. [6]. The apparent differences arise first because we used a quite a rigorous criterion to detect the onset of instability, and second, because the curvature ratio differs from ours in each study. Compared to the R_c/D_h effect, we note that the variation of the critical Dean number with the duct aspect ratio is less regular. The critical Dean number shows a local minimum at $b/a=1$ and increases for aspect ratios smaller than 1 and between 1 and 4. Beyond $b/a=4$, it decreases and reaches a constant value at $b/a=8$, a minimum value that corresponds to the case of curved parallel plates.

In order to better understand the implication of the aspect ratio for the critical Dean number evolution observed in Fig. 9, we consider the relative effect of the secondary flow strength and the confinement. We thus present in Fig. 10 the axial velocity profiles in the horizontal midsurfaces at the exit of the 180 deg curved channel for Dn=55 (below the critical Dean number for all cases) and for aspect ratios ranging from 0.5 to 8. The curvature ratio is held constant at 10. We note that a decrease in the aspect ratio causes a stronger secondary flow; that is, the high-momentum fluid is transferred toward the concave wall and the low-momentum fluid near the concave wall is moved to the center of the channel cross section. This phenomenon promotes the occurrence of Dean instability.

On the other hand, when the aspect ratio increases, the effect of the confinement is less sensitive in the sense that the Dean vortices cover more space and are freer to expand. In fact, when the Dean number and the curvature ratio are kept constant and the channel aspect ratio increases, both the effect of confinement and the resistance to the secondary flow at the center of the channel cross section decrease [26]; i.e., it is easier to form Dean vortices, and the occurrence of instability is advanced.

Thus, when the aspect ratio is increased, these two effects com-

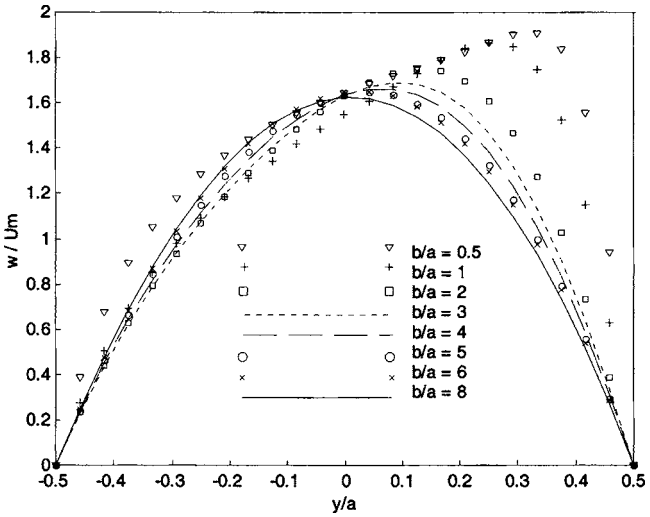

Fig. 10 Effect of aspect ratio on axial velocity profile: Dn=55 and R_c/D_h=10

pete and their relative magnitudes explain the different zones of the critical Dean number evolution. For a low aspect ratio ($b/a < 1$), the confinement effect is predominant and therefore the critical Dean number increases. In the range between 1 and 8, both effects must be considered. However, from 1 to 4, the secondary flow effect predominates and, consequently, the critical Dean number increases in this zone, whereas for aspect ratio from 4 to 8, the effect of nonconfinement becomes predominant and therefore the critical Dean number decrease. Above aspect ratio 8, the influence of the side walls is minimal, and therefore the critical Dean number decreases moderately and the occurrence of Dean instability becomes essentially independent of aspect ratio. Figure 11 shows the vortex organization in the channel cross section at aspect ratios b/a=8 and b/a=0.5 at supercritical Dean number (Dn=300), in order to give a visual feeling for the confinement effect.

4 Dean Instability in Pseudoplastic Fluids

The effect of the power-law index on the axial velocity profile along the horizontal and vertical midsurfaces is illustrated in Fig. 12. The comparison is made for a curved channel with square cross section at the same generalized Dean number of 120. At the inlet of the curved channel, the flow is fully developed laminar straight channel flow.

In the horizontal midsurfaces (x=0), the axial velocity profile is a single peak shifted toward the concave wall due to centrifugal force. When the power-law index decreases, the axial velocity profile shifts more toward the concave wall and tends to flatten more than for the Newtonian fluid. The maximum axial velocity decreases as the power-law index is reduced, so that the pseudoplastic fluids cause the attenuation of the secondary flow. In the vertical midsurfaces ($y=a/2$), the axial velocity profile is double-peaked and symmetric for Newtonian as well as for power-law fluids. The two-peaks shape indicates the existence of two symmetrical Dean cells, and the peaks correspond to the center of the Dean cells. These results are in good agreement with those of Kumar et al. [14] and Ranade and Ulbrecht [27], who observed the same effect of the power-law index.

Figure 13 shows the influence of the power-law index on Dean instability. The critical Dean number decreases with increasing power-law index n. Therefore in non-Newtonian fluids, the local change of apparent viscosity affects the onset of instability. For pseudoplastic fluids, the apparent viscosity is weaker near the wall and higher at the center of the cross section, and thus it is difficult for unstable Dean cells to form. Agrawal et al. [11] showed that

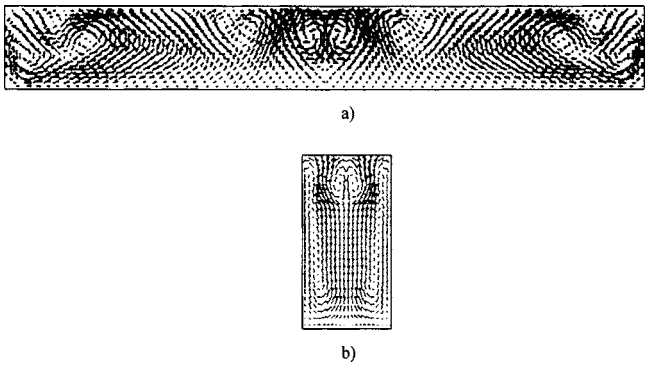

Fig. 11 Vortex organization for two aspect ratios at Dn=300: (*a*) b/a=8 and (*b*) b/a=0.5

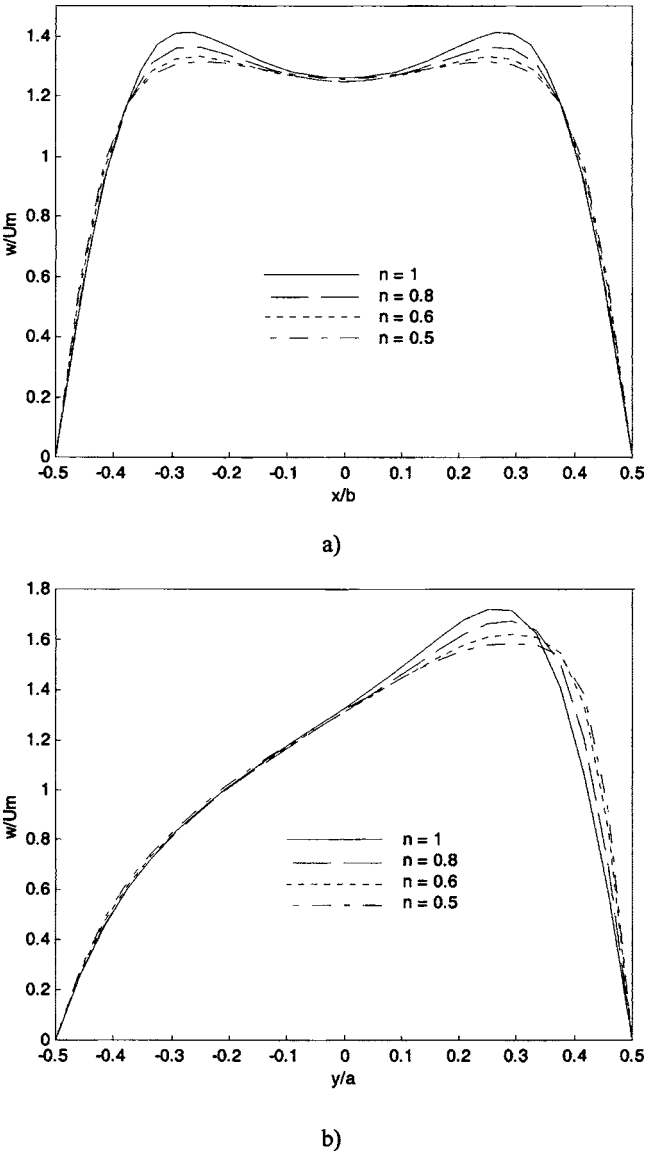

Fig. 12 Effect of power-law index on the axial velocity profiles for a generalized Dean number of 120 in curved square channel with R_c/D_h=10: (*a*) vertical midsurfaces ($y=a/2$) and (*b*) horizontal midsurfaces (x=0)

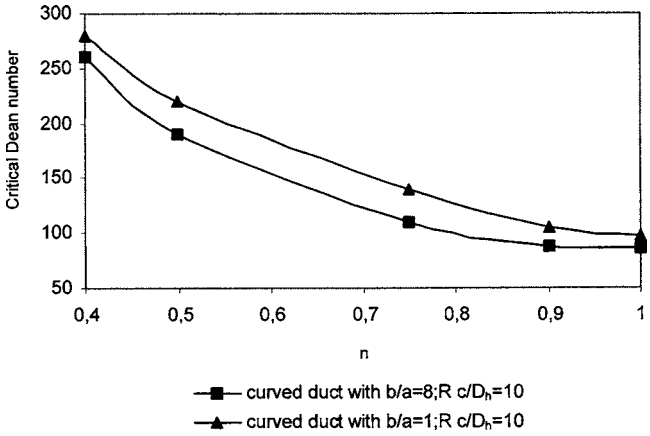

Fig. 13 Effect of power-law index on the onset of instability

pseudoplasticity decreases the intensity of the secondary flow. All these factors lead to a delay in the onset of Dean instability with increasing power-law index.

5 Dean Instability in the Bingham Fluids

The influence of the Bingham number on the instability occurrence is shown in Fig. 14. Increasing Bingham number delays the onset of Dean instability. Alexandrou et al. [28] observed that the size of the plug region increases with the Bingham number. In addition, when the Bingham number increases, the yield stress effect in the flow increases. To overcome the effect of the yield stress increasing, the inertial forces and hence the Dean number must be increased.

6 Conclusions

Dean instability in curved-channel laminar flow of square and rectangular cross sections was studied numerically for Newtonian and non-Newtonian fluids. Using the Papanastasiou model [17] to simulate the flow of yield stress fluids gives results in good agreement with the analytical results. Prediction of the critical Dean number by the precise criterion developed in this work permits detection of the instability closer to its onset than in previous work.

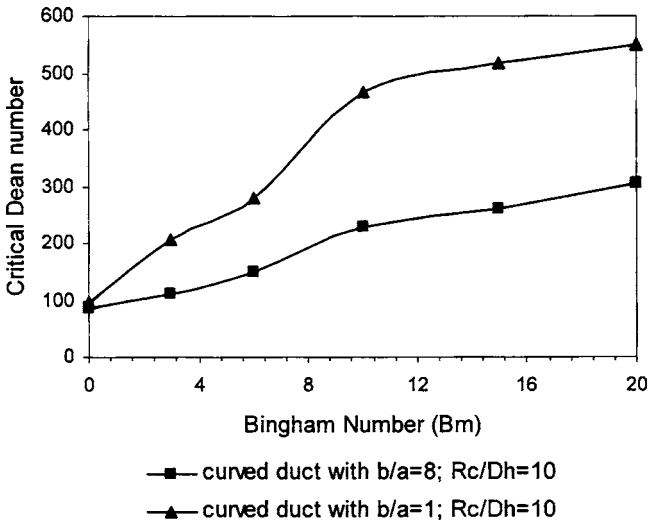

Fig. 14 Effect of Bingham number on the appearance of instability, $R_c/D_h=10$

For all fluids, we show that critical Dean number decreases with increasing duct curvature ratio. The variation of the critical Dean number with the duct aspect ratio is less regular.

The pseudoplastic fluids cause an attenuation of the secondary flow. As the power-law index is reduced, the axial velocity profile shifts toward the concave wall and is flatter than in the Newtonian fluid. The maximum value of the axial velocity decreases, and the onset of Dean instability is delayed with increasing power-law index.

The power-law index and the Bingham number play a significant role in the onset of Dean instability. The same delay is observed in the Bingham fluids when the Bingham number is increased.

Future work will focus on the experimental study of the Dean instability in Newtonian and non-Newtonian fluids.

Nomenclature

a = width of the channel cross section
b = height of the channel cross section
Bm = Bingham number $\mathrm{Bm}=\tau_c D/Um\mu_w$
C_f = friction factor $C_f/2=2\tau_w/\rho Um^2$
D = pipe diameter
D_h = hydraulic diameter
Dn = Dean number $Dn=UmD_h/\nu\sqrt{D_h/R_c}$
k = fluid consistency
L = length of the channel
m = stress growth exponent of the Papanastasiou model
n = power law index
P = pressure
r = radial distance
R = radius of the pipe
R_c = mean curvature radius
Re = Reynolds number $\mathrm{Re}=UmD_h/\nu$
Re_g = generalized Reynolds number
Re_w = Reynolds number of the Bingham fluid defined at the wall
u,v,w = velocity component in x, y, z directions respectively
Uc = velocity of the plastic region (unshared area)
Um = mean velocity
x,y,z = coordinate system

Greek Symbols

ρ = fluid density
μ = fluid viscosity
μ_w = fluid viscosity at the wall
μ_s = solid viscosity
ν = kinematic viscosity
θ = angular position
δ = Bercovier and Engelman model parameter
$\dot{\gamma}$ = shear tensor
$\dot{\gamma}_c$ = critical shear
τ = stress tensor
τ_c = yield stress
τ_w = wall stress
ξ = dimensionless geometrical parameter
ξ_0 = plug flow region (τ_c/τ_w)
ψ_{cc} = yield influence parameter in circular pipe
ψ_{pp} = yield influence parameter in parallel plates channels
Δ = loss

References

[1] Dean, W. R., 1927, "Note on the Motion of Fluid in a Curved Pipe," Philos. Mag., **4**, pp. 208–223.
[2] Eustice, J., 1911, "Experiments of Streamline Motion in Curved Pipes," Proc. R. Soc. London, Ser. A, **A 85**(1), pp. 19–31.

[3] Berger, S. A., Talbot, L., and Yao, L. S., 1983, "Flow in Curved Pipes," Annu. Rev. Fluid Mech., **15**, pp. 461–512.
[4] Cheng, K. C., and Akiyama, M., 1970, "Laminar Forced Convection Heat Transfer in Curved Rectangular Channels," Int. J. Heat Mass Transfer, **13**, pp. 471–490.
[5] Cheng, K. C., Nakayama, J., and Akiyama, M., 1977, "Effects of Finite and Infinite Aspect Ratios on Flow Patterns in Curved Rectangular Channels," Flow Visualization International Symposium, Tokyo, pp. 181–186.
[6] Sugiyama, S., Hayashi, T., and Yamazaki, K., 1983, "Flow Characteristics in the Curved Rectangular Channels (Visualization of Secondary Flow)," Bull. JSME, **26**(216), pp. 964–969.
[7] Chandratilleke, T. T., and Nursubyakto, 2003, "Numerical Prediction of Secondary Flow and Convective Heat Transfer in Externally Heated Curved Rectangular Ducts," Int. J. Therm. Sci., **47**, pp. 187–198.
[8] Cho, Y. I., and Hartnett, J. P., 1982, "Non-Newtonian Fluids in Circular Pipe Flow," Adv. Heat Transfer, **15**, pp. 59–141.
[9] Chen, S. S., Fan, L. T., and Hwang, C. L., 1970, "Entrance Region Flow of the Bingham Fluid in a Circular Pipe," AIChE J., **16**(2), pp. 293–299.
[10] Varadis, G. C., Dougher, J., and Kumar, S., 1993, "Entrance Pipe Flow and Heat Transfer for a Bingham Plastic," Int. J. Heat Mass Transfer, **36**(3), pp. 543–552.
[11] Agrawal, S., Jayaraman, G., Srivastava, V. K., and Nigam, K. D. P., 1993, "Power Law Fluids in a Circular Curved Tube. Part I. Laminar Flow," Polym.-Plast. Technol. Eng., **32**(6), pp. 595–614.
[12] Hsu, C. F., and Patanker, S. V., 1982, "Analysis of Laminar Non-Newtonian Flow and Heat Transfer in Curved Tubes," AIChE J., **24**(4), pp. 610–616.
[13] Shanthini, W., and Nandakumar, K., 1986, "Bifurcation Phenomena of Generalized Newtonian Fluids in Curved Rectangular Ducts," J. Non-Newtonian Fluid Mech., **22**, pp. 35–60.
[14] Kumar, K. R., Rankin, G. W., and Sridhar, K., 1989, "Fully Developed Flow of Power Law Fluids in Curved Ducts With Heat Transfer," Numer. Heat Transfer, Part A, Part A, **16**, pp. 101–118.
[15] Metzner, A. B., and Reed, J. C., 1955, "Flow of Non-Newtonian Fluids: Correlation of the Laminar, Transition, and Turbulent-Flow Regions," AIChE J., **1**, pp. 434–440.
[16] Shan, R. K., and London, A. L., 1978, *Laminar Flow Forced Convection in Ducts*, Academic Press, New York.
[17] Papanastasiou, T. C., 1987, "Flow of Materials With Yield," J. Rheol., **31**(5), pp. 385–404.
[18] Bercovier, M., and Engelman, M., 1980. "A Finite Element Method for Incompressible Non-Newtonian Flows," J. Comput. Phys. **36**, pp. 313–326.
[19] O'Donovan, E. J., and Tanner, R. I., 1984, "Numerical Study of the Bingham Squeeze Film Problem," J. Non-Newtonian Fluid Mech., **15**, pp. 75–83.
[20] Nouar, C., Devienne, R., and Lebouche, M., 1994, "Convection Thermique Pour un Fluide de Herschel-Bulkley dans la Région d'Entrée d'une Conduite," Int. J. Heat Mass Transfer, **37**(1), pp. 1–12.
[21] Itô, H., 1970, "Laminar Flow in Curved Pipes," Rep. Inst. High Speed Mech., Jpn., **22**(224), pp. 161–180.
[22] Bara, B., Nandakumar, K., and Masliyah, J. H., 1992, "An Experimental and Numerical Study of the Dean Problem: Flow Development Towards Two-Dimensional Multiple Solutions," J. Fluid Mech. **244**, pp. 339–376.
[23] Ghia, K. N., and Sokhey, J. S., 1977, "Laminar Incompressible Viscous Flow in Curved Ducts of Rectangular Cross-Section," ASME J. Fluids Eng., **99**, pp. 640–648.
[24] Hille, P., Vehrenkamp, R., and Schulz-Dubois, E. O., 1985, "The Development and Structure of Primary and Secondary Flow in a Curved Square Duct," J. Fluid Mech., **151**, pp. 219–241.
[25] Thangam, S., and Hur, N., 1990, "Laminar Secondary Flows in Curved Rectangular Ducts," J. Fluid Mech., **217**, pp. 421–440.
[26] Komiyama, Y., Mikami, F., Okui, K., and Hori, T., 1984, "Laminar Forced Convection Heat Transfer in Curved Channels of Rectangular Cross-Section," Trans. Jpn. Soc. Mech. Eng., Ser. B, **B 50**(450), pp. 424–434.
[27] Ranade, V. R., and Ulbrecht, J. J., 1982, "Velocity Profiles of Newtonian and Non-Newtonian Toroidal Flows Measured by a LDA Technique," Chem. Eng. Commun., **20**, pp. 253–272.
[28] Alexandrou, A. N., McGilvreay, T. M., and Burgos, G., 2001, "Steady Herschel-Bulkley Fluid Flow in Three-Dimensional Expansions," J. Non-Newtonian Fluid Mech., **100**, pp. 77–96.

Taylor-Couette Instabilities in Flows of Newtonian and Power-Law Liquids in the Presence of Partial Annulus Obstruction

B. V. Loureiro

P. R. de Souza Mendes[1]

L. F. A. Azevedo

Department of Mechanical Engineering,
Pontifícia Universidade
Católica do Rio de Janeiro,
Rua Marquês de São Vicente 225,
Gávea, Rio de Janeiro, RJ, 22453-900, Brazil

The flow inside a horizontal annulus due to the inner cylinder rotation is studied. The bottom of the annular space is partially blocked by a plate parallel to the axis of rotation, thereby destroying the circumferential symmetry of the annular space geometry. This flow configuration is encountered in the drilling process of horizontal petroleum wells, where a bed of cuttings is deposited at the bottom part of the annulus. The velocity field for this flow was obtained both numerically and experimentally. In the numerical work, the equations which govern the three-dimensional, laminar flow of both Newtonian and power-law liquids were solved via a finite-volume technique. In the experimental research, the instantaneous and time-averaged flow fields over two-dimensional meridional sections of the annular space were measured employing the particle image velocimetry (PIV) technique, also both for Newtonian and power-law liquids. Attention was focused on the determination of the onset of secondary flow in the form of distorted Taylor vortices. The results showed that the critical rotational Reynolds number is directly influenced by the degree of obstruction of the flow. The influence of the obstruction is more perceptible for Newtonian than for non-Newtonian liquids. The more severe is the obstruction, the larger is the critical Taylor number. The height of the obstruction also controls the width of the vortices. The calculated steady-state axial velocity profiles agreed well with the corresponding measurements. Transition values of the rotational Reynolds number are also well predicted by the computations. However, the measured and predicted values for the vortex size do not agree as well. Transverse flow maps revealed a complex interaction between the Taylor vortices and the zones of recirculating flow, for moderate to high degrees of flow obstruction. [DOI: 10.1115/1.2136930]

1 Introduction

The flow field generated in the annular region formed by two concentric cylinders due to the rotation of the inner cylinder is a classical problem in fluid mechanics that has received considerable attention in the literature. The flow instabilities generated in the annular space have been investigated since the pioneer work of Taylor [1]. Since then, several other researchers addressed different features of this super critical Couette flow [2,3]. Andereck et al. [4] characterized the supercritical flow regimes in circular Couette flow, while Wereley and Lueptow [5] employed whole-field techniques to measure the flow field in a meridional plane.

In addition to its importance to the fundamentals of fluid mechanics, supercritical circular Couette flow encounters several important practical applications. The present research was motivated by the drilling of horizontal oil and gas wells. Horizontal wells have been extensively used in recent years by the petroleum industry due to its higher efficiency in oil recovery. A challenge posed to the horizontal drilling technique is the ability to efficiently remove the drilling cuttings that tend to settle and accumulate at the lower part of the annular gap between the rotating column and the formation. The design of a successful drilling operation relies on simulations of the flow capability of suspending and removing the cuttings. One of the key inputs to such simulations is the axial velocity profile in the annular space. Often, due to the lack of information about the actual flow, crude approximations for the velocity profile—such as plug flow—are employed. There are a number of articles in the petroleum literature that deal with the influence of shaft rotation on the flow field and on the cleaning efficiency of horizontal wells (e.g., [6–8]).

The present paper reports on the efforts of an ongoing project aimed at studying the flow field and cleaning characteristics of horizontal wells. In the first phase presented here, a simplified model of the problem is studied in detail. The model consists of a horizontal annular space formed by an outer fixed cylinder and an inner rotating cylinder of large length-to-gap ratio. The annular space is limited axially by end walls. No axial flow is present. The bed of cuttings is mimicked by an impermeable horizontal plate that partially obstructs the annular gap, as represented schematically in Fig. 1.

Four distinct regimes were reported [4] for the flow in annular spaces due to rotation of the inner cylinder, which were observed as the angular velocity is increased. These are, in order of increasing angular velocity, (i) the classical Couette flow (purely tangential flow), (ii) the Taylor-vortex flow, (iii) the wavy-vortex flow, and (iv) the modulated-vortex flow. An additional regime was identified and reported by Lim et al. [9], occurring between Taylor- and wavy-vortex flow. It was named secondary Taylor-vortex flow. These five regimes are characterized by a few parameters, namely, a rotational Reynolds number, the ratio of inner to outer annulus radius, and, for some regimes, the angular acceleration imposed on the inner cylinder as it approaches the desired rate of rotation.

[1]Corresponding author. Email: pmendes@mec.puc-rio.br

Contributed by the Fluids Engineering Division of ASME for publication in the JOURNAL OF FLUIDS ENGINEERING. Manuscript received September 20, 2004; final manuscript received September 29, 2005. Assoc. Editor: Dennis Siginer.

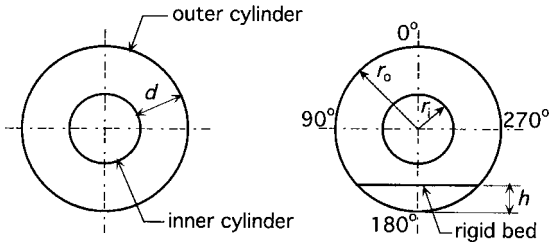

Fig. 1 Cross section of the partially obstructed annular space. Inner cylinder rotates counter-clockwise.

The effect of the annular space radius ratio on the Taylor-Couette stability was investigated mathematically [3] for concentric, infinite-length cylinders. They have shown that the critical rotational Reynolds number that characterizes the onset of Taylor-vortex flow increases with the radius ratio, for radius ratios larger than 0.45.

It has been observed [4,10] that the transition from purely tangential to Taylor-vortex flow depends also on the acceleration ramp imposed on the inner cylinder. A hysteresis curve for the critical rotational Reynolds number was obtained by approaching the transition angular velocity both from below and from above [10]. The hysteresis effect was shown to be negligible if the dimensionless acceleration is smaller than 10. This dimensionless acceleration is defined as

$$a^* = \left(\frac{d}{L}\right)\frac{d\,\mathrm{Re}}{dt^*} \tag{1}$$

where $\mathrm{Re} \equiv \rho\Omega r_i d/\eta_c$ is the rotational Reynolds number, $t^* = t\eta_c/\rho L^2$ is a dimensionless time, $d = r_o - r_i$ is the gap, r_i and r_o are respectively the inner and outer cylinder radii, L is the total axial length, and ρ is the mass density. The characteristic viscosity η_c is defined as $\eta_c \equiv \eta(\dot{\gamma}_c)$, where $\dot{\gamma}_c \equiv \Omega r_i/d$ is the characteristic shear rate [see Eq. (4) below].

A visualization technique was employed to study the influence of the length-to-gap ratio, L/d, on the Taylor-vortex and wavy-vortex instabilities [2]. It was found that the onset of Taylor-vortex instability is not affected by L/d when this parameter is larger than 20, while it should be larger than 50 in the case of the wavy-vortex transition.

The effect of the eccentricity between the inner and outer cylinders on the Taylor vortex instability was investigated [11,12]. Both articles report that the value of the critical Reynolds number that characterizes the onset of Taylor-vortex instability increases with eccentricity.

The objective of the present work is to determine the influence of the partial obstruction on the flow structure within the gap for low rotational Reynolds number values, both for Newtonian and power-law liquids. To this end, a combined experimental and numerical program was conducted where instantaneous, whole-field velocity measurements and three-dimensional computer simulations were employed to help characterize the flow field.

2 Governing Equations and Numerical Solution

The problem investigated is the flow in the gap between two horizontal, concentric cylinders forming an annular space with inner radius r_i and an outer radius r_o, defining the annular space which gap is $d = r_o - r_i$. The outer cylinder is fixed, while the inner cylinder rotates with an angular velocity Ω. A horizontal plate is placed at the lower part of the annular space, at a distance h from the external radius. The axial length of the annular space, L, is the same as that of the plate. A view of the cross section of the partially obstructed geometry studied is shown in Fig. 1. To allow comparisons between numerical and experimental results, the numerical solutions were obtained for a finite-length annular space, delimited axially by two vertical end walls.

The steady isothermal flow of an incompressible, generalized Newtonian liquid is governed by the following mass conservation and momentum equations:

$$\boldsymbol{\nabla}\cdot\mathbf{u} = 0 \tag{2}$$

$$\rho\mathbf{u}\cdot\boldsymbol{\nabla}\mathbf{u} = -\boldsymbol{\nabla}p + \boldsymbol{\nabla}\cdot(\eta\dot{\boldsymbol{\gamma}}) \tag{3}$$

In the above equations, $\mathbf{u}$ is the velocity vector, p is the liquid pressure, ρ and η are, respectively, the mass density and viscosity function of the generalized Newtonian liquid, and $\dot{\boldsymbol{\gamma}} \equiv \boldsymbol{\nabla}\mathbf{u} + \boldsymbol{\nabla}\mathbf{u}^T$ is the rate-of-deformation tensor.

The presence of the horizontal plate in the annular space destroys the circumferential symmetry, and therefore a three-dimensional flow field is expected. The dimensionless parameters that govern the problem are the rotational Reynolds number based on the inner cylinder angular velocity, $\mathrm{Re} \equiv \rho\Omega r_i d/\eta_c$, the inner-to-outer cylinder radius ratio, r_i/r_o, the length-to-gap ratio, L/d, and the dimensionless obstruction height, $\chi = h/d$.

At the inner and outer cylinder walls, the boundary conditions employed were the no-slip/impermeability conditions ($\mathbf{u}=\mathbf{0}$). At the vertical walls that delimit axially the horizontal annular space, two types of boundary conditions were tested. The first kind of boundary condition tested was no-slip/impermeability ($\mathbf{u}=\mathbf{0}$). This condition models the experimental test section constructed. A second type of boundary condition was used as an attempt to simulate the flow in infinitely long annular spaces. To this end, the boundary condition suggested by Coronado-Matutti et al. [13] was implemented, namely, the computational domain is extended and no-slip/impermeability boundary conditions are imposed at the new, farther-apart solid surfaces. At the surface of the inner cylinder that belongs to the extended computational domain the angular velocity is set to zero. This approach provides essentially an additional cavity of fluid that allows freedom to accommodate the vortical flow in the annular space. Coronado-Matutti et al. [13] reported good results employing this type of boundary condition.

In order to try to reduce the computer effort, some numerical solutions were performed employing a symmetry boundary condition at the annular space mid-length. The results obtained with the three boundary conditions described were tested against the experimental results. In order to facilitate future reference in this text, these boundary conditions were labeled as:

Type (a) boundary conditions: symmetry at mid-length and extended domain at vertical end plane;

Type (b) boundary conditions: symmetry at mid-length and no-slip/impermeability condition at vertical end wall;

Type (c) boundary conditions: no-slip/impermeability condition at both vertical end walls (computation of the full domain).

The conservation equations together with the appropriate boundary condition were solved numerically employing the software Fluent version 6.12. This code employs a finite-volume-based discretization of the governing equations, using a power-law interpolation scheme. The pressure-velocity coupling employed was the SIMPLE algorithm [14]. The resulting algebraic system was solved using a multi-grid procedure. Due to memory limitations, axis-symmetric solutions only (no obstruction) were obtained for type (c) boundary conditions. Extensive mesh-sensitivity tests were conducted in order to define an appropriate three-dimensional mesh for solving the problem. Grid independence was obtained for a uniform mesh of $25\times160\times400$ control volumes, deployed, respectively, in the radial, circumferential, and axial directions. For the axis-symmetric cases, grid-independent solutions were achieved with a 40×800 uniform mesh. All the physical dimensions of the domain of computation were chosen to be identical to the ones found in the experimental apparatus, to allow comparisons between predictions and measurements. These dimensions are given in Sec. 4.

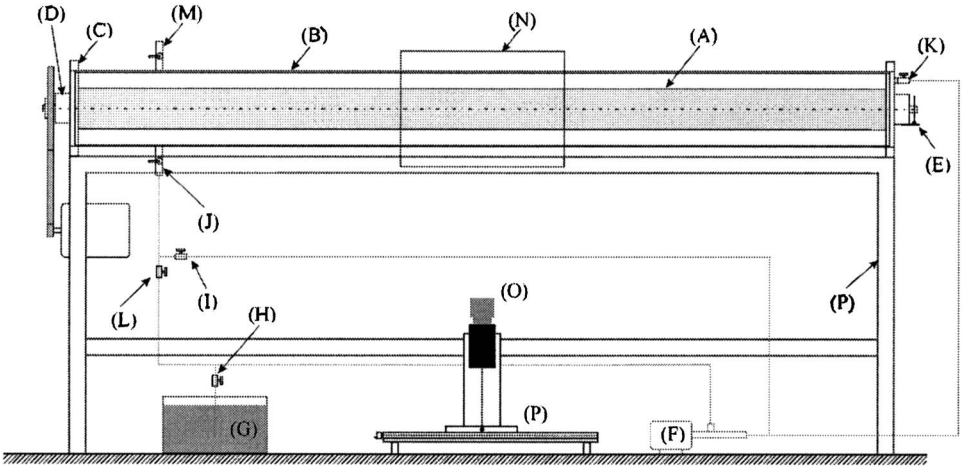

Fig. 2 Schematic view of the experimental setup

3 The Viscosity Function

For the range of angular velocities found in drilling operations, the shear rate is typically large enough to render unimportant the zero-shear-rate plateau region which is often observed in the viscosity function of drilling fluids. Therefore, to consider the shear-thinning behavior of these materials in this flow it suffices to employ the simplest non-Newtonian viscosity function available, namely, the Ostwald-de-Waele or power-law viscosity function:

$$\eta(\dot{\gamma}) = K\dot{\gamma}^{n-1} \tag{4}$$

where K is the consistency index, $\dot{\gamma} \equiv \sqrt{\mathrm{tr}\dot{\boldsymbol{\gamma}}^2/2}$ is the deformation rate and n is the power-law index.

The rheological parameter values pertaining to four non-Newtonian liquids used in the experiments, namely, K and n, were obtained via least-squares fittings to rheological data, and were employed in the numerical simulations.

These parameters are given below:

K(Pa s^n)	n
0.221	0.704
0.567	0.578
1.26	0.406
2.52	0.309

For the Newtonian experiments, the liquid employed was a glycerol/water mixture with a constant viscosity of approximately 0.36 Pa s.

4 Experimental Setup

The experimental setup to be described next was designed and constructed with the objective of allowing the assessment of the influence of the cylinder-to-plate gap on the flow structure inside the annular region, and on the critical rotational Reynolds number that characterizes the transition to the Taylor-vortex flow regime. A more complete description is available in Loureiro [15].

4.1 Test Section. Figure 2 is a schematic representation of the test section employed in the experiments. Capital letters in the figures mark some components of the test section to facilitate the description in the text. A horizontal aluminum hollow shaft (A) was mounted concentrically with a 5 mm thick Plexiglas cylinder (B). The outer diameter of the shaft was $2r_i = 125$ mm, while the inner diameter of the Plexiglas cylinder was equal to $2r_o = 220$ mm, thereby forming an annular gap of $d = 47.5$ mm and a radius ratio of $r_i/r_o = 0.57$. The inner aluminum shaft was machined from a 5 mm thick extruded pipe. One aluminum cap with a protruding 25 mm diameter shaft was installed at each end of the hollow aluminum shaft. During the machining operation, the aluminum shaft was supported on the lathe by its two end shafts, in order to guarantee a perfect rotation of the outer surface of the aluminum shaft around its centerline. At the end of the machining operation, a dial gauge was used to verify that the aluminum shaft rotated with an eccentricity smaller than 0.1 mm. The two end shafts were mounted on ball bearings (D) fixed on Plexiglas discs (C). Each disc was equipped with an O-ring and fixed to one of the end planes of the Plexiglas cylinder, thereby sealing the working liquid in the annular space. The length of the annular space formed was equal to $L = 2475$ mm, which produced a length-to-gap ratio of $L/d = 52.1$.

An electrical motor equipped with a programmable speed control was used to rotate the aluminum shaft. Two pulleys connected with a synchronizing rubber belt were used to drive the aluminum shaft, providing a transmission ration of 7:1. The motor speed control and the low transmission ratio allowed for a smooth control of the shaft angular speed and speed ramp. As will be noted shortly, the ability to control the shaft angular acceleration is critical for the success of the flow transition experiments. An encoder (E) was installed at the tip of the aluminum shaft to monitor its angular motion. The encoder signal was registered by a computer that calculated angular displacement, angular velocity, and acceleration of the shaft. The signal from the encoder was also used to trigger the system used for measuring the instantaneous flow field.

A progressive cavity pump (F) was installed to aid in the preparation of the experiments. The pump was used to fill the annular cavity with the working liquid. In this operation, the working liquid was pumped from a reservoir (G) to the interior of the annular space, by opening valves (H), (I), and (J) and closing valves (L) and (K). Air was purged from the annular space using valve (M). The Newtonian working liquid was formed by a mixture of glycerol, water and a few grams of small, silver-coated, hollow glass spheres used as tracers for the laser technique employed. For non-Newtonian liquids, a mixture of glycerol, carbopol solution at 0.15%, and the same spheres were used. The glycerol was used to reduce the carbopol turbidity and control the power-law index. The pump was also used to circulate the working liquid prior to the measurements in order to keep the tracer particles in suspension. The pump was not used during the experiments.

A Plexiglas box (N) was mounted around the Plexiglas tube with the objective of minimizing the distortions of the image in the annular space due to the curved wall. The box was filled with the working liquid, without the small hollow glass spheres, which provided a good match to the index of refraction of Plexiglas. Two adjacent box walls were made of borosilicate glass, while the other two were made of Plexiglas. The laser sheet of the velocity

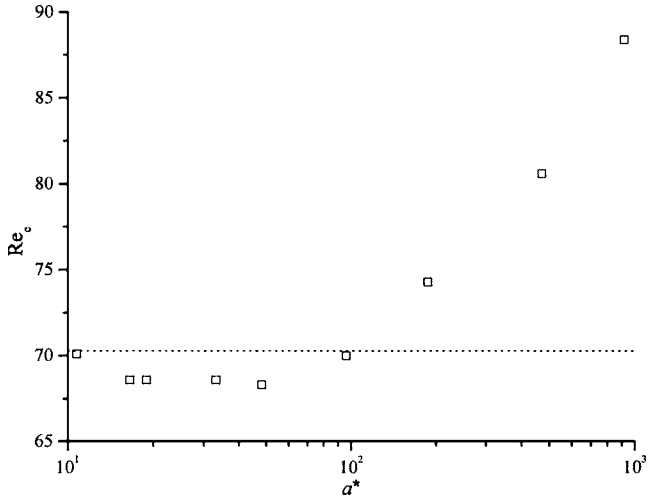

Fig. 3 Influence of dimensionless acceleration on critical Reynolds number for a Newtonian liquid. Experimental results.

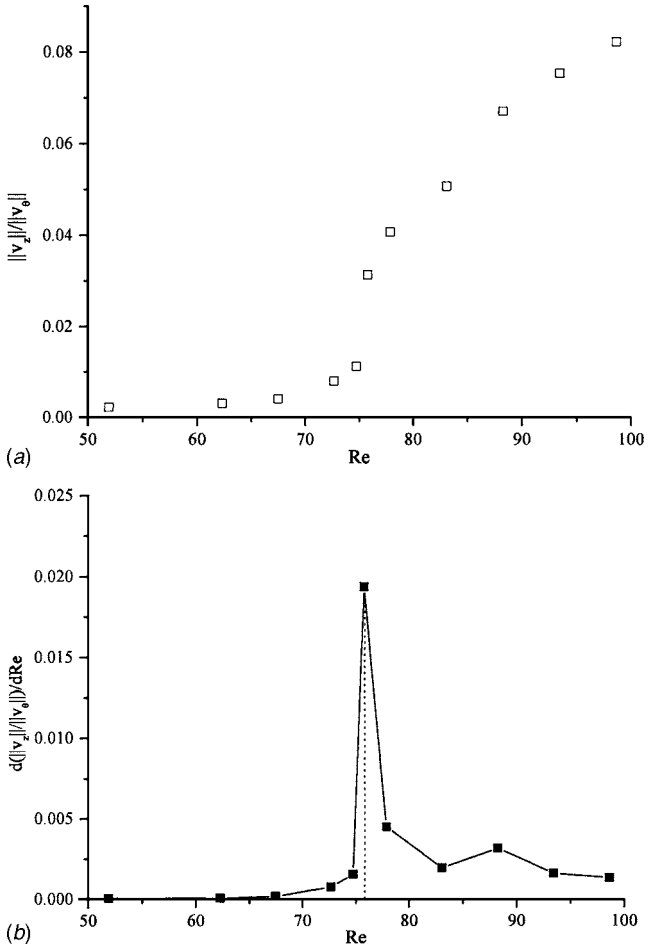

Fig. 4 (*a*) Axial-to-tangent velocity norm ratio as a function of the rotational Reynolds number. (*b*) Derivative of the norm ratio as a function of the rotational Reynolds number (Newtonian liquid, $h/d=0.5$).

measuring system entered through the vertical glass wall, while the images of the illuminated tracer particles were captured through the second, horizontal, lower glass wall.

The focus of the work was on the effect on the flow field within the annular gap caused by the presence of a partial obstruction placed within the gap. A set of five, 4 mm thick Plexiglas plates was carefully machined to serve as the obstruction in the annular gap. The length of each plate matched the length of the annular gap. The width of each plate was calculated so as to produce the cylinder-to-plate spacing required for each particular experiment. The plate was introduced in the annular space by removing one of the Plexiglas end caps that sealed the annular space. The edges of the plates were beveled at an angle that matched the internal curvature of the Plexiglas cylinder. The horizontal plates were fixed in position by a series of bolts that passed through the external surface of the Plexiglas cylinder and matched tapped holes in the inferior surface of the plate.

The complete assembly formed by the inner aluminum shaft, Plexiglas outer cylinder with horizontal plate (when present), and visualization box was mounted on a solid steel frame that was fixed to the laboratory floor using four antivibration bases. The assembly was fixed on the steel frame by mounting the Plexiglas cylinder on four semi-circular Plexiglas bases. Braces fixed the Plexiglas cylinder on the bases. When the braces were not yet tightened, it was possible to rotate the Plexiglas cylinder by hand. The rotation of the cylinder was only necessary in the experiments that used the horizontal plate in the annular gap. In these experiments, the circumferential symmetry of the flow in the annular space is destroyed and there is a need to measure flow fields in the r-z plane for different circumferential positions θ. This was achieved by keeping the illuminating laser sheet horizontal and positioning the Plexiglas cylinder at different circumferential coordinates. It should be mentioned that the visualization box was designed so that the Plexiglas cylinder could be circumferentially moved, while keeping the box in a fixed position with its vertical glass window orthogonal to the incident laser sheet.

4.2 Velocity Measurements. Both time-resolved and average flow fields in the annular gap were obtained via the particle image velocimetry technique (PIV) [16]. In this technique, a pulsed laser sheet illuminates small tracer particles previously distributed in the liquid. A digital camera, mounted orthogonally to the laser sheet, captures the particle positions at two consecutive time instants. An image-processing algorithm calculates the displacements of small groups of particles in the image which, together with the time interval of image capture, produces the desired instantaneous flow field.

In the present study the PIV system used was manufactured by TSI Inc. The system employed a New Wave Research, 120 mJ per pulse, double-cavity laser that is able to fire double pulses at 15 Hz. The minimum time interval between pulses can be adjusted to a few nanoseconds, much less than necessary for the present low-speed experiments. Lenses attached to the laser unit transformed the beam into a divergent laser sheet with an approximate thickness at the beam waist of 0.3 mm. The tracer particles used were silver-coated, hollow glass spheres with mean diameter of 13 μm and density of 1.6 g/cm^3; even though the working liquid density was approximately equal to 1.2 g/cm^3, a very small number of particles was observed to settle over a 24 h period. The camera (O) used to capture the particle images (TSI model PIV-CAM 10–30) had 1000×1000 pixel resolution, working at 30 frames per second. This camera was mounted on a xyz coordinate table (P). Synchronization between laser firing and image capture was accomplished by a TSI model 60030 synchronizer. In the experiments, instantaneous flow fields were captured as the aluminum shaft was accelerated from rest up to the final angular speed desired for a particular experiment. These measurements were accomplished by using the signal from the shaft encoder as a trigger for the TSI synchronizer.

Two types of velocity measurements were obtained: flow fields in the r-z plane and in the r-θ plane. In the former case, the light sheet was placed horizontally and the camera vertically. The tracer particles in this case crossed the light sheet with elevated circum-

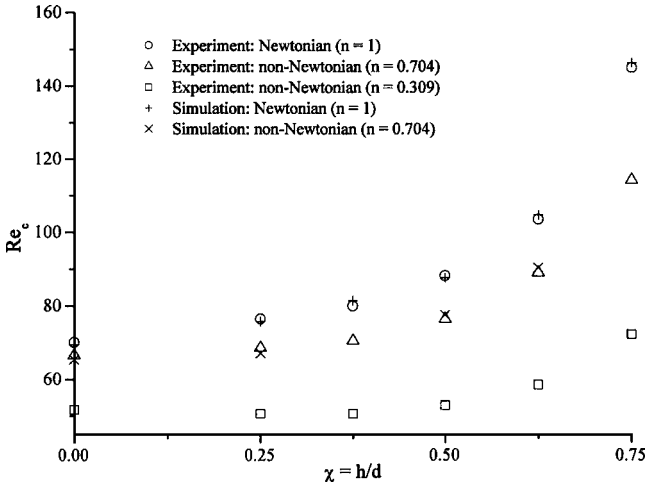

Fig. 5 Critical Reynolds number as a function of the obstruction height

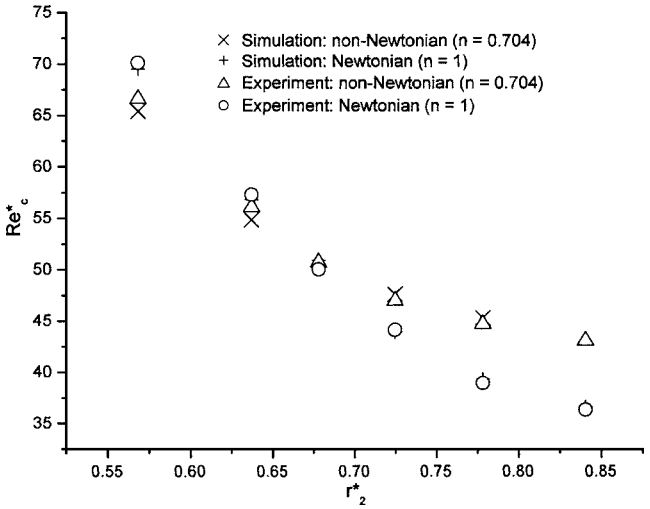

Fig. 6 Critical Reynolds number at the minimum gap as a function of the radius ratio at the minimum gap

ferential velocity, especially in the regions close to the aluminum shaft surface where the velocity is highest. The time interval between laser pulses was adjusted so as to guarantee that the particles did not leave the light sheet during the two pulses and still display a reasonable displacement to allow an accurate measurement.

A cross-correlation-based algorithm was employed to determine the particle displacement field. The algorithm was part of the software Insight version 5.0 developed by TSI Inc. Interrogation windows of 64×64 pixels with a 32 pixel overlap were used in the calculations. An image calibration procedure indicated that the chosen interrogation window corresponded to a 3×3 mm^2 window in the actual flow. Typically, 50×30 (axial $\times$ radial direction) velocity vectors were measured in each plane. The quality of the images obtained was such that the interrogation windows generated only valid vectors, so no vector interpolation scheme was employed. Average velocity fields were obtained by averaging over 100 measured vector fields. This number was limited by the memory of the available computer. Calibrating experiments previously conducted with a solid body rotation apparatus indicated that the experimental accuracy for the PIV system employed is of the order of $\pm1\%$ [17].

5 Results and Discussion

In the following subsections we present and discuss the experimental and numerical results obtained.

5.1 Effect of Angular Acceleration on the Onset of Taylor-Vortex Flow. Park et al. [10] demonstrated the effect of angular acceleration on the critical value of the rotational Reynolds number. A series of experiments was carried out to determine the relationship between angular acceleration and Taylor-vortex onset for the annular region without the partial blockage. In these experiments the aluminum shaft was started from rest and uniformly accelerated to reach a steady-state condition. The shaft encoder recorded the rotation history and sent a signal to trigger the PIV system at every three shaft revolutions. The r-z velocity fields recorded were carefully examinated to detect the onset of radial or axial velocities, which were the indication of the onset of Taylor vortices.

Figure 3 presents the results obtained for a Newtonian liquid. In the figure, the critical rotational Reynolds number is plotted as a function of the dimensionless acceleration. The influence of the acceleration on the value of the critical Reynolds number is clearly noted. For the lowest value of the acceleration tested, the value of the critical Reynolds number slightly over 70 agrees with data from the literature available for $r_i/r_o=0.55$ [3], which is close to the one of the present study ($r_i/r_o=0.57$). All the experiments reported in the present paper were conducted with the minimum possible dimensionless acceleration value allowed by the experimental setup, which was around 10. This value is within the maximum limit suggested by Park et al. [10] to minimize hysteresis effects on Taylor-vortex transition values.

5.2 Taylor-Vortex Onset for Partially Obstructed Annular Space. The onset of Taylor-vortex flow in the partially obstructed annular space was investigated both numerically and experimentally. In the experimental tests, the same methodology described in the previous section was employed for determining the critical rotational Reynolds number values.

In the numerical investigations, the three-dimensional, steady-state flow field was obtained for increasing values of the rotational Reynolds number until the onset of Taylor-vortex flow was detected. The criterion employed for detecting the onset of Taylor-vortex flow was that suggested by Coronado-Matutti [13]. According to this criterion, the ratio of a given norm of the axial velocity field (v_z) to the same norm of the circumferential velocity field (v_θ) is calculated for each value of the rotational Reynolds number. This ratio is given by

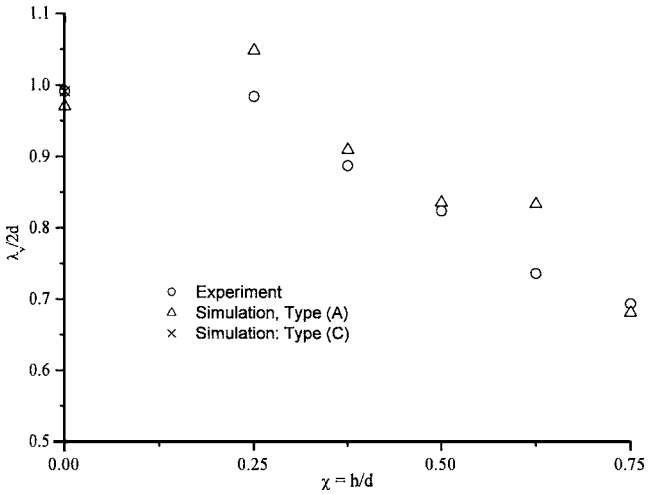

Fig. 7 Vortex length as a function of obstruction height. Newtonian liquid.

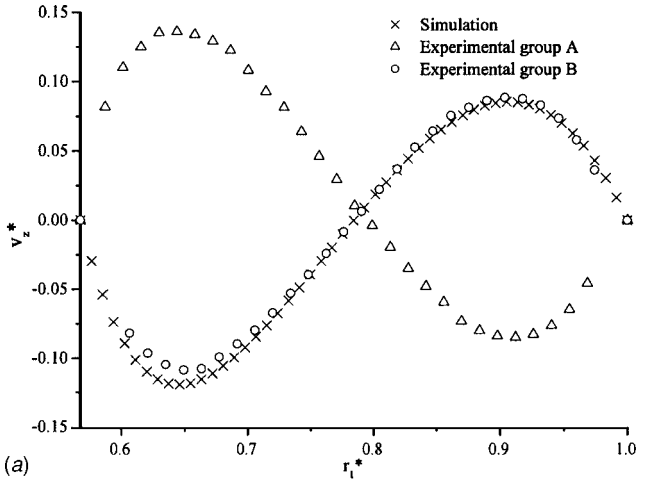

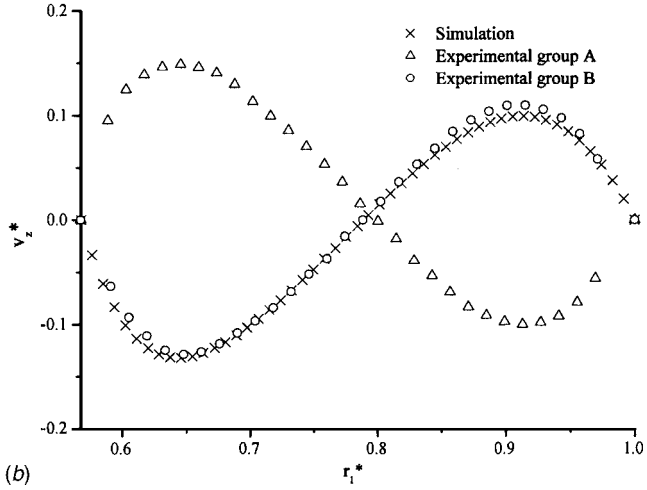

Fig. 8 Axial velocity profiles for Taylor-vortex regime. Unobstructed annulus and Newtonian liquid. (*a*) Re=104. (*b*) Re =126.

$$\frac{\|v_z\|}{\|v_\theta\|} = \frac{\Sigma|v_z|}{\Sigma|v_\theta|} \tag{5}$$

In the three-dimensional calculations, the summations in Eq. (5) were evaluated only over the node points contained in the meridional vertical planes (0 and 180 deg). For a flow configuration below the critical Reynolds number value, it is expected that the ratio of velocity norms be zero, indicating the absence of the axial velocity component. As the Taylor-vortex structure begins to develop, the axial component of velocity appears and the norm ratio increases.

Figure 4(*a*) presents the results obtained from the numerical simulations conducted with the type (a) boundary conditions. In the figure, the ratio of norms is plotted as a function of the rotational Reynolds number for an obstruction of $h/d=0.5$. The departure from zero can be detected for a Reynolds number around 75. A more accurate detection of the critical Reynolds number can be obtained if the derivative of the function is calculated and plotted in terms of the Reynolds number. This is presented in Fig. 4(*b*). The peak in the derivative of the norm function with respect to the Reynolds number clearly determines the transition point. This methodology was adopted in the present study after being tested for $h/d=0$, for which the obtained value for the critical rotational Reynolds number was in close agreement with the already mentioned result available in the literature ($\mathrm{Re}_c \simeq 70$ [3]).

The effect of the flow obstruction on the critical Reynolds number is now examined. Figure 5 presents both numerical and ex-

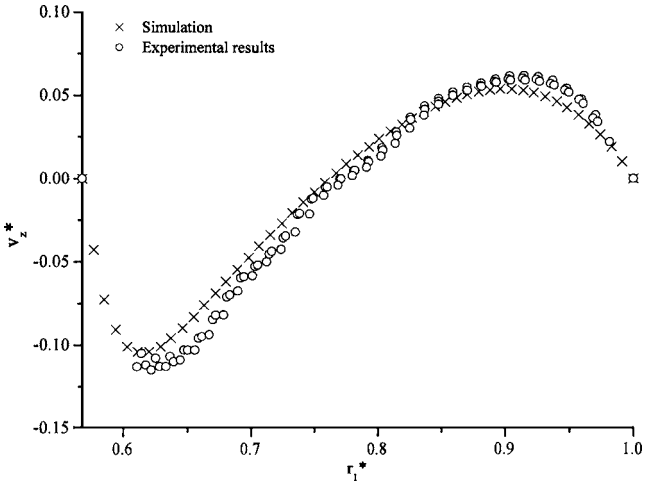

Fig. 9 Axial velocity profiles for Taylor-vortex regime. Unobstructed annulus. $n=0.406$. $\mathrm{Re} \simeq 1.8\mathrm{Re}_c$.

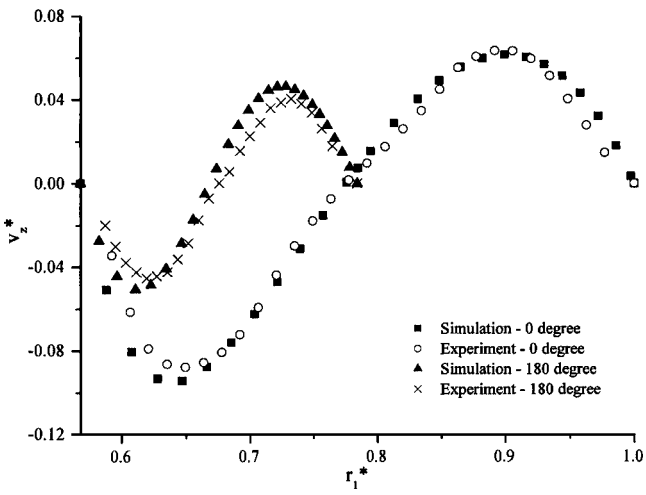

Fig. 10 Velocity profile in the meridional planes 0 and 180 deg for Taylor-vortex regime. Newtonian liquid. $\mathrm{Re} \simeq 1.2\mathrm{Re}_c$, h/d =0.5.

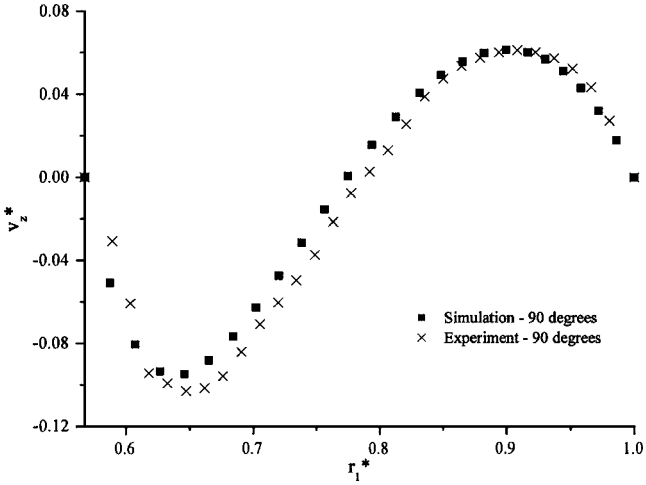

Fig. 11 Velocity profile in the meridional plane 90 deg for Taylor-vortex regime. Newtonian liquid. Re=109, h/d=0.5.

perimental results obtained for the critical rotational Reynolds number as a function of the dimensionless obstruction height, h/d, both for Newtonian and non-Newtonian power-law liquids. According to the definition of h (Fig. 1), when $h/d=1$ the plate touches the inner cylinder, while $h/d=0$ corresponds to the absence of obstruction.

Figure 5 reveals that the obstruction of the annular space delays the transition to the Taylor-vortex flow regime. Indeed, the critical Reynolds number value for the free annular space of roughly 70 increases up to 145 for the maximum obstruction value, namely $h/d=0.75$, and Newtonian liquid. This trend is consistent with the observations for increasing radius ratio values [3] and also for increasing eccentricity [11,12]. Narrower gaps imply larger viscous forces, which render the inertial forces relatively less important and hence a stabilizing effect is observed. These results can be of significant importance for the application that motivated the present work. Indeed, the rate of particle removal of a horizontal bed in an annular space can be directly influenced by the presence and intensity of Taylor vortices.

Another result observed in Fig. 5 is the effect of the power-law index on the transition to the Taylor-vortex flow regime. The more shear-thinning is the liquid, the lower is the critical rotational Reynolds number. This behavior is in agreement with the findings of Ashrafi and Khayat [18].

Figure 5 also illustrates the remarkable agreement between experiments and computation for both the Newtonian and the non-Newtonian liquids. Indeed, the average deviation observed between experiments and computation is of the order of 0.9%, the maximum deviation being 1.83%. The average absolute experimental uncertainties estimated for the Reynolds number were of the order of 0.5.

It is interesting to replot the information given in Fig. 5 in a different form. We can define a Reynolds number evaluated at the minimum gap as follows:

$$\mathrm{Re}^{*} \equiv \frac{\rho \Omega r_i (d-h)}{\eta(\dot{\gamma}_2)} \tag{6}$$

where $\dot{\gamma}_2 \equiv \Omega r_i/(d-h)$ is a representative shear rate at the minimum gap. In Fig. 6 we plot the critical value of Re^{*}, namely Re_c^{*}, as a function of $r_2^{*} \equiv r_i/(r_o-h)$, which is the radius ratio at the minimum gap. We can observe that Re_c^{*} decreases with r_2^{*} which yields that, since Re_c increases with r_i/r_o for the tangential flow in the free annular space [3], then the tangential flow in the partially obstructed annular space with a given obstruction r_2^{*} is less stable than the tangential flow in the free annular space of radius ratio equal to r_2^{*}.

5.3 Taylor-Vortex Characterization: Vortex Length. The influence of the obstruction on the length of the Taylor vortices was investigated both numerically and experimentally. In both cases, the methodologies employed to determine the vortex length were similar. Along a line of constant radial and tangential coordinates close to the inner rotating cylinder, the vortex length was taken as the distance between two consecutive axial positions where the axial velocity component changed direction. This procedure was conducted for different values of the flow obstruction, given by h/d.

Figure 7 presents Taylor-vortex length results for the Newtonian liquid. The dimensionless length of the vortex $\lambda_v/2d$ (λ_v is the axial length of each pair of counter-rotating vortices) is presented as a function of the obstruction parameter h/d. The experimental results are represented in the figure by circles, while numerical results are represented by $\times$'s and triangles. The two numerical solutions differ on the boundary conditions imposed at the r-θ end planes that limit axially the computation domain.

First it is observed that for unblocked annuli $\lambda_v/2d \simeq 1$. This is a well-known result, which holds for a wide range of radius ratio values. Therefore, Fig. 7 illustrates that, although the obstruction reduces the vortex length, the vortices for a given obstruction h/d are larger than those pertaining to an unblocked annulus with gap equal to $d-h$.

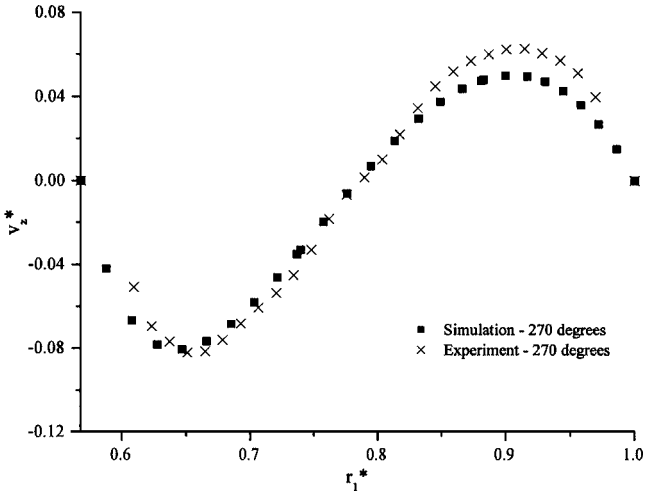

Fig. 12 Velocity profile in the meridional plane 270 deg for Taylor-vortex regime. Newtonian liquid. Re=109, $h/d=0.5$.

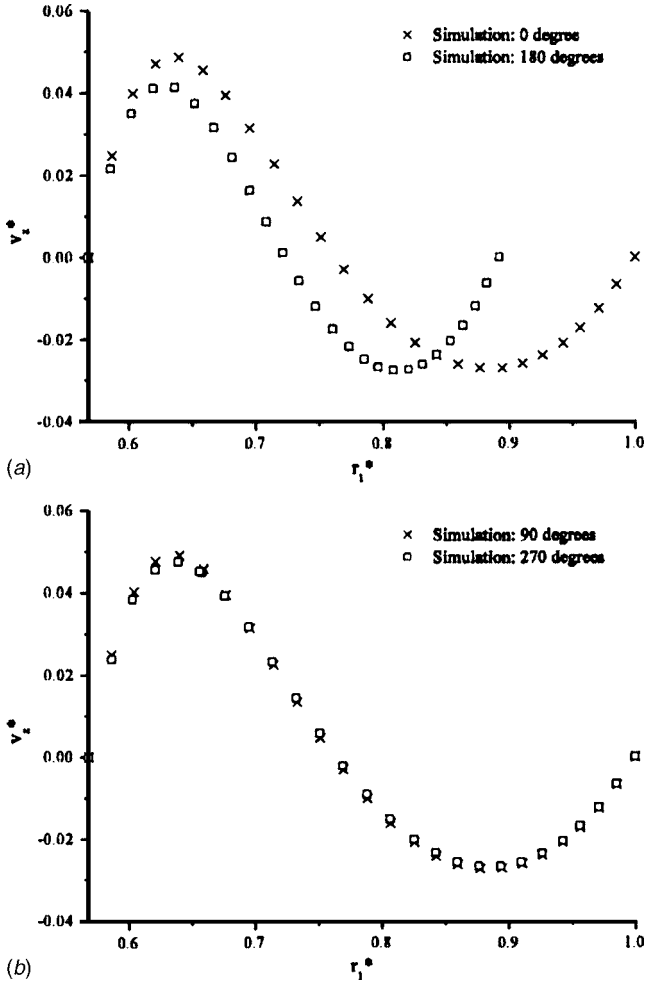

Fig. 13 Velocity profile in the meridional planes (*a*) 0 and 180 deg and (*b*) 90 and 270 deg for Taylor-vortex regime. $n=0.704$. $\mathrm{Re}=69.5 \simeq 1.03\mathrm{Re}_c$, $h/d=0.25$.

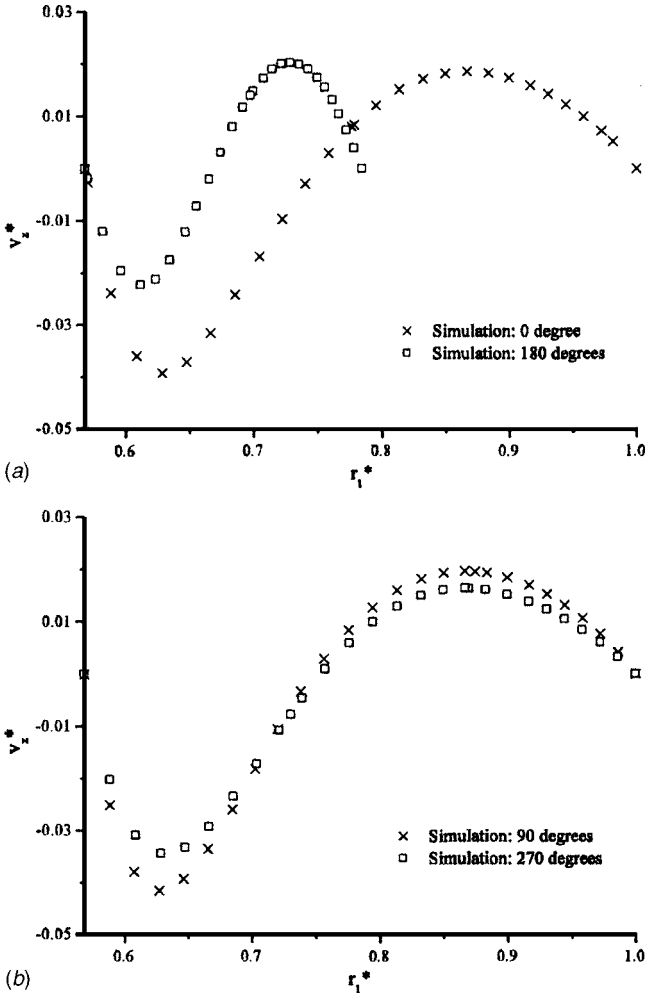

Fig. 14 Velocity profile in the meridional planes (*a*) 0 and 180 deg and (*b*) 90 and 270 deg for Taylor-vortex regime. $n=0.704$. $\mathrm{Re}=80\simeq 1.03\mathrm{Re}_c$, $h/d=0.5$.

It is also interesting to verify in Fig. 7 that, although the agreement between numerical and experimental results for the critical Reynolds number presented in Fig. 5 was excellent, a significant discrepancy is observed for the Taylor vortex length. For h/d equal to 0.375, 0.500, and 0.750, the agreement is very good for the type (b) boundary condition. The same cannot be said for h/d equal to 0, 0.250, and 0.625, where a considerable discrepancy is observed.

These discrepancies were found to be related to the boundary conditions employed. To further investigate the influence of the boundary conditions on the vortex length, numerical simulations were obtained for the computational domain encompassing the whole axial length of the annular space. The boundary conditions imposed in this case were no-slip/impermeability at the solid vertical end caps that limit the annular space. These are labeled in Fig. 7 as boundary conditions of type (c). The computational time and memory requirements for a solution of this type would be significantly larger than those required for a solution that employs boundary conditions of type (b) where just half of the physical domain is solved. For this reason, the runs for the type (c) boundary condition were performed for the $h/d=0$ case only, which could be solved by exploiting axial symmetry, thus reducing the computational requirements to a feasible level.

As shown in Fig. 7, the type (c) numerical result (at $h/d=0$) matches perfectly with the corresponding experimental result, namely, a Taylor vortex length of approximately 47.5 mm, which is also the gap size, as expected. On the other hand, the value obtained for the type (b) condition is 46 mm. Although this difference might not seem significant, it should be mentioned that for type (c) boundary condition 52 vortices were obtained in the annular space, while 54 (27×2) vortices were obtained when type (b) boundary condition was employed. These results show that the symmetry condition at mid-length may lead to unphysical predictions, since type (a) and type (b) boundary conditions yielded the same numerical results.

From Fig. 7 it is also seen that the length of the vortices decreases as h/d is increased. Inspection at other circumferential positions (as obtained both numerically and experimentally) showed that the vortex length is constant all around the annular space. Experimental observations were made at meridional planes located at 0, 90, 180 and 270 deg, as marked in Fig. 1. In order to conduct these measurements, the Plexiglas cylinder was manually rotated relative to the horizontal laser light sheet, as described in the previous section.

5.4 Taylor-Vortex Characterization: Axial Velocity Profile. Experimentally and numerically obtained axial velocity profiles are now presented in dimensionless form ($v_z^*=v_z/\Omega r_i$, $r_1^*=r/r_o$). The axial velocity profiles were obtained at an axial coordinate passing through the eye of the vortex, located approximately at the mid-length of the annular space.

Figure 8 presents the axial velocity profiles for the annular space without obstruction for a Newtonian liquid. Results for two rotational Reynolds number values are presented: 104 and 126. These values correspond respectively to 48% and 80% above the transition value, but below the values for the second transition to the wavy-vortex regime. Two sets of representative experimental

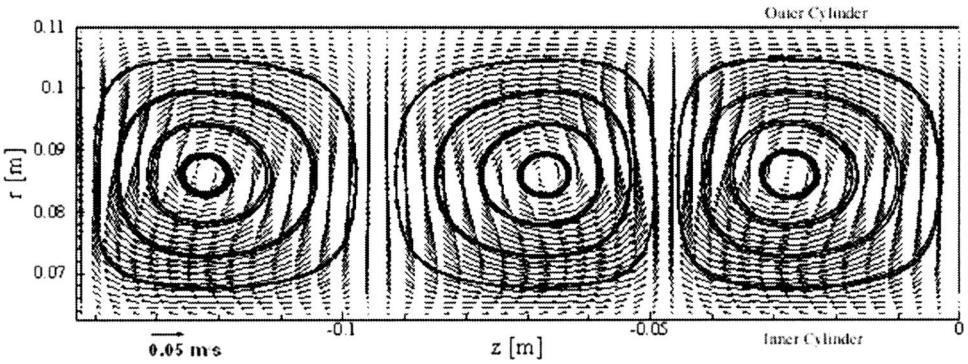

Fig. 15 Velocity distribution in the *r-z* plane and vortex structure. Newtonian liquid. $\mathrm{Re}=85.6$, $h/d=0.0$, $\theta=0$.

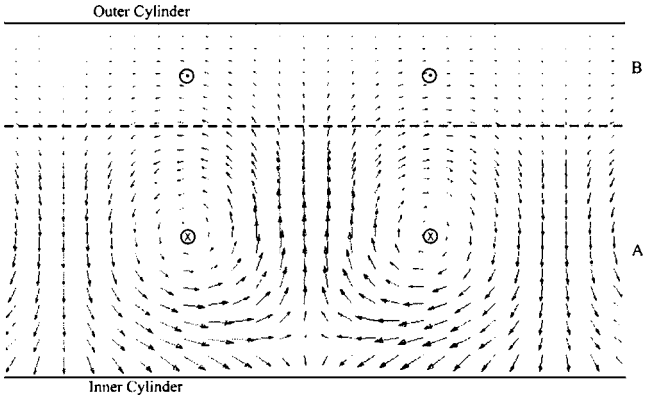

Fig. 16 Velocity distribution in the *r-z* plane and vortex structure. Newtonian liquid. Re=149 $h/d=0.75$, $\theta=0$.

results are presented in the figure, labeled as "group A" and "group B" velocity profiles in Figs. 8(*a*) and 8(*b*). These two sets of results pertain to the same nominal initial and boundary conditions, but are completely different. They were carefully and extensively repeated using the same working liquid at a fixed temperature. The imposed acceleration ramp was the same for all experiments, namely $a^*=10.2$.

Since the camera that registered the particle images was kept at the same axial position in all experiments, the two types of velocity profiles measured are an indication of the existence of two stable solutions for the flow. An obvious observation in Fig. 8 is that group A and group B profiles display opposite signs, indicating that a lateral shift in the vortices had occurred. Although it is not clear in the figure, group A and group B profiles are not symmetric. Group A profiles display maximum axial velocities that are somewhat higher than those measured for group B profiles. This might be an indication that the two solutions observed differ in the number and intensity of the vortices.

Figure 8 also displays numerical predictions of the axial velocity profiles. The boundary conditions employed in the calculations were of type (c), which means that the whole annular space was used as the computation domain with no-slip/impermeability conditions at the end walls. The calculations were obtained by assuming axis-symmetric flow. The results show that the numerically obtained velocity profiles agree well with group B profiles for the two values of the Reynolds number investigated.

Figure 9 presents axial velocity profiles for a non-Newtonian power-law liquid with a power-law index of $n=0.406$. The non-Newtonian liquid is turbid and the image processing becomes more difficult than for the Newtonian transparent liquid, especially in the vicinities of the annulus walls. This is the reason for the lack of experimental data in Fig. 9 pertaining to these flow regions. For this power-law index, the Taylor vortex onset was observed to occur at Re=65.6.

Figure 10 shows axial velocity profiles for a Newtonian liquid and an obstruction of $h/d=0.5$, for a rotational Reynolds number value of 109, which is about 22% above the transition value. The profiles are for an axial coordinate passing through the eye of the vortex. The dimensionless acceleration imposed on the shaft to reach the steady-state condition was the same as in the free annular space, i.e., $a*=10.2\pm0.1$. Figure 10 shows velocity profiles measured at meridional planes positioned both at 0 and 180 deg. Although the presence of the obstruction flattens the vortex radially, the profiles at the two meridional planes have qualitatively the same shape. At the 90 and 270 deg planes the axial velocity profiles are quite similar, although the vortex intensity at the 90 deg plane is higher (Figs. 11 and 12).

It can be seen in Figs. 10–12 that the same level of agreement between numerical and experimental results obtained for the free annular space case of Fig. 8 is achieved for the partially obstructed case, for the planes positioned at 90 and 270 deg. The boundary conditions employed in these 3-D calculations were of type (a).

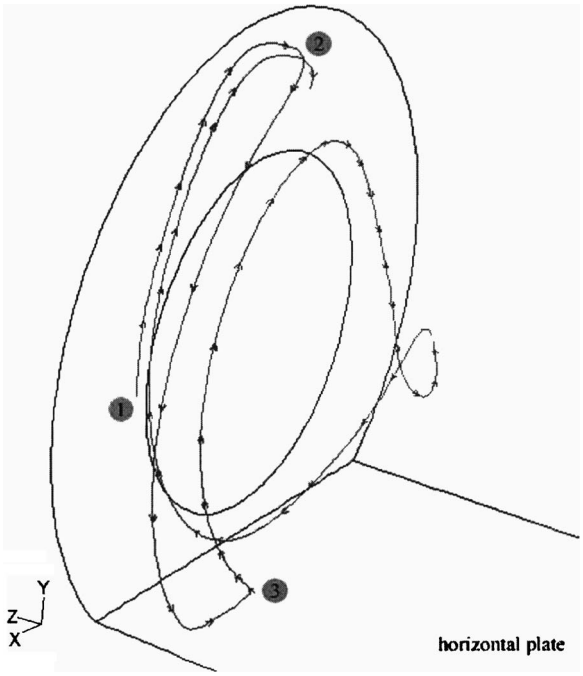

Fig. 17 Particle pathline as given by the numerical solution for a Newtonian liquid. $h/d=0.75$, Re=149.

Finally, Figs. 13 and 14 show axial velocity profiles for the case of the non-Newtonian liquid with $n=0.704$. Figure 13 pertains to an obstruction of $h/d=0.25$, while Fig. 14 shows the profiles for $h/d=0.5$. These figures illustrate that the qualitative trends discussed above for Newtonian axial velocity profiles are also observed for power-law liquids.

5.5 Taylor-Vortex Characterization: Longitudinal Velocity Fields. The Taylor-vortex structure in the annular space is now discussed. Figure 15 shows the velocity distribution in the meridian plane *r-z* for the free annular space, i.e., $h/d=0$. At a given axial position, the velocity magnitude in the neighborhood of the inner cylinder is larger than in the vicinity of the outer cylinder. This is also illustrated in Fig. 8. This occurs due to mass conservation, as explained by Wereley and Lueptow [5]. Furthermore, at a given streamline, the positive radial velocity component is larger in magnitude than the negative one at the same radial position. This behavior is consistent with mass conservation together with the just-discussed axial velocity behavior.

Velocity distributions in the *r-z* plane for partially obstructed annular spaces were also obtained, and they turn out to be rather more complex than the ones observed for a free annular space. Figure 16 shows the velocity distribution in the *r-z* plane for $h/d=0.75$. First, it is observed that adjacent Taylor vortices turn in opposite directions, as expected and independently of the presence of an obstruction. In addition to the vortex recirculation in the *r-z* plane, the liquid particles in a vortex also possess velocity in the θ direction, due to the tangential drag related to the rotation of the inner cylinder. Moreover, due to the flow resistance caused by the obstruction, this tangential velocity may be either in the same direction of the inner cylinder motion or in the opposite direction. This is also illustrated in Fig. 16, where it is indicated by the symbol $\otimes$ that in region A, there is flow into the plane of the picture, while the symbol $\odot$ indicates that the liquid in region B flows tangentially in the opposite direction. To further illustrate the complexity of this flow field, a particle path is represented in

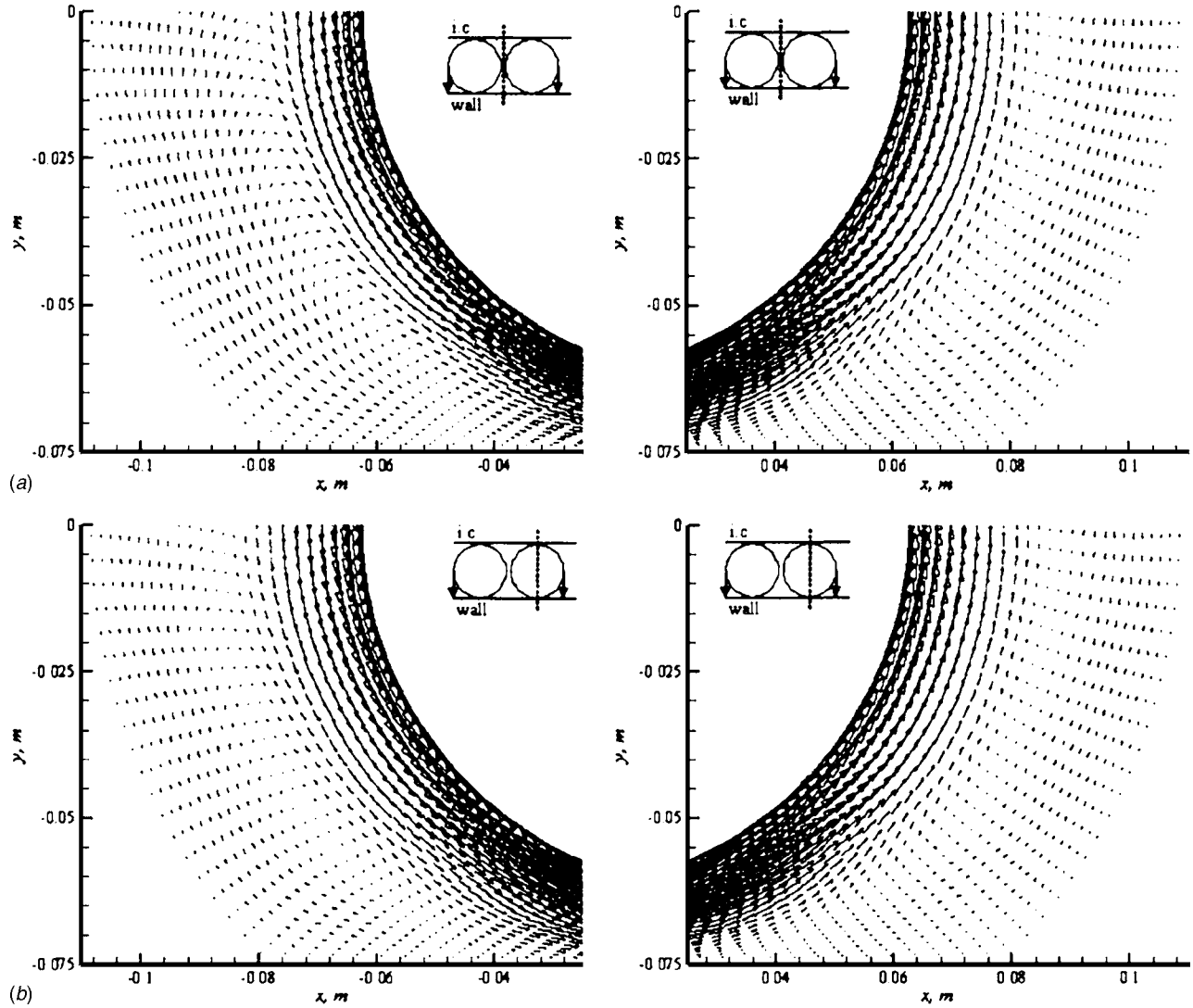

Fig. 18 Velocity distribution in the lower half of the cross section of the annular space (*a*) at the vortex-pair symmetry plane and (*b*) at the vortex midplane (upstream at left and downstream at right). Re=149, h/d=0.75. Counter-clockwise cylinder rotation. Newtonian liquid.

Fig. 17. We start drawing the pathline at point 1. Point 2 corresponds to the first change in direction, when the particle leaves region A and enters region B (see Fig. 16). At point 3 the particle changes again its direction, due to the presence of the partial obstruction.

5.6 Taylor-Vortex Characterization: Transverse Velocity Fields. Velocity distributions in the cross-section plane (r-θ plane) obtained from 3-D numerical solutions for a Newtonian liquid are presented in Fig. 18. The case chosen to illustrate the complex flow pattern induced by the presence of the horizontal plate in the annular gap is characterized by a Reynolds number value of 149 and an obstruction such that h/d=0.75. This Reynolds number value is above the Taylor-vortex transition value, but below the wavy-vortex transition value. Figure 18 shows the lower half of the annular space, between 90 and 270 deg. Because the inner cylinder rotates counter-clockwise, the graphs on the left pertain to the portion of the flow upstream of the obstruction, whereas the graphs on the right show the velocity distributions downstream of the obstruction. In all graphs, the x axes run along the plate, while the y coordinate is zero at the horizontal plane containing the cylinder axis, and increases downwards. The insets in the figures indicate the axial position relative to the pair of counter-rotating Taylor vortices where the r-θ velocity fields are shown. The vortex pairs in the inset are drawn at the 180 deg position, i.e., at the lower part of the annular space. The parallel lines that bound the vortex pair in the inset represent the inner cylinder wall (I.C.) and the plate wall (wall). According to this representation, Fig. 18(*a*) represents the velocity distribution at the symmetry plane between the vortices, while 18(*b*) gives the same information for the midplane of a single vortex.

The velocity distribution presented in Fig. 18(*a*) shows clearly the strong tangential flow passing through the narrow gap passage. This strong flow is fed by the down wash of the vortex pair at the symmetry line. Worth noting is the recirculation zone present both upstream and downstream of the gap passage. The recirculation zones are present in the two axial stations shown. Other results, not shown in the present paper, revealed that the recirculation zone disappears for larger passages, when $h/d<0.5$. For other axial positions, the tangential flow is seen to be less intense.

It should be mentioned that the Taylor vortices completely occupy the annular gap space for all tangential positions. Therefore, at the narrow gap passage by the obstruction, the vortices display the smallest cross sectional area, which increases to a maximum

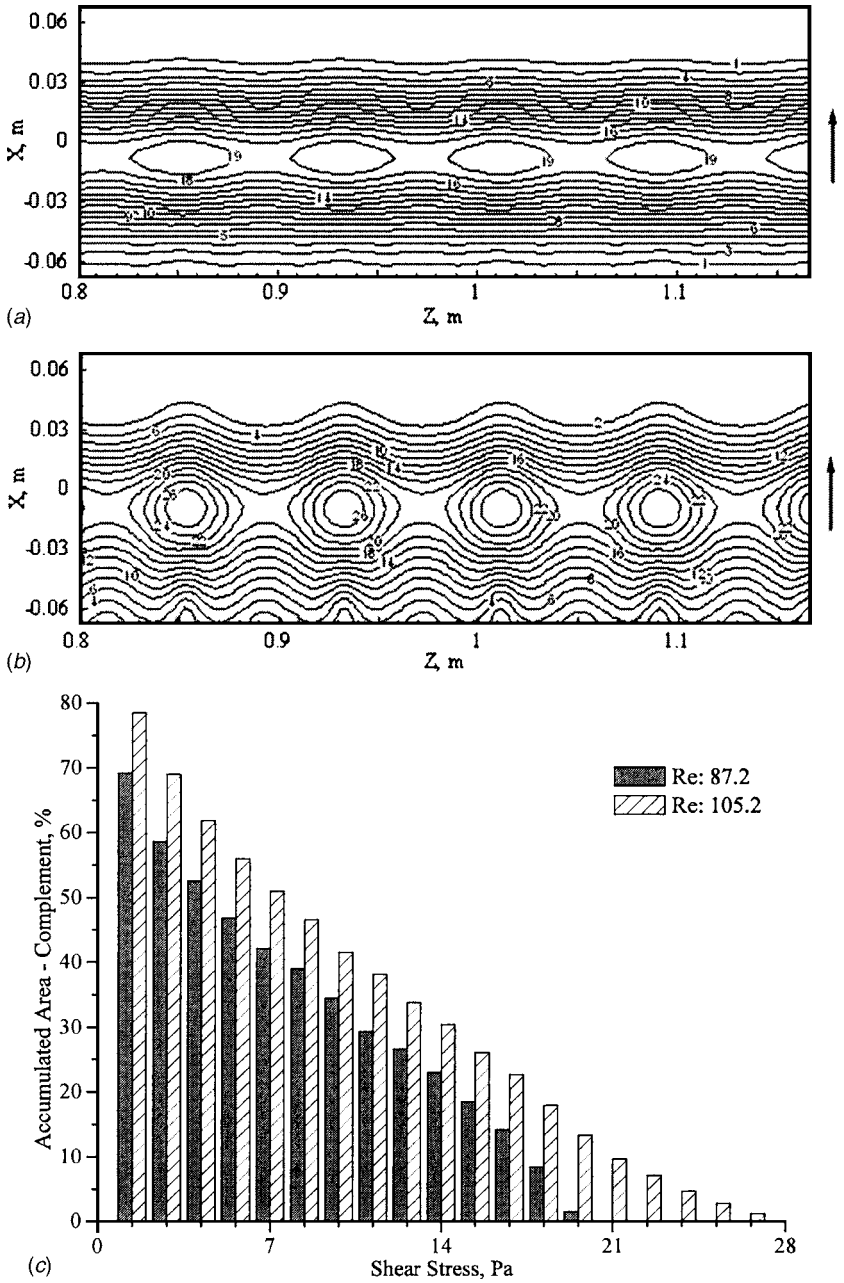

Fig. 19 Shear stress distribution on the plate surface. (*a*) Re=87.2=0.99Re$_c$. (*b*) Re=105.2=1.20Re$_c$. (*c*) Complement of accumulated area (total area-accumulated area). *h*/*d*=0.5. Newtonian liquid.

value 180 deg away. The interaction of the Taylor vortices with the recirculating flow shown in Fig. 16 induces a rather complex flow pattern, as shown in Fig. 17.

5.7 Taylor-Vortex Characterization: Wall Plate Shear Stress. The shear stress distribution on the plate surface was obtained numerically for the flow of a Newtonian liquid in two partially obstructed annular spaces, namely $h/d=0.5$ and 0.75, as shown respectively in Figs. 19 and 20, where the labels of the iso-curves indicate the shear stress in Pascal, and X is a coordinate along the plate and transversal to the axial (z or Z) direction. In each situation, two Reynolds number values were investigated, to illustrate the influence of the transition in the shear stress distribution on the wall plate. The first Reynolds number value was chosen to be 0.99Re$_c$, so that the flow was purely tangential. The second Reynolds number value was chosen to be 1.20Re$_c$, therefore within the Taylor-vortex regime.

The change in wall plate shear stress distribution is striking when the Taylor vortices appear, as a comparison between Figs. 19(a) and 19(b) illustrates for $h/d=0.5$. The shear stress values pertaining to the Taylor-vortex regime are clearly larger, not only due to the increase in Reynolds number. In addition, the wall shear stress distribution changes dramatically due to the vortex structure.

In order to assess the flow capability to displace drilling cuttings from the cuttings bed, it is interesting to compare the stress values caused by the flow on the bed surface with the minimum shear stress needed to displace the cuttings. In this connection, it is useful to evaluate the percent of surface area subjected to shear stresses above different levels. This information is given in in Fig. 19(c). For example, this figure indicates that 30% of the total area

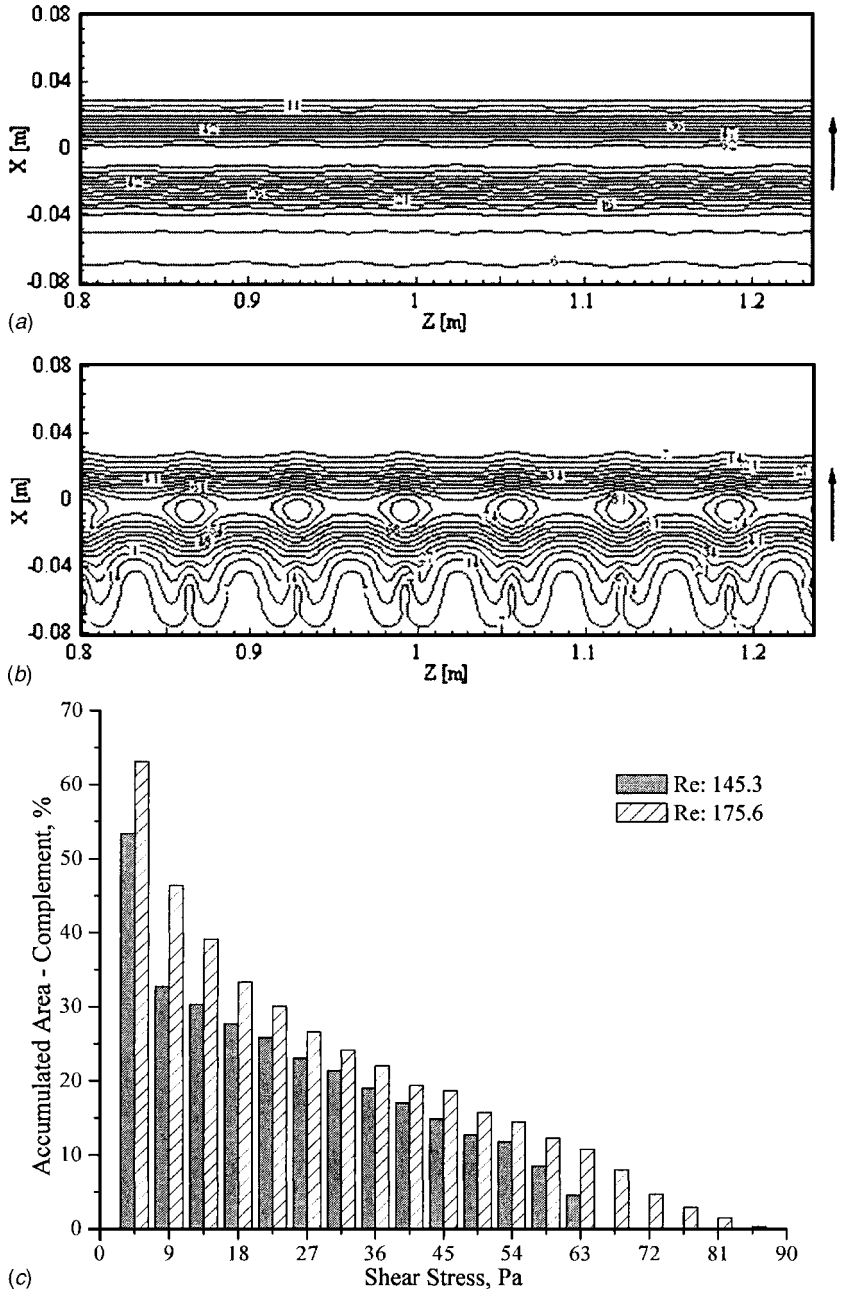

Fig. 20 Shear stress distribution on the plate surface. (*a*) Re=145.3=0.99Re$_c$. (*b*) Re=175.6=1.20Re$_c$. (*c*) Complement of accumulated area (total area-accumulated area). h/d=0.75. Newtonian liquid.

is subject to shear stresses above 14.0 Pa in the presence of Taylor vortices, while only 23% is subject to shear stresses above the same level for purely tangential flow.

The same analysis was performed for h/d=0.75, and the corresponding results are shown in Fig. 20. It is clear that the shear stresses for this case are larger than for the previous case. Figure 20(*c*) shows that approximately 25% of the total plate area for h/d=0.75 is subjected to shear stresses above 27.0 Pa, which is the upper-limit wall shear stress for h/d=0.50.

6 Concluding Remarks

The present paper presented a combined numerical and experimental study of the flow characteristics of a horizontal circular Couette flow with partial obstruction of the annular space. The obstruction consisted of a horizontal plate positioned at the lower part of the annular gap. The presence of the plate destroys the axial symmetry of the problem and affects the transition from purely tangential to Taylor-vortex flow.

The three-dimensional velocity field within the annular space was determined by the numerical solution of the mass and momentum conservation equations for the isothermal steady flow of Newtonian and power-law liquids. Instantaneous and time-averaged velocity fields were determined experimentally by employing the particle image velocimetry technique, PIV.

The results obtained were in the form of critical values for the rotational Reynolds number that characterizes the transition from purely tangential flow to Taylor-vortex flow. Agreement between experimentally obtained and numerically predicted critical Reynolds numbers was excellent for all values of the cylinder-to-plate values investigated. The results have shown that the flow obstruc-

tion delays the transition to Taylor-vortex flow, and that this delay is smaller for non-Newtonian liquids. A significant sensitivity of the critical Reynolds number to the acceleration imposed on the inner rotating cylinder was verified, which confirmed previous results available in the literature.

Excellent agreement was also found between computation and experiments for the axial velocity profiles. The experiments, however, revealed two possible different stable configurations for the axial velocity profiles in the annular space without obstruction. The existence of these two configurations is related to a different number of vortices accommodated within the annular space length.

Although the agreement between computation and experiments was considered excellent for the critical Reynolds number and axial velocity profiles, for some values of the cylinder-to-plate gap the prediction of vortex length presented discrepancies between measured and predicted results. These discrepancies are also related to the different number of vortex pairs accommodated within the annular gap. Different types of boundary conditions employed in the simulations at the vertical end walls that seal the gap have been shown to produce different numbers of counter-rotating pairs of vortices.

Numerically obtained velocity fields in the cross-section, r-θ plane revealed the existence of a rather complex flow structure composed of Taylor vortices and zones of recirculating flow, when the flow passage between the cylinder and the horizontal plate is limited. Further investigation is needed to clarify the detailed structure of this flow.

Acknowledgment

The authors acknowledge the support of the Rio de Janeiro State Research Foundation (FAPERJ), the Brazilian Research Council (CNPq), the Faculdade do Centro Leste (UCL), and Petrobras S.A.

References

[1] Taylor, G. I., 1923, "Stability of a Viscous Liquid Contained Between Two Rotating Cylinders," Philos. Trans. R. Soc. London, Ser. A, **223**, pp. 289–345.
[2] Cole, J. A., 1976, "Taylor-Vortex Instability and Annulus-Length Effects," J. Fluid Mech., **75**(Part 1), pp. 1–15.
[3] DiPrima, R. C., Eagles, P. M., and Ng, B. S., 1984, "The Effect of Radius Ratio on the Stability of Couette Flow and Taylor Vortex Flow," Phys. Fluids, **27**(10), pp. 2403–2411.
[4] Andereck, C. D., Liu, S. S., and Swinney, H. L., 1986, "Flow Regimes in a Circular Couette System With Independently Rotating Cylinders," J. Fluid Mech., **164**, pp. 155–183.
[5] Wereley, S. T., and Lueptow, R. M., 1998, "Spatio-Temporal Character of Non-Wavy and Wavy Taylor-Couette Flow," J. Fluid Mech., **364**, pp. 59–80.
[6] Lockett, T. J., Richardson, S. M., and Worraker, W. J., 1993, "The Importance of Rotation Effects for Efficient Cuttings Removal During Drilling," *SPE/IADC*, 25768.
[7] Philip, Z., Shama, M. M., and Chenevert, M. E., 1998, "The Role of Taylor Vortices in the Transport of Drill Cuttings," *SPE*, 39504.
[8] Sifferman, T. R., and Becker, T. E., 1992, "Hole Cleaning in Full-Scale Inclined Wellbores," SPE, *Drilling Engineering*, June, pp. 115–120.
[9] Lim, T. T., Chew, Y. T., and Xiao, Q., 1998, "A New Flow Regime in a Taylor-Couette Flow," Phys. Fluids, **10**(12), pp. 3233–3235.
[10] Park, K., Crawford, G. L., and Donnelly, R. J., 1981, "Determination of Transition in the Couette Flow in Finite Geometries," Phys. Rev. Lett., **47**(20), pp. 1448–1450.
[11] DiPrima, R. C., and Stuart, J. T., 1972, "Non- Local Effects in Stability of Flow Between Eccentric Rotating Cylinders," J. Fluid Mech., **54**(Part 3), pp. 393–415.
[12] Eagles, P. M., Stuart, J. T., and DiPrima, R. C., 1978, "The Effects of Eccentricity on Torque and Load in Taylor-Vortex Flow," J. Fluid Mech., **87**(Part 2), pp. 209–231.
[13] Coronado-Matutti, O., Souza Mendes, P. R., and Carvalho, M. S., 2004, "Instability of Inelastic Shear-Thinning Liquids in a Couette Flow Between Concentric Cylinders," ASME J. Fluids Eng., **126**(3), pp. 385–390.
[14] Patankar, S. V., 1980, *Numerical Heat Transfer and Fluid Flow*, McGraw-Hill, New York.
[15] Loureiro, B. V., 2004, "Secondary Flow in a Partially Obstructed Annulus With Inner Cylinder Rotation," Ph.D. thesis, Pontifícia Universidade Católica-RJ, Rio de Janeiro, Brazil (in Portuguese).
[16] Raffel, M., Willert, C., and Kompenhans, J., 1998, *Particle Image Velocimetry*, Springer, New York.
[17] Gomes, B. A. A., Thompson, R. L., and Azevedo, L. F. A., 2000, "Solid Body Rotation Flow for Particle Image Velocimetry," in *Proc. VIII ENCIT*, Porto Alegre, RS, Brazil, November.
[18] Ashrafi, N., and Khayat, R. E., 2000, "Shear-Thinning-Induced Chaos in Taylor-Couette Flow," Phys. Rev. E, **61**(2), pp. 1455–1467.

Calculation of the Die Entry Flow of a Concentrated Polymer Solution Using Micro-Macro Simulations

Kathleen Feigl

Deepthika C. Senaratne[1]

Department of Mathematical Sciences,
Michigan Technological University,
1400 Townsend Drive,
Houghton, MI 49931-1295
e-mail: feigl@mtu.edu

A micro-macro simulation algorithm for the calculation of polymeric flow is developed and implemented. The algorithm couples standard finite element techniques to compute velocity and pressure fields with stochastic simulation techniques to compute polymer stress from simulated polymer dynamics. The polymer stress is computed using a microscopic-based rheological model that combines aspects of network and reptation theory with aspects of continuum mechanics. The model dynamics include two Gaussian stochastic processes, each of which is destroyed and regenerated according to a survival time randomly generated from the material's relaxation spectrum. The Eulerian form of the evolution equations for the polymer configurations is spatially discretized using the discontinuous Galerkin method. The algorithm is tested on benchmark contraction domains for a polyisobutylene solution. In particular, the flow in the abrupt die entry domain is simulated and the simulation results are compared to experimental data. The results exhibit the correct qualitative behavior of the polymer and agree well with the experimental data. [DOI: 10.1115/1.2136922]

1 Introduction

Two persistent challenges in polymeric fluid mechanics are the development of accurate rheological models to describe the stress-strain relationship in the fluid and the development of accurate and efficient numerical techniques to solve the resulting governing system of equations. Within the traditional framework of simulations, the stress is calculated using a closed-form macroscopic model. Unfortunately, these models, often in the form of differential or integral equations, fail to various degrees to describe real polymer behavior. Improvements to these models are restricted due to the lack of molecular insight into them. Therefore, the best hope for improvement is to develop microscopic-based, or molecular, models since these models are naturally suited for the inclusion of relevant polymer physics. These models include a description of the polymer molecular dynamics, usually involving the evolution of polymer configuration variables with associated probability density functions, and an expression for the polymer stress as a function of these dynamics.

In order for microscopic-based models to be useful in engineering applications, simulation techniques must be developed that are capable of resolving the multiple levels of description. In 1992, Laso and Öttinger [1] introduced the first such *micro-macro algorithm* for polymeric flow. The strategy of their algorithm, widely known as CONNFFESSIT (Calculation Of Non-Newtonian Flow: Finite Elements and Stochastic Simulation Techniques), is to couple traditional methods, such as finite element techniques, for the calculation of velocity and pressure with stochastic simulation techniques for the calculation of polymer stress from a microscopic-based model. Polymer stress is computed by simulating the dynamics of a large ensemble of the configuration variables and taking an appropriate ensemble average of a function of these variables.

Laso and Öttinger [1] tested the method in one-dimensional flow for various molecular models: the Hookean dumbbell models (upper convected Maxwell model and Oldroyd-B model), and the FENE and FENE-P models. Feigl et al. [2] were the first to extend CONNFFESSIT to two-dimensional flow. This was done for a Hookean dumbbell model. Subsequent studies include those of Hua and Schieber [3] for a reptation model and Bell et al. [4], who used a spectral method, as opposed to a finite element method, for the macro calculation. Each of these studies relied on a particle tracking technique in which an ensemble of model molecules or chains is tracked in the flow field along selected particle paths, and the polymer stress in each element is determined by averaging over all such paths passing through the element.

An improvement to the particle tracking scheme was introduced by Hulsen et al. [5], who replaced the individual polymer molecules or chains by an ensemble of configuration fields, which are defined at every point of the flow domain. These configuration fields, like polymer molecules, convect and deform in the flow field and may be subjected to Brownian motion. With this description, the difficulties associated with particle or ensemble tracking in the original CONNFFESSIT algorithm were avoided. It was also observed that the configuration field approach led to a reduction in the statistical error [6]. A further improvement to the micro-macro simulation of reptation models was reported by Van Heel et al. [7] who used deformation gradient fields instead of configuration fields for these models.

An important advantage of CONNFFESSIT, and other micro-macro algorithms, is the ability to calculate polymeric flow using molecular models for which a closed-form constitutive equation is not known. This means that the physics in a model does not need to be sacrificed for tractability. Moreover, these simulations allow one to study the relationship between the flow process, the flow-induced structure in the fluid, the macroscopic rheological properties of the fluid, the flow stability, and the mechanical properties of the finished product. More details on the state of the art in micro-macro simulations can be found in the recent review given by Keunings [8].

The model considered in this study is a molecular-based model introduced by Feigl and Öttinger [9]. This model combines aspects of microscopic models, specifically reptation and network

[1]Current address: Department of Mathematics and Computer Science, Fayetteville State University, 1200 Murchison Road, Fayetteville, NC 28301.

Contributed by the Fluids Engineering Division of ASME for publication in the JOURNAL OF FLUIDS ENGINEERING. Manuscript received April 28, 2004; final manuscript received May 26, 2005. Assoc. Editor: Dennis Siginer.

models, with aspects of macroscopic models. Comparison of model predictions to experimental data showed that the model described well the material functions of a low-density-polyethylene melt in shear and elongational flow. The goal of the present paper is to develop a two-dimensional micro-macro simulation algorithm incorporating this model and to test it in benchmark flow problems. The fluid considered is a well-characterized polyisobutylene (PIB) solution [10,11], and the flow domains are the tapered and abrupt die entry domains.

The remainder of the paper is organized as follows. In Sec. 2, the general dynamics and stress tensor of the microscopic-based model are described. A particular form of the model is constructed for the PIB solution, and some of the model's predictions are presented and compared to experimental data. The three subsequent sections describe the micro-macro simulation algorithm, the simulation results in the die entry domains, and a summary. Simulation results in the abrupt planar die entry domain are compared to experimental data taken from the PIB solution in this domain.

2 Rheological Model and Material Function Predictions

The isothermal flow of an incompressible fluid with density ρ is governed by the momentum and mass balance equations:

$$\rho\left[\frac{\partial \mathbf{u}}{\partial t}+(\mathbf{u}\cdot\nabla)\mathbf{u}\right]=-\nabla p+\nabla\cdot\tau \tag{1}$$

$$\nabla\cdot\mathbf{u}=0 \tag{2}$$

where p and $\mathbf{u}$ denote the pressure and the velocity fields, respectively, and τ is the extra-stress tensor. In general, the extra-stress tensor τ is represented as a sum of the polymer contribution τ_p and the Newtonian solvent contribution τ_s, given by $\tau_s=\eta_s\dot{\gamma}$, where η_s is the solvent viscosity and $\dot{\gamma}$ is the rate-of-strain tensor. The polymer contribution τ_p to the extra-stress tensor must be modeled with an appropriate rheological model. In this paper, the following microscopic-based rheological model is considered.

2.1 Model Description. The dynamics of the model are described by two independent Gaussian random variables, $\mathbf{Q}_1(t)$ and $\mathbf{Q}_2(t)$, each of which is a 3×1 column vector that is repeatedly created, allowed to evolve according to an equation of motion, and then destroyed in an independent manner. At its time t' of creation, each vector is a standard Gaussian random variable. Associated with each random variable is a lifetime s_i during which the vector evolves according to its corresponding deterministic equation of motion

$$\frac{d\mathbf{Q}_1(t)}{dt}=\kappa(t)\cdot\mathbf{Q}_1(t),\quad t'<t<t'+s_1 \tag{3}$$

$$\frac{d\mathbf{Q}_2(t)}{dt}=-\kappa^{\dagger}(t)\cdot\mathbf{Q}_2(t),\quad t'<t<t'+s_2 \tag{4}$$

These equations are based on the assumption that the vectors deform affinely in the homogeneous flow field represented by the transpose of the velocity gradient tensor κ. At time $t'+s_i$, the vector $\mathbf{Q}_i$ $(i=1,2)$ is destroyed and again (independently) randomly generated according to the standard Gaussian distribution function. Using this newly generated vector as an initial condition, $\mathbf{Q}_i$ again evolves according to Eq. (3) (for $i=1$) or Eq. (4) (for $i=2$) during a second time interval, and so forth over many time intervals until the time at which we want to compute stress is reached.

The vector $\mathbf{Q}_1(t)$ represents the end-to-end configuration vector from network theory of concentrated polymer solutions and polymer melts [12]. It describes the configuration of segments, or tubes, defining the temporary physical entanglements of the macromolecules. The dual vector $\mathbf{Q}_2(t)$ represents the same concept as anisotropic tube cross section in reptation theory [13]. It points from the centerline of the tube to the wall of the tube, where the tube represents the topological constraint imposed by the surrounding macromolecules. It is, therefore, a representation of the tube cross section, or an area element of the segment.

Given the above dynamics, the polymer contribution to the extra-stress tensor τ_p is expressed as the expectation of a function $\mathbf{F}$ of these dynamics. It is most conveniently written in terms of conditional expectations of $\mathbf{F}$ (p. 53 of [14]) as follows:

$$\tau_p(t)=\langle\mathbf{F}(\mathbf{Q}(t))\rangle=\int_{-\infty}^{t}\langle\mathbf{F}(\hat{\mathbf{Q}}(t,t'))\rangle\mu(t-t')dt' \tag{5}$$

where $\mu(t-t')$ is the probability density associated with the random variable representing the creation time of a vector, under the assumption that strain effects and time effects may be factored. The vectors $\hat{\mathbf{Q}}_1(t,t')$ and $\hat{\mathbf{Q}}_2(t,t')$ are the solutions of Eq. (3) and Eq. (4), respectively. We set $\mathbf{Q}(t)=[\mathbf{Q}_1(t),\mathbf{Q}_2(t)]^{\dagger}$ and $\hat{\mathbf{Q}}(t,t')=[\hat{\mathbf{Q}}_1(t,t'),\hat{\mathbf{Q}}_2(t,t')]^{\dagger}$. For sufficiently small dt', the product $\mu(t-t')dt'$ represents the probability that a strand which lives at time t was created in the interval of length dt' around t'.

In the model described here we take

$$\tau_p(t)=G(0)\langle f_1(Q_1^2,Q_2^2)\mathbf{Q}_1(t)\mathbf{Q}_1(t)+f_2(Q_1^2,Q_2^2)\mathbf{Q}_2(t)\mathbf{Q}_2(t)\rangle \tag{6}$$

where the factor $G(0)$ is the relaxation modulus $G(t-t')$ at $t=t'$, and f_1 and f_2 are scalar functions of $Q_i^2=\mathbf{Q}_i\cdot\mathbf{Q}_i$, $i=1,2$. The functions f_1 and f_2 represent the continuum mechanics part of the model. The parameters contained in these functions can be chosen to fit rheological data, if desired. In order to ensure that the correct linear viscoelastic behavior is described by the model, the functions, f_1 and f_2, must satisfy a small deformation constraint, as described in [9].

Both the memory function, $m(t-t')$, of the fluid and the probability density, $\mu(t-t')$, are related to the probability of a strand, $\mathbf{Q}_i$, having survival time s exceeding $t-t'$ via

$$\frac{m(t-t')}{m(0)}=\frac{\mu(t-t')}{\mu(0)}=\int_{t-t'}^{\infty}p(s)ds \tag{7}$$

where $p(s)$ is the probability density for survival time s [9,15]. Through a coordinate transformation, a survival time $s\in[0,\infty)$ can be obtained from a uniform random number $z\in[0,1)$ via the invertible function

$$z(s)=\int_0^s p(s')ds'=1-\frac{m(s)}{m(0)} \tag{8}$$

where $s=t-t'$. Often the memory function of a fluid is available in the form of the Maxwell linear viscoelastic memory function

$$m(s)=\sum_{k=1}^{K}\frac{\eta_k}{\lambda_k^2}e^{-s/\lambda_k} \tag{9}$$

where λ_k and η_k, $k=1,\ldots,K$, are a set of relaxation times and partial viscosities for the material, whose values can be found from linear viscoelastic data, such as the storage and loss moduli measured in small amplitude oscillatory shear flow.

For a single-mode model $(K=1)$, the expression for $z=z(s)$ in Eq. (8) can be inverted analytically to give $s(z)=-\lambda_k\ln(1-z)$. For a multimode memory function $(K>1)$, $z(s)$ cannot be inverted analytically. Since the multimode model can be written as a sum of single-mode models, each mode can be simulated separately and the results added together. Although this is the most convenient and straightforward approach, the computational time increases with the number of relaxation times. Therefore, in this study, a survival time is generated from the entire relaxation spectrum by using a rapidly converging nonlinear iteration scheme

Table 1 Relaxation spectrum for the PIB solution at 25°C, solvent viscosity η_s=0.002 Pa s, polymer viscosity η_p =1.4238 Pa s

Mode Number	λ_i [s]	η_i [Pa s]
1	0.6855	0.0400
2	0.1396	0.2324
3	0.0389	0.5664
4	0.0059	0.5850

(e.g., the Newton-Raphson method) to solve Eq. (8) for s, given a value of z. A very good initial guess is computed using piecewise function approximations.

2.2 Fluid and Predictions of Material Functions. The fluid we consider is a concentrated polymer solution, specifically a 5% polyisobutylene (PIB) solution in tetradecane (C14) at 25°C, described by Quinzani et al. [10,11]. The relaxation spectrum was determined by Quinzani et al. [10] and is given in Table 1.

The form of the strain functions in Eq. (6) was chosen based on past experience [9] to be $f_2=0$ and

$$f_1(Q_1^2,Q_2^2)=\frac{1}{a_0+a_1Q_1^2+a_2Q_2^2} \tag{10}$$

The parameter values were taken to be $a_0=0.635$, $a_1=0.040$, and $a_2=0.038$. These values were chosen to give good predictions to the material functions of the PIB solution and to satisfy the small deformation constraint.

The steady-state and transient material functions were computed for the PIB solution in shear and elongational flows. In all cases, an ensemble of 10^7 trajectories was used for each configuration vector. Vectorization was employed to reduce the computational time, and a variance reduction technique was used to control the statistical error at low shear or strain rates. See [9] for details of the simulation algorithm. The statistical errors for these simulations are so small that the computed values can be regarded as "exact" values of the model predictions. For comparison to the micro-macro simulation algorithm described in Sec. 3, the simulation algorithm here, in homogeneous flow, is referred to as the *standard simulation algorithm.*

A sample of the model's predictions to the material functions is given in Fig. 1. The error bars in the model's predictions are smaller than the size of the symbols and are not visible. The top graph shows the model's predictions of the viscosity, $\eta^+(t)$, in the start-up of shear flow, at two shear rates along with the experimental data report in Quinzani et al. [11]. All experimental data points for the PIB solution were read from the graphs in [11]. The model predicts the start-up behavior very well including the small overshoot at $\dot{\gamma}=100\ s^{-1}$.

The middle graph shows the steady-state shear viscosity η and the first normal stress coefficient, $\Psi_1=(\tau_{11}-\tau_{22})/\dot{\gamma}^2$. Again there is good agreement between the model and the experimental data. The horizontal dashed lines represents the zero-shear-rate viscosity $\eta_0=\eta_p+\eta_s=1.4258$ Pa s and the zero-shear-rate first normal stress coefficient computed from the generalized Maxwell model.

Finally, the bottom graph of Fig. 1 shows the model's predictions of the steady-state second normal stress coefficient, $\Psi_2=(\tau_{22}-\tau_{33})/\dot{\gamma}^2$, and the normal stress ratio, Ψ_2/Ψ_1, in simple shear flow. Although there was no experimental data with which to compare, the magnitudes and behavior of these values is reasonable for this type of fluid.

The model also predicts the correct qualitative behavior in uniaxial elongational flow, such as strain hardening. There was no reliable experimental data in uniaxial elongational flow for this PIB solution.

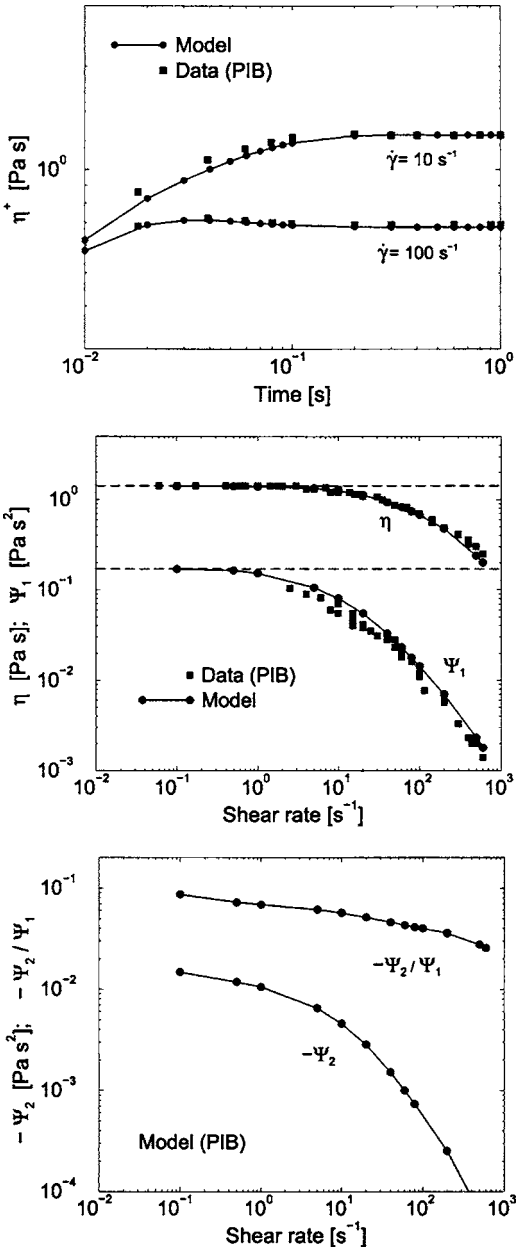

Fig. 1 Model predictions of PIB solution in simple shear flow and comparison to experimental data

3 Micro-Macro Simulation Procedure

We are interested in computing the isothermal, incompressible flow of a polymeric fluid using micro-macro simulations. A decoupled approach is taken in which the velocity and pressure fields are computed in one step, where a previously computed stress tensor enters the momentum equation as a pseudo-body force, and the polymer stress is computed in the second step from this updated velocity field.

The velocity and pressure fields are computed from the momentum and continuity equations, Eqs. (1) and (2), using standard finite element techniques. In accordance with the decoupled approach, the divergence of the extra-stress tensor is treated as a known pseudo-body force. The finite element method is applied to the penalty formulation of Eqs. (1) and (2). The type of finite element used is the crossed-triangle macro-element [16,17], which consists of a quadrilateral divided into four triangles formed by the diagonals of the quadrilateral. On each triangle, linear velocity

interpolants are used and pressure is taken to be constant (via the penalty equation). Rigorous convergence results for this element have been established in [17]. Feigl and co-workers used this element in standard macroscopic finite element simulations of polymeric flow [18–21] and in micro-macro simulations [2]. Regardless of whether the flow is steady or transient, the time derivatives are retained in the momentum equation, and a time-marching scheme is used. For steady problems, this strategy increases stability of the algorithm. Details of the macro part of the algorithm can be found in [16,20].

The micro part of the simulation consists of calculating the polymer stress from the molecular-based model described in Sec. 2. However, since the flow is not homogeneous in arbitrary flow domains, the transpose of the velocity gradient in Eqs. (3) and (4) must be allowed to vary with $\mathbf{x}$ as well as with t. In this case, the equations of motion can be viewed to be in Lagrangian form with the time derivatives being material derivatives. The particle tracking approach to the calculation of polymer stress uses this Lagrangian formulation of the equations of motion.

In the configuration field approach, proposed by vanden Brule and co-workers [5,7], these Lagrangian equations of motion are written in Eulerian form as

$$\frac{\partial \mathbf{Q}_1(x,t)}{\partial t} + \mathbf{u}(\mathbf{x},t)\cdot\nabla\mathbf{Q}_1(\mathbf{x},t) = \kappa(\mathbf{x},t)\cdot\mathbf{Q}_1(\mathbf{x},t) \tag{11}$$

$$\frac{\partial \mathbf{Q}_2(\mathbf{x},t)}{\partial t} + \mathbf{u}(\mathbf{x},t)\cdot\nabla\mathbf{Q}_2(\mathbf{x},t) = -\kappa^{\dagger}(\mathbf{x},t)\cdot\mathbf{Q}_2(\mathbf{x},t) \tag{12}$$

for $t' < t < t' + s_i$, $i=1,2$. In this case, $\mathbf{Q}_1(\mathbf{x},t)$ and $\mathbf{Q}_2(\mathbf{x},t)$ are configuration fields that are defined at every point of the domain. Initially, the configuration fields are spatially uniform. Similar to the Lagrangian approach, associated with each configuration field is a lifetime s_i, during which the field evolves according to Eq. (11) or Eq. (12). Once the lifetime is reached, the entire configuration field is destroyed and immediately reset to a new initially spatially uniform, random configuration field.

The equations of motion, Eqs. (11) and (12), are spatially discretized using the discontinuous Galerkin method. This method reduces coupling between elements and allows the stress and configuration fields to be calculated at the element level. The repeated solution of many large systems of equations is thus avoided. Omitting the details of the derivation, the weak form of Eqs. (11) and (12) can be stated as follows: for each element Ω^e, find $\mathbf{Q}_1$, $\mathbf{Q}_2 \in \mathbf{W}$ at time t such that for all $\psi \in \mathbf{W}$

$$\int_{\Omega^e}\left(\frac{\partial \mathbf{Q}_1}{\partial t} + \mathbf{u}\cdot\nabla\mathbf{Q}_1 - \kappa\cdot\mathbf{Q}_1\right)\cdot\psi d\Omega^e + \int_{\partial\Omega^{e-}}[\mathbf{n}\cdot\mathbf{u}(\mathbf{Q}_1^E - \mathbf{Q}_1)]\cdot\psi d\Gamma = 0 \tag{13}$$

$$\int_{\Omega^e}\left(\frac{\partial \mathbf{Q}_2}{\partial t} + \mathbf{u}\cdot\nabla\mathbf{Q}_2 + \kappa^{\dagger}\cdot\mathbf{Q}_2\right)\cdot\psi d\Omega^e + \int_{\partial\Omega^{e-}}[\mathbf{n}\cdot\mathbf{u}(\mathbf{Q}_2^E - \mathbf{Q}_2)]\cdot\psi d\Gamma = 0 \tag{14}$$

where $\mathbf{W}\subseteq[\mathbf{L}^2(\Omega)]^2$ denotes the functional space for $\mathbf{Q}_1$ and $\mathbf{Q}_2$, and $\mathbf{Q}_i^E$ is the value of $\mathbf{Q}_i$, $i=1,2$, in the element(s) upstream of Ω^e. This quantity is passed, or convected, across the inflow boundary, $\partial\Omega^{e-}$, of the element Ω^e.

Although several types of approximations for the configuration fields are possible, we take $\mathbf{W}^h$ to be the space of piecewise constant functions on the triangles of the velocity elements. This choice of $\mathbf{W}^h$ is consistent with the linear velocity interpolants in the macro calculation of velocity and pressure. With this approximation, the convection of configuration fields in each triangle comes only through the boundary integral term. As a consequence, the resulting semi-discrete system of equations forms an initial-value problem, which can be solved analytically. The fact that no element system of equations needs to be solved is an advantage of using the velocity and configuration field approximations described above.

As a postprocessing step, the trianglewise constant pressure field, stress field, and velocity gradients are projected onto the space of continuous bilinear polynomials based on the vertices of the quadrilateral macro-elements.

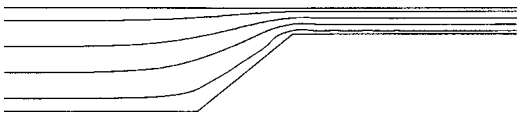

Fig. 2 Streamline patterns in the tapered contraction domain for $Q=30$ cm^2/s

4 Simulation Results

The performance of the micro-macro algorithm is evaluated by simulating the flow of the PIB solution in a planar tapered die entry domain and in a planar abrupt die entry domain. The simulation results were compared to the known behavior of polymers and to available experimental data. Furthermore, since the model quantitatively predicts the behavior of the PIB solution in homogeneous steady-state shear flow (see Fig. 1), the steady-state model predictions from the standard simulation algorithm in homogeneous shear flow are also compared to the stress computed from the micro-macro simulations in the fully developed flow of the downstream channel. Recall that the values from the standard simulation algorithm are exact model predictions.

In both domains, the flow is assumed to be symmetric about the centerline, so that the computational domain is reduced. The boundary conditions imposed for both problems were: no slip along the walls of the channels, the symmetry condition along the centerline, a parabolic velocity profile along the inlet boundary and the fully developed velocity profile along the outlet boundary. The fully developed profile along the outlet boundary was obtained by computing the flow at the same volumetric flow rate in a channel of uniform width equal to the width of the downstream channel of the die entry domain.

4.1 Tapered Die Entry. The relevant dimensions of the tapered contraction domain are the half-height of the upstream channel, $H_u=4$ cm, and half-height of the downstream channel, $H_d=1$ cm. This yields a contraction ratio of 4:1. The contraction occurs in the region $0\leqslant x\leqslant 3$ cm and $x=-8$ cm corresponds to the inflow boundary while $x=13$ cm corresponds to the outflow boundary.

The simulations were performed on two finite element meshes. The first mesh contained 200 quadrilateral macro-elements and 446 velocity nodes. The second, more refined, mesh contained 480 macro-elements and 1029 velocity nodes.

Several flow rates were considered, ranging from $Q=10$ cm^2/s to $Q=50$ cm^2/s. Good convergence was observed for all the flow rates, and with few exceptions, the results were mesh independent. Results for one flow rate, $Q=30$ cm^2/s, are presented below. The behavior at the other flow rates is similar.

Figure 2 shows the typical streamline pattern in the tapered contraction. As expected, all streamlines are open and there is no recirculation. Figure 3 shows the axial velocity profile along the centerline and along an axial cross section in the fully developed flow of the downstream channel. The centerline axial velocity profile displays the typical overshoot immediately after entry into the downstream channel before it reaches a steady value. The size of the overshoot was reduced with the mesh refinement, but is still present. This was the only noticeable mesh dependency observed

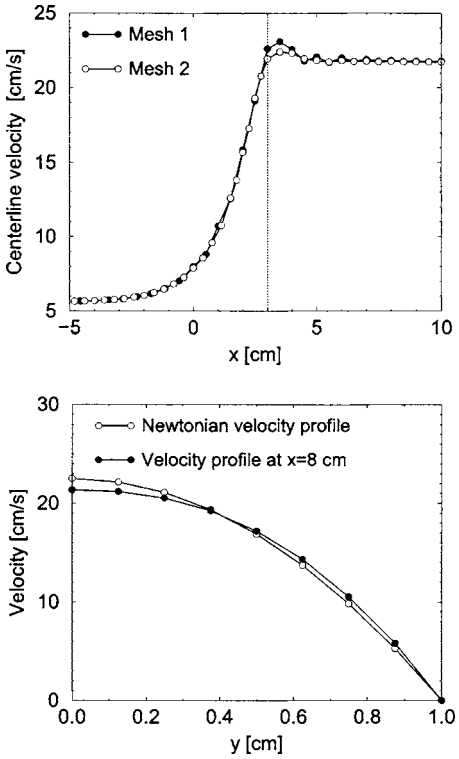

Fig. 3 Axial velocity profiles in the tapered contraction domain along the centerline and along an axial cross section of the downstream channel for $Q=30$ cm^2/s

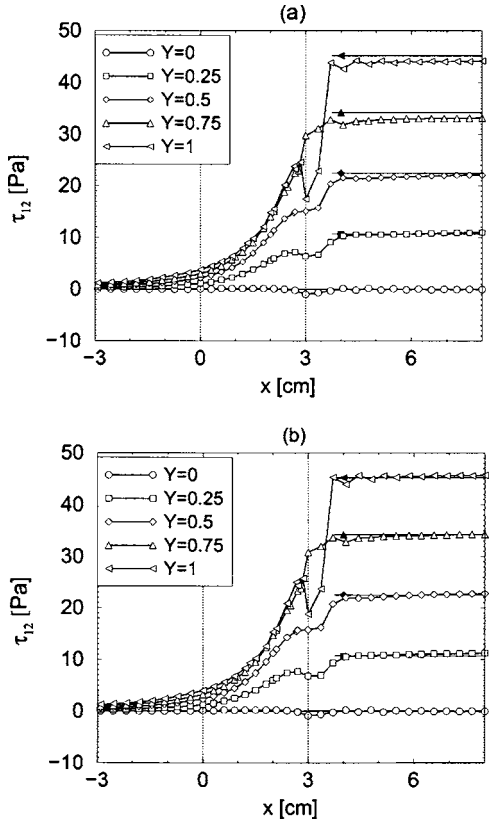

Fig. 4 Simulation results in the tapered contraction domain for $Q=30$ cm^2/s: (*a*) $N_F=2000$ and (*b*) $N_F=4000$. Horizontal lines are the exact steady-state values.

in these calculations. All other velocity and stress profiles were mesh independent. The axial velocity profile at the cross section $x=8$ cm in the downstream channel is shown in the bottom graph of Fig. 3. Although not shown for graphical clarity, all subsequent axial velocity profiles coincide with this one, indicating that the flow is fully developed. The parabolic profile corresponding to a Newtonian fluid at this flow rate is also shown in the graph. Comparison of the two profiles shows the shear-thinning behavior of the PIB solution.

In addition to the velocity profiles of Fig. 3, there is further evidence that the flow in the downstream channel is fully developed shear flow: the stress and shear rates are virtually constant at a given height above the centerline. Since the fully developed flow in the downstream channel is shear flow, the stress values from the micro-macro simulation can be compared to those computed from the standard simulation algorithm in homogeneous shear flow. As discussed in a previous section, the latter values can be considered to be "exact." To make the comparison, the constant shear rate at a given y value in the downstream channel, computed from the micro-macro simulation, is used to calculate the extra-stress from a standard simulation in homogeneous shear flow.

Figures 4 and 5 show the shear stress τ_{12} and first normal stress difference, $N_1=\tau_{11}-\tau_{22}$, at a representative set of y values (normalized by the half-height, H_d, of the downstream channel) for the flow rate $Q=30$ cm^2/s. The results from three different ensemble sizes of configuration fields are shown, $N_F=2000$, $N_F=4000$, and $N_F=8000$. The horizontal lines in each graph, marked by the solid symbols, represent the steady-state values computed from a standard simulation in homogeneous shear flow. There is very good agreement between the values from the micro-macro simulation and the "exact" values calculated in homogeneous flow. The exception is the values of N_1 close to the centerline. As previously mentioned, the stress values were mesh independent.

These graphs also allow us to determine the effect of the ensemble size N_F used in the micro-macro simulations on the calculated stress values. Figure 4 shows that there was almost no effect of N_F on the τ_{12} component of the stress tensor. An ensemble of $N_F=2000$ configuration fields was sufficient to get very good predictions for the shear stress in the downstream channel, and increasing N_F to 4000 yielded excellent agreement. There is more of an effect of N_F on the first normal stress difference, as shown in Fig. 5, particularly close to the wall. Increasing N_F to 8000 produced excellent agreement in N_1 close to the wall, but had less effect on the predictions close to the centerline. Although not shown, it was also observed that the velocity profiles were independent of the ensemble size.

4.2 Abrupt Die Entry Simulations and Comparison to Experimental Data. The abrupt slit die entry experiments, which were simulated in this study, were performed by Quinzani et al. [11]. The dimensions of the slit die were: half-height of the upstream channel, $H_u=1.27$ cm, half-height of the downstream channel, $H_d=0.32$ cm, and half-width of the channel, $W=12.7$ cm. The contraction ratio was 3.97:1.

The simulations were performed on the two-dimensional centerplane of this domain ($x_3=0$). In doing so, it is assumed that the width of the channel is sufficiently large so that the flow in the x_3 direction does not strongly affect the flow in the centerplane. The computational domain was further reduced by taking advantage of symmetry along the centerline ($x_2=0$). The half-heights of the upstream and downstream channels in the computational domain were the same as in the experiment, and the lengths of these channels were $L_u=8$ cm and $L_d=13$ cm.

Two finite element meshes were used. The first mesh contains 613 rectangular macroelements and 1357 velocity nodes, and a second, more refined, mesh consists of 1200 macroelements and

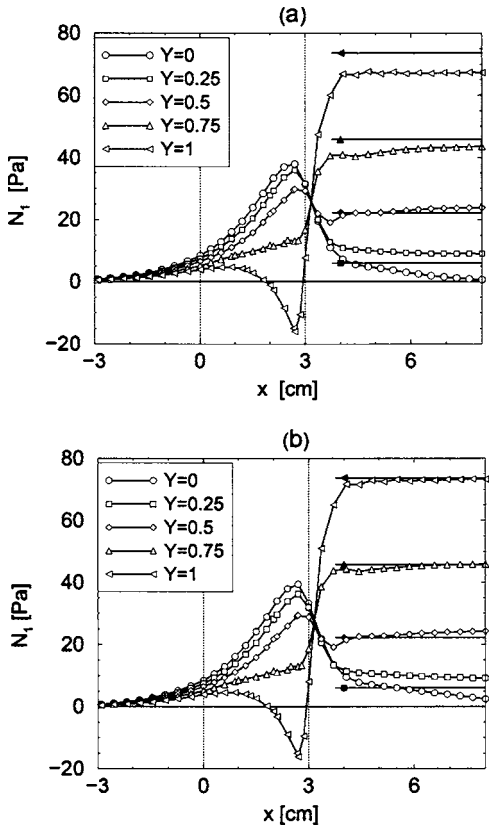

Fig. 5 Simulation results in the tapered contraction domain for $Q=30$ cm^2/s: (*a*) $N_F=2000$ and (*b*) $N_F=8000$. Horizontal lines are the exact steady-state values.

2514 velocity nodes.

Simulations were performed over a range of volumetric flow rates, Q, corresponding to the flow rates $\hat{Q}$ used in the experiments. The latter (in units cubic centimeters per second) were converted to the former (in units square centimeters per second) by assuming that the flow in the x_3 direction was nearly uniform. The results from two flow rates are presented here: $Q=6.42$ cm^2/s and $Q=9.92$ cm^2/s. At all flow rates considered, the simulation results were mesh-independent.

Figure 6 shows the streamline patterns from the numerical simulations for the two flow rates. A significant vortex is observed, as is typical for viscoelastic flows in abrupt contraction domains. Furthermore, over the range of flow rates considered, the size of the vortex did not grow with increased flow rate. This lack of vortex growth is again typical of polymers in planar contractions [18]. At all flow rates, the size of the vortex, $\chi=L_v/(2H_u)$, remained at 0.24, where L_v is the vortex detachment length along the upstream wall. The size of the vortex in the experiments was not reported.

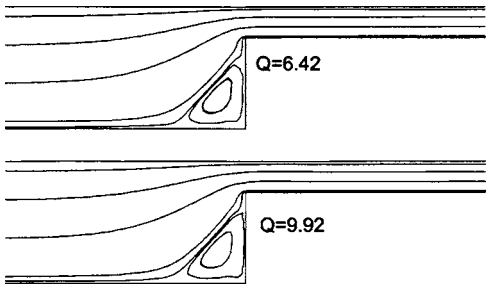

Fig. 6 Streamline patterns in the abrupt contraction domain

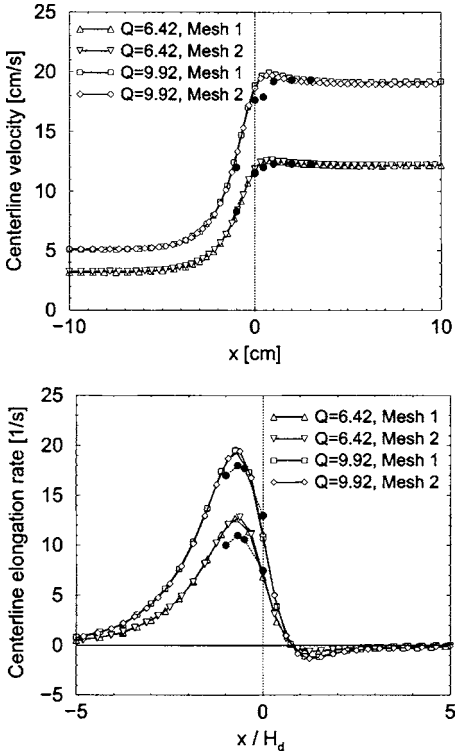

Fig. 7 Centerline velocity profiles and elongation rates: experimental data (closed symbols), simulation (open symbols)

A comparison of the predicted flow kinematics and the experimental data is given in Fig. 7. The top graph shows the comparison of axial velocity along the centerline of the domain, while the bottom graph shows the derived centerline elongation rates. The centerline velocity in the experiments was measured using laser doppler velocimetry [11]. The figure shows that there is generally good agreement. The model and simulation predict well the characteristic velocity overshoot within the die before a constant value is reached. In contrast, a velocity overshoot was not apparent in the experimental data. This difference in velocity is reflected in the elongation rates. Nevertheless, both simulation and experiment show that the maximum elongation rate is reached immediately before the die entry, which is characteristic in die entry flow [18]. Simulation results from both meshes are shown in these figures, verifying mesh independence.

5 Summary

A micro-macro simulation algorithm to calculate the flow of polymeric fluids was developed and implemented. The calculation of the velocity and pressure fields was performed using standard finite element techniques, while the polymer stress was calculated from a microscopic-based rheological model using stochastic simulations. The rheological model considered in this study combines aspects of network and reptation theories for concentrated polymer solutions and melts with aspects of continuum mechanics.

The fluid considered was a concentrated polyisobutylene (PIB) solution. After determining model parameters that produced good agreement between model predictions and experimental data in viscometric flows, the performance of the micro-macro algorithm, as well as the rheological model, was evaluated by simulating the flow of the PIB solution in two benchmark contraction domains. In a tapered contraction domain, the simulations predicted the correct qualitative behavior of polymeric fluids. The simulation results in an abrupt die entry domain also predicted the correct

qualitative behavior and were compared to experimental data. It was found that the computed centerline velocity and elongation rates generally agreed well with the experimental values reported in the literature.

As with all multiscale simulations, the computational cost of the simulations performed here was high. Using 2000 configuration fields for each of the two configuration vectors resulted in computational times of ~0.93 s per triangle per iteration on a Dell Inspiron 8100. This time grew linearly with the increase of configuration fields and elements. A major factor contributing to the high computational time for the current simulations is the accurate determination of a survival time s for each configuration field from the multimode relaxation spectrum of the fluid. Recall that in the single-mode case, there is an analytical expression for s as a function of a uniformly distributed random number z. Therefore, a survival time can be generated through a single-function evaluation. However, in the multimode case, a nonlinear equation for $z(s)$ must be solved every time a new survival time is needed. Even though a fast converging Newton method is used to solve this equation, the process is still time consuming. This is due to the behavior of the memory function, in particular, the locally high gradients, and the fact that a good initial guess must be found to guarantee convergence of the Newton iterates. Although we have seen that it is sometimes possible to reduce this computational time by simulating each mode separately, it is not guaranteed that this will always be the case, particularly when the number of relaxation times increases. This is because additional ensembles must be processed. Currently the most reliable and robust way to reduce computational costs is to parallelize the code with respect to the ensemble of configuration fields.

In conclusion, the micro-macro simulation algorithm presented here performed very well for our molecular-based model in the test die entry domains. The dynamics of the model are very simple and there is substantial room for improvements, such as the inclusion of nonaffine motion of the molecules, finite extensibility and nonlinear restoring forces. Future work includes improving the dynamics of the model, testing the model modifications using the micro-macro algorithm, and extending the algorithm to other molecular-based models.

Acknowledgment

This work was supported by the National Science Foundation under Grant No. NSF DMS-0096847.

References

[1] Laso, M., and Öttinger, H. C., 1993, "Calculation of Viscoelastic Flow Using Molecular Models: The CONNFFESSIT Approach," J. Non-Newtonian Fluid Mech., **47**(1), pp. 1–20.

[2] Feigl, K., Laso, M., and Öttinger, H. C., 1995, "The CONNFFESSIT Approach for Solving a Two-Dimensional Viscoelastic Fluid Problem," Macromolecules, **28**(9), pp. 3261–3274.

[3] Hua, C. C., and Schieber, J. D., 1996, "Application of Kinetic Theory Models in Spatiotemporal Flows for Polymer Solutions, Liquid Crystals and Polymer Melts Using the CONNFFESSIT Approach," Chem. Eng. Sci., **51**(9), pp. 1473–1485.

[4] Bell, T. W., Nyland, G. H., Graham, M. D., and de Pablo, J. J., 1997, "Combined Brownian Dynamics and Spectral Method Simulations of the Recovery of Polymeric Fluids After Shear," Macromolecules, **30**(6), pp. 1806–1812.

[5] Hulsen, M. A., van Heel, A. P. G., and van den Brule, B. H. A. A., 1997, "Simulation of Viscoelastic Flows Using Brownian Configuration Fields," J. Non-Newtonian Fluid Mech., **70**, pp. 79–101.

[6] Öttinger, H. C., van den Brule, B. H. A. A., and Hulsen, M. A., 1997, "Brownian Configuration Fields and Variance Reduced CONNFFESSIT," J. Non-Newtonian Fluid Mech., **70**, pp. 255–261.

[7] Van Heel, A. P. G., Hulsen, M. A., and van den Brule, B. H. A. A., 1999, "Simulation of Doi-Edwards Model in Complex Flow," J. Rheol., **43**(5), pp. 1239–1260.

[8] Keunings, R., 2004, "Micro-Macro Methods for the Multiscale Simulation of Viscoelastic Flow Using Molecular Models of Kinetic Theory," *Rheology Reviews 2004*, D. M. Binding and K. Walters, Eds., British Society of Rheology, pp. 67–98.

[9] Feigl, K., and Öttinger, H. C., 1998, "A New Class of Stochastic Simulation Models for Polymer Stress Calculation," J. Chem. Phys., **109**(2), pp. 815–826.

[10] Quinzani, L. M., McKinley, G. H., Brown, R. A., and Armstrong, R. C., 1990, "Modeling the Rheology of Polyisobutylene Solutions," J. Rheol., **34**, pp. 705–748.

[11] Quinzani, L. M., Armstrong, R. C., and Brown, R. A., 1995, "Use of Coupled Birefringence and LDV Studies of Flow Through a Planar Contraction to Test Constitutive Equations for Concentrated Polymer Solutions," J. Rheol., **39**(6), pp. 1201–1228.

[12] Bird, R. B., Curtiss, C. F., Armstrong, R. C., and Hassager, O., 1987, Dynamics of Polymeric Liquids, Volume 2, *Kinetic Theory*, 2nd ed., Wiley-Interscience, New York.

[13] Öttinger, H. C., 2000, "Thermodynamically Admissible Reptation Models With Anisotropic Tube Cross Sections and Convective Constraint Release," J. Non-Newtonian Fluid Mech., **89**, pp. 165–185.

[14] Öttinger, H. C., 1996, *Stochastic Processes in Polymeric Fluids*, Springer, New York.

[15] Feigl, K., and Öttinger, H. C., 2001, "The Equivalence of the Class of Rivlin-Sawyers Equations and a Class of Stochastic Models for Polymer Stress," J. Math. Phys., **42**(2), pp. 796–817.

[16] Bernstein, B., Malkus, D. S., and Olsen, E. T., 1985, "A Finite Element for Incompressible Plane Flows of Fluids With Memory," Int. J. Numer. Methods Fluids, **5**, pp. 43–70.

[17] Bernstein, B., Feigl, K., and Olsen, E. T., 1996, "A First Order Exactly Incompressible Finite Element for Axisymmetric Fluid Flow," SIAM (Soc. Ind. Appl. Math.) J. Numer. Anal., **33**(5), pp. 1736–1758.

[18] Feigl, K., and Öttinger, H. C., 1996, "A Numerical Study of the Flow of a Low-Density Polyethylene Melt in a Planar Contraction and Comparison to Experiments," J. Rheol., **40**(1), pp. 21–35.

[19] Feigl, K., and Öttinger, H. C., 1994, "The Flow of a LDPE Melt Through an Axisymmetric Contraction: A Numerical Study and Comparison to Experimental Results," J. Rheol., **38**(4), pp. 847–874.

[20] Bernstein, B., Feigl, K., and Olsen, E. T., 1994, "Steady Flows of Viscoelastic Fluids in Axisymmetric Abrupt Contraction Geometry: A Comparison of Numerical Results," J. Rheol., **38**(1), pp. 53–71.

[21] Feigl, K., Tanner, F. X., Edwards, B. J., and Collier, J. R., 2003, "A Numerical Study of the Measurement of Elongational Viscosity of Polymeric Fluids in a Semihyperbolically Converging Die," J. Non-Newtonian Fluid Mech., **115**(2–3), pp. 191–215.

D. Gao[1]
Ames Laboratory,
Ames, IA 50011

R. Fan
Chemical Engineering Department,
Iowa State University,
Ames, IA 50011

S. Subramaniam
Mechanical Engineering Department,
Iowa State University
and Ames Laboratory,
Ames, IA 50011

R. O. Fox
Chemical Engineering Department,
Iowa State University
and Ames Laboratory,
Ames, IA 50011

D. Hoffman
Ames Laboratory,
Ames, IA 50011

Momentum Transfer Between Polydisperse Particles in Dense Granular Flow

We perform molecular dynamics (MD) simulations (based on the soft-sphere model) of a model dry granular system consisting of two types of spherical particles differing in size and/or density to characterize particle-particle momentum transfer (solid drag). The velocity difference between two types of particles is specified in the initial conditions, and the evolution of relative mean velocity and the velocity fluctuations in terms of granular temperature are quantified. The dependence of the momentum transfer is studied as a function of volume fraction, size and density ratio of the two types of particles, inelasticity, and friction coefficient. An existing continuum model of particle-particle momentum transfer is compared to the MD simulations. A modified continuum solid drag model is suggested for a limited range of parameters. [DOI: 10.1115/1.2140803]

Introduction

Granular flows as well as dispersed particle flows (particles in fluid) are widely seen in nature and applied in industrial processes. Two approaches are currently used to model the motion of particle phase: particle (Lagrangian) approach and multiphase fluid model (continuum approach). In a particle approach, individual particles are tracked by solving for particle motion in a discrete element method (DEM) based on the soft-sphere contact model [1–3], which is popularly being called molecular dynamics (MD) [4,5] simulation in recent years. The capability of this approach is largely limited by the computational expense incurred in simulating a large number of particles. In a multiphase fluid model, the particle phase is approximated as a continuum fluid, and thus a set of continuum equations (conservation of mass, momentum, energy) for a control volume is obtained from granular gas kinetics. The advantage of the continuum approach is that it is capable of computing large systems. Particle number is not relevant in the continuum approach. One widely used numerical code, MFIX [6], developed at the National Energy Technology Laboratory (NETL), is based on the continuum approach, and this work is partially motivated by the modeling questions that arise during application of the code.

MFIX is a hydrodynamic model for fluid-solids flows, based on conservation laws of mass, momentum, energy, and species for describing the hydrodynamics, heat transfer, and chemical reactions in dense or dilute fluid-solids flows. The conservative equations must be closed by several constitutive relations including the particle-particle momentum transfer relation we are studying in this work. The model treats the fluid and solid phases as interpenetrating continua. Each solid phase consists of particles with identical particle properties such as density, diameter, and so on. Phase volume fractions are introduced to track the fraction of the averaging volume occupied by various phases. The code is used as a "test-stand" for testing and developing multiphase flow constitutive equations. More about MFIX can be found from the website of www.mfix.org.

The development of kinetic theory [7] of dense granular flows encounters a tremendous difficulty from the fact that particle collisions in granular flows are inelastic. The basic assumptions on which solving the Boltzmann equation [8] for ideal gas molecules (elastic collision) are based do not hold for granular flows. The continuum models have to be closed by employing approximations and empirical relations.

A real granular system consists of several kinds of particles with different sizes, densities, or other properties. For continuum models, each kind of particles is denoted as one solid particle phase and is described by one set of governing equations of continuum mechanics. Each particle phase has to experience internal "fluid-dynamics" [4,9], fluid-particle interaction, and particle-particle interaction, so that the fluid-particle momentum transfer term (also called fluid drag) and particle-particle momentum transfer term (also called solid drag) appear in the momentum equations of each particle phase. In this work, we focus on particle-particle momentum transfer through the study of a dry bidisperse granular mixture.

Existing models for particle-particle momentum transfer are semi-empirical and applicable to a limited range of flows [7] (dilute flows in most cases). In efforts to explore the characteristics of granular flows and enhance predictive ability of continuum models, lots of direct simulations of granular systems have been done. There are in general two methods in such MD simulations: soft-sphere model and hard-sphere model. The soft-sphere contact model is pioneered by Cundall and Strack [1]. In recent years several MD simulations of bidisperse granular systems [10,11] based on hard-sphere model are very attractive to the study of momentum transfer between particle phases.

In this work, we perform MD simulations of a dry bidisperse granular mixture in the soft-sphere framework [1–5] to characterize the solid drag for the simple system and compare the results to an existing continuum model, specifically the model used in MFIX (although other continuum models can also be used for comparison). We compare results from the two approaches, pro-

[1]Corresponding author. Email: gao_ma@yahoo.com
Contributed by the Fluids Engineering Division of ASME for publication in the JOURNAL OF FLUIDS ENGINEERING. Manuscript received May 5, 2004; final manuscript received April 12, 2005. Assoc. Editor: Dennis Siginer.

pose a modified model based on the original MFIX model, and discuss ideas for improving the continuum model for solid drag.

Study System and Solution in Continuum Approach. A simple case, two types of dry particles in a control volume with periodic boundary conditions on all sides, and without external force, but with an initial velocity difference in one velocity component, is a good starting point for the study of particle-particle momentum transfer (or solid drag). The homogeneous and periodic conditions make the system simple for modeling in the continuum approach. The constitutive relations for dynamics inside a solid phase are not involved. In most continuum multiphase modeling [6], the governing equations for such a homogeneous case can be written as

$$\frac{d}{dt}(\epsilon_1\rho_1\mathbf{u}_1) = -F_{12}(\mathbf{u}_1 - \mathbf{u}_2) \tag{1}$$

$$\frac{d}{dt}(\epsilon_2\rho_2\mathbf{u}_2) = F_{12}(\mathbf{u}_1 - \mathbf{u}_2) \tag{2}$$

where $\epsilon_{1,2}$, $\rho_{1,2}$, $\mathbf{u}_{1,2}$ are the volume fraction, particle mass density, and number-weighted mean velocity for particles of type 1 and 2, respectively, and F_{12} is the solid drag coefficient. Due to the periodic conditions on all sides, the volume fractions in the control volume are fixed. Therefore, the velocity difference is obtained from the above equations as

$$\frac{d}{dt}(\mathbf{u}_1 - \mathbf{u}_2) = -\left(\frac{1}{\epsilon_1\rho_1} + \frac{1}{\epsilon_2\rho_2}\right)F_{12}(\mathbf{u}_1 - \mathbf{u}_2) \tag{3}$$

F_{12} is usually a linear function of magnitude of relative mean velocity in the form of

$$F_{12} = C_{12}|\mathbf{u}_1 - \mathbf{u}_2| \tag{4}$$

Here C_{12} is a coefficient that is independent of velocity. The governing equation then becomes

$$\frac{d}{dt}|\mathbf{u}_1 - \mathbf{u}_2| = -\left(\frac{1}{\epsilon_1\rho_1} + \frac{1}{\epsilon_2\rho_2}\right)C_{12}|\mathbf{u}_1 - \mathbf{u}_2|^2$$

The solution is

$$|\mathbf{u}_1 - \mathbf{u}_2| = \left[\left(\frac{1}{\epsilon_1\rho_1} + \frac{1}{\epsilon_2\rho_2}\right)C_{12}t + 1/|\mathbf{u}_1 - \mathbf{u}_2|_0\right]^{-1}$$

The system shares some properties with the homogeneous cooling state such as the asymptotic decay rate of the velocity is like $1/t$, a fact that follows from the lack of inherent time scales. For easy description of the current work, we normalize the solution using a velocity scale as the initial velocity difference $u_0 = |\mathbf{u}_1 - \mathbf{u}_2|_0/2.0$, a length scale as the average diameter of two types of particles $d_0 = (d_1 + d_2)/2$, and a time scale as $t_0 = d_0/u_0$. We use the notation u_{12} to denote the velocity difference $|\mathbf{u}_1 - \mathbf{u}_2|$ and $\tilde{C}_{12}$ to symbolize the term in dimensionless form, but we drop off the $\tilde{}$ on other terms such as velocity and time for simplicity. According to the MFIX model [6,12], we have the dimensionless momentum equation as well as its solution in our final form:

$$\frac{du_{12}}{dt} = -\tilde{C}_{12}u_{12}^2 \tag{5}$$

$$u_{12} = \frac{1}{\tilde{C}_{12}t + 0.5} \tag{6}$$

$$\tilde{C}_{12} = \left(\frac{1}{\epsilon_1\rho_1} + \frac{1}{\epsilon_2\rho_2}\right)\frac{d_1 + d_2}{2}C_{12} \tag{7}$$

$$C_{12} = \frac{3(1+e)(\pi/2 + \mu\pi^2/8)\epsilon_1\rho_1\epsilon_2\rho_2(d_1 + d_2)^2 g_0}{2\pi(\rho_1 d_1^3 + \rho_2 d_2^3)} \tag{8}$$

$$g_0 = \frac{1}{1 + \epsilon_s} + \frac{3d_1d_2}{(1 - \epsilon_s)^2(d_1 + d_2)}\left(\frac{\epsilon_1}{d_1} + \frac{\epsilon_2}{d_2}\right) \tag{9}$$

$$\epsilon_s = \epsilon_1 + \epsilon_2 \tag{10}$$

where e, μ are two microscale particle material properties during contacts: restitution and friction coefficient, ϵ_s is the total volume fraction of particles, $d_{1,2}$ is the particle diameter for particles of type 1 and 2, respectively, and g_0 is the radial distribution function at contact originated by Lebowitz [13].

It can be seen that the dimensionless solution is a function of e, μ, ϵ_1, ϵ_2, d_2/d_1, ρ_2/ρ_1, namely

$$\tilde{C}_{12} = f(e, \mu, \epsilon_1, \epsilon_2, d_1/d_2, \rho_1, \rho_2) \tag{11}$$

The solid drag coefficient is a function of many parameters. We cannot exhaust all the conditions to cover the full range of variation of every variable. In this work, we focus on the equal volume fractions of two particle phases and on medium to dense particle volume fraction.

The coefficient C_{12} in Eq. (8) is derived in MFIX [6,12] by considering two colliding particles located at $\mathbf{r}_1$, $\mathbf{r}_2$ with velocities $\mathbf{c}_1$, $\mathbf{c}_2$, and diameters d_1, d_2, respectively. The average momentum transfer per unit volume between the two types of particles is

$$\mathbf{I}_{12} = d_{12}^2\int_{\mathbf{c}_{12}\cdot\mathbf{n}>0}\mathbf{J}(\mathbf{c}_{12}\cdot\mathbf{n})f_{12}(\mathbf{r}_1, \mathbf{c}_1, \mathbf{r}_1 + d_{12}\mathbf{n}, \mathbf{c}_2)d\mathbf{n}d\mathbf{c}_1\mathbf{c}_2 \tag{12}$$

where $\mathbf{I}_{12}$ is average momentum transferred per unit volume, $d_{12} = (d_1 + d_2)/2$, the relative velocity $\mathbf{c}_{12} = \mathbf{c}_1 - \mathbf{c}_2$, $\mathbf{n}$ is the unit vector from the center of particle 1 to the center of particle 2, $\mathbf{J}$ is the momentum transferred between particles 1 and 2, and f_{12} is the pair distribution function which is assumed to be the product of two single velocity distribution functions

$$f_{12} = g_0 f_1 f_2 \tag{13}$$

The single velocity distribution functions take the form of a delta function

$$f_1 = 6\epsilon_1\delta(\mathbf{c}_1 - \mathbf{u}_1)/\pi d_1^3 \tag{14}$$

$$f_2 = 6\epsilon_2\delta(\mathbf{c}_2 - \mathbf{u}_2)/\pi d_2^3 \tag{15}$$

Following Walton [14], a collision is divided into sticking collision part and sliding collision part, so that the formulation of $\mathbf{J}$ will take into account the repulsion, dissipation, and friction effects.

Soft-Sphere MD Model. GranFlow is a parallel MD simulation code for granular flows that has been developed at Sandia National Lab. and has been evaluated, verified, and applied in many publications [3,5]. Readers who are interested in high-performance numerical algorithms are referred to Ref. [15]. The MD simulation is based on a 3D soft-sphere contact model [1–3] where small deformations and multiple contacts on a sphere are allowed, and friction and rotation are also taken into account. Contact force is first calculated from the deformation through a microscale spring-dashpot model, then is used in Newton's second law for every particle (spherical shape is assumed throughout this work) to update the velocity and angular velocity of each particle. The implementation of contact forces is essentially a reduced version of that employed by Walton and Braun [2], developed earlier by Cundall and Strach [1].

The spheres interact on contact through a Hookean (linear) contact law [1,2]. For two contacting particles $\{i, j\}$, at position $\{\mathbf{r}_i, \mathbf{r}_j\}$, with velocities $\{\mathbf{v}_i, \mathbf{v}_j\}$ and angular velocities $\{\boldsymbol{\omega}_i, \boldsymbol{\omega}_j\}$, a relative normal compression is

$$\boldsymbol{\delta}_{n,ij} = [(d_i + d_j)/2 - r_{ij}]\mathbf{n}_{ij} \tag{16}$$

where $\mathbf{r}_{ij}=\mathbf{r}_i-\mathbf{r}_j$, $r_{ij}=|\mathbf{r}_{ij}|$ and the normal direction $\mathbf{n}_{ij}=\mathbf{r}_{ij}/r_{ij}$. The normal and tangential contact forces for particle i are given by

$$\mathbf{F}_{n,ij} = k_n\boldsymbol{\delta}_{n,ij} - \gamma_n m_{\text{eff}}\mathbf{v}_{n,ij} \tag{17}$$

$$\mathbf{F}_{t,ij} = -k_t\boldsymbol{\delta}_{t,ij} - \gamma_t m_{\text{eff}}\mathbf{v}_{t,ij} \tag{18}$$

where $m_{\text{eff}}=(m^i m^j)/(m^i+m^j)$, $\mathbf{v}_n$ and $\mathbf{v}_t$ are the normal and tangential components of the relative surface velocity, and $k_{n,t}$ and $\gamma_{n,t}$ are spring and damping coefficients, respectively. $\boldsymbol{\delta}_t$ is the elastic tangential displacement between spheres, obtained by integrating surface relative velocities over time during deformation of the contact. The magnitude of $\boldsymbol{\delta}_t$ is truncated as necessary to satisfy a local Coulomb yield criterion $|\mathbf{F}_t| \leqslant \mu|\mathbf{F}_n|$. Frictionless particles can be simulated by setting zero friction coefficient, $\mu=0$.

The presented simulations follow the same framework of Grest et al. [3,5] regarding the particle material parameters. The spring constants are set to $k_n=2\times10^5 m_* g/d_0$, where m_* and d_0 are mass and diameter of the particle in monodisperse mixtures, respectively, g is the gravity acceleration, and $k_t=2k_n/7$. The γ_n is related to restitution coefficient e. Such a correlation can be found in Ref. [3]. For a reference particle, physical experiments often use glass spheres of $d=100$ μm with $\rho=2\times10^3$ kg/m^3.

For the present polydisperse systems with two types of particles, when we investigate size or density effects, we wish to maintain contact parameters k_n, γ_n unchanged for better understanding and comparisons of results. For this purpose, the diameter and mass (or density) of a particle are varied proportionally relative to the corresponding particle. We maintain $d_0=(d_1+d_2)/2$ unchanged, so that d_0 is also equal to the diameter of particles when the two types of particle are the same.

The movement of particle i is described by Newton's second law in dimensionless form based on the normalization scales of m_*, d_0, g as

$$\frac{m_i}{m_*}\frac{d\mathbf{v}_i}{dt} = \sum_j \left(\tilde{k}_n\boldsymbol{\delta}_{n,ij} - \tilde{\gamma}_n\frac{m_{\text{eff}}}{m_*}\mathbf{v}_{n,ij}\right) + \sum_j \left(-\tilde{k}_t\boldsymbol{\delta}_{t,ij} - \tilde{\gamma}_t\frac{m_{\text{eff}}}{m_*}\mathbf{v}_{t,ij}\right) \tag{19}$$

$$0.4\frac{m_i}{m_*}\frac{d\boldsymbol{\omega}_i}{dt} = -\frac{1}{2}\sum_j d_i\mathbf{n}_{ij} \times \left(-\tilde{k}_t\boldsymbol{\delta}_{t,ij} - \tilde{\gamma}_t\frac{m_{\text{eff}}}{m_*}\mathbf{v}_{t,ij}\right) \tag{20}$$

The numerical simulation directly solves the above dimensionless equations, and input and output parameters are all in dimensionless form. We take $\tilde{k}_n=2\times10^5$, $k_t=2k_n/7$, and $\tilde{\gamma}_n=0,50$ (corresponding to $e=1,0.88$). For the Hookean contact model $\gamma_t=0$. Detailed discussion about contact parameters is available in Ref. [3].

To compare to a continuum model based on kinetic theory, the macroscopic terms (average variables) must be obtained from simulation results for the particle mixtures. The phase velocity $\mathbf{u}_{1,2}$ appearing in the continuum approach is equivalent to the average velocity over all particles of a type in the system. For example, for solid phase 1,

$$\mathbf{u}_1 = [u_1, v_1, w_1] = \sum_{i=1}^{N_1} \mathbf{v}_i/N_1 \tag{21}$$

N_1 is the number of particles of type 1. The granular temperature is defined as

$$\theta_1 = \sum_{i=1}^{N_1} [(u_i-u_1)^2 + (v_i-v_1)^2 + (w_i-w_1)^2]/3N_1 \tag{22}$$

where u_1, v_1, w_1 are three average velocity components. In this work, the volume of the simulation cell is $V=24^3 d_0^3$. The particle volume fractions for particle types 1 and 2 are calculated as

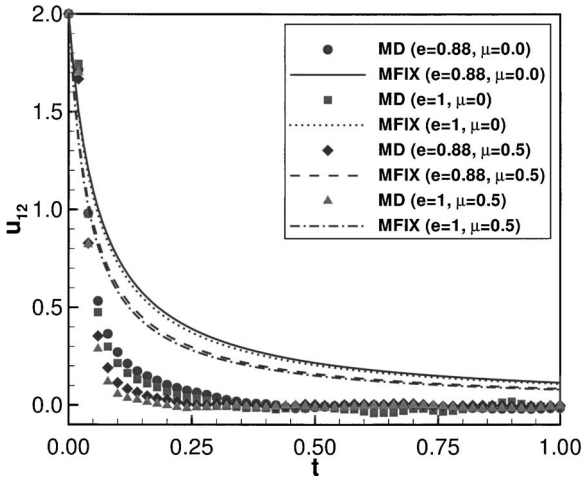

Fig. 1 Velocity difference u_{12} for $\epsilon_1=\epsilon_2=0.262$, $d_2/d_1=1/1$, and $\rho_2/\rho_1=1/1$

$$\epsilon_{1,2} = (\pi d_{1,2}^3 N_{1,2}/6)/V$$

Note that the normalization used here in simulations is different from that used in the previous section. The resultant terms of simulation must be transformed to the same normalization system on which the continuum model is based before any comparison is performed.

The particle mixture must be initialized to be spatially homogeneous. It is difficult to place all particles by random number generation methods, especially for dense mixtures. We use another way to initialize the system in this study. We first set all the particles in a form of lattice arrangements and assign an arbitrary velocity to each one, and then run the simulation to equilibrate the mixture. Because relative velocities of particles in a cooling system decay very fast, one run of the simulation may not result in the homogeneous condition. To ensure homogeneity, the output of a simulation is used as the input of particle positions to the next simulation, but the velocity of each particle is reset to a random value. The output-input procedure may be repeated several times. Finally, the input of particle positions from the homogeneous state is used to study cases with the velocity set to u_0 for one type of the particles and $-u_0$ for the other type.

Results and Discussion

Effects of e, μ, ϵ_s. The results are presented in dimensionless form and the units are omitted. The normalization scales have been given in the second section of deriving continuum solution of the granular system.

We first investigate the dependence of particle-particle momentum transfer on the total volume fraction and on the microscale properties e, μ. The particles in two phases are actually the same with $d_2/d_1=1$, $\rho_2/\rho_1=1$. Four combinations of $e=\{0.88,1\}$, $\mu=\{0.5,0\}$ are considered. According to the MD model, $e=1.0$ represents no energy loss during collision, $\mu=0$ represents no rotation.

The velocity differences u_{12} varying with time are plotted in Figs. 1 and 2, respectively, for total particle volume fraction $\epsilon_s=0.524$, 0.304. The initial momentum rapidly decays as the momentum of particles is redistributed isotropically through collisions (contacts). The granular temperature of the system immediately reaches its maximum. We can see the microscale parameters do make a difference on the momentum transfer, but the difference is relatively small compared with the difference between the MFIX model and MD simulation.

MFIX has captured the basic feature of contact parameters. The MFIX model follows the same trend as the MD simulations. The

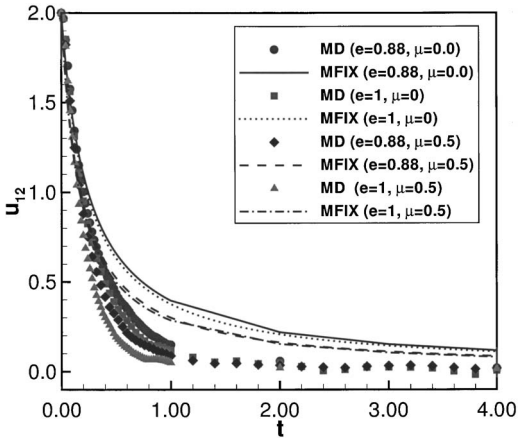

Fig. 2 Velocity difference u_{12} for $\epsilon_1=\epsilon_2=0.152$, $d_2/d_1=1/1$, and $\rho_2/\rho_1=1/1$

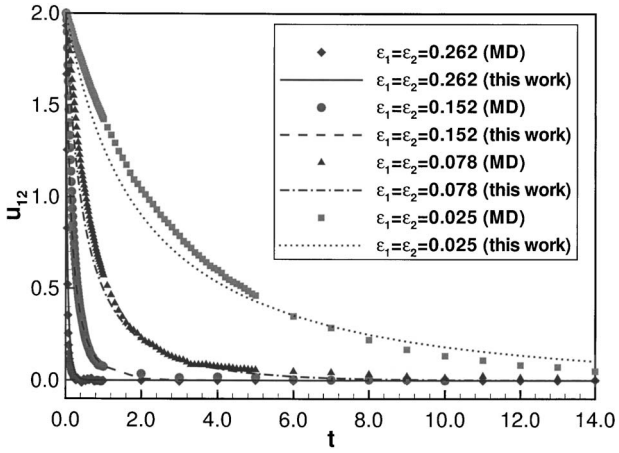

Fig. 4 Velocity difference u_{12} at various total volume fractions for $d_2/d_1=1/1$, $\rho_2/\rho_1=1/1$, $e=0.88$, and $\mu=0.5$

order of lines respective to different e, μ values from MFIX is the same as that from MD simulation. However, what concerns us most is the prominent gaps between the MFIX model and the MD simulation in Figs. 1 and 2, which overshadow the differences the microscale parameters make. It is clearly shown that the MFIX drag model underestimates the momentum transfer. Similar mismatches were observed for a wide range of total volume fractions. Agreement with the MFIX prediction becomes worse as the density of granular mixture increases.

The continuum solid drag model can be improved by separating the drag coefficient into two parts: a velocity-dependent part and a velocity-independent part as follows:

$$\frac{du_{12}}{dt} = -\tilde{C}_{12}u_{12}(1 + b/u_{12})u_{12} \tag{23}$$

The solution to this equation is

$$u_{12} = -b + b\left(1 - \frac{2.0}{2.0+b}\exp(-b\tilde{C}_{12}t)\right)^{-1} \tag{24}$$

In fact, we found that b is a function of total volume fraction ϵ_s, which is shown in Fig. 3. The curve fit gives the linear function

$$b = \epsilon_s + 0.42 \tag{25}$$

The model constant b is a correction to the original dilute granular flow solid drag model. Equation (25) indicates that the correction increases linearly with the total volume fraction.

The comparison of the suggested model and MD simulation for different volume fractions is shown in Fig. 4. The agreement is very good.

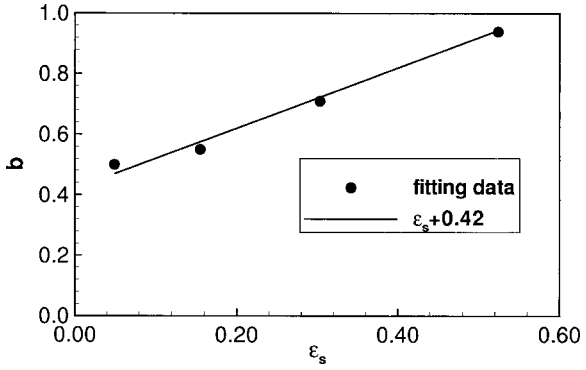

Fig. 3 b as a function of total volume fraction ϵ_s

Effects of Density Ratio. The velocity differences at different particle density ratios but with all other parameters the same ($e=0.88$, $\mu=0.5$, $\epsilon_1=\epsilon_2$, $d_1=d_2$) are plotted in Fig. 5. The results show that both MD and Eqs. (23)–(25) are not sensitive to variation of density. But, we must point out that the density effects could be important if the particle sizes are not the same, or the volume fractions of two particle phases are not equal, or the contact parameters change with the density. The present MD simulation uses the same contact coefficients for colliding particles, which deviates from the reality that material properties have much difference, especially when the densities are different.

Polydispersity. The size ratio plays a critical role in the solid drag model. This can be seen from the cubic power on particle diameters in Eqs. (7) and (8), but the drag model depends on other parameters only to the first power.

Figures 6–8 show the results for particles at different size ratios but with the same particle density $\rho_1=\rho_2$ and volume fraction $\epsilon_1=\epsilon_2=0.152$ for the case of $e=0.88$, $\mu=0.5$. The velocity difference u_{12} and granular temperature θ are plotted in Figs. 6 and 7, respectively. It is interesting to see that the phenomenon of momentum transfer between particle phases exhibits a nearly delta functional dependence on particle size. If the particle size ratio is just a little bit away from 1, specifically $d_2/d_1 \geqslant 1.1/0.9$, all the velocity difference curves settle down on nearly the same decay curve. However, near equal size, here $1 \leqslant d_2/d_1 \leqslant 1.05/0.95$, the velocity difference profiles are quite different from the group with

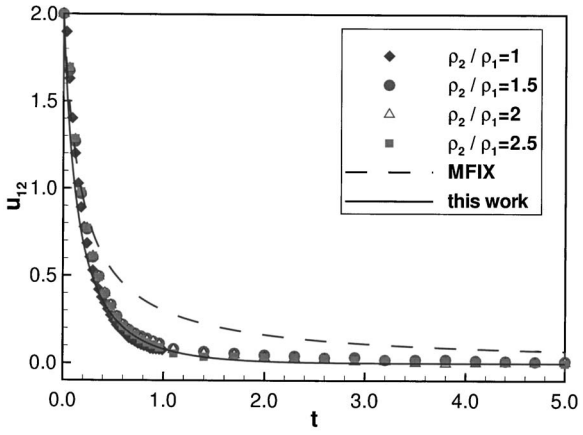

Fig. 5 Velocity difference u_{12} at various densities for $\epsilon_1=\epsilon_2=0.152$ and $d_2/d_1=1/1$

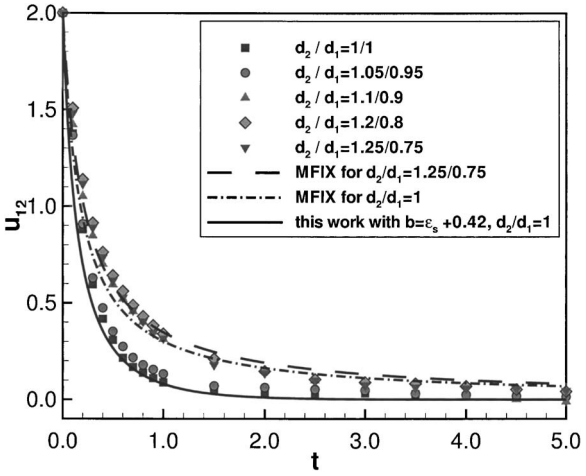

Fig. 6 Velocity difference u_{12} at different sizes for $e=0.88$, $\mu=0.5$, $\epsilon_1=\epsilon_2=0.152$, and $\rho_2/\rho_1=1$

$d_2/d_1 \geqslant 1.1/0.9$: they decay much faster than those with larger size ratios. From the comparison of the result of $d_2/d_1=1.1/0.9$ to that of $d_2/d_1=1.05/0.95$, we can see that a small change of particle size ratio results in a jump of velocity profiles between the two cases. But, in each group ($1 \leqslant d_2/d_1 \leqslant 1.05/0.95$ or $d_2/d_1 \geqslant 1.1/0.9$), the velocity profiles stay close together without obvious gaps among them.

It is encouraging to see that the agreement between Eq. (23) and MD simulation is very good for the particle size ratios which are a little bit away from 1, although the agreement is the worst at $d_2=d_1$. The suggested model of Eq. (23) still holds but needs further modification on b to address the particle size dependence issue:

$$\frac{du_{12}}{dt} = -\tilde{C}_{12}(1 + b/u_{12})u_{12}^2 \tag{26}$$

$$b = (\epsilon_s + 0.42)\left(\frac{d_{min}}{d_{max}}\right)^n \tag{27}$$

where d_{min} is the smaller diameter and d_{max} is the larger. In Eq. (27), the power n may need to be very large to account for the jump feature of solid drag. We found that $n=10$ gives satisfactory fit to the MD simulations.

As we have seen, the original MFIX modeling does not capture the discontinuity. So, the next question is what are the major contributors to the mismatch of the multiphase model with the MD

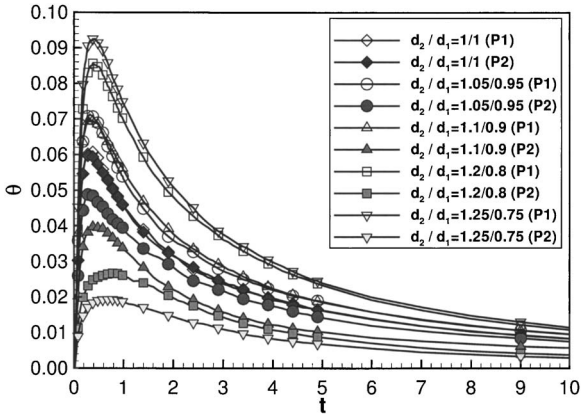

Fig. 7 Granular temperature θ at different sizes for $e=0.88$, $\mu=0.5$, $\epsilon_1=\epsilon_2=0.152$, and $\rho_2/\rho_1=1$. P1 denotes particle phase 1.

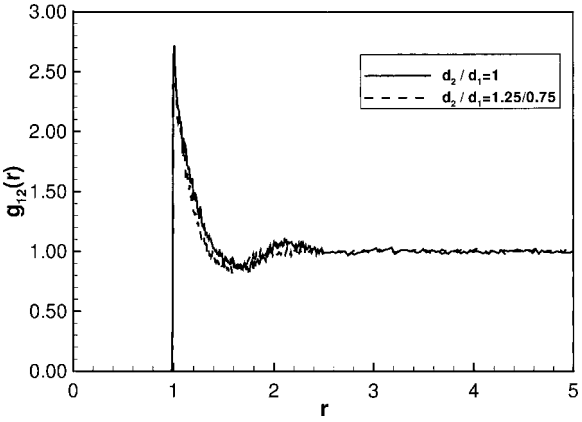

Fig. 8 Radial distribution function $g_{12}(r)$ for two cases of $d_2/d_1=1$ and $d_2/d_1=1.25/0.75$

simulation. The parameter g_0, the radial distribution function at contact, is worth studying. The MD simulation can be used to validate the independency at the specific conditions or to improve the form of g_0 since g_0 is the pair correlation function [16] that is equal to the radial distribution function $g_{12}(r)$ between particle types 1 and 2 evaluated at contact $r=d_0$.

The form of g_0 defined in Eq. (9) is originally from the work of Lebowitz [13]. Another form of g_0 was suggested by Mansoori et al. [17] and is known [18] to be more accurate. However, the inability of present models to predict particle-particle momentum transfer is not because of the form of g_0. As a matter of fact, both forms predict that g_0 is not a function of particle size ratio when the volume fractions of two phases are equal.

The pair velocity distribution function of two particles at contact is generally assumed in the term of product of two single particle velocity distribution functions [6,12,18], namely $f_{12}=g_0 f_1 f_2$. Thus, g_0 appears in the collision term calculation in kinetic theory.

In the case of spatially homogeneous systems as in the present study, $g_{12}(r)$ can be calculated by counting the pairs of separation [16] between particles of type 1 and particles of type 2 with $r-\delta/2 \leqslant |\mathbf{r}_{ij}| \leqslant r+\delta/2$. We use the numerical kernel function method [19] for this work. The g_0 relations given by Lebowitz [13] and Mansoori et al. [17] concern equilibrium states, but the study system in this work is dynamic at early times. We have calculated $g_{12}(r)$ of the granular assembly outputs from MD simulation at several moments. From the calculation, it is indeed found that $g_{12}(r)$ is statistically not a function of time as we expected, although fluctuations with time are found. We also found that the peak of $g_{12}(r)$ is not always exactly at contact distance, but at a slightly larger separation. Figure 8 gives the $g_{12}(r)$ averaged over five time points for two different particle systems. It shows the shape of $g_{12}(r)$ curves is weakly associated with particle sizes at $\epsilon_1=\epsilon_2$ condition. But, for both cases $g_0=g_{12}[(d_1+d_2)/2] \approx 2.5$. The form used in the MFIX model, Eq. (9), gives $g_0=2.37$.

Now, after g_0 has been excluded, we reason that a possible contributor to the disagreement is the assumed delta velocity distribution function during derivation [12] of the drag model in MFIX as shown in Eqs. (14) and (15). The largest momentum transfer happens when two identical particles collide. Due to the delta velocity distribution function, some of size information may be canceled out, leading to underestimation of the momentum transfer at the equal size condition. Other forms for the velocity distribution function could be checked against the simulations. Some models [18] use the Maxwellian distribution function or log-Maxwellian distribution function. Almost all continuous velocity distribution functions are functions of granular temperature in an effort to find out more accurate and general constitutive

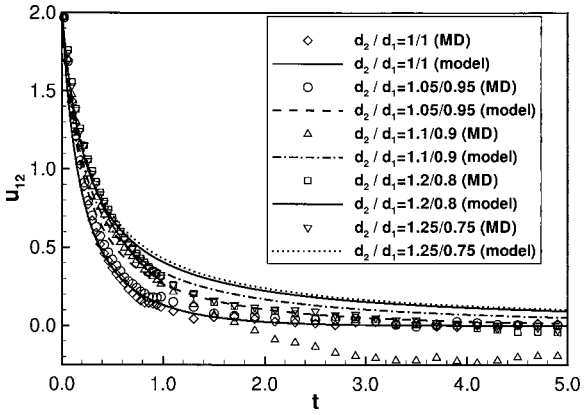

Fig. 9 Velocity difference at different sizes for $e=1.0$, $\mu=0$, $\epsilon_1=\epsilon_2=0.152$, and $\rho_2/\rho_1=1$ "model" means modified model in this work

relations. Note that when granular temperature is involved and a continuous distribution function applied, the near equilibration is often assumed from the point of view of kinetic theory. The application of such a model to a fast decay region starting with zero granular temperature needs to be examined, and the study system here may need to be redesigned in order to validate and explore continuum models.

To better understand the role of granular temperature, it may be helpful to consider frictionless elastic spheres ($e=1.0$, $\mu=0$). The results are shown in Figs. 9 and 10. Oscillation appears in the velocity difference profile when the relative mean velocity approaches zero, since the decay is due to the redistribution of energy in three directions, not to the energy loss. From the comparison of Fig. 9 with Fig. 6, we do see that granular temperature must play a role in the solid drag modeling formulation. For $e=1.0$, $\mu=0$, the velocity profiles from MD simulations diverge from the modeled curves after one time unit. Correspondingly, the granular temperatures increase from zero to the peaks in $t=[0,1]$ and remain at the peaks thereafter as shown in Fig. 10. However, granular temperatures rapidly decay after one time unit for the frictional and inelastic case $e=0.88$, $\mu=0.5$ as shown in Fig. 7. We will continue this work in the future. Note that a discontinuity feature like in Fig. 6 is always a difficult point for continuum modeling. Another discontinuity problem is referred to free-surface flows with surface tension on interfaces [20]. The discontinuity may imply some degree of crystallization at the equal size and equal volume fraction conditions. Away from the condition, crystallization is more unlikely to develop.

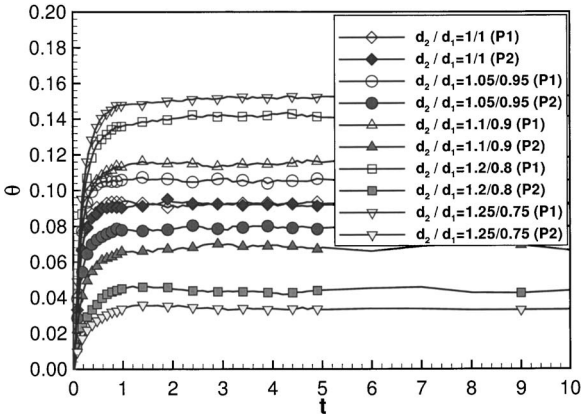

Fig. 10 Granular temperature θ at different sizes for $e=1.0$, $\mu=0$, $\epsilon_1=\epsilon_2=0.152$, and $\rho_2/\rho_1=1$. P1 denotes particle phase 1.

Conclusion and Future Work

We have investigated momentum transfer between particle phases in a limited range of variation of parameters from MD simulation and MFIX continuum drag model and have provided the comparison between them. We found a discontinuous behavior of particle-particle momentum transfer at equal particle sizes from the MD simulation. This discontinuity may point to some degree of crystallization at the condition of equal sizes and equal volume fractions and presents a difficulty in continuum modeling. The current MFIX model is in good agreement with the simulation when particle sizes are different, but underestimates the momentum transfer for particles of equal size. A tentative modified drag model based on the original MFIX model is proposed.

The current model of solid drag has not included the information of granular temperature due to an assumed delta velocity distribution function. Other solid drag models connecting to granular temperature should be considered and compared with simulation data in the future. At the same time, we also need to examine if the model is independent of initial conditions and whether implementation of initial conditions influences results. The study case may need redesign to avoid the zero granular temperature at the initial state. Moreover, all the cases we considered in this work have equal volume fractions for two particle phases. Further detailed study of two-particle phases with different volume fractions is encouraged, and the crystallization or discontinuity that happened at equal sizes and equal volume fractions may disappear. It is perhaps better to rewrite the dependence of solid drag on the governing parameters as

$$\tilde{C}_{12} = f(e, \mu, \epsilon_s, \epsilon_1/\epsilon_2, d_1/d_2, \rho_1/\rho_2) \tag{28}$$

Future work should give attention to the solid drag model varying with ϵ_1/ϵ_2. Indeed, the density ratio may not be negligible if $\epsilon_1 \neq \epsilon_2$. In addition, contact mechanics between different material particles should be taken into account in the MD simulation.

Acknowledgment

This work is supported by the U.S. Department of Energy through project Granular Flow and Kinetics. We thank J.W. Landry and G.S. Grest with help implementing their parallel MD simulation code GranFlow. We are thankful to reviewers for their constructive and informative suggestions.

References

[1] Cundall, P. A., and Strack, O. D. L., 1979. "Discrete Numerical Model for Granular Assemblies," Geotechnique, **29**, pp. 47–64.
[2] Walton, O. R., and Braun, R. L., 1986. "Viscosity, Granular-Temperature, and Stress Calculations for Shearing Assemblies of Inelastic, Frictional Disks," J. Rheol., **30**, p. 949.
[3] Silbert, L. E., Ertas, D., Grest, G. S., et al., 2001," Granular Flow Down an Inclined Plane: Bagnold Scaling and Rheology," Phys. Rev. E, **64**, p. 051302.
[4] Volfson, D., Tsimring, L. S., and Aranson, I. S., 2003, "Partially Fluidized Shear Granular Flows: MD Simulations and Continuum Theory," Phys. Rev. E, **68**, p. 021301.
[5] Landry, J. W., Grest, G. S., Silbert, L. E., and Plimpton, S. J., 2003, "Confined Granular Packings: Structure, Stress, and Forces," Phys. Rev. E, **67**, p. 041303.
[6] Syamlal, M., Rogers, W., and O'Brien, T. J., 1993, "MFIX Documentation: Theory Guide," Tech. Rep. DOE/METC-94/1004, Morgantown Energy Technology Center of U.S. Department of Energy, Morgantown, WV.
[7] Goldhirsch, I., 2003. "Rapid Granular Flows," Annu. Rev. Fluid Mech., **35**, pp. 267–293.
[8] Vincenti, W. G., and Kruger, Jr., C. H., 1965, *Introduction to Physics Gas Dynamics*, John Wiley and Sons, Inc., New York.
[9] Gao, D., Subramaniam, S., Fox, R. O., and Hoffman, D., 2005, "Objective Decomposition of the Stress Tensor in Granular Mixtures," Phys. Rev. E, **71**, p. 021302.
[10] Clelland, R., and Herenya, C. M., 2002, "Simulations of a Binary-Sized Mixture of Inelastic Grains in Rapid Shear Flow," Phys. Rev. E, **65**(3), p. 031301.
[11] Alam, M., and Luding, S., 2003, "Rheology of Bidisperse Granular Mixtures

via Event-Driven Simulations," J. Fluid Mech., **476**(10), pp. 69–103.
[12] Syamlal, M., 1987, "The Particle-Particle Drag Term in a Multiparticle Model of Fluidization," Tech. Rep. DOE/MC/21353-2373, Morgantown Energy Technology Center of U.S. Department of Energy, Morgantown, WV.
[13] Lebowitz, J. L., 1964, "Exact Solution of Generalized Percus-Yevick Equation for a Mixture of Hard Spheres," Phys. Rev., **133**, pp. A895–A899.
[14] Walton, O. R., 1992, "Numerical Simulation of Inelastic, Frictional Particle-Particle Interaction," in *Particulate Two-phase Flow*, M. C. Roco, ed., Butterworth-Heinemann, London, pp. 1249–1253.
[15] Plimpton, S., 1995, "Fast Parallel Algorithms for Short-Range Molecular Dynamics," J. Comput. Phys., **117**, pp. 1–19.
[16] Rapaport, D. C., 1995, *The Art of Molecular Dynamics Simulation*, Cambridge University Press, Cambridge.
[17] Mansoori, G. A., Garnahan, N. F., Starling, K. E., and Leland, Jr., T. W., 1971. "Equilibrium Thermodynamics Properties of the Mixture of Hard Spheres," J. Chem. Phys., **54**(4), pp. 1523–1525.
[18] Huilin, L., Gidaspow, D., and Manger, E., 2001, "Kinetic Theory of Fluidized Binary Granular Mixtures," Phys. Rev. E, **64**, p. 061301.
[19] Stoyan, D., and Stoyan, H., 1994, *Fractals, Random Shapes, and Point Fields: Methods of Geometrical Statistics*, Wiley, Inc., New York.
[20] Gao, D., Morley, N. B., and Dhir, V., 2003, "Numerical Simulation of Wavy Falling Film Flows Using VOF Method," J. Comput. Phys., **192**(10), pp. 624–642.

Jinjia Wei
State Key Laboratory of Multiphase Flow
in Power Engineering,
Xi'an Jiaotong University,
Xi'an, 710049, People's Republic of China

Fengchen Li
2nd Department,
Oshima-lab,
Institute of Industrial Science (IIS),
The University of Tokyo,
Meguro-ku, Tokyo, 153-5805, Japan

Bo Yu
Oil and Gas Storage
and Transportation Engineering,
China University of Petroleum,
Beijing, 102249, People's Republic of China

Yasuo Kawaguchi[1]
e-mail: yasuo@rs.noda.tus.ac.jp
Department of Mechanical Engineering,
Faculty of Science and Technology,
Tokyo University of Science,
Noda, China, 278-8510, Japan

Swirling Flow of a Viscoelastic Fluid With Free Surface—Part I: Experimental Analysis of Vortex Motion by PIV

The swirling flows of water and CTAC (cetyltrimethyl ammonium chloride) surfactant solutions (50–1000 ppm) in an open cylindrical container with a rotating disc at the bottom were experimentally investigated by use of a double-pulsed PIV (particle image velocimetry) system. The flow pattern in the meridional plane for water at the present high Reynolds number of 4.3×10^4 differed greatly from that at low Reynolds numbers, and an inertia-driven vortex was pushed to the corner between the free surface and the cylindrical wall by a counter-rotating vortex caused by vortex breakdown. For the 1000 ppm surfactant solution flow, the inertia-driven vortex located at the corner between the bottom and the cylindrical wall whereas an elasticity-driven reverse vortex governed the majority of the flow field. The rotation of the fluid caused a deformation of the free surface with a dip at the center. The dip was largest for the water case and decreased with increasing surfactant concentration. The value of the dip was related to determining the solution viscoelasticity for the onset of drag reduction.
[DOI: 10.1115/1.2136928]

Introduction

Drag reduction is a flow phenomenon in which the addition of small amount of drag reducers to a fluid causes a reduction in the turbulent friction compared with the pure fluid at the same flow rate. There are mainly two different kinds of drag reducers: polymers and surfactants. For polymer solutions, it has been found that after a period of running, the solution loses its drag-reducing ability. However, this mechanical degradation was not found for surfactant solutions. Therefore, surfactants have been of special interest in recent drag-reducing studies. Dilute surfactant solutions have been found to significantly reduce turbulent friction drag [1–3]. Li et al. [1] and Yu et al. [2] reported a 70%–80% turbulent drag reduction (DR) by use of a very dilute cetyltrimethyl ammonium chloride (CTAC)/sodium salicylate (NaSal) aqueous solution having surfactant mass concentrations of only 30 and 75 ppm, indicating that this surfactant is a very promising drag-reducing additive. It is generally considered that the DR phenomenon is caused by the viscoelasticity of the surfactant solution [4–8]. Therefore, rheological measurements can be used for screening an effective drag-reducing surfactant within a measurable range. However, Li et al. [1] showed that the elasticity of the CTAC solutions is so small that the rheometers could not provide reliable data for the first normal stress and storage modulus. Therefore, the challenge to be addressed is how to determine a surfactant solution with small viscoelasticity having DR ability. From an economic consideration, the amount of the testing surfactant should be as small as possible. Siginer and co-workers initiated an idea of using the free surface shape of a viscoelastic swirling flow to generate information of the constitutive equation for the viscoelastic liquid [9–13]. In the present study, we attempt to solve this problem by using a swirling flow to observe and analyze the effect of the drag-reducing surfactant solution on the vortex inhibition and relate this to the screening of effective low viscoelastic drag reducers.

Swirling flows exist in many areas of engineering and have been widely studied for a number of decades. Experimental observations and/or measurements of Newtonian swirling flows generated in a closed cylindrical container by rotating the disc and/or cylindrical wall have been reported by Bien and Penner [14], Hill [15], Escudier [16], Fujimura et al. [17], and Ogino et al. [18]. An extension of the confined swirling flow to non-Newtonian fluids that have high shear-thinning properties and varying degrees of elasticity has been reported by Bohme et al. [19], Day et al. [20], Escudier and Cullen [21], Xue et al. [22], Bowen et al. [23], and Siginer [24]. To separate elasticity from shear thinning, Stokes et al. [25,26] reported the confined swirling flow of non-Newtonian fluids that have varying degrees of elasticity with constant shear viscosity. Arora et al. [27] investigated the influence of CTAC on closed turbulent swirling flows and observed enhancement in the radial and tangential mean velocities for CTAC solutions compared to that for water swirling flow. Studies of free surface swirling flows in containers are scarce compared to the closed swirling flows. Goller and Ranov [28] dealt with the transient Newtonian flow in an open rotating cylindrical container and Spohn [29] observed the vortex breakdown of the swirling flow in an open cylindrical container with a rotating bottom. Their results showed that the free surface flows differed greatly from the closed container flows. Bohme et al. [30] further studied the open cylinder with rotating bottom disc for a shear-thinning elastic liquid and a constant-viscosity elastic liquid. Reverse flow with a bulge in the free surface was observed at a low Reynolds number. Siginer and co-workers carried out a series of studies experimentally and theoretically on viscoelastic swirling flows with free surface [9–13,31–33].

The Reynolds numbers in all of the aforementioned studies on free surface swirling flows were not high (less than 10,000). It is well known that the rotation of the fluid can cause a deformation of the free surface proportional to the Froude number and that the *Quelleffekt* can be generated by the elasticity of the fluid in swirl-

[1]Corresponding author.

Contributed by the Fluids Engineering Division of ASME for publication in the JOURNAL OF FLUIDS ENGINEERING. Manuscript received June 25, 2004; final manuscript received August 22, 2005. Assoc. Editor: Dennis Siginer.

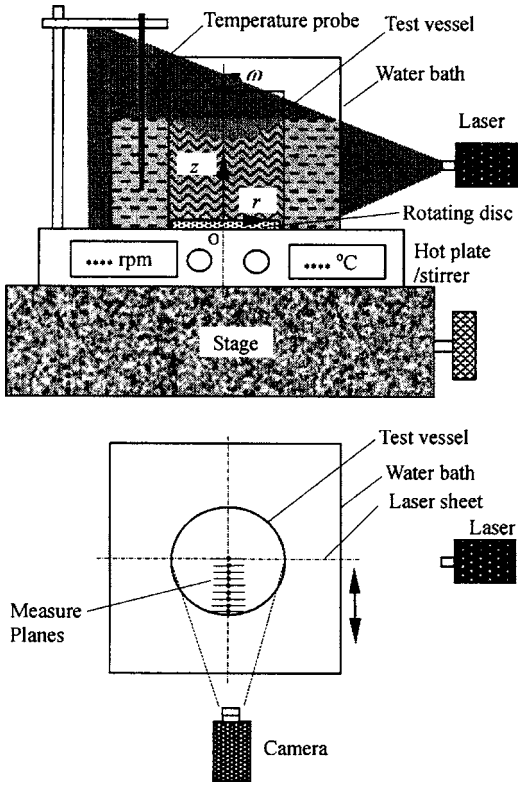

Fig. 1 Schematic of the test facility

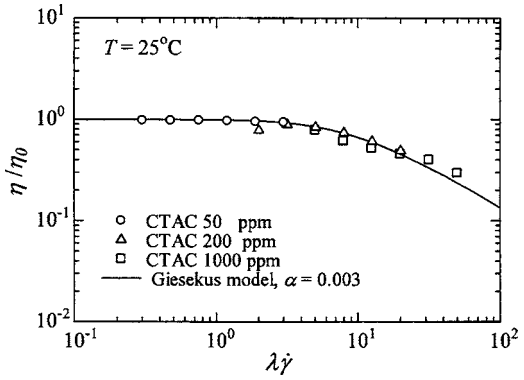

Fig. 2 Fitting results of the measured shear viscosities with the Giesekus model

ing flows capped by a free surface [30]. Therefore, the elasticity of the fluid may be recognized by comparing the degree of the free surface deformation under the same conditions. For the surfactant drag-reducing flow in application, the mass concentration is usually below 1000 ppm and the viscosity is not high (usually in the range of 0.001–0.1 Pa s at room temperature). At a low Reynolds number, the Froude number is usually negligible, which results in a very small deformation of the free surface, and thus a comparison between the Newtonian flow and elastic flow shows no obvious differences. A very high Reynolds number is necessary for showing a clearly visible difference. The vortex motion for a higher Reynolds number is not yet clear, especially for non-Newtonian flow in an open cylinder. In the present study, the swirling flows of water and CTAC surfactant solutions at a high Reynolds number in an open cylindrical container with a rotating disc at the bottom were experimentally investigated by use of a double-pulsed PIV (particle image velocimetry) system. The secondary flow in the meridional plane of the cylinder and the radial distribution of the tangential velocities were measured to analyze the primary vortex motion in the tangential direction and the secondary vortex motion in the meridional plane. Measured also were the swirl decay time (the time between the stopping of the disc rotation and the cessation of the solution movement before recoil) and the tangential velocity evolution after the rotating disc was stopped.

Experimental

Test Facility. The experimental setup is shown in Fig. 1. A glass cylinder having an inner radius of 70 mm was nearly submerged in a cubic water bath constructed from flat transparent perspex walls 130 mm in side length. The purpose of the external water bath was to reduce optical distortion caused by the curved surfaces of the cylinder. A rotating circular disc having a diameter of 65 mm and a thickness of 8.5 mm was placed at the bottom of the cylinder. The water bath was fixed on the surface of a digital hot plate/stirrer and the temperature of the water bath was controlled by use of the heating function of the hot plate/stirrer. The temperature probe of the hot plate/stirrer was inserted into the water bath and the test fluid temperature was measured with a digital thermometer before the PIV measurements. The temperature of the water in the water bath and that of the test fluid in the test vessel were both kept at a constant of 25°C. A magnet bar ($\phi 8 \times 55$ mm^2) was embedded into the rotating disc and the rotational speed was controlled by the magnetic force from the hot plate/stirrer acting on the magnet bar. The axis of the cylinder and the center of the disc were carefully adjusted to align with that of the hot plate/stirrer (magnetic center). The hot plate/stirrer was mounted on a flat stage that could be moved back and forth with an accuracy of 0.1 mm.

Working Fluids. Water and surfactant solutions were used for the test. The surfactant was cetyltrimethyl ammonium chloride (CTAC). Sodium salicylate (NaSal) was selected as the counterion. The surfactant solution was prepared by adding the same mass concentration of surfactant and counterion to the desired amount of distilled water. The surfactant concentration was marked by the concentration of CTAC, and three mass concentrations of 50, 200, and 1000 ppm were tested.

The test fluid was filled into the glass cylinder up to a height H equal to the inner radius of the cylinder, R_w, and thus the aspect ratio of the fluid height to radius, H/R_w, was fixed to unity in the present experiments. The shear viscosities of the three kinds of surfactant solutions at 25°C were also measured in the shear rate range of 10–100 s^{-1} by use of an ARES rheometer equipped with a double-wall Couette cell.

The Reynolds number and the elasticity number (the ratio of elastic to viscous time scales) of the fluid in the present study are defined as

$$\mathrm{Re}_0 = \rho\omega R_d^2/\eta_0, \quad \mathrm{Re} = \rho\omega R_d^2/\eta, \quad \mathrm{E} = \lambda_G \eta/\rho R_d^2 \qquad (1)$$

where η_0 is zero-shear viscosity and λ_G is the relaxation time in the Giesekus model. Shear viscosity η, which is a function of shear rate $\dot{\gamma}$, is evaluated by assuming shear rate $\dot{\gamma}$ equal to the angular velocity ω. The elasticity of the CTAC solutions in the present study is so small that the rheometers could not provide reliable data for the first normal stress and storage modulus. However, our ARES rheometer was able to provide accurate measurements of the shear viscosity data. For evaluating the elasticity of the three surfactant solutions, the relaxation times were extracted by fitting the measured shear viscosity curves to the Giesekus model [34] instead of the Maxwell relaxation time used by the other researchers [20,21]. Figure 2 shows the least square fitting results of the measured shear viscosities of three surfactant solutions with the Giesekus model. α shown in the legend indicates the mobility factor in the Giesekus model. It appears that the Giesekus model can describe their shear viscosity characteristics

Table 1 Values of η_0, λ_G, Re_0, Re, and E

	Water	CTAC 50 ppm	CTAC 200 ppm	CTAC 1000 ppm
η_0 (Pa.s)	1.0×10^{-3}	1.05×10^{-3}	1.21×10^{-2}	4.50×10^{-2}
λ_G (s)	0	0.034	0.25	0.57
Re_0	4.3×10^{4}	3.7×10^{4}	3.2×10^{3}	8.6×10^{2}
Re	4.3×10^{4}	3.9×10^{4}	3.9×10^{3}	1.8×10^{3}
E	0	2.8×10^{-5}	2.0×10^{-3}	1.0×10^{-2}

well. Table 1 lists the values of η_0, λ_G, Re_0, Re, and E for water and the three CTAC solutions. The elasticity number indicates the elasticity effect against the inertia effect.

The Froude number indicates the gravity effect against the inertia effect and is defined as

$$\mathrm{Fr} = \omega^2 R_d^2 / gH \tag{2}$$

In the present study, the Froude number is 4.80, which is large for generating a sizeable deformation of the free surface against the gravity effect in Newtonian swirling flow.

PIV Measurement. The secondary flow pattern in the meridional plane and the tangential velocities were obtained by use of a PIV system consisting of a double-pulsed laser, laser sheet optics, charge-coupled device (CCD) camera, timing circuit (TSI Model 610032), image-sampling computer, and image-processing software (TSI Insight ver. 3.3). The double-pulsed laser (New Wave Research Co., Ltd., MiniLase-II/20 Hz) is a combination of a pair of Nd-YAG lasers, each having an output of 25 mJ/pulse and a maximum repetition rate of 20 Hz. By changing the combination of cylindrical lenses, the laser sheet thickness can be modified from 0.14 to 0.6 mm and the beam spread angle from 4.3 to 13.3 deg. The timing circuit communicates with the CCD camera and computer and generates pulses to control the double-pulsed laser. The CCD camera used (PIVCAM, 10–30, TSI Model 630046) has a resolution of 1280×1024 pixels.

The meridional plane of the swirling flow was illuminated by the double-pulsed laser for measurement of the secondary flow pattern. The tangential velocities were also measured by illuminating the vertical planes parallel to the meridional plane at eight equally spaced radial locations as shown in Fig. 1. The flat stage could be controlled to move back and forth to obtain the desired vertical cross section for illumination and measurement. The interrogation area was set at 32×32 pixels (with 50% overlap in each direction) for velocity vector analyses. PIV images were acquired for 1000 dual frames (2000 double-exposed PIV photographs) for the meridional plane measurements and 100 dual frames for the other measurements. Due to the presence of the cubic water tank, the optical distortion caused by the cylindrical wall was negligible up to a radius of $0.9R_w$. The photograph acquisition rate was 8 Hz, indicating that the velocity field was recorded at 4 Hz. The tracer particles used to seed the flow were acrylic colloids $1-4$ μm in diameter. The particle concentration was adjusted so that on average at least ten particle pairs were observed in an interrogation window for each case.

After a vector field was calculated by interrogating a dual frame, TSI Insight software was used to validate it and remove any erroneous velocity vectors that might have been incorrectly detected during interrogation due to random noise in the correlation function. Empty data cells (holes) that appeared after the removal of erroneous velocity vectors were filled using a FORTRAN program created by interpolation of neighboring velocity vectors.

Results and Discussion

Figures 3(*a*)–3(*d*) respectively show the secondary flow patterns in the meridional plane for water, CTAC 50 ppm, CTAC 200 ppm, and CTAC 1000 ppm. The experimental conditions can be seen in Table 1. The vectors shown in Fig. 3(*d*) are enlarged to three times the size of those in Figs. 3(*a*)–3(*c*). Since the flow at the high Reynolds number in the present study is an unsteady one, the results shown are the average of the instantaneous velocities obtained from 1000 dual frames in the measurements. The average of 100 dual frames shows the same secondary flow pattern,

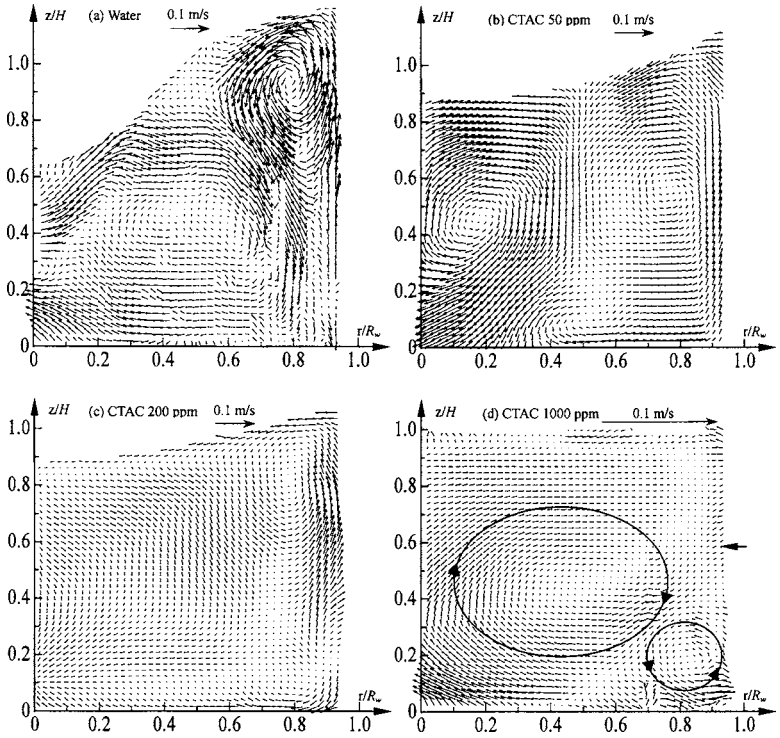

Fig. 3 Secondary flow patterns in the meridional plane

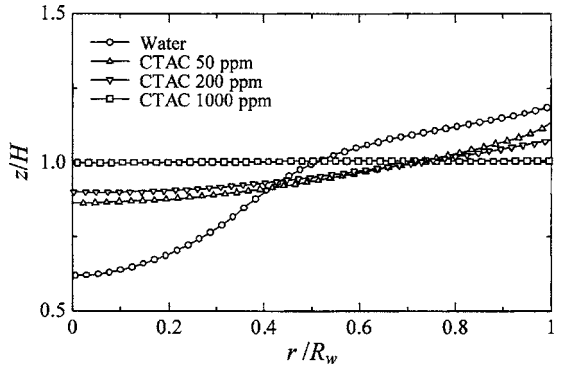

Fig. 4 Free surface shapes for water and surfactant solutions

indicating the statistically stationary nature of the swirling flow. It is well known that for Newtonian swirling flows at a low Reynolds number, the inertia-driven vortex plays a dominant role in the meridional plane. Centrifugal forces cause the fluid to flow radially outwards along the rotating disc, and then the flow is deflected upward along the cylindrical wall. At the free surface, the flow bends towards the center and turns downward to finish its path of circulation. However, the flow pattern in the meridional plane for water at the present high Reynolds number differs significantly from that at low Reynolds numbers, and the inertia-driven vortex is pushed to the corner between the free surface and cylindrical wall by a large counter-rotating vortex. It is considered that the vortex breakdown phenomenon leads to the appearance of the counter-rotating vortex. According to the observations conducted by Spohn et al. [29] on vortex breakdown in an open cylindrical container with a rotating bottom, there is no upper Reynolds number limit at which breakdown disappears, which is very different from the observations of the closed cylindrical container flow conducted by Escudier [16] in which the breakdown bubbles disappear beyond a certain Reynolds number. The breakdown bubble increases in size with increasing Reynolds number. Therefore, it is supposed that the large counter-rotating vortex is the breakdown bubble. From our numerical calculations [35], we also found the existence of the counter-rotating vortex at a large Reynolds number and the inertia-driven vortex is pushed toward the cylindrical wall. For the case of CTAC 50 ppm as shown in Fig. 3(*b*), the size of the counter-rotating vortex becomes smaller and the size of the inertia-driven vortex increases but the intensity decreases compared to the water case. The size increase of the inertia-driven vortex is probably caused by the decrease of the free surface deformation. With further increasing surfactant concentration up to 200 ppm as shown in Fig. 3(*c*), the counter-vortex disappears and the inertial-driven vortex decreases in both size and intensity. This is probably due to the large decrease of local Reynolds number and the competing interaction between elasticity and inertial force, which weakens both the inertia-driven and breakdown vortices. For the CTAC 1000 ppm surfactant solution flow, the inertia-driven vortex locates near the disc-wall intersection whereas an elasticity-driven reverse vortex governs the majority of the flow field. However, the vortex intensity is much smaller compared to that in the water flow case. This differs from a closed disc-cylinder system, in which a large Re and small elasticity number produce Newtonian-like characteristics in the secondary flow in the meridional plane.

Figure 4 shows the free surface shapes for water and surfactant swirling flows. The free surface shapes were also averaged over 1000 frames. We can see that the height of the dip, h, at the center of the free surface (the maximum deflection of the free surface from the horizontal at the central axis) is much smaller for surfactant solutions than that for water and decreases slightly with increasing surfactant concentrations (elasticity numbers). The concrete value of h/H is listed in Table 2. In the present study,

Table 2 Values of free surface deformation h/H, SDT, and flow dissipation ratio D/D_w

	Water	CTAC 50 ppm	CTAC 200 ppm	CTAC 1000 ppm
h/H	0.37	0.13	0.10	0.0
SDT(s)	/	12.33	9.47	2.58
D/D_w	1	1.46	2.71	9.05

although the elasticity number is very small, the elasticity still plays an important role in the shape of the free surface and the secondary flow pattern. Since the local Reynolds number for CTAC 50 ppm is very close to that of Newtonian fluid flow, we do not consider the decrease of the dip to be due to the decrease of the local Reynolds number. The decrease of h/H with elasticity number is the so-called *Quelleffekt* [30]. The sensitivity of the free surface deformation with small elasticity in the open swirling flow may be used as a simple method for the evaluation of DR ability instead of the rheology measurement. A critical value of h/H may exist for the judgment of the lowest viscoelasticity for the onset of DR to overcome the difficulty in screening effective drag reducers by use of a rheometer for the low viscoelasticity case.

To testify this conjecture, we measured the free surface shapes of another three CTAC surfactant swirling flows with low mass concentrations of 25, 30, and 40 ppm, respectively. Figure 5 shows the relationship of h/H with mass concentration C_m. Our measured drag reduction data of CTAC/NaSal surfactant flow in a two-dimensional channel flow at a Reynolds number of 4.3×10^4 for different C_m are also shown in this figure. The values of h/H and DR are the same as that of water for $C_m \leqslant 30$ ppm. At a critical value of C_m=40 ppm, the value of h/H decreases suddenly and the value of DR jumps from 0 to about 60%. This suggests that the viscoelasticity of a 40 ppm CTAC surfactant solution is a critical value for the onset of drag reduction at a Reynolds number of 4.3×10^4, and this critical viscoelasticity can be represented indirectly by the corresponding value of h/H in a free-surface swirling flow. Since the elasticity of the CTAC solutions is small, we did not observe the appearance of a bulge around the center of the free surface even for the 1000 ppm surfactant solution. However, when we inserted a rod into the center of the swirling flow of the 1000 ppm surfactant solution, we found the rod-climbing Weissenberg phenomenon.

Figures 6(*a*)–6(*d*) show the radial distributions of the reduced tangential velocities averaged over 100 dual frames. The experimental conditions are listed in Table 1. The correlation lines are also shown by use of a least square fitting method. For the water case, the tangential velocities increase rapidly with increasing r/R_w up to 0.46, decrease gradually with further increasing r/R_w up to 0.80, and then increase again to a second peak adjacent to the cylindrical wall, whereas for the surfactant solutions, the tan-

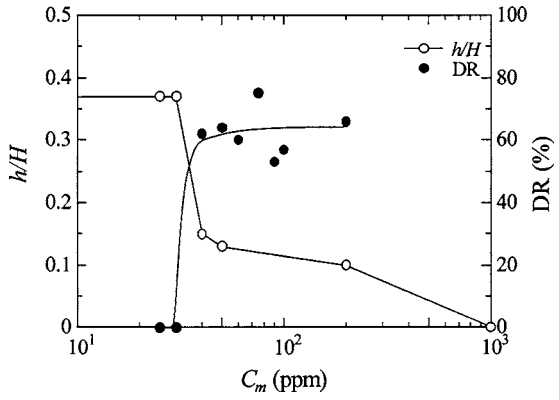

Fig. 5 Relationship of h/H with DR for Re=4.3×10^4

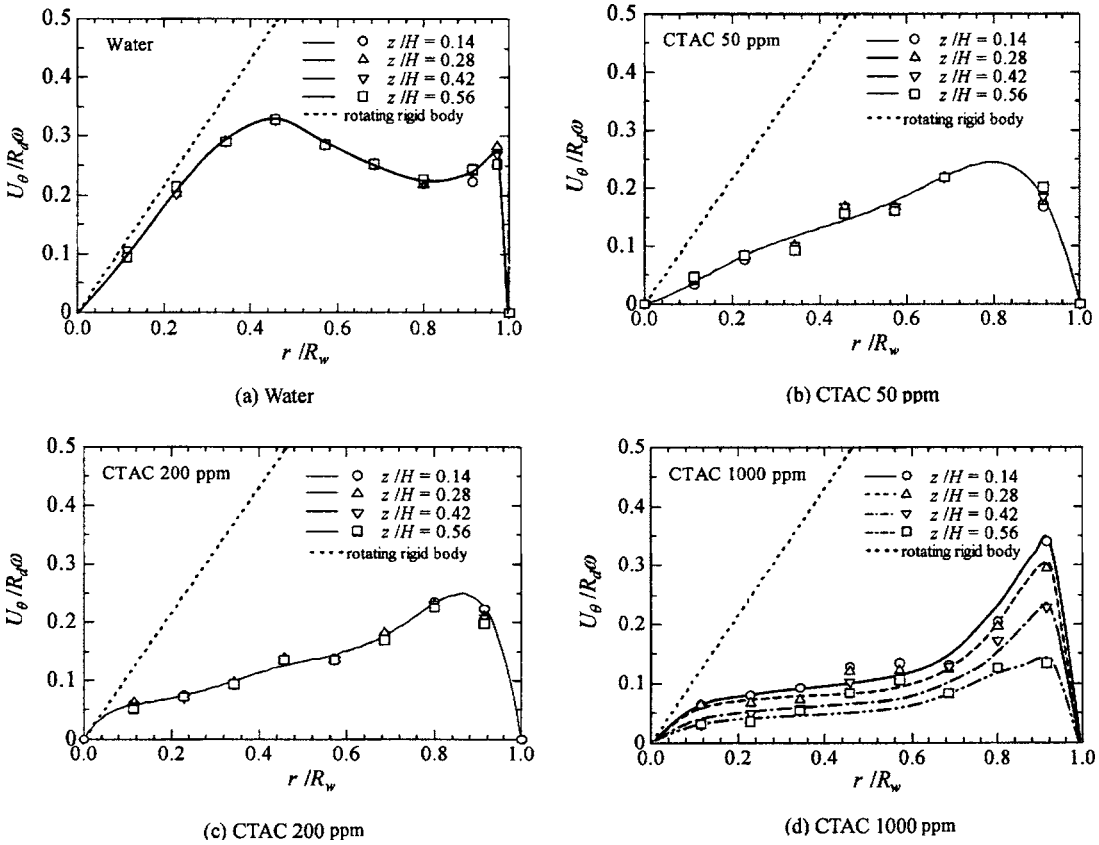

Fig. 6 Radial distributions of the time-averaged tangential velocities

gential velocities increase gradually in the radial outward direction except in the region near the periphery of the rotating disc where the tangential velocities decrease for CTAC 50 ppm and CTAC 200 ppm and increase rapidly for CTAC 1000 ppm. The position of the maximum tangential velocity appears to move outward with increasing surfactant concentration. For the water case, the tangential velocity distribution is different from the numerical calculation at a low Reynolds number [35] in which the tangential velocity increases monotonically in the radial direction to a peak near the cylindrical wall. From the secondary flow pattern shown in Fig. 3(*a*), we can see a very intensive inertia-driven vortex in an anticlockwise direction which may intensify the momentum change in the radial direction and then smear the peak near the cylindrical wall. This is may be the reason that the maximum tangential velocity appears at $r/R_w=0.46$ instead of a place near the cylindrical wall for low Reynolds numbers.

Figure 7 shows the vertical tangential velocity profiles along $r/R_w=0.46$. It can be seen that a large gradient of the tangential velocities exists near the rotating disc. In the region away from the bottom, the velocities for water, CTAC 50 ppm, and CTAC 200 ppm show uniform distribution, which agrees with the well-known Taylor-Proudman theorem, whereas the velocities for CTAC 1000 ppm decreases from $z/H=0.53$ to 0.63 and then levels off. Since the Taylor-Proudman theorem assumes that the inertial term and viscous term in the Navier-Stokes equation in a rotating reference frame are much smaller compared to the Coriolis acceleration term and the reduced pressure gradient term including the centrifugal acceleration and the body force, the swirling flows of water and the surfactant solution with low effective viscosities may satisfy the Taylor-Proudman theorem, whereas that of the surfactant solution with high effective viscosities may not obey it. The tangential velocities are lower than that of water and decrease with increasing elasticity number. Combining this with Figs. 3(*a*)–3(*d*), we can see that the elasticity leads to a weak motion of the swirling flow in both the tangential direction and the meridional plane. This is considered to be due to the addition of elastic dissipation compared to the Newtonian swirling flow in which the main dissipation is viscous dissipation. The viscoelastic dissipation of the swirling flow can be estimated by the following expression:

$$D=\int_0^V \eta\left\{2\left[\left(\frac{\partial U_z}{\partial z}\right)^2+\left(\frac{\partial U_r}{\partial r}\right)^2+\left(\frac{U_r}{r}\right)^2\right]+\left(\frac{\partial U_z}{\partial r}+\frac{\partial U_r}{\partial z}\right)^2+\left(\frac{\partial U_\theta}{\partial z}\right)^2+\left(\frac{\partial U_\theta}{\partial r}-\frac{U_\theta}{r}\right)^2\right\}dv \tag{3}$$

where V is the volume of the swirling flow domain. The measured tangential velocities were interpolated or extrapolated for the dissipation calculation with Eq. (3). The ratio of the solution flow

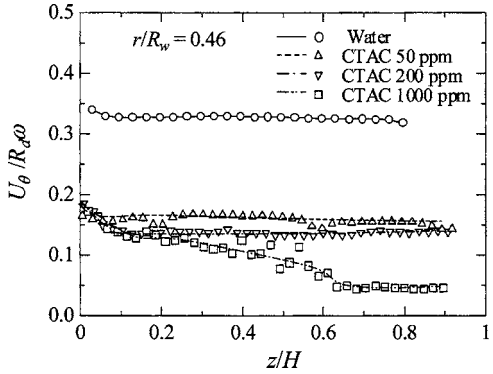

Fig. 7 Vertical tangential velocity profiles along $r/R_w=0.46$

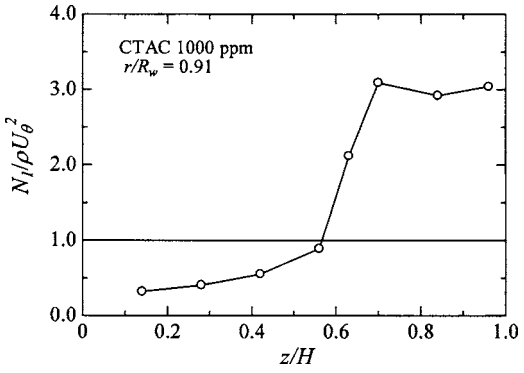

Fig. 8 Comparison of N_1 and ρU_θ^2 along $r/R_w=0.91$

dissipation to the water flow dissipation is listed in Table 2. We can clearly see that the dissipation is larger for the surfactant solutions and increases with increasing surfactant concentration. Therefore, the weakening of the secondary motion and decrease of the tangential velocities with elasticity number further supports the observation that the elasticity in the surfactant solutions plays an important role. Our numerical simulations [35] also show the same phenomenon of elasticity weakening the swirling flow. For a laminar swirling flow at low Reynolds numbers, the dissipation obtained from Eq. (3) equals the input power for the rotation. If the input torque is measured, the effective shear viscosity of the surfactant solution may be obtained.

The momentum equation in the radial direction can be expressed as

$$\rho U_r \frac{\partial U_r}{\partial r} + \rho U_z \frac{\partial U_z}{\partial z} = -\frac{\partial p}{\partial r} + \frac{1}{r}\frac{\partial}{\partial r}(r\tau_{rr}) - \frac{\tau_{\theta\theta}}{r} + \frac{\rho U_\theta^2}{r}$$

$$= -\frac{\partial(p+\tau_{zz})}{\partial r} + \frac{-N_1 + \rho U_\theta^2}{r} - \frac{\partial N_2}{\partial r} \quad (4)$$

where $N_1=\tau_{\theta\theta}-\tau_{rr}$ and $N_2=\tau_{rr}-\tau_{zz}$ are first and second normal stresses, respectively. We consider that the swirling flow near the cylindrical wall has a large shear rate of $\dot{\gamma}_{r\theta}=r(\partial/\partial r)(U_\theta/r)$ for resulting in large N_1 and N_2. The relationship between the first and second normal stresses and shear rate can be expressed as

$$N_1 = \psi_1 \dot{\gamma}_{r\theta}^2, \quad N_2 = \psi_2 \dot{\gamma}_{r\theta}^2 \quad (5)$$

where ψ_1 and ψ_2 are first and second normal stress coefficients, respectively, and can be expressed by the Giesekus model as [36]

$$\frac{\psi_1}{2\eta_0} = \frac{f(1-\alpha f)}{\lambda_G \dot{\gamma}_{r\theta}^2 \alpha(1-f)}, \quad \frac{\psi_2}{\eta_0} = \frac{-f}{\gamma_G \dot{\gamma}_{r\theta}^2} \quad (6)$$

where

$$f = \frac{1-x}{1+(1-2\alpha)x} \quad \text{and} \quad x^2 = \frac{\sqrt{1+16\alpha(1-\alpha)(\lambda_G\dot{\gamma}_{r\theta})^2}-1}{8\alpha(1-\alpha)(\lambda_G\dot{\gamma}_{r\theta})^2}.$$

Then we have

$$\frac{N_2}{N_1} = -\frac{1-f}{2(1/\alpha - f)} \quad (7)$$

In our present study, the mobility factor α has a very small value of 0.003, so N_2 is very small compared to N_1 and can be neglected here. For the case of CTAC 1000 ppm, the free surface is almost flat, so we can further assume that the variation of pressure in radial direction can be neglected. Therefore, from Eq. (4) we can see that the competition between first normal stress N_1 and inertial force term ρU_θ^2 determines the appearance of inertia-driven and elasticity-driven vortices. Figure 8 shows the ratio of N_1 to ρU_θ^2 along an axial line of $r/R_w=0.91$ adjacent to the cylindrical wall for the 1000 ppm surfactant solution. It can be seen that for $z/H<0.6$, ρU_θ^2 is larger than N_1 to generate an inertia-driven vortex, whereas for $z/H>0.6$, N_1 is larger than ρU_θ^2 to generate an elasticity-driven vortex. This theoretical analysis agrees with the secondary flow pattern shown in Fig. 3(*d*) where an arrow indicates the place of $z/H=0.6$ adjacent to the cylindrical wall.

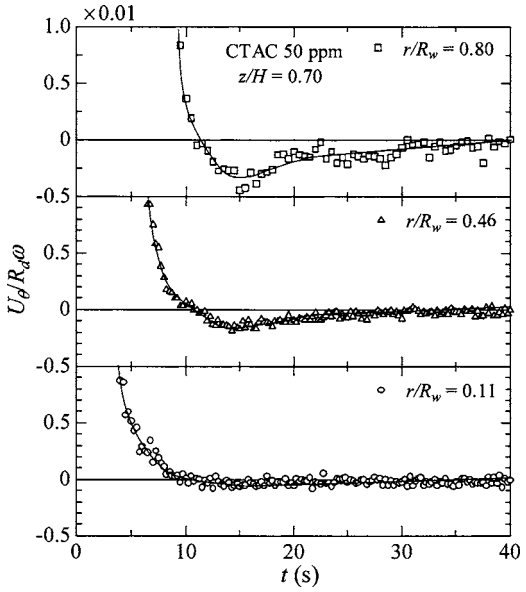

Fig. 9 Time evolution of the tangential velocities at different radial positions after the rotating disc was stopped

It is generally considered that the swirling flow of viscoelastic solution moves in the opposite direction of the rotation after the outer force is removed and the swirl decay time (SDT) can be used to identify the viscoelasticity. In this study, the SDT was measured as the difference between the time at which the rotating disc was stopped and the time when the solution stopped before starting to recoil by use of a stopwatch. The SDT was measured three times and the average values were used as the experimental data. Recoil was observed for all three surfactant solutions and Table 2 lists the measured SDT values. We can see that the SDT decreases with surfactant concentration, indicating that the viscoelasticity increases with surfactant concentration. This is consistent with the results of the elasticity numbers listed in Table 1 and further supports that the decrease of h/H with surfactant concentration is caused by viscoelasticity of the solution. The evolution of the tangential velocities of the solution was also measured after the rotating disc was stopped. Figure 9 shows the time evolution of the normalized tangential velocities for CTAC 50 ppm at $z/H=0.70$ and $r/R_w=0.11$, 0.46 and 0.80. The time was obtained from the photograph acquisition rate and the sequence numbers of the dual frames of PIV images. We can clearly see the decrease of tangential velocity with the elapse of time and the solution started to recoil with the velocity becoming negative at $t=12$ s. This time agrees with the SDT measurements listed in Table 2. Since the velocity at the larger radius is large for easy recognition, in the SDT measurements the recoil process was assumed to start when the solution at the outer radius was observed to start to move in the opposite direction. As expected, the tangential velocity decreases with decreasing r/R_w. The surfactant solution stopped its motion after about 30 s relative to the start-up time of recoil, and the time is shorter for the higher surfactant concentrations. Figure 10 shows the time evolution of the normalized tangential velocities for CTAC 50 ppm at $r/R_w=0.80$ and $z/H=0.01$, 0.42, and 0.70. We can see that there is no great axial-direction dependence of the tangential velocity during the vortex decay and recoil period except at $z/H=0.01$ where the effect of the stationary disc results in a smaller tangential velocity.

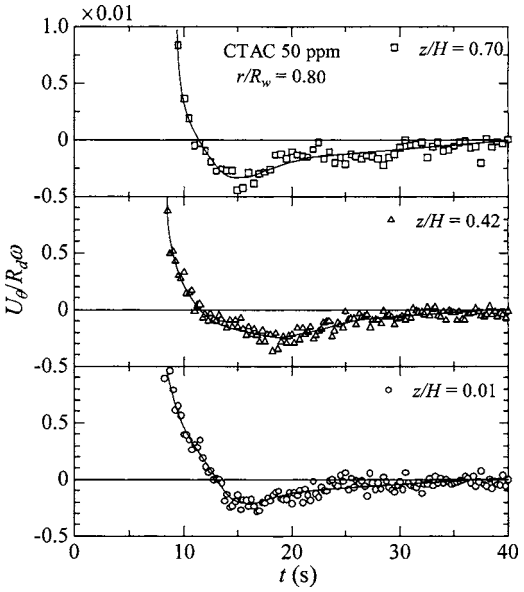

Fig. 10 Time evolution of the tangential velocities at different axial positions after the rotating disc was stopped

Conclusions

An experimental investigation was conducted on the swirling flows of water and dilute CTAC surfactant solutions in an open disc-cylinder system by use of a double-pulsed PIV system. Obtained were the free surface shape, the secondary flow pattern in the meridional plane and the tangential velocities, swirl decay time, and tangential velocity evolution after the rotating disc was stopped. The main conclusions may be summarized as follows:

1. For the water flow, vortex breakdown at high Reynolds numbers resulted in a large counter-vortex at the center part, and the inertia-driven vortex was pushed to the top-right corner near the intersection of the free surface and the wall.
2. Despite the very small elasticity number, the elasticity of the CTAC surfactant solutions greatly affected the free surface shape and the secondary flow pattern in the meridional plane, which was different from in the closed disc-cylinder system. The maximum depression of the free surface, h, decreased with elasticity number.
3. Elasticity resulted in the decrease of the tangential velocities and the weakness of the secondary vortex flow compared to the Newtonian swirling flow.
4. Measurements of swirl decay time and tangential velocity evolution after the rotating disc was stopped showed that the investigated surfactant solutions had viscoelasticity and increased with surfactant concentration, which was consistent with the elasticity number obtained by combining the measured shear viscosity with the Giesekus model.
5. The open cylindrical swirling flow was sensitive to elasticity and the maximum depression of the surface h/H may be used as a simple indexer for determining the viscoelasticity of surfactant solutions required for the onset of turbulent friction drag reduction to overcome the difficulty of screening an effective low viscoelastic drag reducer by use of rheological measurements.

Acknowledgment

This study was carried out as a part of the research project of the Center for Smart Control of Turbulence with the financial support of the Ministry of Education, Culture, Sports, Science and Technology (MECSST), Japan. We are also grateful for the support of NEDO and their international research grant for "Development of Practical Drag-Reduction Systems for District Cooling Systems."

Nomenclature

C = concentration, ppm
D = flow dissipation, W
E = elasticity number
Fr = Froude number
g = gravitational acceleration, m/s^2
h = the dip of the free surface at the center, m
H = the height of the fluid filled into the cylinder, m
N_1 = first normal stress
N_2 = second normal stress
p = pressure, Pa
r = coordinate in radial direction, Fig. 1
R = radius, m
Re = Reynolds number
U = velocity, m/s
v = volume, m^3
V = volume, m^3
z = coordinate in axial direction of the cylinder, Fig. 1

Greek Symbols

α = mobility factor
$\dot{\gamma}$ = shear rate, 1/s
η = shear viscosity, Pa s
ψ_1 = first normal stress coefficient
ψ_2 = second normal stress coefficient
λ = relaxation time, s
ω = angular velocity of the rotating disc, 1/s
ρ = density, kg/m^3
τ = stress, Pa

Subscripts

0 = zero shear strain rate
d = rotating disc
G = Giesekus model
m = mass
r = radial direction
w = cylindrical wall
z = axial direction
θ = tangential direction

References

[1] Li, F. C., Wang, D. Z., Kawaguchi, Y., and Hishida, K., 2004, "Simultaneous Measurement of Velocity and Temperature Fluctuations in Thermal Boundary Layer in a Drag-Reducing Surfactant Solution Flow," Exp. Fluids, **36**, pp. 131–140.
[2] Yu, B., Li, F. C., and Kawaguchi, Y., 2004, "Numerical and Experimental Investigation of Turbulent Characteristics in a Drag-Reducing Flow With Surfactant Additives," Int. J. Heat Fluid Flow, **25**, pp. 961–974.
[3] Nowak, M., 2003, "Time-Dependent Drag Reduction and Ageing in Aqueous Solutions of a Cationic Surfactant," Exp. Fluids, **34**, pp. 397–402.
[4] Elson, T. P., and Garside, J., 1983, "Drag Reduction in Aqueous Cationic Soap Solutions," J. Non-Newtonian Fluid Mech., **12**, pp. 121–133.
[5] Ohlendorf, D., Interthal, W., and Hoffmann, H., 1986, "Surfactant Systems for Drag Reduction: Physico-Chemical Properties and Rheological Behavior," Rheol. Acta, **25**, pp. 468–486.
[6] Rehage, H., Wunderlich, I., and Hoffmann, H., 1986, "Shear Induced Phase Transitions in Dilute Aqueous Surfactant Solution," Prog. Colloid Polym. Sci., **72**, pp. 51–59.
[7] Rose, G. D., and Foster, K. L., 1989, "Drag Reduction and Rheological Properties of Cationic Viscoelastic Surfactant Formulations," J. Non-Newtonian Fluid Mech., **31**, pp. 59–85.
[8] Bewersdorff, H. W., and Thiel, H., 1993, "Turbulence Structure of Dilute Polymer and Surfactant Solution in Artificially Roughened Pipes," Appl. Sci. Res., **50**, pp. 347–368.
[9] Siginer, A., 1984, "General Weissenberg Effect in Free Surface Rheometry, Part I: Analytical Consideration," ZAMP, **35**, pp. 545–558.
[10] Siginer, A., 1984, "General Weissenberg Effect in Free Surface Rheometry, Part II: Experiments," ZAMP, **35**, pp. 618–633.

[11] Siginer, A., 1984, "Free Surface on a Simple Fluid Between Rotating Eccentric Cylinders, Part I: Analytical Solution," J. Non-Newtonian Fluid Mech., **15**, pp. 93–108.
[12] Siginer, A., and Beavers, G. S., 1984, "Free Surface on a Simple Fluid Between Rotating Eccentric Cylinders. Part II: Experiments," J. Non-Newtonian Fluid Mech., **15**, pp. 109–126.
[13] Siginer, A., 1991, "Viscoelastic Swirling Flow With Free Surface in Cylindrical Chambers," Rheol. Acta, **30**, pp. 159–174.
[14] Bien, F., and Penner, S. S., 1970, "Velocity Profiles in Steady and Unsteady Rotating Flows for a Finite Cylindrical Geometry," Phys. Fluids, **13**, pp. 1665–1671.
[15] Hill, C. T., 1972, "Nearly Viscometric flow of Viscoelastic Fluids in the Disk and Cylindrical System, II: Experimental," Trans. Soc. Rheol., **16**, pp. 213–245.
[16] Escudier, M. P., 1984, "Observations of the Flow Produced in a Cylindrical Container by a Rotating End Wall," Exp. Fluids, **2**, pp. 189–196.
[17] Fujimura, K., Koyama, H. S., and Hyun, J. M., 1997, "Time Dependent Vortex Breakdown in a Cylinder With a Rotating Lid," ASME J. Fluids Eng., **119**, pp. 450–453.
[18] Ogino, F., Kawai, K., Dohmoto, T., and Takahashi, T., 1999, "Velocity Distribution of the Flow in a Rotating Cylindrical Container With a Rotating Disc at the Liquid Surface," Kagaku Kogaku Ronbunshu, **25**, pp. 29–36.
[19] Bohme, G., Rubart, L., and Stenger, M., 1992, "Vortex Breakdown in Shear-Thinning Liquids: Experiment and Numerical Simulation," J. Non-Newtonian Fluid Mech., **45**, pp. 1–20.
[20] Day, C., Harris, J. A., Soria, J., Boger, D. V., and Welsh, M. C., 1996, "Behavior of an Elastic Fluid in Cylindrical Swirling Flows," Exp. Therm. Fluid Sci., **12**, pp. 250–255.
[21] Escudier, M. P., and Cullen, L. M., 1996, "Flow of Shear-Thinning Liquid in a Cylindrical Container With a Rotating End Wall," Exp. Therm. Fluid Sci., **12**, pp. 381–384.
[22] Xue, S. C., Phan-Thien, N., and Tanner, R. I., 1999, "Fully Three-Dimensional, Time-Dependent Numerical Simulations of Newtonian and Viscoelastic Swirling Flows in a Confined Cylinder-Part I. Method and Steady Flows," J. Non-Newtonian Fluid Mech., **87**, pp. 337–367.
[23] Bowen, P. J., Davies, A. R., and Walters, K., 1991, "On Viscoelastic Effects in Swirling Flows," J. Non-Newtonian Fluid Mech., **38**, pp. 113–126.
[24] Siginer, D. A., 2004, "On the Nearly Viscometric Torsional Motion of Viscoelastic Liquids Between Shrouded Rotating Disks," ASME J. Appl. Mech., **71**, pp. 305–313.
[25] Stokes, J. R., Graham, L. J. W., Lawson, N. J., and Boger, D. V., 2001, "Swirling Flow of Viscoelastic Fluids. Part 1. Interaction Between Inertia and Elasticity," J. Fluid Mech., **429**, pp. 67–115.
[26] Stokes, J. R., Graham, L. J. W., Lawson, N. J., and Boger, D. V., 2001, "Swirling Flow of Viscoelastic Fluids. Part 2. Elastic Effects," J. Fluid Mech., **429**, pp. 67–115.
[27] Goller, H., and Ranov, T., 1968, "Unsteady Rotating Flow in a Cylinder With Free Surface," J. Basic Eng., **90**, pp. 445–454.
[28] Arora, K., Sureshkumar, R., Scheiner, M. P., and Piper, J. L., 2002, "Surfactant-Induced Effects on Turbulent Swirling Flows," Rheol. Acta, **41**, pp. 25–34.
[29] Spohn, A., Mory, M., and Hopfinger, E. J., 1993, "Observation of Vortex Breakdown in an Open Cylindrical Container With a Rotating Bottom," Exp. Fluids, **14**, pp. 70–77.
[30] Bohme, G., Voss, R., and Warnercke, W., 1985, "Die Frei Oberflache Einer Flussigkeit Uber Einer Rotierenden Scheibe," Rheol. Acta, **24**, pp. 22–23.
[31] Siginer, D. A., and Knight, R. W., 1993, "Swirling Free Surface Flow in Cylindrical Containers," J. Eng. Math., **27**, pp. 245–264.
[32] Siginer, D. A., 1989, "Free Surface on a Viscoelastic Liquid in a Cylinder with Spinning Bottom," Macromol. Chem., **23**, pp. 73–90.
[33] Siginer, D. A., 1986, "Torsional Oscillations of a Rod in a Layered Medium of Simple Fluids," Int. J. Eng. Sci., **24**, pp. 631–640.
[34] Kawaguchi, Y., Wei, J. J., Yu, B., and Feng, Z. P., 2003, "Rheological Characterization of Drag-Reducing Cationic Surfactant Solution: Shear and Elongational Viscosities of Dilute Solution," in Proceedings of the 4th ASME/JSME Joint Fluids Engineering Conference, Honolulu, Hawaii.
[35] Yu, B., Wei, J. J., and Kawaguchi, Y., 2004, "Swirling Flow of a Viscoelastic Fluid With Free Surface, Part II: Numerical Analysis With Extended Marker-and-Cell Method," ASME J. Fluids Eng., **128**, pp. 77–87.
[36] Giesekus, H., 1982, "A Simple Constitutive Equation for Polymer Fluids Based on the Concept Deformation-Dependent Tensorial Mobility," J. Non-Newtonian Fluid Mech., **11**, pp. 69–109.

Swirling Flow of a Viscoelastic Fluid With Free Surface—Part II: Numerical Analysis With Extended Marker-and-Cell Method

Bo Yu
Department of Oil and Gas Storage and Transportation Engineering,
China University of Petroleum,
Beijing, 102249, People's Republic of China

Jinjia Wei
State Key Laboratory of Multiphase Flow in Power Engineering,
Xi'an Jiaotong University,
Xi'an, 710049, People's Republic of China

Yasuo Kawaguchi[1]
Department of Mechanical Engineering,
Faculty of Science and Technology,
Tokyo University of Science,
Noda, Chiba, 278-8510, Japan

In Part I [Wei et al., 2004, 2004 ASME Int. Mech. Eng. Conference], we presented the experimental results for swirling flows of water and cetyltrimethyl ammonium chloride (CTAC) surfactant solution in a cylindrical vessel with a rotating disk located at the bottom for a Reynolds number of around 4.3×10^4 based on the viscosity of solvent. For the large Reynolds number, violent irregular instantaneous secondary flows at the meridional plane were observed by use of a particle image velocimetry system. Because of the limitations of our computer resources, we did not carry out direct numerical simulation for such a large Reynolds number. The LES and turbulence model are alternative methods, but a viscoelastic LES/turbulence model has not yet been developed for the surfactant solution. In this study, therefore, we limited our simulations to a laminar flow. The marker-and-cell method proposed for Newtonian flow was extended to the viscoelastic flow to track the free surface, and the effects of Weissenberg number and Froude number on the flow pattern and surface shape were studied. Although the Reynolds number is much smaller than that of the experiment, the major experimental observations, such as the inhibition of primary and secondary flows and the decrease of the dip of the free surface by the elasticity of the solution, were qualitatively reproduced in the numerical simulations. [DOI: 10.1115/1.2136929]

Introduction

The phenomenon studied in this paper is related to the Weissenberg effect and called *Quelleffekt* as mentioned in Part I [1]. *Quelleffekt* was studied two decades ago for relatively elastic fluids at small Reynolds numbers, the most important reports being those of Bohme et al. [2] and Devvat and Hocq [3] for silicon oil and a 2.5% polyacrymide aqueous solution. Their experimental and numerical simulations show that the viscoelastic fluid in a cylindrical vessel flows upwards along the axis of symmetry and produces a bulge in the free surface around the axis when the fluid is driven by a rotating disk at the bottom of the vessel. Xue et al. numerically studied the effect of small amounts elasticity on the flow pattern for the confined flow [4]. Siginer and his co-workers [5–13] first connected the free surface shape with rheological parameters in the viscoelastic constitutive equation for the viscoelastic liquid.

We did not observe the bulge in our experiments because of the lower elasticity of the CTAC surfactant solution compared to silicon oil and polyacrymide aqueous solution and the extremely large inertial force at the large Reynolds number. To our knowledge, the effects of elasticity on the flow pattern and free surface shape of the swirling flow at a large Reynolds number and small elasticity have not been reported. Those effects were measured experimentally in Part I [1] and are numerically analyzed herein utilizing a viscoelastic Giesekus model.

One of the key issues in the simulation is the proper modeling of the free surface. Several numerical techniques have been developed to deal with free surface flows; for example, the surface height method [14], marker-and-cell (MAC) method [15], volume-of-fluid (VOF) method [16], and level-set method [17]. The MAC method is a simple and effective technique in which Lagrangian marker particles are advected at the velocity of the local fluid, with their distribution determining the instantaneous fluid configuration. The method was designed for Newtonian fluid and has been successfully used in solving a wide range of complex free surface problems. Recently, Tomes et al. [18] applied the MAC technique for the first time to viscoelastic free surface flows in a two-dimensional Cartesian coordinate and achieved satisfactory solutions. In this study, we further extended the MAC method to calculate the viscoelastic axisymmetric swirling flow.

Numerical Method

The flow was described in detail in Part I [1] and is sketched in Fig. 1 herein. The fluid is enclosed in a circular cylinder having radius R, and a disk at the bottom rotates with a constant angular velocity. The radius of the rotating disk is assumed to be equal to that of the cylindrical vessel. Shear thinning and elasticity are two important properties influencing the flow behavior of the surfactant solution when its concentration is larger than a certain value [19], which can be well described by a Giesekus model [20] as shown in Part I. The governing equations of Giesekus fluids can be written as follows:

Continuity equation:

$$\nabla \cdot u = 0 \tag{1}$$

Momentum equation:

$$\rho\frac{Du}{Dt} = -\nabla P + \mu\Delta u + \nabla\cdot\tau + \rho\vec{g} \tag{2}$$

Constitutive equation:

[1]Corresponding author.

Contributed by the Fluids Engineering Division of ASME for publication in the JOURNAL OF FLUIDS ENGINEERING. Manuscript received June 25, 2004; final manuscript received August 20, 2005. Assoc. Editor: Dennis Siginer.

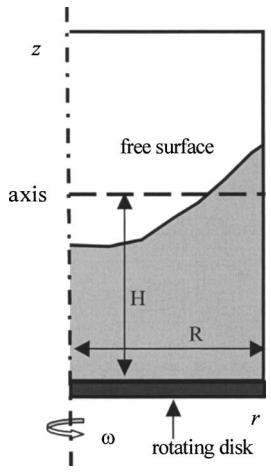

Fig. 1 Sketch of the disk-cylinder swirling flow system

$$\tau+\lambda\left(\frac{\partial\tau}{\partial t}+u\cdot\nabla\tau-\tau\cdot\nabla u-\nabla u^T\cdot\tau+\frac{\alpha}{\eta}\tau\cdot\tau\right)=\eta(\nabla u+\nabla u^T) \tag{3}$$

where λ, μ, η, and α are the relaxation time, solvent viscosity, surfactant contribution to the zero-shear-rate solution viscosity, and mobility factor, respectively. The Giesekus model reduces to an Oldroyd-B model [21] by setting α equal to zero. By introducing the following dimensionless variables

$$u^*=u/(\omega R),\quad \vec{x}^*=\vec{x}/R,\quad \tau^*=\tau/(\eta\omega),\quad P^*=p/(\rho\omega^2R^2)$$

$$\mathrm{Re}=\rho\omega R^2/\mu,\quad \mathrm{We}=\lambda\omega,\quad \mathrm{Fr}=\omega^2R/g,\quad t^*=t\omega,\quad \beta=\eta/\mu$$

the governing equations can be written in dimensionless form as

$$\nabla\cdot u=0 \tag{4}$$

$$\frac{Du}{Dt}=-\nabla P+\frac{1}{\mathrm{Re}}\Delta u+\frac{\beta}{\mathrm{Re}}\nabla\cdot\tau+\frac{1}{\mathrm{Fr}}\frac{\vec{g}}{g} \tag{5}$$

$$\frac{\partial\tau}{\partial t}+u\cdot\nabla\tau=\frac{1}{\mathrm{We}}(\nabla u+\nabla u^T)-\frac{1}{\mathrm{We}}\tau+\tau\cdot\nabla u+\nabla u^T\cdot\tau-\alpha\tau\cdot\tau \tag{6}$$

For simplicity, the superscript *'s in the above nondimensional equations were dropped.

In the experiments, the flows were three-dimensional turbulent ones. DNS could not be carried out for a Reynolds number as high as 4.3×10^4 and LES/turbulence viscoelastic models have not yet been developed. Therefore, we limited our simulations to laminar flows, which can be assumed to be axisymmetric. The axisymmetric swirling flow had ten unknown variables (three velocity components, pressure, and six extra viscoelastic stresses) to be solved. The full components of the Giesekus model for axisymmetric swirling flow were not readily found in a textbook and therefore we worked them out as follows:

Continuity equation:

$$\frac{1}{r}\frac{\partial ru_r}{\partial r}+\frac{\partial u_z}{\partial z}=0 \tag{7}$$

Momentum equation:

$$\frac{\partial u_r}{\partial t}+\frac{1}{r}\frac{\partial ru_ru_r}{\partial r}+\frac{\partial u_zu_r}{\partial z}=-\frac{\partial p}{\partial r}+\frac{1}{\mathrm{Re}}\left[\frac{1}{r}\frac{\partial}{\partial r}\left(r\frac{\partial u_r}{\partial r}\right)+\frac{\partial}{\partial z}\left(\frac{\partial u_r}{\partial z}\right)\right]-\frac{1}{\mathrm{Re}}\frac{u_r}{r^2}+\frac{u_\theta^2}{r}+\frac{\beta}{\mathrm{Re}}\left(\frac{1}{r}\frac{\partial}{\partial r}(r\tau_{rr})+\frac{\partial\tau_{rz}}{\partial z}-\frac{\tau_{\theta\theta}}{r}\right) \tag{8}$$

$$\frac{\partial u_z}{\partial t}+\frac{1}{r}\frac{\partial ru_ru_z}{\partial r}+\frac{\partial u_zu_z}{\partial z}=-\frac{\partial p}{\partial z}+\frac{1}{\mathrm{Re}}\left[\frac{1}{r}\frac{\partial}{\partial r}\left(r\frac{\partial u_z}{\partial r}\right)+\frac{\partial}{\partial z}\left(\frac{\partial u_z}{\partial z}\right)\right]+\frac{\beta}{\mathrm{Re}}\left(\frac{1}{r}\frac{\partial}{\partial r}(r\tau_{rz})+\frac{\partial\tau_{zz}}{\partial z}\right)-\frac{1}{\mathrm{Fr}} \tag{9}$$

$$\frac{\partial u_\theta}{\partial t}+\frac{1}{r}\frac{\partial ru_ru_\theta}{\partial r}+\frac{\partial u_zu_\theta}{\partial z}=\frac{1}{\mathrm{Re}}\left[\frac{1}{r}\frac{\partial}{\partial r}\left(r\frac{\partial u_\theta}{\partial r}\right)+\frac{\partial}{\partial z}\left(\frac{\partial u_\theta}{\partial z}\right)\right]-\frac{1}{\mathrm{Re}}\frac{u_\theta}{r^2}-\frac{u_\theta u_r}{r}+\frac{\beta}{\mathrm{Re}}\left(\frac{1}{r^2}\frac{\partial}{\partial r}(r^2\tau_{r\theta})+\frac{\partial\tau_{\theta z}}{\partial z}\right) \tag{10}$$

Giesekus constitutive equation:

$$\frac{\partial\tau_{rr}}{\partial t}+\frac{1}{r}\frac{\partial ru_r\tau_{rr}}{\partial r}+\frac{\partial u_z\tau_{rr}}{\partial z}=\frac{2}{\mathrm{We}}\frac{\partial u_r}{\partial r}-\frac{1}{\mathrm{We}}\tau_{rr}+2\left(\frac{\partial u_r}{\partial r}\tau_{rr}+\frac{\partial u_r}{\partial z}\tau_{rz}\right)-\alpha(\tau_{rr}^2+\tau_{r\theta}^2+\tau_{rz}^2) \tag{11}$$

$$\frac{\partial\tau_{\theta\theta}}{\partial t}+\frac{1}{r}\frac{\partial ru_r\tau_{\theta\theta}}{\partial r}+\frac{\partial u_z\tau_{\theta\theta}}{\partial z}=\frac{2}{\mathrm{We}}\frac{u_r}{r}-\frac{1}{\mathrm{We}}\tau_{\theta\theta}+2\left[\frac{u_r}{r}\tau_{\theta\theta}+r\frac{\partial}{\partial r}\left(\frac{u_\theta}{r}\right)\tau_{r\theta}+\frac{\partial u_\theta}{\partial z}\tau_{\theta z}\right]-\alpha(\tau_{r\theta}^2+\tau_{\theta\theta}^2+\tau_{\theta z}^2) \tag{12}$$

$$\frac{\partial\tau_{zz}}{\partial t}+\frac{1}{r}\frac{\partial ru_r\tau_{zz}}{\partial r}+\frac{\partial u_z\tau_{zz}}{\partial z}=\frac{2}{\mathrm{We}}\frac{\partial u_z}{\partial r}-\frac{1}{\mathrm{We}}\tau_{zz}+2\left(\frac{\partial u_z}{\partial z}\tau_{zz}+\frac{\partial u_z}{\partial r}\tau_{rz}\right)-\alpha(\tau_{rz}^2+\tau_{\theta z}^2+\tau_{zz}^2) \tag{13}$$

$$\frac{\partial\tau_{r\theta}}{\partial t}+\frac{1}{r}\frac{\partial ru_r\tau_{r\theta}}{\partial r}+\frac{\partial u_z\tau_{r\theta}}{\partial z}=\frac{2}{\mathrm{We}}r\frac{\partial}{\partial r}\left(\frac{u_\theta}{r}\right)-\frac{1}{\mathrm{We}}\tau_{r\theta}+\left[-\frac{\partial u_z}{\partial z}\tau_{r\theta}+r\frac{\partial}{\partial r}\left(\frac{u_\theta}{r}\right)\tau_{rr}+\frac{\partial u_\theta}{\partial z}\tau_{rz}+\frac{\partial u_r}{\partial z}\tau_{\theta z}\right]-\alpha(\tau_{rr}\tau_{r\theta}+\tau_{r\theta}\tau_{\theta\theta}+\tau_{rz}\tau_{\theta z}) \tag{14}$$

$$\frac{\partial\tau_{rz}}{\partial t}+\frac{1}{r}\frac{\partial ru_r\tau_{rz}}{\partial r}+\frac{\partial u_z\tau_{rz}}{\partial z}=\frac{1}{\mathrm{We}}\left(\frac{\partial u_r}{\partial z}+\frac{\partial u_z}{\partial r}\right)-\frac{1}{\mathrm{We}}\tau_{rz}+\left[\frac{\partial u_z}{\partial r}\tau_{rr}+\frac{\partial u_r}{\partial z}\tau_{zz}+\left(\frac{\partial u_r}{\partial r}+\frac{\partial u_z}{\partial z}\right)\tau_{rz}\right]-\alpha(\tau_{rr}\tau_{rz}+\tau_{r\theta}\tau_{\theta z}+\tau_{rz}\tau_{zz}) \tag{15}$$

$$\frac{\partial\tau_{\theta z}}{\partial t}+\frac{1}{r}\frac{\partial ru_r\tau_{\theta z}}{\partial r}+\frac{\partial u_z\tau_{\theta z}}{\partial z}=\frac{1}{\mathrm{We}}\frac{\partial u_\theta}{\partial z}-\frac{1}{\mathrm{We}}\tau_{\theta z}+\left[-\frac{\partial u_r}{\partial r}\tau_{\theta z}+\frac{\partial u_z}{\partial r}\tau_{r\theta}+r\frac{\partial}{\partial r}\left(\frac{u_\theta}{r}\right)\tau_{rz}+\frac{\partial u_\theta}{\partial z}\tau_{zz}\right]-\alpha(\tau_{r\theta}\tau_{rz}+\tau_{\theta\theta}\tau_{\theta z}+\tau_{\theta z}\tau_{zz}) \tag{16}$$

It can be seen that there are five important dimensionless numbers in the above equations to characterize the Quelleffekt flow: Reynolds number Re, Froude number Fr, Weissenberg number We, viscosity ratio β, and mobility factor α.

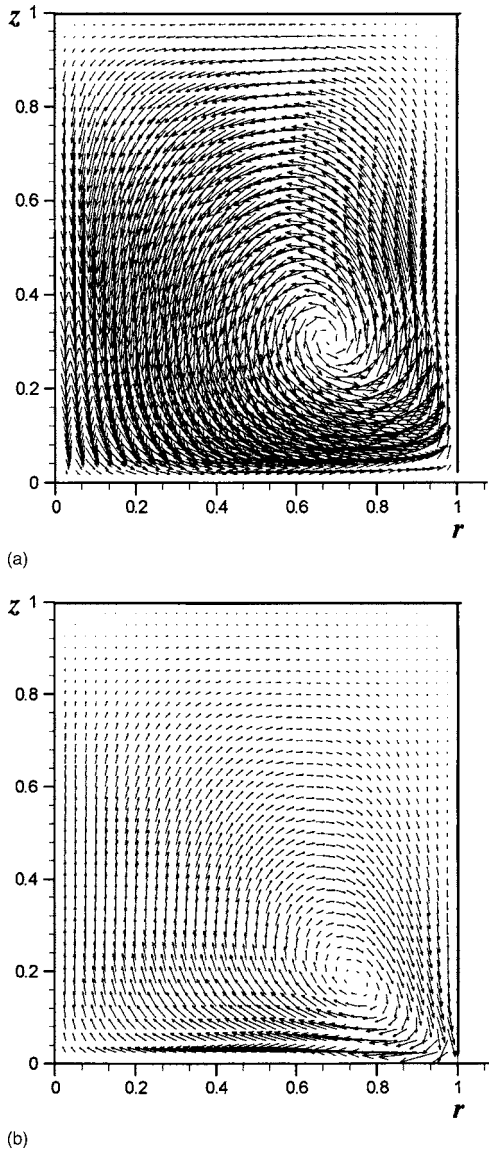

Fig. 2 Secondary flow patterns of a confined swirling flow. (*a*) Inertia-driven vortex of Newtonian flow (Re=100 and *a*=1.0) and (*b*) elasticity-driven vortex of viscoelastic flow (Re=100, We=1.0, β=1.0, α=0 and *a*=1.0).

Special attention should be paid to the treatment of the free surface. In this study, in which surface tension is neglected, the boundary conditions at the free surface are the disappearance of normal and tangential stresses as follows:

$$n \cdot \sigma \cdot n = 0 \tag{17}$$

$$m \cdot \sigma \cdot n = 0 \tag{18}$$

where n and m are the local unit normal and tangential vectors. Equations (17) and (18) can be rewritten as

$$P = \frac{n_r n_r}{\mathrm{Re}}\left(\frac{2\partial u_r}{\partial r} + \beta\tau_{rr}\right) + \frac{2n_r n_z}{\mathrm{Re}}\left(\frac{\partial u_z}{\partial r} + \frac{\partial u_r}{\partial z} + \beta\tau_{rz}\right) + \frac{n_z n_z}{\mathrm{Re}}\left(\frac{2\partial u_z}{\partial z} + \beta\tau_{zz}\right) \tag{19}$$

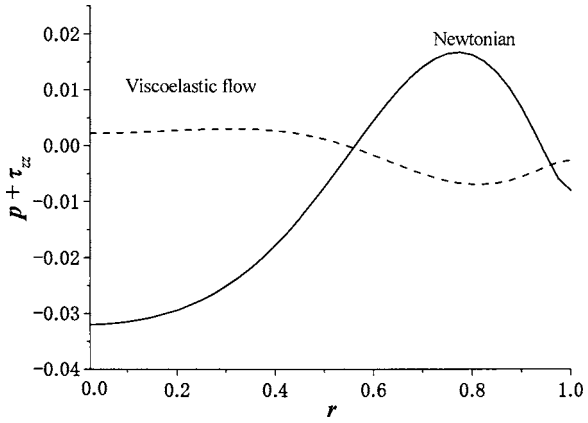

Fig. 3 The total normal pressure exerted on the top disk

$$\frac{n_r n_z}{\mathrm{Re}}\left[2\left(\frac{\partial u_r}{\partial r} - \frac{\partial u_z}{\partial z}\right) + \beta(\tau_{rr} - \tau_{zz})\right] + \frac{n_z n_z - n_r n_r}{\mathrm{Re}} \times \left(\frac{\partial u_z}{\partial r} + \frac{\partial u_r}{\partial z} + \beta\tau_{rz}\right) = 0 \tag{20}$$

In order to apply these conditions we divide the surface conditions into four types.

(a) Horizontal surfaces: These surfaces are identified by surface cells having only one side contiguous with empty cells, and the normal vector is $n=(0,1)$. Then, Eqs. (19) and (20) reduce to

$$P = \frac{1}{\mathrm{Re}}\left(\frac{2\partial u_z}{\partial z} + \beta\tau_{zz}\right) \tag{21}$$

$$\frac{\partial u_z}{\partial r} + \frac{\partial u_r}{\partial z} + \beta\tau_{rz} = 0 \tag{22}$$

(b) Vertical surfaces: These surfaces are identified by surface cells having only one side contiguous with empty cells, and the normal vector is $n=(1,0)$. Then we have

$$P = \frac{1}{\mathrm{Re}}\left(\frac{2\partial u_r}{\partial r} + \beta\tau_{rr}\right) \tag{23}$$

$$\left(\frac{\partial u_z}{\partial r} + \frac{\partial u_r}{\partial z} + \beta\tau_{rz}\right) = 0 \tag{24}$$

(c) 45 deg slope surface cells: The surfaces are identified by surface cells having two adjacent faces contiguous with empty cells. For these cells, the normal vector is assumed to make 45 deg with the axes, i.e., $n=(\pm 1/\sqrt{2}, \pm 1/\sqrt{2})$. For the surface with top and right empty cells, the normal vector is assumed to be $n=(1/\sqrt{2}, 1/\sqrt{2})$ and we have

$$P = \frac{1}{2\,\mathrm{Re}}\left(\frac{2\partial u_r}{\partial r} + \beta\tau_{rr}\right) + \frac{1}{\mathrm{Re}}\left(\frac{\partial u_z}{\partial r} + \frac{\partial u_r}{\partial z} + \beta\tau_{rz}\right) + \frac{1}{2\,\mathrm{Re}}\left(\frac{2\partial u_z}{\partial z} + \beta\tau_{zz}\right) \tag{25}$$

$$2\left(\frac{\partial u_r}{\partial r} - \frac{\partial u_z}{\partial z}\right) + \beta(\tau_{rr} - \tau_{zz}) = 0 \tag{26}$$

For the surface with bottom and right surfaces, we assumed the normal vector $n=(1/\sqrt{2}, -1/\sqrt{2})$ and then we have

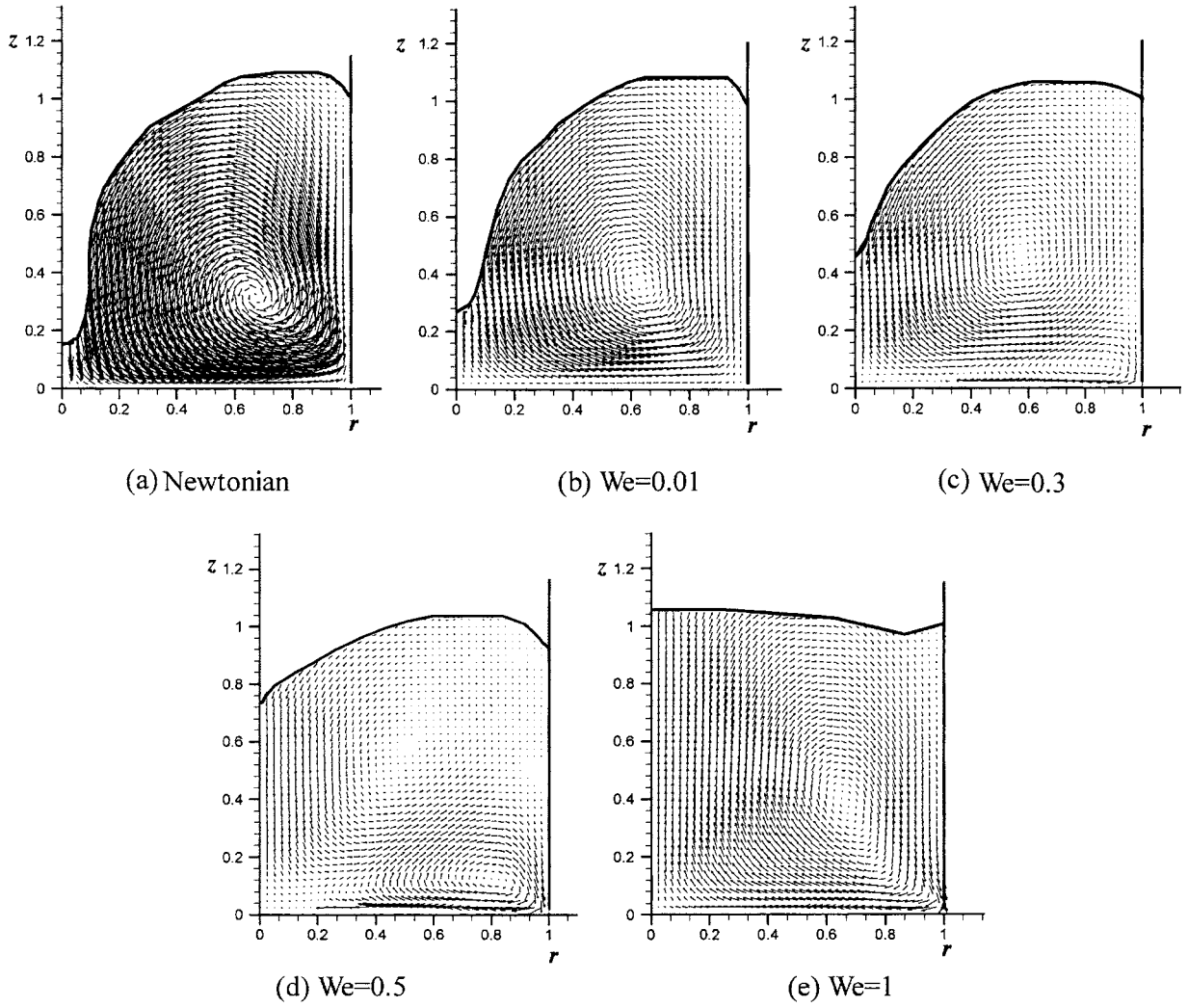

Fig. 4 Secondary flows at various Weissenberg numbers and Re=100, Fr=100, β=1, α=0, and a=1.0

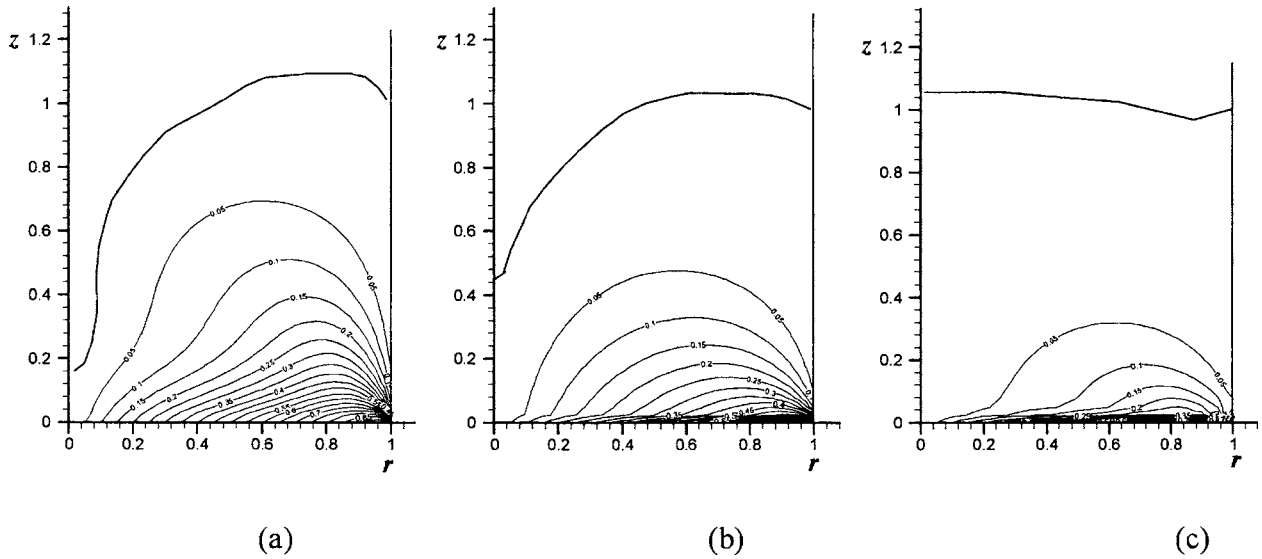

Fig. 5 Contours of the tangential velocity. (*a*) Newtonian fluid Re=100, Fr=100, and a=1.0; (*b*) We=0.3, Re=100, Fr=100, β=1, α=0 and a=1.0; and (*c*) We=1.0, Re=100, Fr=100, β=1, α=0, and a=1.0

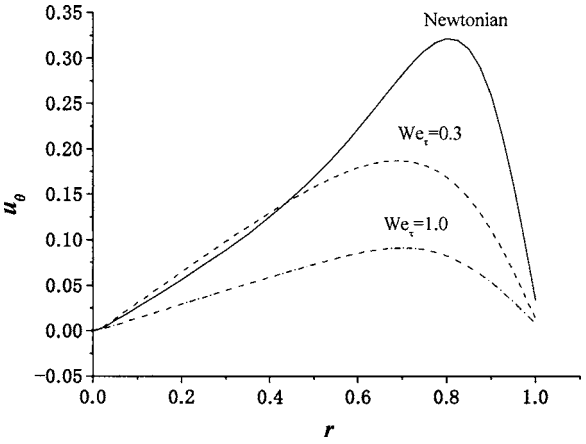

Fig. 6 Tangential velocities at z=0.2

$$P=\frac{1}{2\,\mathrm{Re}}\left(\frac{2\partial u_r}{\partial r}+\beta\tau_{rr}\right)-\frac{1}{\mathrm{Re}}\left(\frac{\partial u_z}{\partial r}+\frac{\partial u_r}{\partial z}+\beta\tau_{rz}\right)+\frac{1}{2\,\mathrm{Re}}\left(\frac{2\partial u_z}{\partial z}+\beta\tau_{zz}\right) \tag{27}$$

$$2\left(\frac{\partial u_r}{\partial r}-\frac{\partial u_z}{\partial z}\right)+\beta(\tau_{rr}-\tau_{zz})=0 \tag{28}$$

For the surface with bottom and left surfaces, we assumed the normal vector $n=(-1/\sqrt{2},-1/\sqrt{2})$ and then we have

$$P=\frac{1}{2\,\mathrm{Re}}\left(\frac{2\partial u_r}{\partial r}+\beta\tau_{rr}\right)+\frac{1}{\mathrm{Re}}\left(\frac{\partial u_z}{\partial r}+\frac{\partial u_r}{\partial z}+\beta\tau_{rz}\right)+\frac{1}{2\,\mathrm{Re}}\left(\frac{2\partial u_z}{\partial z}+\beta\tau_{zz}\right) \tag{29}$$

$$2\left(\frac{\partial u_r}{\partial r}-\frac{\partial u_z}{\partial z}\right)+\beta(\tau_{rr}-\tau_{zz})=0 \tag{30}$$

For the surface with top and left surfaces, we assumed the normal vector $\vec{n}=(-1/\sqrt{2},1/\sqrt{2})$ and then we have

$$P=\frac{1}{\mathrm{Re}}\left(\frac{2\partial u_r}{\partial r}+\beta\tau_{rr}\right)-\frac{1}{\mathrm{Re}}\left(\frac{\partial u_z}{\partial r}+\frac{\partial u_r}{\partial z}+\beta\tau_{rz}\right)+\frac{1}{\mathrm{Re}}\left(\frac{2\partial u_z}{\partial z}+\beta\tau_{zz}\right) \tag{31}$$

$$2\left(\frac{\partial u_r}{\partial r}-\frac{\partial u_z}{\partial z}\right)+\beta(\tau_{rr}-\tau_{zz})=0 \tag{32}$$

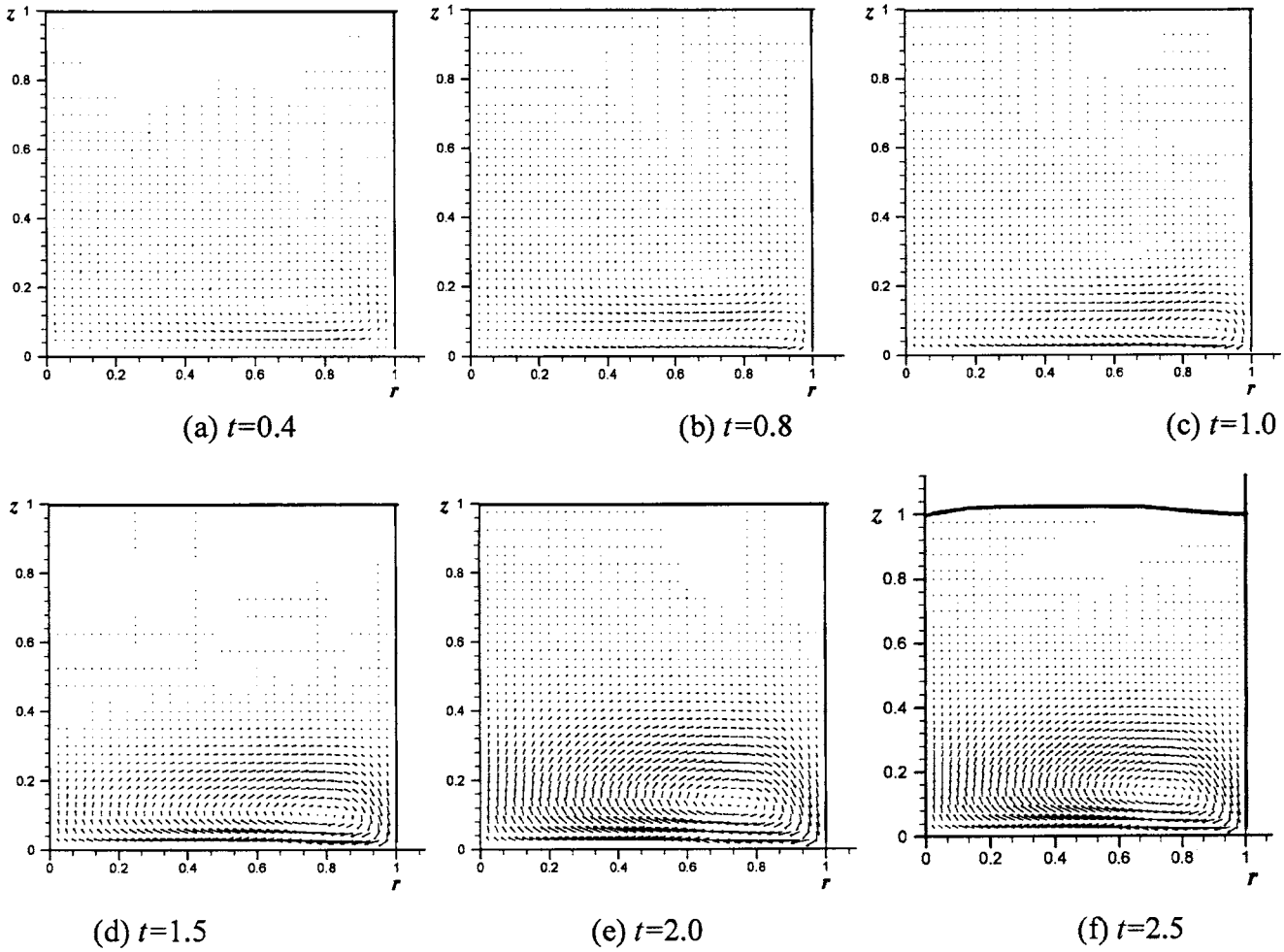

Fig. 7 Transient process of the development of the vortex of viscoelastic flow at Re=100, Fr=100, We=1.0, β=1.0, α=0, and a=1.0 from a static state

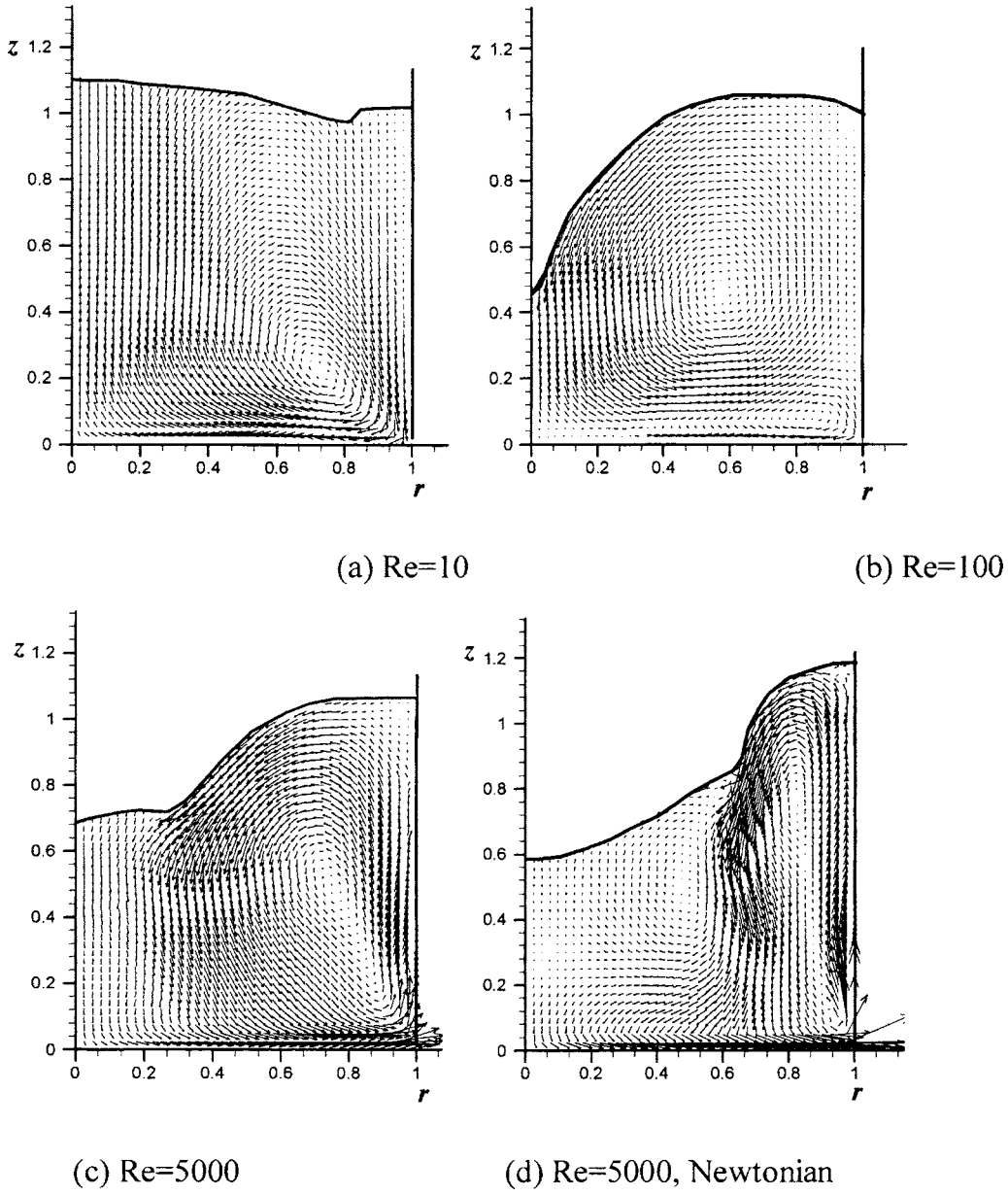

Fig. 8 Secondary flows at various Reynolds numbers with We=0.5, Fr=100, β=1.0, α=0, and a=1.0 for viscoelastic flow [(*a*), (*b*), and (*c*)] and Fr=100 and a=1.0 for Newtonian flow (*d*).

(d) Surfaces with three sides or two opposite sides contiguous with empty cells: For these cases, the pressure is set to zero and adjust at least one velocity on the empty cell faces to satisfy the mass conservation.

A second-order finite difference scheme similar to that of Tomes et al. [18] was used to discretize the governing equations. An explicit method was used for time advancement and the numerical procedure is referred to Tomes et al. [18]

Results and Discussions

A number of experiments and numerical simulations have been carried out for confined swirling flows of Newtonian and viscoelastic fluids [22,23]. The results show that for Newtonian flow, an outward centrifugal force at the meridional plane causes the fluid near the rotating disk to flow radially outward, up the sidewalls of the cylindrical vessel, inward along the top, and finally down near the center, whereas for a highly elastic fluid, an opposite secondary flow is generated by the rotation of the disk due to the induced normal stresses in the fluid. Usually the vortex caused by centrifugal force is called an "inertia-driven vortex" and that due to elasticity is called an "elasticity-driven vortex." In order to validate our code, we first made calculations for the confined swirling flows of Newtonian fluid (Re=100 and a=1.0) and a relatively elastic Oldroyd-B fluid (Re=100, We=1, β=1.0, α=0.0, and a=1.0). Figure 2 shows the secondary flows in the disk-cylinder system, in which the top disk and the sidewall of the cylindrical vessel are stationary and the bottom disk rotates at a constant angular velocity. It is clearly seen that the inertia-driven vortex and elasticity-driven vortex are reproduced by our code. Figure 3 shows the total normal pressure at the top stationary disk. It can be seen that the total pressure exerted on the top disk is larger near the sidewall than near the axis for Newtonian flow. Thus, if we remove the top disk we would expect the fluid to rise near the sidewall and dip near the axis. For the elastic fluid, the total pressure is larger near the axis, thus a bulge would be produced in the free surface around the axis when the disk is re-

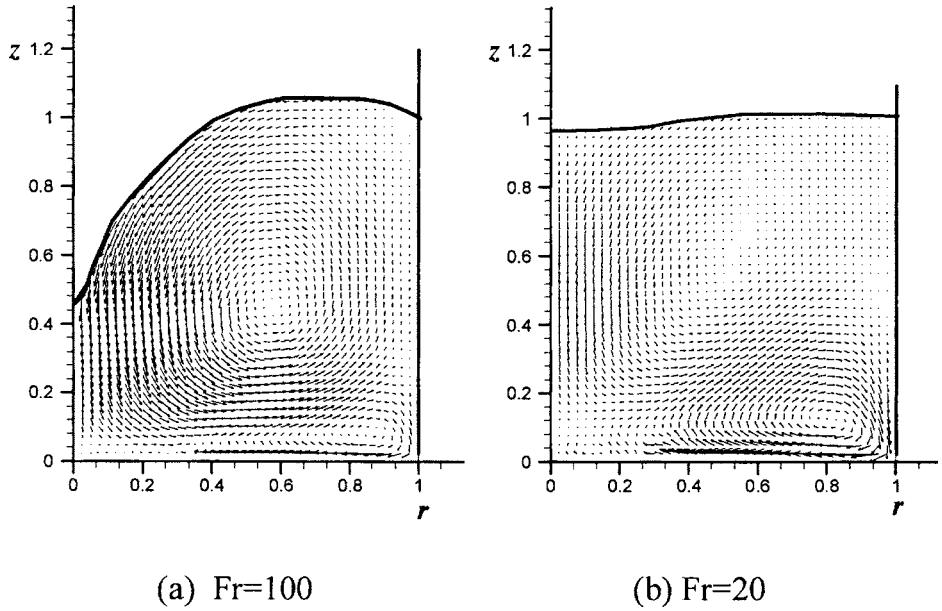

Fig. 9 Effect of Froude number on the free surface at Re=100, We=0.5, β=1.0, α=0.0, and a=1.0

moved. The numerical total pressure distributions are consistent with the analyses of the rod-climbing effect in [24]. Figures 2 and 3 validate our code. We checked the grid resolution using three sets of meshes with grid size of 1/20, 1/40, and 1/80 in each direction, respectively, and found that the grid size of 1/40 is enough to obtain a grid-independent solution.

Next, we discuss free surface calculation. The fluid motion in the swirling flow system with aspect ratio a=1.0 is studied. The flow pattern and surface shape are affected by five important parameters: (1) Weissenberg number, (2) Reynolds number, (3) Froude number, (4) viscosity ratio β, and (5) mobility factor α. Following is a systematic explanation of these effects.

(1) Effect of Weissenberg number: Elasticity is often represented by a Weissenberg number, which is defined as the ratio of relaxation time to the characteristic time of the fluid. Generally, the larger the Weissenberg number, the more important the role that elasticity plays. In this section, four Weissenberg numbers We=0.01, 0.3, 0.5, and 1.0 were studied with other parameters set as Re=100, Fr=100, β=1.0, α=0.0, and a=1.0.

Elasticity number E (E=We/Re) is another important nondimensional number defined as the ratio of the elastic force to the inertial force, which is independent of angular velocity. In the present study, E varies from 0.0001 to 0.01, which is almost the same range as that in Part I.

Figure 4 shows the secondary flows of various Weissenberg numbers at the meridional plane; the results of Newtonian flow are also included for comparison. The effects of the Weissenberg number on flow pattern and surface shape are clearly seen. First, the flow patterns of the Newtonian flow and viscoelastic flow with We=1.0 are, respectively, the same as those in Figs. 2(a) and 2(b); the magnitudes of velocity vectors do not have any apparent change when the top stationary disk is replaced by a free surface. The striking change is seen in the eventual curving of the flat liquid surfaces. The surface shapes of Newtonian flow and the high elastic flow (We=1.0) are completely different: a dip is formed in Newtonian fluid while a bulge is produced in the high elastic fluid near the axis. The surface shapes are consistent with the radial distribution of total pressure in Fig. 3. Secondly, the specific flow pattern and surface shape depends on the balance between the inertial force (Re), elastic force (We or E), and gravity force (Fr). In Fig. 4(a), the flow is controlled by inertia and gravity and an inertia-driven vortex is produced. In Figs. 4(b)–4(e), normal stresses are introduced and the fluid motion is affected by elasticity. Since the Froude number is fixed, a competitive process between the inertial force and elastic force is seen. In Fig. 4(b), the elasticity number is 0.0001 and inertia dominates the flow field. "Newtonian-like flow" is seen, but the strength of the secondary flow field is dramatically suppressed. When the Weissenberg number is increased to 0.3 (E=0.003), 30 times as large at that in Fig. 4(b), an elastic-driven small reverse vortex develops at the outward edge of the rotating disk and the inertia-driven vortex is pushed upward and inward. With the increase of the Weissenberg number to 0.5 the small elasticity-driven vortex grows and with further increase of We to 1.0, the inertia-driven vortex diminishes and the entire domain becomes occupied by the elasticity-driven vortex. Note that when the Weissenberg number is increased from 0.01 to 0.5, the secondary flow becomes weaker. The inhibition of vortex motion at the meridi-

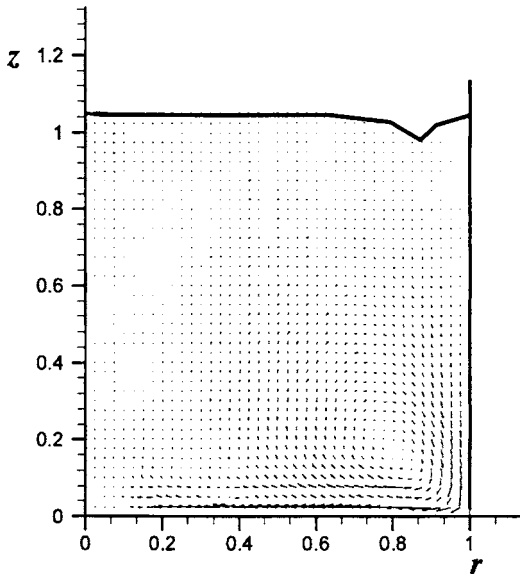

Fig. 10 Secondary flow at Re=100, Fr=100, We=0.3, β=3.0, α=0.0, and a=1.0

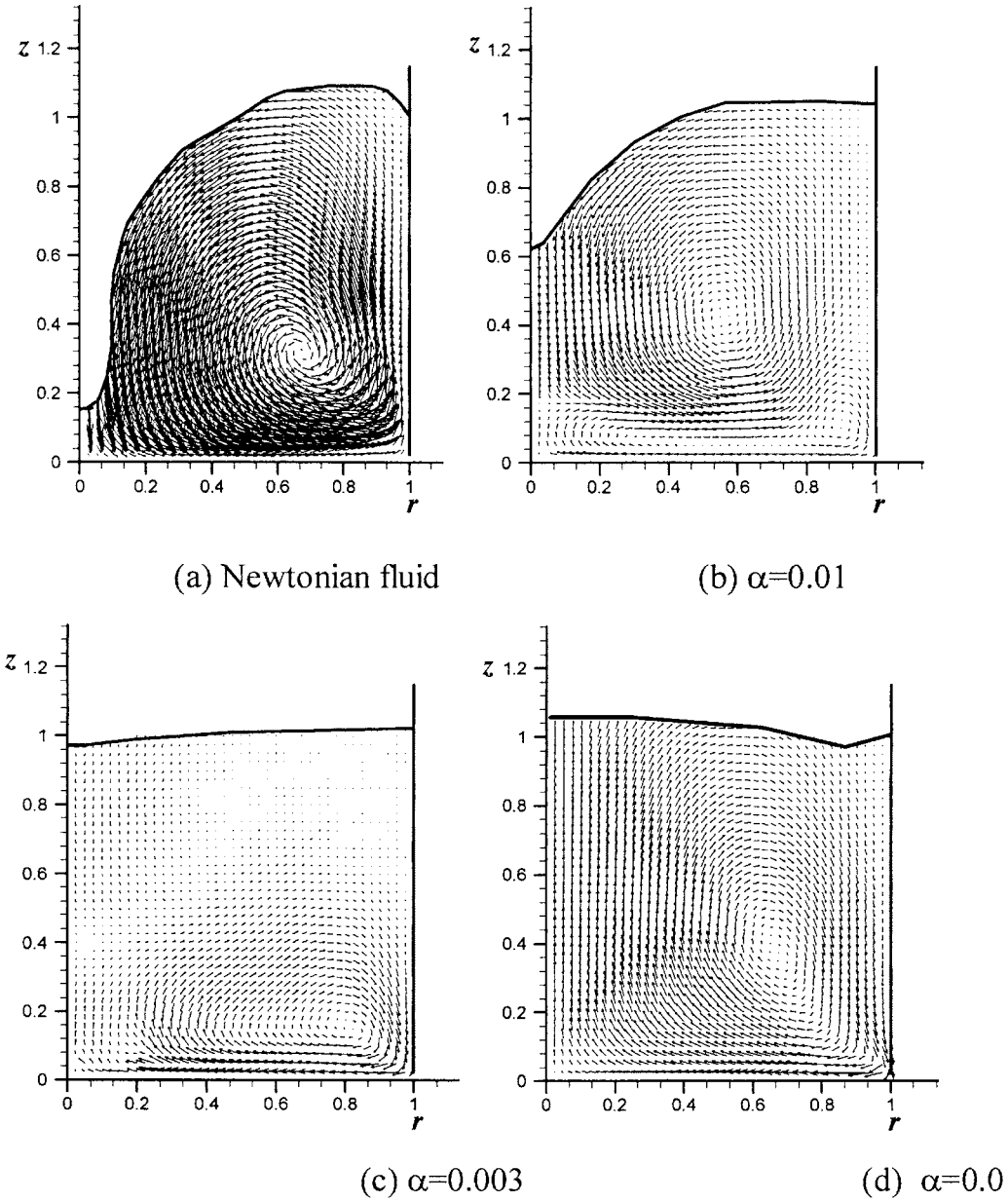

Fig. 11 Secondary flows at various mobility factors and Re=100, We=1.0, Fr=100, β=1, and a=1.0

onal plane agrees with the experimental findings [1]. With further increase of the Weissenberg number to 1.0, the secondary flow increases slightly. At a small Weissenberg number (E=0.0001), the free surface pattern is the same as that of Newtonian flow and the depth of the dip in the free surface is almost the same as that of Newtonian flow. With the increase of the Weissenberg number the dip depth decreases and finally a bulge is produced near the axis and a dip is generated near the sidewall, indicating that elasticity plays an important role in the shape of the free surface, which is in agreement with the experiment [1].

Figure 5 shows the contours of the tangential velocity at the meridional plane. The contour values range from 0.05 to 0.8 and the interval is 0.05. It is clear that elasticity generally weakens the primary flow; the larger the Weissenberg number, the smaller the tangential velocity. The weakened primary flow with the increase of elasticity has been measured in the experiments [1]. The boundary layer becomes thinner with the increase of the Weissenberg number, leading to a larger viscous frictional drag. Figure 6 shows the tangential velocity versus radius at z=0.2 where it becomes

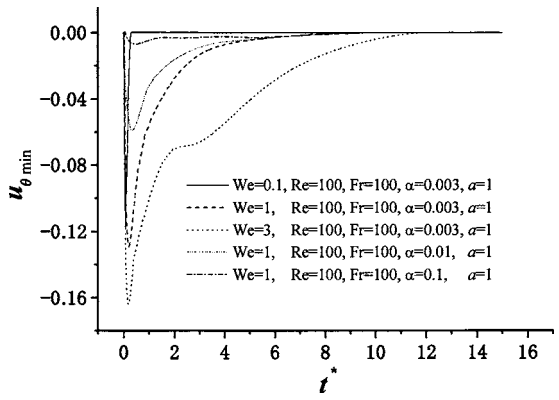

Fig. 12 Evolution of the minimal tangential velocity after the stop of the rotating disk

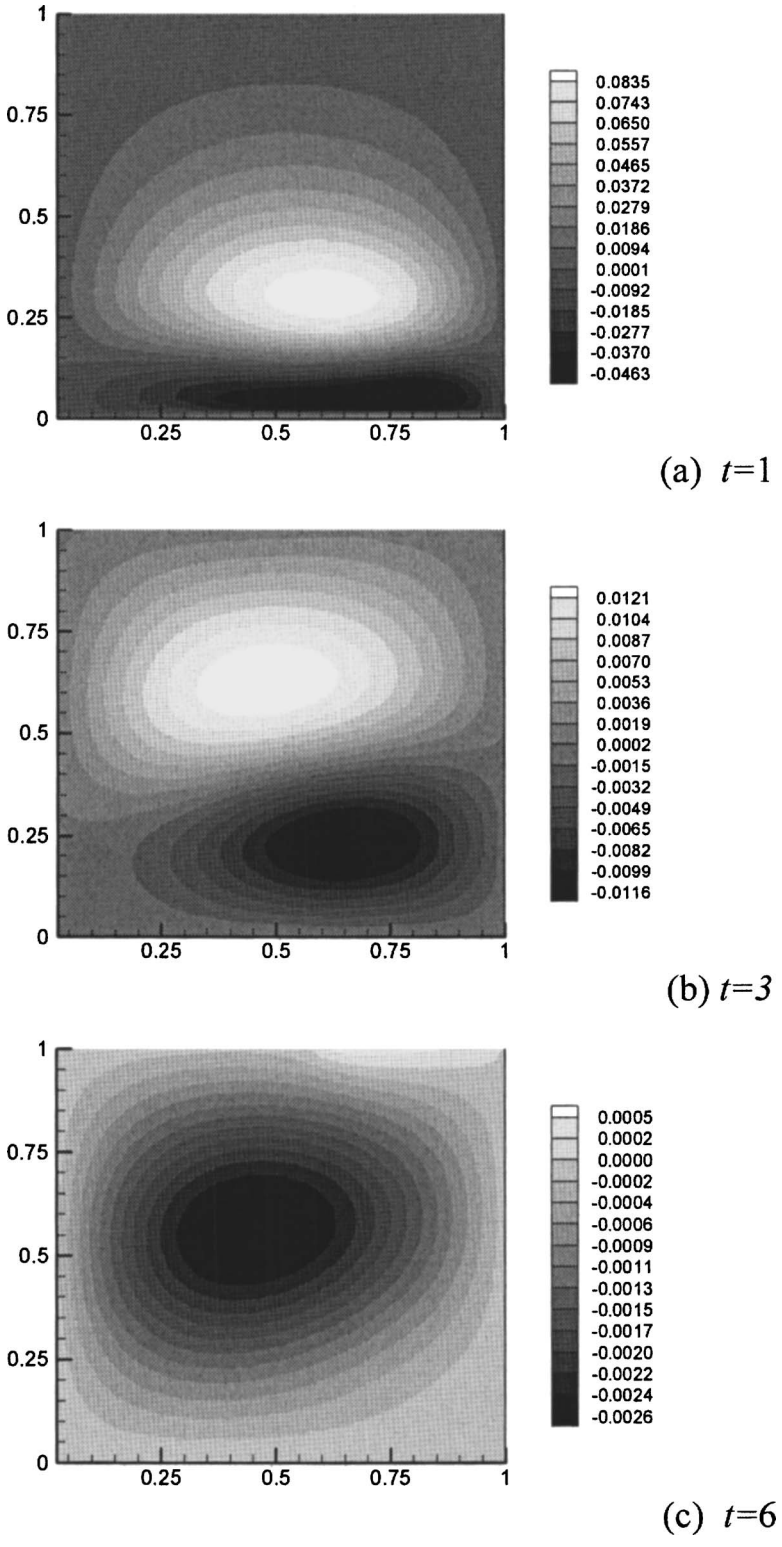

Fig. 13 Contours of the tangential velocity at Re=100, We=1, Fr=100, β =1, α=0.003, and a=1.0

clearer that the tangential flow is inhibited by elasticity. Compared to Newtonian flow, the tangential velocities of viscoelastic flows first increase gradually and then decrease gradually and their peaks shift inward toward the axis. In the experiment, there are two tangential velocity peaks along radial direction for Newtonian fluid due to the effect of the high-Reynolds number. With addition of surfactant additives, it was found that the velocity peak near the axis vanishes and the other peak shifts toward the axis [1]. The shift is in agreement with the numerical simulation.

Figure 7 shows the transient process of the development of the vortex of viscoelastic flow at We=1.0 from a static state. It can be seen that the swirling free surface flow experiences a complex flow process. Below t=0.4, the flow is weak and the secondary flow is inertia driven. At t=0.8, a small elasticity-driven vortex is

generated at the outward edge of the rotating disk that increases gradually and finally occupies the entire field. When t is less than 2.0, inertial and elasticity forces are weak and gravity is the largest force. The gravity force counteracts the inertia-driven and elasticity-driven vortex, producing a flat free surface. However, when t is larger than 2.5, the elasticity force plays the most important role and a bulge is produced at the region near the axis. Finally a steady solution is obtained as shown in Fig. 4(e).

(2) Effect of Reynolds number: Three Reynolds numbers Re =10, 100, and 5000 were studied with other parameters set as We=0.5, Fr=100, β=1.0, α=0.0, and a=1.0. Note that for Re =5000, the flow becomes unstable and it is not possible to achieve a steady converged solution. The secondary flows of various Reynolds numbers at the meridional plane are shown in Fig. 8. It can be seen that the larger the Reynolds number, the more "Newtonian-like" the flow pattern and surface shape become, due to the larger inertial force. One instantaneous snapshot of the secondary flow of the Newtonian fluid at Re=5000 and a=1.0 is also shown in Fig. 8. It can be seen that the one-vortex structure in Fig. 4(a) breaks into two counter-rotating vortices at the much higher Reynolds number. The inertia-driven vortex is pushed toward the sidewall with the vortex center shifted upward. This breakdown phenomenon at the high Reynolds number qualitatively agrees with the experiment [1]. In the experiment the Reynolds number is higher and the inertial vortex is pushed further upward and outward. Both the numerical simulation and experiment show that the strength of the inertia-driven vortex is much stronger than the counter-rotating vortex.

(3) Effect of Froude number: Froude number is defined as the ratio of inertial force to gravitational force. It is found that the Froude number does not change the flow pattern, but greatly affects the free surface. The dip of the free surface shape decreases with the decrease of the Froude number as shown in Fig. 9. This indicates that the gravity can effectively prevent deformation of the free surface when it is much larger than the inertial and elastic forces.

(4) Effect of viscosity ratio β: Kawaguchi et al. [19] show that the larger the concentration of the CTAC solution, the larger the apparent shear viscosity and relaxation time. In section (1) we described the effect of relaxation time (Weissenberg number); in this section, the effect of viscosity due to surfactant additives is described. By increasing the viscosity ratio β from 1.0 to 3.0, the secondary flow [Fig. 4(c)] is significantly weakened, as shown in Fig. 10. The free surface shape completely changes as the dip of the free surface near the axis becomes a bulge. The azimuthal velocities are also suppressed (not shown). It can be seen that the increase of the viscosity ratio is somewhat equal to the increase of the Weissenberg number.

(5) Effect of mobility factor on the flow pattern and surface shape: Figure 11 shows the flow motions at different mobility factors. It is seen that mobility factor also greatly affects the flow pattern and dip height. For a mobility factor α=0.01, the dip height is smaller than that of Newtonian fluid; with the decrease of mobility factor the dip height decreases, and a bulge is reproduced near the axis at α=0. The flow patterns at α=0.01 and α =0.003 are respectively similar to those of Figs. 4(c) and 4(d). This indicates that the increase of mobility factor is somewhat equivalent to a decrease of elasticity.

Figure 12 shows the evolution of the minimal tangential velocity starting from the stop of the rotating disk. For small elasticity We=0.1, though there is an opposite flow at the very beginning after the stop, it lasts very short time. Actually the opposite flow occurs only in the region very near the bottom disk and soon vanishes. The larger the Weissenberg number, the larger the minimal tangential velocity (absolute value) and the recoil process lasts a longer period. Figure 12 also shows that the increase of the mobility factor suppresses the recoil process. A recoil process at Re=100, We=1.0, Fr=100, β=1, α=0.003, and a=1.0 is shown in Fig. 13. It is seen that the opposite flow first occurs in the near wall region and then it spreads to most of the fluid region. When the rotating disk stops, the velocity gradient $\partial u_\theta/\partial z$ at the bottom disk changes from negative value to positive value which makes an abrupt change of $(\beta/\mathrm{Re})(\partial\tau_{\theta z}/\partial z)$. Due to the change of the elastic stress, recoil flow first occurs in the region near the bottom disk.

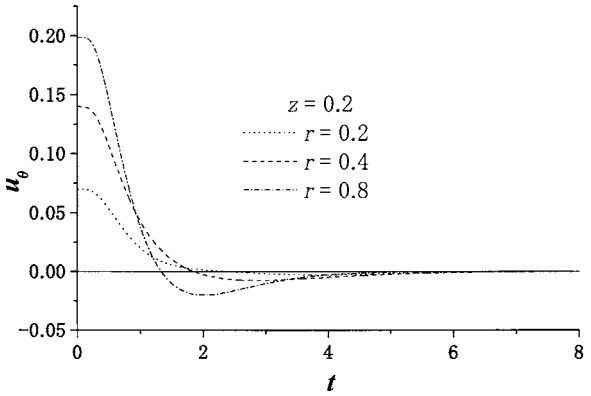

Fig. 14 The evolution of the tangential velocities at different radial position after the stop of the rotating disk at Re=100, We=1, Fr=100, β=1, α=0.003, and a=1.0

Figures 14 and 15 respectively show the evolution of tangential velocities at different radial and axial positions. It is seen clearly that the swirl decay time (SDT) differs greatly with respect to positions, while in the experiments a SDT almost independent of locations is found [1]. The almost constant SDT in the experiments means the spread of the recoil process from bottom disk to entire flow region is very fast. The different SDT feature is quite probably due to the effect of Reynolds number, etc.

Finally, we summarize the relationship between the DR rate, Quelleffekt, recoil process, and rheological properties in Fig. 16. The present numerical simulations and previous direct numerical simulation (DNS) results [25–27] show that Quelleffect and recoil process and drag-reduction rate are strongly dependent on the

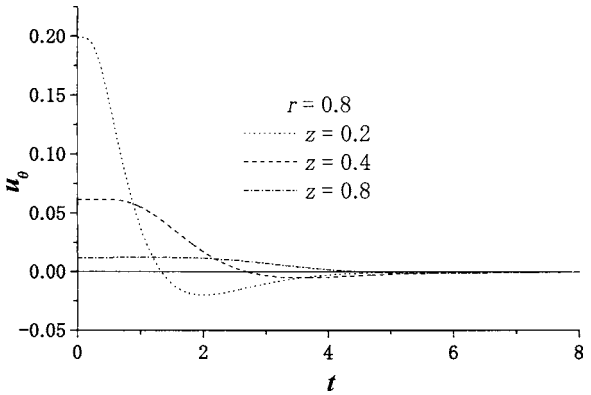

Fig. 15 The evolution of the tangential velocities at different axial position after the stop of the rotating disk at Re=100, We=1, Fr=100, β=1, α=0.003, and a=1.0

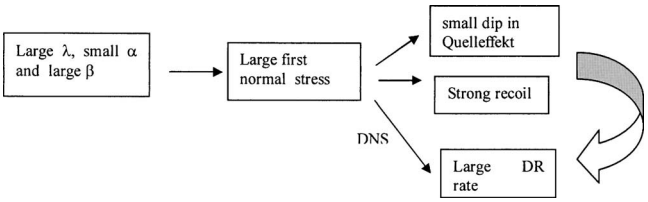

Fig. 16 The relationship between rheological parameters and Quelleffekt, recoil, and drag reduction rate

rheological parameters of the solution. The present numerical tests have shown that generally the larger the relaxation time, the smaller the mobility factor, and the larger the β value, the smaller the dip height. On the other hand, DNS results [25–27] show that the larger the elasticity, the smaller the mobility factor, and the larger the β value, the larger the drag-reduction (DR) rate. Therefore a preliminary judgment can be made that the smaller the dip height, the larger the DR ability. This is in agreement with the report of Wei et al. [1] which experimentally found that the DR rate is related to the dip height; the onset of drag-reduction occurs after a critical dip height. We can also connect DR rate with the recoil process. Generally the stronger the recoil motion, the larger DR capability the solution may possess.

Conclusion

Numerical simulations were performed for the swirling flows of Newtonian and viscoelastic fluids in a cylindrical vessel with a rotating disk at the bottom. The MAC method was extended to axisymmetric swirling viscoelastic flows. The effect of Weissenberg number, Reynolds number, Froude number, surfactant-induced viscosity, and mobility factor were systematically studied. The primary conclusions are summarized as follows. The MAC method can successfully solve axisymmetric viscoelastic flows. The experimentally observed vortex breakdown of Newtonian flow at a large Reynolds number is validated by numerical simulation. The flow pattern and surface shape are greatly dependent on the balance between inertial force, elastic force, and gravity. Elasticity weakens both the primary and secondary flows and makes the boundary thinner, which qualitatively agrees with the experimental results. With the increase of elasticity, the dip of the free surface near the axis decreases and for highly elastic fluid a bulge is generated. For small inertial and elastic forces, gravity can counteract both the inertial motion and elastic motion, thus preventing surface deformation. The dip height can be utilized to preliminarily judge the DR capability of a surfactant solution.

Acknowledgment

This study was supported by the Ministry of Education, Culture, Sports, Science and Technology, through the project "Smart Control of Turbulence: A Millennium Challenge for Innovative Thermal and Fluids Systems, Japan."

Nomenclature

a = aspect ratio$=H/R$
E = elasticity number$=\lambda\mu/\rho R^2$
Fr = Froude number$=\omega^2 R/g$
g = gravitational constant, m/s^2
H = height of fluid in cylindrical vessel at static state, m
m = local unit tangential vector
n = local unit normal vector
p = pressure, Pa
r = radial coordinate
t = time, s
R = radius of the cylindrical vessel radius of the rotating disk, m
Re = Reynolds number$=\rho\omega R^2/\mu$
u = velocity (m/s)
We = Weissenberg number$=\lambda\omega$
z = axial coordinate

Greek Symbols

α = mobility factor
β = viscosity ratio$=\eta/\mu$
η = dynamic viscosity of surfactant contribution, Pa s
λ = relaxation time, s
μ = dynamic shear viscosity of solvent, Pa s
θ = tangential coordinate
ρ = density of the solution, kg/m^3
σ = stress tensor
τ = extra stress due to surfactant
ω = angular velocity, 1/s

References

[1] Wei, J. J., Li, F. C., Yu, B., and Kawaguchi, Y., 2006, "Swirling Flow of a Viscoelastic Fluid With Free Surface, Part I, Experimental Analysis of Vortex Motion by PIV," ASME J. Fluids Eng., **128**, pp. 69–76.
[2] Bohme, G., Voss, R., and Warnercke, W., 1985, "Die Frei Obserflache Einer Flussigkeit Uber Einer Riiterenden Scheibe," Rheol. Acta, **24**, pp. 22–23.
[3] Debbaut, B., and Hocq, B., 1992, "On The Numerical Simulation of Axisymmetric Swirling Flows of Differential Viscoelastic Liquids: The Rod-Climbing Effect and the Quelleffekt," J. Non-Newtonian Fluid Mech., **43**, pp. 103–126.
[4] Xue, S. C., Phan-Thien, N., and Tanner, R. I., 1999, "Fully Three-Dimensional Time-Dependent Numerical Simulations of Newtonian and Viscoelastic Swirling Flows in a Confined Cylinder, Part I. Method and Steady Flows," J. Non-Newtonian Fluid Mech., **87**, pp. 337–367.
[5] Siginer, A., 1984, "General Weissenberg Effect in Free Surface Rheometry, Part I: Analytical Consideration," ZAMP, **35**, pp. 545–558.
[6] Siginer, A., 1984, "General Weissenberg Effect in Free Surface Rheometry, Part II: Experiments," ZAMP, **35**, pp. 618–633.
[7] Siginer, A., 1984, "Free Surface on a Simple Fluid Between Rotating Eccentric Cylinders, Part I: Analytical Solution," J. Non-Newtonian Fluid Mech., **15**, pp. 93–108.
[8] Siginer, A., and Beavers, G. S., 1984, "Free Surface on a Simple Fluid Between Rotating Eccentric Cylinders. Part II: Experiments," J. Non-Newtonian Fluid Mech., **15**, pp. 109–126.
[9] Siginer, D. A., 1986, "Torsional Oscillations of a Rod in a Layered Medium of Simple Fluids," Int. J. Eng. Sci., **24**, pp. 631–640.
[10] Siginer, D. A., 1989, "Free Surface on a Viscoelastic Liquid in a Cylinder With Spinning Bottom," Macromol. Chem., **23**, pp. 73–90.
[11] Siginer, A., 1991, "Viscoelastic Swirling Flow With Free Surface in Cylindrical Chambers," Rheol. Acta, **30**, pp. 159–174.
[12] Siginer, D. A., and Knight, R. W., 1993, "Swirling Free Surface Flow in Cylindrical Containers," J. Eng. Math., **27**, pp. 245–264.
[13] Siginer, D. A., 2004, "On the Nearly Viscometric Torsional Motion of Viscoelastic Liquids Between Shrouded Rotating Disks," ASME J. Appl. Mech., **71**, pp. 305–313.
[14] Nichols, B. D., and Hirt, C. W., 1971, "Calculating Three-Dimensional Free Surface Flows in the Vicinity of Submerged and Exposed Structures," J. Comput. Phys., **12**, p. 234.
[15] Nichols, B. D., and Hirt, C. W., 1975, "Methods for Calculating Multidimensional, Transient Free Surface Flows Past Bodies," Proc. of the First International Conf. On Num. Ship Hydrodynamics, Gaithersburg, MD, Oct. 20–23.
[16] Hirt, C. W., and Nichols, B. D., 1981, "Volume of Fluid Method For the Dynamics of Free Boundaries," J. Comput. Phys., **39**, p. 201.
[17] Koren, B., Lewis, M. R., van Brummelen, E. H., van Leer, B., 2002, "Riemann-Problem and Level-Set Approaches for Homentropic Two-Fluid Flow Computations," J. Comput. Phys., **181**, pp. 654–674.
[18] Tomes, M. F., Mangiavacchi, N., Cuminato, J. A., Castelo, A., and McKee, S., 2002, "A Finite Difference Technique for Simulating Unsteady Viscoelastic Free Surface Flows," J. Non-Newtonian Fluid Mech., **106**, pp. 61–106.
[19] Kawaguchi, Y., Wei, J. J., Yu, B., and Feng, Z. P., 2003, "Rheological Characterization of Drag-Reducing Cationic Surfactant Solution: Shear and Elongational Viscosities of Dilute Solution," in Proc. of the 4th ASME/JSME Joint Fluids Engineering Conference, Honolulu, Hawaii.
[20] Giesekus, H., 1982, "A Simple Constitutive Equation for Polymer Fluids Based on the Concept Deformation-Dependent Tensorial Mobility," J. Non-Newtonian Fluid Mech., **11**, pp. 69–109.
[21] Phillips, T. N., and Williams, A. J., 2002, "Comparison of Creeping and Inertial Flow of an Oldroyd B Fluid Through Planar and Axisymmetric Contractions," J. Non-Newtonian Fluid Mech., **108**, pp. 25–47.
[22] Hill, C. T., 1972, "Nearly Viscometric Flow of Viscoelastic Fluids in the Disk and Cylindrical Geometry, II: Experimental," Trans. Soc. Rheol., **16**, pp. 213–245.
[23] Stokes, J. R., Grahan, L. J. W., Lawson, N. J., and Boger, D. V., 2001, "Swirling Flow of Viscoelastic Fluids. Part I, Interaction Between Inertia and Elasticity," J. Fluid Mech., **429**, pp. 67–115.
[24] Bird, R. B., Armstrong, R. C., and Hassager, O., 1987, *Dynamics of Polymer Liquids, Volume 1, Fluid Mechanics*, John Wiley & Sons, Inc., New York, pp. 64–65.
[25] Dimitropoulos, C. D., Sureshkumar, R., and Beris, A. N., 1998, "Direct Numerical Simulation of Viscoelastic Turbulent Channel Flow Exhibiting Drag-Reduction: Effect of the Variation of Rheological Parameters," J. Non-Newtonian Fluid Mech., **79**, pp. 433–468.
[26] Yu, B., and Kawaguchi, Y., 2003, "Effect of Weissenberg Number on the Flow Structure: DNS Study of Drag-Reducing Flow With Surfactant Additives," Int. J. Heat Fluid Flow, **24**, pp. 491–499.
[27] Yu, B., and Kawaguchi, Y., 2004, "Direct Numerical Simulation of Viscoelastic Drag-Reducing Flow: A Faithful Finite Difference Method," J. Non-Newtonian Fluid Mech., **116**, pp. 431–466.

Swirling Flow of a Viscoelastic Fluid in a Cylindrical Casing

Motoyuki Itoh
Department of Mechanical Engineering,
Nagoya Institute of Technology,
Gokiso-cho, Showa-ku,
Nagoya, 466-8555, Japan

Masahiro Suzuki

Takahiro Moroi

Toyota Industries Corporation,
Kariya, Japan

The swirling flow of a viscoelastic fluid in a cylindrical casing is investigated experimentally, using aqueous solutions of 0.05–1.0 wt. % polyacrylamide as the working fluid. The velocity measurements are made using laser Doppler anemometer. The aspect ratios H/R (H: axial length of cylindrical casing; R: radius of rotating disk) investigated are 2.0, 1.0, and 0.3. The Reynolds numbers Re_0 *based on the zero shear viscosity and the disk-tip velocity are between 0.36 and 50. The velocity measurements are mainly conducted for the circumferential velocity component. The experimental velocity data are compared to the velocity profiles obtained by numerical simulations using Giesekus model and power-law model. It is revealed that at any aspect ratios tested the dimensionless circumferential velocity component* V'_θ *decreases with increasing Weissenberg number We. Both the Giesekus and power-law models could predict the retardation of circumferential velocity fairly well at small We. The extent of the inverse flow region, where the fluid rotates in the direction opposite to the rotating disk, is clarified in detail.*
[DOI: 10.1115/1.2136925]

Keywords: viscoelastic fluid, rotating disk, flow visualization, LDV, power-law model, Giesekus model

Introduction

The confined swirling flows of viscoelastic fluids are commonly encountered in process engineering industries. There have been many investigations concerning the swirling flow of viscoelastic fluids induced by the rotation of a disk in a cylindrical casing. One of the earliest experimental works was performed by Hill [1], and recently, Day et al. [2], Escudier and Cullen [3], Stokes and Boger [4], and Stokes et al. [5,6] have published comprehensive experimental studies. Theoretical or numerical calculations for these flows have also been conducted by using a variety of rheological models [7–10].

The present authors have studied this flow field by applying flow visualization techniques and numerical simulations [11–14]. A good agreement was obtained between the simulation results and experimental ones within a range of relatively small Weissenberg numbers. Moreover, it was found that, when the elasticity number was large, the fluid in the vicinity of the central axis was rotating in the direction opposite to that of the rotating disk. Since the velocity measurements in our previous experiments were conducted using particle tracking velocimetry with a relatively thick (3–5 mm) slit light source, the precise velocity distributions could not be determined at the region of large velocity gradient (near the rotating disk).

In the present work, velocity measurements using a laser Doppler velocimeter (LDV) were carried out to provide experimental data that would be useful for the validation of various constitutive equations. Comparison was made between the experimental and calculated results using the Giesekus and power-law models. Furthermore, the structures of reverse flows near the central axis were closely examined.

Experimental Apparatus and Procedure

The experimental apparatus used in the present work is shown in Fig. 1. The main body consists of a rotating disk enclosed in a casing. The surface of the rotating disk is smooth, and the outside diameter of the disk is 180 mm (R=90 mm). The disk is painted black to reduce the effect of reflected light. The distance H between the casing end wall and the rotating disk can be changed by adjusting the thickness of the disk, and the aspect ratio H/R was set at 0.3, 1.0, and 2.0. The disk is driven by a motor and decelerator with an inverter control. The clear acrylic casing is cylindrical with an inner diameter of 181 mm. The exterior is rectangular, with a length on one side of 215 mm, to minimize the effect of light refraction while observing cross sections.

Aqueous solutions of 0.025–1.0 wt. % polyacrylamide (Sanfloc AH70P, molecular weight of two to four million, Sanyo Kasei Kogyo, Ltd.) were used as the working fluid. Measurements of the shear viscosity η and the first normal stress difference $N1$ of the working fluid were conducted using a cone-and-plate-type viscometer (Tokimec, Visco-Eld, cone angle 1.34 deg, radius 24.0 mm) and cone-and-plate-type rheometer (Rheology, MR-500, cone angle 2.04 deg, radius 20.0 mm). The uncertainty intervals of the data for η and $N1$ are 5% and 7%, respectively, of their absolute values.

Velocity measurements were made with a four-beam two-color LDV system manufactured by KANOMAX Japan Inc. The light source was an Argon laser with an output power of 300 mW. Two Bragg acoustic-optic cells were used to shift the frequency of the light beams. The LDV system was of backscattered fringe mode. The size of the measuring volume was 74 μm dia and 0.89 mm in length. Signal processing was performed by digital signal processors (KANOMAX 8007-IBM). A fiber probe with a focusing distance of 300 mm was mounted on a three-dimensional traversing mechanism with the accuracy of 0.01 mm. The test fluids were seeded with nylon powder (particle diameter 4.15 μm, density 1.02 g/cm^3). The accuracy of the velocity measurements has been checked by comparing the experimental data for a Newtonian fluid (90 wt. % glycerol in water) with results from a numerical simulation for the Newtonian fluid.

The uncertainty for the velocity data is estimated to be ±0.01 for the nondimensional velocity components V'_r, V'_θ, and V'_z.

Numerical Simulation

Numerical simulations were made for the swirling flow of viscoelastic fluid in a cylindrical casing with a radius R and height H when the lower surface (disk) of the casing rotates at a constant

Contributed by the Fluids Engineering Division of ASME for publication in the JOURNAL OF FLUIDS ENGINEERING. Manuscript received July 27, 2004; final manuscript received October 4, 2005. Assoc. Editor: Dennis Siginer.

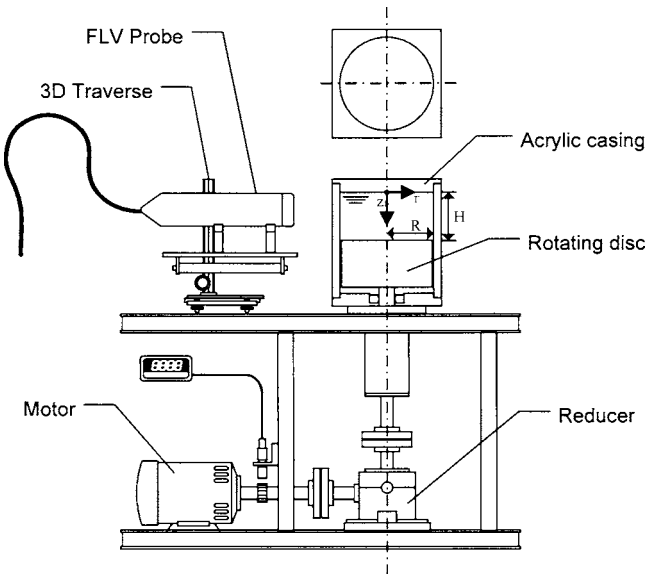

Fig. 1 Experimental apparatus

angular velocity Ω, as shown in Fig. 2. Assuming that the flow is incompressible and axially symmetric, we have the following dimensionless equation of motion (1) and the continuity equation (2):

$$D\mathbf{v}'/Dt' = -\nabla p' + \nabla \cdot \boldsymbol{\tau}' \tag{1}$$

$$\nabla \cdot \mathbf{v}' = 0 \tag{2}$$

where $\mathbf{v}'$ is the velocity vector, p' the pressure, t' the time, and $\boldsymbol{\tau}'$ is the deviatoric stress tensor. The dimensionless values are defined as follows: $\mathbf{v}'=\mathbf{v}/R\Omega$, $\boldsymbol{\tau}'=\boldsymbol{\tau}/\rho(R\Omega)^2$, $p'=p/\rho(R\Omega)^2$, and $t'=t\Omega$.

The power-law model [15] and the Giesekus model [16], as shown in Eqs. (3) and (4), respectively, were used as the constitutive equations

$$\boldsymbol{\tau}' = \left(\frac{1}{\mathrm{Re}}\right)\left(\frac{|2\mathbf{D}'|^2}{2}\right)^{(n-1)/2} \cdot 2\mathbf{D}' \tag{3}$$

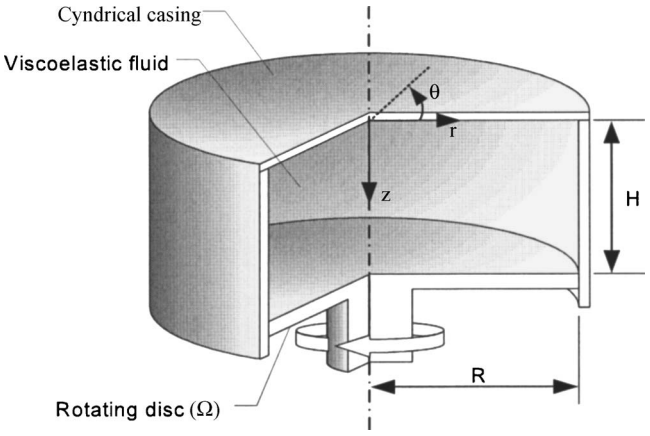

Fig. 2 Disk and cylinder system

$$\boldsymbol{\tau}' + \mathrm{We}\,\overset{\nabla}{\boldsymbol{\tau}}' + \alpha\,\mathrm{Re}_0\mathrm{We}\,\boldsymbol{\tau}'^2 = \left(\frac{2}{\mathrm{Re}_0}\right)\mathbf{D}' \tag{4}$$

where $\mathbf{D}'$ is the rate-of-strain tensor, Re the modified Reynolds number ($\mathrm{Re}=\rho R^n(R\Omega)^{2-n}/K$, $\mathrm{Re}_0=\rho R^2\Omega/\eta_0$) and We the Weissenberg number ($\mathrm{We}=\lambda_G\Omega$):

$$\overset{\nabla}{\boldsymbol{\tau}}' = \frac{D\boldsymbol{\tau}'}{Dt'} - (\nabla\mathbf{v}')^t \cdot \boldsymbol{\tau}' - \boldsymbol{\tau}' \cdot (\nabla\mathbf{v}') \tag{5}$$

is the upper-convected derivative of the stress tensor $\boldsymbol{\tau}'$. α is the mobility factor. In this study, we assumed $\alpha=0.1$. The power-law model does not consider the influence of elasticity, but shows the shear-thinning viscosity in which the apparent shear viscosity decreases with increasing shear rate. The Giesekus model was derived from a molecular model of a Hookean dumbbells with a nonlinear stress term related to anisotropic hydrodynamic drag.

In order to solve Eqs. (1)–(5), numerically, we used a finite-difference method. A staggered grid system in which the locations of definition for normal stress components are the same as those of pressure was used. The velocity components and pressure were solved with the SMAC (simplified marker and cell) method. The Euler explicit scheme and the elastic viscous split stress (EVSS) method [17,18] as in the following equation (6) were applied to Eq. (4) in order to solve the stress tensor:

$$\boldsymbol{\tau}' = \boldsymbol{\xi}' + \boldsymbol{\sigma}' \tag{6}$$

$$\boldsymbol{\xi}' = 2\mathbf{D}'\mathrm{Re}_0 \tag{7}$$

where $\boldsymbol{\xi}'$ is the viscous stress and $\boldsymbol{\sigma}'$ is the elastic stress. $\boldsymbol{\xi}'$ is calculated by Eq. (7), and then $\boldsymbol{\sigma}'$ is calculated by the constitutive equation (4).

The axial symmetric condition for the rotating axis and the no-slip condition for all the wall surfaces were applied as the boundary conditions. When the calculations for large We were carried out, the results for small We were used as initial values to stabilize the calculation. The details of the numerical calculations were reported in our previous paper [11].

Results and Discussion

Rheological Properties of Fluids. The shear viscosity η and the first normal stress difference *N1* for the working fluids were measured using a viscometer and a rheometer. The representative results obtained are shown in Fig. 3 for the aqueous solution of 1.0 wt. % polyacrylamide (PAA). In the figures, the lines of the power-law and Giesekus models are drawn for reference. As can be known from the figures, the power-law model could not represent the measured shear viscosity well at low shear rate, and the Giesekus model gives too low a shear viscosity at high shear rate. On the other hand, the measured *N1* values could be represented fairly well by the Giesekus model. The shear viscosity η was measured for all PAA solutions used in the present experiment, but the first normal stress differences, *N1* for 0.025 and 0.05 wt. % PAA solutions were too small to determine accurately. The relaxation times λ_G for these PAA solutions, therefore, were estimated by extrapolating the data for PAA solutions of higher concentrations, as shown in Fig. 4. It was confirmed that the shear viscosity and the first normal stress difference changed hardly before and after a test run, indicating no appreciable degradation of the working fluid during a test run.

Secondary Flow Patterns. Before proceeding to the presentation of the results concerning the velocity field, it may be appropriate to illustrate the flow regime diagram for identifying the flow pattern in which the velocity field is to be examined. Figures 5 and 6 show the flow regime diagrams in which the patterns of secondary flow in the meridional section (r-z plane) are classified based on the visual observations [13,14].

Figure 5 shows the secondary flow patterns for a large aspect ratio ($H/R=2$). In Fig. 5(a), the typical secondary flow patterns

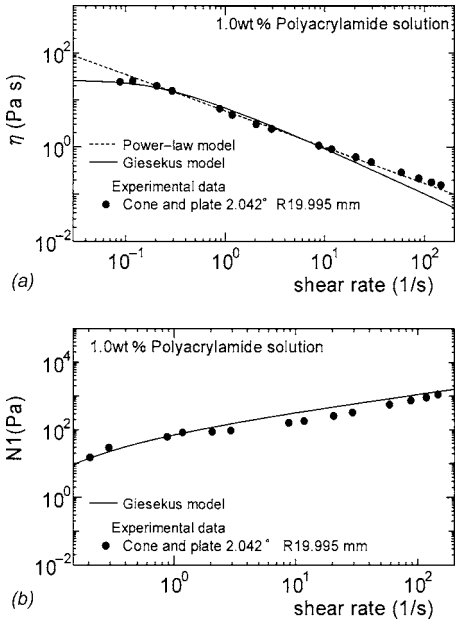

Fig. 3 Rheological characteristics of the working fluid: (*a*) shear viscosity and (*b*) first normal stress difference

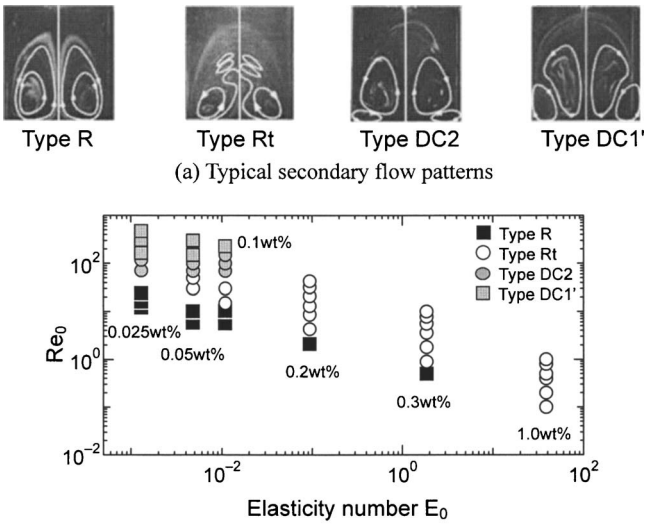

Fig. 5 Secondary flow patterns for a large aspect ratio $H/R=2.0$: (*a*) typical secondary flow patterns and (*b*) secondary flow patterns for various E_0 and Re_0

observed for this aspect ratio are illustrated. The parametric ranges over which the respective secondary flow patterns were observed are shown in Fig. 5(*b*), where Re_0 ($=\rho R^2\Omega/\eta_0$) is the Reynolds number and E_0 ($=We/Re_0=\lambda_G\eta_0/\rho R^2$) is the elasticity number. The elasticity number is a measure of the ratio of the elastic force to the inertial (centrifugal) force acting on the working fluid. When E_0 is relatively small as with 0.05–0.10 wt. % PAA solutions, the changes in the secondary flow patterns with increasing Re_0 are as follows. At the lowest Re_0, the structure in which the flow direction is opposite to that of a Newtonian fluid is observed (type R). The secondary flow direction changes to one opposite to a Newtonian fluid and in an unsteady state in the vicinity of the central axis (type Rt), then to a double-cell structure in which the two cells are aligned vertically in the axial direction (type DC2), and finally to a double-cell structure in which the two cells are aligned laterally in the radial direction (type DC1′).

Figure 6 shows the secondary flow patterns for a small aspect ratio ($H/R=0.3$). The typical secondary flow patterns are illustrated in Fig. 6(*a*). For these small aspect ratios, the structure of the secondary flow changes with increasing Re_0, first into a structure in which the flow direction is opposite to that of a Newtonian fluid (type R), then to a double-cell structure with the two cells aligned in the radial direction (type DC1), and finally to a structure (type N) in which the flow is in the same direction as with a Newtonian fluid. The direction of flow circulation for this type DC1 differs from that of the type DC1′ in Fig. 5(*a*).

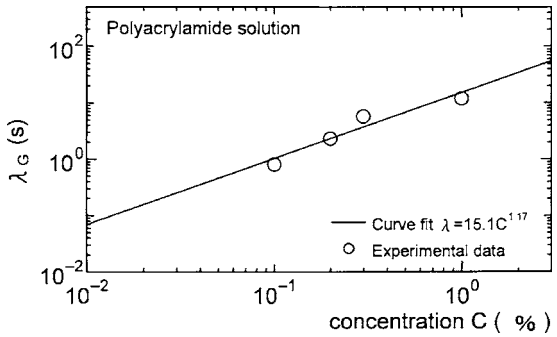

Fig. 4 Relaxation time λ_G

Velocity Distributions. Velocity measurements were made using a laser Doppler anemometer for the Reynolds numbers of $0.36<Re_0<50$. Figures 7 and 8 show the velocity profiles of circumferential component V'_θ ($=V_\theta/r\Omega$) measured at two different radial positions for the Reynolds number $Re_0=5.8$ and 50, respectively, with the aspect ratio $H/R=2$. In the figures, the experimental data for aqueous solutions of 0.05–0.2 wt. % PAA are compared to those obtained by numerical simulations for the Newtonian fluid (dashed lines). Although the secondary flow pattern was type Rt at these Reynolds numbers, velocity fluctuations were hardly detected at the radial positions shown in the figures. It can be known from Figs. 7 and 8 that the profile of V'_θ becomes more decelerated with increasing the concentration of PAA solu-

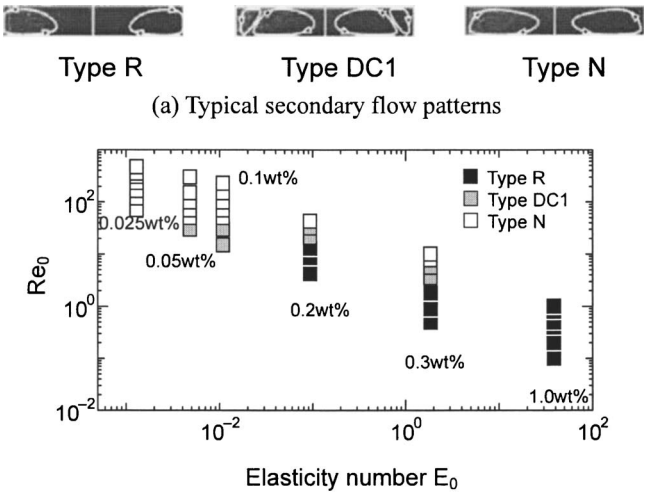

Fig. 6 Secondary flow patterns for a small aspect ratio $H/R=0.3$: (*a*) typical secondary flow patterns and (*b*) secondary flow patterns for various E_0 and Re_0

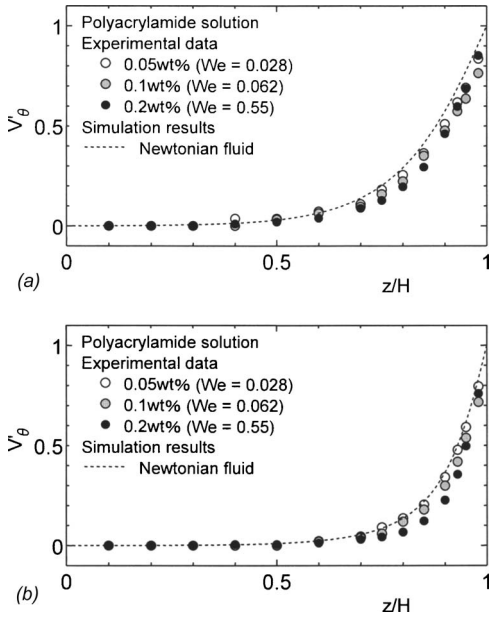

Fig. 7 Profiles of circumferential velocity component (Re_0 =5.8, H/R=2.0): (*a*) r/R=0.5 and (*b*) r/R=0.8

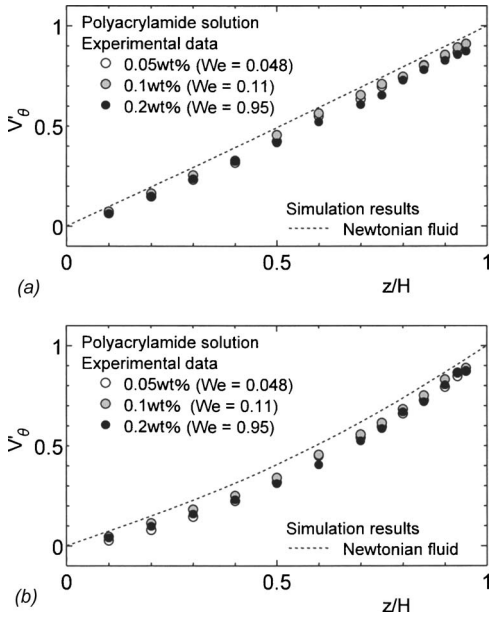

Fig. 9 Profiles of circumferential velocity component (Re_0 =10, H/R=0.3): (*a*) r/R=0.5 and (*b*) r/R=0.8

tion, i.e., increasing the Weissenberg number We. At Re_0=50, the velocity profiles for 0.2 wt. % PAA solution differ significantly from those for the other solutions, especially at r/R=0.5.

The velocity profiles measured for a small aspect ratio H/R =0.3 are shown in Figs. 9 and 10 for Re_0=10 and 50, respectively. It is noted in the figures that the velocity profiles for the PAA solutions vary in the same manner as in Figs. 7 and 8. At this aspect ratio, however, the velocity profiles for 0.2 wt. % PAA solution do not show so much difference from others even at high Reynolds numbers of Re_0=50.

Figure 11 shows the distributions of radial (V'_r), circumferential (V'_θ) and axial (V'_z) velocity components for 1.0 wt. % PAA solution at H/R=1.0 and Re_0=0.36, where all the velocity components are normalized with the disk tip velocity (=$R\Omega$). In the figures, calculated results for Newtonian fluid are also shown for comparison. The type of secondary flow patterns for Fig. 11 was observed to be type Rt of Fig. 5(*a*). It should be mentioned that the measured velocity data were little affected by the unsteady fluid motion near the central axis, i.e., velocity fluctuations were not detectable in the time series of velocity data. The direction of the secondary flow is opposite that for Newtonian fluid, i.e., radially inward along the rotating disk, axially upward near the rotation axis, and axially downward along the cylindrical wall. It is well known that the radial inward flow near the rotating disk is due to the normal stress difference. The magnitude of these velocity components reaches to as large as around 4% of the disk tip speed. It should be remarked that the magnitude of V'_r and V'_z is

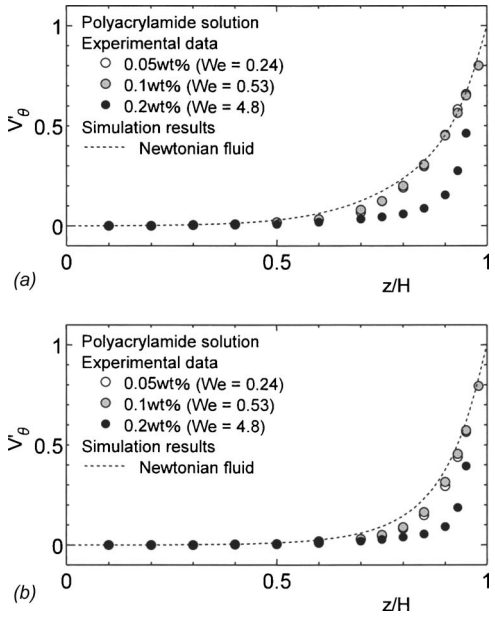

Fig. 8 Profiles of circumferential velocity component (Re_0 =50, H/R=2.0): (*a*) r/R=0.5 and (*b*) r/R=0.8

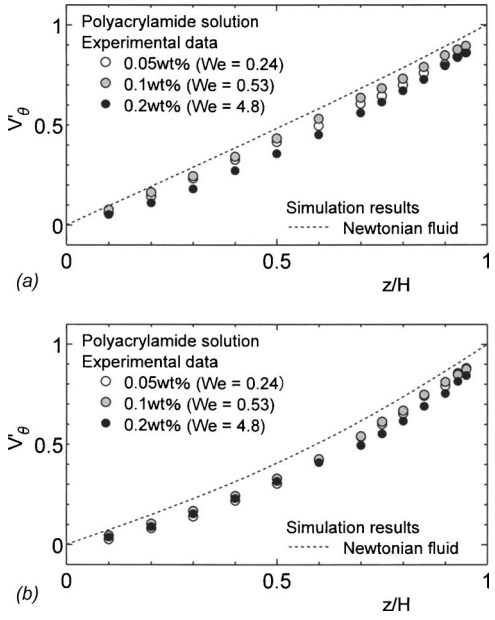

Fig. 10 Profiles of circumferential velocity component (Re_0 =50, H/R=0.3): (*a*) r/R=0.5 and (*b*) r/R=0.8

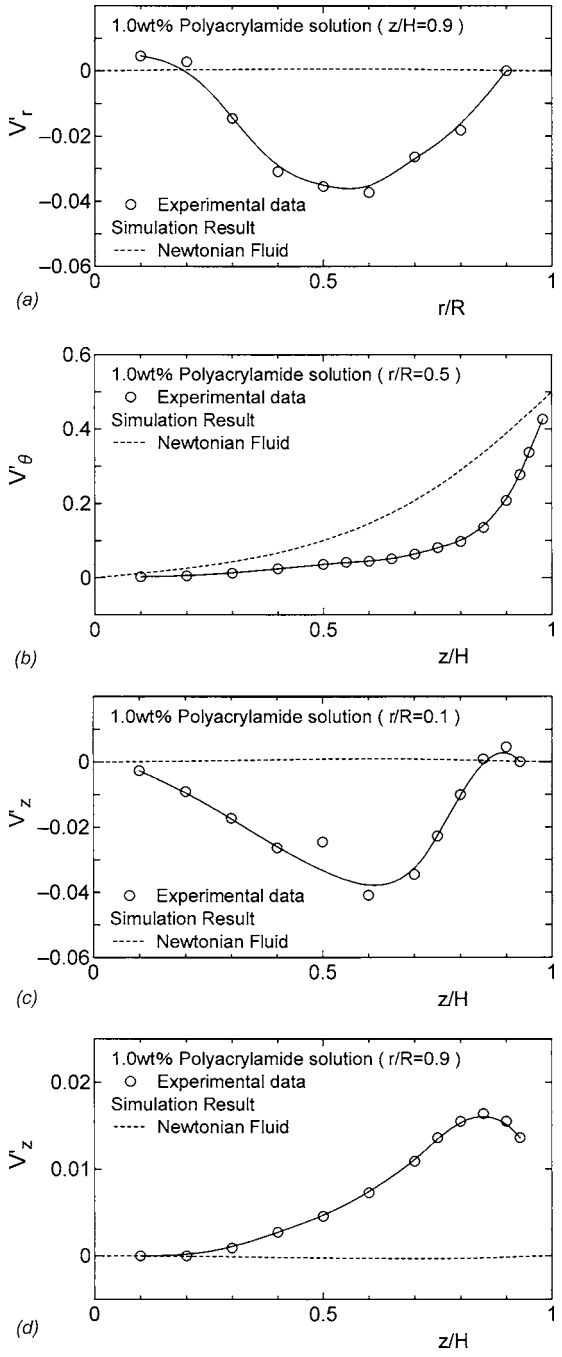

Fig. 11 Velocity distributions for 1.0 wt. % PAA solution (Re_0 =0.36, We=13.7, H/R=1.0): (*a*) radial component V'_r, (*b*) circumferential component V'_θ, (*c*) axial component V'_z, and (*d*) axial component V'_z

much larger for 1.0 wt. % PAA solution than that for the Newtonian fluid. This means that at these small Reynolds numbers the secondary flow due to elastic effects is much stronger than that generated by centrifugal effects. The circumferential velocity component V'_θ is found to be much decelerated, especially at the outer radial position r/R=0.8, compared to that for the Newtonian fluid.

The velocity vectors measured in the meridional plane are shown in Fig. 12. The secondary flow of which direction is opposite to that produced by the centrifugal effect is clearly demonstrated in the figure. The center of the secondary flow circulation is around r/R=0.65 and z/H=0.75.

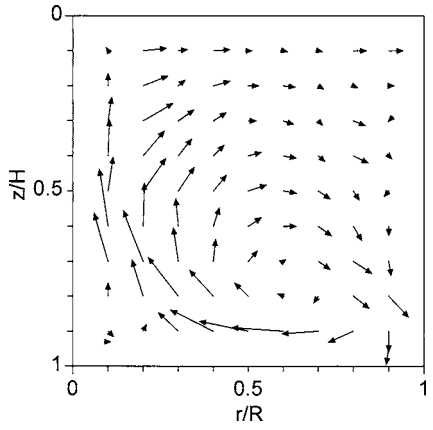

Fig. 12 Secondary flow in the meridional section (1.0 wt. % PAA solution, Re_0=0.36, We=13.7, H/R=1.0)

In Fig. 13, the V'_θ distributions obtained by numerical simulations using the power-law model and the Giesekus model as the constitutive equations are compared to the experimental ones at H/R=1.0. When the Reynolds number Re_0=10 and the Weissenberg number We=0.048 (Fig. 13(*a*)), the calculated V'_θ profiles using the power-law model and the Giesekus model are both in good agreement with the experimental one. At a higher Weissenberg number (We=0.24) as shown in Fig. 13(*b*), however, these two models give too small values for V'_θ near the rotating disk. Considering the fact that the V'_θ profile obtained by using the power-law model becomes more decelerated with increasing We, it is deduced that one of the causes for the decrease of V'_θ with increasing We is the shear-thinning effect of the test fluid, because the power-law model incorporates only the shear-thinning effect.

In our previous experiment [13], a strange phenomenon was observed in which the direction of flow in the r-θ plane was opposite to that of the rotating disk. In the present study, we performed detailed measurements with respect to the circumferential velocity component in order to clarify the flow structure.

Figure 14 shows the domain of unsteady flow for 0.3 wt. %

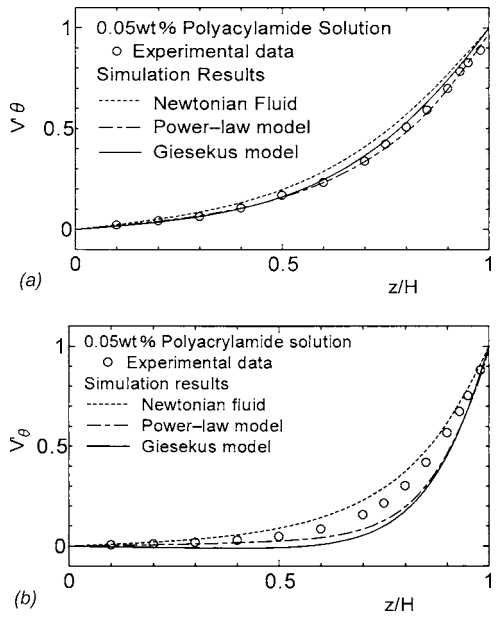

Fig. 13 Comparison of velocity profiles between experiments and numerical simulations (H/R=1.0): (*a*) Re_0=10, We =0.048, r/R=0.5 and (*b*) Re_0=50, We=0.24, r/R=0.8

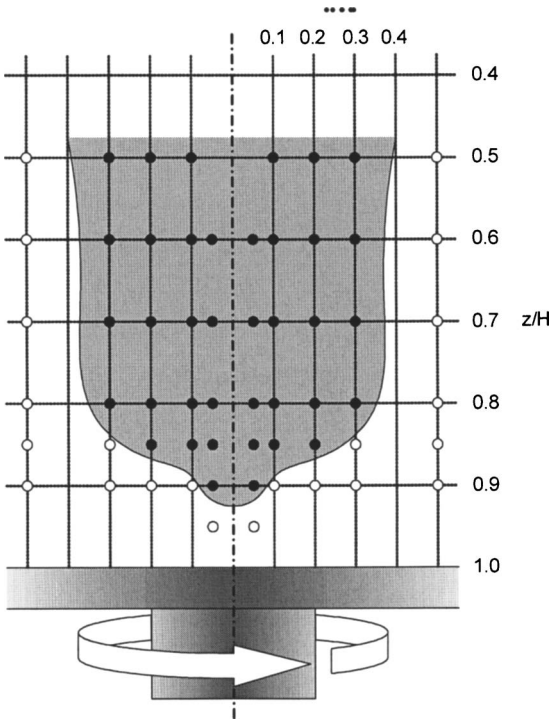

Fig. 14 Structure of unsteady flow region (0.3 wt. %, Re_0 =5.8, We=10.8, H/R=2.0)

PAA solution at H/R=2.0 and Re_0=5.8. The symbol ● in the figure shows the measured points where periodical oscillations were observed in the time series of velocity data, and the symbol ○ represents the steady flow region. It can be known that the periodical velocity fluctuation is caused by the spiral instability [5] in the vicinity of the central axis (type Rt in Fig. 5). In this case, the reverse flow in the r-θ plane has been observed temporally at the region of r/R=0.05–0.5 and z/H=0.5–0.9.

On the other hand, in the case shown in Fig. 15 where the working fluid is 1 wt. % PAA solution and Re_0=0.36, continuous reverse flows in the r-θ plane were observed in the region near the central axis. In the figure, the symbol ● shows the measured points where the continuous reverse flows were observed, the symbol ○ shows the steady fluid motion in the same direction as that of the rotating disk, and the gray circle indicates the point where the working fluid is almost at rest. The maximum value of the reverse flow reaches about V'_θ=0.05. The extent of the striped zone in the figure shows a lump of fluid rotating like a solid body glued on the disk. The reverse flow in Fig. 15 may be explained by the elastic recoil effect of the working fluid. Thus, it is plausible that the tangential force acting on the fluid diminishes rapidly when the fluid moves away from near the rotating disk in the vicinity of the central axis, so that the elastic recoil effect may drive the fluid in the direction opposite to that of the rotating disk.

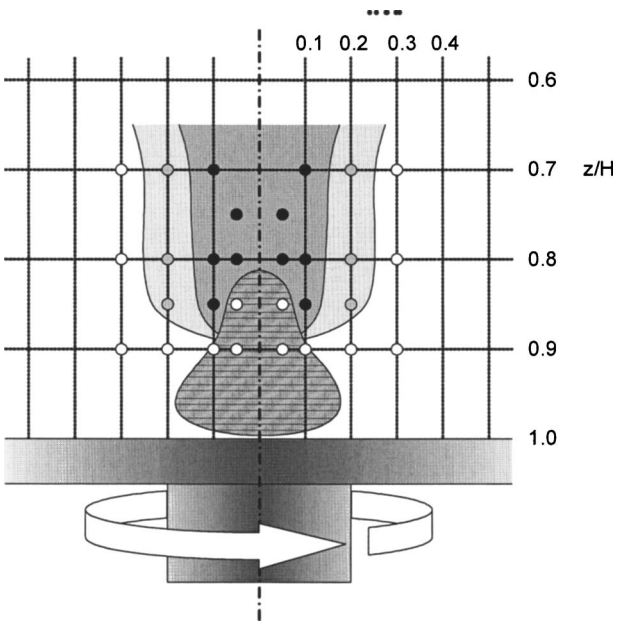

Fig. 15 Structure of reverse flow region (1.0 wt. %, Re_0 =0.36, We=13.7, H/R=2.0)

Conclusions

Swirling flows of viscoelastic fluid in a cylindrical casing with a rotating end wall (disk) have been studied. The results are summarized as follows:

1. Dimensionless circumferential velocity V'_θ decreases with increasing the Weissenberg number We.
2. Both the power-law model and the Giesekus model could predict this retardation of circumferential velocity fairly well at small We (~0.1) With increasing We, however, the V'_θ values calculated using these two models become too small compared to the measured ones.
3. The structure of the inverse flow region where the fluid rotates continuously in the direction opposite to that of the rotating disk was clarified in detail.

Nomenclature

$\mathbf{D}$ = rate of strain tensor
E_0 = elasticity number (=We/Re_0)
H = height of cylindrical casing
K = consistency
n = power-law index
$N1$ = first normal stress difference
R = radius of rotating disk
Re_0 = Reynolds number ($=\rho R^2\Omega/\eta_0$)
r, θ, z = cylindrical coordinates
$\mathbf{v}$ = velocity vector
V_r, V_θ, V_z = velocity components in r, θ, z directions, respectively
We = Weissenberg number ($=\lambda_G\Omega$)
η = shear viscosity
η_0 = zero shear viscosity
λ_G = relaxation time of Giesekus model
$\dot{\gamma}$ = shear rate
ρ = density of fluid
$\boldsymbol{\tau}$ = stress tensor
Ω = angular velocity of the rotating disk

References

[1] Hill, C. T., 1972, "Nearly Viscometric Flow of Viscoelastic Fluids in the Disc and Cylinder System. II: Experimental," Trans. Soc. Rheol., **16**, pp. 213–245.
[2] Day, C., Harris, J. A., Soria, J., Boger, D. V., and Welsh, M. C., 1996, "Behavior of an Elastic Fluid in Cylindrical Swirling Flow," Exp. Therm. Fluid Sci., **12**, pp. 250–255.
[3] Escudier, M. P., and Cullen, L. M., 1996, "Flow of a Shear-Thinning Liquid in a Container With a Rotating End Wall," Exp. Therm. Fluid Sci., **12**, pp. 381–387.
[4] Stokes, J. R., and Boger, D. V., 2000, "Mixing of Viscous Polymer Liquids," Phys. Fluids, **12**(6), pp. 1411–1416.
[5] Stokes, J. R., Lachlan, J. W., Graham, J. W., Lawson, N. J., and Boger, D. V., 2001, "Swirling Flow of Viscoelastic Fluids, Part 1, Interaction between Inertia and Elasticity," J. Fluid Mech., **429**, pp. 67–115.
[6] Stokes, J. R., Lachlan, J. W., Graham, J. W., Lawson, N. J., and Boger, D. V., 2001, "Swirling Flow of Viscoelastic Fluids, Part 2, Elastic Effects," J. Fluid Mech., **429**, pp. 117–153.
[7] Kramer, J. M., and Johnson, M. W., 1972, "Nearly Viscometric Flow in the

Disk and Cylinder System. I: Theoretical," Trans. Soc. Rheol., **16**, pp. 197–212.
[8] Böhme, G., Rubart, L., and Stenger, M., 1992, "Vortex Breakdown in Shear-Thinning Liquids: Experiment and Numerical Simulation," J. Non-Newtonian Fluid Mech., **45**, pp. 1–20.
[9] Xue, S. C., Phan-Thien, N., and Tanner, R. I., 1999, "Fully Three-Dimensional, Time-Dependent Numerical Simulations of Newtonian and Viscoelastic Swirling Flows in a Cylinder Part I. Method and Steady Flows," J. Non-Newtonian Fluid Mech., **87**, pp. 337–367.
[10] Siginer, D. A., 2004, "On the Nearly Viscometric Torsional Motion of Viscoelastic Liquids Between Shrouded Rotating Disks," Trans. ASME, J. Appl. Mech., **71**, pp. 305–313.
[11] Itoh, M., Moroi, T., and Toda, H., 1998, "Viscoelastic Flow Due to a Rotating Disc Enclosed in a Cylindrical Casing," Trans. Jpn. Soc. Mech. Eng., Ser. B, **64**(621), pp. 1351–1358 (in Japanese).
[12] Moroi, T., Itoh, M., and Toda, H., 1998, "Viscoelastic Flow Due to a Rotating Disc Enclosed in a Cylindrical Casing," *Proc. 13th Australasian Fluid Mechanics Conference*, pp. 313–316.
[13] Moroi, T., Itoh, M., and Fujita, K., 1999, "Viscoelastic Flow Due to a Rotating Disc in a Cylindrical Casing (Numerical Simulation and Experiment)," Trans. Jpn. Soc. Mech. Eng., Ser. B, **65**(639), pp. 3361–3568 (in Japanese).
[14] Moroi, T., Itoh, M., Fujita, K., and Hamasaki, H., 2001, "Viscoelastic Flow Due to a Rotating Disc in a Cylindrical Casing (Influence of Aspect Ratio)," JSME Int. J., Ser. B, **44**(3), pp. 465–473.
[15] Bird, R. B., Armstrong, R. C., and Hassager, O., 1987, *Dynamics of Polymeric Liquids*, Vol. 1, Wiley, New York, Chap. 4.
[16] Giesekus, H., 1982, "A Simple Constitutive Equation for Polymer Fluids Based on the Concept of Deformation Dependent Tensorial Mobility," J. Non-Newtonian Fluid Mech., **11**, pp. 69–109.
[17] Kawabata, N., Tachibana, M., and Ashino, I., 1990, "A Numerical Simulation of Viscoelastic Fluid Flow in a Two-Dimensional Channel (Application of Lax's Scheme to the Constitutive Equation)," Trans. Jpn. Soc. Mech. Eng., Ser. B, **56**(523), pp. 47–54 (in Japanese).
[18] Sasmal, G. P., 1990, "Finite Volume Approach for Calculation of Viscoelastic Flow Through an Abrupt Axisymmetric Contraction," J. Non-Newtonian Fluid Mech., **56**, pp. 15–47.

Keizo Watanabe
Graduate School of Technology Management,
Tokyo University of Agriculture
and Technology,
2-24-16 Nakacho,
Koganei-shi, Tokyo 184-8588, Japan
e-mail: mot1z019@cc.tuat.ac.jp

Shu Sumio
JEF Engineering Corporation,
2-1 Suehiro-cho,
Turumi-ku, Yokohama-shi,
Kanagawa 230-8611, Japan
e-mail: sumio-shu@jfe-eng.co.jp

Satoshi Ogata
Graduate School of Engineering,
Tokyo Metropolitan University,
Department of Mechanical Engineering
1-1 Minami Ohsawa,
Hachiooji-shi, Tokyo 192-0397, Japan
e-mail: ogata-satoshi@c.metro-u.ac.jp

Formation of Taylor Vortex Flow of Polymer Solutions

Laser-induced fluorescence (LIF) was applied for the flow visualization of the formation of a Taylor vortex, which occurred in the gap between two coaxial cylinders. The test fluids were tap water and glycerin 60 %wt solution as Newtonian fluids; polyacrilamide (SeparanAP-30) solutions in the concentration range of 10 *to* 1000 *ppm and polyethylene-oxide (PEO15) solutions in the range of* 20 *to* 1000 *ppm were tested as non-Newtonian fluids. The Reynolds number range in the experiment was* $80 < Re < 4.0 \times 10^3$. *The rotating inner cylinder was accelerated under the slow condition* ($dRe^*/dt \leq 1\ min^{-1}$) *in order to obtain a Taylor vortex flow in stable primary mode. Flow visualization results showed that the Görtler vortices of half the number of the Taylor cells occurred in the gap when the Taylor vortex flow was formed in the primary mode. In addition, the critical Reynolds number of the polymer solutions increased, where Taylor vortices occur, because the generation of the Görtler vortices was retarded. In high concentration polymer solutions, this effect became remarkable. Measurements of steady-state Taylor cells showed that the upper and lower cells of polymer solutions became larger in wavelength than those of the Newtonian fluids. The Taylor vortex flow of non-Newtonian fluids was analyzed and the result obtained using the Giesekus model agreed with the experimental result.* [DOI: 10.1115/1.2137350]

1 Introduction

In general, the flow pattern between two coaxial cylinders changes considerably with speed, because of instability. It is known that the pattern can change from a rotational Couette flow to a Taylor-Couette flow with an increase in speed, for a Newtonian fluid between a rotating inner cylinder and a stationary outer cylinder. This flow field is ideal for research into the transition process from laminar to turbulent flow because it is slower than other flow systems and the instabilities are well understood. Thus, much theoretical and experimental research on the transition process using this flow field has been carried out for Newtonian fluids since Taylor's work [1].

Polymer solutions, on the other hand, show a viscoelastic effect. The rheological behavior and flow characteristics depend on the types of polymer additives and their concentrations. In recent years, there has been great interest in the turbulent flows of dilute polymer solutions, and particularly in the phenomenon of drag reduction called the Toms effect [2]. However, there have been few studies on the transition flow from laminar to turbulent flow.

From prior studies conducted using polymer solutions, the problem of a purely elastic Taylor-Couette instability has been noted. Larson et al. [3] showed that, for the Oldroyd-B fluid, there exists an inertia-free mode of instability in a Taylor-Couette flow. By means of a linear stability analysis, they showed that secondary toroidal cells occur when the Deborah number De reaches 20, which was in agreement with the experiments with a solution of 1000 ppm high-molecular-weight polyisobutylene in a viscous solvent. Sadanandan and Sureshkumar [4] studied analytically the influence of elasticity on the budgets of the vorticity and the kinetic energy associated with the most dangerous disturbance to the plane Poiseuille flow of a model polymer solution, using the Oldroyd-B fluid. They showed that the stabilizing effect due to the perturbation shear stress increases monotonically with increasing the elasticity number and also showed a destabilizing influence due to the perturbation normal stress that increases monotonically. Sureshkumar et al. [5] calculated the bifurcating families which correspond to each of the two possible non-axisymmetric patterns emerging at the point of criticality, namely, the spirals and ribbons, to determine their stability. They showed that the unstable oscillatory modes are always non-axisymmetric, and transitions to them are probably discontinuous. Although the extensional nature of the fluid does play an important role, the resulting flow patterns in this case were not shown.

Regarding the character of instability in a Couette-Taylor flow, Groisman and Steinberg [6] showed experimentally that two novel oscillatory flow patterns are observed after small additions of polymers. One of the patterns was essentially due to the fluid elasticity, and the other resulted from an inertial instability modified by the elasticity.

Lee et al. [7] carried out a flow visualization study to reveal the effect of dilute polymer solutions on the Görtler instability between two cylinders. They showed experimental results in which the Görtler instability was stabilized by the polymer additive, which created increase in the local viscosity.

In general, these works found that viscoelasticity increases the critical Taylor number at which a cellular flow is observed. Thus, an increase in viscoelasticity stabilizes the flow against the formation of initial Taylor vortices. However, the formation process of Taylor vortices has not been clarified experimentally in detail. Although it has been speculated that the transition in a Newtonian fluid is different from that in a viscoelastic fluid, the vortex formation process has not been sufficiently studied. In this work, we experimentally examined the formation of Taylor vortices with regard to the effect of high-molecular-polymer additives on the instability, by using a flow visualization technique. The result observed in the stable mode was compared with the analytical result in terms of the elasticity and viscosity effects. The numerical simulation results for polymer solutions produce predictions of the axial wavelength of the Taylor cell.

2 Experimental Apparatus and Procedure

The test fluid is tap water, glycerin solution is used as the Newtonian fluid, and polyacrilamide (Separan AP-30) and polyethleneoxide (PEO15) solutions ranging in concentration from 10 to 1000 ppm and from 20 to 1000 ppm, respectively, are used as polymer solutions. The polymer additives were added to distilled water. Figure 1 shows the flow curve of the polymer solution

Contributed by the Fluids Engineering Division of ASME for publication in the JOURNAL OF FLUIDS ENGINEERING. Manuscript received August 5, 2004; final manuscript received July 13, 2005. Assoc. Editor: Dennis Siginer.

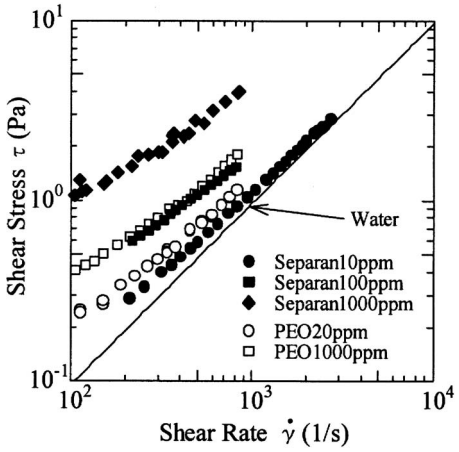

Fig. 1 Flow curve of polymer solutions

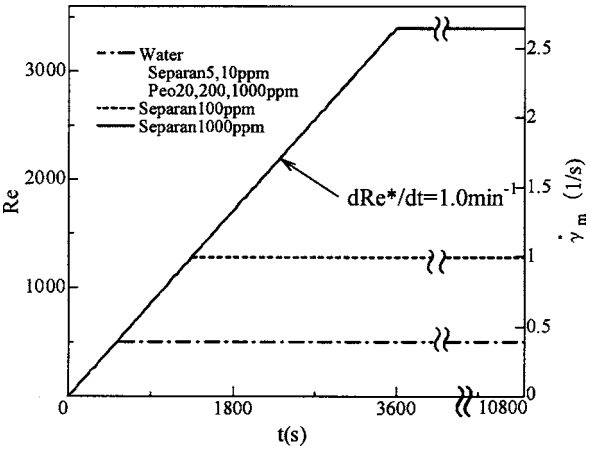

Fig. 3 Acceleration time of rotating inner cylinder

measured using a tube viscometer. After 24 h had elapsed, the polymer solution was carefully transferred to the test section. The temperature of the solution was maintained at $T=13.0\pm0.5°C$ throughout the experiments because the solutions' rheology is temperature dependent. The effect of polymer degradation on the result was examined by means of pipe friction loss measurement at the start and end of the experiment.

The experimental apparatus, shown in Fig. 2, is a two-coaxial-cylinder system in which the inner cylinder is rotated at a constant speed by a servomotor, while the outer cylinder and end wall are kept stationary. The height (L) and the gap between the cylinders are 240 and 39 mm, respectively. The radius of the outer cylinder (R_o) is 120 mm and, since the aspect ratio $\Gamma=(L/\delta)$ is 6.15, six Taylor vortices should appear in the gap. The angular velocity of the inner cylinder ω_i was measured by means of a digital counter. The inner and outer cylinders are made of aluminum and acrylic resin, respectively. An acrylic resin container, filled with tap water to protect the light reflected from the laser sheet, covers the outer cylinder. Test fluids were supplied from a head tank through a nylon tube, to prevent contamination by bubbles.

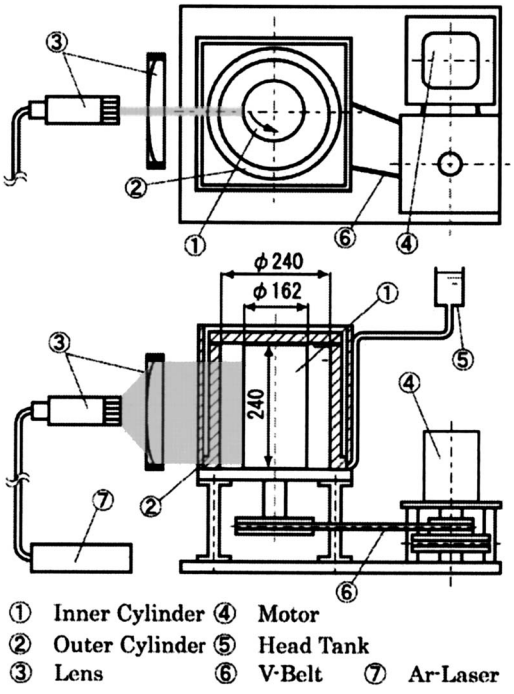

Fig. 2 Experimental apparatus

The formation and evolution of counter-rotating vortices close to the inner cylinder wall were examined by means of a laser-induced-fluorescence (LIF) flow visualization technique. A laser beam was radially directed through the center of the cylinders and spread into a vertical laser sheet by a cylindrical lens, illuminating the flow in the (r,z) plane. The thickness of the sheet was approximately 5 mm. Test fluids were marked with a fluorescent in a dye injected upstream of the laser sheet using a syringe, via a 1 mm tube inserted between the cylinders through a hole in the top of the end plate. The most effective method for marking the flow close to the inner cylinder was to slowly bleed dye directly onto the surface of the inner cylinder, and the near-wall vortices entrained the dyed fluid away from the wall to make the vortices visible. It was confirmed, using a capillary viscometer, that there was no change in the viscosity of the liquid which was mixed with the dye for visualization. Visual records of the LIF experiments were made using a video camera. The range of the nondimensional Taylor number T_a^*, defined as the ratio of the Taylor number Ta to the critical Taylor number Ta_{crit}, was $1\leqslant T_a^*\leqslant 2550$. Here the Taylor number is defined as $T_a=(R_i\omega_i^2\delta^3)/\nu^2$, where ν is kinematic viscosity. In this paper, we calculated the Taylor number using the viscosity value of tap water.

Three acceleration rates were applied to evaluate the effect of acceleration on the formation of Taylor vortices. Figure 3 shows the acceleration of the inner cylinder in this study. We used the slow condition ($d\,\mathrm{Re}^*/dt\leqslant 1.0\ \mathrm{min}^{-1}$) [8] for the rotation. The slow condition in this study was about 0.2 rpm/min in the acceleration and we confirmed that stabilized Taylor cells occurred in the flow.

3 Experimental Results and Discussions

Figure 4 shows the visualization result of the cross section of Taylor cells of Separan 100 ppm solution in the gap. After the rotation starts, we can see that the dye streak has separated from the inner cylinder wall, in Fig. 4(a). With an increase in the rotational speed, a Couette flow forms, as shown in Fig. 4(b). The number of streaks almost agrees with the number of rotations. The secondary flow occurs at the corners of the upper and end plates after $t=600$ s, and the secondary flow range becomes larger. When the size of the vortex reaches approximately one quarter of the cylinder height, the second vortex, which rotates in the reverse direction to the first vortex, is generated. In Fig. 4(f), we recognize the occurrence of a Görtler vortex from the swelling of the dye streak at the center of the cylinder wall. Finally, the six Taylor

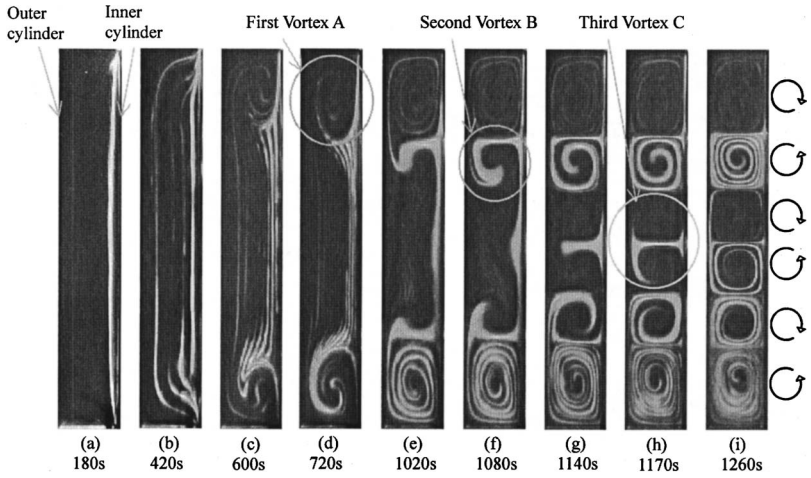

Fig. 4 Forming process of Taylor cells of Separan 100 ppm ($d\,\mathrm{Re}^*/dt = 1\ \mathrm{min}^{-1}$, $T = 13\,^\circ\mathrm{C}$

cells are fixed in the gap, as shown in Fig. 4(*i*). The flow pattern obtained in this experiment is that of a normal mode of Taylor vortex flow.

The formation of the vortices in the secondary flow of the different polymer concentrations is plotted against the Reynolds number in Fig. 5. The phrases written on the vertical axis are the vortex names shown in Fig. 4. The experimental results show that the Reynolds number for the third vortex C appears to be almost the same as the critical Reynolds number given by Taylor [1] for Newtonian fluids. For polymer solutions, the appearance of either vortex is retarded compared with that for Newtonian fluids. Remarkably, it occurs in the second and third vortexes according to the increase in the polymer concentration. These results mean that the secondary flow is suppressed, and it can be considered that the viscoelasticity of polymer solutions has an effect on the phenomena.

On the other hand, drag reduction occurs in surfactant solutions in the turbulent flow region [9], and they exhibit a viscoelastic effect [10]. Watanabe et al. [11] have experimentally shown that the Taylor cells also appear in the case of a 10 ppm surfactant solution of Ethoquad O/12. However, no Taylor cells appear in 50 and 100 ppm solutions. In terms of the flow mode, the difference is clear between polymer and surfactant solutions. In general, the viscoelasticity of these solutions develops markedly with increasing concentration. The dilute solution properties which we can consider are the ratio of the second to the first normal stress for the viscoelasticity, and the ratio of the solvent to the polymer or surfactant contribution to the shear viscosity. As mentioned, the flow curve of surfactant solutions has a shear-induced-structure at low shear rates. Some curious facts are revealed for the contribution of the viscoelasticity of surfactant properties, not only the local shear viscosity, to the stability of the flow.

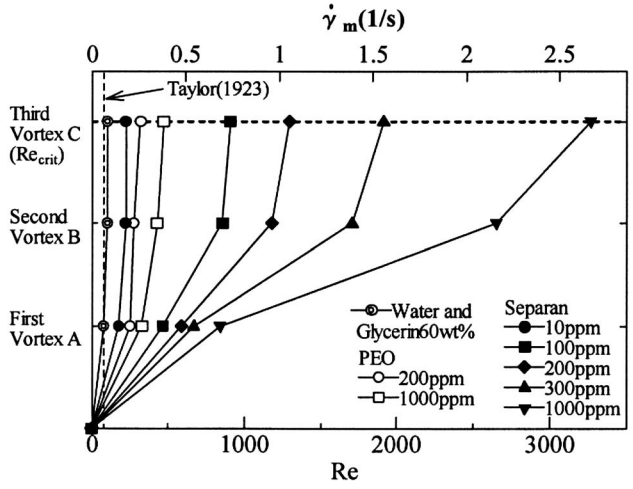

Fig. 5 Effect of polymer concentration on vortex generation

The cross sections of the first vortices of the Separan solution at different concentrations are shown in Fig. 6(*a*). The axial wavelength of the first vortexes becomes larger with increasing polymer concentration. The total axial wavelengths of the PEO and Separan solutions are arranged in Fig. 6(*b*). W_t is the total axial wavelength, and the value of W_t is defined as the wavelength in which the second vortex arises. In the case of Separan solutions, it increases substantially with the increase in polymer concentration.

To grasp the effect of polymer additives on the stable Taylor cell mode, we measured the axial wavelength of each cell in the stable mode. When the flow pattern depends on the time elapsed from the start of rotation of the inner cylinder, it is important to allow the system to achieve stable mode. In this measurement, using Snyder's formula [12] the stable time was determined to be 3 h from the rotation start time. Figure 7 shows the axial wavelength of the six Taylor cells of polymer solutions in the gap. The vertical axis shows the ratio of the wavelength of polymer solutions and that of tap water, and the number on the horizontal axis corresponds to the cell number shown in Fig. 7(*a*). According to the increase of the concentration in the Separan solutions, the lengths of no. 1 and no. 6 cells increase. As a result, other cells become small. The effect of the viscosity on the phenomenon can be neglected because the mode of tap water observed in this measurement agrees with that of the 60% glycerin solution. It can be posited that the change using the PEO solutions is less because of their low viscoelasticities compared to the Separan solutions shown in Fig. 7(*b*).

Figure 8 shows the effect of polymer concentration on the wavelength of the Görtler vortex. The acceleration of the inner cylinder is $d\,\mathrm{Re}^*/dt = 750\ \mathrm{min}^{-1}$. As this acceleration progresses, a fixed Reynolds number is achieved within 1 s. The center-to-center distance was measured and twice this value was taken to be the wavelength λ_G [13]. The experimental values are mean values obtained from 50 to 100 samples. The reported values are best estimates for the results and, with 95% confidence, the true value is believed to lie within ±2% of the present value of tap water. The solid line in Fig. 8 is the experimental result for Newtonian

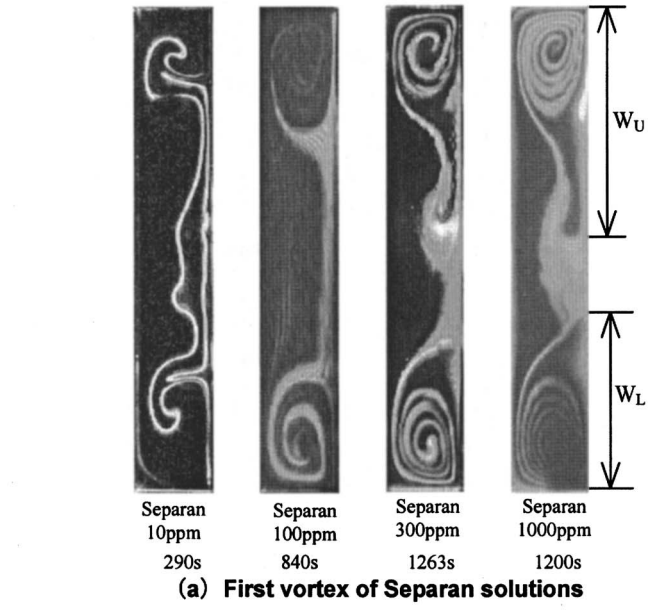

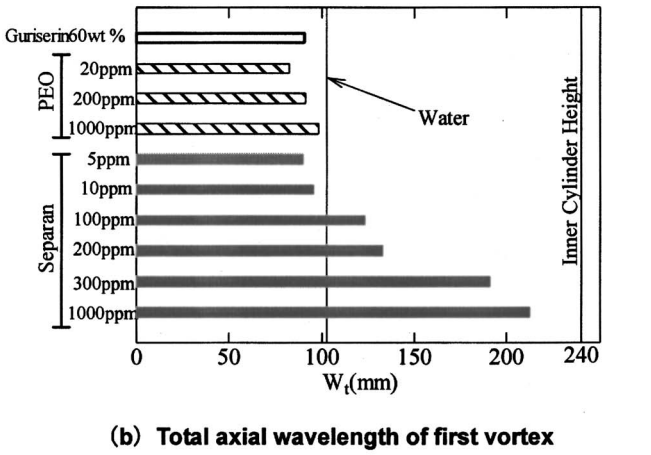

Fig. 6 (a) First vortex of Separan solutions and (b) Total axial wavelength of first vortex

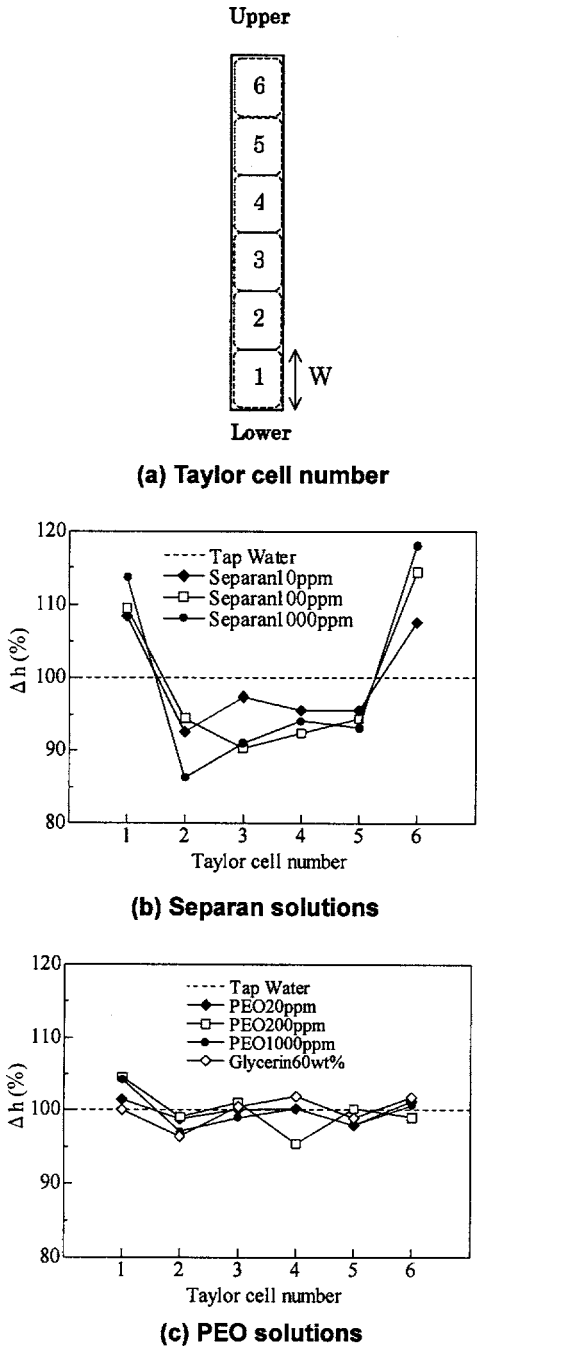

Fig. 7 (a) Taylor cell number; (b) Separan solutions; and (c) PEO solutions

fluids [14]. Although our experimental data for tap water lie slightly above this line, there is a tendency for greater agreement at lower Taylor numbers.

The wavelength of polymer solutions decreases slowly with Re in comparison to tap water, for all concentrations. This means that the solutions' stabilizing effect on the Görtler instability increases with Re and with polymer concentration.

The six cells appear in the Taylor vortex flow of the stable mode for this experimental apparatus because the aspect ratio is $\Gamma=6.15$. The experimental results also showed the phenomena. Generally speaking, the flow is analyzed by the momentum equation for laminar flow [1]. We analyzed the Taylor vortex flow of the stable mode to clarify the effects of viscoelasticity on the flow behavior by using the Giesekus model [15]. The finite-element-based simulation program used was POLYFLOW (Fluent Inc.). The calculated fluid is a viscoelastic fluid, which is equal to Separan 100 ppm solution in terms of the physical constants. In addition, three cases were calculated using the power-law model to examine the effect of the non-Newtonian viscosity. Figure 9 shows the apparent viscosity of the Separan 100 ppm solution, calculated using the Giesekus and power-law models. The power-law model fits the experimental data for many pseudoplastics at an intermediate shear rate and over a range of 10 to 100 fold, but fails both at very low and very high shear rates as shown in the figure. The first normal stress difference of the Separan 100 ppm solution was determined by extrapolation from the high concentrated solutions data, because the experimental data is lacking for dilute polymer solutions.

Figure 10 shows the analytical results of the power-law model. Increased viscosity has a stabilizing effect on the inertial instability; however, the results of the power-law model do not concur with the experimental results. The analytical results of the Giesekus model are shown in Fig. 11, in comparison with the experimental results of the Separan solutions. In Fig. 11, the

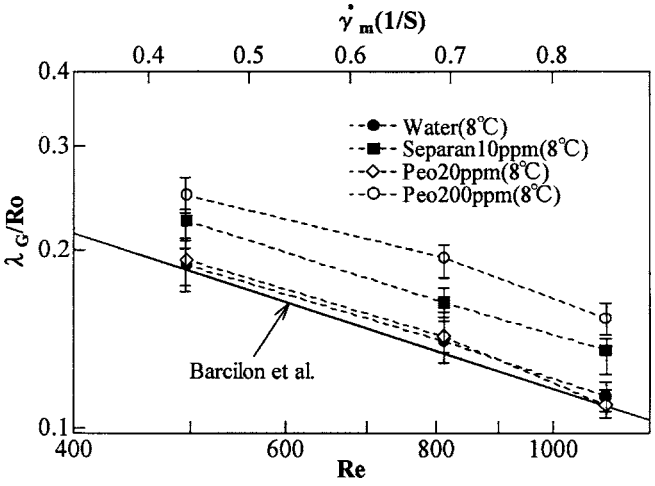

Fig. 8 Görtler wavelength of polymer solutions

dotted lines show the position of Taylor cells no. 1 and no. 6 of the glycerin 60% solution for the case of Newtonian fluids. The calculated results of the viscoelastic fluids agree with the experimental results.

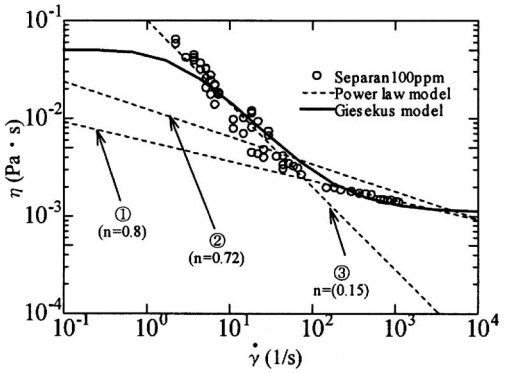

Fig. 9 Apparent viscosity of Separan 100 ppm solution

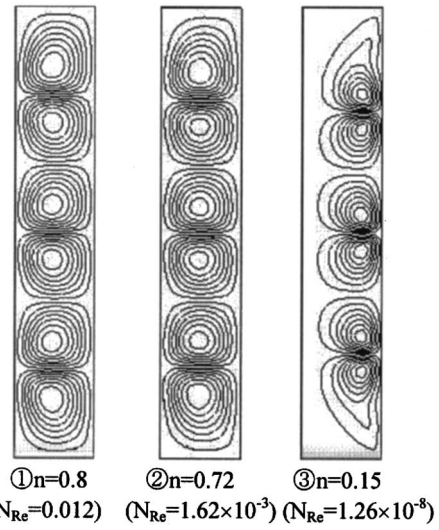

Fig. 10 Analytical results for power law models [$\dot{\gamma}_m$ =0.075(1/s)]

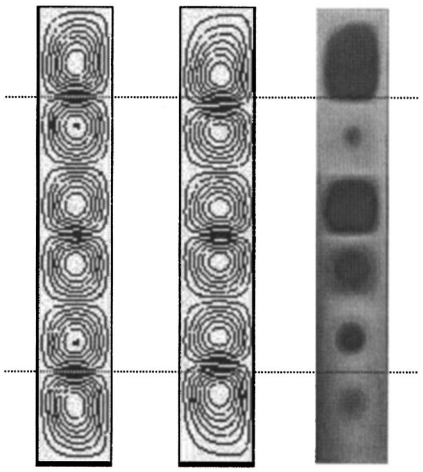

Fig. 11 Analytical results for viscoelastic model [$\dot{\gamma}_m$ =0.075(1/s)]

4 Conclusions

The effect of drag-reducing polymer additives on the formation process of Taylor cells in a Taylor-Couette flow was investigated by means of a laser-induced-fluorescence (LIF) flow visualization technique. Visual observations revealed that Taylor cells were formed in polymer solutions in spite of their not forming in surfactant solutions with viscoelastic properties. This polymer case is consistent with the analytical results for a viscoelastic fluid in the stability mode. Measurements of the wavelength of the Görtler vortices lead to the conclusion that the stabilizing effect on the Görtler instability increases with polymer concentration. However, the role of the elasticity of viscoelastic fluid in relation to the stability of the forming process in the Taylor cell surfactant case remains to be clarified.

Acknowledgment

This work was supported in part under Grant-in Aid for Science Research (B), No. 12450078 of Japan Society for the Promotion of Science.

Nomenclature

DR = drag reduction ratio
Δh = axial wavelength ratio to tap water ($=W_{test\ fluid}/W_{water}\times 100$)
L = cylinder height
N_{Re} = generalized Reynolds number
Re = Reynolds number ($=R_i\omega_i\delta/\nu$)
Re_{crit} = critical Re number to Taylor Couette flow
Re^* = ratio of Re to Re_{crit} ($=\mathrm{Re}/\mathrm{Re}_{crit}$)
R_i = inner cylinder radius
R_o = outer cylinder radius
T = temperature of test fluid
W = axial wavelength of Taylor cell
W_L = axial wavelength of lower Taylor cell
W_U = axial wavelength of upper Taylor cell
W_t = total axial wavelength ($=W_U+W_L$)
t = time of inner cylinder rotation
t_r = relaxation time of Taylor cells
δ = gap width ($=R_i-R_o$)

Γ = aspect ratio
$\dot{\gamma}$ = shear rate
$\dot{\gamma}_m$ = mean shear rate
η = viscosity of test solution
τ = shear stress
λ_G = Görtler wavelength
ν = kinematic viscosity of tap water
ω_i = angular velocity

References

[1] Taylor, G. I., 1923, "Stability of a Viscous Liquid Contained Between Two Rotating Cylinders," Philos. Trans. R. Soc. London, Ser. A, **223**, pp. 289–343.
[2] Toms, B. A., 1948, "Some Observations on the Flow of Linear Polymer Solutions Thorough Straight Tubes at Large Reynolds Number," *Proc. of Int. Conger. on Rheology*, II, pp. 135–138.
[3] Larson, R. G., Shaqfeh, E. S. G., and Muller, S. J., 1990, "A Purely Elastic Instability in Taylor-Couette Flow," J. Fluid Mech., **218**, pp. 573–600.
[4] Sadanandan, B., and Sureshkumar, 2002, "Viscoelastic Effects on the Stability of Wall-Bounded Shear Flows," Phys. Fluids, **14**(1), pp. 41–48.
[5] Sureshkumar, R., Beris, A. N., and Avgousti, M., 1994, "Non-Axisymmetric Subcritical Bifurcations in Viscoelastic Taylor-Couette Flow," Proc. R. Soc. London, Ser. A, **447**, pp. 135–153.
[6] Groisman, A., and Steinberg, V., 1996, "Couette-Taylor Flow in a Dilute Polymer Solution," Phys. Rev. Lett., **77**(8), pp. 1480–1483.
[7] Lee, S. H. -K, Sengupta, S., and Wei, T., 1995, "Effect of Polymer Additives on Görtler Vortices in Taylor-Couette Flow," J. Fluid Mech., **282**, pp. 115–129.
[8] Gorman, M., and Swinney, H. L., 1982, "Spatial and Temporal Characteristics of Modulated Waves in the Circular Couette System," J. Fluid Mech., **117**, pp. 123–142.
[9] Zakin, J. L., and Chang, J. L., 1974, "Polyoxyethylene Alcohol Non-Ionic Surfactants as Drag Reducing Additives," *Proc. of Inter. Conf. on Drag Reduction*, BHRA, pp. D1-1–D1-14.
[10] Imai, S., and Shikata, T., 2001, "Viscoelastic Behavior of Surfactant Thread-like Micellar Solutions; Effect of Additives," J. Colloid Interface Sci., **244**, pp. 399–404.
[11] Watanabe, K., Takayama, T., and Ogata, S., 2002, "Formation Process of Taylor Cells of a Surfactant Solution Proc. of Rheology and Fluid Mechanics of Nonlinear Materials," ASME IMECE FED-259, pp. 1–6.
[12] Snyder, H. A., 1969, "Wave-Number Selection at Finite Amplitude in Rotating Couette Flow," J. Fluid Mech., **35**(2), pp. 273–298.
[13] Wei, T., Kline, E. M., Lee, S. H. -K., and Woodruff, S., 1992, "Görtler Vortex Formation at the Inner Cylinder in Taylor-Couette Flow," J. Fluid Mech., **245**, pp. 47–68.
[14] Barcilon, A., Brindley, L., Lessen, M., and Mobbs, F. R., 1979, "Marginal Instability in Taylor-Couette Flows at a Very High Taylor Number," J. Fluid Mech., **94**(3), pp. 453–463.
[15] Giesekus, H., 1982, "A Simple Constitutive Equation for Polymer Fluids Based on the Concept of Deformation Dependent Tensorial Mobility," J. Non-Newtonian Fluid Mech., **11**, pp. 69–109.

Mizue Munekata
Department of Mechanical Engineering
and Materials Science,
Kumamoto University,
2-39-1, Kurokami, Kumamoto,
860-8555, Japan
e-mail: munekata@gpo.kumamoto-u.ac.jp

Kazuyoshi Matsuzaki
Tokyo Electron LTD.,
650 Mitsuzawa, Hosaka-cho,
Nirasaki City, Yamanashi,
407-0192, Japan
e-mail: kazuyoshi.matsuzaki@tel.com

Hideki Ohba
Department of Mechanical Engineering
and Materials Science,
Kumamoto University,
2-39-1, Kurokami, Kumamoto,
860-8555, Japan
e-mail: ohba@gpo.kumamoto-u.ac.jp

Vortex Motion in a Swirling Flow of Surfactant Solution with Drag Reduction

Surfactants are well known as additives which induce drag reduction in the straight (nonswirling) pipe flow. However, in industrial applications of the drag-reducing effect, many flow fields besides the straight pipe flow need to be considered. The purpose of this study is to investigate the flow characteristics of the surfactant solution in swirling pipe flow. The drag-reducing effect is estimated from the measurement of wall pressure drop and velocity profiles on various pipe sections by two-dimensional LDV (Laser Doppler Velocimeter). Since the surfactant solution has viscoelasticity, interesting flow characteristics are obtained. The decay of swirl, the vortex type and the turbulence intensity are discussed, compared with the swirling flow of the water. As the results, it is concluded that the change from Rankin's combined vortex to the forced vortex at a more upstream section by suppressing progress of free vortex and stretch of forced vortex introduces considerable drag reduction. Oscillation of the vortex core is also investigated, and it is found that the oscillation is independent of swirl number. [DOI: 10.1115/1.2136927]

Keywords: swirling flow, drag reduction, surfactant solution, vortex, LDV

Introduction

It is well known that the addition of certain kinds of surfactants, as well as polymers, to a Newtonian fluid causes considerable drag reduction in the turbulent and nonswirling pipe flow. The drag-reducing rate reaches 80%. Therefore a successful application of this effect would be a great contribution in industrial pipe flow systems. Applications to an air-conditioning system in a building and a district heating/cooling system have attracted special interest recently [1]. Those pipe flow systems have many complicated flow fields produced by curved pipes, branched pipes, and pumping machines. Therefore investigation on various flow fields is required to effectively apply the drag-reducing effect to the systems. We focus the effect of surfactant on swirling flow in a pipe. Swirling flow of Newtonian fluids has been investigated from mid-1950s onwards, for example, Binnie [2] and Nuttal [3] for a central cylindrical region of reversed axial flow and Talbot [4] for a laminar swirling flow.

The surfactant solution has viscoelasticity and shows interesting flow characteristics. Some investigators have studied the rotating flow of non-Newtonian fluids in a container (Stokes et al. [5]). In most of the flow fields the rotational Reynolds number based on a tangential velocity is low. However, in this study, the experiments are performed using high Reynolds numbers (a bulk velocity is taken as a representative velocity). The drag-reducing effect of a surfactant solution in the swirling pipe flow is obtained in the high bulk velocity, which is similar to the case of nonswirling flow. The swirl generator in this study is equipped with guide vanes [6] and installed at the entrance of the test pipe. The wall pressure drop and the velocity profiles on various pipe sections are measured in order to investigate the flow characteristics of the surfactant solution in the swirling pipe flow. Relationships among the type of vortex and the decay of swirl and the oscillating phenomenon of the vortex core are analyzed. The swirl decay in Newtonian fluid has been investigated by Hatazawa [7], Kreith and Sonju [8], Kitoh [9]. Smith [10], Chanaud [11], and Ito [12] reported the oscillating phenomenon in the vortex whistle and the cyclone separator, in which the ratio of the pipe length to the diameter is smaller than that of the pipe used in the present study. In our previous work [13] it has been shown that the forced vortex is easily formed, when the surfactant solution is used instead of the water. One of the reasons for this could be suppressed centrifugal force by the elastic effect of surfactant solution. Oscillating phenomenon of the vortex core often observed in Rankin's vortex is investigated by using the time history data of velocity in the vortex core. The characteristics of oscillating frequency and the relation between the oscillating frequency and the swirl number are discussed.

Experimental Setup and Methods

The swirling flow was generated by swirl generator with 12 guide vanes (Fig. 1), which was installed at the entrance of the pipe. Inclination angles of the vane (α) at 45, 60, and 70 deg were used in order to change the initial swirl intensity, for measurements of the drag-reducing effect. However, for the LDV (Laser Doppler Velocimeter) measurement, we present the results only at $\alpha=60$ deg for convenience of explanation.

Figure 2 shows the experimental setup. The inner diameter, $d(=2R)$, and the length of the test pipe were 44 and 5000 mm ($114d$), respectively. The flow was induced by the difference between the solution levels, H, in the inlet tank and the outlet tank. Two solution levels were kept constant by an overflow system. The solution was kept at a constant temperature ($25\pm0.5\,^{\circ}C$) by cooling and heating coils.

Mass flow rates were measured by a platform scale. Wall pressure was measured at four axial positions of the pipe. At each position, the pressures measured by four pressure taps spaced at an equal distance in the circumferential direction were averaged. The axial and tangential components of velocity were measured by LDV and then averaged in time, and turbulence intensities were obtained, respectively. Oscillation of the vortex was analyzed using time history data of the velocity. Axial position, x, was defined as a distance from the inlet of the pipe. Positive direction of tangential velocity, V_t, is shown in Fig. 1. Profiles of two-component velocity in the radial direction were measured at six

Contributed by the Fluids Engineering Division of ASME for publication in the JOURNAL OF FLUIDS ENGINEERING. Manuscript received August 11, 2004; final manuscript received April 25, 2005. Assoc. Editor: Dennis Siginer.

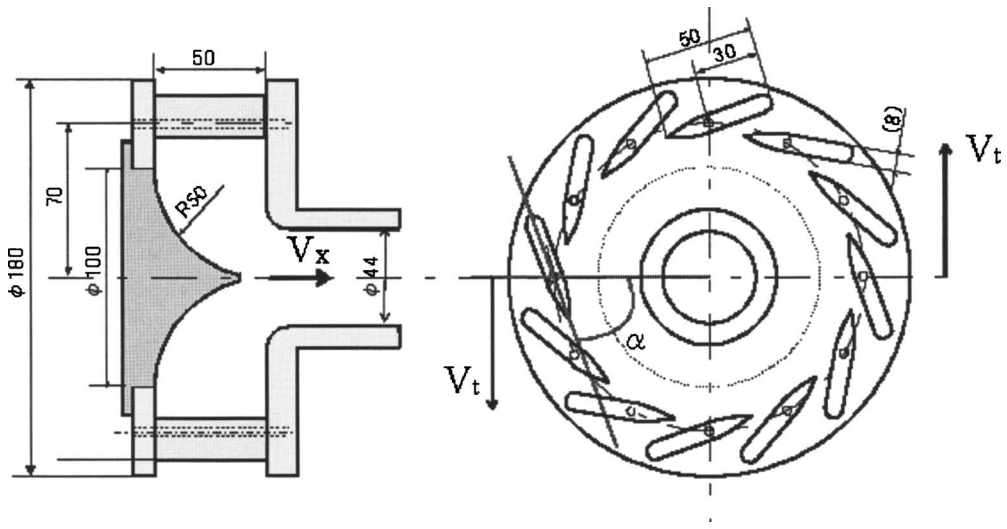

Fig. 1 Swirl generator

sections in the axial direction. Polyethylene particles with 10 μm diameter and a specific gravity of 0.918 were used as seeding particles for LDV measurements.

The surfactant solution (CTAB) used in this study was 500 ppm cetyl-trimetyl ammonium bromide in water containing sodium salicylate at the same molar concentration as cetyl-trimetyl ammonium bromide. CTAB is characterized by "the shear-thinning property," in which the kinematic viscosity increases with a decrease of shear rate. CTAB is also classified into non-Newtonian fluids as a pseudo-plastic fluid and a viscoelastic fluid. However, in this study, a constant kinematic viscosity could not be determined for CTAB in the swirling flow, because shear stresses, as well as axial and tangential velocity profiles at the cross sections of the pipe, changed in the downstream direction. Therefore, $\mathrm{Re}(=V_b d/\nu)$ and $\mathrm{Re}_t(=V_{tm}R/\nu)$ were calculated using the kinematic viscosity of the water. More specifically, Re and Re_t present nondimensional bulk velocity and nondimensional tangential velocity at the upstream end of the pipe, respectively.

Results and Discussions

Effect of Guide Vane Inclination Angle on Friction Coefficient. Because a difference between the total pressure drop and the pressure drop obtained from wall pressure was within 5% in our previous experiment [14], the net energy loss was estimated only by the wall pressure drop. Figure 3 shows the friction coefficient as a function of Reynolds number; the pressure drop is estimated for the axial segment between two positions, which are $48d$ and $99d$ from the inlet of pipe, separated by $51d$. According to Hatazawa's report [15], because they position more downstream than $15d$, it is considered that the friction coefficient has no effect of the entry condition. Data for straight shear flow (nonswirling flow) are also shown in Fig. 3. The friction coefficient for nonswirling water flow is consistent with Blasius's equation for Newtonian fluid flow. For nonswirling CTAB flow, the friction coefficient approaches Virk's maximum drag-reducing asymptote [16] for nonswirling flow as Re increases. The friction coefficients of the water flow become larger as α increases, when Re is higher than 10^4. The friction coefficients of the CTAB flow are lower than those of the water, thus it is shown that significant drag reduction occurs. Furthermore, the friction coefficient of the CTAB decreases until a critical Re and then increases afterwards. The critical Re is shifted lower as α increases. Assuming that an excessive shear stress is put on the shear layer in higher Re, it is likely that the elastic stress of the surfactant solution does not work effectively due to a collapse of micelle structure in the solution, which leads to the increase in friction coefficient. Therefore it is considered that the micelle structure is stressed stronger with increasing of α in higher Re.

Drag-reducing rate (DR) is defined by

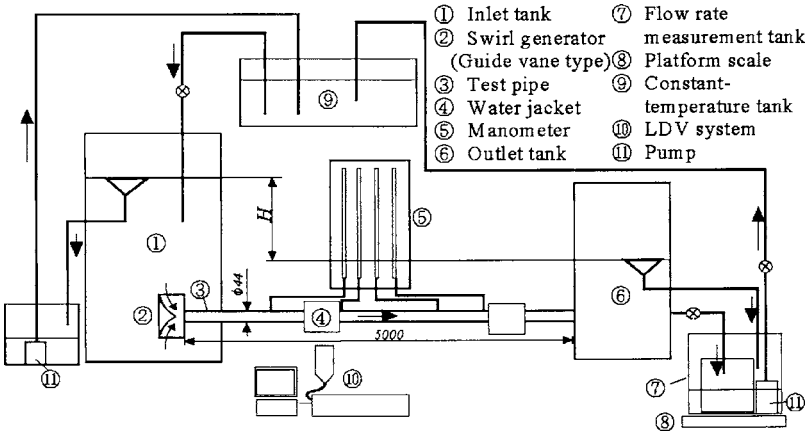

Fig. 2 Experimental setup

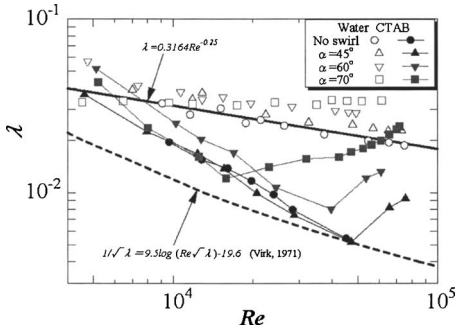

Fig. 3 Friction coefficient vs. Re

$$\mathrm{DR}(\%) = \left(\frac{\lambda_w - \lambda_C}{\lambda_W}\right) \times 100 \tag{1}$$

Here, λ_C and λ_w are friction coefficients at a given Re of the surfactant solution (CTAB) and the water, respectively. The λ_w is estimated by the following equation, when α is 60 deg:

$$\lambda_W = 0.378\,\mathrm{Re}^{-0.24} \tag{2}$$

Figure 4 shows DR vs. Re. Vane angles (α) do not affect DR when Re is lower than the critical Re, but at the Re higher than the critical Re, DR becomes greater with the decrease in α. Maximum DR reaches 80% at α=45 deg. Solid lines indicate DR using λ_w of the nonswirling flow in the water, which is obtained by Blasius's equation ($\lambda = 0.3164\mathrm{Re}^{-0.25}$). The swirling flows of the CTAB induce the drag reduction, even when those are compared to the nonswirling flow of Newtonian fluid. However, at α =70 deg in the Re higher than 6×10^4, the drag reduction of swirling flow, compared with the nonswirling flow, is no longer obtained because the swirl intensity is higher.

Swirl Intensity. Swirl intensity in an axisymmetric flow can be expressed by swirl number, Sw, as follows [17]:

$$\mathrm{Sw} = \frac{\int_0^R V_x V_t r^2 dr}{R\int_0^R V_x^2 r dr} \tag{3}$$

where V_x and V_t are the axial velocity and the tangential velocity, respectively, measured by LDV. Since the swirl flow is not exactly axisymmetric, V_x and V_t are measured across the pipe diameter and then the representative swirl number at a cross section is obtained by averaging two swirl numbers. The swirl number for Newtonian flow decays exponentially in the downstream direction. This behavior can be expressed as follows [9]:

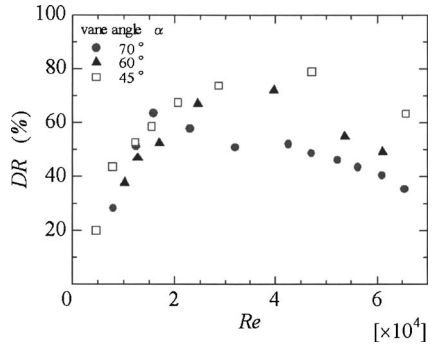

Fig. 4 Drag-reducing rate compared with the friction coefficient in Newtonian swirling flow

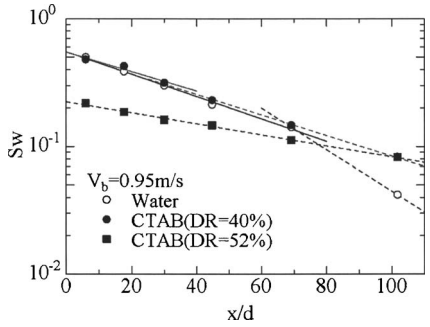

Fig. 5 Decay of Sw in the stream wise direction at α=60 deg; solid lines and dashed lines indicate approximate expressions of swirl decay in Rankin's combined vortex and the forced vortex, respectively

$$\mathrm{Sw} = \mathrm{Sw}_0 \exp[2a_1(x - x_0)/d] \tag{4}$$

where a_1 is the decay coefficient and Sw_0 is the swirl number at a reference position, x_0. The reference position in this study is the upstream end of the pipe. Therefore Sw_0 represents the initial swirl intensity and shows the highest intensity in the experiment.

Decay of the swirl numbers at the bulk velocity of 0.95 m/s ($\mathrm{Re}=4.7\times10^4$, $\mathrm{Re}_t=9.0\times10^3$) is shown in Fig. 5. The decay coefficient a_1 depends on Re (or bulk velocity) as it was shown in the previous reports [9,18]. The magnitude of Sw and the decay of Sw depend on the DR. In the CTAB with DR of 52%, the Sw is lower and the exponential decay of Sw is smaller than that in the CTAB with DR of 40%, which is probably caused by the higher effective viscosity or the viscoelasticity of the CTAB with the DR of 52%. Therefore the change of Sw of the CTAB with DR =52% is similar to that of the CTAB with DR=40% at the Re lower than the estimated Re. In other words, the actual Re of CTAB with DR=52% would be lower than the Re defined using kinematic viscosity for the water, which is used to estimate the Re of the CTAB with DR=40%.

Vortex Type. Figures 6 and 7 show the changes in the profiles of V_x and V_t, respectively, for the water and the CTAB with DR =40% and 52%, in the stream wise direction. Although the mean velocity profile of CTAB with DR=52% is shown by a solid line, the error bounds of all mean velocity profiles including other solutions are within the symbol size in figures. Different vortex types are observed at the upstream sections. For the first vortex type, Rankin's combined vortex has a forced vortex in the core region and a free vortex in the annular region. The tangential mean velocity profile has the gradient of $\partial V_t/\partial r > 0$ and $\partial V_t/\partial r < 0$ in the forced vortex region and the free vortex region, respectively. The second vortex type is the forced vortex all over the cross section of pipe, without free vortex. The upstream vortex type of the water and the CTAB with DR=40% is the Rankin's combined vortex, while the downstream type is the forced vortex. The CTAB with DR=52% forms a forced vortex in all sections as described by the solid line.

We focus on the transition from the Rankin's combined vortex to the forced vortex via the following steps; step 1 is the progress of the free vortex or stretch of the forced vortex, which is found by expansion of the annular region of the free vortex or an increase of the tangential velocity gradient, $\partial V_t/\partial r$, in the core region, and after a vortex breakdown step 2 is the decay of the free vortex or development of the forced vortex in Rankin's combined vortex. In the water, the value of V_x in the core region decreases between the inlet (x/d=6.0) and x/d=17.7, and then increases along the downstream, while the gradient of tangential velocity, $\partial V_t/\partial r$, in the core region increases also between the inlet (x/d =6.0) and x/d=17.7, and then decreases. Between x/d=6.0 and x/d=17.7, the core region becomes narrower with the stretch of

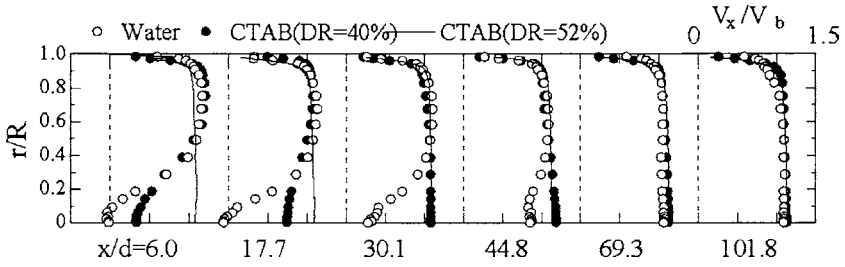

Fig. 6 Axial velocity profiles (V_b=0.95 m/s at α=60 deg)

the forced vortex, in which it has a vortex breakdown bubble. Here, reverse flow is observed. The annular region becomes wider with the progress of free vortex. In the CTAB with DR=40%, values of V_x in the core region of Rankin's combined vortex are larger than that in the water, and the value of V_t at an edge of the free vortex is smaller than that in the water, although they have a similar decay of Sw at the upstream section.

In the water, it is expected that the vortex breakdown between steps 1 and 2 occurs between 17.7 and 30.1 in x/d, and then the transition of the vortex type occurs between 69.3 and 101.8 in x/d as shown in the decay line of Sw (Fig. 5) and velocity profiles (Figs. 6 and 7). In the CTAB with DR=40%, the flow at x/d =6.0 is in step 2 because the increase of $\partial V_t/\partial r$ in the core region in step 1 is not observed, and it is expected that the vortex breakdown occurs before x/d=6.0, and then the transition to the forced vortex occurs between 17.7 and 30.1 in x/d. Now, at x/d=17.7, the vortex type formed in the CTAB with DR=40% is an intermediate between Rankin's combined vortex and the forced vortex, in which the edge of the core region between the forced vortex and the free vortex is indistinct. These results indicate that the change from Rankin's combined vortex to the forced vortex at a more upstream section, by suppressing the progress of the free vortex and the stretch of the forced vortex, would introduce considerable drag reduction in the CTAB.

The flow of the CTAB forms the forced vortex when the Sw is less than about 0.3. The swirl number at which the vortex type

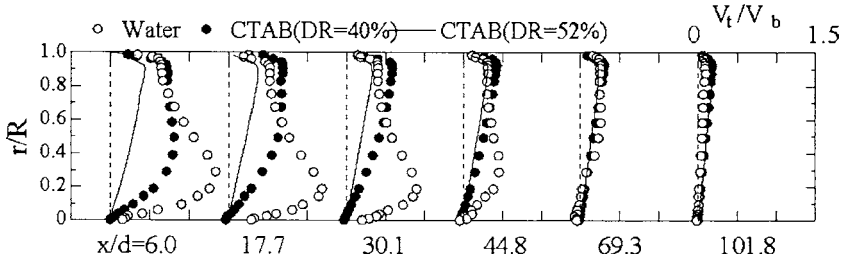

Fig. 7 Tangential velocity profiles (V_b=0.95 m/s at α=60 deg)

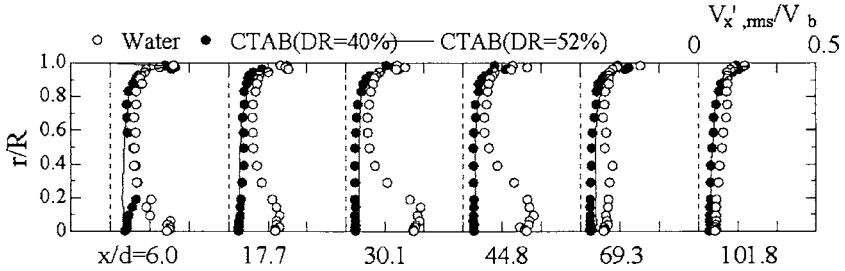

Fig. 8 Turbulence intensity profiles of axial velocity fluctuations (V_b=0.95 m/s at α=60 deg)

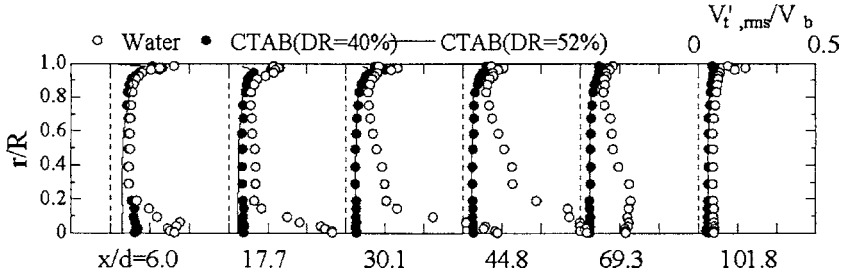

Fig. 9 Turbulence intensity profiles of tangential velocity fluctuations (V_b =0.95 m/s at α=60 deg)

changes is defined as a critical Sw. The critical Sw of the CTAB at $\alpha=60^{\circ}$ is smaller than that at the $\alpha=70^{\circ}$ obtained in the previous study [18], but larger than that of the water. When α is 45°, the critical Sw of the CTAB with DR=30% is 0.2. The critical Sw of the CTAB is influenced by α and DR, although the critical Sw of the water is constant independently of α. Therefore contributing factor to the critical Sw in the CTAB is not clear and require more investigations.

Turbulence Intensity. Figures 8 and 9 show profiles of turbulence intensity of the water and the CTAB with DR=40% and 52%, toward the downstream direction. The turbulence intensity in the Rankin's vortex in the core region is higher than in the annular region, because the velocity gradient is larger and the vortex core is oscillating in the core region as described in the next section. The turbulence intensity becomes stronger as the velocity gradient increases with the progress of free vortex (or the stretch of forced vortex). However, at the cross section immediately after the vortex breakdown, the turbulence intensity in the core region is stronger than the intensity before the vortex breakdown. In the water, the position of the immediate cross section is $x/d=30.1$, and at the downstream cross sections $x/d=44.8$, 69.3, the turbulence intensity in the core region becomes smaller and the core region is extended toward the pipe periphery. Finally, at the position $x/d=101.8$, where the forced vortex is formed over the entire cross section in the water flow, the turbulence intensity has no peak around the center of the pipe.

The turbulence intensity of the CTAB is smaller than that of the water, which is in agreement with the case of $\alpha=70$ deg [18]. It is of interest that the turbulent intensity of the CTAB is smaller in spite of the larger velocity gradient near the wall compared to the water, as shown especially in the tangential velocity gradient (Fig. 7).

Oscillating Phenomenon of the Vortex Core. The time history of the velocity is analyzed in order to investigate the oscillation of the vortex core. Figures 10(*a*) and 10(*b*) show the time history of tangential velocity fluctuation, V_t' at $r/R\approx 0$ of the water and the CTAB with DR=40%, respectively. The wave of velocity fluctuation consists of the high-frequency wave and the low-frequency wave with high amplitude. The low-frequency wave shows the oscillation of the vortex core. In the forced vortex, the clear waves due to the oscillation are not detected. A periodicity of the low-frequency wave and the wave number are affected by the vortex type.

Figure 11 shows the autocorrelation coefficient of tangential velocity fluctuations shown in Fig. 10. The coefficient is calculated from the velocity data for 30 s with the time interval of 0.001 s. In the water, the autocorrelation coefficient and the periodicity are low until $x/d=17.7$. At the position immediately after the maximum stretch of the free vortex in the core region, the highest oscillation frequency and the most periodic oscillating phenomenon are observed. And then the oscillating frequency decreases and the periodicity of oscillating phenomenon diminishes, as the region of the free vortex becomes narrower and finally disappears. It is difficult to detect clearly the oscillating phenomenon at the center of the pipe in the forced vortex region at the downstream section because of the low swirl intensity. On the other hand, in the CTAB (DR=40%), the periodicity of the oscillating phenomenon is not clear at any positions tested except $x/d=6.0$, even at the cross section with Sw higher than that of water. It is suggested that the oscillating frequency is independent of Sw.

Conclusions

The wall pressure drop and the velocity profiles are measured in order to investigate the characteristics of the swirling flow of the surfactant solution. The effect of Re and α on the drag reduction are shown; the critical Re with the maximum DR decreases as α increases; the maximum DR reaches 80% when α is 45 deg. It is found that the magnitude of Sw, the decay of Sw, and the type of vortex formed at the same bulk velocity are affected by the DR, which could be influenced by the effective viscosity and the elasticity. The surfactant solution forms most easily the forced vortex at a higher Sw compared to the water. These results indicate that the change to the forced vortex at a more upstream section by

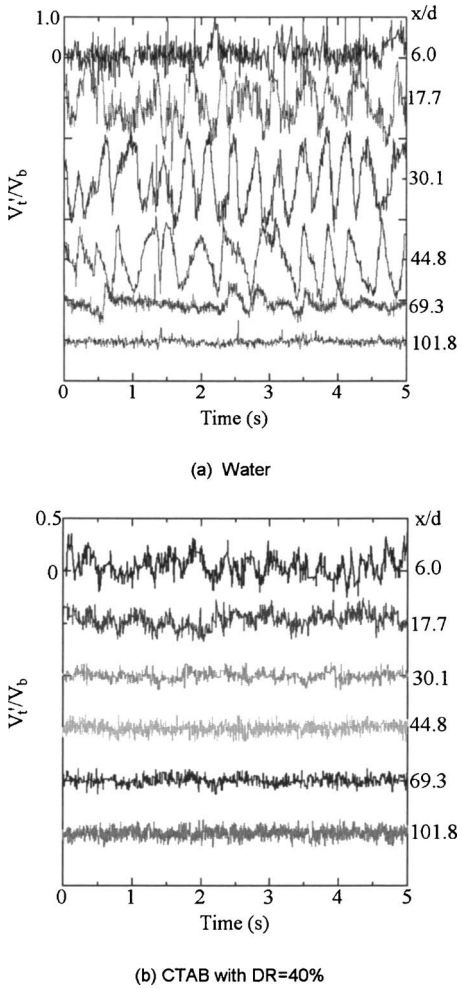

Fig. 10 Fluctuation of nondimensional tangential velocity at $r/R\approx 0$ ($V_b=0.95$ m/s at $\alpha=60$ deg)

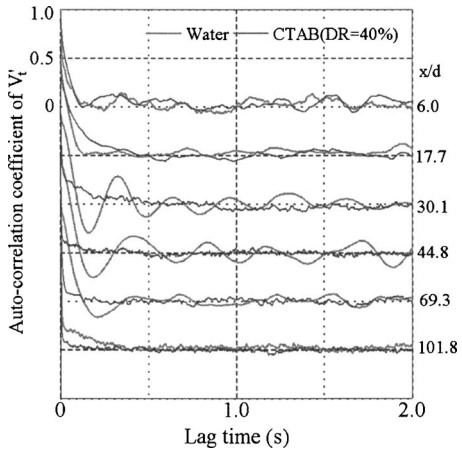

Fig. 11 Autocorrelation coefficient of V_t' at $r/R\approx 0$

suppressing the progress of the free vortex and the stretch of the forced vortex introduces considerable drag reduction. Furthermore, it is of interest that the turbulent intensity of the surfactant solution is smaller in spite of the larger velocity gradient near the wall being larger than that of the water. The turbulence intensity in the Rankin's vortex in the core region is higher than in the annular region, because the velocity gradient is larger and the vortex core is oscillating. However, the periodic oscillation of the surfactant solution is not observed even at the cross section with Sw higher than that of water, suggesting that the oscillating frequency is independent of Sw.

Acknowledgment

The authors would like to thank T. Kawasoe, T. Yoshiura, H. Takaki, and H. Yamakawa for their experimental support. This work was partially supported by Harada memorial financial group in 2003 and Grants-in-Aid for Scientific Research, No. 14750121 from Japan Society for the Promotion Science.

Nomenclature

a_1 = swirl decay coefficient
d(=2R) = inner diameter of the test pipe (=0.044 m)
DR = drag reduction, %
r = radial distance from the axis of the test pipe
R = radius of the test pipe (=0.022 m)
R_i = outside radius of the guide vane wheel
Re = Reynolds number ($=V_b d/\nu$)
Re_t = rotational Reynolds number ($=V_{tm}R/\nu$)
Sw = swirl number
V = mean velocity
V' = velocity fluctuation
V_{ti} = tangential mean velocity at the inlet of guide vane, assuming infinite number of vanes
V_{tm} = tangential mean velocity ($r=R$) at the upstream end of the test pipe ($=V_{ti}R_i/R$)
V_b = bulk velocity
x = axial distance from the upstream end of the test pipe

Greek Letters

α = guide vane inclination angle
λ = friction coefficient in a pipe
ν = kinematic viscosity

Subscripts

0 = reference location
t = tangential component
rms = root mean square
x = axial component

References

[1] Kawaguchi, Y., 2000, "Activities of Eco-Energy City Project, Urban Energy Systems That Support Lifestyle Enrichment While Harmonizing With the Environment," Proc. Joint Iran-Japanese Seminar on Renewable Energy, Tehran, I.R. Iran.
[2] Binnie, A. M., 1957, "Experiments on the Slow Swirling Flow of a Viscous Liquid Through a Tube," Q. J. Mech. Appl. Math. **10**, pp. 276–290.
[3] Nuttal, J. B., 1953, "Axial Flow in a Vortex," Nature (London) **172**, pp. 428–583.
[4] Talbot, L., 1954, "Laminar Swirling Pipe Flow," ASME J. Appl. Mech. **21**, pp. 1–7.
[5] Storks, J. R., Graham, L. J. W., Lawson, N. J., and Boger, D. V., 2001, "Swirling Flow of Viscoelastic Fluids. Part 1. Interaction Between Inertia and Elasticity," J. Fluid Mech. **429**, pp. 67–115.
[6] Kito, O., and Suzuki, Y., 1985, "Effect of Swirl Generator's Character on Swirl Velocity in Pipe," Trans. Jpn. Soc. Mech. Eng., Ser. B **51**(471), pp. 3461–3362.
[7] Hatazawa, M., and Komatsu, Y., 1997, "Characteristics of Turbulent Swirling Flow in a Straight Pipe—Flows Similarities and Flow Reversal Conditions," J. Jpn. Soc. Fluid Mech. **16**, pp. 128–138.
[8] Kreith, F., and Sonju, O. K., 1965, "The Decay of Turbulent Swirl in a Pipe," J. Fluid Mech. **22**, pp. 257–271.
[9] Kitoh, O., 1991, "Experimental Study of Turbulent Swirling Flow in a Straight Pipe," J. Fluid Mech. **225**, pp. 445–479.
[10] Smith, J. L., 1962, "An Experimental Study of the Vortex in the Cyclone Separator," ASME J. Basic Eng., **84**(3), pp. 602–608.
[11] Chanaud, R. C., 1965, "Observations of Oscillatory Motion Certain Swirling Flows," J. Fluid Mech. **21**, part 1, pp. 111–127.
[12] Ito, T., Suematsu, Y., Kanda, N., and Hayase, T., 1983, "On the Oscillatory Phenomena in a Swirling Pipe Flow," Trans. Jpn. Soc. Mech. Eng., Ser. B **48**(436), pp. 2472–2483.
[13] Munekata, M., Matsuzaki, K., and Ohba, H., 2002, "Experimental Study of Swirling Flow With a Surfactant for Drag Reduction in a Pipe," JSME Int. J., Ser. B **45**(1), pp. 35–40.
[14] Shibata, E., Munekata, M., Matsuzaki, K., and Ohba, H., "A Study on Swirling Flow of Surfactant Solution in a Pipe (Velocity Measurement by LDV)," *JSME Kyushu Branch Conference*, No. 018-2, pp. 123–124.
[15] Hatazawa, M., 1999, "Study on Turbulent Swirling Flow in a Straight Pipe (A Study of Pressure Loss)," JSME Fluids Engineering Conference 1999, No. 99-19, pp. 433–434.
[16] Virk, P. S., 1971, "An Elastic Sublayer Model for Drag Reduction by Dilute Polymer Solutions," J. Fluid Mech. **45**, pp. 417–440.
[17] Yajnik, K. S., and Subbsish, M. V., 1973, "Experiments on Swirling Turbulent Flows. Part 1. Similarity in Swirling Flows," J. Fluid Mech. **60**, part 4, pp. 665–687.
[18] Munekata, M., Matsuzaki, K., and Ohba, H., 2002, "Swirling Flow of Surfactant Solution With Drag Reduction in a Pipe (Characteristics of Swirl Decay)," *Proceedings of the Fifth JSME-KSME Fluids Engineering Conference*, Nagoya, Japan.

Three Regimes of Non-Newtonian Rimming Flow

Sergei Fomin[1]
Department of Mathematics and Statistics,
California State University,
Chico, CA 95929

The present study is related to the rimming flow of non-Newtonian fluid on the inner surface of a horizontal rotating cylinder. Using a scale analysis, the main characteristic scales and nondimensional parameters, which describe the principal features of the process, are found. Exploiting the fact that one of the parameters is very small, an approximate asymptotic mathematical model of the process is developed and justified. For a wide range of fluids, a general constitutive law can be presented by a single function relating shear stress and shear rate that corresponds to a generalized Newtonian model. For this case, the run-off condition for rimming flow is derived. Provided the run-off condition is satisfied, the existence of a steady-state solution is proved. Within the bounds stipulated by this condition, film thickness admits a continuous solution, which corresponds to subcritical and critical flow regimes. It is proved that for the critical regime the solution has a corner on the rising wall of the cylinder. In the supercritical flow regime, a discontinuous solution is possible and a hydraulic jump may occur. It is shown that straightforward leading order steady-state theory can work well to study the shock location and height. For the particular case of a power-law model, the analytical solution of a steady-state equation for the fluid film thickness is found in explicit form. More complex rheological models, which show linear Newtonian behavior at low shear rates with transition to power law at moderate shear rates, are also considered. In particular, numerical computations were carried out for the Ellis model. For this model, some analytical asymptotic solutions have also been obtained in explicit form and compared with the results of numerical computations. Based on these solutions, the optimal values of parameters, which should be used in the Ellis equation for the correct simulation of the coating flows, are determined; the criteria that guarantee the steady-state continuous solutions are defined; and the size and location of the stationary hydraulic jumps, which form when the flow is in the supercritical state, are obtained for the different flow parameters. [DOI: 10.1115/1.2137342]

Introduction

The problem of rotational flow on the inner and/or on the outer wall of a hollow horizontal cylinder has been of interest for many years due to its wide range of applications in industry. A schematic sketch of the process is presented in Fig. 1. Rimming flow at high rotation rates, as a limiting case when the motion of the liquid is a small perturbation from a rigid-body motion, was analyzed in [1]. However, as it was demonstrated later [2–4], already at relatively low angular velocities the flow can settle into a steady two-dimensional flow. Based on the previous studies three flow regimes can be identified. When the mass flux through the cross section of the liquid layer on the wall of the cylinder q is below its maximal supportable value q_{max}, then fluid film thickness is a continuous and smooth function of an angular coordinate. This regime is called subcritical. The critical steady-state regime occurs when the mass flux q is equal to its critical value q_{max}. In addition to these two regimes, a third regime, which was named supercritical, is also possible for $q=q_{max}$. This regime is associated with the existence of a steady-state puddle (further hydraulic jump) on the rising wall of the cylinder, which occurs as a result of an excessive mass of the liquid loaded on the wall or a too low rotational rate [see Fig. 1(*c*)]. In [5] it was shown that for the Newtonian model the straightforward leading order steady-state lubrication theory could work well to study hydraulic jumps locations and heights in the supercritical regime. Although the aforementioned investigations highlight the main characteristics of the rimming flow, due respect to the effect of non-Newtonian properties was not given. In the present paper we extend the estimates made for Newtonian fluids by Moffatt [2] and O'Brien and Gath [5] for the more general case of a non-Newtonian fluid. In numerical computations the Ellis constitutive equation is used for the quantitative analysis of three possible steady-state regimes (subcritical, critical, and supercritical) of rimming flow on the inner surface of the horizontal rotating cylinder.

System Model and Analysis

Our main concern is rotational moulding of highly viscous polymers, which exhibit Newtonian behavior at low shear rates with transition to power-law shear thinning at moderate shear rates [6]. The angular velocity of the cylinder, Ω, is relatively low, the liquid film is thin, the effect of the centripetal force is negligibly small (in contrast to the case studied in [1]), and rimming flow is mainly dominated by the interaction of the gravity and viscous forces. In our recent paper related to non-Newtonian fluids [7] only subcritical and critical flow regimes were analyzed. The latter was done numerically on the basis of Carreau-Yasuda constitutive model. In the present studies we utilize the Ellis model and extend our previous estimates to the supercritical flow regime. We assume that the ratio $\delta=h_0/r_0$ of the liquid layer characteristic thickness, h_0, to the radius of the cylinder, r_0, is small and, hence, the simple lubrication theory can be applied. Using a scale analysis, a theoretical description for a steady-state non-Newtonian flow is obtained. The main nondimensional complexes that define the process are derived and their typical numerical values are computed, e.g., it was found that $\delta=(\rho g r_0/\mu\Omega)^{1/2} \approx 0.02$, where ρ and μ are fluid density and typical viscosity, respectively. When the shear rate is large, the shear thinning effect can be significant, but the memory effects may still be negligible because of the long time scale for the flow transitions. The nu-

[1]Tel. +1-530-898-5274; e-mail: sfomin@csuchico.edu

Contributed by the Fluids Engineering Division of ASME for publication in the JOURNAL OF FLUIDS ENGINEERING. Manuscript received June 17, 2004; final manuscript received July 4, 2005. Assoc. Editor: Dennis Siginer.

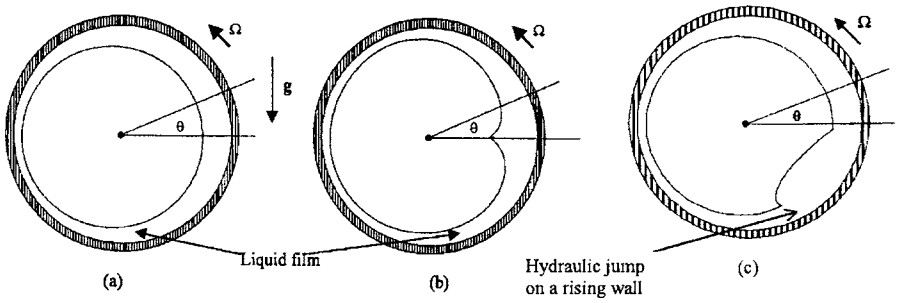

Fig. 1 A schematic sketch of rimming flow in the horizontal cylinder: (*a*) smooth solution in subcritical state, (*b*) critical regime, and (*c*) supercritical regime

merical estimates of elastic effects are based on a typical time scale for liquid polymers λ. This value is well documented for rotational flows [8,9] and normally stays in the range of $10^{-3}-10^{-2}$ s. The time scale for the rimming flow associated with rotation is $T=1/\Omega$. Hence, the Deborah number $\mathrm{De}=\lambda/T=\lambda\Omega$ for the maximal rotational rates, Ω, that occur in rotational moulding (<10 rad s^{-1}), is in the range $\mathrm{De}\sim 10^{-2}-10^{-1}$. Since the Deborah number, which characterizes memory effects, is sufficiently small, the flow is assumed to be viscometric. A general constitutive law for this kind of flow requires only a single function relating shear stress and shear rate that corresponds to a generalized Newtonian model.

The horizontal cylinder is assumed to be of infinite length. A cylindrical system of coordinates is located such that the z axis coincides with the axis of the cylinder and symmetry is assumed along this axis so that the flow picture is two-dimensional (Fig. 1). The balance laws for momentum and mass of an incompressible fluid are

$$\rho\frac{D\mathbf{v}^*}{Dt^*}=\rho\mathbf{g}-\nabla p^*+\nabla\cdot\boldsymbol{\tau}^* \tag{1}$$

$$\nabla\cdot\mathbf{v}^*=0 \tag{2}$$

Accounting for the surface tension, boundary conditions on the free surface are as follows:

$$-p^*+\mathbf{n}\cdot\boldsymbol{\tau}^*\cdot\mathbf{n}=2\kappa\sigma,\quad \mathbf{n}\cdot\boldsymbol{\tau}^*\cdot\mathbf{t}=0, \tag{3}$$

where $\mathbf{n}$ is the external to the liquid layer normal unit, $\mathbf{t}$ is the tangent, $\boldsymbol{\tau}$ is the stress tensor deviator, σ is the surface tension, and κ is the mean curvature of the free surface. The latter is calculated from the equation $2\kappa=\nabla\cdot\mathbf{n}$. The tangent and the normal to the free surface, which is defined as $r^*=r_0-h^*(\theta,t)$, are given by

$$\mathbf{t}=\left(-\frac{\partial h^*}{\partial\theta}\mathbf{e}_r+r^*\mathbf{e}_\theta\right)\Bigg/\left[\left(\frac{\partial h^*}{\partial\theta}\right)^2+r^{*2}\right]^{1/2},$$

$$\mathbf{n}=-\left(\mathbf{e}_r+\frac{1}{r^*}\frac{\partial h^*}{\partial\theta}\mathbf{e}_\theta\right)\Bigg/\left[1+\left(\frac{1}{r^*}\frac{\partial h^*}{\partial\theta}\right)^2\right]^{1/2}$$

On the wall of the cylinder $r^*=r_0$, $\mathbf{v}^*(\nu_r^*,\nu_\theta^*)=(0,\Omega r_0)$. The kinematics condition $D(r^*-r_0+h^*)/Dt^*=0$ on the free surface can be presented in the following form:

$$\frac{\partial h^*}{\partial t^*}+\nu_r^*+\frac{\nu_\theta^*}{r^*}\frac{\partial h^*}{\partial\theta}=0 \tag{4}$$

For the non-Newtonian fluid the constitutive law is given by $\boldsymbol{\tau}^*=2\mu^*(\gamma^*)\mathbf{e}^*$, where $\mathbf{e}^*$ is the rate-of-deformation tensor given by $\mathbf{e}^*=[(\nabla\mathbf{v}^*)+(\nabla\mathbf{v}^*)^T]/2$ and γ^* is a local shear rate, defined by $\boldsymbol{\gamma}^*=[2\,\mathrm{tr}(\mathbf{e}^{*2})]^{1/2}$. In particular, for the power-law fluid the viscosity is given by $\mu^*=k(\gamma^*)^{n-1}$. The stress-strain rate correlations in the 2D case reduce to the following:

$$\tau_{\theta\theta}^*=2\mu^*\left(\frac{1}{r^*}\frac{\partial\nu_\theta^*}{\partial\theta}+\frac{\nu_r^*}{r^*}\right),\quad \tau_{rr}^*=2\mu^*\frac{\partial\nu_r^*}{\partial r^*},$$

$$\tau_{r\theta}^*=\mu\left(\frac{1}{r^*}\frac{\partial\nu_r^*}{\partial\theta}+\frac{\partial\nu_\theta^*}{\partial r^*}-\frac{\nu_\theta^*}{r^*}\right). \tag{5}$$

The characteristic scales for the variables in the rimming flow are obvious and well documented, therefore, the nondimensional variables can be readily introduced as

$$\nu_\theta=\nu_\theta^*/\Omega r_0,\quad \nu_r=\nu_r^*/\Omega_0 r_0\delta,\quad r=r^*/r_0,$$

$$R=(1-r)/\delta,\quad h=h^*/h_0,$$

$$\tau_{r\theta}=\tau_{r\theta}^*\delta/\mu_0\Omega,\quad (\tau_{\theta\theta},\tau_{rr})=(\tau_{\theta\theta}^*,\tau_{rr}^*)/\mu_0\Omega, \tag{6}$$

$$t=t^*\Omega,\quad p=p^*/g\rho r_0$$

Here δ is the ratio of characteristic thickness of the liquid layer h_0 to the radius of the cylinder r_0 and μ_0 is the characteristic dynamic viscosity. As a result of scale analysis of the governing equations and boundary conditions three nondimensional parameters are defined:

$$\delta=\left(\frac{\mu_0\Omega}{\rho g r_0}\right)^{1/2}\ll 1,\quad \mathrm{Re}=\delta^2\frac{\rho\Omega r_0^2}{\mu_0}\ll 0,\quad C_B=\delta^2\frac{\sigma}{r_0\mu_0\Omega}\ll 1. \tag{7}$$

where Re is a Reynolds number and characterizes the ratio of inertial to the viscous forces, and C_B is the inverse of the Bonds number and characterizes the ratio of capillary and gravitational forces. Exploiting parameter δ being very small and to this end ignoring the terms of $O(\delta^2)$, the nondimensional continuity and momentum equations in cylindrical coordinates reduce to

$$-\frac{\partial}{\partial R}[(1-R\delta)\nu_R]+\frac{\partial\nu_\theta}{\partial\theta}=0 \tag{8}$$

$$-\delta\sin\theta+\frac{\partial p}{\partial R}+O(\delta^2)=0 \tag{9}$$

$$-\cos\theta-\frac{1}{1-\delta R}\frac{\partial p}{\partial\theta}-\frac{\partial\tau_{R\theta}}{\partial R}+2\delta\tau_{R\theta}+O(\delta^2)=0 \tag{10}$$

For the viscometric flow

$$\tau_{\theta R}=\mu\left(-\frac{\partial\nu_\theta}{\partial R}-\frac{\partial\nu_\theta}{1-\delta R}\right),\quad \tau_{RR}=-2\mu\frac{\partial\nu_R}{\partial R},$$

$$\tau_{\theta\theta}=\frac{2\mu}{1-\delta R}\left(\frac{\partial\nu_\theta}{\partial\theta}+\delta\nu_R\right) \tag{11}$$

where

$$\mu = \mu(|\dot{\gamma}|), \quad \dot{\gamma} = \frac{\partial \nu_\theta}{\partial R} + \frac{\delta \nu_\theta}{1 - \delta R} + O(\delta^2). \tag{12}$$

The kinematic condition on the free surface $R=h$ in the nondimensional form is given by

$$\frac{\partial h}{\partial t} + \nu_R + \frac{\partial h}{\partial \theta}\frac{\nu_\theta}{(1 - \delta R)} = 0 \tag{13}$$

Integrating the mass conservation equation (8) across the layer and introducing the result into the above equation yields

$$(1 - \delta h)\frac{\partial h}{\partial t} + \frac{\partial}{\partial \theta}\left(\int_0^h \nu_\theta dR\right) = 0 \tag{14}$$

Stress balance conditions on the free surface $R=h$ in tangential and transverse directions, respectively, reduce to

$$\tau_{\theta R} + O(\delta^2) = 0 \tag{15}$$

$$p = C_B\left(1 + h\delta + \delta\frac{\partial^2 h}{\partial \theta^2} + \right) + O(\delta^2) \tag{16}$$

On the wall of the cylinder $R=0$

$$\mathbf{v}(\nu_r, \nu_\theta) = (0,1) \tag{17}$$

For the generalized Newtonian liquid approximately to $O(\delta^2)$

$$\tau_{\theta R} = -\mu(|\dot{\gamma}|)\dot{\gamma} + O(\delta^2), \tag{18}$$

where $\dot{\gamma}$ is defined by Eq. (12).

At this stage it is convenient to introduce a function $G(x)$ as the inverse of function $\mu(\dot{\gamma})\dot{\gamma}$ so that for $x>0$ equations $G[\mu(x)x] = x$ and $\mu(G(x))G(x) = x$ should be satisfied. It is physically evident that shear stress should be a smooth and continuously increasing function of shear rate. Hence, function $\mu(\dot{\gamma})\dot{\gamma}$ can be assumed as an analytical and monotonic function. Due to the monotonic inverse function theorem, the inverse to $\mu(\dot{\gamma})\dot{\gamma}$ function G should also be an analytic and increasing function. For this definition, stress-strain correlation can be converted to its inverse form as follows:

$$\dot{\gamma} = -\operatorname{sgn}(\tau_{\theta R})G(|\tau_{\theta R}|). \tag{19}$$

To determine the dimensionless azimuthal velocity, which should be substituted into Eq. (14), the method of perturbations is utilized. The unknown functions in Eqs. (9)–(11) are expanded in asymptotic series by a small parameter δ with the adopted accuracy of $O(\delta^2)$:

$$p = p^0 + \delta p^1 + O(\delta^2), \quad \tau_{\theta R} = \tau^0_{\theta R} + \delta\tau^1_{\theta R} + O(\delta^2) \tag{20}$$

Substituting formulas (20) into the governing Eqs. (9)–(11) and boundary conditions (15) and (16) and collecting the terms of the same order yields

$$\frac{\partial p^0}{\partial R} = 0, \quad \cos\theta + \frac{\partial p^0}{\partial \theta} + \frac{\partial \tau^0_{R\theta}}{\partial R} = 0 \tag{21}$$

$$\frac{\partial p^1}{\partial R} - \sin\theta = 0, \quad -\frac{\partial p^1}{\partial \theta} - R\frac{\partial p^0}{\partial \theta} - \frac{\partial \tau^1_{\theta R}}{\partial R} + 2\tau^0_{R\theta} = 0 \tag{22}$$

Boundary conditions reduce to the following ones:

$$\text{for } R = h, \quad \tau^0_{\theta R} = 0, \quad p^0 = C_B, \quad p^1 = C_B\left(h + \frac{\partial^2 h}{\partial \theta^2}\right), \quad \tau^1_{\theta R} = 0 \tag{23}$$

Solution of the equations (21) and (22) subject to boundary conditions (23) is straightforward:

$$\tau^0_{\theta R} = (h - R)\cos\theta, \quad p^0 = C_B, \quad p^1 = -(h - R)\sin\theta + C_B\left(h + \frac{\partial^2 h}{\partial \theta^2}\right) \tag{24}$$

$$\tau^1_{\theta R} = -\frac{3}{2}(h - R)^2\cos\theta + (h - R)\left[-\sin\theta\frac{\partial h}{\partial \theta} + C_B\left(\frac{\partial h}{\partial \theta} + \frac{\partial^2 h}{\partial \theta^3}\right)\right] \tag{25}$$

Combining equations (19) and (12), and accounting for boundary conditions (17), the unknown velocity ν_θ can be readily obtained:

$$\nu_\theta = \left(1 - \operatorname{sgn}(\tau_{\theta R})\int_0^R \exp(\delta R)G(|\tau^0_{\theta R} + \delta\tau^1_{\theta R}|)dR\right)\exp(-\delta R), \tag{26}$$

where $\tau^0_{\theta R}$ and $\tau^1_{\theta R}$ are defined by (24) and (25).

Substituting function ν_θ into Eq. (14) and integrating with respect to R leads to the equation for the liquid layer thickness

$$(1 - \delta h)\frac{\partial h}{\partial t} + \frac{\partial}{\partial \theta}\left[h - \delta\frac{h^2}{2} - \operatorname{sgn}(\tau^0_{\theta R} + \delta\tau^1_{\theta R})\int_0^h (h - R)\left(1 - \frac{\delta}{2}(h - R)\right)G(|\tau^0_{\theta R} + \delta\tau^1_{\theta R}|)dR\right] = 0 \tag{27}$$

For $n=1$ it coincides with the equation presented in [5,10] for the Newtonian fluid. In the case of steady-state flow, the leading order equation can be presented in the following form:

$$\frac{\partial}{\partial \theta}\left(h - \operatorname{sgn}(\cos\theta)h^2\int_0^1 yG(h|\cos\theta|y)dy\right) = 0 \tag{28}$$

Integrating the latter leads to a simple algebraic equation

$$h - \operatorname{sgn}(\cos\theta)h^2\int_0^1 yG(h|\cos\theta|y)dy = q, \tag{29}$$

where the constant of integration, q, represents the nondimensional mass flux within the liquid film ($q = q^*/r_0^2\Omega\delta$). Obviously, solution $h=h(\theta)$ of Eq. (29) is periodic, even, and symmetric respective to $\theta=0$. Hence, the azimuthal distribution of h can be represented by its variation on the interval $[0,\pi]$. Differentiating Eq. (29) with respect to h and equalizing this derivative to 0 leads to the equation $1 - h\operatorname{sgn}(\cos\theta)G(h|\cos\theta|) = 0$. Once the solution of the latter equation $h=h_*(\theta)$ is found, the maximal supportable mass flux q_{max} can be readily computed from Eq. (29) setting in it $h=h_*$ and $\theta=0$.

Results and Discussion

For the further analysis of the process it is convenient to introduce a new auxiliary function f by the equation

$$f(h) = h - \operatorname{sgn}(\cos\theta)h^2\int_0^1 yG(h|\cos\theta|y)dy - q, \tag{30}$$

whose derivative with respect to h is the following:

$$\partial f/\partial h = 1 - h\operatorname{sgn}(\cos\theta)G(h|\cos\theta|). \tag{31}$$

Qualitative analysis of function (30) with its derivative (31) for the subcritical regime ($q < q_{max}$) readily shows that (a) at the interval $[\pi/2,\pi]$ Eq. (29) has the unique solution $h=h(\theta)$ which satisfies an inequality $0 < h < q$ and (b) on the interval $[0,\pi/2]$ Eq. (29) has two solutions $h=h_1(\theta)$ and $h=h_2(\theta)$, which satisfy inequalities $q < h_1 < h_*$ and $h_2 > h_*$, and $h_2 \to \infty$ for $\theta \to \pi/2$. Apparently, solution $h=h_2(\theta)$ for this regime has no physical meaning and, hence, should be omitted. Possible distributions of film thicknesses in the subcritical regime are illustrated in Fig. 2.

Quantitative analysis of Eq. (30) for the critical flow regime ($q=q_{max}$) leads to the following conclusions: (a) for this regime Eq. (29) reduces to an identity at $h=h_*$ and $\theta=0$. Hence, in the point $\theta=0$ functions $h_1(\theta)$ and $h_2(\theta)$ intersect, i.e., $h_1(0)=h_2(0)$

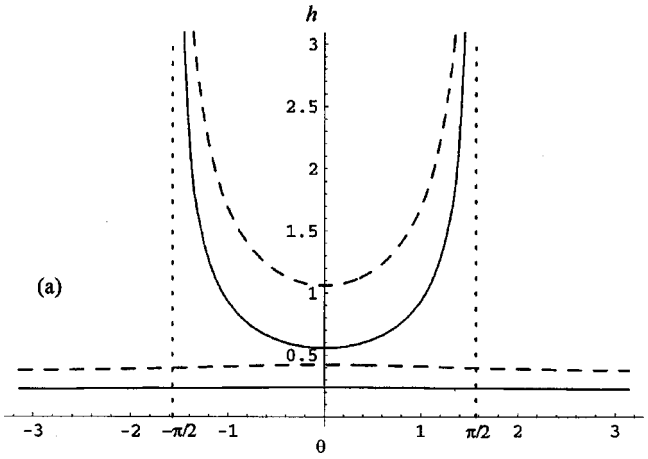

Fig. 2 Thickness of the liquid film in subcritical flow regime (*a*) when $q<q_{max}$. Solution is obtained by Eq. (36) for $n=\frac{1}{3}$; solid lines correspond to *Wi*=5 and dashed lines to *Wi*=1.

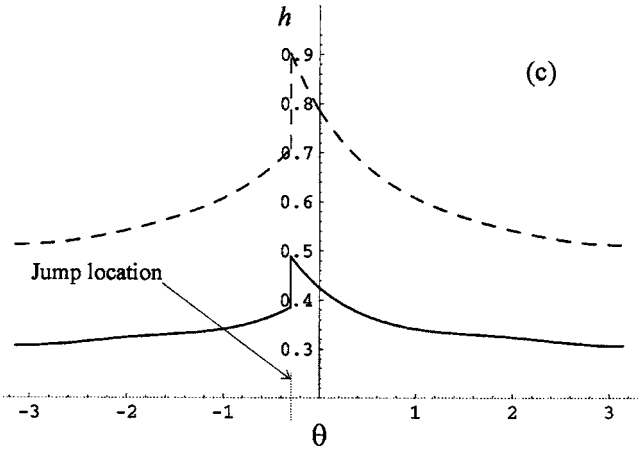

Fig. 4 Solution of Eq. (36) for supercritical flow regime (*c*) when $n=\frac{1}{3}$, $q=q_{max}$, and $H_0>H_c$; solid lines correspond to *Wi* =5 and dashed lines to *Wi*=1

$=h_*(0)$. (b) $h_1(\theta)$ decreases on $[0,\pi/2]$. At $\theta=0$ it reaches maximal value and for $\theta\to\pi/2-0$, $h_1\to q$. In contrast, $h_2(\theta)$ exhibits monotonous growth on $[0,\pi/2]$ and $h_2\to\infty$ for $\theta\to\pi/2-0$. It can be readily shown that the unique solution $h=h(\theta)$ defined on $[\pi/2,\pi]$ is a smooth continuation of function $h_1(\theta)$ in the domain $[\pi/2,\pi]$. Possible distributions of film thicknesses in the critical regime are illustrated in Fig. 3.

The critical conditions when solution of the steady-state equation (29) exists are defined in the terms of critical mass flux, i.e., $q\leqslant q_{max}$. Technologically, it is more natural to operate with such quantities as a total mass and volume of the liquid inside a cylinder or the rate of rotation. To this end, it is sensible to reformulate the critical condition in terms of the above-mentioned quantities. The mass of the liquid W^* inside the rotating cylinder can be calculated by the following equation (the asterisks are used to denote dimensional quantities):

$$W^*=\rho[\pi r_0^2-\pi(r_0-H_0^*)^2]=\rho\pi(2r_0H_0^*-H_0^{*2}), \tag{32}$$

where H_0^* is a mean thickness of the liquid layer $H_0^*=(1/2\pi)\int_0^{2\pi}h^*d\theta$. Denoting $W=W^*/\rho\pi r_0^2$, $H_0=1/2\pi\int_0^{2\pi}hd\theta$ and staying in the bounds of adopted accuracy [i.e., neglecting the terms of $O(\delta)$], Eq. (32) can be converted to the following nondimensional one:

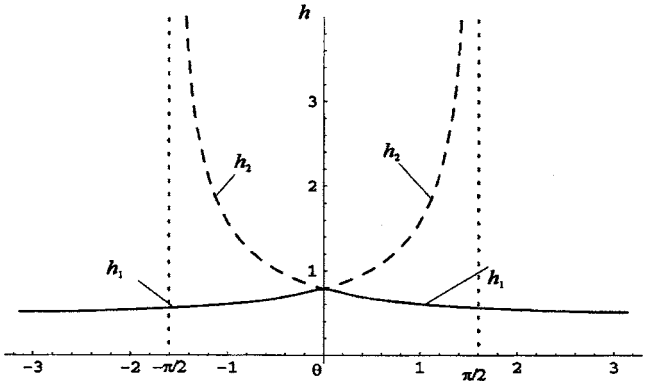

Fig. 3 Thickness of the liquid film in critical flow regime (*b*) when $q=q_{max}$. Solution is obtained by Eq. (36) for $n=\frac{1}{3}$ and *Wi* =1.

$$H_0=\frac{1}{2\pi}\int_0^{2\pi}hd\theta=\frac{W}{2\delta} \tag{33}$$

The mean thickness H_0 is obtained by the numerical evaluation of the integral (33), where h is the solution of Eq. (29). H_0 is equal to its critical value H_c when solution h of the equation (29) corresponds to the maximal mass flux $q=q_{max}$. For instance, for a Newtonian liquid H_c is equal to 0.707, which coincides with the results of the previous authors [1–5]. Thus, summing the above reasoning one can conclude that steady-state flow can be sustained while the inequality $H_0\leqslant H_c$ is satisfied. Accounting for Eq. (33), the latter condition can be converted to the form of the run-off condition, as it was formulated by Moffatt [2] and Preziosi and Joseph [3]. In the dimensional form this condition is the following:

$$(W/\rho r_0^2)\delta^{1/2}\leqslant H_c \tag{34}$$

Equation (34) provides the principal bounds for the steady-state rimming flow. By introducing the appropriate volume of liquid inside the cylinder and the speed of rotation, the inequality (34) should be satisfied. It will guarantee the steady-state flow of the liquid. However, the steady-state flow can be also sustained even when the left-hand side of (34) exceeds the value on the right-hand side, i.e., when $H_0>H_c$. In this supercritical case the discontinuous solution of Eq. (29) is possible and a steady hydraulic jump may occur [4,5], which can be the source of further instabilities. Possible distributions of the liquid film thicknesses in the supercritical regime are illustrated in Fig. 4.

It should be noted that even though the curves on Figs. 2–4 can be plotted approximately, as a result of qualitative analysis of functions (30) and (31) for different flow regimes, in fact they were obtained by exact numerical computations on the basis of the Ellis model. The Ellis model is one of the simplest models, which accounts for shear-thinning properties and simulates the Newtonian features for the low shear rates. For the Ellis model the inverse function can be defined explicitly, $G(x)=x(1+x^{1/n-1})$, and, hence, the shear rate-stress relationship can be presented as follows in nondimensional form [10,11]:

$$\dot\gamma=-\tau_{\theta R}[1+(Wi|\tau_{\theta R}|)^{1/n-1}] \tag{35}$$

In Eq. (35) parameter $Wi=\Omega/\dot\gamma_t\delta$ is the shear thinning parameter, where $\dot\gamma_t$ is a transitional value of shear rate, characterizing either the Newtonian (for $\dot\gamma<\dot\gamma_t$) or shear-thinning behavior (for $\dot\gamma>\dot\gamma_t$). Thus, for the Ellis model, equation (29) reduces to the following:

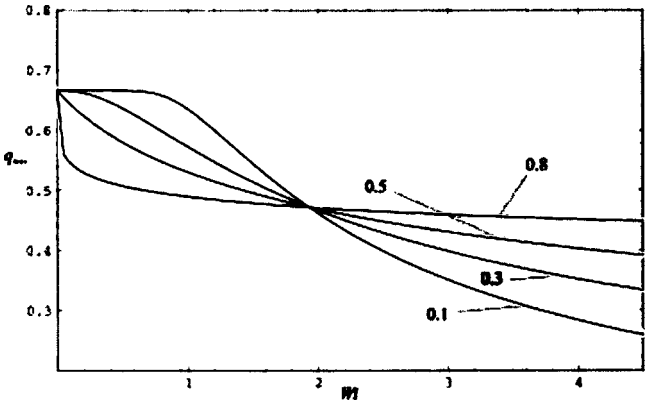

Fig. 5 Variation of the critical mass flux in the Ellis liquid film with respect to *Wi* for different values of flow index *n* =0.8, 0.5, 0.3, 0.1

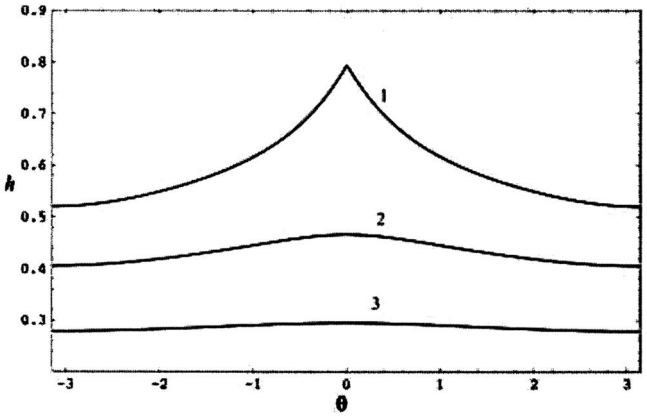

Fig. 6 Thickness of the Ellis liquid film along the wall of the cylinder for *Wi*=1 and $n=\frac{1}{3}$; (1) $q=q_{max}$, (2) $q=\frac{3}{4}q_{max}$, and (3) $q=\frac{1}{2}q_{max}$

$$h - h^3 \cos\theta\left(\frac{1}{3} + \frac{n(Wi|\cos\theta|h)^{(1-n)/n}}{2n+1}\right) = q, \quad 0 < n < 1. \tag{36}$$

Similar to the Carreau-Yasuda model, which was discussed in [7], the Ellis model also possesses Newtonian and power-law limits, though the transition from Newtonian to shear-thinning behavior is very gradual. For Ellis model the change in the maximal mass flux q_{max} *vs* parameter *Wi* is illustrated in Fig. 5. For this model, the interval of the steady-state flow $(0, q_{max})$ is wider (higher values of q_{max}) for smaller shear-thinning numbers *Wi* and reduces with the growth of this parameter. It is interesting to note that for $Wi \approx 1.9$ the flow is not affected by the parameter *n*, which defines shear-thinning properties of the fluid. For small *Wi* less than unity and $n \leqslant \frac{1}{3}$ the Ellis model provides the same steady-state-flow interval as a Newtonian fluid since $q_{max} \approx \frac{2}{3}$. As can be seen from the Fig. 5, the Ellis model can be used for modeling rimming flow if $n \leqslant \frac{1}{3}$. Only for these flow indexes can the transition from shear thinning to Newtonian behavior for low shear rates be recovered. For flow indexes above $\frac{1}{3}$ the Ellis model leads to unphysical results. This phenomenon follows from the Ellis constitutive equation and definition of the corresponding inverse function *G*. Substituting this function into the equation for the maximal liquid layer thickness $h=h_c$ at $\theta=0$, $1-h_c G[h_c Wi]/Wi=0$ and ignoring the terms of higher degree of smallness with respect to $Wi<1$ yields the asymptotic formula $h_c=1-Wi^{1/n-1}/2+o(Wi^{1/n-1})$. Substituting this approximate expression for h_c into Eq. (36) at $\theta=0$ and again ignoring the terms of higher degree of smallness the critical mass flux can be estimated asymptotically as $q_{max}=\frac{2}{3}-[1/(1/n+2)]Wi^{1/n-1}+o(Wi^{1/n-1})$. As it can be readily seen, this simple asymptotic equation perfectly explains the variation of q_{max} for small values of *Wi* (small shear rates). If $n=\frac{1}{3}$, the curvature of the curve, which is determined by the second derivative of the function $q_{max}(Wi)$, is finite for $0<Wi<1$ and if $n<\frac{1}{3}$, the curvature of the plot tends to zero in vicinity of $Wi=0$. On the contrary, if $n>\frac{1}{3}$, the curvature of the plot tends to infinity as $Wi \to 0$. Hence, for modeling the rimming flow with the Ellis constitutive equation, the restriction $n \leqslant \frac{1}{3}$ should be satisfied in order to ensure the Newtonian behavior at the small shear rates (interval $0<Wi<1$) and smooth transition to a shear-thinning flow for $Wi>1$.

Figure 6 illustrates distribution of the liquid film along the wall of the cylinder at the critical state $q=q_{max}$ (curve 1 with corner at $\theta=0$) and the subcritical state (curves 2 and 3) computed by Eq. (36). The solution for the Ellis liquids below critical values of mass fluxes are everywhere smooth, the local maximum at $\theta=0$ is flat, and for $q<q_{max}/2$ the thickness is practically uniform, which is very beneficial to technical applications where the resulting uniform thickness of the film is of a main concern.

Conclusions

1. The leading order lubrication model can be used for estimating the limits of steady-state behavior of a liquid film in the rimming flow of a non-Newtonian fluid. The application of the generalized Newtonian model for the approximate description of the flow of a liquid polymer is justified by the scale analysis.
2. The run-off condition for a generalized-Newtonian fluid on the wall of a rotating cylinder is derived and used for estimating the flow parameters. The maximum supportable load allowed by the generalized-Newtonian model, which exhibits transition from shear-thinning to Newtonian behavior, is smaller than for a Newtonian liquid and depends on the flow index *n*.
3. While using the Ellis constitutive equation, the restriction $n \leqslant \frac{1}{3}$ should be satisfied in order to ensure the Newtonian behavior at the small shear rates (interval $0<Wi<1$) and smooth transition to a shear-thinning flow for $Wi>1$.
4. Relatively uniform thickness can be achieved by ensuring that the rotational moulding process operates substantially below its critical conditions, for instance by applying the restriction $q<q_{max}/2$. Mathematically exact uniform thickness can be reached only in micro-gravity conditions when the centrifugal forces dominate.
5. Supercritical regimes can be analyzed within the bounds of leading order model; locations and dimensions of the hydraulic jumps can be detected.

Nomenclature

C_B = inverse to the Bond number
D = full derivative
$\mathbf{e}$ = rate of deformation tensor
$\mathbf{e}_r, \mathbf{e}_\theta$ = radial and azimuthal axes vectors, respectively
$\mathbf{g}$ = gravity vector
G = inverse function to $\mu(\dot{\gamma})\dot{\gamma}$
H_0 = nondimensional mean thickness of the liquid layer
H_c = nondimensional critical mean thickness of the liquid layer
h = nondimensional thickness of the liquid layer

h_0 = characteristic thickness of the liquid layer
$\mathbf{n}$ = normal to the free surface
p = nondimensional pressure
q = nondimensional mass flux
r = nondimensional radial coordinate as defined by Eqs. (6)
r_o = radius of the cylinder
R = modified nondimensional radial coordinate=$(1-r)/\delta$
Re = Reynolds number
t = nondimensional time
$\mathbf{v}$ = nondimensional fluid velocity
v_r, v_θ = nondimensional radial and azimuthal components of the fluid velocity, respectively
W = total mass of the liquid
Wi = shear-thinning number ($Wi=\Omega/\dot{\gamma}_t\delta$)

Greek Symbols

δ = ratio of the characteristic liquid layer thickness and radius of the cylinder
$\dot{\gamma}$ = nondimensional shear rate
$\dot{\gamma}_t$ = nondimensional transitional value of shear rate
κ = mean curvature of the free surface
μ = dynamic viscosity
θ = azimuthal coordinate
ρ = liquid density
σ = surface tension
τ = nondimensional deviator of the stress tensor
$\tau_{\theta R}, \tau_{RR}, \tau_{\theta\theta}$ = nondimensional components of τ
Ω = angular velocity of the cylinder

Superscripts

* = dimensional quantities
0,1 = zeroth- and first-order approximations, respectively

Subscripts

0 = characteristic quantity
θ, r = azimuthal and radial components, respectively

References

[1] Ruschak, K. J., and Scriven, L. E., 1976, "Rimming Flow of Liquid in a Rotating Horizontal Cylinder," J. Fluid Mech., **76**, pp. 113–125.
[2] Moffatt, H. K., 1977, "Behaviour of Viscous Film on the Surface of a Rotating Cylinder," J. Mec., **16**, pp. 651–673.
[3] Preziosi, L., and Joseph, D. D., 1988, "The Run-Off Condition for Coating and Rimming Flows," J. Fluid Mech., **187**, pp. 99–113.
[4] Melo, F., 1993, "Localized States in Film-Dragging Experiments," Phys. Rev. E, **48**, pp. 2704–2712.
[5] O'Brien, S. B. G., and Gath, E. G., 1998, "Location of a Shock in Rimming Flow," Phys. Fluids, **10**, pp. 1040–1042.
[6] Harkin-Jones, E., and Crawford, R. J., 1996, "Rotational Moulding of Liquid Polymers," in *Rotational Moulding of Plastics*, R. J. Crawford (Ed.), John Wiley & Sons, London, pp. 243–255.
[7] Fomin, S., Watterson, J., Raghunathan, S., and Harkin-Jones, E., 2002, "Steady-State Rimming Flow of the Generalized Newtonian Fluid," Phys. Fluids, **14**(9), pp. 3350–3353.
[8] Jenekhe, S. A., 1983, "The Rheology and Spin Coating of Polyimide Solutions," Polym. Eng. Sci., **23**, pp. 830–834.
[9] Jenekhe, S. A., and Schuldt, S. B., 1984, "Coating of Non-Newtonian Fluids on a Flat Rotating Disk," Ind. Eng. Chem. Fundam., **23**, pp. 432–436.
[10] Lawrence, C. J., and Zhou, W., 1991, "Spin Coating of Non-Newtonian Fluids," J. Non-Newtonian Fluid Mech., **39**, pp. 137–187.
[11] Bird, R. B., Armstrong, R. C., and Hassager, O., 1977, *Dynamics of Polymeric Liquids, Vol. 1, Fluid Dynamics*, Wiley, New York.

Experimental Study on the Helical Flow in a Concentric Annulus With Rotating Inner Cylinder

Nam-Sub Woo
e-mail: nswoo@skku.edu

Young-Ju Kim
e-mail: kyjp7272@kigam.re.kr

Young-Kyu Hwang
e-mail: ykhwang@skku.edu

School of Mechanical Engineering,
Sungkyunkwan University,
300 Chunchun-dong, Jangan-gu,
Suwon 440-746, South Korea

This experimental study concerns the characteristics of vortex flow in a concentric annulus with a diameter ratio of 0.52, whose outer cylinder is stationary and inner one is rotating. Pressure losses and skin friction coefficients have been measured for fully developed laminar flows of water and of 0.4% aqueous solution of sodium carboxymethyl cellulose, respectively, when the inner cylinder rotates at the speed of 0–600 rpm. The results of the present study show the effect of the bulk flow Reynolds number Re and Rossby number Ro on the skin friction coefficients. They also point to the existence of a flow instability mechanism. The effect of rotation on the skin friction coefficient depends significantly on the flow regime. In all flow regimes, the skin friction coefficient is increased by the inner cylinder rotation. The change in skin friction coefficient, which corresponds to a variation of the rotational speed, is large for the laminar flow regime, whereas it becomes smaller as Re increases for transitional flow regime and, then, it gradually approaches to zero for turbulent flow regime. Consequently, the critical bulk flow Reynolds number Re_c *decreases as the rotational speed increases. The rotation of the inner cylinder promotes the onset of transition due to the excitation of Taylor vortices.*
[DOI: 10.1115/1.2136923]

Keywords: vortex flow, concentric annulus, rotating cylinder, skin friction coefficient

1 Introduction

Rotating flows in annular passages with rotation of the inner cylinder are important because they have many engineering applications in bearings, rotating-tube exchangers, and, especially, annulus flows of mud in the case of slim hole drilling of the oil well.

It is well known that the stability of a viscous flow in a small annular gap between concentric cylinders with rotation of the inner one was first considered experimentally and theoretically by Taylor [1]. He also found that the flow is stable when the inner cylinder is stationary and the outer one is rotating. Conversely, if the outer cylinder is stationary, the flow becomes unstable. Diprima [2] applied the nonlinear theory to investigate the relation between the Taylor number and the stability.

Watanabe and Yamada [3] also indicated that the flow is relatively stable when the outer cylinder is rotating, and thus, the critical bulk flow Reynolds number Re_c is larger than that for the case of the inner cylinder rotating. Nouri and Whitelaw [4] revealed that the value of Re_c, decreases as both the rotational Reynolds number Re_w and the ratio of eccentricity m increases.

Escudier and Gouldson [5] investigated the influence of rotation on the axial velocity distribution and knew that it is most apparent at low bulk flow Reynolds number Re. Delwiche et al. [6] showed that the variations of an annular gap, wellbore eccentricity, and shaft rotational speed have strong effect on the pressure loss of fluid flowing in a narrow annulus of slim hole drilling. Because of these factors, it is very difficult to calculate accurately and control pressure losses in slim hole wellbores.

Siginer and Bakhtiyarov [7] carried out an analytical and experimental study on the flow of glycerol/water mixture and oil field spacer fluid in an eccentric annulus. Escudier et al. [8] presented numerical results for the flow of an inelastic shear-thinning power-law fluid through an eccentric annulus. They also summarized the literature of theoretical and numerical investigations of laminar flow of non-Newtonian fluids through annular channels.

This paper concerns an experimental study of fully developed laminar flows of Newtonian and non-Newtonian fluids through a concentric annulus in combination with bulk axial flow and inner cylinder rotation. The pressure losses and skin friction coefficients through the rotating annulus with diameter ratio of 0.52 have been measured under the fully developed flow condition of water and of 0.4% carboxylmethyl cellulose (CMC) aqueous solution. The rotational speed of the inner cylinder is between 0 and 600 rpm. The axial bulk flow Reynolds number is in range of $100 \leqslant \mathrm{Re} \leqslant 12,000$. The effects of shaft rotation, flow rate, and fluid rheology on the pressure loss, skin friction coefficient, and flow instability are investigated by the present experimental work. Namely, the value of critical Reynolds number Re_c is obtained for various combinations of the bulk flow Reynolds number and rotational speed of the inner cylinder. The effect of rotation on the skin friction coefficient depends significantly on the flow regime. For laminar flow regime, the change of skin friction coefficient corresponding to the variation of rotational speed is large, whereas it becomes smaller as the axial Reynolds number increases for transitional flow regime. For turbulent flow regime, it gradually approaches to zero.

2 Data Reduction

The equation of the average axial velocity in a concentric annulus without the rotation can be expressed in terms of the pressure loss dp/dz as follows [9]:

$$\bar{v}_z = \left(\frac{dp}{dz}\right)\frac{R_2^2}{8\mu}\left(\frac{1-\eta^4}{1-\eta^2} - \frac{1-\eta^2}{\ln(1/\eta)}\right) \tag{1}$$

where, $\eta\ (=R_1/R_2)$ is the ratio of radius. Also, the skin friction coefficient C_f can be obtained as

Contributed by the Fluids Engineering Division of ASME for publication in the JOURNAL OF FLUIDS ENGINEERING. Manuscript received July 20, 2004; final manuscript received September 22, 2005. Assoc. Editor: Dennis Siginer.

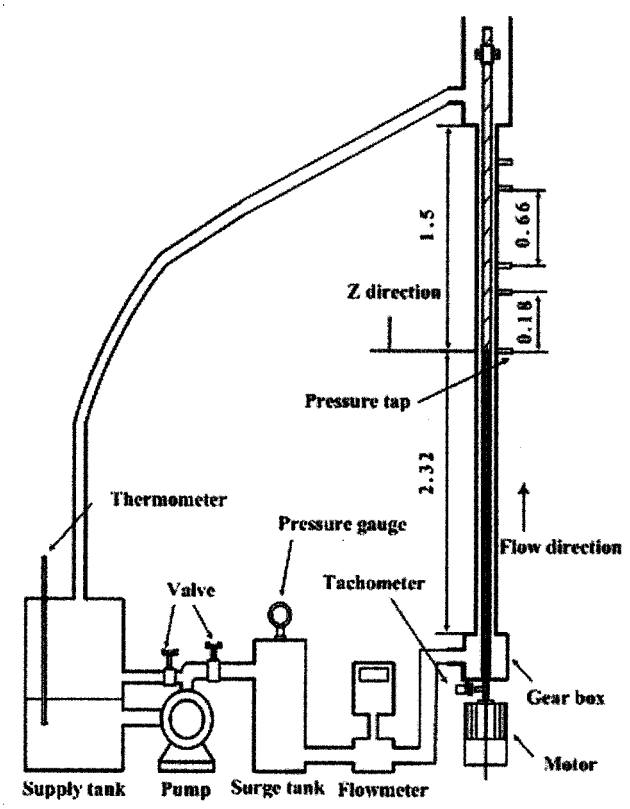

Fig. 1 Schematic diagram of experimental apparatus (all dimensions in meters)

$$C_f = \frac{dp}{dz} \cdot \frac{D_h}{2\rho \bar{v}_z^2} \tag{2}$$

where D_h $(=2(R_2-R_1))$ is the hydraulic diameter. Equations (1) and (2) are combined as

$$C_f = \frac{16}{\mathrm{Re}}\left(\frac{1-\eta^4}{1-\eta^2} - \frac{1-\eta^2}{\ln(1/\eta)}\right)(1-\eta)^2 \tag{3}$$

where Re $(=\bar{v}_z^{2-n} D_h^n / \nu)$ is the Reynolds number for Newtonian and non-Newtonian fluids.

3 Experimental Method

3.1 Experimental Apparatus. The experimental setup consists of a cylindrical section, supporting parts, fluid-providing and rotating part, and measuring part, which measure the flow rate, pressure loss, and the temperature as shown in Fig. 1. A centrifugal pump delivers the working fluid from a supply tank to a surge tank. The surge tank located immediately after the pump outlet acts to remove pulsation in the flow prior to entry into the test section. The fluid flow into the annular passage with an outer brass pipe of nominal inside diameter D_2 of 38.4 mm and 3.82 m long and an inner stainless steel rod of diameter D_1 of 20 mm. To insure fully developed flow in the measuring section, the length of straight pipe upstream of the test section is 2.32 m, corresponding to 126 hydraulic diameters, in order to produce an artificially thickened boundary layer. The rotating cylinder with the length of 1.5 m, and the nonrotating counterpart are connected by bronze bearings in order to prevent vibration and eccentricity caused by the rotation of the inner cylinder.

Static pressures are measured with holes of 0.5 mm dia distributed longitudinally in the outer cylinder. Five static pressure taps are installed along the flow direction in measuring part as shown in Fig. 1. The static pressures are read from a calibrated manometer bank with ±1 mm resolution. The specific gravity of the manometer fluid CCl_4 is 1.88, and it gives a height in the range of 20–600 mm.

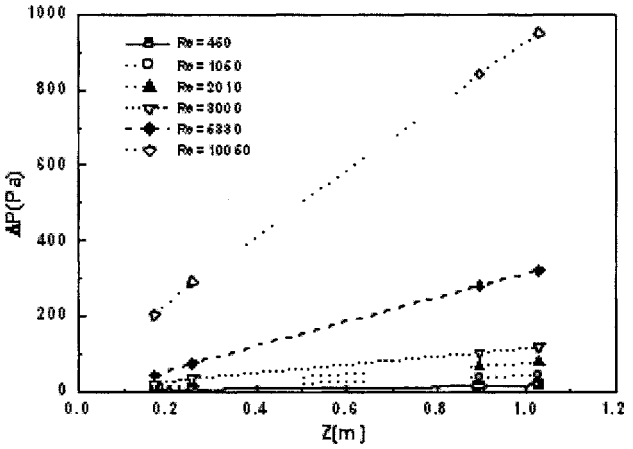

Fig. 2 Pressure differences of water as a function of *z* with various Re

In the experiment, the pressure losses have been measured by

$$\frac{dp}{dz} = \frac{gh \sin\theta(\rho_{ccl_4} - \rho)}{\Delta z} \tag{4}$$

where ρ, ρ_{CCl_4}, θ, h, and Δz denote the density of the fluid, the density of CCl_4, the inclined angle of the manometer, the difference of head of the manometer, and the distance between pressure holes, respectively. The experimental values of the skin friction coefficient in the laminar region can be evaluated by substituting Eq. (4) into Eq. (2).

The viscosity of 0.4% CMC solution was measured using the rotating type viscometer (Brookfield DV-III$^+$ Programmable Rheometer). In the case of a nonrotating annulus, we compared the experimental value of the skin friction coefficient obtained from the experiment with the theoretical value calculated by Eq. (5). For a nonrotating eccentric annulus, the skin friction coefficient was proposed by Yamada and Watanabe [10] as

$$C_f = \frac{23.8}{\mathrm{Re}\left(1 + \frac{3}{2}m^2\right)} \tag{5}$$

where m is the eccentricity of an annulus. The measured value has the discrepancy of 2.3% with the theoretical value. Thus, it is confirmed that the eccentricity (m) is within 0.12. The outer cylinder and the rotating inner cylinder are supported by an H-beam of 4 m long construction steel (SK40).

The flow rate has been measured with a magnetic flow meter whose accuracy is within the limit of ±0.5%. The temperature of the working fluid has been measured with a digital multimeter. The inner cylinder may be rotated at any speed up to a maximum of 1000 rpm by means of an AC motor. The temperature of the fluid within the pipe rig is maintained at 25±0.5°C.

3.2 Experimental Method. The development of the flow is identified by the change of the axial pressure gradient. Therefore, the value of pressure losses with Reynolds number has been measured between the tap 1 and taps 2–5 along the z direction of Fig. 1 to check the development of the flow.

In the case of water, the measured pressure losses along the flow of the z direction at each tap are shown in Fig. 2 to confirm the development of the flow with various Reynolds numbers. Since the measured values of $\Delta P_{1,2}$ and $\Delta P_{1,3}$ have large errors due to the short distances between taps, experiments have been repeated several times to minimize the errors. For Re≥1000, the

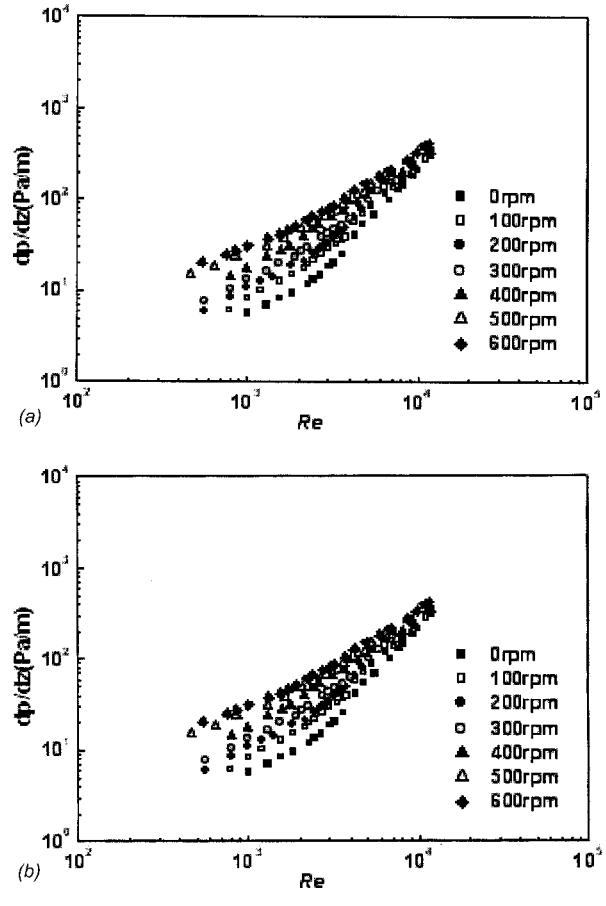

Fig. 3 (*a*) Pressure losses and (*b*) skin friction coefficients of water as a function of Re at 0–600 rpm

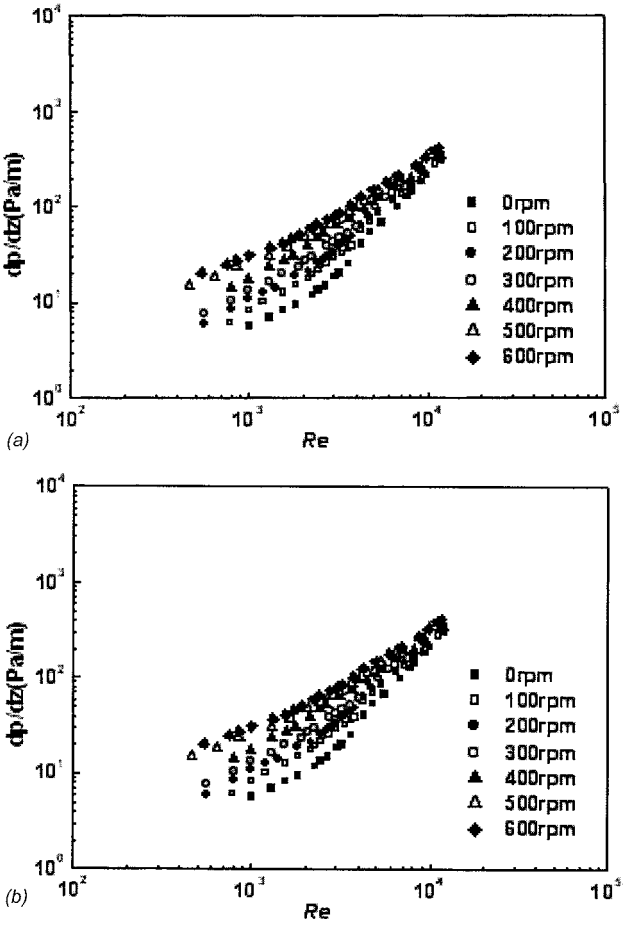

Fig. 4 (*a*) Pressure losses and (*b*) skin friction coefficients of 0.4% CMC solution as a function of Re at 0–600 rpm

maximum uncertainties are less than ±6% and ±3% for the flow of water and of 0.4% CMC solution, respectively.

3.3 Properties of Working Fluid. Non-Newtonian fluids are those for which the strain rate and shear stress curve are not linear, i.e., the viscosity of non-Newtonian fluids is not constant at a given temperature and pressure but depends on other factors, such as the rate of shear in the fluid, the apparatus in which the fluid is contained, or even the previous history of the fluid.

In the case of 0.4% CMC solution, $n<1$ and the power law relating the shear stress τ to the shear rate γ is given by

$$\tau = k\gamma^n \tag{6}$$

where n is the flow behavior index and K is the consistency factor. The apparent viscosity μ_a for a power-law fluid may be expressed in terms of n and K as follows:

$$\mu_a = k\gamma^{n-1} \tag{7}$$

The effective viscosity of 0.4% CMC solution for the same flow rate of 6 lpm becomes 22 cp at 0 rpm and 18 cp at 200 rpm and n is measured as 0.76.

4 Results and Discussion

The relations between the pressure loss dp/dz and Re are shown in Fig. 3(*a*), for the various rotational speeds in the range of water flow rate 1–40 lpm. Also, the relations between C_f and Re are shown in Fig. 3(*b*). In laminar flow regime without rotation, the variation of C_f with water is similar to those of Nouri and Whitelaw [4] and Shah and London [11].

In the case of water, it is difficult to measure the pressure loss accurately because it is so small at low Reynolds number. The errors of C_f have appeared at the maximum of ±7% for Re <1000 and ±5% for Re >1000. However, in the case of 0.4% CMC solution, it is relatively easy to measure the pressure loss since its viscosity is larger than that of water. In this case, the errors of C_f are less than ±3% for all laminar flow regimes.

The measurement of pressure loss for 0.4% CMC solution has been carried out for 1–50 lpm. Figures 4(*a*) and 4(*b*) show the effects of rotation on dp/dz and C_f, respectively, for 0.4% CMC solution. The critical Reynolds number for 0.4% CMC solution is found to be slightly lower than that for water because of the different viscosity at the same rotational speed.

4.1.1 Laminar Regime. Laminar flow regime has been confined to the range of $\mathrm{Re}<\mathrm{Re}_c$, where, the critical Reynolds number Re_c decreases with the increase of rotational speed as shown in Fig. 5. From the experimental results of pressure losses for both water and 0.4% CMC solution, the gradient of the skin friction coefficients is almost unchanged, which is irrespective of the change of the rotational speed $N<200$ rpm, but it becomes steeper for $N\geqslant 300$ rpm as shown in Figs. 3 and 4. This is due to the change of flow regime from laminar to laminar-Taylor vortices.

The relative skin friction coefficient C_f^* is defined as Eq. (8). Where, suffixes s and R represents the skin friction coefficient for non-rotation and that for rotation, respectively.

$$C_f^* = [(C_{f,R} - C_{f,s})/C_{f,R}] \tag{8}$$

In the case of water, we can obtain C_f^* by Eq. (8) as shown in Fig. 6(*a*). The value of C_f^* significantly increases from 40 to 76% in the laminar regime as N increases from 100 to 400 rpm. On the

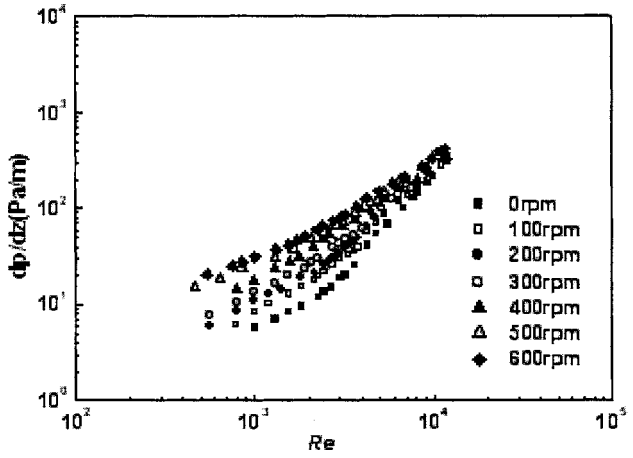

Fig. 5 Pressure losses of 0.4% CMC solution as a function of Re at 200–600 rpm

other hand, in the case of 0.4% CMC solution as shown in Fig. 6(*b*), the value of C_f^* slightly increases from 4 to 26% as N increases from 100 to 600 rpm. That is, the influence of the rotational speed on the skin friction coefficients for 0.4% CMC solution is relatively weaker than that for water because of the difference of rheological characteristics. Note that the Rossby number is defined as $\mathrm{Re}_\omega/\mathrm{Re}$, which represents the ratio of the inertial force to the Coriolis force.

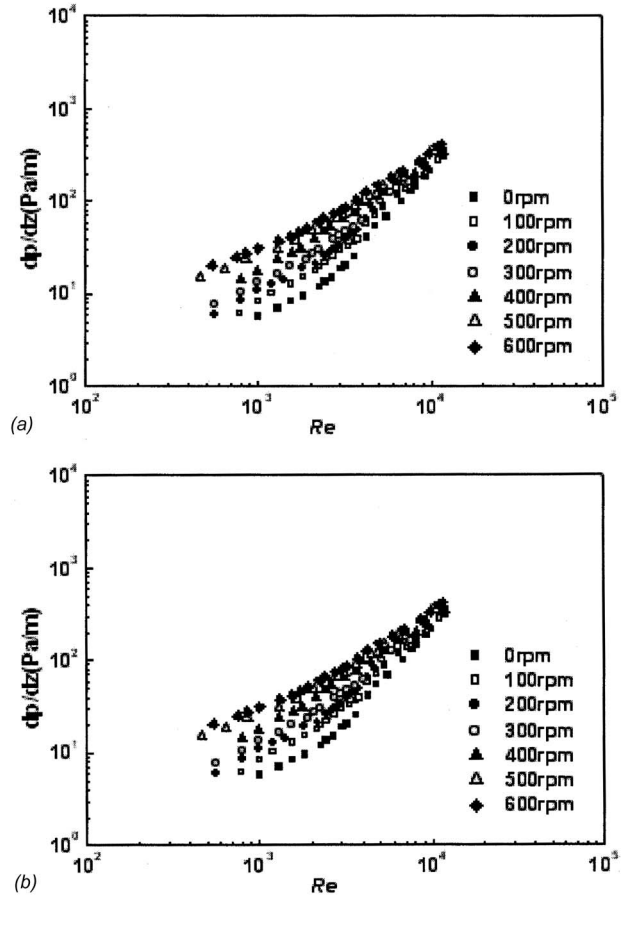

Fig. 6 Normalized relative skin friction coefficients C_f^* of water and 0.4% CMC solution as a function of Re at 100–600 rpm: (*a*) water and (*b*) 0.4% CMC solution

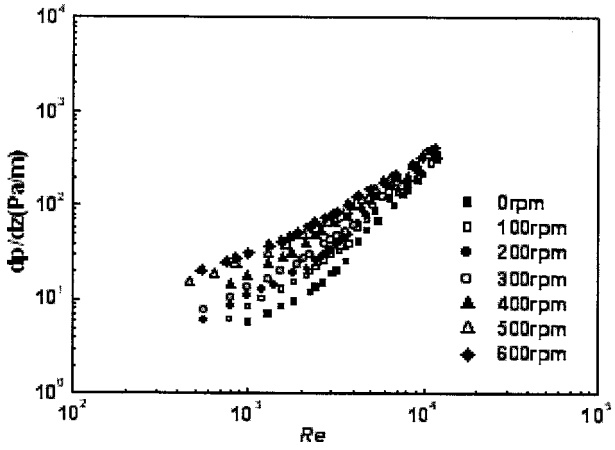

Fig. 7 Relation of C_f Re with Ro for laminar flow in water

Variations of the pressure losses with Reynolds number and rotational speed for 0.4% CMC solution are shown in Fig. 5. The previous researchers also observed that laminar-Taylor vortex exists in the range of $131 \leqslant \mathrm{Re} \leqslant 927$ [12]. It is found from the present results that the laminar-Taylor vortex exists in the range $0 \leqslant \mathrm{Re} \leqslant \mathrm{Re}_{l,t}$. The value of $\mathrm{Re}_{l,t}$ increases as N increases. If the bulk flow increases for $\mathrm{Re} > \mathrm{Re}_{l,t}$, the flow belongs to the laminar flow regime where the Taylor vortex has the least influence.

Figures 7 and 8 show the relation between C_f Re and Ro for water and 0.4% CMC solution, respectively. The effect of rotation with axial flow on the axial pressure loss in a rotating annulus can be explained with these figures. The skin friction coefficient can be correlated with Ro and Re as Eq. (9) for water and Eq. (10) for 0.4% CMC solution, asymptotically.

The index on Rossby number indicates the effect of rotation. From the Eqs. (9) and (10), we can also see that the effect of rotation on the pressure losses is larger in water than in 0.4% CMC solution. The deviation of experimental data with the correlations is within ±9%.

$$C_f \mathrm{Re} = 45.3\ \mathrm{Ro}^{-0.44} \tag{9}$$

$$C_f \mathrm{Re} = 77.3\ \mathrm{Ro}^{-0.10} \tag{10}$$

4.1.2 Transitional Regime. It is evident from the experimental results of 0.4% CMC solution that the critical Reynolds number is

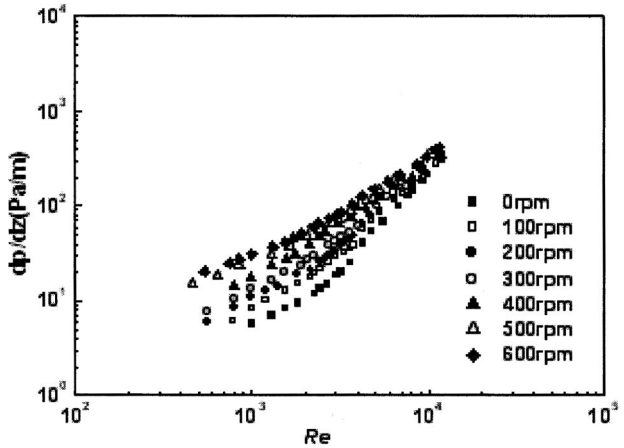

Fig. 8 Relation of C_f Re with Ro for laminar flow in 0.4% CMC solution

dependent on the rotational speed and Rossby number as shown in Fig. 5. The value of axial critical Reynolds number decreases as the rotational speed of the inner cylinder N increases. Namely, the critical Reynolds number decreases as Rossby number decrease.

When C_f^* is used to express the influence of N on the skin friction coefficients in a transition regime, C_f^* is consistently unchanged in the laminar regime as seen in Fig. 6. But, C_f^* tends to increase in a transition regime for $\mathrm{Re} \approx \mathrm{Re}_c$, and to decrease abruptly in a turbulent regime. However, this tendency decreases as N increases due to the Taylor vortex. In the case of water at $N=100$ rpm, the relative skin friction coefficient is about 65% due to the rotation.

5 Conclusions

In this study, the effects of the rotational speeds, the flow rates, and the working fluids on the pressure losses and skin friction coefficients have been investigated experimentally for the rotating flow between the stationary outer cylinder and the rotating inner one. From the present results, the new correlations with the skin friction coefficients, the Rossby numbers, and Reynolds numbers of water and 0.4% CMC solution have been presented with the reasonable limits of the accuracy in the laminar flow region.

It is clear that the critical Reynolds number of 0.4% CMC solution has a slightly lower value than that of water due to the difference of rheological characteristics of fluids. The effects of rotation on water are much greater than on 0.4% CMC solution because of this rheological difference.

The pressure loss slightly increases as the rotational speed increases although the relative skin friction coefficient C_f^* decreases as the Reynolds number increases in the regime of the transition and turbulence.

The value of critical Reynolds number decreases with the increasing of rotational speed. Also, the increase of flow disturbance caused by the Taylor vortex between the concentric cylinders results in the decrease of the critical Reynolds number and the increase of skin friction coefficient.

Acknowledgment

This work was supported by the academic research fund of the Korea Energy Management Corporation.

Nomenclature

C_f = skin friction coefficients
D_h = hydraulic diameter, $2(R_2-R_1)$
dp/dz = pressure loss (Pa/m)
e = displacement of inner cylinder axis from outer cylinder axis
K = consistency factor (Pa sn)
m = eccentricity, $e/(R_2-R_1)$
n = flow behavior index
N = rotational speed of inner cylinder (rpm)
ΔP = difference of pressure (Pa)
R_1 = radius of inner cylinder (mm)
R_2 = radius of outer cylinder (mm)
Re = Reynolds number, $\bar{v}_z^{2-n} D_h^n / \nu$
Re_c = critical Reynolds number
Re_w = rotational Reynolds number, $\omega R1(R_2-R_1)/v$
Ro = Rossby number, $2\bar{v}_z/\omega R_1$
$\bar{v}_z$ = average velocity in z-direction (m/s)
Δz = distance between pressure taps (mm)

Greek Symbols

η = ratio of radius, R_1/R_2
μ = absolute viscosity (Pa s)
μ_a = apparent viscosity
ν = kinematic viscosity (m^2/s)
ρ = density of fluid (kg/m^3)
ω = angular velocity of inner cylinder (rad/s)

References

[1] Taylor, G. I., 1923, "Stability of a Viscous Fluid Contained Between Two Rotating Cylinders," Philos. Trans. R. Soc. London, Ser. A, **223**, pp. 289–343.
[2] Diprima, R. C. 1960, "The Stability of a Viscous Fluid Between Rotating Cylinders With a Bulk Flow," J. Fluid Mech., **366**, pp. 621–631.
[3] Watanabe, S., and Yamada, Y., 1973, "Frictional Moment and Pressure Drop of the Flow Through Co-Axial Cylinders With an Outer Rotating Cylinder," Bull. JSME, **16**(93), pp. 551–559.
[4] Nouri, J. M., and Whitelaw, J. H., 1994, "Flow of Newtonian and Non-Newtonian Fluids in a Concentric Annulus With Rotation of the Inner Cylinder," ASME J. Fluids Eng., **116**, pp. 821–827.
[5] Escudier, M. P., and Gouldson, I. W., 1995, "Concentric Annular Flow With Centerbody Rotation of a Newtonian and a Shear-Thinning Liquid," Int. J. Heat Fluid Flow, **16**, pp. 156–162.
[6] Delwiche, R. A., Lejeune, M. W. D., and Stratabit, D. B., 1992, "Slimhole Drilling Hydraulics," SPE Paper No. 24596, pp. 521–541.
[7] Siginer, D. A., and Bakhtiyarov, S. I., 1998, "Flow of Drilling Fluids in Eccentric Annuli," J. Non-Newtonian Fluid Mech., **78**, pp. 119–132.
[8] Escudier, M. P., Oliveira, P. J., and Pinho, F. T., 2002, "Fully Developed Laminar Flow of Purely Viscous Non-Newtonian Liquids Through Annuli, Including the Effects of Eccentricity and Inner-Cylinder Rotation," Int. J. Heat Fluid Flow, **23**, pp. 52–73.
[9] Bird, R. B., Lightfoot, E. N., and Stewart, W. E., 1960, *Transport Phenomena*, pp. 34–70.
[10] Yamada, Y., and Watanabe, S., 1973, "Frictional Moment and Pressure Drop of the Flow Through Co-Axial Cylinders With an Outer Rotating Cylinder," Bull. JSME, **12**(93), pp. 551–559.
[11] Shah, R. K., and London, A. L., 1978, *Laminar Flow Forced Convection*, Academic Press, New York.
[12] Wereley, S. T., and Lueptow, R. M., 1998, "Spatio-Temporal Character of Non-Wavy and Wavy Taylor-Couette Flow," J. Fluid Mech., **364**, pp. 59–80.

On the Mechanism Responsible for Turbulent Drag Reduction by Dilute Addition of High Polymers: Theory, Experiments, Simulations, and Predictions

J. Jovanović

M. Pashtrapanska

B. Frohnapfel

F. Durst

Lehrstuhl für Strömungsmechanik,
Universität Erlangen-Nürnberg,
Cauerstrasse 4, 91058 Erlangen, Germany

J. Koskinen
Neste Jacobs Oy,
POB 310,
06101 Porvoo, Finland

K. Koskinen
Outokumpu Research Oy,
POB 60,
28101 Pori, Finland

Turbulent drag reduction by dilute addition of high polymers is studied by considering local stretching of the molecular structure of a polymer by small-scale turbulent motions in the region very close to the wall. The stretching process is assumed to restructure turbulence at small scales by forcing these to satisfy local axisymmetry with invariance under rotation about the axis aligned with the main flow. It can be shown analytically that kinematic constraints imposed by local axisymmetry force turbulence near the wall to tend towards the one-component state and when turbulence reaches this limiting state it must be entirely suppressed across the viscous sublayer. For the limiting state of wall turbulence, the statistical dynamics of the turbulent stresses, constructed by combining the two-point correlation technique and invariant theory, suggest that turbulent drag reduction by homogeneously distributed high polymers, cast into the functional space which emphasizes the anisotropy of turbulence, resembles the process of reverse transition from the turbulent state towards the laminar flow state. These findings are supported by results of direct numerical simulations of wall-bounded turbulent flows of Newtonian and non-Newtonian fluids and by experiments carried out, under well-controlled laboratory conditions, in a refractive index-matched pipe flow facility using state-of-the art laser-Doppler anemometry. Theoretical considerations based on the elastic behavior of a polymer and spatial intermittency of turbulence at small scales enabled quantitative estimates to be made for the relaxation time of a polymer and its concentration that ensure maximum drag reduction in turbulent pipe flows, and it is shown that predictions based on these are in very good agreement with available experimental data.
[DOI: 10.1115/1.2073227]

1 Introduction

Turbulent drag reduction due to the addition of small amounts of dilute polymers to flowing liquids has been known for more than 50 years. This phenomenon was discovered by Toms in 1948 and owing to his pioneering contribution it is often termed Tom's effect in the literature. In spite of enormous research efforts in recent decades in attempts to provide at least a qualitative understanding of the mechanisms involved, no satisfactory explanation has yet been obtained. In this respect, the early studies of Metzner and Park [1], Lumley [2,3], Virk [4], and Berman [5] and the more recent contributions of Tabor and Gennes [6], Ryskin [7], Thirumalai and Bhattacharjee [8], and Sreenivasan and White [9] should be mentioned.

Only recently, with advances in optical measuring techniques, has it become possible to measure turbulence in polymer drag reducing flows. The experimental work of Rudd [10] and Logan [11] and subsequent contributions of Reischman and Tiederman [12], Luchik and Tiederman [13], Walker and Tiederman [14], Willmarth et al. [15], Wei and Willmarth [16], and Warholic et al. [17] provided important information on modifications of the statistical properties of turbulence in wall-bounded flows by presence of polymer additives. Most of these experimental investigations were carried out for a low percentage of drag reduction (DR). The mean velocity profile was found not to follow a classical log law. The root mean square of the streamwise and normal velocity fluctuations, normalized with the wall friction velocity determined for the polymer flow, were larger and lower, respectively, than in Newtonian liquid. These trends became more pronounced as DR increased. For large DR, experiments showed that the turbulent shear stress is approximately zero, indicating that turbulence is not maintained by the well-known mechanism (which ensures that rates of energy generation and viscous dissipation are in balance) and that the persistence of turbulence is associated with the statistical dynamics of extra polymer stresses.

In order to gain a more detailed insight into the phenomena of polymer drag reduction, direct numerical simulations have been performed by Toonder et al. [18], Sureshkumar et al. [19], Dimitropulos et al. [20], Sibilla and Baron [21], Angelis et al. [22], and Dubief [23]. These numerical studies provided considerable information about the behavior of turbulence in the presence of a polymer solution in the flow: the influence of a polymer on the mean flow and turbulence stresses and their detailed budgets including instantaneous three-dimensional flow patterns. These simulations, like those of Newtonian turbulence, cannot themselves lead to improved understanding without a firm theory capable of distinguishing the cause from the consequence. A lack of generally accepted and well-supported theory for the remarkable evidence that one drop of a long-chain polymer properly mixed with a few hundred liters of liquid can reduce up to 80% of friction drag in a pipe flow illustrates the huge gap that exists in our current knowledge of wall turbulence. This situation immediately

Contributed by the Fluids Engineering Division for publication of ASME in the JOURNAL OF FLUIDS ENGINEERING. Manuscript received April 9, 2004; final manuscript received August 2, 2005. Assoc. Editor: Steven Ceccio.

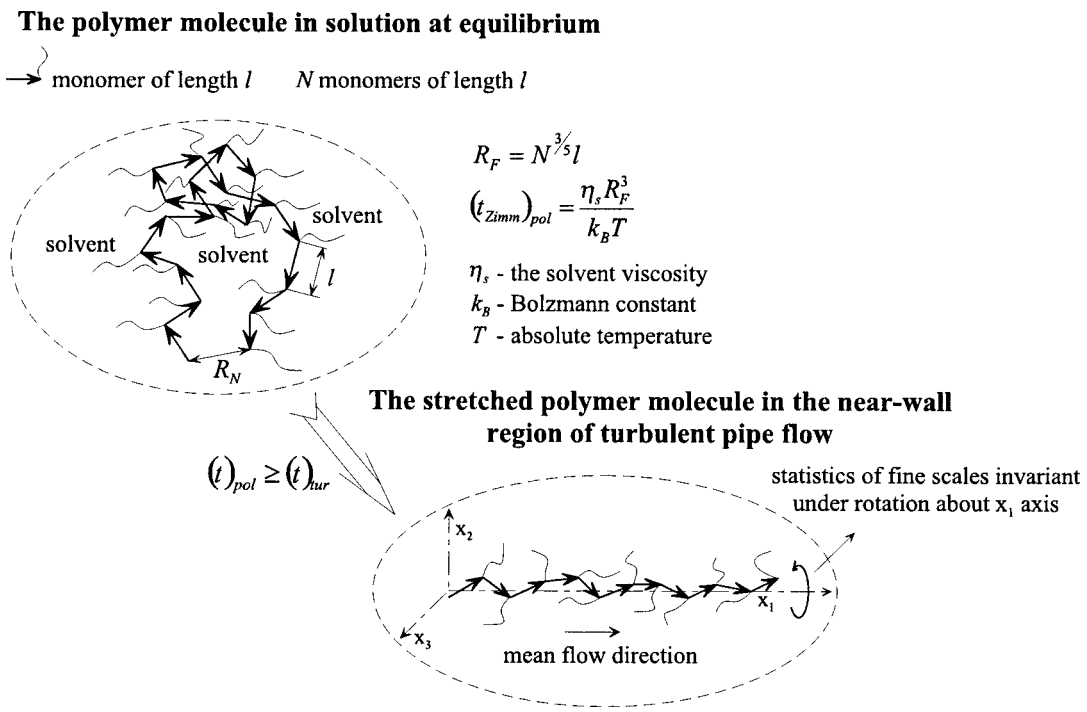

Fig. 1 Behavior of a polymer in solution at equilibrium (top) and its response to stretching by turbulent motions at small scales very close to the wall (bottom). Here R_N and R_F are hydrodynamical and Flory radius, respectively.

suggests that something substantial and very fundamental can be learned about turbulence by studying the mechanism of polymer drag reduction.

The theory of turbulent drag reduction in simple, nearly parallel wall-bounded flows with homogeneous distribution of the polymer can be worked out proceeding from the basic equations that govern the turbulent stresses and by using (*but not misusing*) the turbulence closure based on the application of the two-point correlation technique and invariant theory [24]. Conclusions emerging from the theory can be tested by direct comparisons with numerical simulations or experiments. The mechanism responsible for large drag reduction can be identified without appeal to the empirical input or auxiliary approximation. However, its description might not be digestible for those who reason about turbulence (in a deterministic fashion) exclusively in the physical space where observations usually take place: exposition and usage of arguments and resulting deductions may therefore seem unreasonable, confusing, or entirely wrong. If the matter is analyzed in the functional space formed by the two scalar invariants which emphasize the anisotropy of turbulence, the problem of large drag reduction turns out to be the first one to attack because of its simplicity, and specific and unconventional usage of arguments then appears logical and transparent.

Knowing the mechanism of turbulent drag reduction in advance, it became necessary to reverse the order of reasoning to arrive at the conceptual scenario of how long-chain polymers interact with turbulence. By arguing in the real space and the functional space [25] it is possible to specify this interaction in the form of kinematic constraints and to show how these constraints force suppression of turbulence close to the wall, leading to significant drag reduction.

2 The Mechanism of Homogeneous Polymer Drag Reduction

The problem of polymer drag reduction remains poorly understood mainly because the interaction between a polymer and turbulence is essentially at the molecular level of the former. This interaction involves modification of the molecular structure of a polymer by turbulent motions in the near-wall region. Figure 1 shows a conceptual scenario where, under very special circumstances, turbulence in the near-wall region forces rolled-up chains of a polymer to partially unroll and stretch in the mean flow direction.

In the unrolled state, polymer chains dictate characteristic length scales associated with the fine structure of turbulence. These scales are elongated in the streamwise direction and are therefore strongly anisotropic. In the most extreme case, polymer chains form a filament structure with a length-scale arrangement which is almost axisymmetric around the axis aligned with the mean flow. Hence it is reasonable to assume that the mechanism of drag reduction is related to the ability of the activated polymer to restructure turbulence at small scales by forcing them to satisfy constraints imposed by local axisymmetry.

Local axisymmetry as illustrated in Fig. 1 requires that the statistics of higher-order velocity derivatives, which contribute to the turbulent dissipation correlations, must satisfy invariance under rotation about the axis orientated in the mean flow direction (see [25]).

In the near-wall region, the presence of the polymer increases not only the anisotropy in length scales but also anisotropies in the dissipation and turbulent stresses, since these are closely related across the viscous sublayer. This can be shown using the two-point correlation technique and invariant theory [24]. If the polymer concentration (c) and its relaxation time (t_{pol}) are appropriately matched to the properties of turbulence, it will undergo considerable modification and reach, at the wall, a state of maximum anisotropy. This state can be identified on the anisotropy-invariant map shown in Fig. 2 and corresponds to the one-component limit ($\mathrm{II}_a = 2/3$). For these limiting conditions Jovanović and Hillerbrand [25] provided an analytical proof which shows that if turbulence (at small scales) close to the wall is locally axisymmetric as illustrated in Fig. 1, it must undergo very rapid laminarization and therefore considerable drag reduction

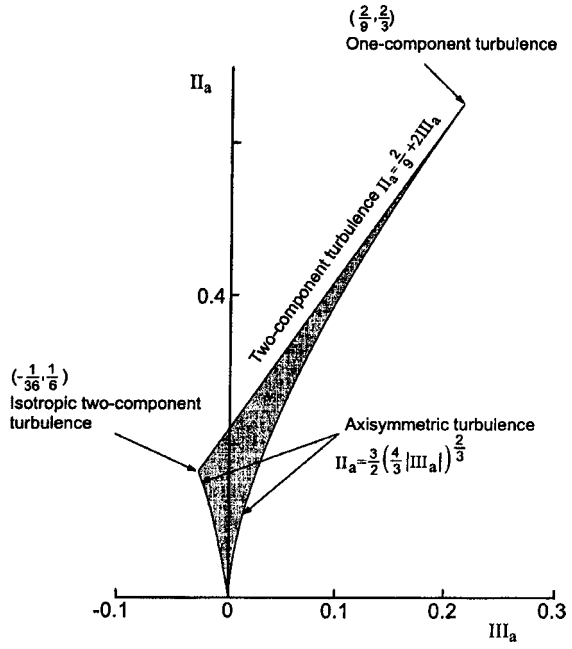

Fig. 2 Anisotropy-invariant map of the tensor $a_{ij}=\overline{u_iu_j}/q^2-1/3\delta_{ij}$ and the limiting values of scalar invariants $II_a=a_{ij}a_{ji}$ and $III_a=a_{ij}a_{jk}a_{ki}$ for the different states of the turbulence, after Lumley and Newmann [26]. Here $\overline{u_iu_j}$ is the Reynolds stress tensor and $q^2=\overline{u_su_s}$. According to Lumley [27], all realistic turbulence must exist within the area delineated by the map.

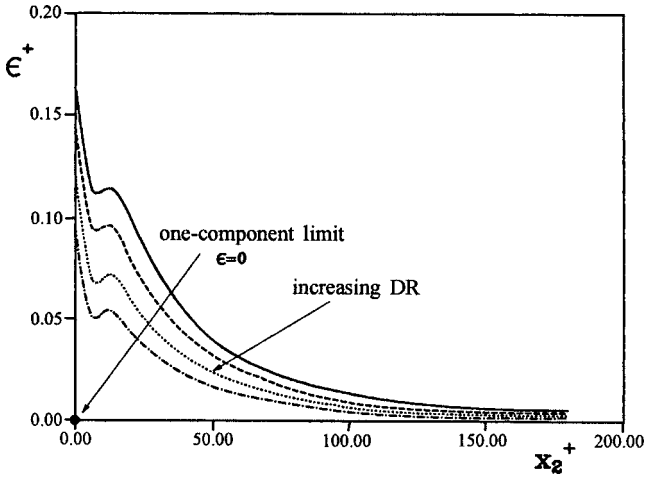

Fig. 3 Distribution of the turbulent dissipation rate ϵ versus distance from the wall, normalized on the inner variables u_τ and ν, in a plane channel flow (DR=0) from direct numerical simulations of Kim et al. [28], sketched ϵ profiles for nonvanishing DR, and the limiting state at the wall for maximum DR

owing to suppression of the turbulent dissipation rate ϵ, which, under common circumstances, reaches a maximum at the wall (see Fig. 3).

For an extreme situation, when $(II_a)_{wall}\to 2/3$ and $(\epsilon)_{wall}\to 0$, the statistical dynamics of the turbulent stresses constructed by combining the two-point correlation technique and invariant theory written in Cartesian notation [24]:[1]

$$\frac{\partial \overline{u_1^2}}{\partial t}\simeq P_{11}+a_{11}P_{ss}+\mathcal{F}\left(\frac{1}{3}P_{ss}-P_{11}\right)+(\mathcal{C}-2\mathcal{A}\epsilon_h)a_{11}-\frac{2}{3}\epsilon_h-\frac{\partial}{\partial x_2}\frac{\overline{u_1^2}}{q^2}\overline{u_su_su_2}+\frac{1}{2}\nu\underbrace{\frac{\partial^2\overline{u_1^2}}{\partial x_2^2}}_{\to 0\ \text{if}(II_a)_{wall}\to 2/3}, \tag{1}$$

$$\frac{\partial \overline{u_2^2}}{\partial t}\simeq a_{22}P_{ss}+\frac{1}{3}\mathcal{F}P_{ss}+(\mathcal{C}-2\mathcal{A}\epsilon_h)a_{22}-\frac{2}{3}\epsilon_h-\frac{\partial}{\partial x_2}\frac{\overline{u_2^2}}{q^2}\overline{u_su_su_2}+\frac{1}{2}\nu\underbrace{\frac{\partial^2\overline{u_2^2}}{\partial x_2^2}}_{\to 0\ \text{if}(II_a)_{wall}\to 2/3}, \tag{2}$$

$$\frac{\partial \overline{u_3^2}}{\partial t}\simeq a_{33}P_{ss}+\frac{1}{3}\mathcal{F}P_{ss}+(\mathcal{C}-2\mathcal{A}\epsilon_h)a_{33}-\frac{2}{3}\epsilon_h-\frac{\partial}{\partial x_2}\frac{\overline{u_3^2}}{q^2}\overline{u_su_su_2}+\frac{1}{2}\nu\underbrace{\frac{\partial^2\overline{u_3^2}}{\partial x_2^2}}_{\to 0\ \text{if}(II_a)_{wall}\to 2/3}, \tag{3}$$

[1]In (1)–(4) $P_{ij}=-\overline{u_iu_k}\partial\bar{U}_j/\partial x_k-\overline{u_ju_k}\partial\bar{U}_i/\partial x_k$ represents the production of the turbulent stresses by mean motion, x_2 measures the distance from the wall, ϵ_h is the homogeneous part of the turbulent dissipation rate defined by (10), and $\mathcal{A}$, $\mathcal{C}$, and $\mathcal{F}$ are scalar functions that depend on the anisotropy invariants and the turbulent Reynolds number.

$$\frac{\partial \overline{u_1u_2}}{\partial t}\simeq P_{12}+a_{12}P_{ss}-\mathcal{F}P_{12}+(\mathcal{C}-2\mathcal{A}\epsilon_h)a_{12}-\frac{\partial}{\partial x_2}\frac{\overline{u_1u_2}}{q^2}\overline{u_su_su_2}+\frac{1}{2}\nu\underbrace{\frac{\partial^2\overline{u_1u_2}}{\partial x_2^2}}_{\to 0\ \text{if}(II_a)_{wall}\to 2/3}, \tag{4}$$

suggest that the viscous diffusion process can almost be neglected, $\partial^2\overline{u_iu_j}/\partial x_2^2\to 0$, forcing turbulence to tend towards the axisymmetric state with the streamwise intensity larger than in the other two directions, $\overline{u_1^2}>\overline{u_2^2}=\overline{u_3^2}$. Since in axisymmetric turbulence there is no shear stress $\overline{u_1u_2}$, it is to be expected that for large DR there will be no traditional mechanism of the energy production $P_k=-\overline{u_1u_2}\partial\bar{U}_1/\partial x_2$ which ensures self-maintenance of turbulence in wall-bounded flows.

The system (1)–(4) therefore permits an insight into the two important issues of turbulent drag reduction that need to be distinguished: modifications of turbulence induced in the region of the viscous sublayer are of a causal nature and the significant reduction of turbulent energy production in the flow region away from the wall is a consequence of the mechanism associated with drag reduction. Under these circumstances, turbulence can persist in polymer flows only if interaction between the polymers and turbulence induces additional polymers stresses. Thus, the evolution of turbulence in drag-reducing flows resembles the reverse transition process in the limit when $\mathrm{Re}\to(\mathrm{Re})_{crit}$ as illustrated in Fig. 4.

The specific process by which an increase in the anisotropy of turbulence influences drag reduction is related to the ability of dilute flexible polymers to decrease the contribution of turbulence to the average energy dissipation rate. For a pipe flow this can be expressed as the rate of work done against the wall shear stress per unit mass of fluid:

$$\bar{\epsilon}\simeq\frac{\tau_w\pi DL\bar{U}_B}{\rho\pi\frac{1}{4}LD^2}=\frac{4u_\tau^2\bar{U}_B}{D}, \tag{5}$$

where D and L are the pipe diameter and its length, respectively, $\bar{U}_B$ represents bulk velocity, τ_w corresponds to the wall shear stress, $\tau_w=\mu(\partial\bar{U}_1/\partial x_2)_{wall}$, and u_τ is the wall friction velocity, $u_\tau=(\tau_w/\rho)^{1/2}$. From this equation, we may conclude that for a given mean flow $(\bar{U}_B)$ and pipe diameter (D), only a decrease in $\bar{\epsilon}$ en-

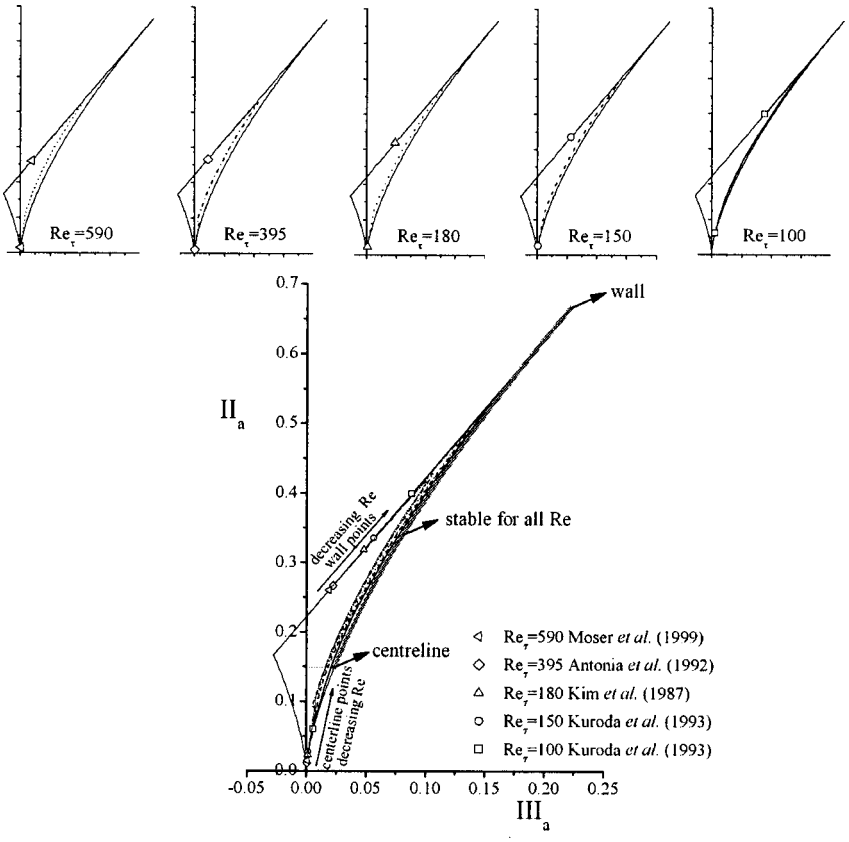

Fig. 4 Anisotropy invariant mapping of turbulence in a channel flow reproduced from [28–33]. Data which correspond to low Reynolds number (based on the channel half-width and the wall friction velocity) show the trend as $Re \rightarrow (Re)_{crit}$ towards the theoretical solution valid for small, neutrally stable, statistically stationary axisysmmetric disturbances [34]. The shading indicates the area occupied by the stable disturbances: for such disturbances it is expected that the laminar regime in a flat plate boundary layer will persist up to very high Reynolds numbers.

sures drag reduction. It is therefore not surprising that measurements of the energy spectra of turbulence in drag-reducing flows display attenuation of fluctuations at high wave numbers (small-scales) across the entire flow [17]. These fluctuations contribute substantially not only to $\bar{\epsilon}$ but also to the dynamics of the dissipation process, which are extremely complicated.

In this paper, we first present the analytical result which illustrates implicitly the mechanism involved in turbulent drag reduction. The basics were derived in the work of Jovanović and Hillerbrand [25] in connection with the flow control of a laminar boundary layer at very high Reynolds numbers and formed the basis for experimental investigations of turbulent drag reduction using uniformly distributed polymer additives. These investigations confirmed the major conclusion which emerged from the above-mentioned theoretical work, namely that the mechanism of drag reduction is associated with an increase in anisotropy of turbulence at the wall.

This paper also provides consideration of the two most important issues related to maximum turbulent drag reduction for pipe flows: determination of the relaxation time of a polymer and its concentration. Following the elastic theory, the relaxation time of a polymer (t_{pol}) is determined by requiring that it should be larger than the characteristic time-scale of turbulent motions in the dissipation range (t_K). Since the small-scale structure of turbulence in the dissipation range is universal, the concentration of a polymer is determined from its spatial extent using well-established relations which hold in isotropic turbulence and the experimental evidence that the mean separation between regions associated with motions at Kolmogorov's scale is comparable to the integral length-scale of turbulence.

3 The Limiting State of Turbulence at the Wall

Using the two-point correlation technique, it is possible to show and demonstrate, utilizing experimental [35] or numerical databases [36], that local axisymmetry for the small-scale part of turbulence must hold by definition in axisymmetric turbulence in order to satisfy the constraint of coincidence for the two-point correlations [37,38,24]. Logic, following the basics of invariant theory introduced by Lumley [27], suggests that we may expect fluctuations in the near-wall region to satisfy constraints imposed by the local axisymmetry when these tend asymptotically towards the one-component limit. This limit corresponds to the vertex on the right-hand side of the anisotropy-invariant map, shown in Fig. 2, where the axisymmetric state merges with the two-component state of the fluctuations. For this very special case, two-component, turbulent motions close to the wall must additionally satisfy axisymmetry at large and small scales, which are closely interrelated [39], and therefore also constraints imposed by local axisymmetry.

Using the Taylor series expansion of the instantaneous velocity fluctuations about the wall which satisfies the continuity equation as presented by Monin and Yaglom [40] and inserting it into the relation for statistics of the velocity derivatives that were derived

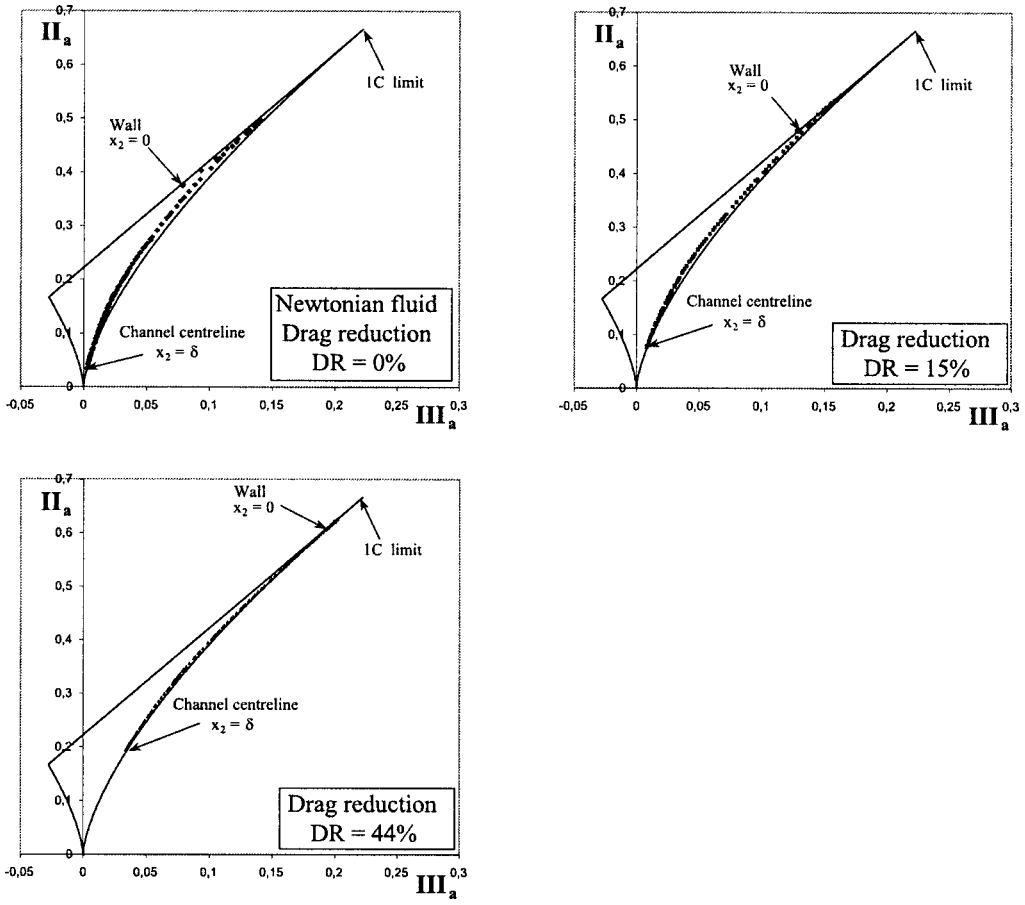

Fig. 5 Anisotropy-invariant mapping of turbulence in a fully developed channel flow with drag reduction from direct numerical simulations of Dimitropulos et al. [20]. The trend in the data at the wall (x_2=0) strongly supports the conclusion that DR increases as turbulence approaches the one-component limit.

by George and Hussein [41] for fluctuations locally invariant to rotation about the x_1 axis, it can be shown that all coefficients of the series expansion must vanish in order to satisfy constraints imposed by the local axisymmetry. We may conclude, therefore, that inhomogeneous but locally axisymmetric turbulence, whose statistical properties in the dissipation range are invariant under rotation about the axis aligned with the mean flow direction, must vanish in close proximity of solid boundaries. Therefore, also the dissipation rate, $\epsilon=\nu\overline{(\partial u_i/\partial x_k)^2}$, at the wall will vanish, causing significant suppression of turbulence in the near-wall region. The expectation that the turbulent dissipation rate at the wall tends to zero as the one-component limit is approached is confirmed by all available data from direct numerical simulations as shown by Jovanovic and Hillerbrand [25].

Figure 5 shows trajectories of the joint variation of the invariants of a_{ij} across the anisotropy-invariant map from the numerical database of drag-reducing, fully developed, turbulent channel flow from Dimitropoulos et al. [20]. This figure confirms that with increasing drag reduction (DR), which is accompanied by suppression of wall turbulence [17], the point that corresponds to the position at the wall x_2=0 moves upwards in the direction of the one-component limit.

This example along with the DNS data sets for Newtonian flows analyzed by Jovanović and Hillerbrand [25] strongly support the major conclusion which emerges from the statistical analysis: the most effective way to suppress turbulence in the near-wall region and achieve large drag reduction is to force the velocity fluctuations to be predominantly one-component near the wall.

4 Determination of the Relaxation Time of a Polymer for Maximum Drag Reduction

In the previous section, we provided an explanation for the physical mechanism that causes turbulent drag reduction by homogeneously distributed polymers. It is associated with modifications of turbulence at small scales by changes in the molecular structure of a polymer. It is therefore reasonable to assume that turbulent motions at high wave numbers are responsible for interaction between turbulence and a polymer. These motions are characterized by Kolmogorov's length scale, defined as

$$\eta_K=\left(\frac{\nu^3}{\epsilon}\right)^{1/4}, \tag{6}$$

and additional scales which can be derived from ν and η_K:

- velocity scale $u_K=\nu/\eta_K$
- time scale $t_K=\eta_K^2/\nu$,
- pressure scale $p_K=\rho\nu^2/\eta_K$.

To ensure that the polymer produces drag reduction, the characteristic time scale of turbulence ($t_{\text{tur}}\simeq t_K$) must be smaller than the relaxation time of a polymer (t_{pol}) in order to activate rolled-up chains of a polymer to unroll and in this way initialize drag reduction [2]. This requirement may be formulated in the form

$$t_K \leqslant t_{\text{pol}}. \tag{7}$$

Using the well-known relationship for interpretation of the turbulent dissipation rate in terms of the energy ($2k=q^2=\overline{u_s u_s}$) and the

Taylor microscale (λ) that holds in homogeneous turbulence,

$$\epsilon = 5\nu\frac{q^2}{\lambda^2}, \tag{8}$$

from (6) we find

$$t_K = \frac{\sqrt{5}}{5}\frac{\lambda}{q}. \tag{9}$$

It is possible to show, using the two-point correlation technique developed by Jovanović et al. [42], that the turbulent dissipation rate in wall-bounded flows may be interpreted in terms of the Taylor microscale as follows:

$$\epsilon = \frac{1}{4}\nu\frac{\partial^2 q^2}{\partial x_k\,\partial x_k} + \underbrace{5\nu\frac{q^2}{\lambda^2}}_{\epsilon_h}. \tag{10}$$

Exploring the series expansion for the instantaneous velocity fluctuations about the wall [22,42], it is possible to show that λ and q are linear functions of the distance from the wall:

$$\left.\begin{aligned}\lambda &= \sqrt{10}x_2,\\ q &= \sqrt{\overline{a_1^2} + \overline{c_1^2}}\,x_2,\end{aligned}\right\} \text{ as } x_2 \to 0. \tag{11}$$

For pipe and channel flows, experimental investigations and numerical simulations indicate that the limiting behavior of turbulence intensities close to the wall is nearly independent of the Reynolds number [43,44]:

$$\left.\begin{aligned}\sqrt{\overline{u_1^2}}/\bar{U}_1 &\approx 0.4,\\ \sqrt{\overline{u_3^2}}/\bar{U}_1 &\approx 0.2,\end{aligned}\right\} \text{ as } x_2 \to 0. \tag{12}$$

This behavior yields

$$\overline{a_1^2} \approx 0.16\frac{u_\tau^4}{\nu^2}, \tag{13}$$

$$\overline{c_1^2} \approx 0.04\frac{u_\tau^4}{\nu^2}. \tag{14}$$

From the above limiting behavior of intensity components close to the wall, we deduce from (9) the time scale t_K of turbulence at the wall:

$$(t_K)_{\text{wall}} \approx \sqrt{10}\frac{\nu}{u_\tau^2}. \tag{15}$$

Another estimate of the time scale t_K follows from consideration of turbulence at the pipe centerline. For this flow region, experiments show that all three intensity components are nearly equal and scale with the wall friction velocity [43,54]:

$$\sqrt{\overline{u_1^2}} \approx \sqrt{\overline{u_2^2}} \approx \sqrt{\overline{u_3^2}} \approx 0.75u_\tau. \tag{16}$$

This experimental evidence suggests the relation for the upper estimation of the time scale t_K:

$$(t_K)_{\text{center}} \approx 0.265(\text{Re}_\lambda)_{\text{center}}\frac{\nu}{u_\tau^2}, \tag{17}$$

where $(\text{Re}_\lambda)_{\text{center}}$ is the turbulent Reynolds number $\text{Re}_\lambda = q\lambda/\nu$ at the pipe centerline, which can be calculated approximately using the correlation suggested by Jovanović and Pashtrapanska [46]:

$$\text{Re}_\lambda \approx 1.996\left(\frac{u_\tau D}{\nu}\right)^{1/2} + 0.108. \tag{18}$$

By requiring that the relaxation time of the polymer t_{pol} is larger than (15) and smaller than or equal to (17),

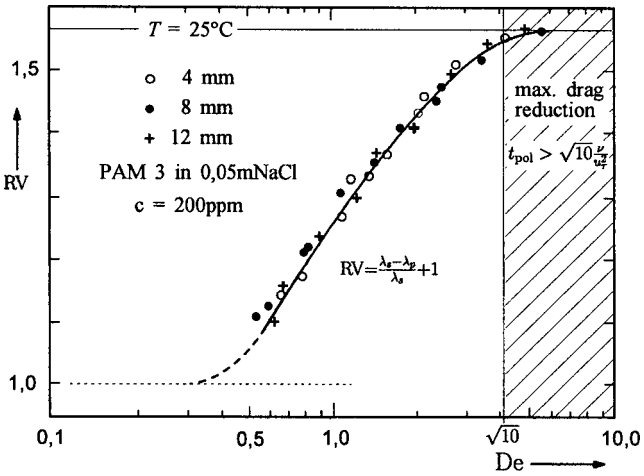

Fig. 6 Drag reduction in pipes of different diameters versus a polymer time scale normalized by a viscous time scale ν/u_τ^2 in a fully developed turbulent pipe flow (from Durst et al. [45]) and the predicted value of a Deborah number for the maximum drag reduction effect

$$\sqrt{10}\frac{\nu}{u_\tau^2} < t_{\text{pol}} \leqslant 0.265(\text{Re}_\lambda)_{\text{center}}\frac{\nu}{u_\tau^2}, \tag{19}$$

we obtain the condition that needs to be fulfilled in order that polymer molecules become substantially elongated, resulting in maximum drag reduction. The lower bound for t_K (15) is far more representative than the upper bound (17), since effects close to the wall are of the causal nature for nearly all production of turbulence in wall-bounded flows and therefore strongly influence its contribution to the viscous drag.

Figure 6 shows experimental results of Durst et al. [45] for polymer drag reduction, defined in terms of the dimensionless coefficients of resistance λ:

$$\frac{\Delta p}{L} = \frac{\lambda}{D}\frac{1}{2}\rho\bar{U}_B^2, \tag{20}$$

for the solvent (λ_s) and a dilute polymer solution (λ_p) versus the Deborah number:

$$\text{De} = \frac{t_{\text{pol}}}{\nu/u_\tau^2}. \tag{21}$$

These experimental results, which were obtained in a turbulent pipe flow at moderate Reynolds numbers, confirm that maximum drag reduction is already reached when the Deborah number exceeds a value of about $\text{De} \geqslant \sqrt{10}$. This finding is in close agreement with the conclusion that emerges from the time-scale argumentation discussed above and is in agreement with the lower bound of the constraint derived (19) for the relaxation time of a polymer. Considering that the molecular weight of a polymer (M) is distributed according to the probability density distribution the onset of drag reduction at $\text{De} \approx 0.5$ is not surprising. If the right-hand side tail of the probability density distribution of the molecular weight of a polymer extends to three times of the mean value ($\bar{M}$), then the requirement $t_{\text{pol}} \geqslant (t_K)_{\text{wall}}$, which corresponds to $\bar{M}$, together with the Zimm relation for t_{pol} suggests that the onset of drag reduction starts already at $\text{De} \approx 0.44$ (see also Fig. 1).

5 The Optimum Concentration of a Polymer

If we assume that the entire interaction between a polymer and turbulence is localized in the dissipation range of the spectrum, this implies that the volume occupied by fluid motions which scale with Kolmogorov's variables (η_k, t_K, u_K, and p_K) should be equal to the volume of a polymer in order to obtain maximum

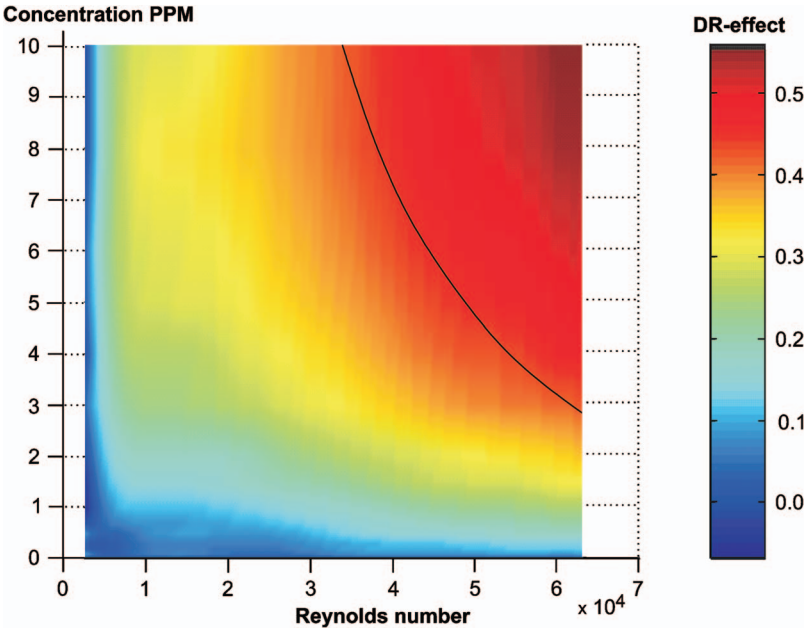

Fig. 7 Measured drag reduction effects at different PAA concentrations in aqueous solutions as a function of the Reynolds number; from Tilli et al. [53]. The solid line represents prediction of the optimum concentration of a polymer for the maximum drag reduction effect.

drag reduction. Since the small-scale structure of turbulence is (believed to be) universal for all turbulent flows, the volume occupied by it can be determined by considering well-established results which hold for isotropic turbulence.

For isotropic turbulence at large Reynolds numbers, the turbulent dissipation ϵ may be related to the integral length scale of the energy containing range by [47,48]

$$\epsilon \simeq 0.192\frac{q^3}{L_f}, \quad \mathrm{Re}_\lambda \gg 1. \tag{22}$$

At very low Reynolds numbers, e.g., in the final decay period of classical grid-generated turbulence, the expression for ϵ can be derived analytically [49]:

$$\epsilon = 1.959\nu\frac{q^2}{L_f^2}, \quad \mathrm{Re}_\lambda \ll 1. \tag{23}$$

Following the suggestion of Rotta [50], we combine (22) and (23) to obtain an interpolation equation for ϵ valid for low and large Reynolds numbers:

$$\epsilon \approx 1.959\nu\frac{q^2}{L_f^2} + 0.192\frac{q^3}{L_f}. \tag{24}$$

Expressing ϵ in terms of Taylor's microscale, using (8), with (24) we are in a position to correlate the length scale ratio λ/L_f in terms of the turbulent Reynolds number:

$$\frac{\lambda}{L_f} \approx -0.049\mathrm{Re}_\lambda + \frac{1}{2}(0.009\,604\mathrm{Re}_\lambda^2 + 10.208)^{1/2}, \tag{25}$$

which attains a maximum value of 1.597 when $\mathrm{Re}_\lambda \to 0$ and vanishes for $R_\lambda \to \infty$. Using (6) and (8), the above ratio λ/L_f can be transformed to the ratio of Kolmogorov's length scale to the length scale L_f:

$$\frac{\eta_K}{L_f} \approx -0.0327\mathrm{Re}_\lambda^{1/2} + 0.3343\mathrm{Re}_\lambda^{-1/2}(0.009\,604R_\lambda^2 + 10.208)^{1/2}. \tag{26}$$

Experimental investigations of statistical properties of the fine scale structure of turbulence by Batchelor and Townsend [51] and Kuo and Corrsin [52] reveal that the mean separation between flow regions in space where turbulent motions correlate well with Kolmogorov's length scale is comparable to the (integral) length scale L_f of turbulence. This finding implies that there is one Kolmogorov structure (η_K) inside the large-scale structure of turbulence (L_f), so that the volume occupied by a polymer (c) relative to the volume of entire fluid (V) can be estimated as follows:

$$\frac{c}{V} \approx \left(\frac{\eta_K}{L_f}\right)^3 \approx [-0.0327\mathrm{Re}_\lambda^{1/2} + 0.3343\mathrm{Re}_\lambda^{-1/2}(0.009\,604\mathrm{Re}_\lambda^2 + 10.208)^{1/2}]^3. \tag{27}$$

It is important to note that the above expression predicts a decrease of c/V with increasing Reynolds number.

Using (18) and (27), and the Blasius correlation formula for the friction coefficient, the optimum concentration of a polymer for the maximum drag reduction effect was predicted for pipe flow and in Fig. 7 the results are compared with measurements carried out by Tilli et al. [53] for polyacrylic acid (PAA) dissolved in water. The predicted concentration is seen to follow very closely the measurements performed in the Reynolds number range $\mathrm{Re} = 1.0\times10^4$–$7.2\times10^4$.

6 Experimental Verification of the Mechanism of Polymer Drag Reduction

In order to provide further experimental evidence that supports theoretical considerations of the mechanism responsible for polymer drag reduction, we decided to initiate an experimental program using state-of-the-art laser-Doppler (LDA) measuring technique. This technique allows accurate experimental data to be

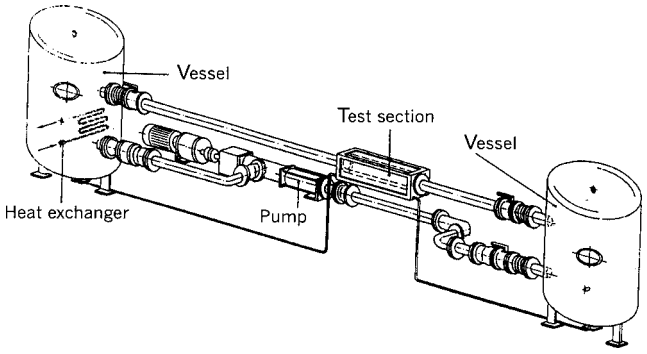

Fig. 8 Closed-loop pipe flow test section

obtained deep inside the viscous sublayer, enabling a quantitative basis to be formed for the interpretation of the dynamics of turbulence using the tools of invariant theory.

6.1 Test Section and Instrumentation. Measurements were performed in the refractive index-matched pipe-flow facility at the Lehrstuhl für Srömungsmechanik in Erlangen. The setup is shown in Fig. 8. This test rig has been used extensively for different LDA measurements. It is a closed-loop pipe flow installation driven by a screw conveyor pump. Flow rates between 0.6 and 20 m^3h^{-1} can be achieved with a tolerance of 1%. With a pipe diameter of 50 mm a maximum Reynolds number of $Re=4.4\times10^4$ can be realized. The test section is made of DURAN-50 glass. The flow was supplied from a large settling tank to the working section that was located about 4 m downstream, providing a development length of about 100 pipe diameters. In the present experiments, the flow was tripped at the pipe inlet to ensure additionally fully developed flow conditions. A more detailed description of the experimental apparatus can be found in Durst et al. [43].

The test fluid (a mixture of two diesel oils) was selected to match the refractive index of the glass. For simplification of the measurement and the traversing system, the pipe was mounted in a rectangular box (made of DURAN 50) through which the refractive index-matched fluid was also guided. Hence, the displacement of the LDA measuring control volume was directly proportional to the traversing performed.

The LDA measuring system was mounted on a 3-D traversing table, which could be moved in the plane normal to the pipe axis by using computer-controlled stepping motors and along the pipe axis with the help of a manual traversing system. The positions were read by digital indicators. The arrangement of the LDA optical system and the test section is shown in Fig. 9. The optical

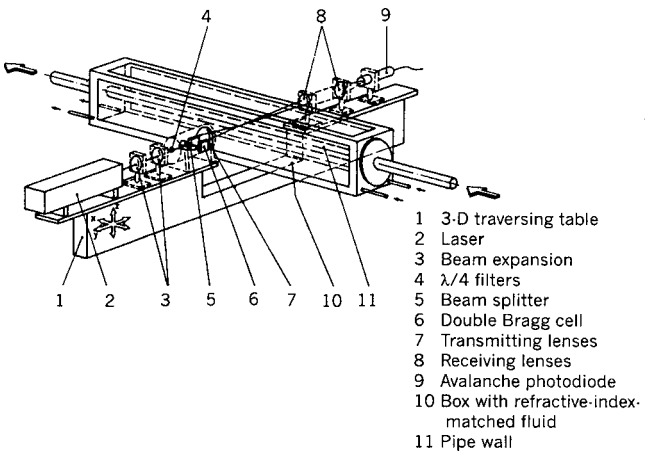

Fig. 9 Layout of the LDA optical system

system consisted of a 15 mW helium-neon laser and a double Bragg cell unit. For measurements in the region away from the wall Bragg cells were driven at 40.0 and 41.5 MHz, providing a shift frequency of 1.5 MHz. In the near-wall region measurements were performed with the Bragg cells operated at 40.0 and 40.3 MHz, providing a shift frequency of 300 kHz. The measuring control volume was about 60 μm in diameter (minor axis d_2) and had a length of 230 μm (major axis d_1). These values, based on the e^{-2} intensity cutoff point, were calculated from

$$d_2 = \frac{4\lambda f}{E\pi d_{beam}\cos(\varphi)}, \tag{28}$$

$$d_1 \frac{4\lambda f}{E\pi d_{beam}\sin(\varphi)}, \tag{29}$$

where E is the beam expansion factor, λ is the laser wavelength, f is the focal length of the transmitting lens, d_{beam} is the diameter of the unfocused laser beam, and φ is half the intersection angle of the beams.

The LDA system employed was operated in the forward scattering mode. The image of the measuring volume was directed onto a pinhole in front of an Avalanche photodiode. In order to minimize the influence of noise on the measured data, the output signal from this diode was bandpass filtered before being processed by a TSI Model 1990 counter.

6.2 Turbulent Pipe Flow Without Polymer Additives. Preliminary measurements without the addition of polymer additives were performed at a Reynolds number of 3×10^4 to verify the accuracy of the measurements. For velocity measurements in the axial direction, the LDA system was traversed in the vertical direction. By rotating the transmitting optics by 90°, the tangential velocity component $\overline{u_3^2}$ was measured in the horizontal and the radial velocity component $\overline{u_2^2}$ in the vertical plane. For axial turbulence intensity measurements, the expression [43]

$$\overline{u_{1\text{meas}}^2} = \overline{u_{1\text{true}}^2} + \frac{d_2^2}{16}\left(\frac{d\bar{U}_1}{dx_2}\right)^2_{\text{true}} \tag{30}$$

was used for correcting the measured data for the finite size of the measuring control volume. The resulting corrections were of the order of less than 8% in the near-wall region. The mean velocity does not require a correction since the leading term of the correction represents the curvature of the velocity profile, which is negligible close to the wall. Since the mean velocity in the tangential and radial direction is approximately zero, no corrections concerning the finite size of the measuring control volume had to be applied to those quantities. Figure 10 shows the obtained results for mean velocity and second-order statistics. For measurements of the fluctuating component in the tangential direction $\overline{u_3^2}$, the optical system was arranged in such a way that the major axis of the elliptical measuring volume was normal to the wall. Therefore, the spatial resolution in the tangential direction was limited and prevented measurements closer than ~230 μm from the wall. It can be seen that measurement errors exist in the region $x_2^+<10$. The dimensionless size of the measuring volume was

$$d_1^+ = \frac{d_1 u_\tau}{\nu} \approx 7, \tag{31}$$

which indicates that it covered not only the near-wall region but also parts of the wall. With the addition of polymers, u_τ decreases drastically. Therefore, the dimensionless size of the measuring volume decreases and correct measurements of the tangential intensity component in the near-wall region become possible.

The deviations for second-order statistics in the buffer region and across the outer part of the flow are due to the influence of the Reynolds number, whereas the turbulence statistics in the viscous sublayer scale as discussed in detail by Durst et al. [43] and Fischer et al. [44]. The study of Lammers [57] provides additional

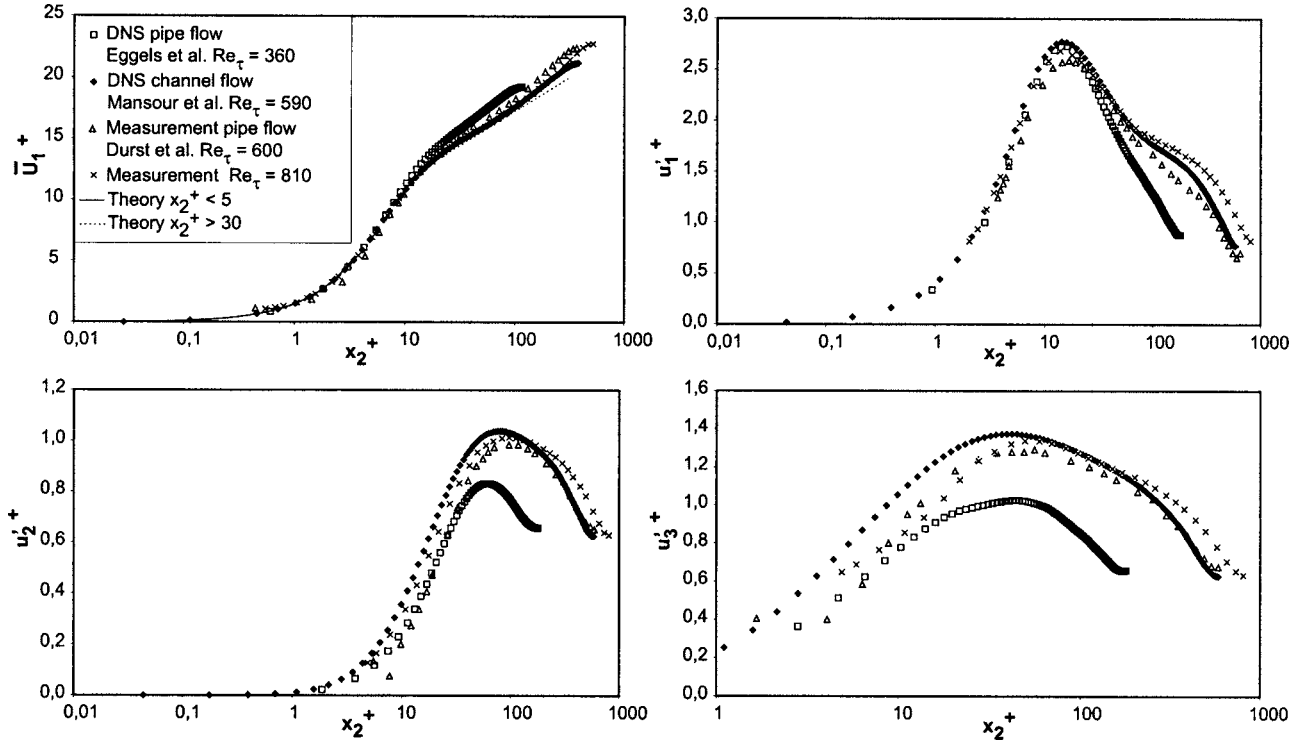

Fig. 10 Measurements at Re_τ=810 in comparison with experimental results of Durst et al. [43] and DNS results of Mansour et al. [55] and Eggels et al. [56]

information on the influence of domain size and grid resolution on the turbulence quantities in the near-wall region obtained by direct numerical simulation. His results show that the peak value of the turbulence intensity $\overline{u_1^2}$ is (weakly) sensitive to the size of the computational domain in the streamwise direction.

6.3 Turbulent Flow with Polymer Additives. The polymer can be added to the flow in different ways. It can be injected into the flow at different concentrations or a homogeneous mixture can be prepared in advance. In order to guarantee a homogeneous mixture from the start it was decided to prepare the mixture outside the installation. A 50 ppm solution of a FORTUM polymer, illustrated in Fig. 11, mixed with diesel oil was prepared. This mixture was stirred slowly for 1 week before distributing it to four 200 l kegs of diesel oil yielding 5 and 10 ppm solutions, respectively. These solutions were stirred for another 24 h before being returned to the installation. Since the polymer is sensitive to mechanical straining, all these steps were performed very carefully and slowly. The viscosity was measured for the pure mixture of the two diesel oils and the 50 ppm solution, yielding a constant kinematic viscosity of $\nu=3.2\times10^{-6}$ m s^{-2}.

Since the polymer solution showed a rather short lifetime, with detectable degradation effects after 1 h of continuous operation, it was not possible to obtain the entire velocity profile of the flow in one session of measurements. Owing to the elaborate preparation procedure of the polymer solutions, the measurement of the entire velocity profile was abandoned and measurements at one point inside of the viscous sublayer at a physical wall distance of 150 μm were taken until the polymer had degraded and no further drag reduction could be observed. Measurements were taken at a Reynolds number of 2.5×10^4. This was chosen to be lower than in the preliminary experiments to increase the size of the viscous

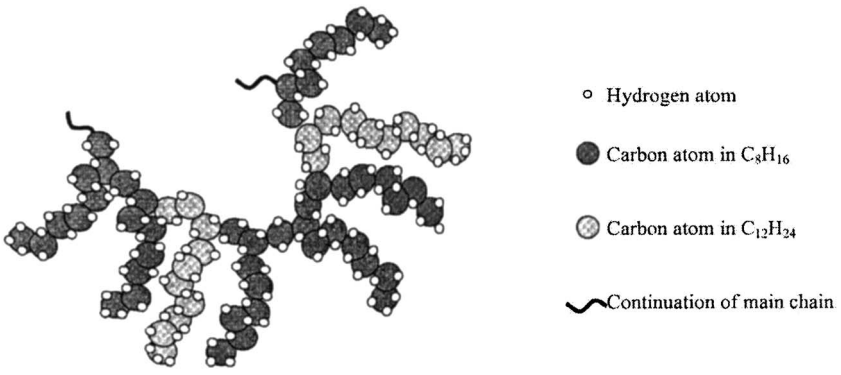

Fig. 11 Illustration of the molecular structure of a FORTUM polymer sample after Koskinen [58]: $M\approx25\times10^6$ g mol^{-1}, $M_{dodecane}$=168.4320 g mol^{-1}, M_{octane} =112.2880 g mol^{-1}, l=2×1.54 Å, $r_{d/o}=C_{12}H_{24}/C_8H_{16}=1/3$, $N_{monomer}=M_{polymer}/[r_{d/o}M_{octane}+(1-r_{d/o})M_{dodecane}]$

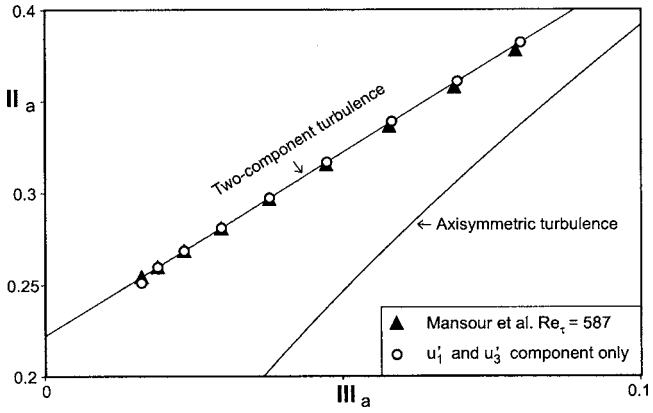

Fig. 12 DNS data from Mansour et al. [55] for $x_2^+<5$ plotted on expanded scale in the anisotropy invariant map

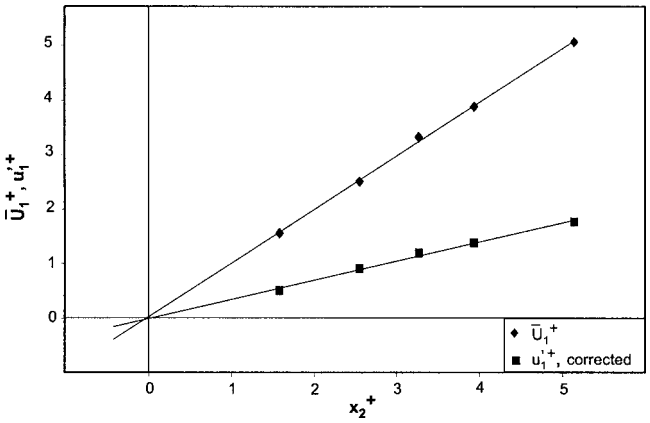

Fig. 13 Velocity profile and turbulent intensity profile in the region very close to the wall

sublayer. At regular time intervals, a sample of a working fluid was taken in order to check its kinematic viscosity, which was found to maintain a constant value.

To quantify drag reduction, which is defined as

$$\mathrm{DR} = 1 - \frac{\tau_{w,pol}}{\tau_\omega}, \tag{32}$$

it was necessary to determine the wall shear stress τ_w. This was accomplished by measuring the mean velocity at a fixed and predetermined position from the wall which was always within the viscous sublayer.

In order to analyze the structure of turbulence in a drag-reduced flow using invariant theory, the second-order moments are required. For measurements in the viscous sublayer ($x_2^+<5$) it is possible to plot data in the anisotropy invariant map using axial and tangential fluctuation values only. Figure 12 shows DNS results of Mansour et al. [55] for $x_2^+<5$ plotted in the anisotropy invariant map: once using all Reynolds stress components and once using the $\overline{u_1^2}$ and $\overline{u_3^2}$ components only. It can be seen that there is no significant difference in the values obtained.

Therefore, the mean velocity and the fluctuating components $\overline{u_1^2}$ in axial and $\overline{u_3^2}$ in tangential direction at a fixed position inside the region of the viscous sublayer were sufficient for the purpose of this investigation.

In order to obtain statistically accurate results, measurements were taken for 4 min at each point. This period corresponds almost to the time during which the entire oil circulated once through the experimental loop and therefore cannot be selected higher. Sufficient particles were in the oil to measure the turbulent fluctuations. The data rate of 150 Hz was smaller than the maximum particle arrival rate (which can be estimated from the flow velocity and the diameter of the measuring control volume) but larger than the Kolmogorov frequency estimated from the mean flow and the average dissipation rate [43]. Thus, 7500 statistically independent samples were obtained for each measurement point, resulting in an relative error of 0.6% for the mean velocity and 2.3% for the second-order statistics. Mean velocity and turbulence intensities in axial and tangential directions were measured for each of the solutions. Measurements were taken for about 10 h. Subsequently, the exact location of the measurement control volume was verified.

The wall shear velocity u_τ was calculated from the slope of the measured mean velocity profile in the viscous sublayer. Figure 13 confirms the linear dependence of the mean velocity $\bar{U}_1$ and of the corrected turbulence intensity $\overline{u_1^2}$ on the dimensionless wall distance $x_2^+=x_2u_\tau/\nu$. Additionally, u_τ was estimated from the Clauser diagram ($u_\tau=0.080\,88$ m s^{-1}) and using the Blasius formula for the friction coefficient:

$$\frac{\tau_w}{\frac{1}{2}\rho\bar{U}_B^2} = 0.0791\left(\frac{\bar{U}_B D}{\nu}\right)^{-1/4}. \tag{33}$$

With a bulk velocity of $\bar{U}_B=1.40$ m s^{-1} the wall shear velocity yields $u_\tau=0.079\,68$ m s^{-1}. This value deviates less than 2% from the calculated value of $u_\tau=0.080\,96$ m s^{-1}.

Results of the measurements with polymer additives are presented in Figs. 14–16. The higher the concentration of the polymer, the lower is the velocity. This implies a less steep velocity gradient at the wall, as expected for a drag reduced flow. As time

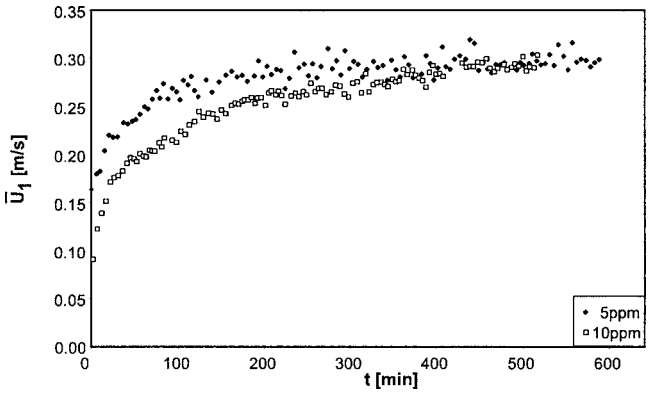

Fig. 14 Behavior of the mean velocity with time for degrading polymer solutions

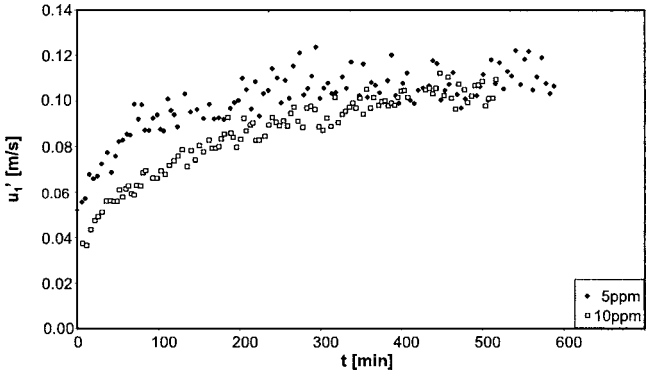

Fig. 15 Behavior of the axial turbulent intensity component in degrading polymer solutions

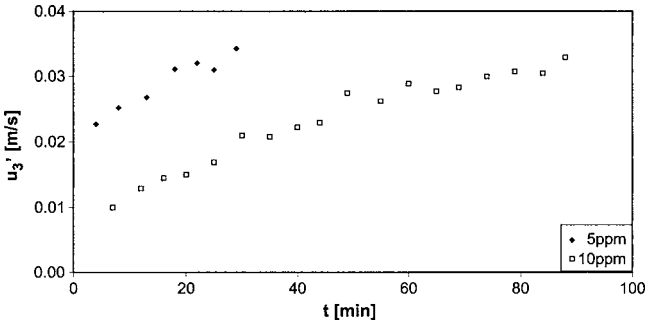

Fig. 16 Behavior of the tangential turbulent intensity component in degrading polymer solutions. The measurement resolution decreases in time since the dimensionless size of the measuring volume increases; the plotted results are therefore limited to that time period when the measuring volume did not extend out of the viscous sublayer

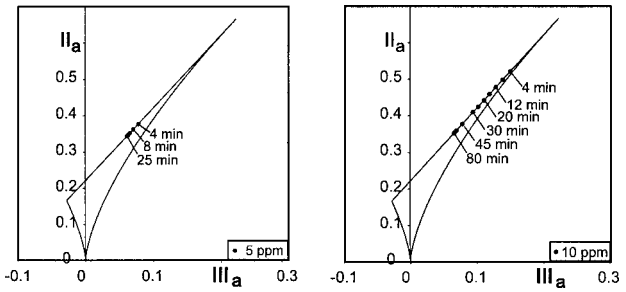

Fig. 18 Measurement results plotted on the anisotropy invariant map (together with those shown in previous figure) demonstrate that with decreasing DR the data points move away from the one-component limit

passes, the influence of the polymer vanishes and the value of the velocity increases until a steady value is reached. The same trend can be observed in histories of the turbulence intensities.

Owing to polymer addition, the wall shear velocity u_τ decreased drastically. Thus, the initial dimensionless size of the measuring control volume (major axis) was calculated to be

$$d_1^+ = \frac{d_1 u_{\tau,initial}}{\nu} \approx 3.2, \tag{34}$$

so that precise measurements in the viscous sublayer with $x_2^+ < 5$ were possible. With degradation of the polymer u_τ increased and also the dimensionless size of the measured control volume. At the point of 30% drag reduction, the major axis d_1^+ assumed a value larger than the thickness of the viscous sublayer. For this reason, measurements in the viscous sublayer did not yield correct results for a low percentage of DR. Therefore Fig. 16 and all results derived from those measurements are limited to DR values above 30%.

As shown in Fig. 17, drag reduction DR,

$$\mathrm{DR} = 1 - \frac{\tau_{w,pol}}{\tau_w}, \tag{35}$$

decreased fast within the first 2 h. With an addition of 10 ppm polymers a maximum drag reduction of 70% could be observed. The effect had completely vanished after continuous operation for 7.5 h. The highest value of drag reduction with a 5 ppm polymer concentration was around 50%. For this concentration of polymer, the effect had disappeared 4 h after the beginning of the measurements.

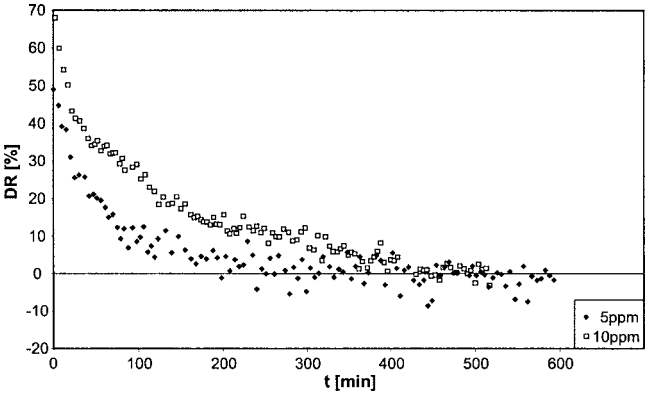

Fig. 17 Drag reduction for different concentrations of a polymer

The measured data were analyzed by plotting these on the anisotropy invariant map. Figure 18 shows the obtained results. The position of the initial point in the anisotropy invariant map depends on the polymer concentration and induced DR. With higher concentrations of polymer its location moves closer to the one-component limit. As shown earlier, the same trend can be observed in Newtonian fluids for decreasing Reynolds numbers (see Fig. 4). As time passes, the data indicate a clear tendency to move downwards along the two-component state from a position close to the one-component limit toward the isotropic two-component limit. These results are in close agreement with those obtained from direct numerical simulations displayed in Fig. 5. The polymer degrades with time and the flow returns to its Newtonian behavior.

7 Conclusions

Statistical analysis of the dynamic equations for turbulent stresses, using the two-point correlation technique and invariant theory, have been performed to investigate polymer drag reduction phenomena. By considering local stretching of the molecular structure of a polymer by small-scale turbulent motions in the region of the viscous sublayer, a conceptual scenario was inferred from theory for the behavior of a polymer and its interaction with turbulence that leads to significant drag reduction effects. According to this scenario, the stretching process is responsible for the restructuring of turbulence at small scales close to the wall by forcing it to satisfy local axisymmetry with invariance under rotation about the axis aligned with the mean flow. Analytical considerations lead to the conclusion that under these circumstances turbulence at the wall tends towards the one-component limit and when it reaches this limiting state turbulence must be entirely suppressed near the wall. In addition to these findings, qualitative analysis of the turbulent transport equations, when projected into the invariant space, suggested that drag reduction by high polymers mimics reverse transition from the fully turbulent state towards the laminar flow state. These analytical deductions were supported by all available results from direct numerical simulations of wall-bounded turbulent flows including those of non-Newtonian fluids.

Examination of the statistical dynamics of the turbulent stresses for conditions of large DR suggests that suppression of the viscous diffusion process at the wall is the major cause for polymer drag reduction and significant reduction of turbulent energy production in the flow region away from the wall can be regarded as a logical consequence. These effects are reflected in a significant reduction of the average turbulent dissipation rate $\bar{\epsilon}$ which controls the turbulent drag. These findings are illustrated in Fig. 19, which shows distributions of the root mean square of the stream-

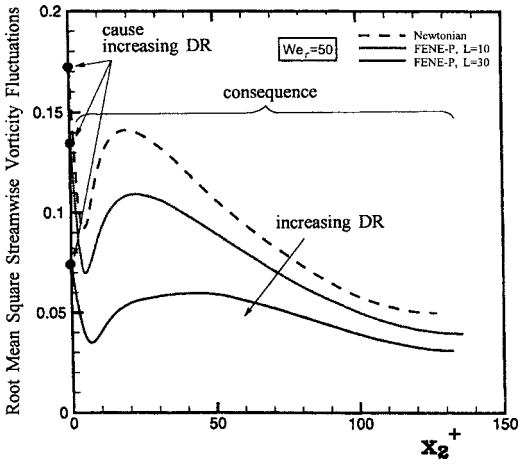

Fig. 19 Illustration of the mechanism responsible for polymer drag reduction utilizing the results of direct numerical simulations of Dimitropulos et al. [20]

wise vorticity fluctuations $(\overline{\omega_1^2})^{1/2}$, which are the largest contribution to the turbulent dissipation rate, $\epsilon \simeq \nu \overline{\omega_i \omega_i}$, in a turbulent channel flow.

Parametrization of the mechanism associated with polymer drag reduction was accomplished by considering the elastic behavior of a polymer and accounting for spatial intermittency of turbulence at small scales. The analysis assumed that the interaction between a polymer and turbulence is localized in motions at small scales which are of the intermittent nature and responsible for the viscous destruction of the turbulent dissipation rate. Favorable agreement was obtained between predictions, based on theoretical considerations, and available experimental results for the relaxation timescale of a polymer and its concentration that produce the maximum drag reduction effect.

High spatial resolution laser-Doppler measurements were performed in a refractive index-matched pipe flow facility in order to provide additional experimental evidence that supports fundamentals associated with the mechanism responsible for polymer drag reduction. Special care was taken to maintain well-controlled flow conditions during the experiments and to account for all possible interferences that can influence the interpretation of the measured LDA signals. The experimental results for the mean velocity and turbulence intensity components obtained deep in the viscous sublayer permitted the evolution of turbulence to be traced across the anisotropy invariant map. Anisotropy-invariant mapping of turbulence in the viscous sublayer reveals that with decrease of DR the anisotropy near the wall decreases along the line which characterizes the two-component state starting from nearly the one-component limit which correspond to large DR. These observations, extracted from the experimental results, are in close agreement with the theoretical analysis and support the notion that turbulent drag reduction by dilute, homogeneous addition of high polymers is associated with the ability of long-chain polymers to induce an increase in the anisotropy of turbulence in close proximity to the wall.

Acknowledgment

The authors gratefully acknowledge the donation of the required oil by ESSO AG, Refinary Ingolstadt.

References

[1] Metzner, A. B. and Park, M. G., 1964, "Turbulent flow characteristics of viscoelastic fluids," J. Fluid Mech., **20**, pp. 291–303.
[2] Lumley, J. L., 1969, "Drag reduction by additives," Annu. Rev. Fluid Mech., **1**, pp. 367–384.
[3] Lumley, J. L., 1973, "Drag reduction in turbulent flow by polymer additives," J. Polym. Sci. Macromol. Rev., **7**, pp. 290–363.
[4] Virk, P. S., 1975, "Drag reduction fundamentals," AIChE J., **21**, pp. 625–656.
[5] Berman, N. S., 1978, "Drag reduction by polymers," Annu. Rev. Fluid Mech., **10**, pp. 47–64.
[6] Tabor, M., and de Gennes, P. G., 1986, "A cascade theory of drag reduction," Europhys. Lett., **2**, pp. 519–522.
[7] Ryskin, G., 1987, "Turbulent drag reduction by polymers: a quantitative theory," Phys. Rev. Lett., **59**, pp. 2059–2062.
[8] Thirumalai, D., and Bhattacharjee, J. K., 1996, "Polymer-induced drag reduction in turbulent flows," Phys. Rev. E, **53**, pp. 546–551.
[9] Sreenivasan, K. R., and White, C. M., 2000, "The onset of drag reduction by dilute polymer additives and the maximum drag reduction asymptote," J. Fluid Mech., **409**, pp. 149–164.
[10] Rudd, M. J., 1972, "Velocity measurements with a laser-Doppler meter on the turbulent flow of a dilute polymer solution," J. Fluid Mech., **51**, pp. 673–685.
[11] Logan, S. E., 1972, "Laser velocimeter measurements of Reynolds stress in dilute polymer solutions," AIAA J., **10**, pp. 962–964.
[12] Reischman, M. A., and Tiederman, W. G., 1975, "Laser-Doppler anemometer measurements in drag reduction g channel flow," J. Fluid Mech., **70**, pp. 369–392.
[13] Luchik, T. S., and Tiederman, W. G., 1988, "Turbulent structure in low-concentration drag-reducing channel flow," J. Fluid Mech., **198**, pp. 241–263.
[14] Walker, D. T., and Tiederman, W. G., 1990, "Turbulent structure in a channel flow with polymer injection at the wall," J. Fluid Mech., **204**, pp. 377–403.
[15] Willmarth, W. W., Wei, T. and Lee, O., 1987, "Laser anemometer measurements of Reynolds stress in a turbulent channel flow with drag reducing polymer additives," Phys. Fluids, **30**, pp. 933–935.
[16] Wei, T., and Willmarth, W. W., 1992, "Modifying turbulent structure with drag-reducing polymer additives in turbulent channel flows," J. Fluid Mech., **245**, pp. 619–641.
[17] Warholic, M. D., Massah, H., and Hanratty, T. J., 1999, "Influence of drag-reducing polymers on turbulence: effects of Reynolds number, concentration and mixing," Exp. Fluids, **27**, pp. 461–472.
[18] den Toonder, J. M. J., Hulsen, M. A., Kuiken, G. D. C., and Nieuwstadt, F., 1997, "Drag reduction by polymer additives in turbulent pipe flow: numerical and laboratory experiments," J. Fluid Mech., **337**, pp. 193–231.
[19] Sureshkumar, R., Beris, A. N., and Handler, R. A., 1997, "Direct numerical simulations of turbulent channel flow of a polymer solution," Phys. Fluids, **9**, pp. 743–755.
[20] Dimitropoulos, C. D., Sureshkumar, R., and Beris, A. N., 1998, "Direct numerical simulation of viscoelastic turbulent channel exhibiting drag reduction: effect of the variation of rheological parameters," J. Non-Newtonian Fluid Mech., **79**, pp. 433–468.
[21] Sibilla, S., and Baron, A., 2002, "Polymer stress statistics in the near-wall turbulent flow of a drag-reducing solution," Phys. Fluids, **14**, pp. 1123–1136.
[22] Angelis, E. D., Casciola, C. M., and Piva, R., 2002, "DNS of wall turbulence: dilute polymers and self-sustaining mechanisms," Comput. Fluids, **31**, pp. 495–507.
[23] Dubief, Y., White, C. M., Terrapon, V. E., Shaqfeh, E. S. G., Moin, P., and Lele, S. K., 2004, "On the coherent drag-reducing and turbulence-enhancing behaviour of polymers in wall flows," J. Fluid Mech., **514**, pp. 271–280.
[24] Jovanović, J., 2004, *The Statistical Dynamics of Turbulence*, Springer-Verlag, Berlin.
[25] Jovanović, J., and Hillerbrand, R., 2005, "On peculiar properties of the velocity fluctuations in wall-bounded flows," J. Therm. Sci., **9**, pp. 3–12.
[26] Lumley, J. L., and Newman, G., 1977, "The return to isotropy of homogeneous turbulence," J. Fluid Mech., **82**, pp. 161–178.
[27] Lumley, J. L., 1978, "Computational modeling of turbulent flows," Adv. Appl. Mech., **18**, pp. 123–176.
[28] Kim, J., Moin, P., and Moser, R., 1987, "Turbulence statistics in a fully developed channel flow at low Reynolds numbers," J. Fluid Mech., **177**, pp. 133–166.
[29] Antonia, R. A., Teitel, M., Kim, J., and Browne, L. W. B., 1992, "Low-Reynolds-number effects in a fully developed turbulent channel flow," J. Fluid Mech., **236**, pp. 579–605.
[30] Moser, R. D., Kim, J., and Mansour, N. N., 1999, "Direct numerical simulation of turbulent channel flow up to Re_τ=590," Phys. Fluids, **11**, pp. 943–945.
[31] Gilbert, N., and Kleiser, L., 1991, "Turbulence model testing with the aid of direct numerical simulation results," *Proc. Eighth Symp. on Turbulent Shear Flows*, Munich, pp. 26.1.1–26.1.6.
[32] Horiuti, K., 1992, "Establishment of the direct numerical simulation data base of turbulent transport phenomena," Ministry of Education, Science and Culture Japan, Co-operative Research No. 012302043, http://www.thtlab.t.u-tokyo.ac.jp/.
[33] Kuroda, A., Kasagi, N., and Hirata, M., 1993, "Direct numerical simulation of the turbulent plane Couette-Poiseulle flows: effect of mean shear on the near wall turbulence structures," *Proc. Ninth Symp. on Turbulent Shear Flows*, Kyoto, pp. 8.4.1-8.4.6, http://www.thtlab.t.u-tokyo.ac.jp/.
[34] Jovanović, J., Hillerbrand, R., and Pashtrapanska, M., 2001, "Mit statistischer DNS-Datenanalyse der Enstehung von Turbulenz auf der Spur," KONWIHR Q. **31**, pp. 6–8.
[35] Schenck, T., and Jovanović, J., 2002, "Measurements of the instantaneous velocity gradients in plane and axisymmetric wake flows." ASME J. Fluids Eng., **124**, pp. 143–153.
[36] Antonia, R. A., Kim, J., and Browne, L. W. B., 1991, "Some characteristics of small-scale turbulence in a turbulent duct flow," J. Fluid Mech., **233**, pp. 369–388.
[37] Chou, P. Y., 1945, "On the velocity correlation and the solution of the equation

of turbulent fluctuation," Q. Appl. Math., **3**, pp. 38–54.
[38] Kolovandin, B. A., and Vatutin, I. A., 1969, "On statistical theory of non-uniform turbulence," Int. J. Heat Mass Transfer, Herceg-Novi, Yugoslavia.
[39] Jovanović, J., Otić, I., and Bradshaw, P., 2003, "On the anisotropy axisymmetric strained turbulence in the dissipation range," ASME J. Fluids Eng., **125**, pp. 1–13.
[40] Monin, A. S., and Yaglom, A. M., 1987, *The Statistical Fluid Mechanics*, Vol. 1, MIT Press, Cambridge, MA.
[41] George, W. K., and Hussein, H. J., 1991, "Locally axisymmetric turbulence," J. Fluid Mech., **233**, pp. 1–23.
[42] Jovanović, J., Ye, Q.-Y., and Durst, F., 1995, "Statistical interpretation of the turbulent dissipation rate in wall-bounded flows," J. Fluid Mech., **293**, pp. 321–347.
[43] Durst, F., Jovanović, J., and Sender, J., 1995, "LDA measurements in the near-wall region of a turbulent pipe flow," J. Fluid Mech., **295**, pp. 305–335.
[44] Fischer, M., Jovanović, J., and Durst, F., 2001, "Reynolds number effects in the near-wall region of turbulent channel flows," Phys. Fluids, **13**, pp. 1755–1767.
[45] Durst, F., Hass, R., Interhal, W., and Keck, T., 1982, "Polymerwirkung in Strömungen-Mechanismen und praktische Anwendungen," Chem.-Ing.-Tech., **54**, pp. 213–221.
[46] Jovanović, J., and Pashtrapanska, M., 2005, "On the criterion for the determination transition onset and breakdown to turbulence in wall-bounded flows," ASME J. Fluids Eng., **126**, pp. 626–633
[47] Kolmogorov, A. N., 1941, "Local structure of turbulence in an incompressible fluid at very high Reynolds numbers," Dokl. Akad. Nauk SSSR, **30**, 299–303.
[48] Sreenivasan, K. R., 1984, "On the scaling of the turbulence energy dissipation rate," Phys. Fluids, **27**, pp. 1048–1051.
[49] Hinze, J. O., 1975, *Turbulence*, 2nd ed., McGraw-Hill, New York.
[50] Rotta, J., 1951, Statistische Theorie nichthomogener Turbulenz," Z. Phys. **129**, pp. 547–572.
[51] Batchelor, G. K., and Townsend, A. A., 1947, "Decay of vorticity in isotropic turbulence," Proc. R. Soc. London, Ser. A, **190**, p. 534.
[52] Kuo, A. Y., and Corrsin, S., 1971, "Experiments on internal intermittency and fine-structure distribution functions in fully turbulent fluid," J. Fluid Mech., **50**, pp. 285–319.
[53] Tilli, M., Maaranen, J., Timonen, J., Kataja, M., and Korppi-Tommola, J., 2003, "Effect mechanisms of DR molecules," Technical Report, University of Jyväskylä, Finland.
[54] Durst, F., Fischer, M., Jovanović, J., and Kikura, H., 1998, "Methods to set up and investigate low Reynolds number, fully developed turbulent plane channel flows, ASME J. Fluids Eng., **120**, pp. 496–503.
[55] Mansour, N. N., Moser, R. D., and Kim, J., 1998, "Fully developed turbulent channel flow simulations," in AGARD Advisory Report 345, pp. 119–121.
[56] Eggels, J. G. M., Unger, F., Weiss, M. H., Westerweel, J., Adrian, R. J., Friedrich, R., and Nieuwstadt, F. T. M., 1994, "Fully developed turbulent pipe flow: a comparison between direct numerical simulation and experiment," J. Fluid Mech., **268**, pp. 175–209.
[57] Lammers, P., 2004, "Direct numerical simulations of wall-bounded flows at low Reynolds numbers using the lattice Boltzmann method, Ph.D. thesis, Friedrich-Alexander University Erlangen-Nuremberg, Germany, pp. 47–72.
[58] Koskinen, K. K., 2004, "On investigating turbulent reactive flows: case studies of combustion and drag reduction by polymer additives," ongoing Ph.D. thesis, Tampere University of Technology, Tampere, Finland.

Theoretical Analysis of the Onset of Gas Entrainment from a Stratified Two-Phase Region Through Two Side-Oriented Branches Mounted on a Vertical Wall

Mahmoud A. Ahmed
Department of Mechanical Engineering,
Assiut University,
Assiut 71516, Egypt
e-mail: aminism@aun.edu.eg

A theoretical analysis has been developed to predict the critical height and the location of the onset of gas entrainment during discharge from a stratified two-phase region through two oriented-side branches mounted on a vertical wall. In this analysis, a point sink model was first developed, followed by a more accurate three-dimensional finite branch model. The models are based on a new modified criterion for the onset of gas entrainment. The theoretically predicted critical height and the location of the onset of gas entrainment are found to be a function of the mass rate of each branch (Fr_1 *and* Fr_2*), the distance between the centerlines of the two branches (*L/d*), and the inclination angle (*θ*). The effects of these variables on the predicted critical height and the onset location were investigated. Furthermore, comparison between the theoretically predicted results and the available experimental data was carried out to verify the developed models. The comparison shows that the predicted results are very close to the measured data within a deviation percentage of 12% at* $\mathrm{Fr}_1 > 10$*. This small deviation percentage reflects a good agreement between the measured and predicted results.* [DOI: 10.1115/1.2140804]

Keywords: onset of gas entrainment, dual discharges, side branches

1 Introduction

The importance of two-phase discharge from a stratified region, due to its relevance to many industrial applications, has motivated theoretical investigations for determining the onset of gas entrainment using different configurations. Knowledge of the critical height of the gas-liquid interface at onset under different operating conditions is required because the type of discharging flow can then be related to the height of the interface. This is a prerequisite for being able to determine the mass flow rate and quality of the discharging flow. For single discharge from a large channel containing stratified two-phase flow, Zuber [1] came to the conclusion that two individual phenomena may occur depending on the location of the gas-liquid interface relative to the break. If the horizontal gas-liquid interface is located above the break, the gas may be entrained by a vortex or vortex-free flow through the break into the predominantly liquid flow (onset of gas entrainment, OGE) while, if the horizontal gas-liquid interface is located below the break, the liquid may be entrained in the predominating gas flow through the break (onset of liquid entrainment, OLE). Detailed experimental data and correlations were developed for the onset of gas entrainment through a general oriented single branch (e.g., Smoglie and Reimann [2], Yonomoto and Tasaka [3,4], Micaelli and Memponteil [5], Hassan et al. [6], and Hassan [7]). For the theoretical study of the onset of gas entrainment from a stratified two-phase region, Ahmed et al. [8] developed a new criterion for the onset of gas entrainment based on the instability of an invicid liquid surface accelerated vertically. Based on this criterion, two different models were developed to predict the critical height at the onset of gas entrainment. They indicated that the comparisons between measured and predicted critical height show a very good agreement. It is worth mentioning that Xue and Yue [9], Miloh and Tyvand [10], Lubin and Springer [11], Zhou and Grabel [12], and Zhou [13] investigated the flow due to side and bottom submerged point sink. They concluded that the dip formation or the onset of air at the free surface occurs at a specific value of a dimensionless parameter, which is related to the sink strength, and the height above the point sink.

For multiple discharges from a stratified two-phase region, Parrott et al. [14] and Parrott [15] experimentally investigated the phenomenon of onset of gas entrainment from a stratified two-phase region during dual discharge through vertically aligned branches located on the sidewall of a reservoir. They indicated that the critical height corresponding to the onset of gas entrainment was found to be a function of the two discharge rates and vertical distance between the centerlines of two branches. Hassan et al. [16] experimentally investigated the onsets of gas and liquid entrainment, mass flow rate, and quality during discharge from two horizontal branches with centerlines falling in a common horizontal plane. Maier [17] performed an experimental work on the onset of gas and liquid entrainment during dual discharges from a stratified two-phase region through two horizontal branches with centerlines falling in a common plane with variable inclinations in order to determine the critical height and location for the onset. He indicated that four distinguishable modes of entrainment were observed. These modes can be defined as initial vortex entrainment, continuous vortex entrainment, initial depression entrainment, and continuous depression entrainment. For the same configuration, Maier et al. [18,19] reported that the critical height and the location of the onset of both phenomena were

Contributed by the Fluids Engineering Division of ASME for publication in the JOURNAL OF FLUIDS ENGINEERING. Manuscript received May 31, 2004; final manuscript received August 14, 2005. Assoc. Editor: Malcolm J. Andrews.

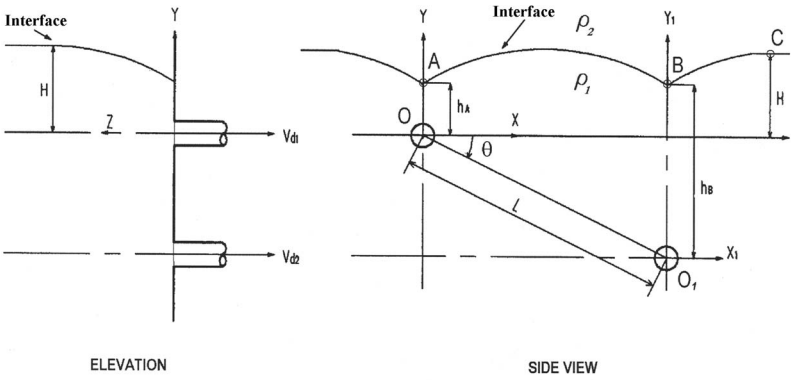

Fig. 1 Geometry and coordinate system for finite-branch analysis

found to be dependent on the flow rates through the branches, the distance between the branches, and the inclination angle.

For the theoretical prediction of the critical height at the onset of gas entrainment from a stratified region through dual branches, Ahmed et al. [20] developed theoretical models using the criterion developed by [8] to investigate the onset of gas entrainment through two vertically aligned side branches. They stated that the theoretically predicted critical height at the onset of gas entrainment was found to be in a good agreement with experimental data.

The objective of the present investigation is to extend the previous study [20] by developing an analysis to predict the onset of gas entrainment during discharge from two branches with centerlines falling in an inclined plane. In the current analysis, two models have been developed: a simplified point-sink model and a more-accurate three-dimensional finite-branch model. These models are based on a new modified criterion for the onset of gas entrainment. Moreover, comparisons with measured data are provided to validate the developed models.

2 Theoretical Analysis

The configuration to be considered, shown in Fig. 1, is composed of stratified layers of two immiscible fluids, having densities ρ_1 and ρ_2, contained in a large reservoir with two branches mounted on a vertical wall. The plane passing through the branch centerlines is inclined with an angle θ and it rotates clockwise from the positive x axis. The distance between branch centerlines is L. The mass flow rates of upper and lower branches are $\dot{m}_1$ and $\dot{m}_2$, respectively. The analysis presented in this article is based on the following assumptions:

1. The two fluids are considered to be invicid, homogenous, and incompressible.
2. The flow of the higher density fluid is considered to be irrotational, vortex free, and quasi-steady. Therefore, the transient free surface flow is not considered in this study.
3. The lower density fluid is considered stagnant.
4. Surface tension effect is ignored.
5. The flow field is extending over $-\infty \leqslant x \leqslant \infty$, $0 \leqslant z \leqslant \infty$.
6. The change in the surface elevation is considered to be very small, which can be acceptably neglected.

2.1 Equilibrium of the Interface. In order to find an analytical expression of the velocity at point (A), applying the Bernoulli equation on a streamline coincident with the interface from the heavier fluid side between point A and point C of Fig. 1, we get

$$P_C + \tfrac{1}{2}\rho_1 V_C^2 + \rho_1 g H = p_A + \tfrac{1}{2}\rho_1 V_A^2 + \rho_1 g h_A \tag{1}$$

On the side of the stagnant lighter fluid, the hydrostatic equilibrium gives

$$p_C + \rho_2 g H = p_A + \rho_2 g h_A \tag{2}$$

When $H=H_{OGE}$, $V_C=0.0$, the velocity of the liquid at point A can be given as

$$V_A^2 = 2g\frac{\Delta\rho}{\rho_1}(H_{OGE} - h_A) \tag{3}$$

Again applying the Bernoulli equation on a streamline coincident with the interface from the heavier fluid side between points B and C of Fig. 1, then following the same procedure, the velocity of the liquid at point B may be given as

$$V_B^2 = 2g\frac{\Delta\rho}{\rho_1}[H_{OGE} - (h_B + L\sin\theta)] \tag{4}$$

2.2 The Modified Criterion of the Onset of Gas Entrainment. As indicated by Ahmed et al. [8,20], the criterion used to predict the onset of gas entrainment is based on the equality between the acceleration of the higher density fluid directly above the branch and the acceleration of gravity. Any further increase of liquid acceleration above the acceleration of gravity will cause flow instability. This instability results in a catastrophic change in the free surface shape. This criterion is based on the assumption that the density of lighter fluid is very small compared to the density of heavier fluid so, acceptably, it may be neglected. However, when the density of the lighter fluid is comparable with the density of the heavier fluid, this significant density difference $\Delta\rho$ reduces the gravitational effect. Then, we can neglect the lighter density fluid, and the interface is considered as a free surface under the action of reduced gravity of $g'=g(\Delta\rho/\rho_1)$. Consequently, the modified criterion for the onset of gas entrainment will be written as follows:

$$[a]_A = -g' = -g\left(\frac{\Delta\rho}{\rho_1}\right). \tag{5}$$

At a very small value of density of the lighter fluid, $\Delta\rho \simeq \rho_1$ and $g'=g$.

2.3 Point-Sink Analysis. In the present analysis, the two branches are simulated as two point sinks with corresponding strengths m_1 and m_2. Relating the sink strengths m_1 and m_2 to the mass flow rates $\dot{m}_1$ and $\dot{m}_2$ gives the following:

$$\dot{m}_1 = 2\pi\rho_1 m_1 \quad \dot{m}_2 = 2\pi\rho_1 m_2 \tag{6}$$

Regarding the upper branch, the velocity field of the heavier fluid can be developed by following Schetz and Fuhs [21]. The potential function Φ is given by

$$\Phi = \Phi_1 + \Phi_2 = \frac{m_1}{\sqrt{x^2+y^2+z^2}} + \frac{m_2}{\sqrt{(x-L\cos\theta)^2+(y-L\sin\theta)^2+z^2}} \tag{7}$$

The criterion used for the prediction of the critical height at the onset of gas entrainment is defined previously in Eq. (5) as $[a]_A = -g(\Delta\rho/\rho_1)$.

The acceleration of the fluid particle at point A can be written as

$$[a]_A = \frac{\partial V_y}{\partial t} + V_x\frac{\partial V_y}{\partial x} + V_y\frac{\partial V_y}{\partial y} + V_z\frac{\partial V_y}{\partial z} \tag{8a}$$

where

$$\frac{\partial V_y}{\partial t} = 0.0 \quad \text{(quasi-steady assumption)}$$

$$V_Z = 0.0 \quad \text{(no flow crossing the wall at point A)}$$

Then, the final form of the acceleration of fluid particle at point A can be written in terms of potential function Φ as

$$[a]_A = \left\{\left(\frac{\partial\Phi}{\partial y}\right)\left(\frac{\partial^2\Phi}{\partial y^2}\right) + \left(\frac{\partial\Phi}{\partial x}\right)\left(\frac{\partial^2\Phi}{\partial x\partial y}\right)\right\}_{A[x=z=0.0,y=h_A]} \tag{8b}$$

Although the whole terms of acceleration shown by equation (8*b*) are included in the point-sink and finite branch analysis, it is worth noting that, based on the calculations of critical height at the onset of gas entrainment, the effect of the last term $(\partial\Phi/\partial x)\times(\partial^2\Phi/\partial x\partial y)$ within the studied range of variables is found not to exceed 0.2%. Consequently, it is reasonable to assume that the value of $(\partial\Phi/\partial x)$ approaches zero at the onset. By getting the first and second derivatives of Eq. (7), and then applying in Eq. (8*b*), the relationship in dimensionless form between the height above the branch h_A^*, Fr_1, Fr_2, L^*, and θ can be defined as follows:

$$\begin{aligned}\frac{\mathrm{Fr}_1^2}{h_A^{*5}} - \frac{\mathrm{Fr}_1\mathrm{Fr}_2}{2.0}\Bigg(&\frac{1.0}{h_A^{*2}[(L^*\cos\theta)^2+(h_A^*-L^*\sin\theta)^2]^{3/2}} \\ &- \frac{3(h_A^*-L^*\sin\theta)^2}{h_A^{*2}[(L^*\cos\theta)^2+(h_A^*-L^*\sin\theta)^2]^{5/2}} \\ &- \frac{2(h_A^*-L^*\sin\theta)}{h_A^{*3}[(L^*\cos\theta)^2+(h_A^*-L^*\sin\theta)^2]^{3/2}}\Bigg) \\ - \frac{\mathrm{Fr}_2^2}{2.0}\Bigg(&\frac{(h_A^*-L^*\sin\theta)}{[(L^*\cos\theta)^2+(h_A^*-L^*\sin\theta)^2]^3} \\ &- \frac{(L^*\cos\theta)^2(h_A^*-L^*\sin\theta)}{[(L^*\cos\theta)^2+(h_A^*-L^*\sin\theta)^2]^4} \\ &- \frac{3(h_A^*-L^*\sin\theta)^3}{[(L^*\cos\theta)^2+(h_A^*-L^*\sin\theta)^2]^4}\Bigg) - 1.0 = 0.0\end{aligned} \tag{9}$$

By substituting in Eq. (3), the dimensionless critical height H_{OGE}/d corresponding to the onset of gas entrainment at point A can be determined as follows:

$$\begin{aligned}\left.\frac{H_{OGE}}{d}\right|_A = \frac{h_A^*}{2} + \frac{1}{8}\Bigg\{&\left[\frac{\mathrm{Fr}_1}{h_A^{*2}}\right. \\ &\left. + \left(\frac{\mathrm{Fr}_2(h_A^*-L^*\sin\theta)}{[(L^*\cos\theta)^2+(h_A^*-L^*\sin\theta)^2]^{3/2}}\right)\right]^2 \\ &+ \left(\frac{\mathrm{Fr}_2 L^*\cos\theta}{[(L^*\cos\theta)^2+(h_A^*-L^*\sin\theta)^2]^{3/2}}\right)^2\Bigg\}.\end{aligned} \tag{10}$$

For any specific value of Fr_1, Fr_2, L/d, and θ, the height above the branch h_A^* can be estimated by solving Eq. (9) using an iterative procedure. Consequently, the critical height corresponding to the onset of gas entrainment at point A, $H_{OGE}/d|_A$, can be determined from Eq. (10).

Regarding the lower branch, the critical height at the onset of gas entrainment can be developed using the same procedure as for the upper branch. The final relationship between the height above the branch h_B^*, Fr_1, Fr_2, L^*, and θ can be analytically expressed as follows:

$$\begin{aligned}\frac{\mathrm{Fr}_2^2}{h_B^{*2}} - \frac{\mathrm{Fr}_1\mathrm{Fr}_2}{2.0}\Bigg(&\frac{1.0}{h_B^{*2}[(L^*\cos\theta)^2+(h_B^*+L^*\sin\theta)^2]^{3/2}} \\ &- \frac{3(h_B^*+L^*\sin\theta)^2}{h_B^{*2}[(L^*\cos\theta)^2+(h_B^*+L^*\sin\theta)^2]^{5/2}} \\ &- \frac{2(h_B^*+L^*\sin\theta)}{h_B^{*3}[(L^*\cos\theta)^2+(h_B^*+L^*\sin\theta)^2]^{3/2}}\Bigg) \\ - \frac{\mathrm{Fr}_1^2}{2.0}\Bigg(&\frac{(h_B^*+L^*\sin\theta)}{[(L^*\cos\theta)^2+(h_B^*+L^*\sin\theta)^2]^3} \\ &- \frac{(L^*\cos\theta)^2(h_B^*+L^*\sin\theta)}{[(L^*\cos\theta)^2+(h_B^*+L^*\sin\theta)^2]^4} \\ &- \frac{3(h_B^*+L^*\sin\theta)^3}{[(L^*\cos\theta)^2+(h_B^*+L^*\sin\theta)^2]^4}\Bigg) - 1.0 = 0.0\end{aligned} \tag{11}$$

The dimensionless critical height H_{OGE}/d at the onset of gas entrainment at point B can be expressed as follows:

$$\begin{aligned}\left.\frac{H_{OGE}}{d}\right|_B = \left(\frac{h_B^*+L^*\sin\theta}{2}\right) + \frac{1}{8}\Bigg\{&\left[\frac{\mathrm{Fr}_2}{h_B^{*2}}\right. \\ &\left. + \left(\frac{\mathrm{Fr}_1(h_B^*+L^*\sin\theta)}{[(L^*\cos\theta)^2+(h_B^*+L^*\sin\theta)^2]^{3/2}}\right)\right]^2 \\ &+ \left(\frac{\mathrm{Fr}_1 L^*\cos\theta}{[(L^*\cos\theta)^2+(h_B^*+L^*\sin\theta)^2]^{3/2}}\right)^2\Bigg\}\end{aligned} \tag{12}$$

Again, by knowing Fr_1, Fr_2, L/d, and θ, the height above the branch h_B^* can be calculated by solving Eq. (11) using an iterative procedure. Based on the value of h_B^*, the critical height corresponding to the onset of gas entrainment at point B, $H_{OGE}/d|_B$, can be determined from Eq. (12).

Based on the calculated values of $H_{OGE}/d|_A$ and $H_{OGE}/d|_B$, two objectives are considered. The first one is to locate the sink or sinks where the onset of gas entrainment would occur and the critical height corresponding to this onset. For a specific value of Fr_1, Fr_2, L/d, and θ, the critical height corresponding to the onset of gas entrainment for both branches can be calculated. Then, if $H_{OGE}/d|_A > H_{OGE}/d|_B$, it means that the onset of gas entrainment occurs at branch 1, and the critical height will be $H_{OGE}/d = H_{OGE}/d|_A$. If $H_{OGE}/d|_B > H_{OGE}/d|_A$, this means that the onset of gas entrainment occurs at branch 2 and the critical height will be $H_{OGE}/d = H_{OGE}/d|_B$, and, if $H_{OGE}/d|_A = H_{OGE}/d|_B$, in this case the onset of gas entrainment occurs at both branches at the same time—a situation which is called a dual onset and the critical height will be $H_{OGE}/d = H_{OGE}/d|_A = H_{OGE}/d|_B$. Furthermore, if $\mathrm{Fr}_2 = 0.0$ or $\mathrm{Fr}_1 = 0.0$, the value of H_{OGE}/d is the same as for the case of a single branch.

It is clear based on Eqs. (9)–(12) that for limiting case $\mathrm{Fr}_1 = \mathrm{Fr}_2 = 0.0$, the critical height corresponding to the onset of gas entrainment approaches zero. However, the correct limit should be $d/2$. This means that the results of point sink analysis are not accurate for low discharges. A more accurate analysis, therefore, is presented in the following section in which all previously mentioned assumptions will be considered, except for considering the branch size.

2.4 Finite-Branch Analysis. In this analysis, the real dimensions of the branches are considered. The flow is caused by the two discharges with uniform velocity V_{d1} from branch 1, located

at $x=y=z=0.0$, and the velocity V_{d2} from branch 2, located at $x=L\cos\theta$, $y=L\sin\theta$, and $z=0.0$ as shown in Fig. 1. The continuity equation using the Cartesian coordinate system can be written in dimensionless form as follows:

$$\frac{\partial V_x^*}{\partial x^*}+\frac{\partial V_y^*}{\partial y^*}+\frac{\partial V_z^*}{\partial z^*}=0.0 \tag{13}$$

where V_x^*, V_y^*, and V_z^* are the dimensionless velocity components in x^*, y^*, and z^* directions. Introducing a dimensionless scalar potential function Φ^* such that

$$V_x^*=\frac{\partial \Phi^*}{\partial x^*} \quad V_y^*=\frac{\partial \Phi^*}{\partial y^*} \quad \text{and} \quad V_z^*=\frac{\partial \Phi^*}{\partial z^*} \tag{14}$$

Then, Eq. (13) can be written as follows:

$$\frac{\partial^2 \Phi^*}{\partial x^{*2}}+\frac{\partial^2 \Phi^*}{\partial y^{*2}}+\frac{\partial^2 \Phi^*}{\partial z^{*2}}=0.0 \tag{15}$$

with the following boundary conditions:

(a) At $z^*=0.0$,

$$\frac{\partial \Phi^*}{\partial z^*}=\begin{cases}-V_{d_1}^* & -\sqrt{1-y^{*2}}\leq x^*\leq+\sqrt{1-y^{*2}},\ \text{and}\ -1\leq y^*\leq+1\\ -V_{d2}^* & L^*\cos\theta-\sqrt{1-(y^*-L^*\sin\theta)^2}\leq x^*\leq L^*\cos\theta+\sqrt{1-(y^*-L^*\sin\theta)^2},\ \text{and}\ L^*\sin\theta-1\leq y^*\leq L^*\sin\theta+1\\ 0.0 & \text{for other values of } x^* \text{ and } y^*\end{cases}$$

(b) At $x^*\to\pm\infty$, $z^*\to+\infty$, Φ^* is finite.

As indicated in (b), one more assumption is considered in order to get an analytical solution of Eq. (15) which is that the lighter density fluid is ignored; consequently, the higher density fluid is unbounded (i.e., $y=\pm\infty$). Craya [22] indicated that assuming the liquid is unbounded in the upwards and downwards directions does not markedly alter the results as long as the top and bottom surfaces are located sufficiently far from the interface. Furthermore, an assessment of the influence of this assumption was proved by many researchers (e.g., Soliman and Sims [23,24], Maier et al. [18], and Ahmed et al. [8,20]). The solution of Eq. (15) subjected to the boundary conditions given by (a) and (b) was obtained using the method of separation of variables as follows:

$$\begin{aligned}\Phi^*(x^*,y^*,z^*)=&\int_0^\infty\int_0^\infty\frac{\cos(\beta y^*)\cos(\lambda x^*)e^{-z^*\sqrt{\lambda^2+\beta^2}}}{\lambda\sqrt{\lambda^2+\beta^2}}\left(\frac{2V_{d_1}^*}{\pi^2}\int_{-1}^{+1}\sin(\lambda\sqrt{1-y^{*2}})\cos(\beta y^*)dy^*+\frac{V_{d_2}^*}{\pi^2}\int_{L^*\sin\theta-1}^{L^*\sin\theta+1}\sin\{\lambda[L^*\cos\theta\right.\\&\left.+\sqrt{1-(y^*-L^*\sin\theta)^2}]\}\cos(\beta y^*)dy^*-\frac{V_{d_2}^*}{\pi^2}\int_{L^*\sin\theta-1}^{L^*\sin\theta+1}\sin\{\lambda[L^*\cos\theta-\sqrt{1-(y^*-L^*\sin\theta)^2}]\}\cos(\beta y^*)dy^*\right)d\lambda d\beta\\&+\int_0^\infty\int_0^\infty\frac{\cos(\beta y^*)\sin(\lambda x^*)e^{-z^*\sqrt{\lambda^2+\beta^2}}}{\lambda\sqrt{\lambda^2+\beta^2}}\left(\frac{V_{d_2}^*}{\pi^2}\int_{L^*\sin\theta-1}^{L^*\sin\theta+1}\cos\{\lambda[L^*\cos\theta-\sqrt{1-(y^*-L^*\sin\theta)^2}]\}\cos(\beta y^*)dy^*\right.\\&\left.-\frac{V_{d_2}^*}{\pi^2}\int_{L^*\sin\theta-1}^{L^*\sin\theta+1}\cos\{\lambda[L^*\cos\theta+\sqrt{1-(y^*-L^*\sin\theta)^2}]\}\cos(\beta y^*)dy^*\right)d\lambda d\beta\\&+\int_0^\infty\int_0^\infty\frac{\sin(\beta y^*)\cos(\lambda x^*)e^{-z^*\sqrt{\lambda^2+\beta^2}}}{\lambda\sqrt{\lambda^2+\beta^2}}\left(\frac{2V_{d_1}^*}{\pi^2}\int_{-1}^{+1}\sin(\lambda\sqrt{1-y^{*2}})\sin(\beta y^*)dy^*+\frac{V_{d_2}^*}{\pi^2}\int_{L^*\sin\theta-1}^{L^*\sin\theta+1}\sin\{\lambda[L^*\cos\theta\right.\\&\left.+\sqrt{1-(y^*-L^*\sin\theta)^2}]\}\sin(\beta y^*)dy^*-\frac{V_{d_2}^*}{\pi^2}\int_{L^*\sin\theta-1}^{L^*\sin\theta+1}\sin\{\lambda[L^*\cos\theta-\sqrt{1-(y^*-L^*\sin\theta)}]\}\sin(\beta y^*)dy^*\right)d\lambda d\beta\\&+\int_0^\infty\int_0^\infty\frac{\sin(\beta y^*)\sin(\lambda x^*)e^{-z^*\sqrt{\lambda^2+\beta^2}}}{\lambda\sqrt{\lambda^2+\beta^2}}\left(\frac{V_{d_2}^*}{\pi^2}\int_{L^*\sin\theta-1}^{L^*\sin\theta+1}\cos\{\lambda[L^*\cos\theta-\sqrt{1-(y^*-L^*\sin\theta)^2}]\}\sin(\beta y^*)dy^*\right.\\&\left.-\frac{V_{d_2}^*}{\pi^2}\int_{L^*\sin\theta-1}^{L^*\sin\theta+1}\cos\{\lambda[L^*\cos\theta+\sqrt{1-(y^*-L^*\sin\theta)^2}]\}\sin(\beta y^*)dy^*\right)d\lambda d\beta\end{aligned} \tag{16}$$

As indicated before, the criterion for the onset of gas entrainment can be written as

$$[a^*]_A=-g^*\left(\frac{\Delta\rho}{\rho_1}\right) \tag{17}$$

where

$$[a^*]_A=\left\{\left(\frac{\partial\Phi^*}{\partial y^*}\right)\left(\frac{\partial^2\Phi^*}{\partial y^{*2}}\right)+\left(\frac{\partial\Phi^*}{\partial x^*}\right)\left(\frac{\partial^2\Phi^*}{\partial x^*\partial y^*}\right)\right\}_{A[x^*=z^*=0.0,y^*=h_A^*]} \tag{18}$$

The values of the first and second derivatives of the stream functions Φ^* at point A can be written as follows:

$$\Phi^*_{y^*}|_A=\frac{V_{d1}^*}{\pi^2}[I_1(h_A^*)]+\frac{V_{d2}^*}{\pi^2}[I_2(h_A^*)] \tag{19}$$

$$\Phi^*_{y^*y^*}|_A = \frac{V^*_{d1}}{\pi^2}[I_3(h^*_A)] + \frac{V^*_{d2}}{\pi^2}[I_4(h^*_A)] \tag{20}$$

$$\Phi^*_{x^*}|_A = \frac{V^*_{d2}}{\pi^2}[I_5(h^*_A)] \tag{21}$$

$$\Phi^*_{x^*y^*}|_A = \frac{V^*_{d2}}{\pi^2}[I_6(h^*_A)] \tag{22}$$

where

$$I_1(h^*_A) = \int_0^\infty \int_0^\infty \int_{-1}^{+1} \frac{2\beta}{\lambda\sqrt{\lambda^2+\beta^2}}\{\sin[\beta(y^* - h^*_A)] \times [\sin(\lambda\sqrt{1-y^{*2}})]\}dy^* d\beta d\lambda$$

$$I_2(h^*_A) = \int_0^\infty \int_0^\infty \int_{L^*\sin\theta-1}^{L^*\sin\theta+1} \frac{-\beta\sin(\beta(y^* - h^*_A))}{\lambda\sqrt{\lambda^2+\beta^2}}(\sin\{\lambda[L^*\cos\theta - \sqrt{1-(y^* - L^*\sin\theta)^2}]\} - \sin\{\lambda[L^*\cos\theta + \sqrt{1-(y^* - L^*\sin\theta)^2}]\})dy^* d\beta d\lambda$$

$$I_3(h^*_A) = \int_0^\infty \int_0^\infty \int_{-1}^{+1} \frac{2\beta^2}{\lambda\sqrt{\lambda^2+\beta^2}}\{\cos[\beta(y^* - h^*_A)] \times \sin(\lambda\sqrt{1-y^{*2}})\}dy^* d\beta d\lambda$$

$$I_4(h^*_A) = \int_0^\infty \int_0^\infty \int_{L^*\sin\theta-1}^{L^*\sin\theta+1} \frac{-\beta^2\cos(\beta(y^* - h^*_A))}{\lambda\sqrt{\lambda^2+\beta^2}}(\sin\{\lambda[L^*\cos\theta - \sqrt{1-(y^* - L^*\sin\theta)^2}]\} + \sin\{\lambda[L^*\cos\theta + \sqrt{1-(y^* - L^*\sin\theta)^2}]\})dy^* d\beta d\lambda$$

$$I_5(h^*_A) = \int_0^\infty \int_0^\infty \int_{L^*\sin\theta-1}^{L^*\sin\theta+1} \frac{\cos[\beta(y^* - h^*_A)]}{\sqrt{\lambda^2+\beta^2}}(\cos\{\lambda[L^*\cos\theta - \sqrt{1-(y^* - L^*\sin\theta)^2}]\} - \cos\{\lambda[L^*\cos\theta + \sqrt{1-(y^* - L^*\sin\theta)^2}]\})dy^* d\beta d\lambda$$

$$I_6(h^*_A) = \int_0^\infty \int_0^\infty \int_{L^*\sin\theta-1}^{L^*\sin\theta+1} \frac{-\beta\sin[\beta(y^* - h^*_A)]}{\sqrt{\lambda^2+\beta^2}}(\cos\{\lambda[L^*\cos\theta - \sqrt{1-(y^* - L^*\sin\theta)^2}]\} - \cos\{\lambda[L^*\cos\theta + \sqrt{1-(y^* - L^*\sin\theta)^2}]\})dy^* d\beta d\lambda$$

Substituting Eqs. (19)–(22) into Eq. (18) will give

$$\mathrm{Fr}_1^2[I_1(h^*_A)I_3(h^*_A)] + \mathrm{Fr}_1\mathrm{Fr}_2[I_2(h^*_A)I_3(h^*_A) + I_1(h^*_A)I_4(h^*_A)] + \mathrm{Fr}_2^2[I_2(h^*_A)I_4(h^*_A) + I_5(h^*_A)I_6(h^*_A)] + \pi^4 = 0.0 \tag{23}$$

By substituting in Eq. (3), the critical height corresponding to the onset of gas entrainment may be written as

$$\left.\frac{H_{OGE}}{d}\right|_A = \frac{h^*_A}{2} + \frac{1}{2\pi^4}(\{\mathrm{Fr}_1[I_1(h^*_A)] + \mathrm{Fr}_2[I_2(h^*_A)]\}^2 + \{\mathrm{Fr}_2[I_5(h^*_A)]\}^2) \tag{24}$$

The procedures to calculate the critical height corresponding to the onset of gas entrainment of branch A, for specific values of independent variables Fr_1, Fr_2, L/d, and θ, can be summarized as follows.

1. Calculate the integral functions I_1, I_2, I_3, I_4, I_5, and I_6 using the proper numerical integration technique as indicated by [25].
2. Solve Eq. (23) using an iterative procedure to obtain the value of h^*_A.
3. Determine the critical height at the onset of gas entrainment using Eq. (24).

Regarding branch 2, the critical height for the onset of entrainment can be obtained by following the same technique as for branch 1. The final analytical equation can be expressed in the following form:

$$\mathrm{Fr}_2^2[J_1(h^*_B)J_3(h^*_B)] + \mathrm{Fr}_1\mathrm{Fr}_2[J_2(h^*_B)J_3(h^*_B) + J_1(h^*_B)J_4(h^*_B)] + \mathrm{Fr}_1^2[J_2(h^*_B)J_4(h^*_B) + J_5(h^*_B)J_6(h^*_B)] + \pi^4 = 0.0 \tag{25}$$

The critical height corresponding to the onset of gas entrainment can be written as

$$\left.\frac{H_{OGE}}{d}\right|_B = \left(\frac{h^*_B + L^*\sin\theta}{2}\right) + \frac{1}{2\pi^4}(\{\mathrm{Fr}_2[J_1(h^*_B)] + \mathrm{Fr}_1[J_2(h^*_B)]\}^2 + (\mathrm{Fr}_1[J_5(h^*_B)])^2) \tag{26}$$

where

$$J_1(h^*_B) = \int_0^\infty \int_0^\infty \int_{-1}^{+1} \frac{-2\beta}{\lambda\sqrt{\lambda^2+\beta^2}}\{\sin[\beta(y^*_1 - h^*_B)] \times [\sin(\lambda\sqrt{1-y^{*2}_1})]\}dy^*_1 d\beta d\lambda$$

$$J_2(h^*_B) = \int_0^\infty \int_0^\infty \int_{-L^*\sin\theta-1}^{-L^*\sin\theta+1} \frac{-\beta\sin(\beta(y^*_1 - h^*_B))}{\lambda\sqrt{\lambda^2+\beta^2}}(\sin\{\lambda[-L^*\cos\theta - \sqrt{1-(y^*_1 + L^*\sin\theta)^2}]\} - \sin\{\lambda[-L^*\cos\theta + \sqrt{1-(y^*_1 + L^*\sin\theta)^2}]\})dy^*_1 d\beta d\lambda$$

$$J_3(h^*_B) = \int_0^\infty \int_0^\infty \int_{-1}^{+1} \frac{2\beta^2}{\lambda\sqrt{\lambda^2+\beta^2}}\{\cos[\beta(y^*_1 - h^*_B)] \times \sin(\lambda\sqrt{1-y'^{*2}})\}dy^*_1 d\beta d\lambda$$

$$J_4(h^*_B) = \int_0^\infty \int_0^\infty \int_{-L^*\sin\theta-1}^{-L^*\sin\theta+1} \frac{-\beta^2\cos(\beta(y^*_1 - h^*_B))}{\lambda\sqrt{\lambda^2+\beta^2}} \times (\sin\{\lambda[-L^*\cos\theta - \sqrt{1-(y^*_1 + L^*\sin\theta)^2}]\} + \sin\{\lambda[-L^*\cos\theta + \sqrt{1-(y^*_1 + L^*\sin\theta)^2}]\})dy^*_1 d\beta d\lambda$$

$$J_5(h^*_B) = \int_0^\infty \int_0^\infty \int_{-L^*\sin\theta-1}^{-L^*\sin\theta+1} \frac{\cos(\beta(y^*_1 - h^*_B))}{\sqrt{\lambda^2+\beta^2}}(\cos\{\lambda[-L^*\cos\theta - \sqrt{1-(y^*_1 + L^*\sin\theta)^2}]\} - \cos\{\lambda[-L^*\cos\theta + \sqrt{1-(y^*_1 + L^*\sin\theta)^2}]\})dy^*_1 d\beta d\lambda$$

$$J_6(h^*_B) = \int_0^\infty \int_0^\infty \int_{-L^*\sin\theta-1}^{-L^*\sin\theta+1} \frac{-\beta\sin[\beta(y^*_1 - h^*_B)]}{\sqrt{\lambda^2+\beta^2}}(\cos\{\lambda[-L^*\cos\theta - \sqrt{1-(y^*_1 + L^*\sin\theta)^2}]\} - \cos\{\lambda[-L^*\cos\theta + \sqrt{1-(y^*_1 + L^*\sin\theta)^2}]\})dy^*_1 d\beta d\lambda$$

Similar to the previous procedures for the upper branch, the critical height corresponding to the onset of gas entrainment of the lower branch can be summarized as follows.

1. Calculate the integral functions J_1, J_2, J_3, J_4, J_5, and J_6 using the proper numerical integration technique.
2. Solve Eq. (25) using an iterative procedure to obtain the value of h^*_B.

3. Determine the critical height at the onset of gas entrainment using Eq. (26).

The conclusion is that for a specific value of Fr_1, Fr_2, L/d, and θ, the critical height at the onset of gas entrainment is calculated for both branches and H_{OGE}/d is selected as the largest one as previously explained. Also, if $H_{OGE}/d|_A = H_{OGE}/d|_B$, it means that the onset of gas entrainment occurs at both branches at the same time—a situation which is called a dual onset and the critical height will be $H_{OGE}/d = H_{OGE}/d|_A = H_{OGE}/d|_B$.

3 Results and Discussion

In this section, the theoretically predicted critical height at the onset of gas entrainment and the location of the onset by point-sink and finite-branch models were investigated at different values of mass flow rate of upper branch (Fr_1), lower branch (Fr_2), distance between the centerlines of two branches (L/d), and the inclination angle (θ) where it rotates clockwise from the positive x axis. The objective of this investigation is to clarify how these independent variables (Fr_1, Fr_2, L/d, and θ) control the values of critical height as well as the onset location. In addition, comparisons between the theoretically predicted results by both models and the experimental data were performed to provide a validation for the present developed models. The sets of experimental results selected for this comparison were measured by Parrott et al. [14] and Maier et al. [19] at continuous depression entrainment mode during dual horizontal discharge from two 6.35 mm diameter branches with centerlines in an inclined plane located on the side of a large reservoir under a stratified (air-water) condition and air pressure of 510 kPa. Also, the direction of rotation of angle θ shown in Fig. 1 is the same as the direction shown in the experimental setup used for measurements by Maier et al. [19].

For dual branches, Fig. 2 shows the comparison of the present predicted results using both models with the experimental data by Maier et al. [19] at $L/d=1.5$, and varying the mass flow rate of lower branch ($Fr_2=14$, 28.5, and 42.5), while θ is set to 0.0, 30.0, and 60 deg. As shown in Fig. 2(a), where θ is set to 0.0 deg, the present models predict well the critical height at the onset of gas entrainment (H_{OGE}/d) and the location of the dual onset point. However, in Fig. 2(b), where $\theta=30.0$ deg, the models slightly overpredicted the dual onset point at $Fr_2=42.5$. In Fig. 2(c), where $\theta=60.0$ deg, the present models accurately predict the critical height at the onset of gas entrainment (H_{OGE}/d) and the location of the dual onset point.

Comparing Figs. 2(a)–2(c) indicates that by increasing the angle θ, the dual onset point shifts towards the lower Fr_1. It means that the value of Fr_1 at the dual onset point decreases by increasing the inclination angle θ.

Figure 3 illustrates the comparison of the predicted critical height and the location of the onset with the measured values by Maier et al. [19] at $L/d=2$, and Fr_2 varies (14.0, 28.5, and 42.5) when θ is set to 0.0 deg as in Fig. 3(a), θ is set to 30.0 deg as in Fig. 3(b), and θ is set to 60.0 deg as in Fig. 3(c). It is obvious from Fig. 3(a) that both models accurately predict the measured values of (H_{OGE}/d) and the location of dual onset point, whereas in Fig. 3(b) the models slightly overpredicted the dual onset points. Increasing the inclination angle θ up to 60.0 deg results in the onset of gas entrainment at the upper branch, while there is no onset of gas entrainment at the lower branch. Comparison between Figs. 3(a) and 3(b) shows that with increasing the angle θ, the value of Fr_1 corresponding to the location of dual onset point decreases.

In a similar way, comparison of the predicted H_{OGE}/d and the location of the onset point with that measured by Maier et al. [19] at $L/d=8.0$, while Fr_2 varies ($Fr_2=14.0$, 28.5, and 56.6) at two different values of θ (0.0 and 30.0 deg), is shown in Fig. 4. As shown in Fig. 4(a), where $\theta=0.0$ deg, the theoretical models predict well the experimental values of H_{OGE}/d and the location of the dual onset point. However, in Fig. 4(b), where $\theta=30.0$ deg, the experimental data were slightly overpredicted by both models at $Fr_1<10.0$, while for $Fr_1>10.0$ the model predicted well the measured values. Also, the values of the critical height are independent of Fr_2 within the measured range 0.0–42.5 and the value

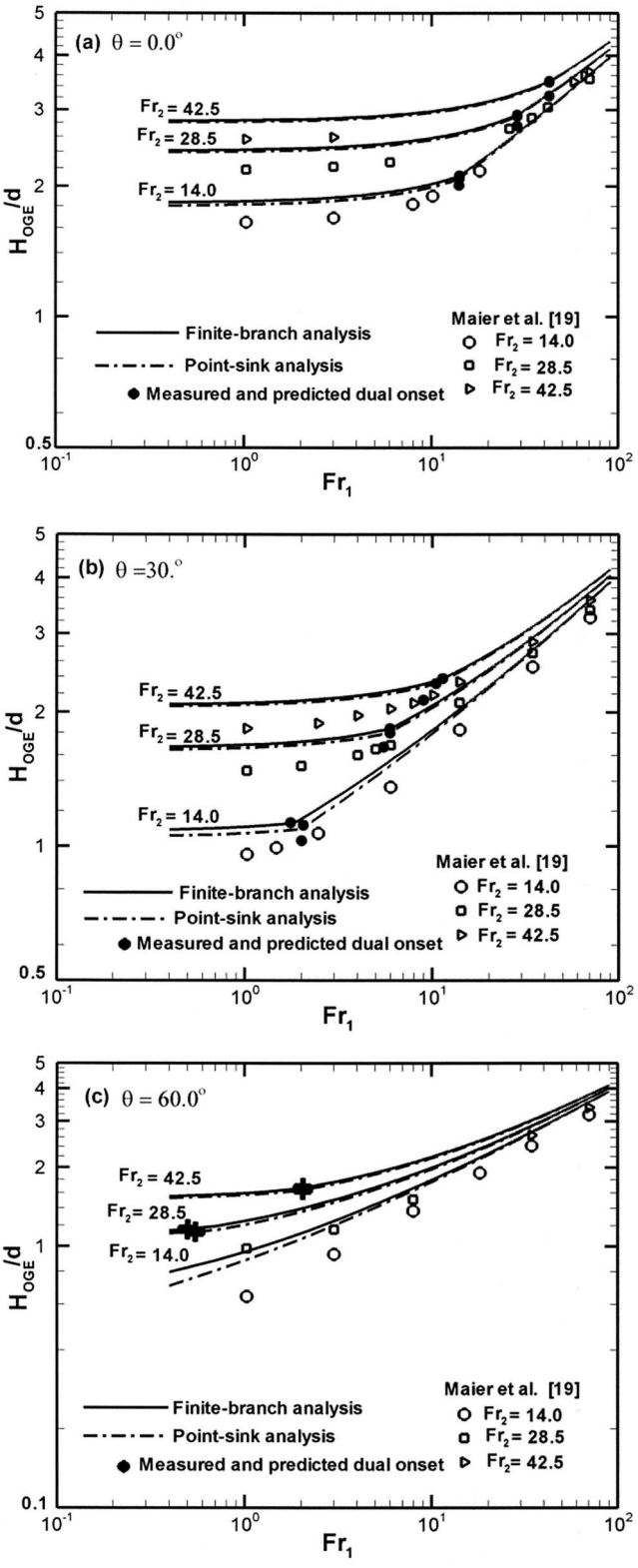

Fig. 2 Comparisons between predicted and experimental results at different values of θ (0.0, 30, and 60 deg) for $L/d=1.5$

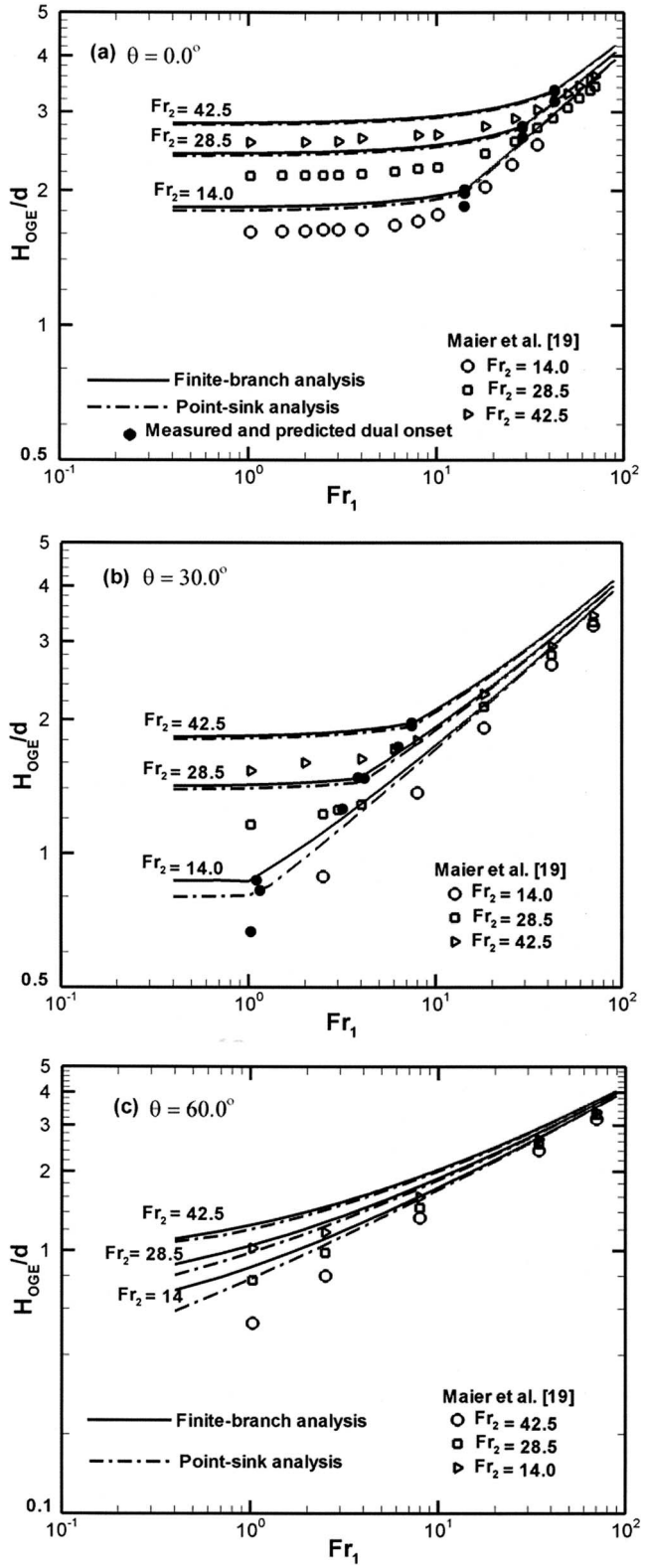

Fig. 3 Comparisons between predicted and experimental results at different values of θ (0.0, 30, and 60 deg) for L/d=2.0

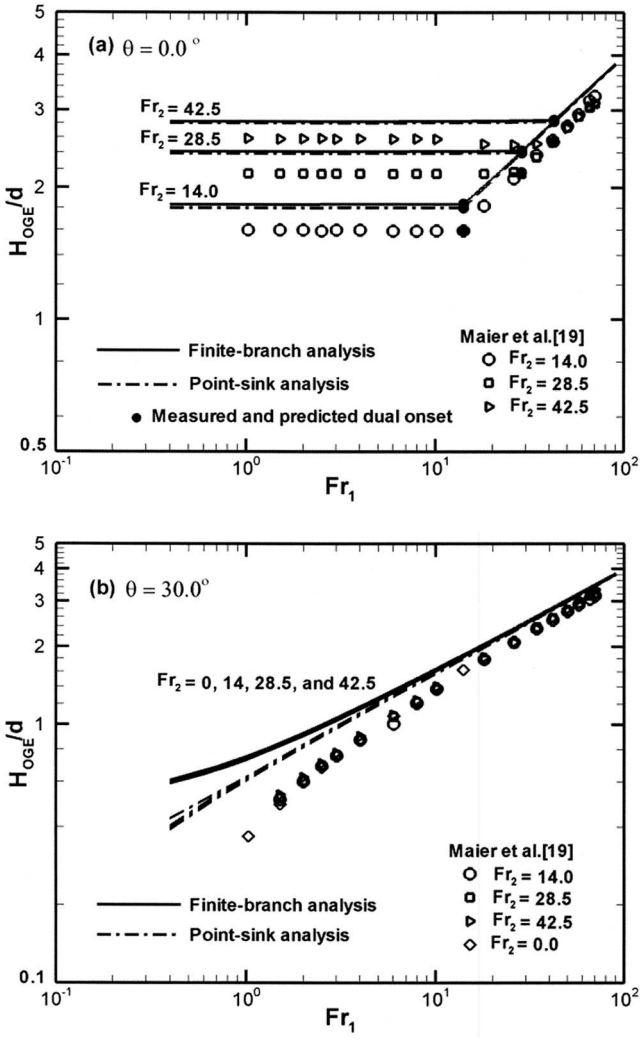

Fig. 4 Comparisons between predicted and experimental results at different values of θ (0.0 and 30 deg) for L/d=8.0

of critical height at the onset is the same as a single branch. Comparison between Figs. 4(*a*) and 4(*b*) indicates that increasing the inclination angle up to 30.0 deg results in the onset of gas entrainment at the upper branch only while there is no onset of gas entrainment at the lower branch.

The effect of Fr_2 on the critical height (H_{OGE}/d) and onset location can be observed from Figs. 2–4. It is clear based on these figures that by increasing Fr_2, the critical height at the onset of gas entrainment increases. For a fixed value of Fr_1, the onset of gas entrainment occurs at branch 2 for low values of Fr_1. There is a slight increase of critical height as Fr_1 increases up to the point where the onset of gas entrainment occurs at both branches—a situation which is called a dual onset point. Beyond this point, the onset shifts to branch 1 and the critical height increases significantly with Fr_1. Also, the value of Fr_1 at the point of dual onset increases as Fr_2 increases.

Figure 5 elucidates the comparison between the theoretically predicted results and the experimental data measured by Maier et al. [19] at θ=0.0, 30, and 60.0 deg, and by Parrott et al. [14] at θ=90.0 deg. Parrott et al. collected two different sets of experimental data for the critical height at the onset of gas entrainment, $H_{OGE,f}$ and $H_{OGE,m}$. The first set of experiments ($H_{OGE,f}$) is defined as the height between the flat surface at the interface and the branch centerline, at the onset of gas entrainment, while the second set ($H_{OGE,m}$) is defined as $H_{OGE,m}=H_{OGE,f}$+the meniscus height of 3.3 mm. As indicated by Parrott [15] for low liquid level heights associated with low discharge rates, $H_{OGE,m}$ appeared to be more meaningful to the phenomenon than $H_{OGE,f}$, while for high discharge rates, the difference between $H_{OGE,f}/d$ and

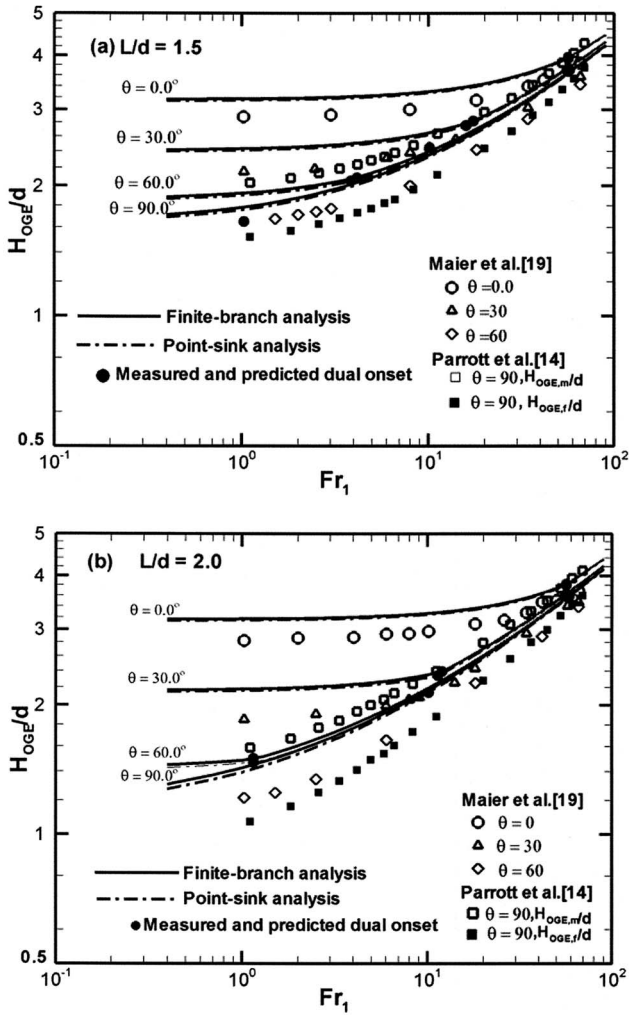

Fig. 5 Comparisons between predicted and experimental results at different values of L/d (1.5 and 2) for $Fr_2=56.6$

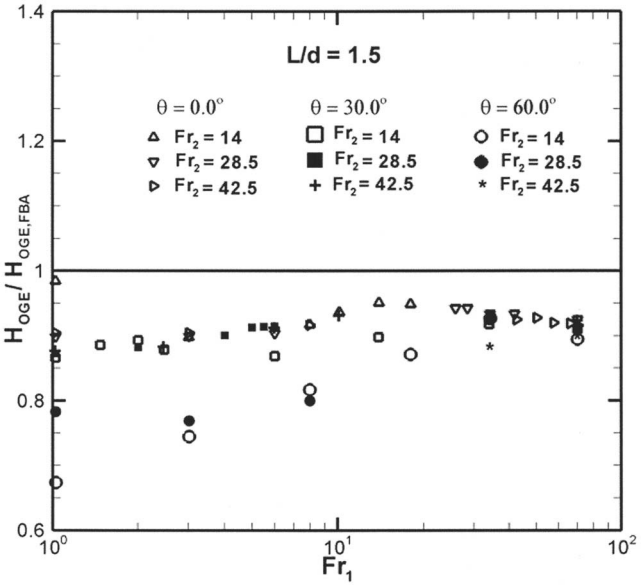

Fig. 6 Percent deviation from the predicted critical height by finite branch model using the experimental data of Maier et al. [19] at $L/d=1.5$ and $\theta=0$, 30, and 60 deg

$H_{OGE,m}/d$ appeared to be relatively small. As shown in Fig. 5(a), where L/d is set to 1.5, the models overpredicted the dual onset points at $\theta \geqslant 30.0$ deg, while at $\theta=90.0$ deg the models were found to be consistent with the average value of $H_{OGE,f}/d$ and $H_{OGE,m}/d$. In Fig. 5(b), where $L/d=2.0$, similar results are observed. Comparison between Figs. 5(a) and 5(b) shows that increasing L/d leads to the decrease of the critical height at values of $\theta \geqslant 30.0$ deg and the value of Fr_1 at dual onset point.

The effect of the inclination angle θ on H_{OGE}/d and location of the onset is observed from Fig. 5 for different values of L/d, with a constant $Fr_2=56.6$. These results show that H_{OGE}/d decreases as θ increases for the same value of Fr_1, Fr_2, and L/d. At $\theta=90.0$ deg, and $L/d=2.0$, the onset takes place at branch 1 at the values of $Fr_1>0.5$ as shown in Fig. 5(b). Moreover, the value of Fr_1 corresponding to the dual onset point decreases as θ increases.

The conclusion based on Figs. 2–6 is that the critical height at the onset of gas entrainment increases by increasing Fr_1, or Fr_2, whereas increasing the inclination angle θ and/or the distance between branches (L/d) decreases the critical height at the onset. This may be explained by the effect of inertia due to the discharge of each branch. Increasing Fr_1 or Fr_2 results in the increase of the inertia effect and, consequently, the critical height at the onset, whereas increasing the inclination angle and/or the distance between branch centerlines causes the increase of the height between the interface and the lower branch. This will reduce the inertia effect and hence the influence of the lower branch. Further increase of L/d results in a single branch approximation.

The comparisons between the predicted and experimental results of the critical height are shown in Figs. 6–9. These figures show the percent deviation of the experimental data from the finite branch prediction which is defined as $H_{OGE}/H_{OGE,FBA}$. At $L/d=1.5$ and 2.0, the effect of the inclination angle ranging from 0.0 to 60 deg on the percent deviation is presented in Figs. 6 and 7. Based on the figures, it is obvious that at $Fr_1>3.0$, the percent deviation of measurements is around 15%, while at $Fr_1<3.0$ the percent deviation reaches 38%. At $L/d=8.0$, the effect of the inclination angle ranging from 0.0 to 30.0 deg on the percent deviation is shown in Fig. 8. When $\theta=0.0$, the percent deviation is about 10% at all values of Fr_1, and when $\theta=30.0$ deg, the percent

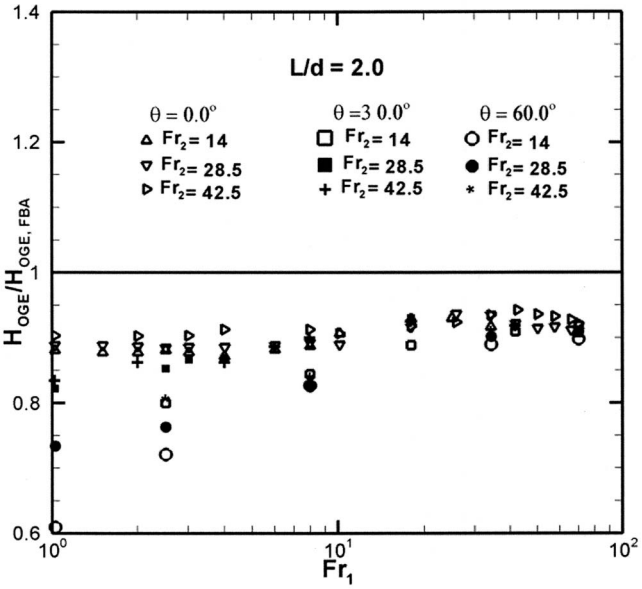

Fig. 7 Percent deviation from the predicted critical height by finite branch model using the experimental data of Maier et al. [19] at $L/d=2.0$ and $\theta=0$, 30, and 60 deg

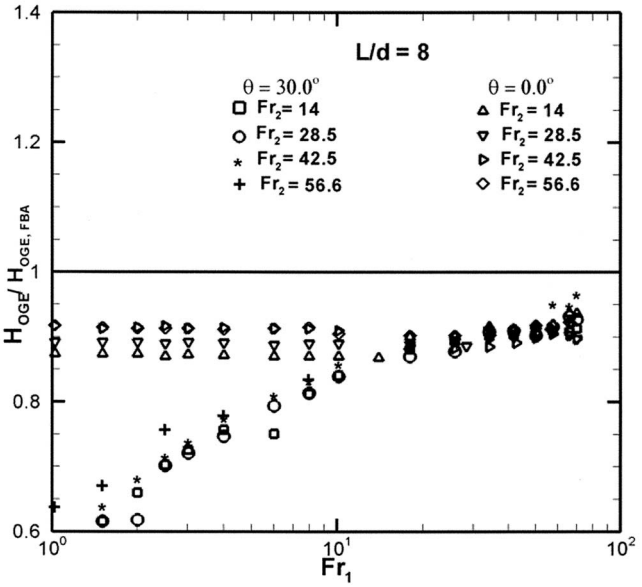

Fig. 8 Percent deviation from the predicted critical height by finite branch model using the experimental data of Maier et al. [19] at L/d=8.0 and θ=0 and 30 deg

deviation is about 10% at $Fr_1 > 10$, and about 38% at $Fr_1 < 10$. Figure 9 represents the percent deviation at Fr_2=56.6 and L/d =1.5 and 2.0 while θ varies from 0.0 to 90 deg. It is found that the percent deviation is about ±12% in case of $Fr_1 > 10$ and about 25% at $Fr_1 < 10$.

The conclusion based on Figs. 6–9 is that for $Fr_1 > 10$, the maximum deviation varied from 6.0% to about 12%, whereas at low Froude number ($Fr_1 < 10$), the maximum deviation varied from 12% to about 38%. The reason is most likely due to the viscous effect where it is expected to have a significant influence on the predicted critical height at low values of Fr_1. However, at higher values of Fr_1 ($Fr_1 > 10$) the inertia effect is dominant and the viscous effect may be insignificant.

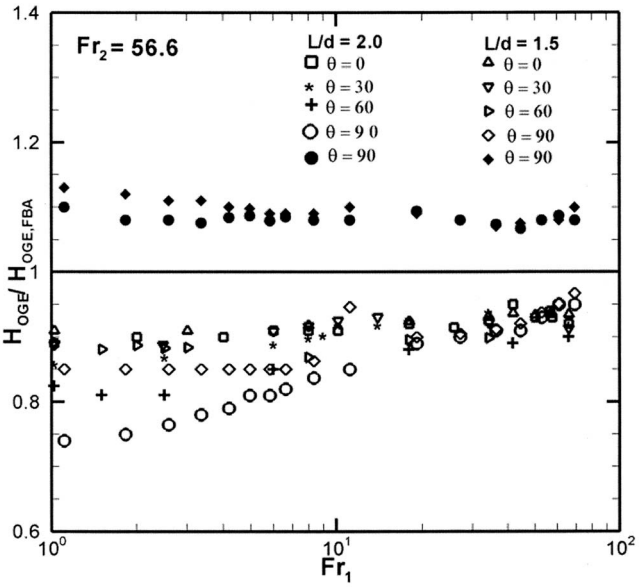

Fig. 9 Percent deviation from the predicted critical height by finite branch model using the experimental data of Maier et al. [19] and Parrott et al. [14] at Fr_2=56.6 and L/d=1.5 and 2.0

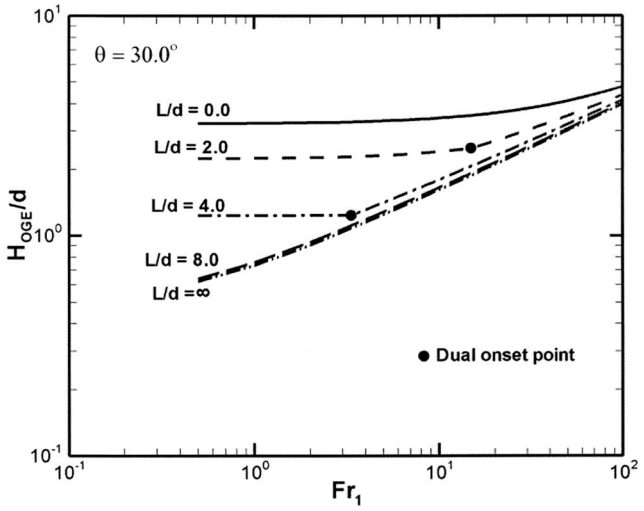

Fig. 10 Influence of L/d on H_{OGE}/d and dual onset point for Fr_2=60

Increasing L/d and θ or decreasing Fr_2 will increase the deviations between predicted and measured critical height at $Fr_1 < 10$, whereas at $Fr_1 > 10$ there is no effect of these variables on the deviations. This may be attributed to the viscous effect where increasing L/d and/or θ reduces the effect of Fr_2 and consequently the influence of the lower branch. This will result in a single branch approximation and consequently will increase the viscous effect at lower values of Fr_1 ($Fr_1 < 10$). Therefore, considering the viscous effect in the model would probably reduce the deviations between measured and predicted values of critical height especially at low values of Froude number ($Fr_1 < 10$).

The effect of L/d on H_{OGE}/d and location of the dual onset using the finite branch model is shown in Fig. 10 for Fr_2=60.0, and θ=30.0 deg. It is clear from the figure that increasing L/d decreases the H_{OGE}/d and the value of Fr_1 at the dual onset point. For L/d=8.0 a single branch is closely approximated and the onset of gas entrainment takes place only at the upper branch.

The effect of Fr_1 on the behavior of the critical height and the location of dual onset point using the finite branch model is presented in Fig. 11. It shows the variation of H_{OGE}/d against θ for various values of Fr_1 with Fr_2=60 and L/d=2.0. Based on the

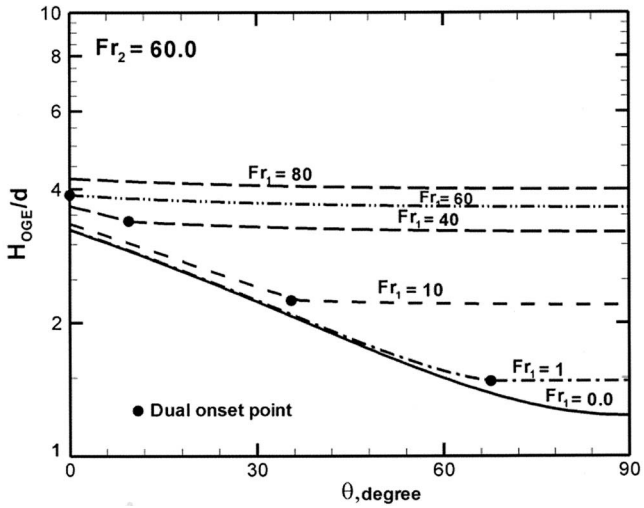

Fig. 11 Influence of Fr_1 on H_{OGE}/d and dual onset point for L/d=2.0

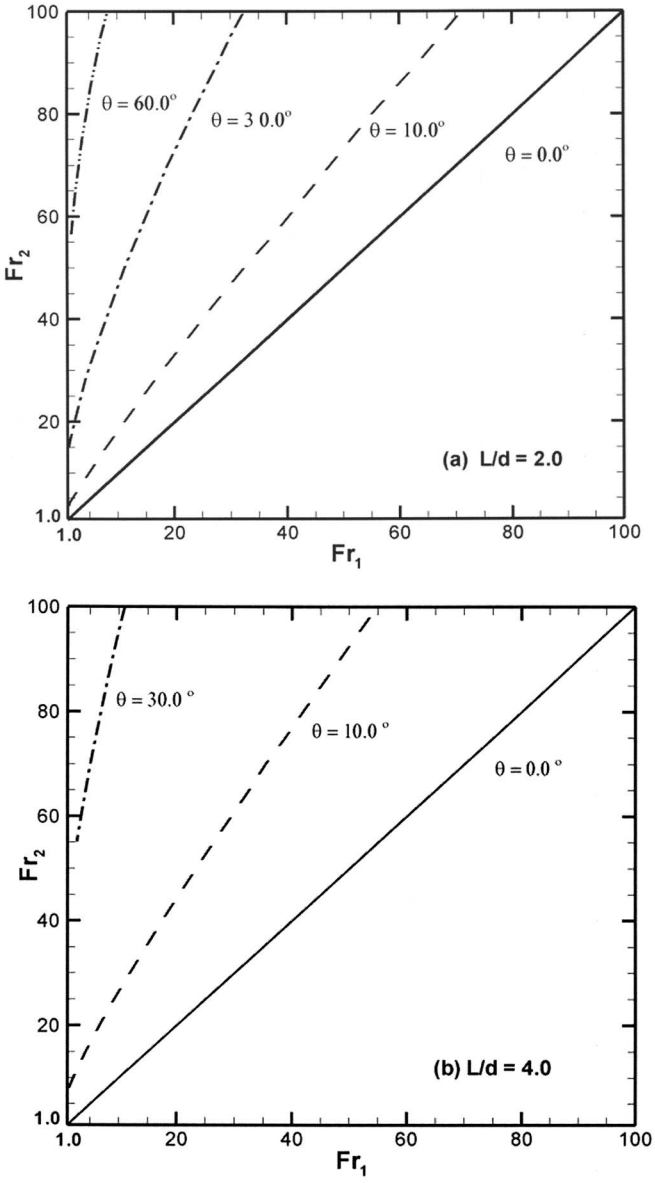

Fig. 12 Prediction of the dual onset at different vales of *L*/*d* (2 and 4)

figure, it is clear that for $Fr_1 > Fr_2$ the onset of gas entrainment occurs at the upper branch and H_{OGE}/d slightly decreases with θ. For $Fr_1 = Fr_2$, the onset of gas entrainment occurs at both branches (dual onset point) for $\theta = 0.0$. In the case of $Fr_1 < Fr_2$, the onset of gas entrainment occurs first at branch 2 up to a certain value of θ where the dual onset point occurs, beyond which entrainment shifts to branch 1. In addition, decreasing Fr_1 increases the value of θ at the dual onset point and, for $Fr_1 = 0.0$, the onset of gas entrainment occurs at the lower branch for all values of θ.

The behavior of the dual onset where $H_{OGE}/d = H_{OGE}/d|_A = H_{OGE}/d|_B$, as a function of Fr_1 and Fr_2 at different values of θ, is presented in Fig. 12(*a*) for $L/d = 2$ and in Fig. 12(*b*) for $L/d = 4.0$. It is clear based on Fig. 12(*a*) that, for $\theta = 0.0$, the dual onset occurs at $Fr_1 = Fr_2$. If $Fr_1 > Fr_2$, the onset occurs only at branch 1, whereas in the case of $Fr_1 < Fr_2$ the onset occurs only at branch 2. Furthermore, increasing the inclination angle θ results in an increase of the value of Fr_2 required for dual onset to occur. It means that at a constant value of Fr_1, the greater the angle θ, the higher the value of Fr_2 required for the dual onset to occur. By increasing L/d to 4, as shown in Fig. 12(*b*), a similar trend was obtained. Comparing Fig. 12(*a*) for $L/d = 2.0$, with Fig. 12(*b*) for $L/d = 4$, it was found that at $\theta = 0.0$, the location of the dual onset occurs at $Fr_1 = Fr_2$ and is independent of L/d. This is referred to as, at $\theta = 0.0$ deg, both branches having the same height from the interface and each branch behaving as an independent single one. Therefore, the critical height for each branch is independent of the separation distance between the two branches, whereas, for $\theta > 0.0$, increasing the distance between branches L/d leads to an increase of the value of Fr_2 for dual onset to occur. Because of an increase in the inclination angle θ, the height above branch 2 increases. Consequently, the value of Fr_2 required for the onset to occur increases. The same effect was found due to the increase of the distance between two branches L/d.

4 Conclusion

A theoretical analysis has been developed to predict the critical height and the location of the onset of gas entrainment during discharge from a stratified two-phase region through two oriented-side branches mounted on a vertical wall. In this analysis, a point sink model was first developed, followed by a more accurate three-dimensional finite branch model. The models are based on a new modified criterion for the onset of gas entrainment. The predicted critical height and the location of the onset of gas entrainment were found to be in a good agreement with the available experimental data at different values of Fr_1, Fr_2, L/d, and θ. The percentage of deviation of the experimental data from the finite branch prediction is about 12% at $Fr_1 > 10$.

Based on these models, it was found that increasing Fr_1 or/and Fr_2 increases the critical height at the onset of gas entrainment, whereas increasing the inclination angle θ and the distance between branch centerlines (L/d) decreases the critical height. Furthermore, at $\theta = 0.0$ deg, the dual onset takes place at $Fr_1 = Fr_2$ and is independent of L/d. At $\theta > 0.0°$, the dual onset occurs at $Fr_2 > Fr_1$ and is dependent on L/d. Increasing the inclination angle θ or the distance between branches L/d results in the increase of Fr_2 required for the dual onset to occur.

Nomenclature

- a = acceleration
- a^* = dimensionless acceleration
- d = branch diameter, m
- Fr_1 = Froude number of the upper branch, $(4/\pi)\dot{m}_1/\sqrt{32gr_o^5\rho_1\Delta\rho}$
- Fr_2 = Froude number of the lower branch, $(4/\pi)\dot{m}_2/\sqrt{32gr_o^5\rho_1\Delta\rho}$
- g = gravitational acceleration, m/s^2
- g^* = dimensionless gravitational acceleration, $gr_o/V_{d_1}^2 + V_{d_2}^2$
- H_{OGE} = critical height corresponding to the onset of gas entrainment, m
- H = distance between the upper branch centerline and point C as defined in Fig. 1, m
- h_A = distance between the upper branch centerline and the point A as defined in Fig. 1, m
- h_B = distance between the lower branch centerline and the point B as defined in Fig. 1, m
- h_A^*, h_B^* = dimensionless distance, $h_A^* = h_A/r_o$, $h_B^* = h_B/r_o$
- L = distance between the centerlines of the two branches, m
- L^* = dimensionless distance between the centerlines of the two branches, L/r_o
- m_1 = strength of the upper point-sink, m^3/s
- m_2 = strength of the lower point-sink, m^3/s
- $\dot{m}_1$ = mass flow rate of the upper branch, kg/s
- $\dot{m}_2$ = mass flow rate of the lower branch, kg/s

P_A = static pressure of the interface at point A, N/m^2

P_B = static pressure of the interface at point B, N/m^2

P_C = static pressure of the interface at point C, N/m^2

x, y, z = cartesian coordinate system O, as defined in Fig. 1

x^*, y^*, z^* = dimensionless variables, $(x/r_o, y/r_o, z/r_o)$

x_1, y_1, z_1 = auxiliary set of Cartesian coordinate system O_1, as defined in Fig. 1

x_1^*, y_1^*, z_1^* = dimensionless variables, $(x_1/r_o, y_1/r_o, z_1/r_o)$

r_o = branch radius, m

V_x, V_y, V_z = velocity components in x, y, and z directions, m/s

V_x^*, V_y^*, V_z^* = dimensionless velocity components in x^*, y^*, and z^* directions, $V_x/\sqrt{V_{d_1}^2+V_{d_2}^2}, V_y/\sqrt{V_{d_1}^2+V_{d_2}^2}, V_z/\sqrt{V_{d_1}^2+V_{d_2}^2}$

V_A = velocity of fluid at point A, as defined in Fig. 1

V_B = velocity of fluid at point B, as defined in Fig. 1

V_C = Velocity of fluid at point C, as defined in Fig. 1

V_{d_1} = discharge velocity of the upper branch, m/s

V_{d_2} = discharge velocity of the lower branch, m/s

$V_{d_1}^*$ = dimensionless discharge velocity of the upper branch, $V_{d_1}/\sqrt{V_{d_1}^2+V_{d_2}^2}$

$V_{d_2}^*$ = dimensionless discharge velocity of the lower branch, $V_{d_2}/\sqrt{V_{d_1}^2+V_{d_2}^2}$

I_1, I_2, I_3, I_4, I_5, and I_6 = integral functions related to the onset of upper branch

J_1, J_2, J_3, J_4, J_5, and J_6 = integral functions related to the onset of lower branch

Greek Letters

$\Delta\rho$ = density difference between two fluids, $(\rho_1-\rho_2)$, kg/m^3

ρ_1 = density of heavier fluid, kg/m^3

ρ_2 = density of lighter fluid, kg/m^3

λ, β = constants

Θ = inclination angle rotates clockwise from the positive x axis.

Φ, Φ_1, Φ_2 = potential functions, m^2/s

Φ^* = dimensionless potential function

$\Phi_{y^*}^*$ = first derivative of the dimensionless potential function with respect to y^*

$\Phi_{y^*y^*}^*$ = second derivative of the dimensionless potential function with respect to y^*

$\Phi_{x^*}^*$ = first derivative of the dimensionless potential function with respect to x^*

$\Phi_{x^*y^*}^*$ = second derivative of the dimensionless potential function with respect to x^* and y^*

References

[1] Zuber, N., 1980, "Problems in Modeling of Small Breaks LOCA," Nuclear Regulatory Commission, Report No. NUREG-0724.

[2] Smoglie, C., and Reimann, J., 1986, "Two-Phase Flow Through Small Breaks in A Horizontal Pipe with Stratified Flow," Int. J. Multiphase Flow, **12**, pp. 609–625.

[3] Yonomoto, T., and Tasaka, K., 1988, "New Theoretical Model for Two-Phase Flow Discharged from Stratified Two-Phase Region Through Small Break," J. Nucl. Sci. Technol., **25**, pp. 441–455.

[4] Yonomoto, T., and Tasaka, K., 1991, "Liquid and Gas Entrainment to a Small Break Hole From A Stratified Two-Phase Region," Int. J. Multiphase Flow, **17**, pp. 745–765.

[5] Micaelli, J. C., and Memponteil, A., 1989, "Two-Phase Flow Behaviour in a Tee-Junction—The Cathare Model," Proceedings of the Fourth International Topical Meeting on Nuclear Reactor Thermal-Hydraulics, Karlsruhe, Germany, Vol. 2, pp. 1024–1030, October 10–13.

[6] Hassan, I. G., Soliman, H. M., Sims, G. E., and Kowalski, J. E., 1998, "Two-Phase Flow From A Stratified Region Through a Small Side Branch," ASME J. Fluids Eng., **120**, pp. 605–612.

[7] Hassan, I. G., 1995, "Single, Dual and Triple Discharge from a large, Stratified, Two-Phase Region Through Small Branches," Ph.D. thesis, University of Manitoba, Winnipeg, MB.

[8] Ahmed, M., Hassan, I., and Esmail, N., 2003, "Modeling of The Onset of Gas Entrainment Through A Finite-Side Branch," ASME J. Fluids Eng., **125**, pp. 902–909.

[9] Xue, M., and Yue, D. P., 1998, "Nonlinear Free Surface Flow Due to an Impulsively Started Submerged Point Sink," J. Fluid Mech., **364**, pp. 325–347.

[10] Miloh, T., and Tyvand, P. A., 1993, "Nonlinear Transient Free Surface Flow and Dip Formation Due to Point Sink," Phys. Fluids A, **5**(6), pp. 1368–1375.

[11] Lubin, B. T. and Springer, G. S., 1966, "The Formation of a Dip on the Surface of a Liquid Draining from a Tank," J. Fluid Mech., **29**(2), pp. 385–390.

[12] Zhou, Q. N., and Graebel, W. P., 1990, "Axisymmetric Draining of a Cylindrical Tank with A Free Surface," J. Fluid Mech., **221**, pp. 511–532.

[13] Zhou, Q. N., 1989, "Numerical Solution of Nonlinear Interaction of Density Interface with a Drain," Ph.D. thesis, Department of Mechanical Engineering and Applied Science, The University of Michigan, Ann Arbor.

[14] Parrott, S. D., Soliman, H. M., Sims, G. E., and Krishnan, V. S., 1991, "Experiments on the Onset of Gas Pull-Through During Dual Discharge from a Reservoir," Int. J. Multiphase Flow, **17**, pp. 119–129.

[15] Parrott, S. D., 1993, "Experiments on The Onsets of Gas Pull-Through and Liquid Entrainment During Dual Discharge From a Large Reservoir," M.Sc. thesis, University of Manitoba, Winnipeg, MB, Canada.

[16] Hassan, I. G., Soliman, H. M., Sims, G. E., and Kowalski, J. E., 1996, "Experimental Investigation of the Two-Phase Discharge From A Stratified Region Through Two Side Branches," Exp. Therm. Fluid Sci., **13**, pp. 117–128.

[17] Maier, M. R., 1998, "Onsets of Entrainment during Dual Discharge from a Stratified Two-Phase Region through Horizontal Branches with Centerlines Falling in an Inclined Plane," M.Sc. thesis, University of Manitoba, Winnipeg, MB.

[18] Maier, M. R., Soliman, H. M., Sims, G. E., and Armstrong, K. F., 2001, "Onsets of Entrainment During Dual Discharge from a Stratified Two-Phase Region through Horizontal Branches With Centerlines Falling in an Inclined Plane: Part I—Analysis of Liquid Entrainment," Int. J. Multiphase Flow, **27**, pp. 1011–1028.

[19] Maier, M. R., Soliman, H. M., Sims, G. E., and Armstrong, K. F., 2001, "Onsets of Entrainment During Dual Discharge from a Stratified Two-Phase Region through Horizontal Branches with Centerlines Falling in an Inclined Plane: Part 2—Experiments on gas and Liquid Entrainment," Int. J. Multiphase Flow, **27**, pp. 1029–1049.

[20] Ahmed, M., Hassan, I., and Esmail, N., 2004, "The Onset of Gas Pull-Through During Dual Discharge From Stratified Two-Phase Region-Theoretical Analysis," Phys. Fluids, **16**(9), pp. 3385–3392.

[21] Schetz, J. A., and Fuhs, A. E., 1996, *Handbook of Fluid Dynamics and Fluid Machinery*, Fundamentals of Fluid Mechanics, Vol. 1, Wiley, New York.

[22] Craya, A., 1949, "Theoretical Research on the Flow of Non-Homogeneous Fluids," Houille Blanche, **4**, pp. 44–55.

[23] Soliman, H. M., and Sims, G. E., 1991, "Theoretical Analysis of the Onset of Liquid Entrainment for Slots of Finite Width," Int. J. Heat Fluid Flow, **12**, pp. 360–364.

[24] Soliman, H. M., and Sims, G. E., 1992, "Theoretical Analysis of the Onset of Liquid Entrainment for Orifices of Finite Width," Int. J. Multiphase Flow, **18**, pp. 229–235.

[25] Stroud, A. H., 1971, *Approximate Calculation of Multiple Integrals*, Prentice-Hall, Englewood Cliffs, NJ.

A Thermal Lattice Boltzmann Two-Phase Flow Model and Its Application to Heat Transfer Problems—Part 1. Theoretical Foundation

Peng Yuan
e-mail: pey1@pitt.edu

Laura Schaefer
e-mail: laschaef@engr.pitt.edu

Mechanical Engineering Department,
University of Pittsburgh,
Pittsburgh, PA, 15261

*A new and generalized lattice Boltzmann model for simulating thermal two-phase flow is described. In this model, the single component multi-phase lattice Boltzmann model proposed by Shan and Chen is used to simulate the fluid dynamics. The temperature field is simulated using the passive-scalar approach, i.e., through modeling the density field of an extra component, which evolves according to the advection-diffusion equation. By coupling the fluid dynamics and temperature field through a suitably defined body force term, the thermal two-phase lattice Boltzmann model is obtained. In this paper, the theoretical foundations of the model and the validity of the thermal lattice Boltzmann equation method are laid out, illustrated by analytical and numerical examples. In a companion paper (P. Yuan and L. Schaefer, 2006, ASME J. Fluids Eng., **128**, pp. 151–156), the numerical results of the new model are reported.* [DOI: 10.1115/1.2137343]

Keywords: lattice Boltzmann equation (LBE) method, two-phase flow, interparticle potential, passive-scalar

1 Introduction

Recently, the lattice Boltzmann equation (LBE) method has been successfully applied to simulate fluid flow and transport phenomena [1]. Unlike conventional CFD methods, the LBE method is based on microscopic models and mesoscopic kinetic equations in which the collective behavior of the particles in a system is used to simulate the continuum mechanics of the system. Due to this kinetic nature, the LBE method has been found to be particularly useful in applications involving interfacial dynamics and complex boundaries, e.g., multiphase or multicomponent flows [2].

Several lattice Boltzmann (LB) multiphase fluid models have been recently proposed. The first immiscible LB model uses red- and blue-colored particles to represent two kinds of fluids [3]. The phase separation is then produced by the repulsive interaction based on the color gradient. The model proposed by Shan and Chen (SC) imposes a nonlocal interaction between fluid particles at neighboring lattice sites [4–6]. The interaction potentials control the form of the equation of state (EOS) of the fluid. Phase separation occurs automatically when the interaction potentials are properly chosen. There is also the so-called free-energy-based approach proposed by Swift et al. [7,8]. The free energy model has a sound physical basis, and, unlike the SC model, the local momentum conservation is satisfied. However, this model does not satisfy Galilean invariance and some unphysical effects will be produced [9].

Despite the progress made by these models in simulating multiphase and multicomponent flows, there is a crucial missing part: the lack of a satisfactory thermal model for multiphase flows. The entire above-mentioned multiphase LBE models are all isothermal models. For single-phase flow, however, there are several LB thermal models, which generally fall in two categories, namely, the multispeed approach [10] and the passive-scalar approach [11]. In the passive-scalar approach, the temperature field is passively advected by the fluid flow and can be simulated as an additional component of the fluid system. This means in order to solve for the temperature field in the multiphase isothermal LBE framework, one only needs to solve an auxiliary LBE. Thus, the overall complexity of the scheme does not significantly increase. Additionally, the passive-scalar approach does not implement energy conservation and therefore has the same stability as the isothermal LBE models.

This paper addresses the multiphase isothermal LBE model as well as the single phase thermal LBE (TLBE) model using the passive-scalar approach. First, the LBE method will be briefly described, with the simulation results of a 2-D lid-driven square cavity flow presented to validate the code. Then, the multiphase LBE model and passive-scalar approach will be introduced, respectively, together with some test problem results to assess the actual ability of these techniques for practical applications. Finally, in the companion paper [12], by combining these two models, the thermal two-phase LBE model will be proposed and numerical results for this model will be reported.

2 Lattice Boltzmann Equation Method

The standard LBE with the Bhatnagar-Gross-Krook approximation (often referred to as the LBGK) model can be written as

$$f_\alpha(\mathbf{x}+\mathbf{e}_\alpha\delta t, t+\delta t) = f_\alpha(\mathbf{x},t) - \frac{1}{\tau}[f_\alpha(\mathbf{x},t) - f_\alpha^{eq}(\mathbf{x},t)],$$

$$\alpha = 0,1,\ldots,N, \tag{1}$$

where $\mathbf{x}$ denotes the position in space, t is time, δt is the time step, f_α is the particle distribution function (PDF) along the αth direction and f_α^{eq} is its corresponding equilibrium particle distribution function, $\mathbf{e}_\alpha$ is the particle velocity in the αth direction, and τ is the single relaxation time. N is the number of discrete particle velocities.

Contributed by the Fluids Engineering Division of ASME for publication in the JOURNAL OF FLUIDS ENGINEERING. Manuscript received December 18, 2004; final manuscript received August 10, 2005. Assoc. Editor: Malcolm J. Andrews.

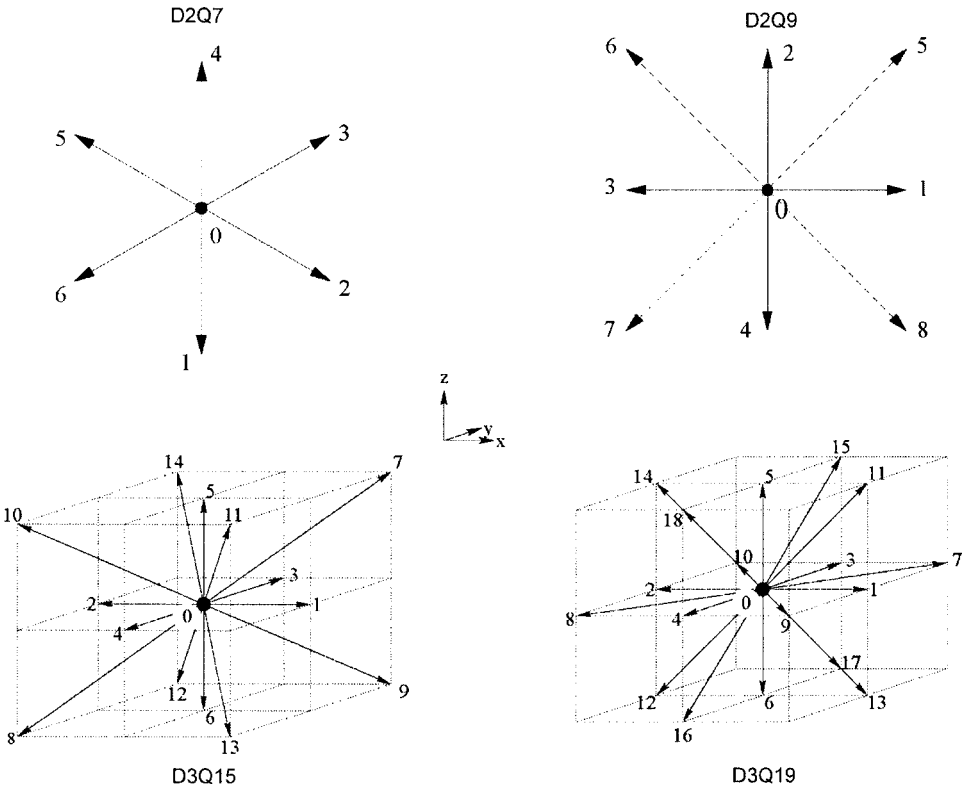

Fig. 1 Discrete velocity vectors for some commonly used 2-D and 3-D particle speed models

For 2-D flow, the nine-velocity LBE model on the 2-D square lattice, denoted as the D2Q9 model, has been widely used. For simulating 3-D flow, there are several cubic lattice models, such as the D3Q15, D3Q19, and D3Q27 models. Figure 1 presents the most common lattices.

The equilibrium distribution for all of the D2Q9, D3Q15, D3Q19, and D3Q27 models can be expressed in the form

$$f_\alpha^{eq} = \rho w_\alpha \left(1 + \frac{3}{c^2}\mathbf{e}_\alpha \cdot \mathbf{u} + \frac{9}{2c^4}(\mathbf{e}_\alpha \cdot \mathbf{u})^2 - \frac{3}{2c^2}\mathbf{u} \cdot \mathbf{u} \right) \tag{2}$$

where w_α is the weighting factor, $c = \delta x / \delta t$ is the lattice speed, δx is the lattice constant, and $\mathbf{u}$ is the macroscopic velocity.

In this paper, we use D2Q9 and D3Q19 for the 2-D and 3-D simulations, respectively. The weighting factor and discrete velocity for these two models are given below.

D2Q9:

$$\mathbf{e}_\alpha = \begin{cases} (0,0), & \alpha = 0; \\ (\pm 1,0)c, (0,\pm 1)c, & \alpha = 1,2,3,4; \\ (\pm 1,\pm 1)c, & \alpha = 5,6,7,8. \end{cases} \tag{3a}$$

$$w_\alpha = \begin{cases} \frac{4}{9}, & \alpha = 0; \\ \frac{1}{9}, & \alpha = 1,2,3,4; \\ \frac{1}{36}, & \alpha = 5,6,7,8. \end{cases} \tag{3b}$$

D3Q19:

$$\mathbf{e}_\alpha = \begin{cases} (0,0,0), & \alpha = 0; \\ (\pm 1,0,0)c, (0,\pm 1,0)c, (0,0,\pm 1)c, & \alpha = 1,2,\ldots,6; \\ (\pm 1,\pm 1,0)c, (\pm 1,0,\pm 1)c, (0,\pm 1,\pm 1)c, & \alpha = 7,8,\ldots,18. \end{cases} \tag{4a}$$

$$w_\alpha = \begin{cases} \frac{1}{3}, & \alpha = 0; \\ \frac{1}{18}, & \alpha = 1,2,\ldots,6; \\ \frac{1}{36}, & \alpha = 7,8,\ldots,18. \end{cases} \tag{4b}$$

In most LBE simulations, Eq. (1) is solved in two steps: collision and streaming. In the collision step, the PDFs for each direction are relaxed toward quasi-equilibrium distributions. Then, at the streaming step, the distributions move to the neighboring nodes. The local mass density ρ and the local momentum density $\rho\mathbf{u}$ are given by

$$\rho = \sum_{\alpha=0}^{N} f_\alpha = \sum_{\alpha=0}^{N} f_\alpha^{eq} \tag{5a}$$

$$\rho\mathbf{u} = \sum_{\alpha=0}^{N} f_\alpha \mathbf{e}_\alpha = \sum_{\alpha=0}^{N} f_\alpha^{eq} \mathbf{e}_\alpha \tag{5b}$$

It can be shown that the above formulation of the LBE recovers the Navier-Stokes (N-S) equations for fluid flows near the incompressible limit (low Mach number) [13]. The viscosity in the N-S equations derived from Eq. (1) is

$$\nu = \left(\tau - \tfrac{1}{2}\right) c_s^2 \delta t \tag{6}$$

where c_s is the lattice sound speed. This option of the viscosity makes the LBGK scheme a second-order method for solving incompressible flow [14].

How to correctly implement boundary conditions is an important issue in LB simulations, since they will influence the accuracy and stability of the computation. The most common and simplest boundary condition is the bounce-back boundary condition. In this boundary condition, when a particle distribution streams to a wall node, it scatters back to the fluid node along its incoming link. However, the bounce-back boundary condition only gives

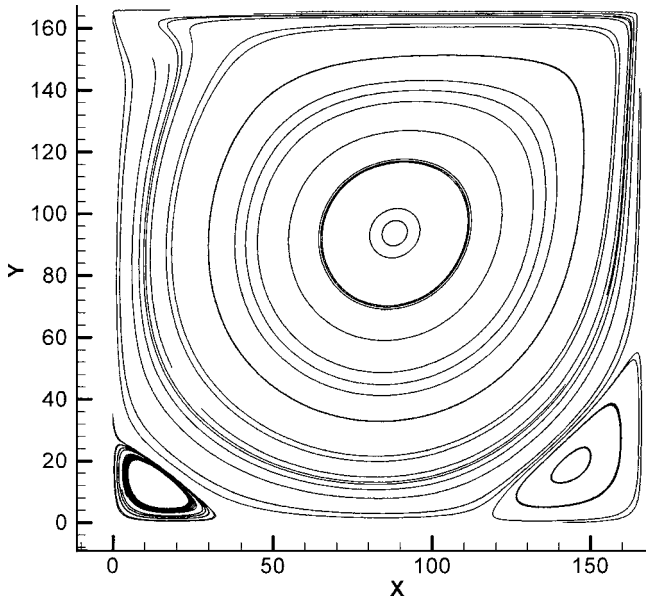

Fig. 2 Streamlines of 2-D lid-driven cavity flow at Re=10³

first-order numerical accuracy. To improve it, many boundary conditions have been proposed in the past [15,16]. Among them, the halfway bounce-back scheme [17] is easy to implement and gives second-order accuracy for straight walls. The boundary condition proposed by Mei [18] has the ability of handling complex geometry, e.g., a curved boundary. In this work, we employed these two boundary treatments in our simulations.

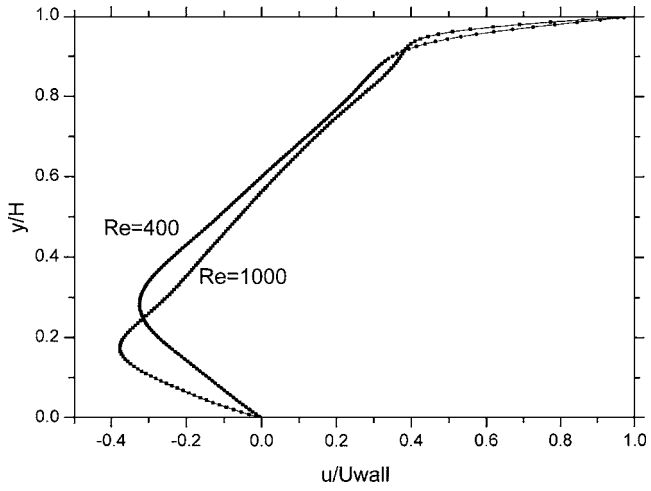

Fig. 3 Velocity profiles for *u* along the vertical geometric centerline of the cavity

3 Single Component Single Phase LBE Model

To validate the code, numerical simulations were carried out for a 2-D lid-driven cavity flow for Re=400 and 1000 on a 167 $\times$ 167 lattice, which gives grid independent results. Furthermore, for every problem presented in this paper, grid independency was checked by conducting simulations on different grid resolutions. The driving lid is placed at the top with a uniform velocity of $Uwall=0.1$ in lattice units. Figure 2 shows the streamlines for Re=1000. The flow structure is in good agreement with the previous work. Figure 3 shows the velocity component **u** at the vertical centerline ($x/H=1/2$) of the cavity.

To quantify the results, the maximum and minimum values of the stream functions and x and y coordinates of the primary and secondary vortex centers are listed in Table 1. The results predicted by the LBE method agree well with other previous work [19].

4 Single Component Multiphase LBE Model

Microscopically, the segregation of a fluid system into different phases is due to the interparticle forces. In the single component multiphase LBE model proposed by Shan and Chen, a simple interaction potential is defined to describe the fluid/fluid interaction. Then the model incorporates the forcing due to the potential by shifting the velocity in the equilibrium distribution. The fluid/fluid interaction force is defined as [20]

$$\mathbf{F}_1(\mathbf{x}) = -\psi(\mathbf{x})\sum_{\mathbf{x}'} G(\mathbf{x},\mathbf{x}')\psi(\mathbf{x}')(\mathbf{x}'-\mathbf{x}) \tag{7}$$

where $\mathbf{x}$ and $\mathbf{x}'$ denote position (site) in space and $G(\mathbf{x},\mathbf{x}')$ is Green's function and satisfies $G(\mathbf{x},\mathbf{x}')=G(\mathbf{x}',\mathbf{x})$. It reflects the intensity of the interaction, with $G(\mathbf{x},\mathbf{x}')<0$ representing attractive forces between particles. In our study, the interactions of nearest and next-nearest neighbors are considered. For a D3Q19 lattice model, this leads to

$$G(\mathbf{x},\mathbf{x}') = \begin{cases} g_f, & |\mathbf{x}-\mathbf{x}'|=1; \\ g_f/2, & |\mathbf{x}-\mathbf{x}'|=\sqrt{2}; \\ 0, & \text{otherwise}. \end{cases} \tag{8}$$

$\psi(\mathbf{x})$ is called the "effective mass" and is defined as a function of the local density. In the SC model, the function of $\psi(\mathbf{x})$ can be varied, and different choices will give a different EOS. Using the Chapmen-Enskog method of successive approximation, one can obtain the macroscopic fluid equation of the LBE model. Meanwhile, the EOS is also obtained as $p=c_s^2\rho+c_0 g_f[\psi(\mathbf{x})]^2$, where c_0 is a constant and equals 3.0 for the D2Q9 and D3Q19 models.

In this study, $\psi(\mathbf{x})$ is taken to be $\psi(\mathbf{x})=\rho_0[1-\exp(-\rho/\rho_0)]$, which gives a nonmonotonic pressure-density relationship. Hence for a certain range of g_f values, at a single pressure, two densities of the same material can coexist. Here, we can say the intensity of the fluid/fluid interaction g_f takes the role of a pseudo-temperature. For example, when g_f falls below a critical value, phase separation will occur.

Table 1 Vortex centers: stream function and location

		Primary vortex			Lower left vortex			Lower right vortex		
Re	Mesh=167 $\times$ 167	φ_{max}	x	y	φ_{min}	x	y	φ_{min}	x	y
400	U. Ghia	0.1139	0.5547	0.6055	−1.42E−05	0.0508	0.0469	−6.42E−04	0.8906	0.1250
	S. Hou	0.1121	0.5608	0.6078	−1.30E−05	0.0549	0.0510	−6.19E−04	0.8902	0.1255
	Present work	0.1120	0.5551	0.6054	−1.28E−05	0.0505	0.0463	−6.15E−04	0.8858	0.1222
1000	U. Ghia	0.1179	0.5313	0.5625	−2.31E−04	0.0859	0.0781	−1.75E−03	0.8594	0.1094
	S. Hou	0.1178	0.5333	0.5647	−2.22E−04	0.0902	0.0784	−1.69E−03	0.8667	0.1137
	Present work	0.1161	0.5319	0.5652	−2.13E−04	0.0821	0.0769	−1.66E−03	0.8652	0.1125

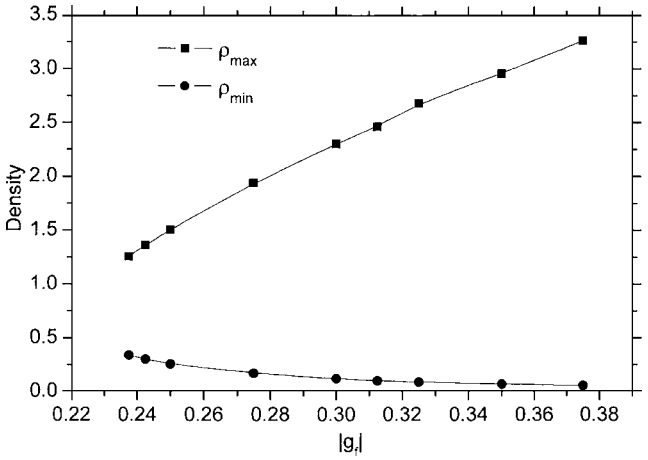

Fig. 4 Maximum and minimum density values as a function of $|g_f|$

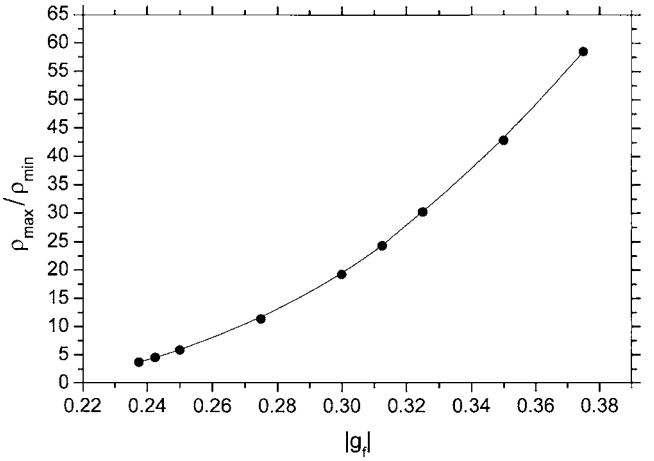

Fig. 5 Density ratio as a function of $|g_f|$

At the fluid/solid interface, similarly, a force between fluid particles and solid surfaces can be introduced into the SC model as follows [21]:

$$\mathbf{F}_2(\mathbf{x}) = -\rho(\mathbf{x})\sum_{\mathbf{x}'} G_w(\mathbf{x},\mathbf{x}')\rho_w(\mathbf{x}')(\mathbf{x}'-\mathbf{x}) \tag{9}$$

where $G_w(\mathbf{x},\mathbf{x}')$ reflects the intensity of the fluid/solid interaction and has the same form as $G(\mathbf{x},\mathbf{x}')$. For the D3Q19 lattice model,

$$G_w(\mathbf{x},\mathbf{x}') = \begin{cases} g_w, & |\mathbf{x}-\mathbf{x}'| = 1; \\ g_w/2, & |\mathbf{x}-\mathbf{x}'| = \sqrt{2}; \\ 0, & \text{otherwise}. \end{cases} \tag{10}$$

g_w controls the strength between fluid and the wall. g_w is positive for a nonwetting fluid and negative for a wetting fluid. Adjusting the value of g_w can give a different wettability. $\rho_w(\mathbf{x}')$ is the wall density, which equals one at the wall and zero in the fluid.

Constant body forces such as gravity can be expressed as

$$\mathbf{F}_3 = \rho(\mathbf{x})\mathbf{a} \tag{11}$$

where $\mathbf{a}$ is the acceleration due to the body force.

All of these forces can be incorporated into the model by shifting the velocity in the equilibrium distribution. That means the velocity $\mathbf{u}$ in Eq. (2) is replaced with

$$\mathbf{u}^{eq} = \mathbf{u} + \frac{\tau\mathbf{F}_{total}}{\rho(\mathbf{x})} \tag{12}$$

where $\mathbf{F}_{total}=\mathbf{F}_1+\mathbf{F}_2+\mathbf{F}_3$.

Then, by averaging the moment before and after the collision, the whole fluid velocity $\mathbf{U}$ is

$$\rho(\mathbf{x})\mathbf{U} = \rho(\mathbf{x})\mathbf{u} + \tfrac{1}{2}\mathbf{F}_{total} \tag{13}$$

There are also other approaches for incorporating fluid/fluid interactions such as the direct body forcing approach, where the interaction is incorporated into the body force term of the Boltzmann equation by adding an additional term after the collision process [22,23].

To validate and illustrate the outcomes of this model, we now present some results of simulations for a 3-D single component system. First, we observe the transitions from a single-phase fluid to a two-phase fluid. Initially, the density is evenly distributed on a $50\times50\times50$ lattice with a small random perturbation. Periodical boundary conditions are applied in all three coordinate directions. Figure 4 shows the maximum and minimum densities as functions of $|g_f|$, with $g_f<0$ for the attraction between particles. When the fluid/fluid interaction strength g_f decreases under some critical value g_f^c, the system separates from the single-phase to a heavier/liquid phase and a lighter/vapor phase. Figure 5 is a plot of the density ratio changing with $|g_f|$.

After finding the relation between the density ratio and the interaction strength g_f, we conducted some static bubble tests. Again, the $50\times50\times50$ lattice and periodical BCs are used in all of the tests [24]. Initially, a droplet is placed at the center of the domain with a radius of $r_{init}=10.0$. To ensure that the droplet's size will not expand or shrink too much, we specify that the initial density inside/outside the droplet is close to the maximum/minimum density obtained in the bifurcation test under the same g_f value. Otherwise, the droplet's radius is not controllable and the droplet may sometimes even expand to the boundaries. The droplet's radius oscillates for the first 800 time steps and then goes to a constant value. Each test was run for 10,000 time steps. At that point, the relative differences of the maximum magnitudes of the velocities at time step t and $t-1000$ are on the order of 10^{-6}, which means that steady state is reached. For $g_f=-0.35$, the density and velocity fields in the xy plane at the midpoint of $z=25$ are plotted in Figs. 6 and 7, respectively. Other g_f values will give similar results.

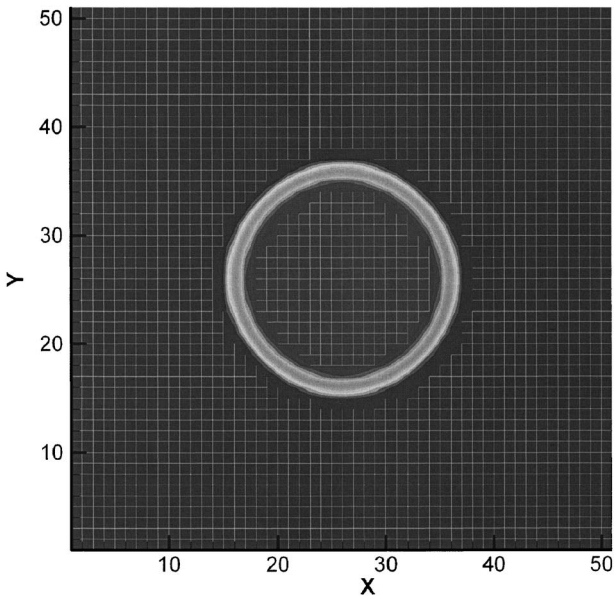

Fig. 6 Density contours plot in the *xy* plane at *z*=25 (symmetry plane)

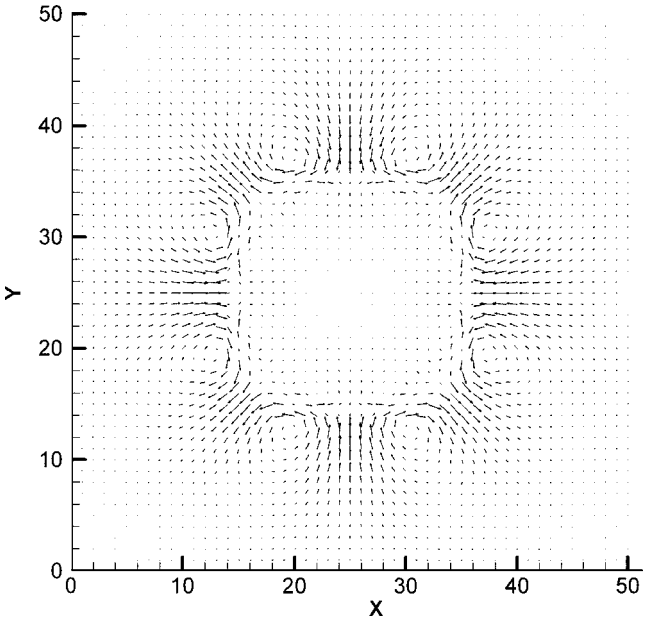

Fig. 7 Velocity vectors plot in the *xy* plane at *z*=25 (symmetry plane)

The nonzero velocity vectors in Fig. 7 indicate the deviation from the real physical situation. These unphysical velocities are called spurious currents and reach their maximum value at the interface region. The maximum magnitude of spurious currents as a function of $|g_f|$ is shown in Fig. 8. The maximum magnitude of the spurious currents increases slowly before $|g_f|$ reaches 0.32 (the corresponding density ratio is around 30), and after that it grows rapidly. For $|g_f|=0.3125$, its value is 0.015 29, while for $|g_f|=0.35$, the value is 0.051 41. We know that the LBE method is valid only in the incompressible limit $|\mathbf{u}|/c_s \to 0$, which requires that $|\mathbf{u}|$ is smaller than 0.13. So, in our later simulations, we restrict $|g_f| \leqslant 0.35$, corresponding to a highest density ratio of 42, which is adequate for many liquid-vapor systems. It is not suitable for a system with a density ratio higher than 100. However, by changing the EOS, we can greatly reduce the spurious currents. We defer this discussion to a future publication.

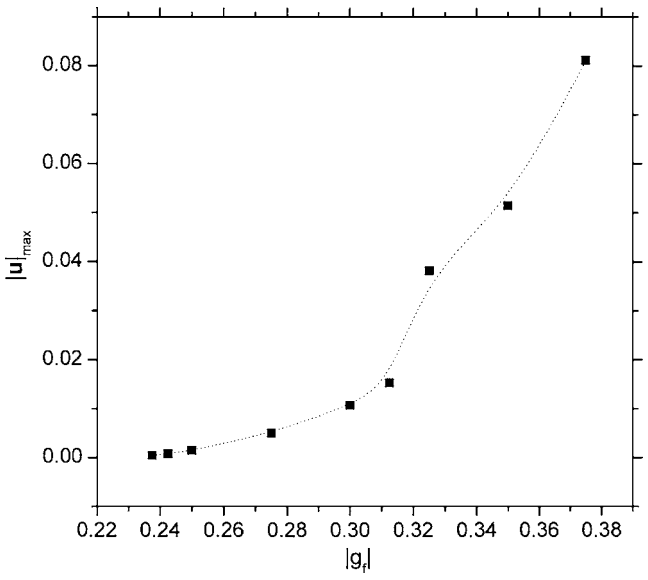

Fig. 8 The maximum magnitude of spurious currents changes with $|g_f|$

We also conducted some static droplet tests with a solid wall interaction by replacing the periodical BCs in the y and z directions with wall BCs. Similar density and velocity fields were obtained and the spurious currents did not increase.

The static contact angle can be adjusted in LB simulations by changing the value or form of $G_w(\mathbf{x},\mathbf{x}')$ or even by changing the form of Eq. (9); say, e.g., by changing the density term in Eq. (9) to some function of local density. In this way, we can easily control the wettability.

In our simulations, initially a half liquid drop of radius 10.0 is placed at the bottom of the solid wall with its center at the geometric center of the bottom wall. The lattice size is $50\times50\times50$ with periodical BCs in the x direction and wall BCs in the y and z directions.

Figure 9 shows two contact angles obtained by adjusting g_w. Figure 10 gives the corresponding velocity fields. The maximum spurious current stays at the same level as in the static bubble test.

Figure 11 plots the contact angle varying with g_w, which is almost a linear relation. This is in agreement with the work of other researchers [25].

For large g_w values ($g_w > 0.08$), after the half liquid drop is placed on the bottom, because of the large interaction between the fluid and solid, the liquid phase contacting with the solid will shrink very fast and will generate some unphysical phenomena. In this case, g_w must be increased step by step until a stable contact angle is obtained.

We also conducted simulations for a different form of Eq. (9). For example, instead of using $\rho(\mathbf{x})$, we used the "effective mass," i.e., $\psi(\mathbf{x})=\rho_0[1-\exp(-\rho/\rho_0)]$. For this case, the linear relation between the contact angle θ and the fluid/solid interaction strength g_w is still obtained. However, the slope will change. For the effective mass case, the slope is smaller than using local density directly. Also, different values of g_w for the liquid and vapor phases can be used. If these values are properly specified, the linear relation between contact angle θ and the liquid/solid interaction strength g_w^l will again be obtained (in this case, vapor/solid interaction strength g_w^v is fixed).

One necessary point with respect to these results is that although any static contact angle can be obtained, there is no guarantee that the fluid dynamics near the contact line are correctly simulated [23]. The details of the fluid/solid interaction are not fully understood and need future research.

5 Thermal LBE Model Using the Passive-Scalar Approach

In spite of the success achieved in isothermal flow simulations, the progress in thermal flow simulations is rather limited. Generally, the existing TLBE models fall into two categories, namely, the multispeed approach and the passive-scalar approach. The multispeed approach implements energy conservation by adding additional speeds and by including the higher-velocity terms in the equilibrium distribution. Although theoretically possible, the multispeed approach suffers severe numerical instability [26,27]. Another limitation for the multispeed approach is that the Prandtl number is fixed (at 0.5) for the simulation [10]. However, if the viscous and compressive heating effects are negligible, the temperature field satisfies a much simpler passive-scalar equation, which can be simulated by solving an additional LBE.

The fluid dynamics can be solved as before by using Eqs. (1) and (2). The temperature field satisfies the following passive-scalar equation:

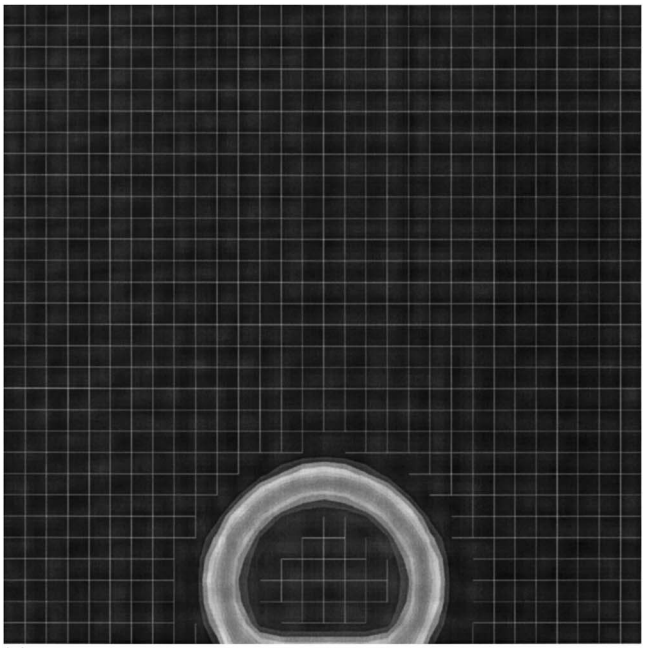

(*a*)

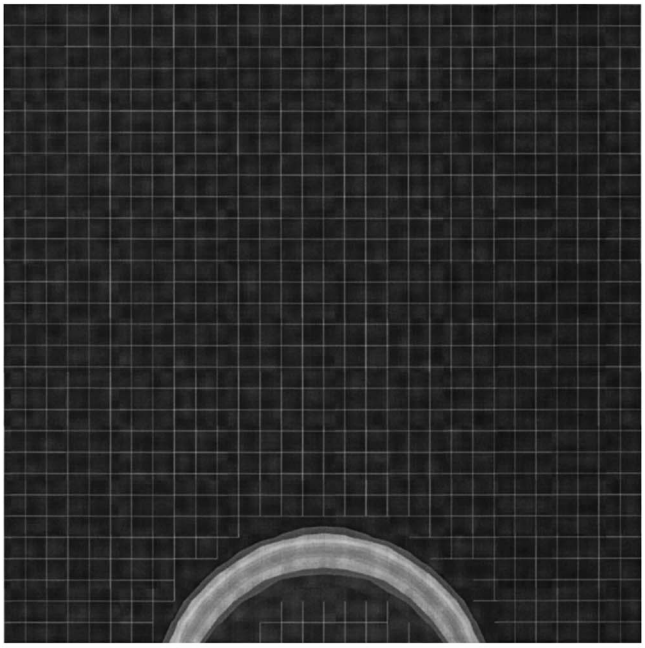

(*b*)

Fig. 9 Density contours for different values of g_w (different wettabilities): (*a*) g_w=0.06, θ=120.6° and (*b*) g_w=−0.03, θ=71.3°

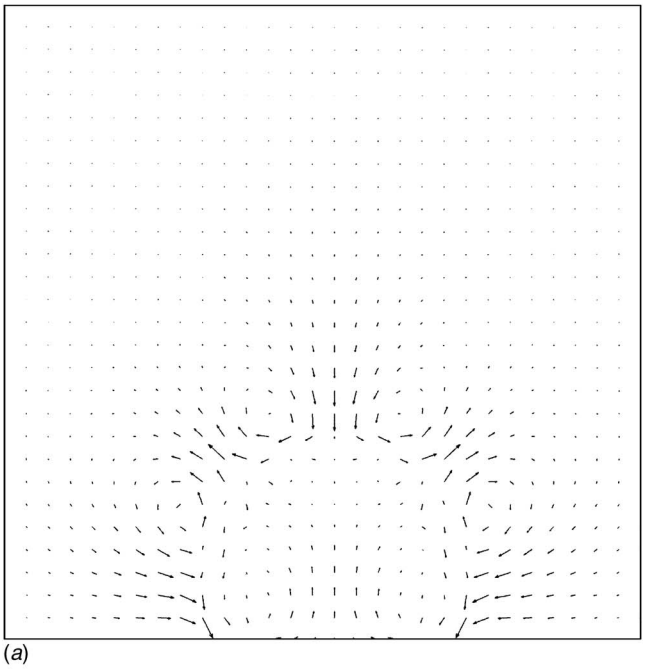

(*a*)

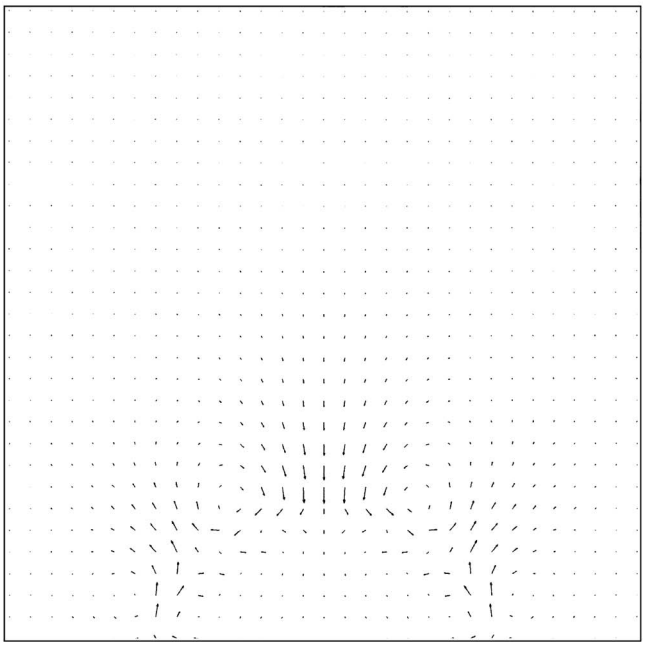

(*b*)

Fig. 10 Velocity fields for different values of g_w: (*a*) g_w=0.06 and (*b*) g_w=−0.03

$$\frac{\partial T}{\partial t} + \mathbf{u} \cdot \nabla T = \nabla \cdot (\alpha \nabla T) + \Psi \tag{14}$$

where $\mathbf{u}$ is the whole fluid velocity, α is the thermal diffusivity, and Ψ is the source term.

Equation (14) can be solved in the LB framework by also using Eqs. (1) and (2), except that τ will be replaced by τ_T (the dimensionless single relaxation time for temperature) and the summation of PDFs will give the temperature value.

As before, $\alpha=(\tau_T-\frac{1}{2})c_s^2\delta t$ and thus the Prandtl number will be

$$\mathrm{Pr} = \frac{\nu}{\alpha} = \frac{2\tau - 1}{2\tau_T - 1} \tag{15}$$

By changing τ and/or τ_T, we can generate a different Prandtl number.

Two different thermal BCs were tested in our simulations. Here we explain them in the context of a D2Q9 model.

(i) Isothermal wall: Suppose the temperature is fixed as T_B at the bottom wall. After streaming, f_2, f_5, and f_6 are unknowns. Assume these unknown PDFs equal their equilibrium distribution given by Eq. (2) with ρ replaced by some unknown temperature T'. Summing these three PDFs together, we have [28]

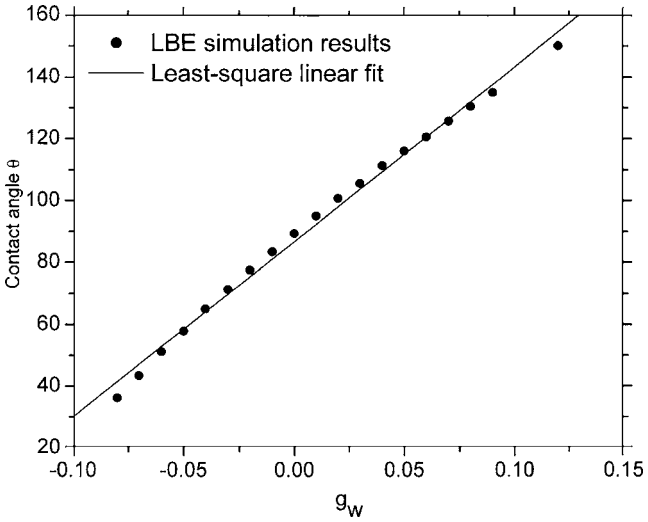

Fig. 11 The relation between the contact angle θ of the bubble and the fluid/solid interaction strength g_w

$$f_2 + f_5 + f_6 = \tfrac{1}{6}T'(1 + 3u_y + 3u_y^2) \tag{16}$$

where u_y is the velocity normal to the wall. If we know T', we will be able to solve for f_2, f_5, and f_6. Meanwhile, we notice that for the isothermal wall, $\Sigma_{\alpha=0}^{8} f = T_B$. Substituting Eq. (16) into this, T' then can be calculated as follows:

$$T' = \frac{6}{1 + 3u_y + 3u_y^2}(T_B - f_0 - f_1 - f_3 - f_4 - f_7 - f_8) \tag{17}$$

Finally, f_2, f_5, and f_6 can be obtained by substituting T' into Eq. (2). This method can be easily extended to the 3-D case.

(ii) Heat flux BC: After streaming, the temperature of the inner domain can be obtained. A second-order finite difference scheme is used to get the temperature on the wall [29], i.e., for the bottom wall at $y=0$, $\partial T/\partial y|_{i,1} = (4T_{i,2} - T_{i,3} - 3T_{i,1})/2\Delta y$. After finding the wall temperature, the same procedure as described in the isothermal wall case is used to calculate the unknown PDFs.

A good benchmark test for a thermal fluid system is Rayleigh-Bénard convection (RBC), where a horizontal layer of viscous fluid is heated from the bottom and the top boundary is maintained at a lower temperature [30]. When the temperature difference between the bottom and top boundaries exceeds some threshold, the static conduction becomes unstable. Any small perturbation will make the system become convective.

We simulated 2-D and 3-D RBC by using the D2Q9 and D3Q19 models, respectively. In the 2-D simulation, the temperatures at the bottom wall ($y=0$) and top wall ($y=1$) are kept at $T_B=1$ and $T_T=0$, respectively. So, $\Delta T = T_B - T_T = 1$. A lattice size of 101×50 is used in the simulation. The two nondimensional terms used to describe the system are the Prandtl number and the Rayleigh number. The Prandtl number is defined in Eq. (15). The Rayleigh number is defined as

$$\mathrm{Ra} = \frac{g\beta\Delta T N_y^3}{\nu\alpha} \tag{18}$$

where g is the acceleration due to gravity, β is the thermal expansion coefficient, and N_y is the lattice size in the y direction.

The Boussinesq approximation is used, which assumes that the material properties are independent of temperature except in the body force term. For the gravitational term, the density is assumed to be a linear function of the temperature. In the LBE method, a fluid is always compressible. By introducing gravity we inevitably introduce a compressibility error into the system. In order to eliminate this compressible effect, the part of the gravity force

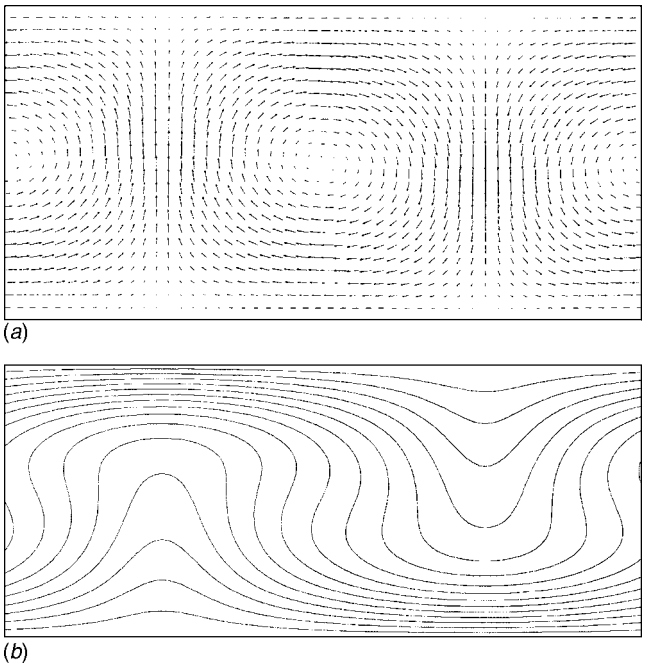

Fig. 12 Velocity vectors and isotherms at Ra=5000 and Pr =1.0: (*a*) velocity vectors and (*b*) isotherms

which corresponds to the buoyancy force in the static conduction state is absorbed in the pressure term, which leads to the following expression of the external force:

$$\rho\mathbf{G} = \rho\beta g(T - T^*)\mathbf{j} \tag{19}$$

where $T^* = T_B - y\Delta T$. This body force can be incorporated into the simulation by using the method given in Sec. 4 (the so-called shifting equilibrium velocity method) or by adding an additional term after the collision process.

We calculated the RBC at different Ra and Pr numbers. Figure 12 plots the typical velocity vectors and isotherms at Ra=5000 and Pr=1.0.

In order to evaluate the accuracy of the method, the onset of RBC was also tested. The simulation was conducted at different Ra numbers around the critical Ra number Ra_c, and then the growth rate (rate of increase of the maximum velocity in the y direction) was measured. The results are shown in Fig. 13, in which the growth rates are plotted against the Ra number. The zero growth rate corresponds to the critical Ra number. Using a

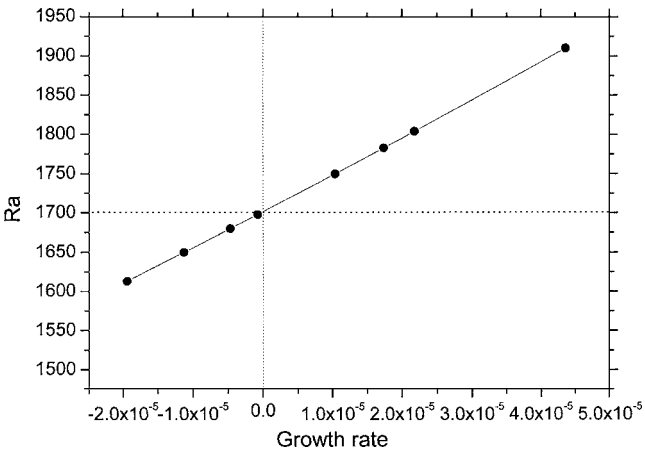

Fig. 13 Growth rate of instability vs Ra number

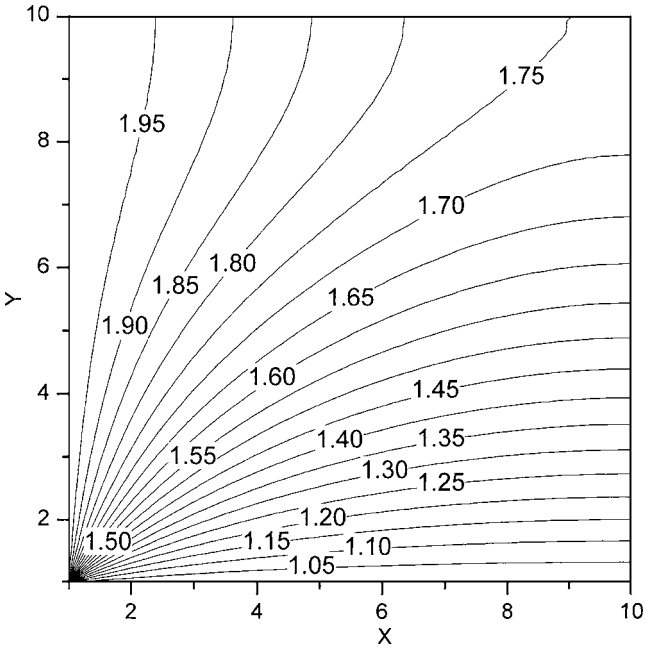

Fig. 14 Isotherms at steady state obtained by the LBE method

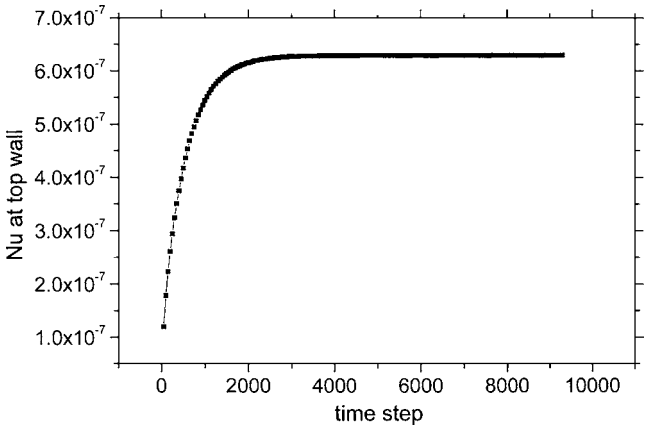

Fig. 15 Nusselt number at the top wall with respect to the time step obtained by the LBE method

least squares fit, the critical Ra number is found to be 1702.436, which agrees well with the theoretical value of 1707.762 obtained by linear stability theory. The relative error is 0.3119%.

Another useful test for code validation is a 2-D heat conduction problem with heat generation inside the domain. A square domain (length $L=1.0$, height $H=1.0$) with an adiabatic BC at the top and right walls, a uniform temperature $T_L=2.0$ at the left wall, and a uniform temperature $T_B=1.0$ at the bottom wall are calculated in a 50×50 mesh. Additionally, there is heat generation q''' inside the domain. Initially, the domain has a uniform temperature of 2.0.

To represent heat generation properly in the LB context, we compare the nondimensional heat generation in a real problem and in the LBE method. These two values should equal. This means that

$$q^* = \frac{q'''L^2}{kT_0} = \frac{q'''_{Lu}L^2_{Lu}}{k_{Lu}T_{0,Lu}} = \frac{q'''_{Lu}L^2_{Lu}}{\alpha_{Lu}\rho_{Lu}c_{V,Lu}T_{0,Lu}} \tag{20}$$

where the subscript "*Lu*" denotes a lattice unit, T_0 is some reference temperature, and k is the thermal conductivity. In the LBE method, we only specify the thermal diffusivity α. Hence ρ_{Lu} and $c_{V,\mathrm{Lu}}$ are set to be unity. Then

$$q'''_{Lu} = \frac{q^*\alpha_{Lu}T_{0,Lu}}{L^2_{Lu}} \tag{21}$$

Similarly, the time step in the LBE method can be related to the physical time through

$$t^* = \frac{\alpha t}{L^2} = \frac{\alpha_{Lu}t_{Lu}}{L^2_{Lu}} \tag{22}$$

For comparison, the finite difference (FD) method is also used to evaluate the same problem. Using the same grid resolution, the average error is $E\approx 8.4\times 10^{-4}$, where E is defined by

$$E = \frac{\sqrt{\sum_x\sum_y[T_{LBE}(x,y)-T_{FD}(x,y)]^2}}{\sqrt{\sum_x\sum_y T^2_{FD}(x,y)}} \tag{23}$$

Figure 14 shows the isotherms at the steady state obtained by the LBE method. Figure 15 shows the Nusselt number at the top wall (adiabatic wall) with respect to the time step in the LBE simulation, which is a very small value. This test shows that the heat flux BC and heat source term are properly incorporated in the LBE method. Furthermore, the heat source term can be related to the viscous and compressive heating terms, which will greatly extend the scope of the method.

6 Discussion

We have demonstrated the applicability of the LBE method in simulating multiphase flow and thermal flow systems. The single component multiphase LBE model has the ability to simulate phase separation, variable wettability, and different EOS as well as complex BCs. Additionally, the simulation results of the thermal system using the passive-scalar TLBE model are in good agreement with established analytical or numerical results. Combining these two models, in Part 2 [12] we will propose a thermal two-phase LBE model with the fluid dynamics simulated by an isothermal single component multiphase LBE, and the temperature field determined by an additional passive-scalar equation. The coupling of these two parts is through a suitably defined body force term in the isothermal LBE.

Acknowledgment

This work has been supported by NSF Grant No. CTS-0238841. The authors also thank Dr. Qinjun Kang at Los Alamos National Laboratory for helpful discussions.

Nomenclature

$\mathbf{a}$ = acceleration
c = lattice speed
c_s = lattice sound speed
c_V = specific heat capacity
$\mathbf{e}_\alpha$ = lattice particle's speed
f_α = particle distribution function
f^{eq}_α = equilibrium particle distribution function
$\mathbf{F}$ = force per unit mass
g = gravitational constant
g_f = intensity of fluid/fluid interaction
g_w = intensity of fluid/solid interaction
$\mathbf{G}$ = buoyancy force per unit mass
$G(\mathbf{x},\mathbf{x}')$ = Green's function (related to the fluid/fluid interaction potential)
$G_w(\mathbf{x},\mathbf{x}')$ = Green's function (related to the fluid/solid interaction potential)
H = height of the domain
k = thermal conductivity
L = length of the domain
N_y, N_z = lattice size in the y and z directions

q''' = heat generation per volume
q^* = nondimensional heat
t = time
t^* = nondimensional time
T = temperature
T^* = reference temperature
$\mathbf{u}, \mathbf{U}$ = fluid velocity
$\mathbf{u}^{eq}$ = equilibrium velocity
U' = characteristic velocity
w_α = weight coefficients
$\mathbf{x}, \mathbf{x}'$ = position
α = thermal diffusivity
β = thermal expansion coefficient
ΔT = temperature difference
ρ = density
ρ_w = wall density
ν = kinematic viscosity
τ = relaxation time
τ_T = relaxation time for temperature field
ψ = effective mass
Ψ = heat source term

References

[1] Chen, S., and Doolen, G. D., 1998, "Lattice Boltzmann Method for Fluid Flows," Annu. Rev. Fluid Mech., **30**, pp. 329–364.
[2] Yu, D., Mei, R., Luo, L., and Shyy, W., 2003, "Viscous Flow Comutations With the Method of Lattice Boltzmann Equation," Prog. Aerosp. Sci., **39**, pp. 329–367.
[3] Chen, S., Chen, H., Martinez, D., and Matthaeus, W., 1991, "Lattice Boltzmann Model for Simulation of Magnetohydrodynamics," Phys. Rev. Lett., **67**, pp. 3776–3779.
[4] Shan, X., and Chen, H., 1993, "Lattice Boltzmann Model for Simulation Flows With Multiple Phases and Components," Phys. Rev. E, **47**, pp. 1815–1819.
[5] Shan, X., and Chen, H., 1994, "Simulation of Nonideal Gases and Liquid-Gas Phase Transitions by the Lattice Boltzmann Equation," Phys. Rev. E, **49**, pp. 2941–2948.
[6] Shan, X., and Doolen, G. D., 1995, "Multicomponent Lattice-Boltzmann Model With Interparticle Interaction," J. Stat. Phys., **81**, pp. 379–393.
[7] Swift, M., Osborn, W., and Yeomans, J., 1995, "Lattice Boltzmann Simulation of Nonideal Fluids," Phys. Rev. Lett., **75**, pp. 830–833.
[8] Swift, M., Orlandini, S., Osborn, W., and Yeomans, J., 1996, "Lattice Boltzmann Simulations of Liquid-Gas and Binary-Fluid Systems," Phys. Rev. E, **54**, pp. 5041–5052.
[9] Nourgaliev, R., Dinh, T., Theofanous, T., and Joesph, D., 2003, "The Lattice Boltzmann Equation Method: Theoretical Interpretation, Numerics and Implications," Int. J. Multiphase Flow, **29**, pp. 117–169.
[10] Alexander, F. J., Chen, S., and Sterling, J. D., 1993, "Lattice Boltzmann Thermohydrodynamics," Phys. Rev. E, **47**, pp. R2249–R2252.
[11] Shan, X., 1997, "Simulation of Rayleigh—Bénard Convection Using a Lattice Boltzmann Method," Phys. Rev. E, **55**, pp. 2780–2788.
[12] Yuan, P., and Schaefer, L., 2006, "A Thermal Lattice Boltzmann Two-Phase Flow Model and Its Application to Heat Transfer Problems—Part 2. Integration and Validation," ASME J. Fluids Eng., **128**, pp. 151–156.
[13] Succi, S., 2001, *The Lattice Boltzmann Equation for Fluid Dynamics and Beyond*, Oxford University Press, Oxford, UK.
[14] He, X., and Luo, L., 1997, "Theory of the Lattice Boltzmann Method: From the Boltzmann Equation to the Lattice Boltzmann Equation," Phys. Rev. E, **56**, pp. 6811–6817.
[15] Chen, S., Martinez, D., and Mei, R., 1996, "On Boundary Conditions in Lattice Boltzmann Method," Phys. Fluids, **8**, pp. 2527–2536.
[16] Inamuro, T., Yoshino, M., and Ogino, F., 1995, "A Non-Slip Boundary Condition for Lattice Boltzmann Simulations," Phys. Fluids, **7**, pp. 2928–2930.
[17] He, X., Zou, Q., Luo, L., and Dembo, M., 1997, "Analytic Solutions and Analysis on Non-Slip Boundary Condition for the Lattice Boltzmann BGK Model," J. Stat. Phys., **87**, pp. 115–136.
[18] Mei, R., Luo, L., and Shyy, W., 1999, "An Accurate Curved Boundary Treatment in the Lattice Boltzmann Method," J. Comput. Phys., **155**, pp. 307–329.
[19] Hou, S., 1995, "Lattice Boltzmann Method for Incompressible Viscous Flow," Ph.D. thesis, Department of Mechanical Engineering, Kansas State Univ., Manhattan, Kansas, USA.
[20] Sukop, M., and Or, D., 2004, "Lattice Boltzmann Method for Modeling Liquid-Vapor Interface Configurations in Porous Media," Water Resour. Res., **40**, W01509.
[21] Kang, Q., Zhang, D., and Chen, S., 2002, "Displacement of a Two-Dimensional Immiscible Droplet in a Channel," Phys. Fluids, **14**, pp. 3203–3214.
[22] Buick, J., and Greated, C., 2000, "Gravity in the Lattice Boltzmann Model," Phys. Rev. E, **61**, pp. 5307–5320.
[23] Martys, N. S., and Chen, H., 1996, "Simulation of Multicomponent Fluids in Complex Three-Dimensional Geometries by the Lattice Boltzmann Method," Phys. Rev. E, **53**, pp. 743–750.
[24] Hou, S., Shan, X., Zou, Q., Doolen, G., and Soll, W., 1997, "Evaluation of Two Lattice Boltzmann Models for Multiphase Flows," J. Comput. Phys., **138**, pp. 695–713.
[25] Yang, Z., Dinh, T., Nourgaliev, R., and Sehgal, B., 2001, "Numerical Investigation of Bubble Growth and Detachment by the Lattice-Boltzmann Method," Int. J. Heat Mass Transfer, **44**, pp. 195–206.
[26] McNamara, G., Garcia, A. L., and Alder, B. J., 1995, "Stabilization of Thermal Lattice Boltzmann Models," J. Stat. Phys., **81**, pp. 395–408.
[27] Pavlo, P., Vahala, G., and Vahala, L., 1998, "Higher Order Isotropic Velocity Grids in Lattice Methods," Phys. Rev. Lett., **80**, pp. 3960–3963.
[28] Inamuro, T., Yoshino, M., Inoue, H., Mizuno, R., and Ogino, F., 2002, "A Lattice Boltzmann Method for a Binary Miscible Fluid Mixture and Its Application to a Heat-Transfer Problem," J. Comput. Phys., **179**, pp. 201–215.
[29] Shu, C., Peng, Y., and Chew, Y., 2002, "Simulation of Natural Convection in a Square Cavity by Taylor Series Expansion- and Least Squares-Based Lattice Boltzmann Method," Int. J. Mod. Phys. C, **13**, pp. 1399–1414.
[30] Busse, F., 1986, *Hydrodynamics Instabilities and the Transition to Turbulence*, 2nd ed., Springer-Verlag, Berlin, Germany.

A Thermal Lattice Boltzmann Two-Phase Flow Model and Its Application to Heat Transfer Problems—Part 2. Integration and Validation

Peng Yuan
e-mail: pey1@pitt.edu

Laura Schaefer
e-mail: laschaef@engr.pitt.edu

Mechanical Engineering Department,
University of Pittsburgh,
Pittsburgh, PA 15261

*In the previous paper (Part 1) (P. Yuan and L. Schaefer, 2006, ASME J. Fluids Eng., **128**, pp. 142–150), the multiphase isothermal lattice Boltzmann equation (LBE) model and single phase thermal LBE (TLBE) model were described. In this work, by combining these two models, the thermal two-phase LBE model is proposed. The coupling of the two models is through a suitably defined body force term. Due to the external nature of this coupling, the new model will have the same stability as the isothermal two-phase model. The applicability of the model is shown by the numerical simulation results of a thermal two-phase flow system in a rectangular channel. Our preliminary studies show that different equations of state, variable wettability, gravity and buoyancy effects, and relatively high Rayleigh numbers can be readily simulated by this new model.*
[DOI: 10.1115/1.2137344]

Keywords: lattice Boltzmann equation (LBE) method, two-phase flow, interparticle potential, passive-scalar

1 Introduction

The lattice Boltzmann equation (LBE) method is a kinetic approach, which assumes that a fluid consists of mesoscopic fluid particles with repeating collision and streaming patterns and is used to solve for the hydrodynamic phenomena of various systems. Due to its kinetic nature, the LBE method has been found to be particularly useful in applications involving interfacial dynamics and complex boundaries, e.g., multiphase or multicomponent flows [1,2].

In the previous paper (Part 1) [3], the theoretical foundation of the multiphase isothermal LBE model and single phase thermal LBE model were described, along with numerical simulations that validate their applications.

In the multiphase LBE model proposed by Shan and Chen (SC) [4–6], the nonlocal interaction potentials between fluid particles at neighboring lattice sites were imposed to mimic the interparticle forces and the phase separation occurs automatically. The form of the equation of state (EOS) was also controlled by the interaction potentials. A strong limitation of these types of multiphase models, however, is that they are all isothermal models. Researchers have developed thermal LBE (TLBE) models, but they focus on single-phase flow, a highly restrictive application. These TBLE models generally fall in two categories, namely, the multispeed approach [7–9] and the passive-scalar approach [10,11]. The passive-scalar approach has many advantages in that the temperature field is passively advected by the fluid flow and can therefore simply be simulated as an additional component of the fluid system. Thus, the overall complexity of the scheme does not significantly increase, and the passive-scalar approach has the same stability as isothermal LBE models.

In order to provide a more generalized approach to the kinetic modeling of complex flows, this paper presents a multi-dimensional and multiphase fluid model with thermal effects. First, the multiphase isothermal LBE model proposed by SC and the single phase TLBE model using the passive-scalar approach will be briefly recapped, while the full description and numerical validation of the techniques are given in Part 1 [3]. Then, by combining these two models, our thermal multiphase LBE model is proposed. The coupling of the two models is through a suitably defined body force term. In order to show the applicability of the new model, numerical simulation results for a thermal two-phase flow system in a rectangular channel are presented. The effects of varying different parameters will also be discussed. The paper concludes with a discussion about the method's applicability and perspectives.

2 The 3-D Isothermal Multiphase LBE

The standard LBE with the Bhatnagar-Gross-Krook approximation (often referred to as the LBGK) model can be written as

$$f_\alpha(\mathbf{x}+\mathbf{e}_\alpha\delta t, t+\delta t) = f_\alpha(\mathbf{x},t) - \frac{1}{\tau}[f_\alpha(\mathbf{x},t) - f_\alpha^{eq}(\mathbf{x},t)],$$

$$\alpha = 0,1,\ldots,N \tag{1}$$

where $\mathbf{x}$ denotes the position in space, t is time, δt is the time step, f_α is the particle distribution function (PDF) along the αth direction and f_α^{eq} is its corresponding equilibrium particle distribution function, $\mathbf{e}_\alpha$ is the particle velocity in the αth direction, τ is the single relaxation time, and N is the number of discrete particle velocities.

For 2-D flow, the nine-velocity LBE model on the 2-D square lattice, denoted as the D2Q9 model, has been widely used. For simulating 3-D flows, there are several cubic lattice models, such as the D3Q15, D3Q19, and D3Q27 model. The equilibrium distribution for all the D2Q9, D3Q15, D3Q19, and D3Q27 models can be expressed in the form

Contributed by the Fluids Engineering Division of ASME for publication in the JOURNAL OF FLUIDS ENGINEERING. Manuscript received December 18, 2004; final manuscript received August 10, 2005. Assoc. Editor: Malcolm J. Andrews.

$$f_\alpha^{eq} = \rho w_\alpha \left(1 + \frac{3}{c^2}\mathbf{e}_\alpha \cdot \mathbf{u} + \frac{9}{2c^4}(\mathbf{e}_\alpha \cdot \mathbf{u})^2 - \frac{3}{2c^2}\mathbf{u} \cdot \mathbf{u} \right) \tag{2}$$

where w_α is the weighting factor, $c = \delta x / \delta t$ is the lattice speed, δx is the lattice constant, and $\mathbf{u}$ is the macroscopic velocity.

In this paper, we use the D3Q19 model, for which the weighting factor and discrete velocity are given below:

$$\mathbf{e}_\alpha = \begin{cases} (0,0,0) & \alpha = 0; \\ (\pm 1,0,0)c, (0,\pm 1,0)c, (0,0,\pm 1)c, & \alpha = 1,2,\ldots,6; \\ (\pm 1,\pm 1,0)c, (\pm 1,0,\pm 1)c, (0,\pm 1,\pm 1)c, & \alpha = 7,8,\ldots,18. \end{cases} \tag{3a}$$

$$w_\alpha = \begin{cases} \frac{1}{3}, & \alpha = 0; \\ \frac{1}{18}, & \alpha = 1,2,\ldots,6; \\ \frac{1}{36}, & \alpha = 7,8,\ldots,18. \end{cases} \tag{3b}$$

In most LBE simulations, Eq. (1) is solved in two steps: collision and streaming. In the collision step, the PDFs for each direction are relaxed toward quasi-equilibrium distributions. Then, at the streaming step, the distributions move to the neighboring nodes. The local mass density ρ and the local momentum density $\rho\mathbf{u}$ are given by

$$\rho = \sum_{\alpha=0}^{N} f_\alpha = \sum_{\alpha=0}^{N} f_\alpha^{eq} \tag{4a}$$

$$\rho\mathbf{u} = \sum_{\alpha=0}^{N} f_\alpha \mathbf{e}_\alpha = \sum_{\alpha=0}^{N} f_\alpha^{eq} \mathbf{e}_\alpha \tag{4b}$$

It can be shown that the above formulation of the LBE recovers the Navier-Stokes (N-S) equations for fluid flows near the incompressible limit (low Mach number) [12]. The viscosity in the N-S equations derived from Eq. (1) is

$$\nu = \left(\tau - \tfrac{1}{2}\right) c_s^2 \delta t \tag{5}$$

where c_s is the lattice sound speed.

Microscopically, the segregation of a fluid system into different phases is due to the interparticle forces. In this work, the interaction potential model of SC is employed to simulate these interaction forces. In the SC model, the fluid/fluid interaction force is defined as [13]

$$\mathbf{F}_1(\mathbf{x}) = -\psi(\mathbf{x}) \sum_{\mathbf{x}'} G(\mathbf{x},\mathbf{x}')\psi(\mathbf{x}')(\mathbf{x}' - \mathbf{x}) \tag{6}$$

where $G(\mathbf{x},\mathbf{x}')$ is interaction potential and satisfies $G(\mathbf{x},\mathbf{x}') = G(\mathbf{x}',\mathbf{x})$. It reflects the intensity of the interaction, with $G(\mathbf{x},\mathbf{x}') < 0$ representing attractive forces between particles. In our study, the interactions of nearest and next-nearest neighbors are considered. For a D3Q19 lattice model, this leads to

$$G(\mathbf{x},\mathbf{x}') = \begin{cases} g_f, & |\mathbf{x} - \mathbf{x}'| = 1; \\ g_f/2, & |\mathbf{x} - \mathbf{x}'| = \sqrt{2}; \\ 0, & \text{otherwise}. \end{cases} \tag{7}$$

$\psi(\mathbf{x})$ is called the "effective mass" and is defined as a function of the local density. In the SC model, the function of $\psi(\mathbf{x})$ can be varied and different choices will give different EOS. The EOS is determined by $p = c_s^2\rho + c_0 g_f[\psi(\mathbf{x})]^2$, where c_0 is a constant and equals 3.0 for the D3Q19 model. In this study, $\psi(\mathbf{x})$ is taken to be $\psi(\mathbf{x}) = \rho_0[1 - \exp(-\rho/\rho_0)]$, which gives a nonmonotonic pressure-density relationship.

Similarly, at the fluid/solid interface, a force between fluid particles and solid surfaces can be introduced as follows:

$$\mathbf{F}_2(\mathbf{x}) = -\rho(\mathbf{x}) \sum_{\mathbf{x}'} G_w(\mathbf{x},\mathbf{x}')\rho_w(\mathbf{x}')(\mathbf{x}' - \mathbf{x}) \tag{8}$$

where $G_w(\mathbf{x},\mathbf{x}')$ reflects the intensity of the fluid/solid interaction and has the same form as $G(\mathbf{x},\mathbf{x}')$. For the D3Q19 lattice model,

$$G_w(\mathbf{x},\mathbf{x}') = \begin{cases} g_w, & |\mathbf{x} - \mathbf{x}'| = 1; \\ g_w/2, & |\mathbf{x} - \mathbf{x}'| = \sqrt{2}; \\ 0, & \text{otherwise}. \end{cases} \tag{9}$$

g_w controls the strength between fluid and the wall. g_w is positive for a nonwetting fluid and negative for a wetting fluid. Adjusting the value of g_w can give a different wettability. $\rho_w(\mathbf{x}')$ is the wall density, which equals one at the wall and zero in the fluid.

Finally, constant body forces such as gravity can be expressed as

$$\mathbf{F}_3 = \rho(\mathbf{x})\mathbf{a} \tag{10}$$

where $\mathbf{a}$ is the acceleration due to the body force.

All of these forces can be incorporated into the model by shifting the velocity in the equilibrium distribution. That means we replace the velocity $\mathbf{u}$ in Eq. (2) with

$$\mathbf{u}^{eq} = \mathbf{u} + \frac{\tau \mathbf{F}_{total}}{\rho(\mathbf{x})} \tag{11}$$

where $\mathbf{F}_{total} = \mathbf{F}_1 + \mathbf{F}_2 + \mathbf{F}_3$.

Then, by averaging the moment before and after the collision, the whole fluid velocity $\mathbf{U}$ is found by:

$$\rho(\mathbf{x})\mathbf{U} = \rho(\mathbf{x})\mathbf{u} + \tfrac{1}{2}\mathbf{F}_{total} \tag{12}$$

3 Single Phase Thermal 3-D LBE Model

The SC model is an isothermal model. In order to take thermal effects into account, we introduced the single phase TLBE model using the passive-scalar approach.

If the viscous and compressive heating effects are negligible, the temperature field satisfies a much simpler passive-scalar equation:

$$\frac{\partial T}{\partial t} + \mathbf{u} \cdot \nabla T = \nabla \cdot (\alpha \nabla T) + \Psi \tag{13}$$

where $\mathbf{u}$ is the whole fluid velocity, α is the thermal diffusivity, and Ψ is the source term.

Equation (13) can be solved in the LB framework by also using Eqs. (1) and (2), except that τ will be replaced by τ_T (the dimensionless single relaxation time for temperature) and the summation of PDFs will give the temperature value. In this way, the temperature field can be simulated by solving an additional LBE.

As before, $\alpha = (\tau_T - \frac{1}{2})c_s^2 \delta t$, and thus the Prandtl number will be

$$\mathrm{Pr} = \frac{\nu}{\alpha} = \frac{2\tau - 1}{2\tau_T - 1} \tag{14}$$

By changing τ and/or τ_T, we can generate a different Prandtl number.

4 Multiphase Thermal 3-D LBE Model

Combining the single component two-phase LBE model (SC model) and the passive-scalar TLBE model, the single component two-phase TLBE model is proposed. In this model, the fluid dynamics are simulated by an isothermal LBE model with the interparticle potential incorporated. The temperature field is determined by an additional passive-scalar equation and the coupling of these two parts is through a suitably defined body force term in the isothermal LBE model. In dealing with this body force, the Boussinesq approximation is adopted, which assumes that the material properties are independent of temperature except in the body force term. For the gravitational term, the density is assumed to be

a linear function of the temperature. Therefore, the buoyancy term induced by the gravity and temperature difference can be expressed as

$$\rho(\mathbf{x})\mathbf{G} = \rho(\mathbf{x})g\left(1 - \frac{\langle\rho\rangle}{\rho(\mathbf{x})}\right)\mathbf{k} - \beta\rho g(T - T^*)\mathbf{k} \tag{15}$$

where $\langle\rho\rangle$ is the average density of the mixture in the entire domain; g is the acceleration due to gravity; T^* is the reference temperature, which is usually equal to the temperature at the pure conduction state; and β is the thermal expansion coefficient, which we assume is equal for the two phases. However, β can also easily be specified to be different values for different phases. In Eq. (15), the first term on the right-hand side (RHS) represents the buoyancy force due to the density difference. The second term on the RHS represents the buoyancy force due to the temperature difference.

Although conceptually very simple, this model can produce a nonideal gas EOS and capture the temperature field at the same time. In comparison to other multi-phase TLBE models, it is easy to realize and more stable because it does not require adding more particle speeds or tracking the energy evolution. The stability is determined by the fluid dynamics, and the temperature field has no influence on it. Also, the energy source term Ψ reserves the space for adding viscous and compressive heating terms in the future.

Another important point is that we have not considered phase transition and latent heat in the current model. In general, the phase transition phenomena are strongly related to the thermodynamics and are very complicated in mechanics. The phase transition rate is a function of thermodynamic properties such as temperature and pressure. In order to consider phase transition in the LB context, one needs to consider how to link the phase transition rate with these thermodynamic properties and how to incorporate latent heat into the scheme. Some pioneering work has been done by using simple approximations. For example, Kono and Ishizuka [14] specify a constant phase change rate in their model and relate it to the latent heat. Miller and Succi [15] studied anisotropic crystal growth from melt. They use a phase-field equation to simulate the phase transition and consider latent heat as an extra force term.

5 Simulation Results

We simulated the thermal two-phase system in a rectangular channel under different conditions (different Reynolds number, different Rayleigh number, and different boundary conditions). Most of the simulations were conducted on a $50\times50\times50$ lattice size with a periodical boundary condition (BC) in the x direction and wall boundary conditions (BCs) in the y and z directions for the fluid dynamics. Grid independency was checked for all of the different resolutions used in the paper by varying the lattice sizes, as detailed in Part 1 [3].

A body force in the x direction is included. Defining the characteristic velocity U' (in lattice units) as $U' = \rho(\mathbf{x})aN_z^2/\mu = aN_z^2/\nu$, the Reynolds number will hence be

$$\mathrm{Re} = \frac{U'N_z}{\nu} = \frac{aN_z^3}{\nu^2} \tag{16}$$

where a is the acceleration due to the body force.

For the simulation, the bottom wall and top wall are kept at fixed temperatures of 1.0 and 0.0, respectively. The vertical walls are adiabatic. Therefore, the Rayleigh number is defined as

$$\mathrm{Ra} = \frac{g\beta\Delta TN_y^3}{\nu\alpha} \tag{17}$$

where ΔT is the characteristic temperature difference (in the simulation $\Delta T = T_B - T_T = 1$) and N_z is the lattice size in the z direction.

Initially, a droplet is placed at the center of the domain with no force on it. After several hundred time steps, the droplet reaches equilibrium. This equilibrium process is needed; otherwise, the code fails to converge. Next the buoyancy force in the z direction and the body force in the x direction will be turned on. Because of the buoyancy force, the droplet will fall until it reaches the bottom wall. Due to different wettabilities at the wall, it can form different contact angles. If the relative difference of the maximum magnitude of the velocities at time step t and at $t-100$ is smaller than a given tolerance, steady state is considered to be reached (in this case, all other variables also have a small relative change). If steady state cannot be reached (in this case, usually the system will exhibit some periodical feature), the duration of the simulation (more than 20,000 time steps in lattice units) will produce statistical results.

5.1 Multiphase Thermal Flow Base Case. First, we present our results for two-phase flow at given Rayleigh numbers. The strength of the interparticle force $g_f = -0.35$ and the initial droplet radius is 7.0. The Reynolds number is held at 100.

Figure 1 shows the isotherm contours, density contours, and velocity vectors in the xz plane at $y=25$ (the symmetric plane) for Ra=10,000 and Re=100. The isotherms form ascending and descending fluid sheets in the vapor phase. In the liquid phase, the isotherms are flattened. This is mainly because the buoyancy force due to the temperature difference is balanced by the buoyancy force due to the density difference in the liquid phase. Currently, the liquid and vapor phases in our model have the same properties except for densities. However, the code has the potential for specifying different properties for different phases and also specifying different EOS. This will be the next step of our research.

In our static bubble test, we observed that there exist nonzero velocity vectors in the flow field which indicate deviation from the real physical situation. These unphysical velocities are called spurious currents and reach their maximum value at the interface region. The spurious currents have an influence on the temperature field and will affect local heat transfer results. This is verified because we are using the velocity of the flow as the advection velocity of the temperature. The fluctuation of the isotherms near the top interface of the droplet shows this influence. However, as for the large scale or overall heat transfer results, we can ignore this influence for two reasons. First, these spurious currents are mostly constrained to be in the interface region and will not extend to a distance far away from the interface. Second, for $|g_f| \leqslant 0.35$, compared with the main flow velocity, the magnitude of the spurious currents is relatively small and can be neglected. Also, by changing the EOS, we can greatly reduce the spurious currents. This relationship will be explored further in our future work.

5.2 Effect of Varying Rayleigh Number. Figure 2 shows the isotherms and density contours in the xz-plane at $y=25$ for Ra =5000 and 15,000. As the Rayleigh number increases, the temperature gradient near the wall becomes sharper: in the Ra =5000 case, the isotherms are almost straight lines and evenly distributed, while in the Ra=15,000 case the isotherms are highly curved and much thicker near the wall. Also, as the Rayleigh number increases, the ascending and descending fluid sheets become narrower.

5.3 Nusselt Number Variation. The Nusselt number of the bulk flow is defined as

$$\mathrm{Nu} = 1 + \frac{\langle u_z(T - T^*)\rangle N_z}{\alpha\Delta T} \tag{18}$$

where u_z is the velocity in the z direction; T^* is the reference temperature, here using the temperature at the pure conduction state; N_z is the lattice size in the z direction; and $\langle\cdot\rangle$ represents the average over the whole flow domain.

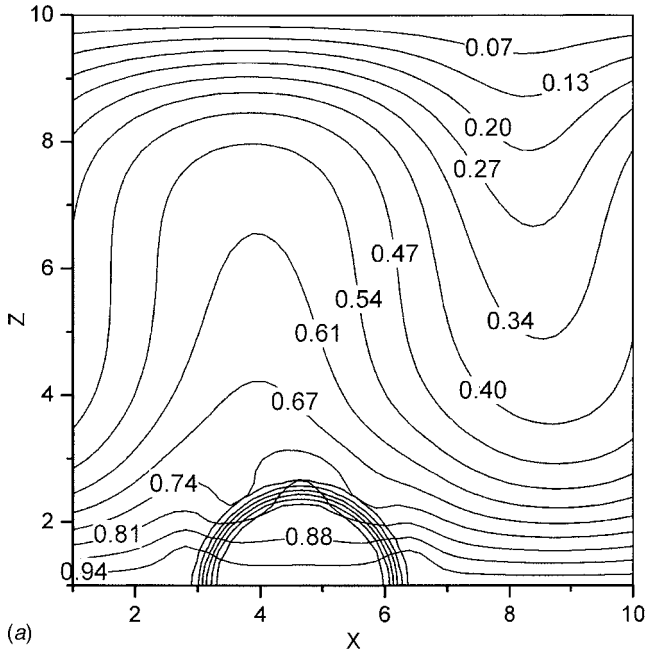

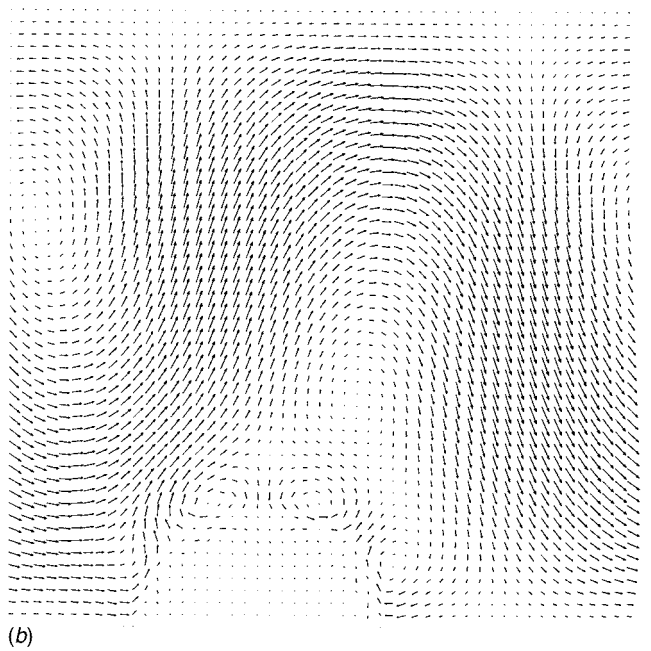

Fig. 1 Isotherms, density contours, and velocity vectors at Ra=10,000 and Re=100: (a) isotherms and density contours and (b) velocity vectors

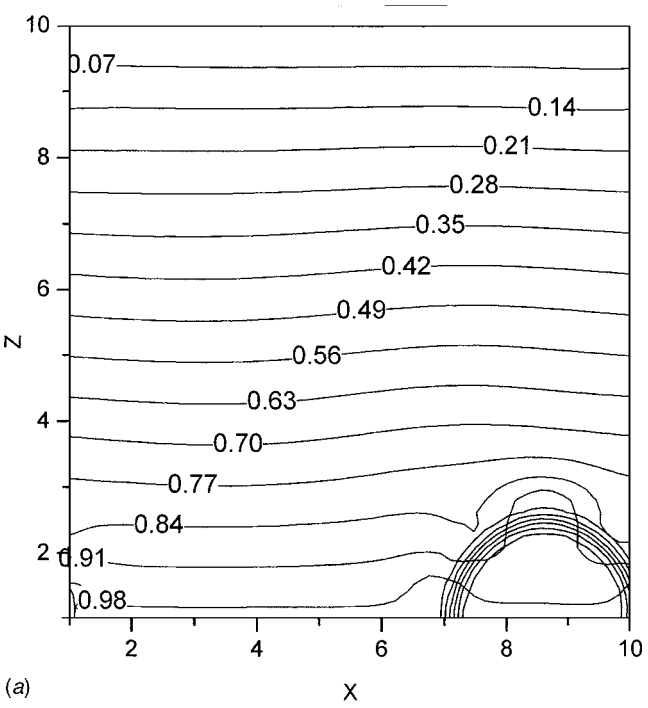

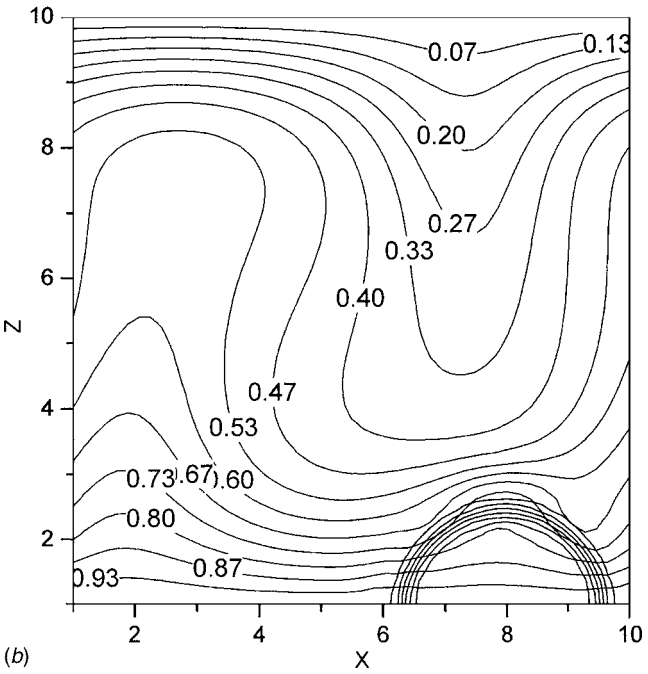

Fig. 2 Isotherms and density contours at different Rayleigh number: (a) Ra=5000 and (b) Ra=15,000

The Nusselt number of the bulk flow, at the top wall, and at the bottom wall as functions of the time step are shown in Fig. 3, with Ra=10,000 and Re=100.

Instead of approaching a constant value, all three values have small fluctuations throughout the simulation. The fluctuation exhibits periodical features. The characteristic Nusselt number can be obtained by averaging the instantaneous values over time.

Figure 4 shows the bulk Nusselt number changing with the time step at different Rayleigh numbers. The bulk Nusselt number increases as the Rayleigh number increases. The magnitude of the fluctuations also increases with increasing Rayleigh number.

The two-phase flow system under different Reynolds numbers is also simulated. The Rayleigh number is fixed at 10,000 and the Reynolds number takes the value 20, 100, and 500, respectively. Figure 5 shows the bulk Nusselt number changing with time step at different Reynolds numbers. For Re=20, the bulk Nusselt number is 1.808, which is slightly higher than that of Re=100 (1.771), and the fluctuation is much smaller (almost a constant value). For Re=500, the bulk Nusselt number (1.493) as well as the Nusselt number at the top and bottom walls is smaller than the Re=100 case.

These results seem counter-intuitive. We believe the main reason is that the larger velocity in the x direction suppresses the convection in the z direction. In this problem, the temperature difference between the upper wall and the lower wall is the main driving force for the heat transfer. Therefore, a better convection

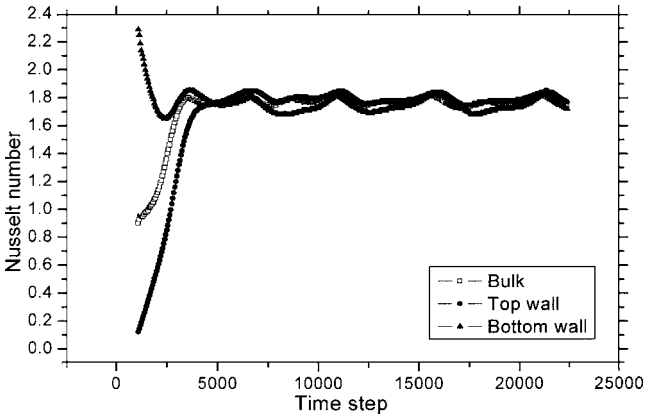

Fig. 3 Nusselt number of the bulk flow, at the top wall, and at the bottom wall as functions of the time step (Ra=10,000, Re =100)

in the z direction will result in a higher Nusselt number. However, as the Reynolds number increases, the convection in the z direction decreases, which can be seen from the isotherms of the xz plane (y=25) in Fig. 6 (Re=500 case), where the isotherms are almost straight lines in the x direction. Also shown in Fig. 6 are the isotherms in the yz plane (x=25), which form some ascending and descending fluid sheets. Compared with Fig. 1(a) (Re=100 case), these fluid sheets are wider and flatter.

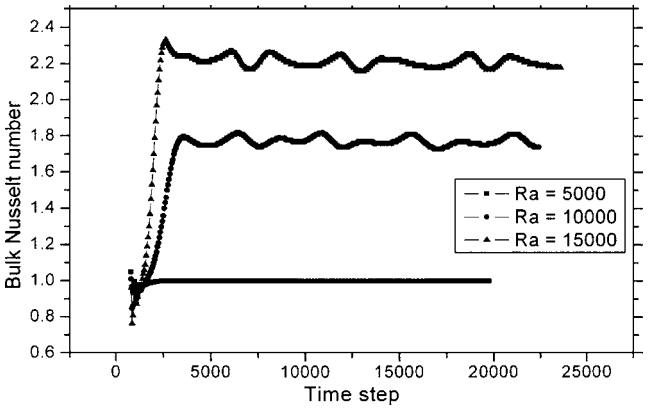

Fig. 4 The bulk Nusselt number changing with time step at different Rayleigh numbers

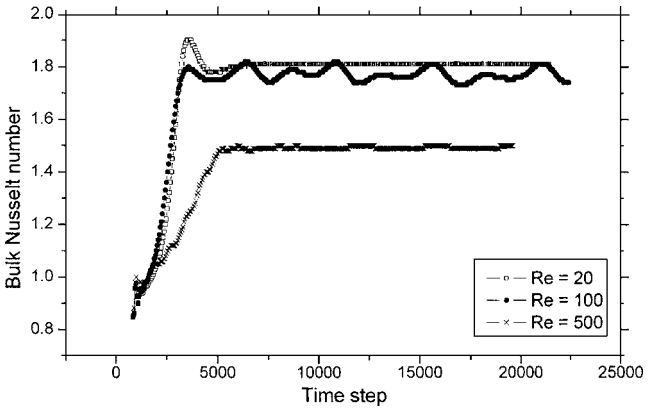

Fig. 5 The bulk Nusselt number changing with time step at different Reynolds numbers

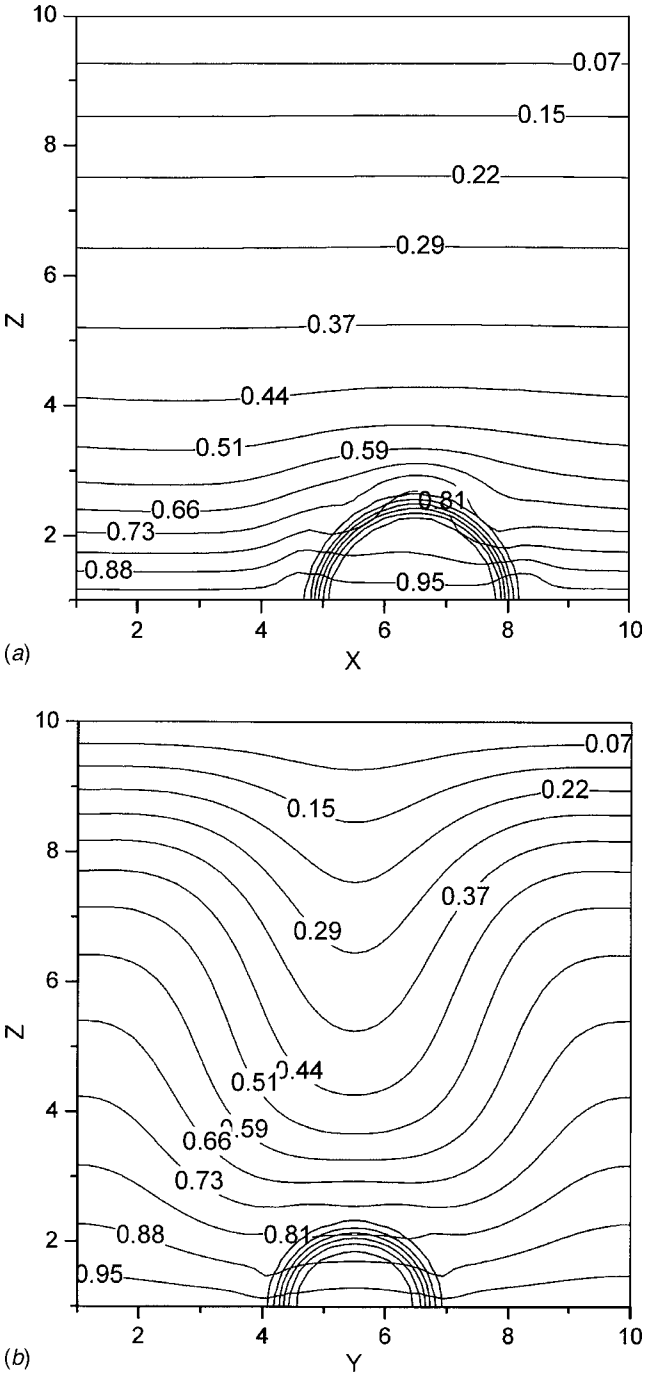

Fig. 6 Isotherms and density contours at Ra=10,000 and Re =500: (*a*) *xz* plane (*y*=25) and (*b*) *yz* plane (*x*=25)

5.4 Effect of Fluid/Solid Interaction Strength. The influence of the fluid/solid interaction on the system is also investigated. Different g_w values (0.06 and −0.03) are used, which represent a typical nonwetting and wetting fluid. The contact angles for these two cases are 120.6 and 71.3 deg, respectively. The Reynolds number and Rayleigh number are fixed at 100 and 10,000. Table 1 lists the Nusselt number of the bulk flow, at the top wall, and at the bottom wall under different g_w values. Because of the fluctuation, the Nusselt number is averaged over the time steps. Compared to the no fluid/solid interaction case, the wetting case (g_w=−0.03) has a higher Nusselt number at the top wall and a lower Nusselt number at the bottom wall, and the bulk Nusselt number is increased. On the other hand, the nonwetting case (g_w

Table 1 Nusselt number at different g_w values

	g_w		
Nu	Bulk	Top wall	Bottom wall
−0.03	1.852	1.918	1.698
0	1.771	1.797	1.741
0.06	1.733	1.722	1.954

=0.06) has a lower Nusselt number at the top wall and a higher Nusselt number at the bottom wall, and the bulk Nusselt number is decreased.

An explanation for this phenomenon is that as the g_w value increases, the contact area between the droplet and the wall decreases, and the height of the droplet increases. This will increase the convection at the bottom wall since more area is exposed to the convection of the vapor phase. However, the bulk Nusselt number is decreased because the droplet extends deeper to the center and hampers the convection in that region.

6 Discussion

In this work, we have proposed a thermal two-phase LBE model. In this model, the fluid dynamics is simulated by an isothermal single component multiphase LBE, and the temperature field is determined by an additional passive-scalar equation. The coupling of these two parts is through a suitably defined body force term in the isothermal LBE. The applicability of our model is demonstrated through numerical simulations. This new model can simulate a thermal two-phase flow system with a non-ideal gas EOS. Because the coupling is external, the new model has the same stability as the isothermal LBE model. Furthermore, it is simple and easy to code. Our preliminary studies show that different EOS, variable wettability, gravity and buoyancy effects, and relatively high Rayleigh numbers can be readily simulated by the new model. Also, the new model has the ability to handle complex BCs. For the future, further research is needed in incorporating a more realistic EOS, handling two phases with a higher density ratio, reducing the spurious currents, and dealing with phase transition.

Acknowledgment

This work has been supported by NSF Grant No. CTS-0238841. The authors also thank Dr. Qinjun Kang at Los Alamos National Laboratory for helpful discussions.

Nomenclature

$\mathbf{a}$ = acceleration
c = lattice speed
c_s = lattice sound speed
c_V = specific heat capacity
$\mathbf{e}_\alpha$ = lattice particle's speed
f_α = particle distribution function
f_α^{eq} = equilibrium particle distribution function
$\mathbf{F}$ = force per unit mass
g = gravitational constant
g_f = intensity of fluid/fluid interaction
g_w = intensity of fluid/solid interaction
$\mathbf{G}$ = buoyancy force per unit mass
$G(\mathbf{x},\mathbf{x}')$ = Green's function (related to the fluid/fluid interaction potential)
$G_w(\mathbf{x},\mathbf{x}')$ = Green's function (related to the fluid/solid interaction potential)
N_z = lattice size in the z direction
t = time
T = temperature
T^* = reference temperature
$\mathbf{u},\mathbf{U}$ = fluid velocity
$\mathbf{u}^{eq}$ = equilibrium velocity
U' = characteristic velocity
w_α = weight coefficients
$\mathbf{x}$, $\mathbf{x}'$ = position
α = thermal diffusivity
β = thermal expansion coefficient
ΔT = temperature difference
ρ = density
ρ_w = wall density
ν = kinematic viscosity
τ = relaxation time
τ_T = relaxation time for temperature field
ψ = effective mass
Ψ = heat source term

References

[1] Chen, S., and Doolen, G. D., 1998, "Lattice Boltzmann Method for Fluid Flows," Annu. Rev. Fluid Mech., **30**, pp. 329–364.
[2] Yu, D., Mei, R., Luo, L., and Shyy, W., 2003, "Viscous Flow Comutations With the Method of Lattice Boltzmann Equation," Prog. Aerosp. Sci., **39**, pp. 329–367.
[3] Yuan, P., and Schaefer, L., 2006, "A Thermal Lattice Boltzmann Two-Phase Flow Model and Its Application to Heat Transfer Problems—Part 1. Theoretical Foundation," ASME J. Fluids Eng., **128**, pp. 142–150.
[4] Shan, X., and Chen, H., 1993, "Lattice Boltzmann Model for Simulation Flows With Multiple Phases and Components," Phys. Rev. E, **47**, pp. 1815–1819.
[5] Shan, X., and Chen, H., 1994, "Simulation of Nonideal Gases and Liquid-Gas Phase Transitions by the Lattice Boltzmann Equation," Phys. Rev. E, **49**, pp. 2941–2948.
[6] Shan, X., and Doolen, G. D., 1995, "Multicomponent Lattice-Boltzmann Model With Interparticle Interaction," J. Stat. Phys., **81**, pp. 379–393.
[7] Alexander, F. J., Chen, S., and Sterling, J. D., 1993, "Lattice Boltzmann Thermohydrodynamics," Phys. Rev. E, **47**, pp. R2249–R2252.
[8] McNamara, G., Garcia, A. L., and Alder, B. J., 1995, "Stabilization of Thermal Lattice Boltzmann Models," J. Stat. Phys., **81**, pp. 395–408.
[9] Pavlo, P., Vahala, G., and Vahala, L., 1998, "Higher Order Isotropic Velocity Grids in Lattice Methods," Phys. Rev. Lett., **80**, pp. 3960–3963.
[10] Shan, X., 1997, "Simulation of Rayleigh—Bénard Convection Using a Lattice Boltzmann Method," Phys. Rev. E, **55**, pp. 2780–2788.
[11] Inamuro, T., Yoshino, M., Inoue, H., Mizuno, R., and Ogino, F., 2002, "A Lattice Boltzmann Method for a Binary Miscible Fluid Mixture and its Application to a Heat-Transfer Problem," J. Comput. Phys., **179**, pp. 201–215.
[12] Succi, S., 2001, *The Lattice Boltzmann Equation for Fluid Dynamics and Beyond*, Oxford University Press, Oxford, UK.
[13] Sukop, M., and Or, D., 2004, "Lattice Boltzmann Method for Modeling Liquid-Vapor Interface Configurations in Porous Media," Water Resour. Res., **40**, p. W01509.
[14] Kono, K., Ishizuka, T., Tsuda, H., and Kurosawa, A., 2000, "Application of Lattice Boltzmann Model to Multiphase Flows With Phase Transition," Comput. Phys. Commun., **129**, pp. 110–120.
[15] Miller, W., and Succi, S., 2002, "A Lattice Boltzmann Model for Anisotropic Crystal Growth From Melt," J. Stat. Phys., **107**, pp. 173–186.

Shihai Feng[1]
e-mail: sfeng@lanl.gov

Alan L. Graham

Patrick T. Reardon

Los Alamos National Laboratory,
Los Alamos, NM 87545

James Abbott
High Performance Computing Center,
Texas Tech University,
Lubbock, TX 79409

Lisa Mondy
Sandia National Laboratories,
Albuquerque, NM 87185-0834

Improving Falling Ball Tests for Viscosity Determination

Laboratory experiments and numerical simulations are performed to determine the accuracy and reproducibility of the falling-ball test for viscosity determination in Newtonian fluids. The results explore the wall and end effects of the containing cylinder and other possible sources that affect the accuracy and reproducibility of the falling ball tests. A formal error analysis of the falling-ball method, an evaluation of the relative merits of calibration and individual measurements, and an analysis of reproducibility in the falling-ball test are performed. Recommendations based on this study for improving both the accuracy and reproducibility of the falling-ball test are presented.
[DOI: 10.1115/1.2137345]

1 Introduction

A falling ball viscometer is one of the simplest, yet most accurate, means of determining the low shear rate viscosity of liquids [1]. It provides a standard way to check quality in plastics processing (ISO 12058) and is applicable for testing of petroleum products, pharmaceuticals, and beverage and food products, to name a few [2]. Because a falling ball viscometer is simple to construct and operate, it can be a cost- and time-effective means to determine properties of transparent liquids, especially for research applications or in cases in which measurements are only required infrequently. It is especially useful in applications concerning highly viscous liquids, where capillary tube viscometry can be inconvenient. However, the danger in constructing a homemade viscometer is that the precision may not be as well understood. We will examine the major causes of inaccuracies in falling ball viscometry and make recommendations on ways to improve both the accuracy and reproducibility of these measurements.

In falling-ball rheometry, a sphere is allowed to fall under the influence of gravity in a quiescent liquid. The sphere, initially at rest, will accelerate until it reaches a constant velocity. At steady state, the sum of all of the forces on the ball must be zero and the gravitational force exactly balances the buoyant and kinetic forces on the particle. The governing equation for falling-ball rheometry is derived from Stokes' solution to the conservation of momentum equation for uniform, low Reynolds number flow past a sphere for the kinetic forces [3] combined with the steady-state force balance in an unbounded Newtonian liquid under conditions such that only hydrodynamic forces exert an appreciable effect. The results show that the terminal velocity, v_t, is a known function of the fluid viscosity, μ, the physical characteristics of the falling ball, and the material properties of the liquid:

$$v_t = \frac{2}{9} \cdot \frac{g(\rho_f - \rho_{fl})a^2}{\kappa\mu}. \tag{1}$$

Here ρ_f is the density of the falling ball, ρ_{fl} is the density of the fluid, a is the radius of the falling ball, and κ is a correction factor used to account for effects not in Stokes' original formulation (i.e., wall effects, inertial effects) [4–7]. Using this simple formula, experiments can be designed to measure the viscosity of a fluid at low shear rates using relatively precise and inexpensive methods.

In order to obtain high precision results in systems contained in finite-sized cylinders, falling-ball rheometry must be corrected for the additional drag due to the presence of bounding walls. In Stokes' original assumptions, it was specified that the fluid was unbounded and infinite. Subsequently, several researchers have devised methods for corrections to the Stokes drag force due to wall effects. Faxen [4] performed the initial study that derived a theoretical prediction of the correction factor for balls settling along the centerline of a cylinder that is accurate to first-order terms of a/R (the ratio of the falling ball to containing cylinder radii) and Reynolds number (based on the falling ball diameter) of zero. Bohlin [5] extended this work by developing an infinite series for a/R terms, valid for a/R ratios between 0 and 0.6. He gives the formula for K through the tenth power as

$$\kappa = 1 \Bigg/ \left[1 - 2.104\,43\left(\frac{a}{R}\right) + 2.088\,77\left(\frac{a}{R}\right)^3 - 0.948\,13\left(\frac{a}{R}\right)^5 - 1.372\left(\frac{a}{R}\right)^6 + 3.87\left(\frac{a}{R}\right)^8 - 4.19\left(\frac{a}{R}\right)^{10} + \cdots \right]. \tag{2}$$

Haberman and Sayre [6] further extended this work by posing a theory that provides a much more accurate correction for $0.6 < a/R < 0.8$ as well as validating Bohlin's correction for $0.6 < a/R$.

The corrections described above provide wall corrections for the axisymmetric case in which the trajectory of the falling ball is along the axis of the cylinder. Brenner and Happel [7] first developed corrections for an off-center case. They define κ as

$$\kappa = \frac{1}{1 - f(b/R) \cdot (a/R)}, \tag{3}$$

where b is the distance between the center of the ball and the axis of the cylinder. The eccentricity function, $f(b/R)$, is in terms of integrals of an infinite series of Bessel functions. Famularo [8] calculated values for this function for several values of b/R. These results are tabulated in [9]. For small values of a/R and $b/R \to 0$, the following function is valid:

$$f\left(\frac{b}{R}\right) = 2.104\,44 - 0.6977\left(\frac{b}{R}\right)^2 + O\left(\frac{b}{R}\right)^4. \tag{4}$$

[1]Corresponding author.

Contributed by the Fluids Engineering Division of ASME for publication in the JOURNAL OF FLUIDS ENGINEERING. Manuscript received February 24, 2005; final manuscript received August 11, 2005. Assoc. Editor: Theodore Heindel.

Papers by Falade and Brenner [10] and Higdon and Muldowney [11] extend these results and provide correction terms for higher a/R and b/R ratios. Ambari and co-workers [12] confirmed Happel and Brenner's corrections experimentally using a falling-ball apparatus with a magnetic ball whose position can be controlled via an external magnetic field. Ilic et al. [13] and Graham et al. [14] also confirmed these corrections in numerical simulations and in physical experiments.

The intent of this paper is to combine theoretical analysis with numerical simulations and laboratory experiments to study the sources that affect the accuracy and reproducibility of falling-ball tests in Newtonian fluids. In the following sections, a theoretical analysis of accuracy and reproducibility in falling-ball tests is presented; then a series of numerical simulations and experiments based on the theoretical analysis are described. Finally, conclusions and recommendations to improve the falling-ball tests are given based on these results.

2 Analysis of Accuracy and Reproducibility in Falling-Ball Experiments

In falling-ball rheometry, the viscosity of a fluid is related to the terminal settling velocity of a ball and is a function of the time of flight, t_f, the length of flight, L_f, the radius size of the ball, a, the radius of the containing cylinder, R, the density of the ball, ρ_f, the mass of the ball, m_f, the fluid, ρ_l, the tilt of the containing cylinder, α, the distance from the ball center to the tube center, b, and the local acceleration of gravity, g. Furthermore, the viscosity is a function of the temperature of the fluid, T. In order to determine the sensitivity of each of these measured quantities and the overall possible accuracy of the falling ball technique, we have performed an error analysis of the procedure. We start with the equation mentioned above: In a Newtonian fluid, t_f is related to the viscosity of the fluid, μ, by Stokes law [3]:

$$\mu(t_f,L_f,a,R,m_f,\rho_l,\alpha,b,g)=\frac{2}{9}\frac{a^2\rho_d g_\alpha t_f \kappa^{-1}}{L_f}, \tag{5}$$

where κ is the wall effects correction described in the previous section. Expression for ρ_d and g_α are developed below. The density difference in terms of measured quantities can be written

$$\rho_d=\frac{m_f}{(4\pi/3)a^3}-\rho_l, \tag{6}$$

The local acceleration of gravity depends on the latitude and elevation and any local gravitational anomalies. For example, there are no gravitational measurements in the USGS data base in the immediate area of the laboratory at Texas Tech. The gravitational "constant" averaged over six nearby stations (located within a radius of about 21.5 km) is 979.309 24 $\mathrm{cm/s^2}$ with a standard deviation of 0.004 59. This variation is small, but the difference between this value and the appropriate value at a different location could be more significant. We also want to take into account that there is a possible change in the driving force due to the cylinder tilt,

$$g_\alpha=g\cos(\alpha). \tag{7}$$

To determine how uncertainties in the experimental parameters affect the overall uncertainty in the calculated viscosity, a perturbation analysis of Eq. (5) with respect to the independent variables is used to give

$$\Delta\mu=\frac{\partial\mu}{\partial t_f}\Delta t_f+\frac{\partial\mu}{\partial L_f}\Delta L_f+\frac{\partial\mu}{\partial a}\Delta a+\frac{\partial\mu}{\partial R}\Delta R+\frac{\partial\mu}{\partial m_f}\Delta m_f+\frac{\partial\mu}{\partial\rho_l}\Delta\rho_l+\frac{\partial\mu}{\partial\alpha}\Delta\alpha+\frac{\partial\mu}{\partial b}\Delta b+\frac{\partial\mu}{\partial g}\Delta g. \tag{8}$$

Each term of $\Delta\mu$ will now be evaluated. The partial derivatives for t_f and L_f are simply given by Eqs. (9) and (10)

$$\frac{\partial\mu}{\partial t_f}=\frac{2}{9}\frac{a^2\rho_d g_\alpha}{\kappa L_f}=\frac{\mu}{t_f}, \tag{9}$$

$$\frac{\partial\mu}{\partial L_f}=-\frac{2}{9}\frac{a^2\rho_d g_\alpha t_f}{\kappa L_f^2}=-\frac{\mu}{L_f}. \tag{10}$$

Somewhat more complicated is the expression for the falling-ball size because it not only appears directly in the equation but also affects the κ and ρ_d terms. Here the expansion gives the result as

$$\frac{\partial\mu}{\partial a}=\frac{4}{9}\frac{a\rho_d g_\alpha t_f}{\kappa L_f^2}+\frac{2}{9}\frac{a^2 g_\alpha t_f}{\kappa L_f}\frac{\partial\rho_d}{\partial a}-\frac{2}{9}\frac{a^2 g_\alpha t_f}{L_f}\frac{\partial\kappa^{-1}}{\partial a}$$
$$=\mu\left(\frac{2}{a}+\frac{1}{\rho_d}\frac{\partial\rho_d}{\partial a}+\kappa\frac{\partial\kappa^{-1}}{\partial a}\right)$$
$$=\mu\left(\frac{2}{a}-\frac{3m_f}{(4\pi/3)a^3\rho_d}\frac{1}{a}+\kappa\frac{\partial\kappa^{-1}}{\partial a}\right).$$

The expression $\partial\kappa^{-1}/\partial a$ can be evaluated by differentiating Eq. (2) with respect to λ, in terms of a dimensionless sphere size, $\lambda=a/R$, to give

$$\frac{\partial\kappa^{-1}}{\partial a}=\frac{\partial\kappa^{-1}}{\partial\lambda}\frac{\partial\lambda}{\partial a}=\frac{\lambda}{a}\frac{\partial\kappa^{-1}}{\partial\lambda}, \tag{11}$$

and

$$\frac{\partial\kappa^{-1}}{\partial\lambda}=-2.104\,43+6.266\,31\lambda^2-4.7407\lambda^4-8.232\lambda^5+31.\lambda^7-41.9\lambda^9. \tag{12}$$

Two of the terms are evaluated numerically because the known analytical solutions are not applicable for the relatively large size falling ball used in our experiments. These are the terms that deal with how the ball falls off-axis but parallel to the axis of the tube and how the ball falls when the cylinder is tilted. For the first term we find that

$$\frac{\partial\mu}{\partial b/R}=-0.178\frac{b}{R}\mu, \tag{13}$$

and for the second term we find that

$$\frac{\partial\mu}{\partial\alpha}=[1.32\alpha-\tan(\alpha)]\mu. \tag{14}$$

The first part of Eq. (14) arises because, if the tube is tilted, the ball will drift off-axis which changes the wall effect κ. The second part arises because of the reduced gravity along the axis of the tube as given by Eq. (7).

In a similar fashion, the rest of the terms can be evaluated. The results are Eqs. (15)–(20):

$$\frac{\partial\mu}{\partial R}=\mu\kappa\frac{\partial\kappa^{-1}}{\partial R}, \tag{15}$$

$$\frac{\partial\mu}{\partial b}=-\frac{\mu}{\kappa}\frac{\partial\kappa}{\partial b}, \tag{16}$$

$$\frac{\partial\kappa^{-1}}{\partial R}=\frac{\partial\kappa^{-1}}{\partial\lambda}\frac{\partial\lambda}{\partial R}=-\frac{\lambda}{R}\frac{\partial\kappa^{-1}}{\partial\lambda}, \tag{17}$$

$$\frac{\partial\mu}{\partial m_f}=\frac{\mu}{\rho_d}\frac{\partial\rho_d}{\partial m_f}=\frac{\mu}{(4\pi/3)a^3\rho_d}=\frac{\mu}{m_f-(4\pi/3)a^3\rho_f}, \tag{18}$$

$$\frac{\partial\mu}{\partial\rho_l}=\frac{\mu}{\rho_d}\frac{\partial\rho_d}{\partial\rho_l}=-\frac{\mu}{\rho_d}, \tag{19}$$

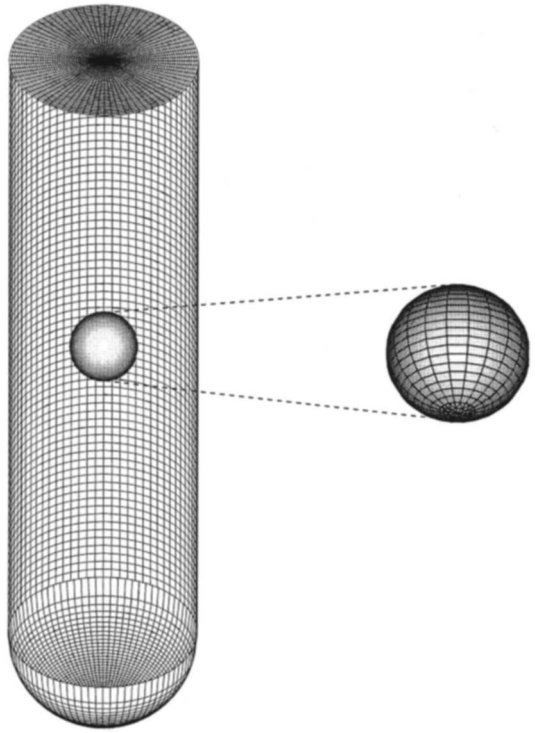

Fig. 1 A three-dimensional BEM mesh of a spherical ball in a tube. Note the vertical wall mesh has been cut in half in order to view the ball clearly.

$$\frac{\partial \mu}{\partial g} = \frac{\mu}{g_\alpha}\frac{\partial g_\alpha}{\partial g} = \frac{\mu}{g}. \tag{20}$$

Combining terms and substituting back into Eq. (8) gives the results below,

$$\frac{\Delta \mu}{\mu} = \frac{\Delta t_f}{t_f} - \frac{\Delta L_f}{L_f} + \left(2 - \frac{3\rho_f}{\rho_d} + \kappa\lambda\frac{\partial \kappa^{-1}}{\partial \lambda}\right)\frac{\Delta a}{a} - \kappa\lambda\frac{\partial \kappa^{-1}}{\partial \lambda}\frac{\Delta R}{R} + \frac{\rho_f}{\rho_d}\frac{\Delta m_f}{m_f} - \frac{\Delta \rho_l}{\rho_d} - \tan(\alpha)\Delta\alpha - \frac{\partial \kappa}{\partial b}\frac{\Delta b}{\kappa} + \frac{\Delta g}{g}. \tag{21}$$

For most liquids, the following behavior is observed for viscosity as a function of temperature,

$$\mu(T) = \gamma e^{\beta/T}, \tag{22}$$

where T is the temperature in Kelvin, and γ and β are experimentally determined parameters. The uncertainty associated with temperature can be described by $(\partial \mu/\partial T)\Delta T$. This yields the following expression for the partial derivative:

$$\frac{\partial \mu}{\partial T} = -\frac{\beta}{T^2}\mu. \tag{23}$$

Therefore, the magnitude of relative error in calculating the viscosity can be bounded by estimating the magnitude of each of the terms in Eqs. (21) and (23). In the following section, numerical simulations and experiments are designed to evaluate each individual term in these equations.

3 Numerical Simulations and Falling-Ball Experiments

3.1 Numerical Methods. Boundary element method (BEM) simulations are used in this study to model the flow of neutrally buoyant suspensions of uniform spheres in Newtonian fluids. A basic feature of the method is that the object needs to be discretized into elements only along the boundaries. These are line contours for a two-dimensional flows and the containing surfaces for three-dimensional flows. The basic governing equations of the problem are solved for the whole domain but written in a manner that the unknowns involved are the values of the parameters (such as velocity, traction) at nodes located on the boundary only. Because no nodes exist in the interior of the object, the unknowns of the problem are reduced significantly. This reduction decreases the number of equations that must be solved. However, the resulting matrix is fully dense. Having determined the nodal parameters on the boundary, the governing equations can be used again to derive simple algebraic relations to obtain values at the interior points with reference to parameters along the boundary nodes. A detailed description of the BEM can be found elsewhere [15,16].

The three-dimensional boundary element mesh of the spherical ball and the tube is shown in Fig. 1. There are 120 and 3200 elements on the ball and the surface of the tube, respectively. No-slip boundary conditions are implemented on the surfaces of the tube and the falling ball, that is $u=0$, $v=0$, and $w=0$ are set on the surfaces of the tube (including the hemispheric bottom end)

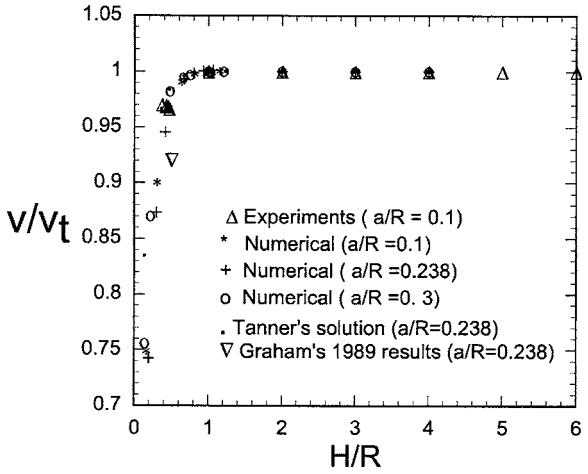

Fig. 2 Falling balls reach terminal velocity in Newtonian fluids when the gap between the falling ball and the ends of the tube is greater than the tube radius. Here *H* is the gap between the falling ball and the surfaces of the fluid, and v_t is the terminal velocity. Included are data from Tanner [17] and Graham [14].

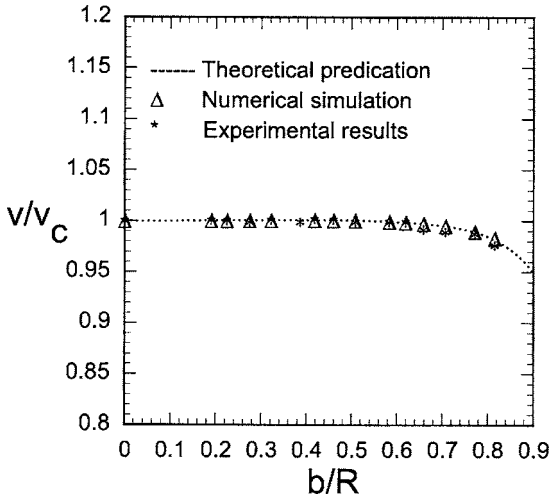

Fig. 3 The falling-ball velocity, *v*, of the ball when falling off-center normalized by the velocity of the ball falling along the centerline, v_c, as a function of the dimensionless eccentricity. Note *a*/*R*=0.1 in this figure.

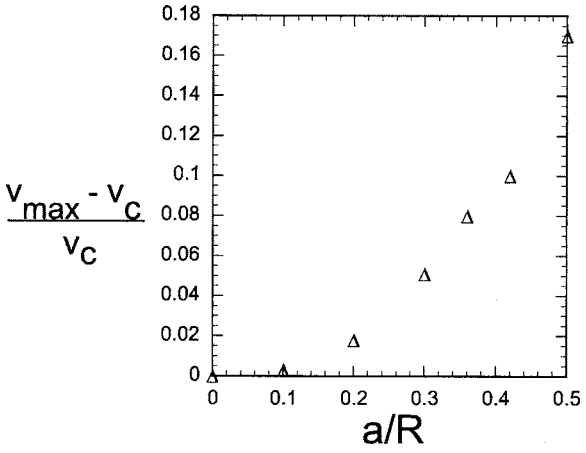

Fig. 4 Maximum increased falling-ball velocity as a function of the ratio of ball radius, *a*, to tube radius, *R*. Here v_{max} is the maximum falling-ball velocity for different sized balls when falling off-center.

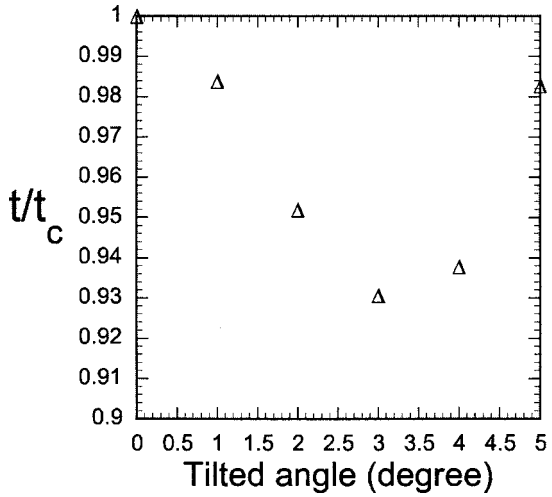

Fig. 6 Numerically simulated normalized time for the falling ball to pass through the timing zone chosen as 5*R* from the top surface and 4*R* from the bottom of the cylinder plotted against the tilt angle of the tube. Results are for *a*/*R*=0.3.

and the falling ball, where u, v, and w are the velocity components in the x, y, and z directions, respectively. However, on the top surface of the tube, free surface boundary conditions are set, that is, $t_x=0$, $t_y=0$, and $w=0$ on the top surface of the tube, where t_x and t_y are the traction components in the x and y directions, respectively.

3.2 Experimental Methods. It was shown in previous work that the larger the a/R ratio in the falling-ball geometry, the more susceptible to error and less reproducible are the experiments [14]. The intent of these experiments was to quantify these errors and reproducibility. We also wished to establish baseline data for the falling-ball tests and to produce a guideline for performing the falling-ball experiments in geometries that are the least sensitive to experimental error and with the most reproducibility.

The settling balls, obtained from Salem Specialty Ball Co., Inc. (West Simsbury, CT), were made of Anti-Friction Bearing Manufacturer's Association (AFMBA) grade 200 brass (specific gravity 8.5) with a tolerance of ±0.005 mm in sphericity and 0.025 mm in diameter. The cylinders were either custom built from plastic tube to achieve the desired length-to-diameter ratio or commercially available glass cylinders when the aspect ratio was appropriate. The cylinders ranged in length from 216 to 1707 mm. The inside diameter of the cylinders was measured using a Mitutoyo Absolute Digimatic micrometer with a tolerance of ±0.03 mm. Timing marks were evenly placed on the cylinder wall all the way from the top of the cylinder to the bottom. The settling spheres were timed with stop watches with a tolerance ±0.01 s for the fluids that were transparent through measured zones in the cylinder. The velocity of the settling balls was determined by measuring time and distance between marks as the balls settled toward the bottom of the cylinder. The beginning of the measurement zone was at least one cylinder diameter from the top fluid level in the cylinder, and ended as the settling ball hit the bottom. Lids were machined to fit the cylinders and holes were drilled at measured positions in order to insure the ball drop started along known positions of the containing cylinder.

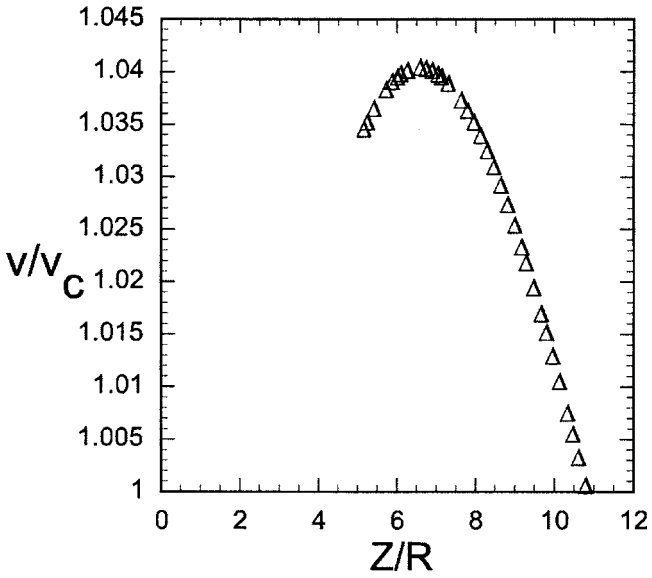

Fig. 5 Numerically simulated vertical settling velocity of the falling ball plotted against the distance between the center of the falling ball to the top surface of the fluid, *Z*, for the specific cases when the tube is tilted at 3° and *a*/*R*=0.3. Data are shown for the measurement zone chosen as 4*R* from the top surface and 3.5*R* from the bottom of the cylinder.

The test fluid was UCON oil HB-90,000 a polyethylene glycol from Union Carbide Corp. A series of dynamic and oscillatory rheometry experiments were used to determine that, under the testing conditions, there were no shear thinning or measurable normal stress differences. Experiments were performed in an Ubbelohde viscometer tube (Cannon Instrument Co., State College, PA) to determine the viscosity of the test fluid (49.4 Pa·s at 25°C). These capillary viscometer results are accurate to within <1% according to the manufacturer. At 25°C, UCON has a specific gravity of 1.0833 as determined by using a Mettler-Toledo Density Meter. In our falling-ball tests, the temperature was carefully controlled in these experiments to ±0.1°C. This is equivalent to a change in viscosity of the test fluid of 0.22 Pa·s. Fresh balls were characterized, weighed, and thermally equilibrated before each drop.

4 Results and Discussion

4.1 End Effect Study. A series of fully three-dimensional transient calculations was performed using the mesh and boundary conditions already described. In these simulations, the sphere was started just beneath the surface of the liquid from rest and allowed to settle to the bottom of the tube. The results of the study are shown in Fig. 2. The simulation and experimental observations showed excellent agreement. The predicted end-effect zone was

Table 1 Contributions of each independent variable to the overall error in the accuracy in estimating the viscosity of UCON 90,000

Variable	Nominal value	Uncertainty	Formula	% error	% of total error
a	3.96 mm	0.01	$\left(2-\frac{3\rho_f}{\rho_d}+\kappa\lambda\frac{\partial\kappa^{-1}}{\partial\lambda}\right)\frac{\Delta a}{a}$	0.75	20.3
α	0°	1	$\tan(\alpha)\Delta\alpha$	0.69	18.6
t_f	57 s	0.3	$\frac{\Delta t_f}{t_f}$	0.52	14.1
T	25°C	0.1	$\frac{\beta\Delta T}{T^2}$	0.46	12.4
R	11 mm	0.03	$\kappa\lambda\frac{\partial\kappa^{-1}}{\partial\lambda}\frac{\Delta R}{R}$	0.42	11.4
L_f	25 mm	0.1	$\frac{\Delta L_f}{L_f}$	0.40	10.8
b	0 mm	0.1	$\frac{\partial\kappa}{\partial b}\frac{\Delta b}{\kappa}$	0.26	7.0
m_f	0.26 g	0.0003	$\frac{\rho_f}{\rho_d}\frac{\Delta m_f}{m_f}$	0.13	3.5
g	980 cm/s^2	0.1	$\frac{\Delta g}{g}$	0.01	0.0
ρ_l	1.0833 g/cm^3	0.001	$\frac{\Delta\rho_l}{\rho_d}$	0.01	0.0
Total				3.7	

less than one cylinder radius up from the bottom and down from the top. The falling-ball reaches its terminal velocity approximately one tube radius from its starting point. As shown in Fig. 2, the velocity profile normalized by the steady-state velocity is to a first approximation only a function of the gap distance between the ball surface and the cylinder bottom. These numerical experiments established that in pure Newtonian fluids the settling-ball size has little effect on the length of the end-effect zone. The results are in good agreement with Tanner's analysis [17] and Graham's predication [14].

4.2 Off-Center Effect Study. In these simulations, the velocity for a falling sphere as a function of the distance from the centerline axis of the containing cylinder was determined away from the cylinder ends to minimize the end effects. The results of the study are shown in Figs. 3 and 4. Here the radial distance from the axis of the tube, b, is normalized with the radius of the containing tube, R.

Shown in Fig. 3 is the velocity of the falling ball normalized with the centerline velocity as a function of b/R. Though it cannot be seen due to the scale, as b/R increases that the velocity first increases slightly ($\leqslant 0.5\%$). This is due to less drag force posed upon the falling ball by the cylinder wall [9]. The velocity in the falling-ball test goes through a maximum as the ball starts further and further off-center. The velocity then decreases as drag forces start to increase when the trajectory brings the ball very close to the wall. It is shown in Fig. 4 that the maximum falling-ball velocity associated with an eccentric trial increases dramatically as the ratio a/R increases.

4.3 Nonvertical Tube Effect Study. If the cylinder is not perfectly vertical, the problem becomes more complicated. The actual falling length is shorter than the distance between the timing marks due to the tilt of the tube. Less time is required to fall between timing marks, giving an apparent velocity greater than that experienced with a vertical tube. Also, the ball inevitably falls off-center due to the tilt of the tube causing the forces on the falling ball to be different from those of a vertical tube. The falling velocity is different from what is experienced for on-center trajectories. There is no theory available for this tilt effect, though one could envision asymmetric wall effects and differing drag forces altering the forces on the falling ball, and, hence, the velocities. A transient BEM code was used to calculate the time required for the ball to pass between marks in the nonvertical tube geometry.

In these simulations, the tube is tilted at a small angle, α, and initially the ball is on the axis of the tube. Numerical results for the case when the tube is tilted at 3° are presented in Fig. 5, where the apparent vertical settling velocity is plotted against the distance from the bottom of the tube. Note $l/R=15$ and $a/R=0.3$, where l is the tube length. When the tube is tilted, it is seen that the falling ball's apparent vertical settling velocity increases by

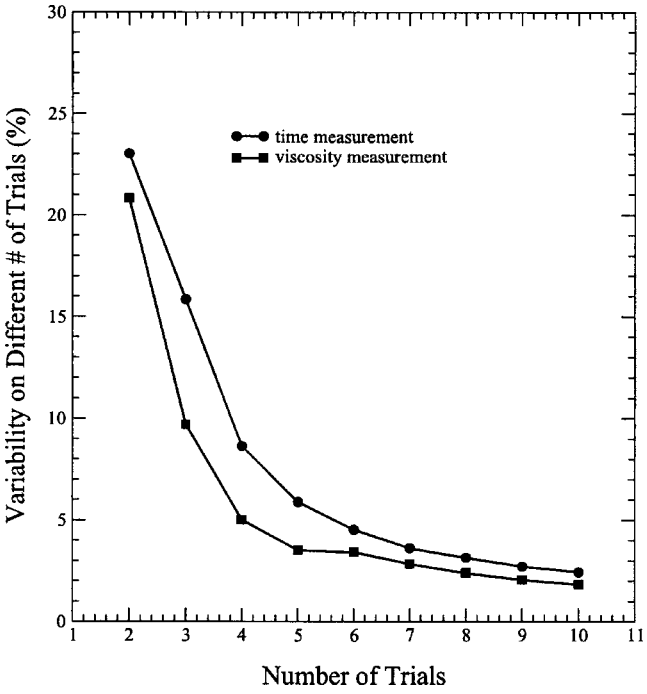

Fig. 7 Variability in 95% percent confident limit decreases as the number of trials increases.

about 4% and then begins to decrease as it gets closer to the cylinder walls. This effect is the sum of the shorter traveling distance and the varying drag effect caused by the wall.

Figure 6 shows the numerically simulated normalized falling time for the ball to pass through the timing zone plotted against the tilt angle of the tube. Based on the typical experimental measurement, the timing zone is chosen to be five tube radii from the top surface and four tube radii from the bottom surface. It is seen that a small angle of tilt ($\leqslant 5°$) of the tube will create a maximum of about 7% decrease in the settling time of the falling ball (at about 3°). When the tilt angle is within 1°, there is only a marginal decrease of the time of flight of the falling ball ($\leqslant 2\%$).

4.4 Reproducibility and Error Analysis. The magnitude of relative error in calculating the viscosity can be bounded by estimating the magnitude of each of the terms in Eqs. (21) and (23). Based on experiments and numerical simulations, we give an example on how to use Eqs. (21) and (23) to analyze data. The results of the analysis are shown in Table 1.

Table 1 shows that the largest errors in accuracy for these experiments as measured by percent of the total error were ball size, tilt degree, and measured time. The timing error is mostly due to human error which is about ±0.3 s for an average technician in our experiments. These experiments used a set of falling balls in a series of different tubes. Several of the factors, such as the tilt degree and measured time, can be improved by using a careful and skilled technician. Other random fluctuations, such as ball size and fall distance, can be improved by using the same ball and tube for all experiments, if practical. As shown in Fig. 7, random fluctuations can be reduced by correcting for variations in the apparatus geometry and converting the falling times to viscosities.

The reproducibility of the viscosity estimate is independent of the accuracy. Shown in Table 2 is the relative contribution of the variables in determining the reproducibility of the viscosity estimates. Many of the same important factors as described above in the accuracy analysis are involved, but the relative weighting is different. Note this analysis is based on taking a single falling-ball test to estimate the properties of a Newtonian fluid with a well-characterized viscosity. A single test gives an estimate of the viscosity, but there is no information about the quality of the measurement.

Table 2 Contributions of each independent variable to the overall reproducibility in estimating the viscosity in a single tube of UCON 90,000

Variable	Nominal value	Uncertainty	% error	% of total error
α	0°	1	0.69	36.3
t_f	57 s	0.3	0.52	27.4
T	25°C	0.1	0.46	24.2
b	0 mm	0.1	0.26	13.7
ρ_l	1.0833 g/cm^3	0.001	0.01	0.0
Total			1.9	

Figure 7 shows the number of experiments is a major factor in determining the reproducibility of a set of experiments. For two tests, the 95% confidence limits on the mean are more than ±20%. However, the 95% confidence limits reduce to ±3%–5% for five trials. This reduction in the uncertainty emphasizes how important multiple falling-ball tests are in obtaining high accuracy results. Note the difference between falling-ball test results averaged over five trials and the measurements of Ubbelohde viscometer tube is less than 5%.

5 Conclusions

In this paper, a combination of theoretical analysis, experiments, and numerical simulations was used to study falling-ball viscometers in Newtonian fluids. The sources that affect the accuracy and reproducibility of these tests were identified. Based on these studies, the following recommendations are presented in order to obtain high precision results.

Use falling balls that are very consistent in size, sphericity, and surface finish. Higher AFMBA grade balls provide more consistent results. Choose a falling ball and cylinder to get a small a/R ratio ($a/R \leqslant 0.1$) which will reduce off-center error dramatically. Make sure that the apparatus is vertical and the ball falls on axis. Multiple trials improve reproducibility and reduce uncertainty in the measurement. Use the material properties such as viscosity rather than the falling time to account for minor variations in falling ball apparatus. Improve the accuracy of the time measurement.

Acknowledgment

The authors would like to thank Jay Mehta and Professor Marc S. Ingber for their help and thoughtful discussions. The authors would also like to thank Dr. David Chaffin and Dr. Sam Subia for their help in numerical modeling. The authors gratefully acknowledge support for this work from Noramco Inc.; the Advanced Research Program from the Texas Higher Education Coordinating Board; the U.S. Department of Energy, Division of Chemical Sciences, Geosciences and Biosciences, Office of Basic Energy Science; U.S. Department of Energy, Environmental Projects Division; National Energy Technology Laboratory, Los Alamos National Laboratory, and Sandia National Laboratories. Sandia National Laboratories is a multiprogram laboratory operated by Sandia Corporation, a Lockheed Martin Company, for the United States Department of Energys National Nuclear Security Administration under Contract No. DE-AC04-94AL85000.

References

[1] Tanner, R. I., 1963, "End Effects in Falling-Ball Viscometry," J. Fluid Mech., **17**, pp. 161–170.

[2] Van Wazer, J. R., Lyons, J. W., Kim, K. Y., and Colwell, R. E., 1963, *Viscosity and Flow Measurement: A Laboratory Handbook of Rheology*, Interscience Publishers, New York.

[3] Stokes, G. G., 1851, "On the Effect of the Internal Friction of Fluids on the Motion of Pendulums," Trans. Cambridge Philos. Soc., **9**, pp. 8–106.
[4] Faxén, H., 1923, "Die Bewegung Einer Starren Kugel Längs der Achse Eines Mit Zäher Flüssigkeit Gefüllten Rühres," Ark. Mat., Astron. Fys., **17**(1), pp. 45–46.
[5] Bohlin, T., 1960, "On the Drag on a Rigid Sphere Moving in a Viscous Liquid Inside a Cylindrical Tube," Trans. R. Inst. Tech. (Stockholm), **155**, pp. 1–63.
[6] Haberman, W. L., and Sayre, R. M., 1958, "David Taylor Model Basin Report No. 1143," U.S. Navy Department, Washington DC.
[7] Brenner, H., and Happel, H., 1958, "Slow Viscous Flow Past a Sphere in a Cylindrical Tube," J. Fluid Mech., **4**, pp. 195–213.
[8] Famularo, J., 1962, "D. Eng. Sci. Thesis," Ph.D. thesis, New York University, New York.
[9] Happel, J., and Brenner, H., 1965, *Low Reynolds Number Hydrodynamics*, Martinus Nijhoff Publishers, Prentice-Hall, Englewood Cliffs, NJ.
[10] Falade, A., and Brenner, H., 1985, "Stokes Wall Effects for Particles Moving Near Cylindrical Boundaries," J. Fluid Mech., **154**, pp. 145–162.
[11] Higdon, J. J. L., and Muldowney, G. P., 1996, "Resistance Functions for Spherical Particles, Droplets and Bubbles in Cylindrical Tubes," J. Fluid Mech., **298**, pp. 193–210.
[12] Ambari, A., Gauthier-Manuel, B., and Guyon, E., 1985, "Direct Measurement of Tube Wall Effect on the Stokes Force," Phys. Fluids, **28**(5), pp. 1155–1167.
[13] Ilic, V., Tullock, D., Phan-Thien, N., and Graham, A. L., 1992, "Translation and Rotation of Spheres Settling in Square and Circular Conduits: Experiments and Numerical Predictions," Int. J. Numer. Methods Fluids, **18**(6), pp. 1061–1068.
[14] Graham, A. L., Mondy, L. A., Miller, J. D., Wagner, N. J., and Cook, W. A., 1989, "Numerical Simulations of Eccentricity and End Effects in Falling Ball Rheometry," J. Rheol., **33**(7), pp. 1107–1128.
[15] Ingber, M. S., 1989, "Numerical Simulation of the Hydrodynamic Interaction Between a Sedimenting Particle and a Neutrally Buoyant Particle," Int. J. Numer. Methods Fluids, **9**, pp. 263–273.
[16] Dingman, S. E., 1992, "Three-Dimensional Simulation of Fluid-Particle Interactions Using the Boundary Element Method," Ph.D. thesis, The University of New Mexico, Albuquerque, NM.
[17] Tanner, R. I., 1963, "End Effects in Falling-Ball Viscometry," J. Fluid Mech., **17**(2), pp. 161–170.

Surfactant Use for Slug Flow Pattern Suppression and New Flow Pattern Types in a Horizontal Pipe

R. J. Wilkens
D. K. Thomas
S. R. Glassmeyer

University of Dayton,
300 College Park,
Dayton, OH 45469-0246

A set of experiments was performed to study flow pattern suppression in horizontal air-water pipe flow by means of surfactant additive. Results suggest that addition of the surfactant to the gas-liquid flow significantly reduces the occurrence of slug flow. In addition, previously unreported flow patterns were observed to exist between slug and dispersed bubble flows. It is concluded that new mechanisms for slug flow transition need to be considered. [DOI: 10.1115/1.2062747]

Introduction

Drag reduction and flow pattern suppression are important to the increase of oil and gas production rates and to reduce recovery and transportation costs. Drag reducing agents (DRA) have been investigated for industrial and military applications since the discovery of Toms [1]. In addition to drag reduction, researchers have indicated that in gas-liquid flow DRA can reduce the range of conditions for which some flow patterns occur [2,3]. Of particular importance is the reduction or elimination of slug flow occurrence. In slug flow gas forces slugs of liquid to completely fill the pipe diameter, accelerate to the gas velocity, and dramatically increase pressure drop.

Clearly the most through work in the DRA area has been the study of polymer-based DRA for single-phase drag reduction. Two critical issues exist with polymer DRAs in terms of hydrocarbon transport; dry out and shear degradation. Polymer DRA requires a co-solvent. In the presence of a gas the co-solvents have a tendency to dry out, causing precipitation of the DRA. Shear degradation is a phenomenon that has been well documented. Under high shear conditions (e.g., a pumping station), long polymer DRAs chains are permanently broken, thus reducing or eliminating the drag reduction capabilities of the DRA. It is common practice to reinject the DRA downstream of pumping stations.

These critical issues could be eliminated with the use of surfactant drag reducing agents (SDRA). Surfactants are soluble in most liquid phases and therefore do not require a co-solvent and are thus not subject to dry out. Surfactants go to the liquid surface and act to reduce the surface tension. Above the critical micelle concentration (CMC) additional surfactant molecules no longer migrate to the interface and they begin to form micelle structures in the liquid. It has been proposed that in single-phase flow, surfactant drag reduction occurs if the micelle structures formed are rodlike [4]. The benefit of these self-assembling structures is that they break apart when subjected to conditions of high shear but then reassemble through fast self-assembly kinetics downstream. This is an additional benefit over a polymer DRA in that it does not need to be re-injected following a high-shear condition (i.e., it reassembles).

Limited work has been reported in the area of SDRA in multiphase flow [2]. It has been shown that drag reduction can occur in stratified gas-liquid flow with low concentrations of surfactant (i.e., low enough not to form drag reducing micelles) [5]. Glassmeyer [6] proposed that this is due to the reduction of interfacial stress and modification of interfacial wave structures. Waters and Grotberg [7] studied the motion of surfactant laden liquid plugs in airways. While their models are not of a scale to directly apply to multiphase transport lines (e.g., capillary effects were significant at their scale), they did make two pertinent observations to the present work. As the surfactant concentration was increased there was an increase in the elasticity parameter (related to the Marangoni number) and subsequently an increase in pressure drop across a liquid plug. The increase of surfactant concentration also decreased the pressure drop required for the liquid plug to burst. Thus, increasing the surfactant concentration leads to a decrease in the stability of the liquid plug.

In multiphase flow numerous mechanisms are available to reduce pressure loss, including: bulk (single phase) mechanisms, wall roughness reduction, reduction of interfacial shear stress, reduction of effective density (vertical flow), change in liquid holdup, change in flow pattern. Proper micelle formation is necessary for the bulk mechanism of surfactant drag reduction to occur, as described previously, and has a primary affect in reducing the drag between the liquid and the wall. Wall roughness reduction can be effective in gas or liquid flow in terms of drag between the fluid and the wall. In gas-liquid flow there is an interfacial roughness that can be affected by surfactants.

Surfactants have been shown to reduce the occurrence of slug flow [5]. While a general literature review of flow patterns is not in the scope of this work, the change in flow pattern and newly formed flow patterns due to the addition of surfactant are addressed here due to their potential to reduce pressure losses. Therefore it is important to first review the commonly reported gas-liquid pipe flow patterns for horizontal flow (Fig. 1).

Consider concurrent air/water flow in a horizontal pipe. At low gas and liquid velocities the two phases flow separately, segregated by gravity, with a smooth interface. This flow is termed *stratified smooth* [Fig. 1(*a*)]. With increasing gas velocity and low liquid velocity the interface becomes wavy. This flow is termed *stratified wavy* [Fig. 1(*b*)]. At low gas and moderate liquid velocity the liquid fills the pipe while the gas forms pockets that gently sweep liquid away from the upper section of the pipe in full pipe regions. This flow is termed *plug flow* [Fig. 1(*c*)]. As the gas velocity increases from plug flow, the liquid filled region develops rotation in the leading section, entraining air bubbles and passing them through the body of the liquid. This type of flow is termed *slug flow* [Fig. 1(*d*)]. Slug flow is of great interest in the present work. In addition to enhanced pressure drop, slug flow creates tremendous forces at pipe beds and enhanced corrosion rates.

Four additional commonly reported flow types exist for the air/

Contributed by the Fluids Engineering Division of ASME for publication in the JOURNAL OF FLUIDS ENGINEERING. Manuscript received June 25, 2004; final manuscript received July 12, 2005. Assoc. Editor: Steven Ceccio.

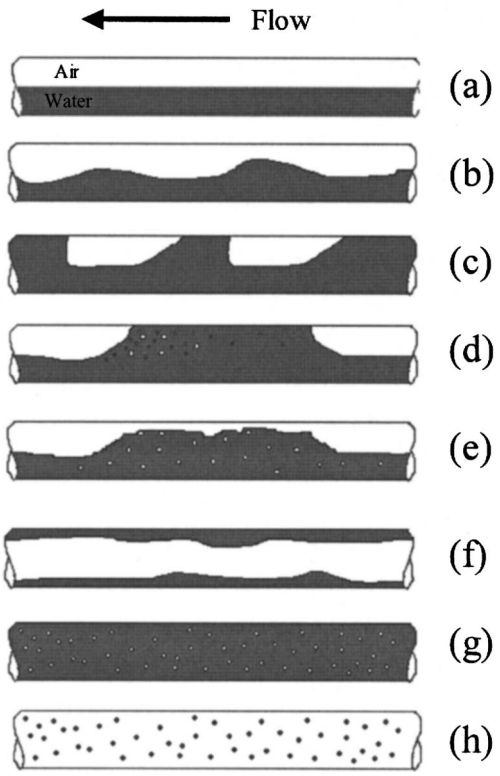

Fig. 1 Common gas-liquid horizontal flow patterns: (a) stratified smooth, (b) stratified wavy, (c) intermittent plug, (d) intermittent slug, (e) pseudoslug, (f) annular, (g) dispersed bubble, (h) mist.

water system. These include *pseudo-slug* [Fig. 1(*e*)], *annular* [Fig. 1(*f*)], *dispersed bubble* [Fig. 1(*g*)], and *mist* [Fig. 1(*h*)]. Pseudoslug flow is similar to slug flow but allows gas to pass through the slugs from the tail section. The liquid does not form a competent bridge and the slug travels at a lower velocity than in true slug flow. Annular flow occurs at very high gas velocities and is observed as a central gas core with wetted walls (due to wave spreading and droplet deposition). Dispersed bubble flow occurs at very high liquid flow rates. The liquid forms a continuous competent bridge across the pipe while the gas moves through the liquid bulk in small bubbles due to the high level of turbulence. Mist flow occurs at very high gas and low liquid velocities. The gas fills the pipe while the liquid is fully entrained in the turbulent gas flow.

Often the intermittent flow patterns (plug, slug, pseudoslug) are lumped together and termed *intermittent*. It is necessary in this work to be more specific.

Methodology

Experiments were arranged to study the effects of surfactant concentration and surface tension on gas-liquid flow pattern. A horizontal multiphase flow loop (Fig. 2) was used for the evaluation of the flow patterns. A predetermined liquid composition was charged into a 200-gal(0.76 m^3) storage/separation tank. The liquid was pumped with a 3-hp(2.2 kW) centrifugal pump through a flow metering section to the inlet of the multiphase pipe. Air was supplied at 100 psi(0.79 MPa). It also flowed through a metering section to the multiphase pipe inlet.

The multiphase flow occurred in a 2-in Sch. 40 (0.052 m-id) clear PVC pipe. For clarity, all locations in the piping system are listed by their length to diameter (L/D) ratio. The storage/separation tank was located at $L/D=300$. The flow patterns were visually determined at $L/D=275$. In addition flow patterns were videotaped at $L/D=250$.

After the multiphase flow entered the separator, the air was vented to the atmosphere. The pressure in the test section is effectively atmospheric (<1 psig). The temperature of the fluid in the test section ranged from 30 to 40°C. This range is not expected to have a significant impact on the flow patterns observed.

Both hard water, 10 grains per gallon (gpg) municipal supply, and soft water, 0 gpg deionized, were available for experimentation. Two surfactants were used in this study: sodium dodecyl sulfate (SDS) and linear alkyl benzene sulphonate (LAS).

Instrumentation details for this system have been reported elsewhere [6].

Results/Discussion

Several new flow patterns were observed that have been previously unreported to the authors' knowledge. A sketch summary of the new flow patterns is shown in Fig. 3.

Stratified Wavy With Bubbles [Fig. 3(*a*)]. This flow pattern is similar to stratified wavy (Fig. 2) but with bubbles on the gas-liquid interface. These bubbles are not present in sufficient quantity to cover the entire interface and suppress waves as in stratified gas-bubble-liquid flow (discussed later).

Intermittent Bubble Top Plug [Fig. 3(*b*)]. This flow pattern is like plug flow; however the plug cannot reach the top of the pipe due to a layer of bubbles.

Intermittent Bubble Top Slug [Fig. 3(*c*)]. Like intermittent bubble top plug flow, the liquid in a bubble top slug does not

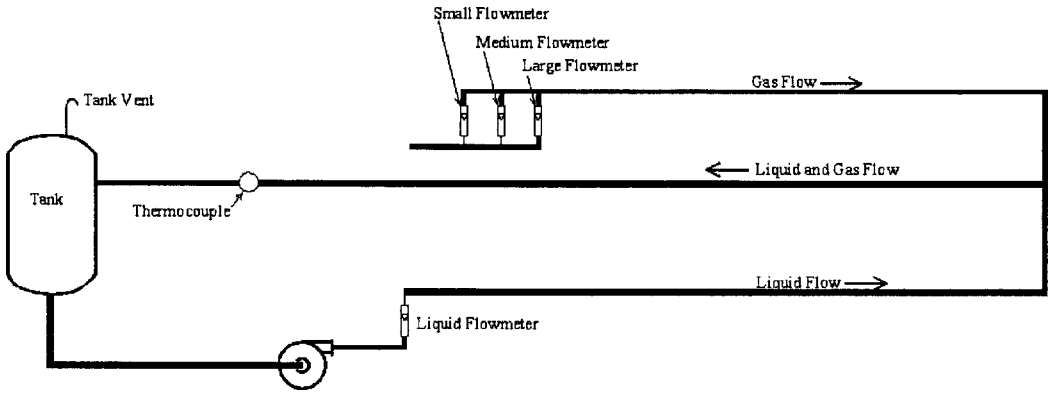

Fig. 2 University of Dayton multiphase flow loop

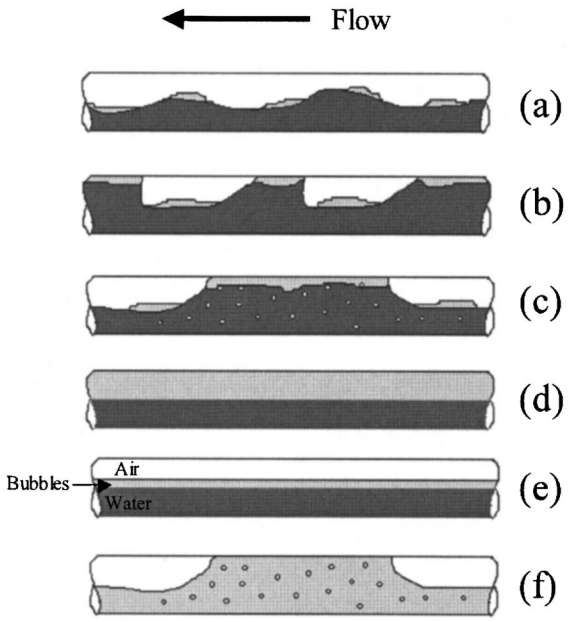

Fig. 3 New flow patterns: (a) stratified wavy with bubbles, (b) intermittent bubble top plug, (c) intermittent bubble top slug, (d) stratified bubble-liquid, (e) stratified gas-bubble-liquid, (f) intermittent bubbly slug

reach the top of the pipe due to a layer of bubbles. This is similar to pseudo-slug observations (Fig. 2) but with a layer of bubbles on top of the slugs as opposed to a gas pocket.

Stratified Bubble-Liquid [Fig. 3(*d*)]. This flow pattern can be visualized as two-phase stratified flow where the lower phase is liquid and the upper phase is a layer of gas bubbles (like foam).

Stratified Gas-Bubble-Liquid [Fig. 3(*e*)]. This flow pattern is similar to stratified bubble-liquid but has three distinct regions. The lower region is liquid, the middle is a layer of bubbles, and the upper region is gas.

Intermittent Bubbly Slug [Fig. 3(*f*)]. This is a slug flow pattern with gas passing along a film of bubbles and pushing slugs of bubbles down the pipe.

For comparison to previous work a flow pattern map for air and water was generated (Fig. 4). The legend for Fig. 4 (and all flow pattern maps) has been placed in Table 1. The results for air/water flow without surfactant were deemed reasonable when compared to the flow pattern map of Mandhane et al. [8]. The solid symbols represent intermittent flow patterns. Four flow patterns were observed for this range of conditions. All patterns fell largely within their designated regions. The transition from stratified to intermittent flow was found to occur at a superficial liquid velocity of around 0.1 m/s. Intermittent flow was observed, and expected, to occur well above a superficial liquid velocity of 1.0 m/s.

Figure 5 is a flow pattern map for air and deionized water (0 gpg) with 220 ppm SDS. The surface tension of this liquid was 64 mN/m (dyn/cm). In comparison to the air/water flow pattern map (Fig. 4) there are 3 additional flow patterns: stratified bubble-liquid, intermittent bubble top slug, pseudoslug.

Table 1 Legend for Figs. 4–8

+	stratified smooth
×	stratified wavy
■	stratified bubble-liquid
⊠	stratified gas-bubble-liquid
✱	stratified wavy with bubbles
●	intermittent plug
■	intermittent slug
▨	intermittent bubbly slug
○	intermittent bubble top plug
□	intermittent bubble top slug
◇	pseudo-slug
△	dispersed bubble
—	[8]

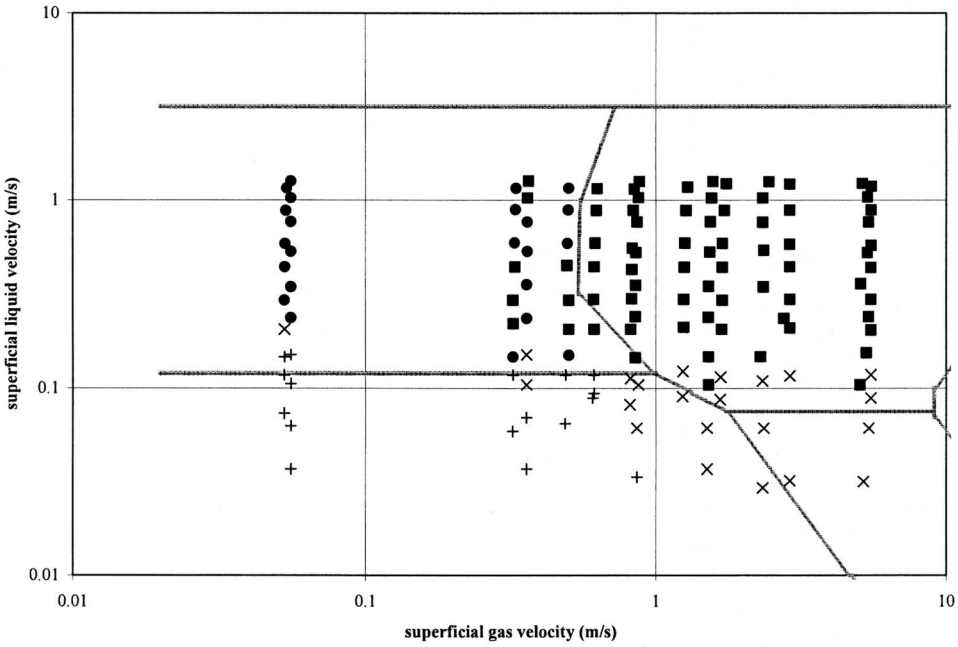

Fig. 4 Experimental flow pattern map for air/water (surface tension=72 mN/m). Shaded lines are the flow pattern map as observed in the literature [8]. The data shows good agreement with expected behavior.

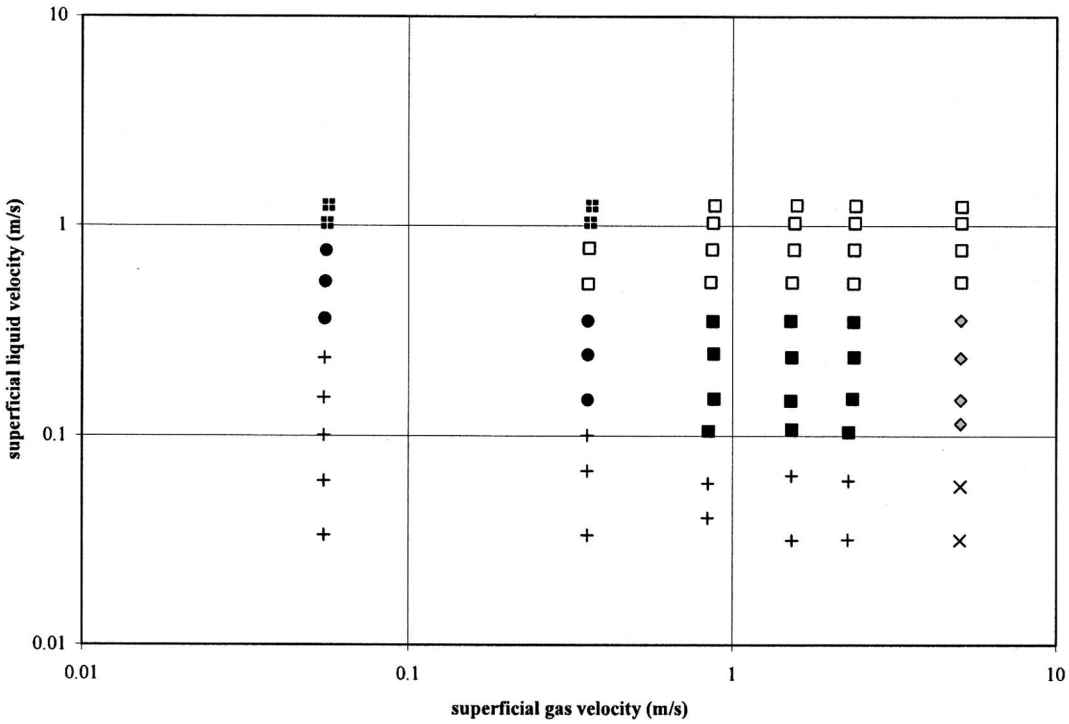

Fig. 5 Flow pattern map for air/220 ppm SDS in 0 gpg water (surface tension=64 mN/m). Note that the intermittent slug pattern has been significantly suppressed in favor of intermittent bubbly slug pattern, especially at high superficial velocities.

The new flow patterns occur largely in place of slug flow. At high gas flow rates pseudoslug flow ensues. At high liquid flow rates intermittent bubble top slug flow occurs. This is unique as true slug flow is only observed to occur up to a superficial liquid velocity of about 0.4 m/s. At low gas and high liquid flow rates the plug flow is replaced with stratified bubble-liquid flow. No change is apparent at low liquid flow rates; the transition from stratified wavy/smooth to intermittent matches that of air/water within the resolution of the data collected.

Figure 6 is a flow pattern map for air and deionized water with 1340 ppm SDS. The surface tension of this liquid was 48 mN/m. This represents both an increase in surfactant concentration and a

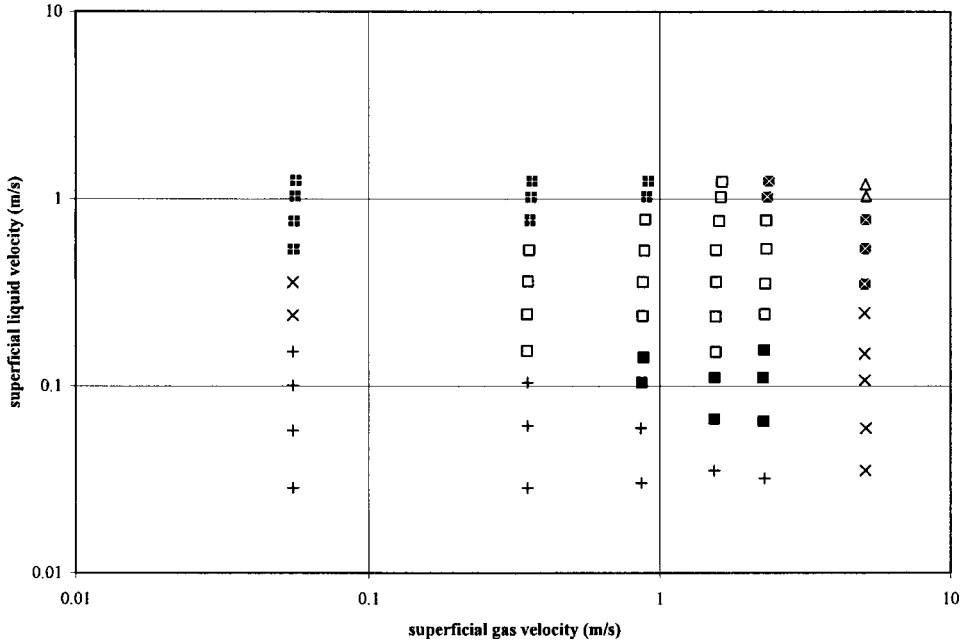

Fig. 6 Flow pattern map for air/1340 ppm SDS in 0 gpg water (surface tension=48 mN/m). Note that the intermittent slug pattern has been almost completely suppressed in favor of intermittent bubbly slug pattern.

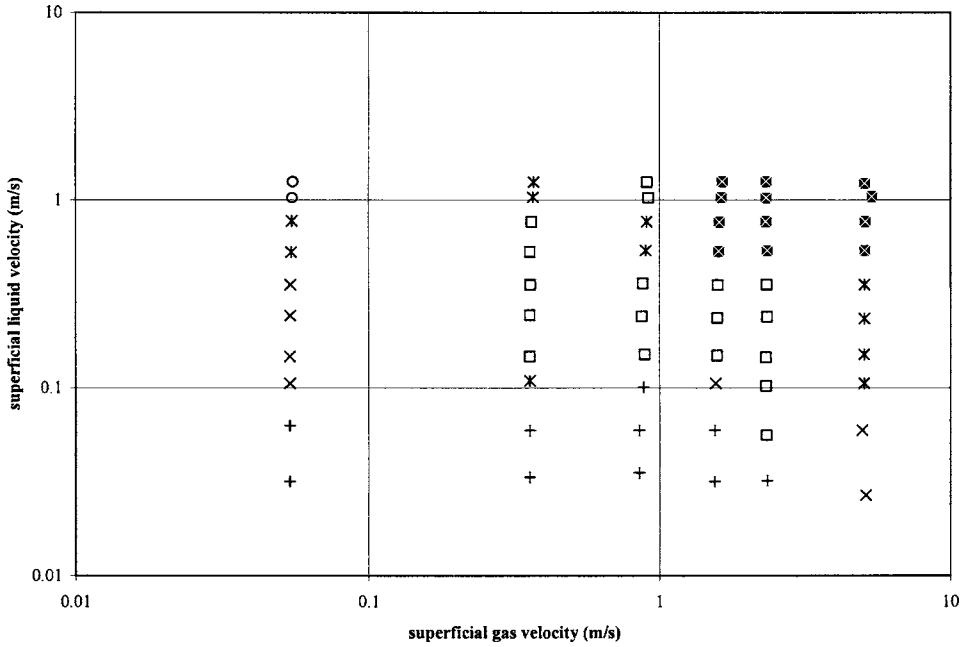

Fig. 7 Flow pattern map for air/1140 ppm SDS in 10 gpg water (surface tension =30 mN/m). Note that the intermittent slug flow pattern has been totally suppressed. Comparing this to Fig. 6 shows that surfactant addition is even more effective in suppression of slug flow pattern when the water is hard than when the water is deionized.

decrease in surface tension compared to the data presented in Fig. 5. By increasing the SDS concentration, 2 new flow patterns are observed (stratified gas-bubble-liquid and dispersed bubble) and 2 flow patterns are eliminated (plug and pseudoslug).

The range of conditions for slug flow existence is further decreased (i.e., only up to a superficial liquid velocity of about 0.2 m/s). For high liquid and gas flow rates, slug flow is replaced by stratified gas-bubble-liquid flow. A large region of the slug flow is replaced with intermittent bubble top slug flow. Plug flow is replaced by stratified wavy and stratified bubble-liquid flow. Little changes at the transition from stratified wavy/smooth to intermittent flow.

The observation of dispersed bubble flow occurs at the highest gas and liquid flow rates. The actual flow pattern was nearly indistinguishable between dispersed bubble and annular flow. A better technique for distinguishing these two flow patterns in surfactant flow is needed. It is also recommended that further data be collected at higher flow rates to determine whether the flow pattern transition was shifting significantly.

The increase of SDS in going from the conditions in Fig. 5 to the conditions in Fig. 6 represents an increase in concentration and a decrease in surface tension. The single-phase liquid properties did not change significantly (i.e., viscosity, density, shear stress [5]).

To isolate the effect of surface tension from surfactant concentration, a flow pattern map for air with 1140 ppm SDS in tap water (10 gpg) was created (Fig. 7). The surface tension of this liquid was 30 mN/m. For these conditions true slug flow was eliminated. Two new flow patterns (stratified wavy with bubbles and intermittent bubble top plug flow) were observed and the dispersed bubble flow pattern disappeared. Despite the lack of slug flow, the flow pattern map is still dominated by intermittent flow. However, intermittent flow has yielded more conditions to stratified flows at high liquid flow rates. The transition from stratified wavy/smooth to intermittent flow does not significantly change.

These conditions represented a further decrease in surface tension while decreasing the surfactant concentration. Thus it might be concluded that the surface tension is a driving factor in the suppression of slug flow. This would counter field observations of slug flow in oil and gas transport.

To further investigate the surface tension hypothesis a flow pattern map for air with 1375 ppm LAS in tap water (10 gpg) was created (Fig. 8). The surface tension of this liquid was 30 mN/m. This map is more like that of Fig. 6 (48 mN/m) than that of Fig. 7 (30 mN/m) indicating that surface tension is not the only missing factor in flow pattern determination (slug flow is observed up to about 0.3 m/s/superficial liquid velocity). The only additional flow pattern observed in Fig. 8 from Fig. 6 is intermittent bubbly slug flow at one condition of high gas and liquid flow rate. Figure 8 does appear to have more stratified gas-bubble and gas-bubble-liquid conditions than observed in Fig. 6. This is similar to what was observed in Fig. 7. As with all of the flow pattern maps, the transition from stratified wavy/smooth to intermittent does not appear to have changed significantly whereas the slug flow region appears to be disappearing from the top (i.e., at higher superficial liquid velocities).

It should be noted that SDS and LAS do not have the same molecular weight (the molar concentrations of surfactant in Fig. 6 and Fig. 8 are not similar). The molecular weight of SDS is 288 and the molecular weight of LAS is 348.

Conclusions

In addition to the summary of new flow patterns, several conclusions can be drawn from the multiphase flow observations. For a given surfactant system a decrease in surface tension causes a decrease in slug flow occurrence. The slug flow regime is largely replaced by a new stratified flow pattern at high liquid flow rates. These stratified flows have a layer of bubbles that appear to dampen wave growth and stabilize the interface. For such conditions, low gas rates yield bubble-liquid stratified flow and high gas rates yield gas-bubble-liquid stratified flow.

Surface tension had little affect on the stratified wavy/smooth to intermittent flow transition. This is most intriguing as many proposed mechanisms suggest wave instability as the mechanism for

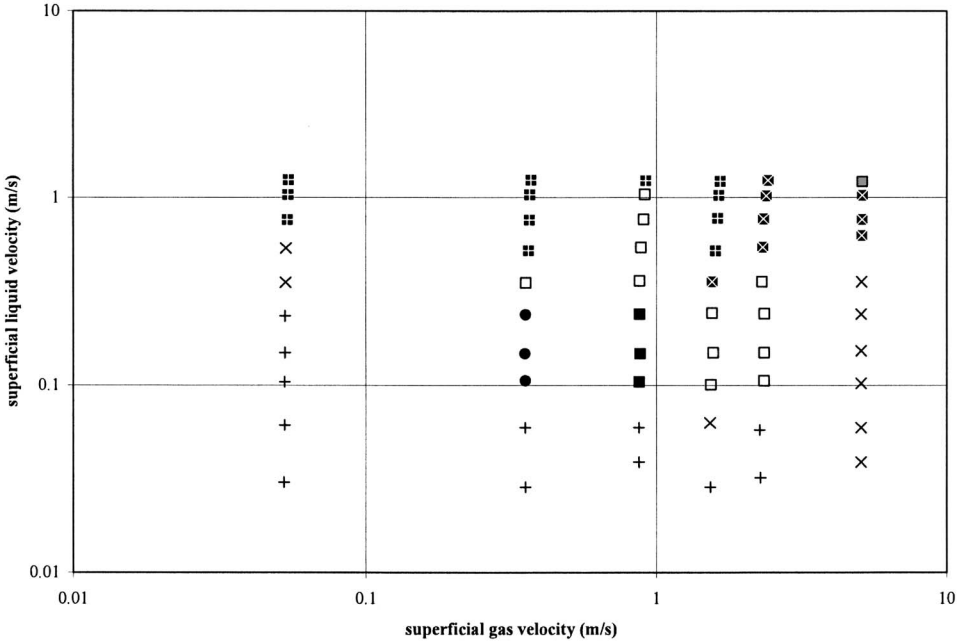

Fig. 8 Flow pattern map for air/1375 ppm LAS in 10 gpg water (surface tension=30 mN/m). Surface tension alone does not establish the flow pattern map.

slug formation from stratified flow. This does not preclude the reduction of slug flow at low liquid velocities. Rather, it is interesting to see it have a much greater affect at higher liquid velocities and to see the presence of new flow pattern types.

Surface tension is not the lone driving factor for slug flow suppression. It appears to be related to the tendency to foam. It is clear that the mechanisms for this phenomenon need to be identified to enhance the general understanding of gas-liquid flow.

No surface tension effect was observed for the annular or dispersed bubble transitions for the range of flow rates investigated. Using common mechanistic models for horizontal flow [9], none were expected.

References

[1] Toms, B. A., 1949, "Some Observations on the Flow of Linear Polymer Solutions through Straight Tubes at Large Reynolds Numbers," in *Proceedings of the International Congress on Rheology*, Holland, Amsterdam, pp. II-135–II-141.

[2] Manfield, P. D., Lawrence, C. J., and Hewitt, G. F., 1999, "Drag Reduction With Additives in Multiphase Flow: A Literature Survey," Multiphase Sci. Technol., **11**, pp. 197–221.

[3] Kang, C., Jepson, W. P., and Gopal, M., 1999, "Effect of Drag-Reducing Agent on Slug Characteristics in Multiphase Flow in Inclined Pipes," J. Energy Resour. Technol., **121**, pp. 86–90.

[4] Ohlendorf, D., Inherthal, W., and Hoffman, H., 1986, "Surfactant Systems for Drag Reduction: Physico-Chemical Properties and Rheological Behaviour," Rheol. Acta, **26**, pp. 468–486.

[5] Glassmeyer, S. R., and Wilkens, R. J., 2002, "Drag Reduction of Surfactants in Multiphase Flow: The Effect of Hydrophobicity," Paper 95j, Annual AIChE National Conference, Indianapolis, IN.

[6] Glassmeyer, S. R., 2003, "Suppressing Intermittent Flow Patterns and Reducing Pressure Loss in Two-Phase Horizontal Pipe Flow Using Surfactants," M.S. thesis, University of Dayton, Ohio.

[7] Waters, S. L., and Grotberg, J. B., 2002, "The Propogation of a Surfactant Laden Liquid Plug in a Capillary Tube," Phys. Fluids, **14**, pp. 471–480.

[8] Mandhane, J. M., Gregory, G. A., and Aziz, K., 1974, "A Flow Pattern Map for Gas-Liquid Flow in Horizontal Pipes: Predictive Models," Int. J. Multiphase Flow, **1**, pp. 537–553.

[9] Taitel, Y., and Dukler, A. E., 1976, "A Model for Predicting Flow Regime Transitions in Horizontal and Near Horizontal Gas-Liquid Flow," AIChE J., **22**, pp. 47–55.

Relaxation Effects in Small Critical Nozzles

Aaron N. Johnson
e-mail: aaron.johnson@nist.gov

Charles L. Merkle

Michael R. Moldover

John D. Wright

National Institute of Standards and Technology,
100 Bureau Drive, Stop 8361,
Gaithersburg, Maryland, 20899-8361

We computed the flow of four gases (He, N_2, CO_2, and SF_6) through a critical flow venturi (CFV) by augmenting traditional computational fluid dynamics (CFD) with a rate equation that accounts for τ_{relax}, a species-dependent relaxation time that characterizes the equilibration of the vibrational degrees of freedom with the translational and rotational degrees of freedom. Conventional CFD ($\tau_{relax}=0$) underpredicts the flow through small CFVs (throat diameter $d=0.593$ mm) by up to 2.3% for CO_2 and by up to 1.2% for SF_6. When we used values of τ_{relax} from the acoustics literature, the augmented CFD underpredicted the flow for SF_6 by only 0.3%, in the worst case. The augmented predictions for CO_2 were within the scatter of previously published experimental data (±0.1%). As expected, both conventional and augmented CFD agree with experiments for He and N_2. Thus, augmented CFD enables one to calibrate a small CFV with one gas (e.g., N_2) and to use these results as a flow standard with other gases (e.g., CO_2) for which reliable values of τ_{relax} and the relaxing heat capacity are available. [DOI: 10.1115/1.2137346]

1 Introduction

Critical flow ventruis (CFVs), also called critical nozzles, have been used for decades as secondary standards for measuring large gas flows because they are passive, extraordinarily stable, and easy to use [1,2]. In an effort to exploit these desirable qualities at the lower flow ranges encountered in semiconductor processing (10 to 300 standard[1] $cm^3\ s^{-1}$), we used computational fluid dynamics (CFD) to predict the flow through a small, well-characterized CFV (nominal throat diameter $d=0.593$ mm).[2] In Fig. 1, we compare our CFD results with previously published measurements for four gases [3]. The variables used for this comparison are those conventionally used to describe CFVs. Thus, the ordinate is the discharge coefficient $C_d \equiv \dot{m}/\dot{m}_i$, where $\dot{m}$ is actual mass flow and $\dot{m}_i$ is the mass flow calculated using an idealized one-dimensional, inviscid model. The abscissa is the inverse square root of the Reynolds number: $\mathrm{Re}=4\dot{m}_i/\pi d\mu_o$ where μ_o is the viscosity evaluated upstream of the CFV at stagnation conditions. As shown in Fig. 1, the present CFD model predicts the mass flow through the small CFV for all four gases to within ±0.31% for flow rates spanning at least a factor of 4 for each gas. Previously existing CFD models and analytical predictions [4–11] account for several species-dependent effects (virial coefficients and temperature-dependent heat capacity) and for boundary layers and curvature of the sonic line. In order to obtain good agreement with the measurements for CO_2 and SF_6, we had to augment existing equilibrium CFD models to account for τ_{relax}, the species-dependent relaxation time that characterizes the equilibration of the vibrational degrees of freedom with the translational and rotational degrees of freedom. The relaxation time must be compared to $\tau_{transit}$, the average time required for a fluid element of fixed mass to move from the CFV inlet to the CFV throat. For any ISO standardized CFV geometry [12] (Fig. 2), the approximate transit time is $\tau_{transit} \approx 10d/c$ where d is the diameter of the throat and c is the speed of sound in the gas at the CFV throat. Thus, small CFVs, such as the one considered here for use at low flow rates, have short transit times and can encounter larger values of the ratio $\Gamma=\tau_{relax}/\tau_{transit}$. Conventional CFD and analytical theories for CFVs assume $\tau_{relax}=0$. Such theories agree with the present results for N_2 and He within their scatter (0.1%, root mean square); however, as shown in the lower panel of Fig. 1, conventional theories ($\tau_{relax}=0$) underpredict the flow through this small CFV by up to 2.3% for CO_2 and up to 1.2% for SF_6. The augmented CFD model provides better understanding of how gas species effects influence the discharge coefficient for both CO_2 and SF_6 in small CFVs. The results help to quantify the level of correction needed when a CFV is calibrated using a standard gas (e.g., N_2 or air, Ar, etc.) where $\tau_{relax}=0$, but applied to other gases (e.g., CO_2 or SF_6) where vibrational relaxation effects are prevalent.

Our CFD model characterizes the vibrational degrees of freedom within each fluid element by its energy $\varepsilon_{vib}(T_{vib})$, where T_{vib} is the vibrational temperature. As the gas flows through the CFV, the temperature of the external modes, T_{ext}, drops quickly while T_{vib} lags behind for molecules where Γ is close to or greater than unity. (Here, we follow Bhatia [13] who called the translational and rotational degrees of freedom "external modes.") To account for the lag, our CFD model couples the Navier-Stokes equations to a local relaxation equation that contains two species-dependent parameters. One is $\varepsilon_{vib}(T_{vib})$ which is obtained from spectroscopy [13,14] and the second is τ_{relax} which is obtained from ultrasonic absorption and dispersion data [15,16]. The CFD flow field is determined by solving the coupled equations simultaneously.

Our results show that relaxation effects must be considered whenever small CFVs are used for slowly relaxing gases over temperatures ranges for which the vibrational states are significantly populated. Both CO_2 and SF_6 meet these conditions; however, N_2 does not because, at ambient temperature, nearly all N_2 molecules are in their lowest vibrational state.

2 CFV Geometry and Principle of Operation

2.1 CFV Geometry. Figure 2 shows the contour of an ISO toroidal throat CFV that was used in this study. It consists of a circular arc of radius $R_c=2d$ that merges smoothly into a conical section with a vertex half-angle of $\theta=3°$.

2.2 Baseline Mass Flow Model. For any CFV, the ratio of the downstream pressure to upstream pressure is maintained so that the gas velocity near the CFV throat reaches sonic velocity. This condition is commonly referred to as choking the CFV. The largest pressure ratio that just chokes the CFV is called the choking pressure ratio, and CFVs must be operated at or below this thresh-

[1]Standard reference conditions are at 293.15 K and 101.325 kPa.

[2]The measured value of the throat diameter was adjusted by less than one micron by matching the experimental C_d data to the computed results for N_2.

Contributed by the Fluids Engineering Division of ASME for publication in the JOURNAL OF FLUIDS ENGINEERING. Manuscript received July 10, 2003; final manuscript received August 10, 2005. Review conducted by Joseph Katz.

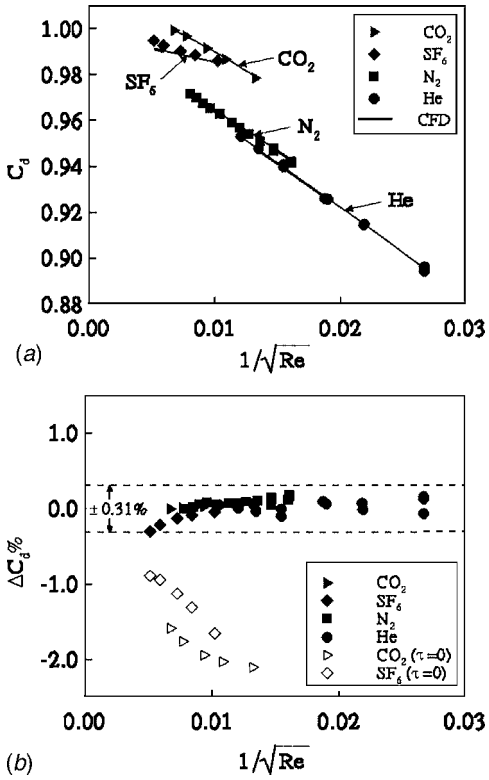

Fig. 1 Comparison of experimental calibration data of four gases with equilibrium (open symbols in (*b*)) and nonequilibrium CFD data (closed symbols) over a Reynolds number range from 2000 to 40,000

old. For choked conditions, a long standing *baseline* mass flow model has been developed that is capable of predicting the actual mass flow to within 10% or better, depending on Reynolds number. This model is based on the following three assumptions: (1) the flow field is one-dimensional, (2) the flow field is inviscid, and (3) the gas behaves ideally and has constant heat capacities. Herein, these assumptions are collectively called the *baseline CFV assumption*. Several engineering texts [17–19] use this assumption to derive a baseline mass flow

$$\dot{m}_{\mathrm{i}} = \frac{P_{\mathrm{o}} A^* C_{\mathrm{s}}^{\mathrm{i}}}{\sqrt{RT_{\mathrm{o}}}} \tag{1}$$

where P_{o} is the upstream stagnation pressure, T_{o} is the upstream stagnation temperature, $A^* = \pi d^2/4$ is the CFV throat area, R is the gas constant for a given species (the universal gas constant divided by the molecular weight), and $C_{\mathrm{s}}^{\mathrm{i}}$ is the ideal critical flow function

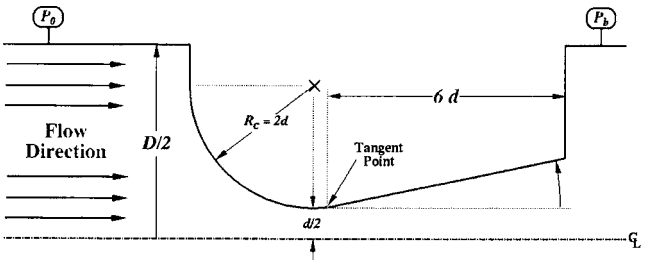

Fig. 2 Critical nozzle used in this study. The diameter of the throat was *d*=0.593 mm.

$$C_{\mathrm{s}}^{\mathrm{i}} = \sqrt{\gamma}\left(\frac{\gamma+1}{2}\right)^{(1+\gamma/2(1-\gamma))} \tag{2}$$

where the superscript "i" is added to denote the gas is ideal and $\gamma = C_P/C_V$ is the ratio of the constant-pressure specific heat to the constant-volume specific heat.

2.3 Experimental Calibration. In CFV applications, none of the three assumptions used to derive the baseline mass flow are perfectly satisfied, and consequently the actual CFV mass flow does not equal $\dot{m}_{\mathrm{i}}$. However, the baseline mass flow plays a vital role in CFV calibrations, being used as the normalizing parameter in the definition of the discharge coefficient

$$C_{\mathrm{d}} \equiv \frac{\dot{m}}{\dot{m}_{\mathrm{i}}} = \frac{\dot{m}\sqrt{RT_{\mathrm{o}}}}{P_{\mathrm{o}} A^* C_{\mathrm{s}}^{\mathrm{i}}} \tag{3}$$

where $\dot{m}$ is the experimentally measured mass flow. Calibration curves typically plot the discharge coefficient versus a function of the Reynolds number

$$\mathrm{Re} = \frac{4\dot{m}_i}{\pi d \mu_o} \tag{4}$$

where μ_o is the molecular viscosity evaluated at the stagnation conditions.

The C_{d} values resulting from experimental calibration curves are most reliable when they are applied using the same conditions (i.e., gas species, stagnation conditions, ambient temperature, inlet velocity profile, beta ratio, etc.) for which the CFV was calibrated. This paper focuses on how species effects impact the discharge coefficient when the calibration and application gas differ and one or both of these gases experiences vibrational relaxation. It is important to understand this phenomenon because this physical mechanism is not captured by the standard Reynolds number parameterization. In a similar manner, species effects attributed to real gas behavior (i.e., virial effects) also result in uncoupling between the discharge coefficient and Reynolds number. While the physical mechanisms differ, we introduce linear CFV theory and use it to show that the methodology used to account for real gas behavior can also be applied to correct for vibrational relaxation phenomenon.

In CFV flows, real gas behavior is taken into account by using the real gas critical flow function, $C_{\mathrm{s}}^{\mathrm{r}}$, in the place of the ideal critical flow function, $C_{\mathrm{s}}^{\mathrm{i}}$, in Eq. (3). When real gas behavior is accounted for in this way, the corresponding discharge coefficient depends predominantly on Reynolds number.[3] In a similar manner, we introduce an *effective* critical flow function, $C_{\mathrm{s}}^{\mathrm{eff}}$, to correct for vibrational relaxation effects. The effectiveness of this correction parameter, like the correction for real gas behavior, depends on vibrational relaxation phenomena being uncoupled from the other higher order effects (i.e., boundary layer development, the shape of the sonic line, and virial effects). Higher order CFV models, which correct the baseline mass flow model, can be used to justify the use of this correction factor.

2.4 Higher Order CFV Models. Higher order CFV models improve upon the baseline mass flow model by eliminating the three assumptions used to derive $\dot{m}_i$. These higher order models are based on solutions of the Navier-Stokes equations that govern the fluid dynamics of conventional CFV flows. Because of the complexity of the Navier-Stokes equations, no analytical solutions have been found when all three of the baseline CFV assumptions are eliminated simultaneously. Instead, researchers have found three different solutions by removing only one of the three baseline CFV assumptions while enforcing the other two. These three solutions include (1) a solution to account for the boundary layer

[3]Even after correcting for real gas behavior the discharge coefficient has a weak dependence on γ that diminishes with increasing Reynolds number.

development along the CFV wall [6–8], (2) an inviscid axisymmetric solution to account for the curvature of the sonic line at the CFV throat [4], and (3) a solution to account for real gas behavior [20–24]. We briefly discuss each of these three solutions.

In the late 1960s and early 1970s both Tang [6,7] and Geropp [8] independently developed models predicting how the discharge coefficient is affected by boundary layer development along the CFV wall. The viscous discharge coefficient developed by these researchers

$$C_{d_1} = f_1(\mathrm{Re}, \gamma, \Omega) \tag{5}$$

is denoted by the subscript "1" and is a function of the Reynolds number, the specific heat ratio, and the CFV geometry which is accounted for via the curvature parameter $\Omega = d/2r_c$ where r_c is the throat radius of curvature.

The second model, developed by Hall in 1962, predicts the effects of sonic line curvature on the discharge coefficient. Hall eliminated the one-dimensional assumption by considering the flow to be axisymmetric, but he retained the assumptions that the fluid behaves as a perfect gas and the flow is inviscid. The axisymmetric inviscid discharge coefficient

$$C_{d_2} = f_2(\gamma, \Omega) \tag{6}$$

is denoted by the subscript "2" and is a function of the specific heat ratio and the curvature parameter. The third model was developed by Johnson [20–24] who included real gas behavior, but assumed that the flow was inviscid and one-dimensional. This solution requires an accurate thermodynamic database and is typically implemented numerically as described in Refs. [20–24]. For convenience, Johnson expressed the numerically calculated mass flow in the same format as the baseline model

$$\dot{m}_3 = \frac{P_o A^* C_s^r}{\sqrt{RT_o}} \tag{7}$$

and lumped all of the real gas effects into the parameter C_s^r, which replaces the ideal critical flow function. The real discharge coefficient is denoted by the subscript "3" and is defined as the ratio of $\dot{m}_3$ and the baseline mass flow

$$C_{d_3} \equiv \frac{\dot{m}_3}{\dot{m}_i} = \frac{C_s^r}{C_s^i} \tag{8}$$

but by Eqs. (1) and (7) is also equal to the ratio of the real gas critical flow function to the ideal critical flow function. The real gas critical flow function, which is often called the *Johnson coefficient*, is generally either tabulated as a function of P_o and T_o or given as a surface fit of these parameters for various gas species.

2.5 Linear CFV Theory. For simplicity, in this paper, the three CFV models are referred to as models 1, 2, and 3, respectively. Linear CFV theory is used to combine the individual results of these three models into a single model capable of predicting the discharge coefficient for a general CFV flow where none of the baseline CFV assumptions apply. The results of the linear theory [11] show that to second-order accuracy the discharge coefficient equals

$$C_d = C_{d_1} C_{d_2} C_{d_3} \tag{9}$$

the product of the C_d's from models 1, 2, and 3, respectively. This expression clearly shows how the discharge coefficient depends on real gas behavior via C_{d_3}. This dependence can be eliminated by dividing Eq. (9) by C_{d_3}, and modifying the discharge coefficient definition to be

$$C_d' \equiv C_d / C_{d_3} = C_{d_1} C_{d_2}. \tag{10}$$

Based on the functionality of C_{d_1} and C_{d_2} given in Eqs. (5) and (6) the modified discharge coefficient is completely free of virial effects, being a function of Re, γ, and Ω. Physically, C_d' is made independent of real gas behavior by using $\dot{m}_3$ as the normalizing parameter

$$C_d' \equiv \frac{\dot{m}}{\dot{m}_3} = \frac{\dot{m}\sqrt{RT_o}}{P_o A^* C_s^r}, \tag{11}$$

which is equivalent to using the real gas critical flow function in place of the ideal critical flow function. Mathematically, Eq. (11) is derived by substituting Eqs. (3) and (8) into Eq. (10).

The definition of the discharge coefficient given in Eq. (11) is preferred over the definition in Eq. (3) because the real gas behavior in Eq. (3) has the undesired quality of possibly permitting the discharge coefficient to be greater than unity. That is, depending on the gas and CFV operating conditions, C_{d_3} could either be greater than or less than unity. In cases where $C_{d_3} > 1$, it could cause the discharge coefficient in Eq. (3) to be greater than unity. On the other hand, the definition in Eq. (11) is only dependent on boundary layer effects and curvature of the sonic line as shown in Eq. (10). Both of these effects cause the discharge coefficient to be less than unity. The boundary layer introduces a region of fluid where both the density and velocity are reduced relative to the core flow. The density is lower because of the higher temperatures in the boundary layer attributed to viscous heating as the flow stagnates at the CFV wall, and the fluid velocity is lower due to the no-slip condition imposed by the wall. In the axisymmetric core flow, the curvature of the sonic line stipulates that the Mach number distribution across the CFV throat cross section is not uniformly equal to unity, but has values both below and above this value. Since compressible flow theory requires that the maximum mass flux coincide with a unity mach number [17], the predicted mass flow will be lower than $\dot{m}_i$.

3 Methodology

In this section, we present the Navier-Stokes equations that are solved in a conventional equilibrium CFD analysis [9]. We then introduce the extensions required to account for molecular relaxation and we conclude with a description of the numerical algorithms that we used.

3.1 Conventional CFD Equations. For Reynolds numbers below 10^6, the axisymmetric, steady, compressible flow in a CFV is governed by the laminar Navier-Stokes equations [9]. The large favorable pressure gradient in the converging section of the CFV is believed to relaminarize what would otherwise be a turbulent flow [25]. Evidence that the flow is laminar is observed in myriads of calibration data where, as predicted by laminar flow theory, the discharge coefficient scales linearly with the inverse square root of the Reynolds number (e.g., Fig. 1).

In CFD, the four scalar conservation equations, including continuity, axial and radial momentum, and energy that constitute the axisymmetric Navier-Stokes equations, are often combined into a single vector equation as explained in Refs. [26,27]. In the present numerical investigation the vector form of the Navier-Stokes equations is expressed as

$$\Upsilon \frac{\partial Q_v}{\partial t} + \frac{\partial E}{\partial x} + \frac{\partial F}{\partial r} = H + \zeta(Q_v) \tag{12}$$

where the time derivative is retained to facilitate a time marching numerical procedure to the desired steady-state solution.[4] This vector representation of the Navier-Stokes equations is developed by grouping the appropriate variables from the four scalar conservation equations. In particular, those variables having like derivative operators are combined into vectors. For example, the time derivative vector, $Q_c = [\rho, \rho u_x, \rho u_r, e]^T$, consists of the temporal terms from continuity, axial and radial momentum, and energy equations where $e = \rho[\varepsilon + 1/2(u_x^2 + u_r^2)]$ is the sum of the internal

[4]The time marching approach differs from commonly used iterative approaches which omit the time derivative term when applied to steady state problems.

and kinetic energy per unit volume. In Eq. (12) the time derivative is multiplied by the Jacobian matrix, $Y=\partial Q_c/\partial Q_v$, so that via the chain rule of vector calculus [28], $Q_c=[\rho,\rho u_x,\rho u_r,e]^T$, is replaced by $Q_v=[P,u_x,u_r,T]^T$. This transformation to the dependent vector, Q_v, conveniently allows thermodynamic properties to be evaluated explicitly as a function of temperature and pressure in the numerical procedure.

The remaining vectors, E and F, on the left-hand side of Eq. (12) are determined in a manner analogously to Q_c. These vectors, commonly called the inviscid flux vectors, are defined as

$$E=\begin{bmatrix}\rho u_x\\ \rho u_x^2+P\\ \rho u_x u_r\\ (e+P)u_x\end{bmatrix},\quad F=\begin{bmatrix}\rho u_r\\ \rho u_r u_x\\ \rho u_r^2+P\\ (e+P)u_r\end{bmatrix} \tag{13}$$

and account for the convective terms in the mass, momentum, and energy equations. On the right-hand side of Eq. (12), the viscous operator, ζ, is defined by

$$\zeta=\frac{\partial}{\partial x}\left(R_{xx}-\frac{\partial}{\partial x}\right)+\frac{\partial}{\partial x}\left(R_{xr}\frac{\partial}{\partial r}\right)+\frac{\partial}{\partial r}\left(R_{rx}\frac{\partial}{\partial x}\right)+\frac{\partial}{\partial r}\left(R_{rr}\frac{\partial}{\partial r}\right) \tag{14}$$

where the viscous matrices, R_{xx}, and R_{xr} are given by

$$R_{xx}=\begin{bmatrix}0&0&0&0\\ 0&\frac{4}{3}\mu&0&0\\ 0&0&\mu&0\\ 0&\frac{4}{3}\mu u_x&\mu u_r&\kappa\end{bmatrix}\quad R_{xr}=\begin{bmatrix}0&0&0&0\\ 0&0&-\frac{2}{3}\mu&0\\ 0&\mu&0&0\\ 0&\mu u_r&-\frac{2}{3}\mu u_r&0\end{bmatrix} \tag{15}$$

with R_{rx} and R_{rr} having analogous forms. Finally, the vector H contains the axisymmetric source terms as given in Ref. [27].

3.2 Thermodynamic and Nonequilibrium Considerations. We follow conventional CFD for dilute gases by computing the density from the equation of state, $\rho=P/[RT(1+B\rho)]$, where the second virial coefficient $B(T)$ accounts for real gas behavior. Data for the second virial coefficient and its temperature derivatives were obtained from Refs. [29,30]. We used the transport property data as a function temperature (at $P=101.325$ kPa) from Refs. [31,32]. In conventional CFD, the equilibrium internal energy $\varepsilon^{eq}(\rho,T)$ is calculated from a reference state by integrating the ideal-gas constant-volume specific heat C_{V_i} and subtracting a correction term to account for real gas effects

$$\varepsilon^{eq}(\rho,T)=\int_{T_{ref}}^{T}C_{V_i}dT-R\rho T^2\frac{dB}{dT} \tag{16}$$

This formula for $\varepsilon^{eq}(\rho,T)$ is unsatisfactory for the CFV in Fig. 2 for certain gases. For this CFV, $\tau_{transit}\approx 20\ \mu s$. Vibrational relaxation times range from 0.0001 to 10 μs depending on gas species, temperature, and density. Thus, the conventional CFD assumption $\Gamma=\tau_{relax}/\tau_{transit}=0$ is a poor approximation for gases with slowly relaxing vibrational modes, especially near the throat of the CFV where the acceleration of the gas is largest. The increase in kinetic energy near the CFV throat is balanced by a decrease in the internal energy of the translational and rotational modes. This reduces the temperature T_{ext} that characterizes these modes. Because the vibrational modes relax slowly, the temperature characterizing them, T_{vib}, is significantly higher than T_{ext}. Consequently, the value of internal energy is not accurately predicted by Eq. (16).

To accurately predict the internal energy when $T_{vib}\neq T_{ext}$, we sum the relevant molecular components including contributions from translational, rotational, and vibrational modes[5]

$$\varepsilon(\rho,T_{vib},T_{ext})\equiv\varepsilon_{ext}(\rho,T_{ext})+\varepsilon_{vib}(T_{vib}) \tag{17}$$

The second term, $\varepsilon_{vib}(T_{vib})$, accounts for the vibrational modes. We assume that the vibrational modes are always in internal equilibrium with each other and we compute $\varepsilon_{vib}(T_{vib})$ by summing the contribution of each vibrational mode

$$\varepsilon_{vib}(T_{vib})=\sum_{n=1}^{N}\frac{g_n R\theta_n}{\exp(\theta_n/T_{vib})-1} \tag{18}$$

where g_n is the degeneracy for the nth vibrational mode, θ_n is the characteristic vibrational temperature for the nth mode, and N is the number of active vibrational modes [13,14]. The first term in Eq. (17), $\varepsilon_{ext}(\rho,T_{ext})$, is called the *external molecular energy*, which consists of both the translational and rotational molecular components. Both of these components are taken to be fully equilibrated so that T_{ext} equals the thermodynamic temperature T. The external molecular energy can be defined by subtracting the equilibrium vibrational energy from the equilibrium internal energy

$$\varepsilon_{ext}(\rho,T_{ext})=\varepsilon^{eq}(\rho,T_{ext})-\varepsilon_{vib}(T_{ext}). \tag{19}$$

In this way $\varepsilon_{ext}(\rho,T_{ext})$ consists only of the translational and rotational components, yet retains real gas behavior that traditional ideal gas models of the translational and rotational components omit.

The exchange of energy between vibrational modes and the combined translational and rotational modes was modeled using the vibrational rate equation [13]

$$\frac{D\varepsilon_{vib}(T_{vib})}{Dt}=\frac{\varepsilon_{vib}(T_{ext})-\varepsilon_{vib}(T_{vib})}{\tau_{relax}} \tag{20}$$

where D/Dt is the time derivative following a fluid element of fixed mass. Bhatia developed this equation for diatomic molecules having only a single vibrational degree of freedom and therefore only one relaxation time [13]. However, Eq. (20) works well for polyatomic molecules at temperatures low enough so that only the lowest vibrational degree of freedom is active (e.g., CO_2 near ambient temperature). Often Eq. (20) is used to model relaxation in sound and shock propagation through polyatomic gases, such as SF_6, where the highest vibrational modes relax quickly so that the entire heat capacity relaxes at a single relaxation time. However, for certain polyatomic gases (e.g., C_2H_6) more than one relaxation time is needed as discussed by Lambert [33].

For steady flow along a streamline the vibrational rate equation is given by

$$\Gamma\frac{d\varepsilon_{vib}(T_{vib})}{dz}=\varepsilon_{vib}(T_{ext})-\varepsilon_{vib}(T_{vib}) \tag{21}$$

where $\Gamma=\tau_{relax}/\tau_{transit}$ is the ratio of the local relaxation time to the local flow transit time, and $z=s/L$ is the normalized distance along a streamline ***where s is the distance along a streamline starting at the CFV entrance, and L is the total distance along the streamline***. Here, $\tau_{transit}=L/\|\vec{u}\|$ is the time that it takes for a fluid particle to move a distance L along a streamline, and $\|\vec{u}\|$ is the magnitude of average velocity over that distance. The relaxation time changes with the local thermodynamic conditions according to the phenomenological Landau and Teller relation [34]

[5]The contribution of the electronic energy is negligible over the temperature range of interest.

$$\tau_{\text{relax}} = \frac{K_1 \exp[(K_2/T_{\text{ext}})^{1/3}]}{P} \tag{22}$$

where the constants K_1 and K_2 were obtained by fitting ultrasonic relaxation data [15,16].

3.3 Numerical Solution. The vibrational rate equation and the Navier-Stokes equations must be solved as a coupled system of equations. In this work these equations are solved by globally iterating between the Navier-Stokes equations and the vibrational rate equation until both are simultaneously satisfied. The iterative procedure begins by solving the Navier-Stokes equations with a guessed value of the molecular vibrational energy, $\varepsilon_{\text{vib}}(T_{\text{vib}})$. From the latest solution of the Navier-Stokes, the input parameters, $\Gamma = \tau_{\text{relax}}/\tau_{\text{transit}}$ and $\varepsilon_{\text{vib}}(T_{\text{ext}})$, are determined for the vibrational rate equation. Next, the vibrational rate equation is integrated along streamlines to determine the updated vibrational energy, $\varepsilon_{\text{vib}}(T_{\text{vib}})$, which is used to determine the modified internal energy, $\varepsilon(\rho, T_{\text{vib}}, T_{\text{ext}})$, in the next iteration of the Navier-Stokes equations. Consequently, the Navier-Stokes solution and the vibrational rate solution are co-dependent.

3.4 Numerical Solution of the Navier-Stokes Equations. The Navier-Stokes equations are solved in a conventional body-fitted coordinate system [35] with a physical domain equivalent to the CFV geometry shown in Fig. 2. Grid-independent solutions are obtained using a mesh with 201 axial grid points and 101 radial grid points. The axial grid points are uniformly spaced while the radial grid points are spaced exponentially with a higher grid density near the CFV wall to resolve the boundary layer.

An alternating-direction implicit (ADI) numerical algorithm [26,27] is used for integrating the Navier-Stokes equations. Time advancement is obtained using first-order, backward finite differences. Both inviscid and viscous time-derivative preconditioning [36–38] are employed for accelerated convergence rates over a wide range of Mach numbers and Reynolds numbers. Spatial discretization is accomplished using third-order up-winded flux differences for the convective terms and central differences for the diffusive terms. The resulting numerical scheme consists of two tridiagonal matrices that are inverted at each time step using a block version of the Thomas algorithm [26,27].

In these computations boundary conditions are specified at the CFV inlet, at the CFV exit, along the CFV wall, and on the centerline. At the inlet, the stagnation pressure, stagnation temperature, and flow angle are specified. Characteristic boundary conditions [39] are specified at the supersonic CFV exit. On the CFV centerline, symmetry boundary conditions are used. The CFV wall is taken to be adiabatic with a zero normal pressure gradient and a no-slip velocity boundary condition.

3.5 Numerical Solution of the Vibrational Rate Equation. In contrast to the Navier-Stokes equations, which are expressed in a Eulerian sense, the vibrational rate equation is expressed in a Lagrangian sense. Specifically, the vibrational rate equation describes the rate of relaxation of the vibrational modes of a gas particle of fixed identity moving through the flow field. The Lagrangian paths of particles of fixed identity correspond to streamlines in the flow field. The trajectories of these streamlines must be estimated from the Navier-Stokes solution before the vibrational rate equation can be solved. In the coupling procedure between the two equation sets, the streamlines in the flow field are computed after each time step using the most recent approximation to the Navier-Stokes solution. The vibrational rate equation is then solved on each streamline by a space-marching procedure that integrates between consecutive points on a streamline.

The space-marching procedure begins at the CFV inlet where the vibrational energy on each streamline is equal to its equilibrium value. To find the value of the vibrational energy, $\varepsilon_{\text{vib}}(T_{\text{vib}})$, at the next adjacent grid point along the stream line, the vibrational rate equation is analytically integrated using variation of parameters [40]. In turn, this value of $\varepsilon_{\text{vib}}(T_{\text{vib}})$ serves as an initial condition for the next point, and so on, until the complete streamline has been updated. This process is then repeated for each streamline in the flow field.

4 Results

4.1 Validation of CFD Model. The CFD methodology followed the procedure used for the experimental calibration, where the mass flow was controlled by varying the stagnation pressures in the range 50 kPa $< P_o <$ 200 kPa while maintaining the stagnation temperature at 298.15 K. For these operating conditions, the corresponding Reynolds number varied from 1000 to 40,000 for the small throat ISO standardized CFV. The CFD results were verified by comparisons with experimental data for four gases including He, N_2, SF_6, and CO_2.

The experimental data shown in Fig. 1 were obtained by Japan's national flow standard, which measures flow using a gravimetric timed-collection technique with an uncertainty of 0.1% [3]. As shown in Fig. 1, the nonequilibrium CFD model predicted the discharge coefficient to better than 0.3% for all of the gases over the entire Reynolds number range. In agreement with experimental results, the nonequilibrium CFD model predicted larger C_d values for SF_6 and CO_2—gases affected by relaxation. As expected, the nonequilibrium CFD model correctly predicted C_d for He and N_2, gases that are not influenced by vibrational nonequilibrium.

4.2 Increase in C_d due to Vibrational Nonequilibrium Flow. When slowly relaxing gases are used in small CFVs, the measured mass flow exceeds the predicted value given by models that assume $\tau_{\text{relax}}=0$. Indeed, the discharge coefficient as defined in Eq. (3) or (11) may even be greater than unity. To understand this phenomenon, it is helpful to consider the limiting cases for the ratio $\Gamma = \tau_{\text{relax}}/\tau_{\text{transit}}$. The limit $\Gamma \to 0$ is the case of equilibrium flow; the limit $\Gamma \to \infty$ is "frozen" flow in which energy in vibrational modes remains constant. In both limiting cases, the gas dynamic equations are uncoupled from the vibrational rate equation.

In the limit of frozen flow, relaxation does not occur or, equivalently $\varepsilon_{\text{vib}}(T_{\text{vib}}) = \varepsilon_{\text{vib}}(T_o) = \text{const}$ throughout the flow field. Because $\varepsilon_{\text{vib}}(T_o)$ is constant, the frozen flow heat capacity of the vibrational degrees of freedom is zero ($C_{V_{\text{vib}}}=0$). Consequently, the specific heat ratio for frozen flow, γ^{fr}, is larger than the equilibrium value, γ^{eq}. The ideal gas model can be used to demonstrate this fact. For an ideal gas, the specific heat ratio is expressible in terms of the translational, rotational, and vibrational heat capacities [18]

$$\gamma_{\text{ideal}} = 1 + \frac{R}{C_{\text{v}_{\text{trans}}} + C_{\text{v}_{\text{rot}}} + C_{\text{v}_{\text{vib}}}}. \tag{23}$$

where γ^{fr} is calculated by setting $C_{V_{\text{vib}}}=0$. For diatomic or polyatomic gases, having a least one active vibrational mode, $C_{V_{\text{vib}}} > 0$ so that $\gamma^{\text{fr}} > \gamma^{\text{eq}}$.

The increased value of the specific heat ratio in the case of frozen flow results in a higher sound speed in the gas than would exist for equilibrium flow. In addition, as the gas expands and accelerates through the CFV it cools to a lower temperature in the case of frozen flow than it would for equilibrium flow. This lower temperature subsequently results in a higher density. Both the higher speed of sound and the higher density, in the case of frozen flow, increase the mass flow through the CFV as shown by combining Eqs. (1) and (2) using the larger frozen flow specific heat ratio in place of normal value of γ. Finally, in the intermediate case of vibrational relaxation, previous CFD results have shown that the mass flow is increased above the equilibrium value, but is less than the frozen flow value [10].

When vibrational relaxation is present, the discharge coefficient as defined by either Eq. (3) or (11) is higher than would be pre-

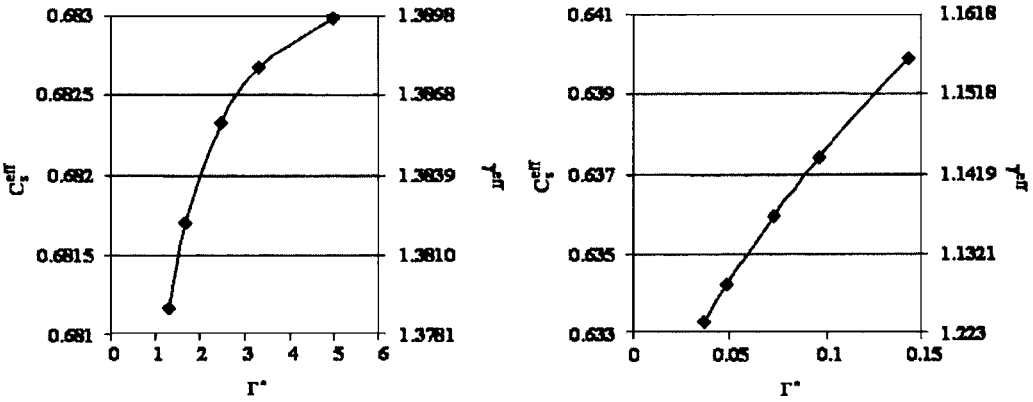

Fig. 3 Effective critical flow function versus reference value of Γ^* evaluated at the nozzle throat for CO_2 (left) and SF_6 (right)

dicted by conventional equilibrium models. The larger discharge coefficient results because the normalizing parameter $\dot{m}_i$ or $\dot{m}_3$ does not account for increased mass flow attributed to vibrational relaxation. Moreover, these definitions allow values of the discharge coefficient that are greater than unity [11]. To avoid this nonphysical situation,[6] the discharge coefficient should be defined using a normalizing parameter that accounts for vibrational relaxation effects.

4.3 Generalizing the Critical Flow Function to Account for Vibrational Relaxation. Vibrational relaxation can be accounted for by generalizing the critical flow function, which itself is a generalization of the discharge coefficient. Based on linear CFV theory it can be shown that an *effective* critical flow function can be defined as

$$C_s^{\text{eff}} \equiv C_s^{\text{r}}\left(\frac{C_d^{\text{vib}}}{C_d^{\text{eq}}}\right) \tag{24}$$

where C_d^{vib} is the discharge coefficient computed with the present vibrational relaxation flow model, and C_d^{eq} is the discharge coefficient computed with the equilibrium flow model.

Figure 3 shows the *effective* critical flow function for both CO_2 and for SF_6 gases as a function of $\Gamma^*(T_o, P_o) = \tau^*_{\text{relax}}/\tau^*_{\text{transit}}$ where τ^*_{relax} is evaluated at the throat conditions using Eq. (22) and $\tau^*_{\text{transit}} = d/c^*$ is the time required for a gas particle to travel one CFV throat diameter at the speed of sound, $c^* = \sqrt{\gamma R T^*}$. The effective critical flow function defined in this way is valid for an ISO standard CFV geometry for T_o near room temperature. For a given gas, C_s^{eff} depends not only on Γ^*, but also on $C_{\text{vib}}/C_v = (\gamma^{\text{fr}} - \gamma^{\text{eq}})/(\gamma^{\text{fr}} - 1)$, the ratio of the vibrational specific heat to the total constant-volume specific heat. This ratio, which gives an indication of the number of active vibrational modes, is strongly dependent on temperature so that Fig. 3 is only valid for T_o near room temperature.

The *effective* critical flow function defines an *effective* specific heat ratio according to the relationship

$$C_s^{\text{eff}} = \sqrt{\gamma^{\text{eff}}}\left(\frac{\gamma^{\text{eff}}+1}{2}\right)^{(1+\gamma^{\text{eff}})/(1-\gamma^{\text{eff}})}. \tag{25}$$

For both gases CO_2 and SF_6 the effective specific heat ratio lies between the equilibrium and frozen flow limit and can be used to assess the degree of vibrational relaxation.

By using C_s^{eff} in the expression for the ideal theoretical mass flow given in Eq. (1), the generalized discharge coefficient accounts for vibrational relaxation. The resulting C_d curves for CO_2 and SF_6 will then agree with analytical C_d predictions, having C_d values that are less than unity and that scale with the Reynolds number and the specific heat ratio.

Conclusions

A model for flow through CFVs that incorporates the influence of the relaxation time of vibrational degrees of freedom has been presented. The model agrees with experimental measurements of the discharge coefficient for four gas species (including CO_2 and SF_6) within 0.31% whereas prior models differed from experiments by as much as 2.3%. The new model couples nonequilibrium thermodynamics with the equations of flow. The pertinent quantities are the energy of vibrational modes and the ratio of the vibrational relaxation time to the transit time for the gas to move from the CFV entrance to its throat. The nonequilibrium phenomena causes an increase in mass flow through the CFV that can be explained by the limiting cases of "frozen" and equilibrium flow. Linear CFV theory is introduced and used to define the appropriate form of the *effective* critical flow function necessary to cancel the effects of vibrational relaxation. The effective values of the specific heat ratio and the critical flow function, presented herein, allow a user to use calibration data performed with N_2 to calculate the flow of CO_2 or SF_6 through a CFV without utilizing the computational model.

Acknowledgment

Computational support was provided by the High Performance Systems and Services Division of the Information Technology Laboratory at NIST. In addition, thanks is extended to Nate Briggs for his ideas and support of this work.

References

[1] Wright, J. D., 1998, "The Long Term Calibration Stability of Critical Flow Nozzles and Laminar Flowmeters," NCSL Conference Proceedings, Albuquerque, NM, pp. 443–462.
[2] Wright, P. H., 1985, "The Application of Sonic Nozzles to the Automated Accuracy Testing of Gas Flow Meters," Proc. International Conference on Flow Measurement, Australia, pp. 152–156.
[3] Nakao, S., Hirayama, T., and Takamoto, M., 1997, "Effects of Thermalphysical Properties of Gases on the Discharge Coefficients of the Sonic Venturi Nozzle," Proceedings of the 1997 ASME Fluids Engineering Division Summer Meeting, Vancouver, British Columbia, Canada, June 22–26.
[4] Hall, I. M., 1962, "Transonic Flow in Two-Dimensional and Axially-Symmetric Nozzles," Q. J. Mech. Appl. Math., **XV**, Pt. 4, pp. 487–508.
[5] Smith, R. E., and Matz, R. J., 1962, "A Theoretical Method of Determining Discharge Coefficients for Venturis Operating at Critical Flow Conditions," J. Basic Eng., **19**, pp. 434–446.
[6] Tang, S. P., 1969, "Theoretical Dependence of the Discharge Coefficients of Axisymmetric Nozzles Under Critical Flows," Technical Report PR-118-PU, Department of Mechanical Engineering, Princeton Univ., Princeton, NJ.
[7] Tang, S., 1969, "Discharge Coefficients for Critical Flow Nozzles and Their

[6] Greater than unity C_d values are sometimes caused by inaccurate values of the CFV throat diameter. This is especially true for small-sized CFVs where the throat diameter is more difficult to measure.

Dependence on Reynolds Numbers," Ph.D. thesis, Princeton Univ., Princeton, NJ.
[8] Geropp, D., 1971, "Laminare Grenzschichten In Ebenen Und Rotationssymmetrischen Lavalduesen," Deutsche Luft-Und Raumfart, Forschungsbericht, pp. 71–90.
[9] Johnson, A. N., Espina, P. I., Mattingly, G. E., Wright, J. D., and Merkle, C. L., 1998, "Numerical Characterization of the Discharge Coefficient in Critical Nozzles," *Proceedings of the 1998 NCSL Workshop Symposium*, Albuquerque, NM.
[10] Johnson, A. N., Wright, J. D., Nakao, S., Merkle, C. L., and Moldover, M. R., 2000, "The Effect of Vibrational Relaxation on the Discharge Coefficient of Critical Flow Venturis," Flow Meas. Instrum., **11**, pp. 315–327.
[11] Johnson, A. N., 2000, "Numerical Characterization of the Discharge Coefficient in Critical Nozzles," Ph.D. thesis, The Pennsylvania State University, University Park, PA.
[12] ISO 9300: (E)., 1990, "Measurement of Gas Flow by Means of Critical Flow Venturi Nozzles," Geneva Switzerland.
[13] Bhatia, A. B., 1967, *Ultrasonic Absorption: An Introduction to the Theory of Sound Absorption and Dispersion in Gases, Liquids, and Solids*, Oxford University Press, Inc., London.
[14] O'Connor, L. C., 1954, "Thermal Relaxation of Vibrational States in Sulfur Hexafluoride," J. Acoust. Soc. Am., **2**(3), pp. 361–364.
[15] Estrada-Alexanders, A. F., and Trusler, J. P. M., 1999, "Speed of Sound in Carbon Dioxide at Temperatures between (200 and 450) K and Pressures up to 14 MPa," J. Chem. Thermodyn., **31**(5), pp. 1589–1601.
[16] Breshears, W. D., and Blair, L. S., 1973, "Vibrational Relaxation in Polyatomic Molecules: SF6," J. Chem. Phys., **59**(11), pp. 5824–5827.
[17] John, J. E., 1984, *Gas Dynamics*, 2nd ed., Allyn and Bacon, Inc., Boston.
[18] Anderson, J. D., Jr., 1982, *Modern Compressible Flow with a Historical Perspective*, McGraw-Hill, Inc., New York.
[19] Shapiro, A. H., 1954, *The Dynamics and Thermodynamics of Compressible Fluid Flow, Vol. II*, The Ronald Press Co., New York.
[20] Johnson, R. C., 1963, "Calculation of Real-Gas Effects in Flow Through Critical-Flow-Nozzles," ASME paper no. 63-WA-71.
[21] Johnson, R. C., 1964, "Calculations of Real-Gas Effects in Flow Through Critical Nozzles," J. Basic Eng., **1964**, p. 519.
[22] Johnson, R. C., 1965, "Real-Gas Effects in Critical-Flow-Through Nozzles and Tabulated Thermodynamic Properties," Nasa Technical Note D-2565, National Aeronautics and Space Administration, Washington, DC
[23] Johnson, R. C., 1968, "Real-Gas Effects in Critical Flow Through Nozzles and Thermodynamic Properties of Nitrogen and Helium at Pressures to 300 $\times$105 Newtons Per Square Meter (Approx. 300 atm)," NASA Technical Note SP-3046, National Aeronautics and Space Administration, Washington, DC.
[24] Johnson, R. C., 1971, "Real Gas Effects in Flowmetering," Symposium on Flow, ISA, Pittsburgh, PA.
[25] White, F. M., 1991, *Viscous Fluid Flow*, McGraw-Hill Inc., New York.
[26] Hirsch, C., 1988, *Numerical Computation of Internal and External Flows: Volume 1, Fundamentals of Numerical Discretization*, John Wiley & Sons, Inc., New York.
[27] Hirsch, C., 1990, *Numerical Computation of Internal and External Flows: Volume 2, Computational Methods for Inviscid and Viscous Flows*, John Wiley & Sons, Inc., New York.
[28] Davis, D. F., and Snider, A. D., 1991, *Introduction to Vector Analysis, Sixth Edition*, Wm. C. Brown Publishers, Dubuque, IA.
[29] Hilsenrath, J., Beckett, C. W., Benedict, W. S., Fano, L., Hoge, H. J., Masi, J. F., Nuttall, R. L., Touloukian, Y. S., and Wooley, H. W., 1955, "Tables of Thermal Properties of Gases," U.S. Department of Commerce NBS Circular 564.
[30] McCarty, R. D., and Arp, V. D., 1990, "A New Wide Range Equation of State for Helium," Adv. Cryog. Eng., **35**, pp. 1465–1475.
[31] Arp, V. D., McCarty, R. D., and Friend, D. G., 1998, "Thermophysical Properties of Helium-4 from 0.8 to 1500 K with Pressures to 2000 MPa," NIST Technical Note 1334, Boulder, CO.
[32] Hands, B. A., and Arp, V. D., 1981, "A Correlation of Thermal Conductivity Data for Helium," Cryogenics, **21**(12), pp. 697–703.
[33] Lambert, J. D., 1977, *Vibrational and Rotational Relaxation in Gases*, Oxford University Press, Oxford.
[34] Kruger, C. H., and Walter, G. V., 1965, *Introduction to Physical Gas Dynamics*, John Wiley & Sons, Inc., New York.
[35] Anderson, D. A., Tannehill, J. C., and Pletcher, R. H., 1984, *Computational Fluid Mechanics and Heat Transfer*, Hemisphere Publishing Corporation, New York.
[36] Buelow, P., Venkateswaran, S., and Merkle, C. L., 1994, "The Effect of Grid Aspect Ratio on Convergence," AIAA J., **32**, pp. 2401–2406.
[37] Feng, J., and Merkle, C. L., 1990, "Evaluation of Preconditioning Methods for Time Marching Systems," AIAA paper no. 90-0016, AIAA 28th Aerospace Sciences Meeting, Reno, NV.
[38] Buelow, P. E. O., 1995, "Convergence Enhancement of Euler and Navier-Stokes Algorithms," Ph.D. thesis, Department of Mechanical Engineering, The Pennsylvania State University, University Park, PA.
[39] DuChateau, P., and Zachmann, D., 1989, "Applied Partial Differential Equations," Harper and Row Publishers, Inc., New York.
[40] Edwards, C. H., and Penny, D. E., 1989, "Elementary Differential Equations With Boundary Value Problems," Prentice-Hall, Inc., Englewood, NJ.

Romeo Susan-Resiga
Professor
Hydraulic Machinery Department,
"Politehnica" University of Timişoara,
Bvd. Mihai Viteazu 1,
RO-300222, Timişoara, Romania
e-mail: resiga@mh.mec.utt.ro

Gabriel Dan Ciocan
Ecole Polytechnique Fédérale de Lausanne,
Laboratory for Hydraulic Machines,
Av. de Cour 33Bis, CH-1007,
Lausanne, Switzerland
e-mail: GabrielDan.Ciocan@epfl.ch

Ioan Anton
Professor
Member of the Romanian Academy
"Politehnica" University of Timişoara,
Hydraulic Machinery Department,
Bvd. Mihai Viteazu 1,
RO-300222, Timişoara, Romania

François Avellan
Professor
École Polytechnique Fédérale de Lausanne,
Laboratory for Hydraulic Machines,
Av. de Cour 33Bis, CH-1007,
Lausanne, Switzerland
e-mail: francois.avellan@epfl.ch

Analysis of the Swirling Flow Downstream a Francis Turbine Runner

An experimental and theoretical investigation of the flow at the outlet of a Francis turbine runner is carried out in order to elucidate the causes of a sudden drop in the draft tube pressure recovery coefficient at a discharge near the best efficiency operating point. Laser Doppler anemometry velocity measurements were performed for both axial and circumferential velocity components at the runner outlet. A suitable analytical representation of the swirling flow has been developed taking the discharge coefficient as independent variable. It is found that the investigated mean swirling flow can be accurately represented as a superposition of three distinct vortices. An eigenvalue analysis of the linearized equation for steady, axisymmetric, and inviscid swirling flow reveals that the swirl reaches a critical state precisely (within 1.3%) at the discharge where the sudden variation in draft tube pressure recovery is observed. This is very useful for turbine design and optimization, where a suitable runner geometry should avoid such critical swirl configuration within the normal operating range. [DOI: 10.1115/1.2137341]

1 Introduction

Swirling flow behavior in various technical applications has long been an intensive subject of research. Usually swirl effects are seen as either the desired result of design or unavoidable, possibly unforseen, side effects [1]. However, the hydraulic turbine draft tube on one hand benefits from the swirl at the runner outlet in order to mitigate flow detachment in the cone, but on the other hand suffers from the flow instabilities leading to pressure fluctuations and ultimately to the draft tube surge.

The draft tube of a hydraulic turbine is the machine component where the flow exiting the runner is decelerated, thereby converting the excess of kinetic energy into static pressure. In the case of machine rehabilitation of an existing power plant, mostly only the runner and the guide vanes are currently modified. For economical and safety reasons, the spiral casing and the draft tube are seldom redesigned, even if these components present some undesirable behavior. However, the installation of an upgraded runner requires a reliable prediction of the flow in a compact draft tube in order to avoid the peculiar and undesirable efficiency curve from Fig. 1. The efficiency drop as the discharge is increased above the best efficiency point value is found to be related to a corresponding sudden variation in the draft tube pressure recovery coefficient at the same discharge. It is this phenomenon we address in this paper.

The obvious practical importance of predicting the complex flow downstream the turbine runner, in the draft tube, led to the FLINDT research project of Flow Investigation in Draft Tubes [2]. The main objective of this project was to investigate the flow in hydraulic turbines draft tubes, for a better understanding of the physics of these flows and to build up an extensive experimental data base describing a wide range of operating points which can provide a firm basis for the assessment of the CFD engineering practice in this component. The extensive experimental investigation of the draft tube flow has been complemented with three-dimensional numerical flow simulations [3,4] aimed at elucidating the swirling flow evolution up to the turbine outlet as well as the phenomena that led to the peculiar sudden drop in the turbine efficiency.

Other investigations have been mainly focused on the ability of the CFD tools to accurately reproduce the complex three-dimensional velocity and pressure field in draft tubes for Kaplan turbines [5,6]. One important issue addressed in these studies was the sensitivity of numerical results to the boundary conditions, particularly the inlet ones.

The present paper focuses on the structure of the swirl produced by the constant pitch turbine runner and further ingested by the draft tube. The corresponding hydrodynamic field is a direct outcome of the runner design and the operating point. Since changing the runner design, while keeping the same draft tube, may lead to an unexpected sudden efficiency drop for a certain discharge, it would be preferable that some design criteria be put forward as far as the runner outlet swirl is concerned. The present analysis shapes such criteria by using relative simple mathematical and numerical tools. Of course, the complex three-dimensional and unsteady flow in the draft tube cannot be quantitatively predicted only by analyzing the draft tube inlet swirl. However, if the runner outlet swirl structure displays a sudden change with respect to appropriate criteria, and this change occurs at a discharge close to the experimental one where the sudden drop in turbine efficiency is observed, these criteria should be taken into account when designing or redesigning the runner.

In analyzing a swirling flow one benefits from a large body of literature on this subject. In laboratory investigations swirl was

Contributed by the Fluids Engineering Division of ASME for publication in the JOURNAL OF FLUIDS ENGINEERING. Manuscript received July 9, 2004; final manuscript received July 31, 2005. Review conducted by Joseph Katz.

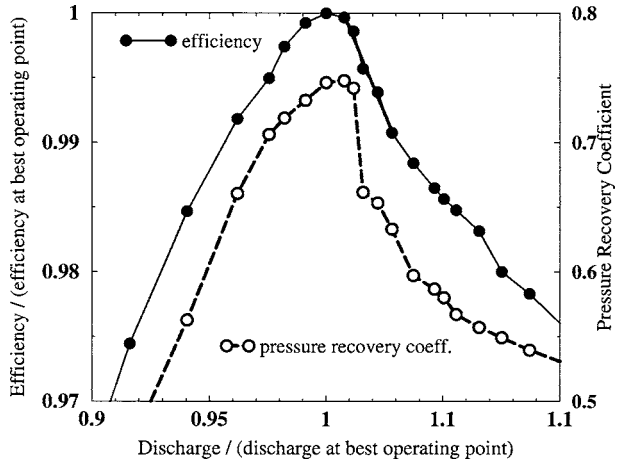

Fig. 1 Efficiency break off obtained by increasing the discharge and keeping the specific energy constant. Model test of a Francis turbine with specific speed 0.56.

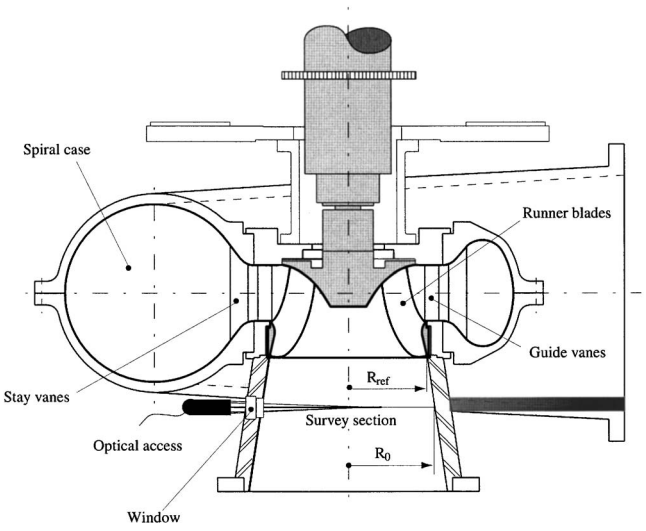

Fig. 2 Sketch of the Francis turbine model and LDA setup for the flow survey section at runner outlet-draft tube inlet

generated by adjustable guidevanes, by fixed vanes similar to those employed in combustors, or by tangential inflow through a long slit [1]. The closest setup to the hydraulic turbine case seems to be the adjustable radial guidevane apparatus, which has been largely used for more than 50 years to investigate, both experimentally and numerically, the so-called vortex breakdown (VB) phenomenon [7–10]. The formulas employed in these studies to fit both axial and circumferential velocity component radial variation are of particular relevance for our study.

Several theoretical developments have been devoted to explain the VB. However, a general consensus over the definition of this phenomenon has not been reached yet. For example, Benjamin [11] considers the VB to be a finite transition between two dynamically conjugate states of axisymmetric flow, analogous to the hydraulic jump in open-channel flow. A similar definition was later adopted by Keller [12], who argued that various authors or even schools have conflicting views on the correct interpretation of the physics of VB. Leibovich [13] relates VB to a disturbance characterized by the formation of an internal stagnation point on the vortex axis, followed by reversed flow in a region of limited axial extent. Goldshtik and Hussain [14] consider that VB occurs due to solution nonuniqueness in some range of inflow parameters when the entire steady flow experiences a jump to another metastable steady state with the same boundary conditions. They stress that VB is a loss-free process and, hence, analogies with shocks or hydraulic jumps are misleading and must be abandoned. All theories for confined swirling flows consider axisymmetric geometries with constant or variable cross section (e.g., slowly diverging pipes). It is difficult to imagine that a simplified theory could be elaborated for a swirling flow in an actual draft tube with both cross-section shape and area variation, as well as changes in the flow direction. However, at least for the draft tube cone where most of the pressure recovery occurs, swirling flow theories might provide valuable results for design evaluation and optimization.

Mauri et al. [15,3] developed and applied original techniques to analyze the three-dimensional flow in the FLINDT draft tube. They explain the draft tube efficiency drop from Fig. 1 by a global instability triggered by the flow rate increase. The topological structure of the velocity field changes abruptly with the emergence of a saddle point and a focus in the skin friction lines pattern on the elbow wall, leading to a global Werlé-Legendre separation that blocks the right channel. However, there is an important question to be answered: is this phenomenon the primary cause of the draft tube efficiency drop or it is one of the consequences of a corresponding abrupt change in the swirling flow ingested by the draft tube as the discharge increases? It is this question we address in this paper, by investigating the swirling flow on the draft tube inlet section within the general framework of vortex breakdown theories.

In Sec. 2 we briefly present the experimental setup and measuring techniques used to investigate the flow in a Francis turbine draft tube. In this paper we examine the flow on a section at the runner outlet/draft tube inlet. Laser Doppler anemometry has been employed to investigate the velocity components, with particular attention paid to the data error control.

Section 3 is devoted to the analytical representation of velocity components radial variation. A critical analysis of swirling flow models available in literature is followed by the development of a model particularly suited to hydraulic turbines. It is shown that a three-vortex system accurately represents the experimental data, and a least squares technique is employed for computing the model parameters. Finally, the velocity profiles are parametrized only by the discharge coefficient, thus allowing a swirl behavior analysis as the operating point changes continuously.

The nonlinear Long-Squire equation is used in Sec. 4 as a mathematical model for the swirling flow at the draft tube inlet. The finite element method is employed to solve the corresponding boundary value problem for the stream function.

The solution behavior is examined in Sec. 5 using the linearized operator spectrum analysis. It was found that the critical state of the swirl configuration, defined by Benjamin [11], is in good agreement with the abrupt change experimentally observed in the draft tube pressure recovery coefficient.

The paper conclusions are summarized in Sec. 6.

2 Experimental Investigation of the Velocity Field on the Draft Tube Inlet

The FLINDT project [2] experimental investigations were carried out on a Francis turbine scaled model of specific speed 0.56 (Fig. 2). The turbine model has a spiral casing of double curvature type with a stay ring of 10 stay vanes, a distributor made of 20 guide vanes, a 17-blade runner of a 0.4 m outlet diameter, and a symmetric elbow draft tube with one pier. The global measurements for flow rate, head, and efficiency were performed according to the IEC 60193 International Standard [16].

The experimental data used in this paper were obtained with a two-component probe Laser Doppler Anemometer (LDA), using back-scattered light and transmission by optical fiber, with a laser of 5 W argon-ion source. The main characteristics of the optical system are laser wave lengths 488/514.5 nm, probe diameter

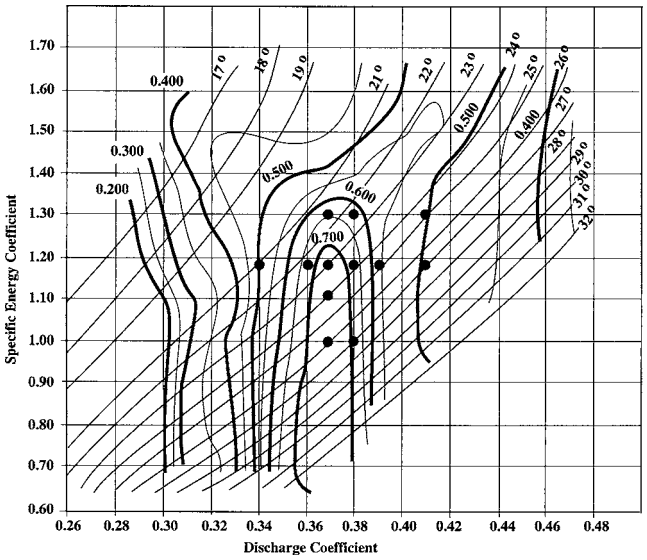

Fig. 3 Pressure recovery isolines (thick lines) for the draft tube investigated in the FLINDT project. The turbine operating points (discharge coefficient-specific energy coefficient) are shown with filled circles.

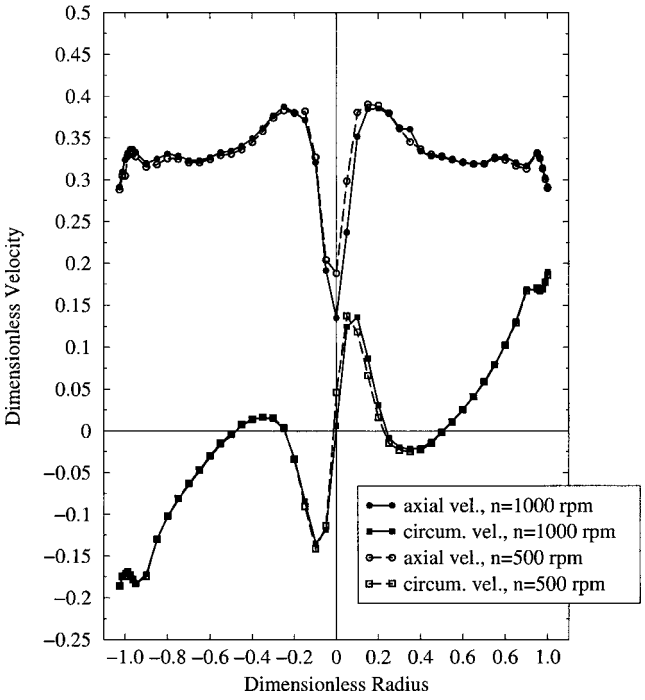

Fig. 4 Reynolds number influence on the dimensionless velocity profiles at operating point with discharge coefficient 0.368 and energy coefficient 1.18

60 mm, beam spacing probe with beam expander 73.3 mm, focal length 1000 mm, fringe spacing ~5.3 nm, and measuring volume $\sigma_x=\sigma_y\sim 0.2$ mm, $\sigma_z\sim 6$ mm.

Spherical silver-coated glass particles are introduced in the test rig flow. These particles are hollowed in order to match the water density and are able to follow flow fluctuations frequency up to 5 kHz [17]. The mean diameter of these particles is 10 μm.

In order to control the position of the measurement volume, a ray tracing technique is used for calculating direct and inverse light paths of laser beams through the different media (air, window, water). An optical window with plane and parallel faces is used as an interface. The measuring point geometrical location is controlled within a 0.05 mm accuracy. Both axial and circumferential components of the velocity are measured. The uncertainties of the velocity measurements are estimated to be 2% of the measured value [18].

The global "efficiency" of the draft tube is quantified using the static pressure recovery coefficient, defined as

$$\chi=\frac{(p/\rho+gz)_{out}-(p/\rho+gz)_{ref}}{Q^2/2A_{ref}^2}. \tag{1}$$

Figure 3 presents isolines of the pressure recovery coefficient in discharge coefficient-energy coefficient coordinates. The operating points further referenced in this paper, where full velocity measurements are performed on the survey section from Fig. 2, are also marked. The turbine efficiency break-off, Fig. 1, is found to be produced by a corresponding drop in the draft tube pressure recovery. This phenomenon occurs practically at the same discharge value for a specific energy coefficient lower than 1.30.

Throughout this paper the velocity is made dimensionless by the *runner angular speed*×*runner outlet radius*, and lengths are made dimensionless with respect to the *runner outlet radius* R_{ref} (Fig. 2).

In order to assess the Reynolds number influence on the velocity field at the runner outlet, the same operating point (discharge coefficient, specific energy coefficient) has been investigated for two runner rotational speed values, 500 and 1000 rpm, respectively. The data for dimensionless axial and circumferential velocity components corresponding to the same operating point in Fig. 3 but at two runner rotational speeds are plotted in Fig. 4. According to the IEC 60193 Standard [16], the characteristic Reynolds number Re of the turbine is defined as $\mathrm{Re}=UD/\nu=\pi nD^2/60\nu$. The corresponding Reynolds number of the reduced scale model is changed from 4.2×10^6 (at $n=500$ rpm) to 8.4×10^6 (at $n=1000$ rpm) without any significant variation in the dimensionless velocity profiles. Moreover, the axial and circumferential velocity profiles measured at the same discharge coefficient value are not sensitive to specific energy coefficient changes within the investigated range 1.0–1.3, as one can observe Fig. 5. This led us to the conclusion that the only relevant parameter for the investigation further presented in this paper is the turbine discharge coefficient.

3 Analytical Representation of Axial and Circumferential Velocity Profiles

Several swirling flow models have been considered in the literature to study either the vortex stability or the vortex breakdown. We briefly review these models in order to develop a suitable representation for the swirl at the Francis runner outlet. Historically, vortex flow have been first studied in unbounded media and as a result the velocity circulation at very large distance from the vortex axis was naturally chosen as a vortex parameter. Since we are dealing with confined vortices, it is convenient to use the angular velocity at the vortex axis, Ω. A second parameter is a characteristic vortex radius R which measures the vortex core radial extent. These two parameters define the Rankine vortex circumferential velocity,

$$w(r)=\begin{cases}\dfrac{\Omega R^2}{r} & \text{for } r\geqslant R,\\ \Omega r & \text{for } r<R\end{cases}, \tag{2}$$

where r is the radial distance from the vortex axis. This simplified model provides a continuous function for $w(r)$, but the derivative is discontinuous. A rigorous theoretical foundation is provided for the Burgers vortex (also known as the Lamb vortex), which gives the circumferential velocity profile as

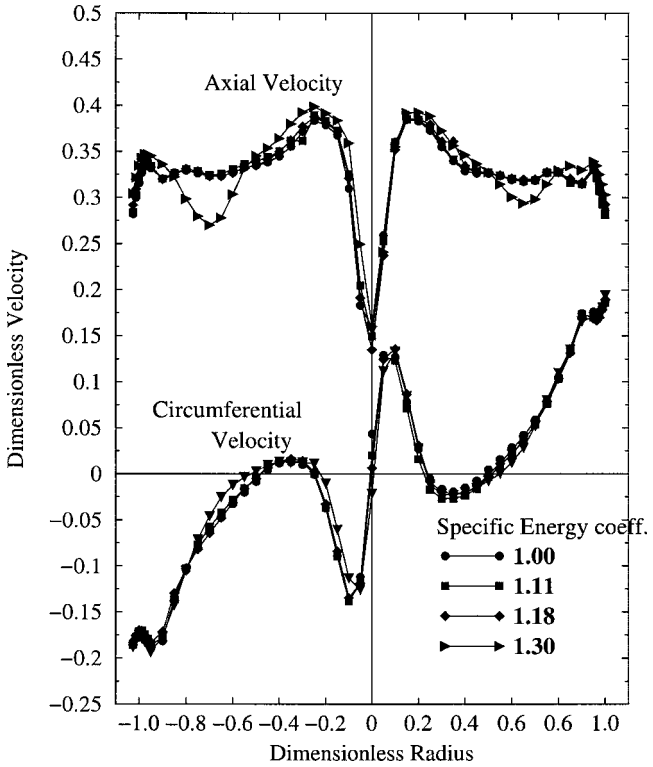

Fig. 5 Specific energy coefficient influence on the dimensionless velocity profiles at operating points with discharge coefficient 0.368

$$w(r) = \frac{\Omega R^2}{r}\left[1 - \exp\left(-\frac{r^2}{R^2}\right)\right]. \tag{3}$$

Formula (3) is an exact solution for a viscous vortex produced by radial inflow and axial outflow where the conditions at large radial distance are irrotational. The relationship between Rankine vortex (2) and Burgers vortex (3) models can be easily seen from Fig. 6. If we take the limit for $r \ll R$ in (3) we get Ωr, while for $r \gg R$ we obtain $\Omega R^2/r$. In conclusion, the Rankine vortex represents the asymptotic behavior of the Burgers vortex for large and small radius with respect to the vortex core extent R.

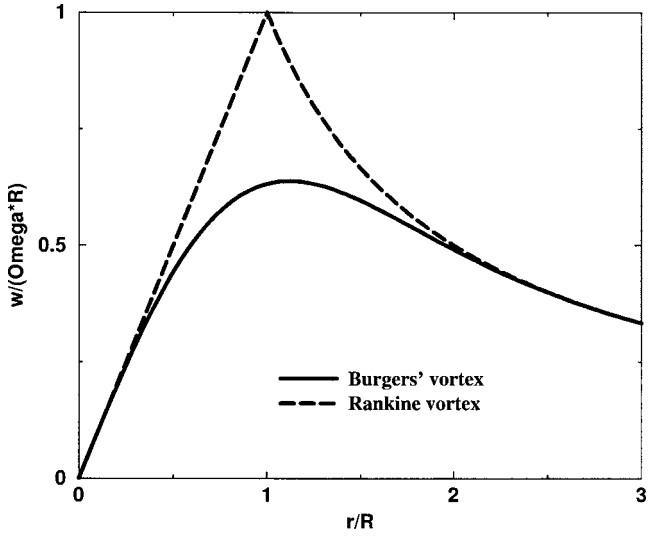

Fig. 6 Circumferential velocity profile for Rankine and Burgers vortex models, respectively

Both the above models consider a uniform axial velocity. It was Batchelor [19] who pointed out that a radial variation in circumferential velocity must be accompanied by a variation in the axial velocity. He showed that in the case of a trailing vortex from one side of a wing in an infinite body of fluid all streamlines originate in a region where the pressure is uniform and the fluid velocity is uniform with only an axial component U_0. When a Rankine vortex circumferential velocity (2) is induced by viscous effects in the boundary layer of the wing, the axial velocity inside the vortex core increases as

$$u = \begin{cases} U_0 & \text{for } r \geqslant R, \\ \sqrt{U_0^2 + 2\Omega^2(R^2 - r^2)} & \text{for } r < R, \end{cases} \tag{4}$$

Applying the same considerations for the Burgers vortex (3), we obtain

$$u^2 = U_0^2 + \int_r^\infty \frac{1}{r^2}\frac{\partial K^2}{\partial r}dr = U_0^2 + 2\Omega^2 R^2\left[\mathrm{Ei}_1\left(\frac{r^2}{R^2}\right) - \mathrm{Ei}_1\left(2\frac{r^2}{R^2}\right)\right],$$

where $K \equiv rw$ is $(2\pi)^{-1}$ times the circulation around a symmetrically placed circle and Ei_1 is the exponential integral of order one. On the axis the axial velocity is $\sqrt{U_0^2 + 2\ln(2)\Omega^2 R^2}$, which is smaller than the corresponding value for the Rankine vortex $\sqrt{U_0^2 + 2\Omega^2 R^2}$.

Faller and Leibovich [8] have used the following axial velocity functional form to fit their experimental data for a radial guide-vane swirl generator,

$$u(r) = U_0 + U_1 \exp\left(-\frac{r^2}{R^2}\right), \tag{5}$$

where U_1 is the difference between the axial velocity on the axis and the axial velocity far away from the axis, U_0. Note that when using (5) together with (3) the vortex core radius R is the same. When $R \gg r$, Eq. (3) becomes $u(r) \approx \Omega r$ since $\lim_{x\to 0}[1 - \exp(-x^2)]/x^2 = 1$, and Eq. (5) becomes $u(r) \approx U_0 + U_1 = \text{const}$.

It was specifically stated in [8] that no theoretical justification for (5) is available. Indeed, in comparison with the axial velocity profile obtained, according to Batchelor, within the constant total head hypothesis

$$\frac{u(r)}{U_0} = \sqrt{1 + 2\left(\frac{\Omega R}{U_0}\right)^2\left[\mathrm{Ei}_1\left(\frac{r^2}{R^2}\right) - \mathrm{Ei}_1\left(2\frac{r^2}{R^2}\right)\right]}, \tag{6a}$$

the functional form (5) rewritten to have the same axial velocity

$$\frac{u(r)}{U_0} = 1 + \left[-1 + \sqrt{1 + 2\ln(2)\left(\frac{\Omega R}{U_0}\right)^2}\right]\exp\left(-\frac{r^2}{R^2}\right), \tag{6b}$$

seems to be completely different. However, one can easily conclude from Fig. 7 that (6*b*) is a rather good approximation for (6*a*). Obviously, (6*b*) or the more general form (5) is more convenient for analytical manipulation.

A more rigorous justification for (5) is attempted by Alekseenko et al. [20] who consider swirling flows with helical symmetry, i.e., the flow characteristics conserve their values along helical lines of pitch $2\pi l$. For axisymmetrical (columnar) helical vortices with a circumferential velocity as in (3) they obtain the axial velocity profile of the form

$$u(r) = U_{\text{axis}} - \frac{\Omega R^2}{l}\left[1 - \exp\left(-\frac{r^2}{R^2}\right)\right], \tag{7}$$

where $U_{\text{axis}} \equiv U_0 + U_1$. One can identify from (7) the characteristic velocity $U_1 = \Omega R^2/l$, and eventually use the length $l = (2\pi)^{-1} \times$ pitch instead of U_1 as a free parameter.

So far we have considered only an elementary vortex representation. However, the experimental data display a more complex structure which should be modeled by a combination of simple vortices. There are two possibilities to consider such combinations. One idea put forward by Alekseenko et al. [20] is to con-

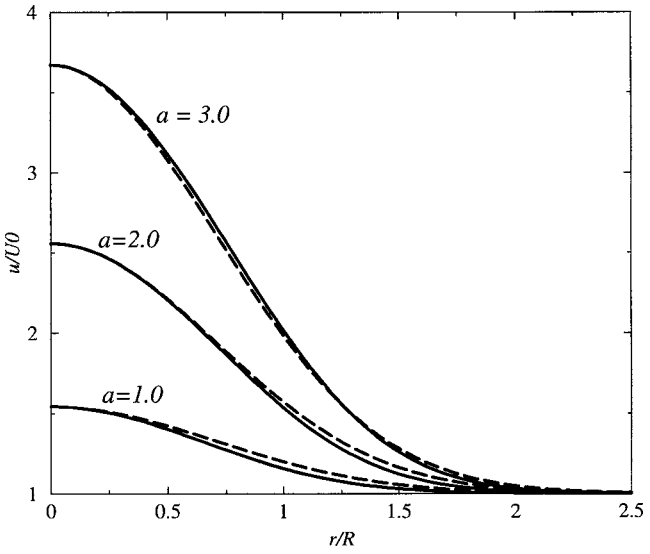

Fig. 7 Axial velocity profiles computed with (6*a*)—solid lines and (6*b*)—dashed lines, respectively, for several values of the dimensionless parameter $a \equiv \Omega R / U_0$

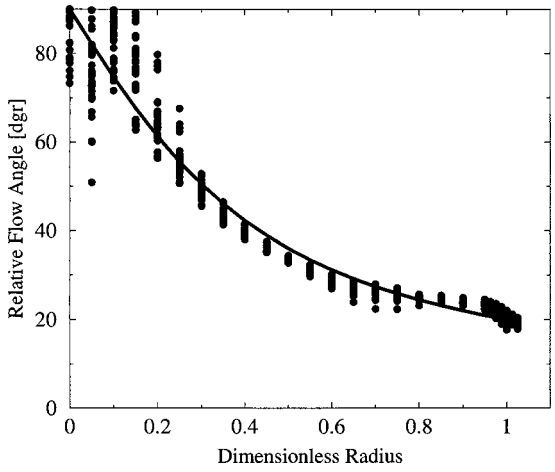

Fig. 8 Relative flow angle computed from the experimental data for axial and circumferential velocity components on the survey section. The solid curve is a least squares fit considering a rigid body rotation for the circumferential velocity and a constant axial velocity.

sider nonoverlapping regions along the radius, with piecewise continuous vorticity distribution. The resulting velocity profiles (both axial and circumferential) are made continuous by a proper choice of the integration constants. Another idea was put forward by Mattner et al. [9] who considered a sum of elementary velocity profiles for both axial and circumferential components. Essentially this second approach becomes equivalent to the first one if the vortices are well separated, i.e., the characteristic radii are well distinct one from each other.

In order to build a suitable vortex combination we should first consider a base flow. Using the dimensionless velocity components u and w, as well as the dimensionless runner tangential velocity, which coincides with the dimensionless radius r according to Sec. 2, the relative flow angle is

$$\beta = \arctan \frac{u}{r - w}. \tag{8}$$

Since the swirling flow examined in this paper is produced by a constant pitch Francis turbine runner, the relative flow angle should be consistent with an approximation corresponding to a solid body rotation, $w = \Omega_0 r$ and $u = U_0$. Indeed, the relative flow angle computed from the experimental data for circumferential and axial velocity can be reasonably fitted with $\beta = \arctan(\text{const}/r)$, as shown in Fig. 8. However, a solid body rotation is a rather crude approximation of the actual velocity profiles. Figures 4 and 5 suggest that two Batchelor vortices, one co-rotating and the other counter-rotating with respect to $w = \Omega_0 r$, and co-flowing/counter-flowing with respect to $u = U_0$, respectively, should be superimposed for consistency with experimental data for circumferential and axial velocity profiles:

$$w(r) = \Omega_0 r + \Omega_1 \frac{R_1^2}{r}\left[1 - \exp\left(-\frac{r^2}{R_1^2}\right)\right] + \Omega_2 \frac{R_2^2}{r}\left[1 - \exp\left(-\frac{r^2}{R_2^2}\right)\right], \tag{9a}$$

$$u(r) = U_0 + U_1 \exp\left(-\frac{r^2}{R_1^2}\right) + U_2 \exp\left(-\frac{r^2}{R_2^2}\right). \tag{9b}$$

If R_0 is the dimensionless survey section radius, then the discharge coefficient can be obtained by integrating the axial velocity profile (9*b*),

$$\varphi = U_0 R_0^2 + U_1 R_1^2\left[1 - \exp\left(-\frac{R_0^2}{R_1^2}\right)\right] + U_2 R_2^2\left[1 - \exp\left(-\frac{R_0^2}{R_2^2}\right)\right]. \tag{10}$$

The functional forms (9) have an eight-parameter set $\mathbf{\Pi} \equiv \{R_1, R_2, \Omega_0, \Omega_1, \Omega_2, U_0, U_1, U_2\}$ to be determined by fitting the experimental data. For each operating point under consideration, with a set of experimental data $(r_j, u_j, w_j) j = 1, \ldots, N$, the error vector $\mathbf{e}(\mathbf{\Pi}) = \{e_k(\mathbf{\Pi})\}$, $k = 1, 2, \ldots, 2N$ is defined as

$$e_k(\mathbf{\Pi}) = \begin{cases} u(r_k, \mathbf{\Pi}) - u_k & \text{for } k = 1, 2, \ldots, N, \\ w(r_{k-N}, \mathbf{\Pi}) - w_{k-N} & \text{for } k = N+1, \ldots, 2N. \end{cases} \tag{11}$$

The error vector includes both axial and circumferential velocity data since the vortex core radii R_1 and R_2 correspond to both velocity components. The parameter set is found by minimizing $\Sigma_{k=1}^{2N}[e_k(\mathbf{\Pi})]^2$, leading to a least squares estimate of $\mathbf{\Pi}$. Let $\mathbf{\Pi}_c$ be the current estimate of $\mathbf{\Pi}$. A new estimate is given by $\mathbf{\Pi}_c + \mathbf{\Pi}_c^*$, where $\mathbf{\Pi}_c^*$ is a solution to

$$[\mathbf{J}^T(\mathbf{\Pi}_c)\mathbf{J}(\mathbf{\Pi}_c) + \mu_c \mathbf{I}]\mathbf{\Pi}_c^* = \mathbf{J}^T(\mathbf{\Pi}_c)\mathbf{e}(\mathbf{\Pi}_c). \tag{12}$$

Here $\mathbf{J}(\mathbf{\Pi}_c)$ is the Jacobian $(2N) \times 8$ matrix evaluated analytically at $\mathbf{\Pi}_c$. The iterative algorithm uses a "trust region" approach with a step bound of δ_c. A solution of Eqs. (12) is first obtained for $\mu_c = 0$. If $\|\mathbf{\Pi}_c^*\|^2 < \delta_c$ this update is accepted. Otherwise, μ_c is set to a positive value and another solution is obtained.

Swirl parameters found by fitting formulas (9) to experimental data for 17 operating points are listed in Table 1. The last two columns contain the values of the discharge coefficient φ computed with (10), and the corresponding relative error with respect to the measured value shown in the first column. This error is a good indicator for the accuracy of the fit, as well as for the measurements overall accuracy. We conclude that (9*b*) is a very good representation for the axial velocity at the runner outlet and the superposition of three vortices in (9*a*) accurately represents the experimental data for the circumferential velocity over the whole discharge range under investigation.

Figures 9–14 display the data as well as the curves fitted with (9) for the first six points in Table 1. These operating points cover the investigated discharge domain at a constant head corresponding to the turbine best efficiency operating point. The quality of the fit can be assessed by observing that most of the time the curves approach the experimental points within the measurement

Table 1 Swirl parameters from Eqs. (9) for 17 turbine operating points

Operating point			Swirl parameters								Discharge coefficient	
Discharge coefficient	Energy coefficient	Speed (rpm)	Ω_0	Ω_1	Ω_2	U_0	U_1	U_2	R_1	R_2	Computed Eq. (10)	Error
0.340	1.18	1000	0.31765	−0.62888	2.2545	0.30697	0.01056	−0.31889	0.46643	0.13051	0.344	+1.1%
0.360	1.18	1000	0.26675	−0.79994	3.3512	0.31501	0.07324	−0.29672	0.36339	0.09304	0.363	+0.8%
0.368	1.18	1000	0.27113	−0.80310	3.4960	0.31991	0.08710	−0.27350	0.37291	0.08305	0.372	+1.0%
0.380	1.18	1000	0.27536	−0.81730	3.5187	0.32447	0.10618	−0.23545	0.38125	0.07188	0.381	+0.2%
0.390	1.18	1000	0.27419	−0.86579	3.2687	0.32916	0.12677	−0.19061	0.37819	0.06502	0.389	−0.2%
0.410	1.18	1000	0.28802	−0.96687	1.4590	0.33623	0.19121	−0.09215	0.39108	0.05012	0.409	−0.3%
0.368	1.00	1000	0.27710	−0.77440	3.3913	0.31704	0.08107	−0.24619	0.38128	0.08289	0.368	+0.1%
0.380	1.00	1000	0.26726	−0.83772	3.1082	0.32442	0.11387	−0.19284	0.35948	0.07312	0.380	+0.1%
0.370	1.11	1000	0.28119	−0.77668	3.5520	0.31731	0.08308	−0.25254	0.38947	0.07904	0.369	−0.1%
0.368	1.30	1000	0.29078	−0.79348	3.4239	0.31599	0.10086	−0.25499	0.39536	0.07939	0.371	+0.8%
0.380	1.30	1000	0.27618	−0.85846	3.2696	0.32691	0.12280	−0.19933	0.37413	0.06734	0.386	+1.5%
0.410	1.30	1000	0.27670	−0.96571	2.2165	0.33816	0.17829	−0.10984	0.37930	0.05021	0.407	−0.6%
0.370	1.11	500	0.27854	−0.77371	3.4491	0.31685	0.09058	−0.21118	0.38535	0.07827	0.370	+0.1%
0.340	1.18	500	0.29630	−0.67299	2.7487	0.30509	0.02987	−0.32612	0.41942	0.11679	0.345	+1.6%
0.368	1.18	500	0.27151	−0.78970	3.5902	0.31617	0.09131	−0.22465	0.37450	0.07914	0.369	+0.2%
0.380	1.18	500	0.27659	−0.79568	3.3111	0.32135	0.11063	−0.17502	0.38765	0.07002	0.379	−0.3%
0.410	1.18	500	0.28624	−0.93559	0.76010	0.33243	0.19587	−0.06119	0.39588	0.05147	0.406	−0.9%

errors of 2%. The wall boundary layer is not correctly reproduced since the swirling flow model (9) was specifically built for an inviscid flow analysis.

A main goal of this paper is to find a suitable parametric representation for the swirling flow at the Francis runner outlet. Figure 15 shows the variation of vortex characteristic angular velocities with respect to φ. Linear least squares fits accurately represent $\Omega_0(\varphi)$ and $\Omega_1(\varphi)$, while for $\Omega_2(\varphi)$ a parabolic fit seems to be quite satisfactory. Moreover, one should note that Ω_0 is almost constant over the investigated operating range. The variation of vortex characteristic axial velocities with respect to φ is shown in Fig. 16, together with the corresponding linear fits. Finally, Fig. 17 displays the dependence of the vortex core radii on φ. A first conclusion from Figs. 15–17 is that swirl parameters in (9) have a smooth, generally linear, variation in φ over the investigated range. As a result, one obtains the velocity components as C^∞ functionals $w(r,\varphi)$ and $u(r,\varphi)$, further employed in a parametric study of the flow stability or other properties.

According to the qualitative picture of the three vortex system presented in Table 2, Vortex 0 is a rigid body rotation with angular speed Ω_0 and we can associate with it a constant axial velocity U_0. Vortex 1, which has a vortex core extent about half the wall radius, is counter-rotating and co-flowing with respect to vortex 0. The strength of this vortex, both in Ω_1 as well as in U_1 is growing

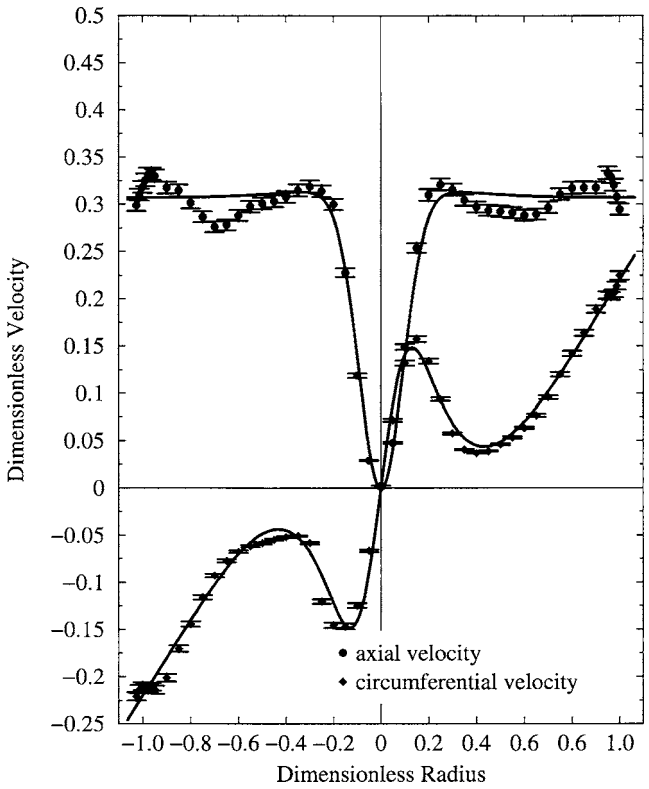

Fig. 9 Axial and circumferential velocity profiles at discharge φ=0.340

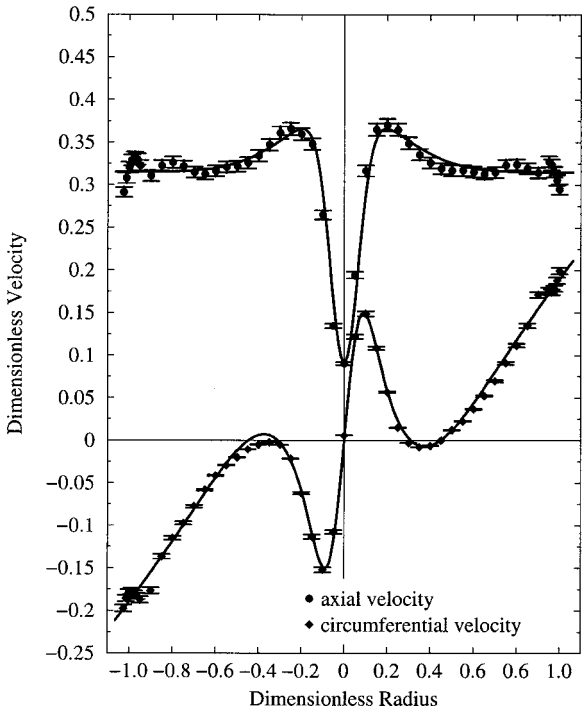

Fig. 10 Axial and circumferential velocity profiles at discharge φ=0.360

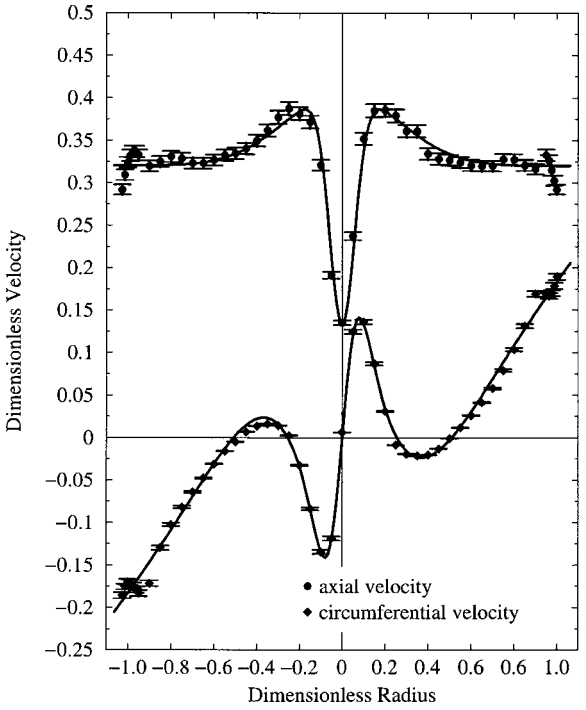

Fig. 11 Axial and circumferential velocity profiles at discharge φ=0.368

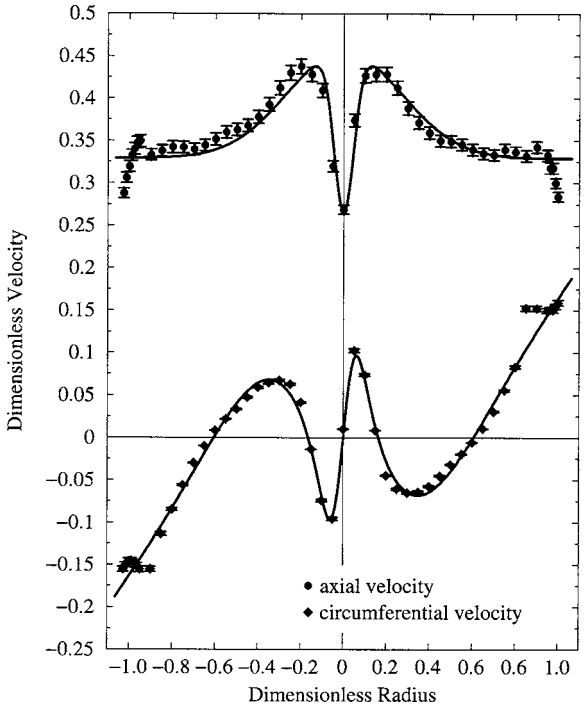

Fig. 13 Axial and circumferential velocity profiles at discharge φ=0.390

as the flow rate increases. Vortex 2 has a core at least four times smaller than vortex 1, is co-rotating and counter-flowing with respect to vortex 0, and its strength increases as the flow rate decreases. Note that as the flow rate increases (eventually beyond the upper limit in our investigation) vortex 2 will vanish. These two Batchelor vortices are mainly responsible for the swirling flow behavior. For φ smaller than the design value a wake-like axial velocity is developed (Fig. 9) while for larger φ the axial velocity has a jetlike profile (Fig. 14).

4 Swirling Flow Mathematical Model and Numerical Approach

Theoretical analysis of swirling flows can employ tools ranging from simplified axisymmetric, inviscid steady [11] or unsteady

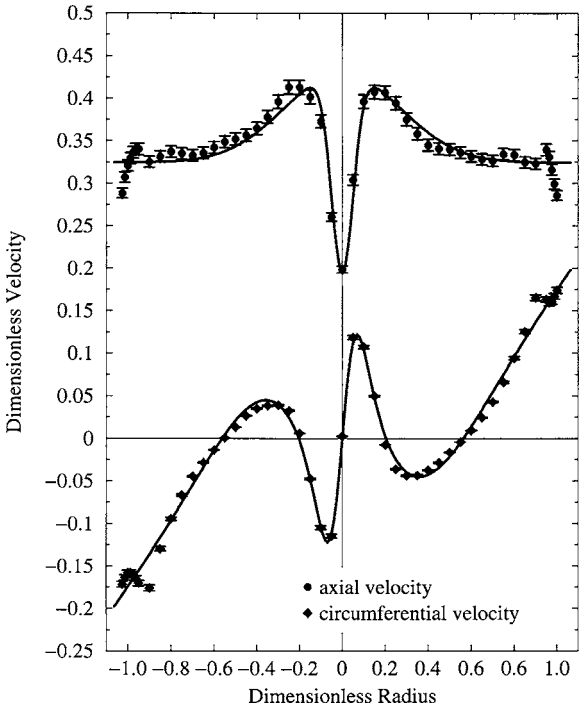

Fig. 12 Axial and circumferential velocity profiles at discharge φ=0.380

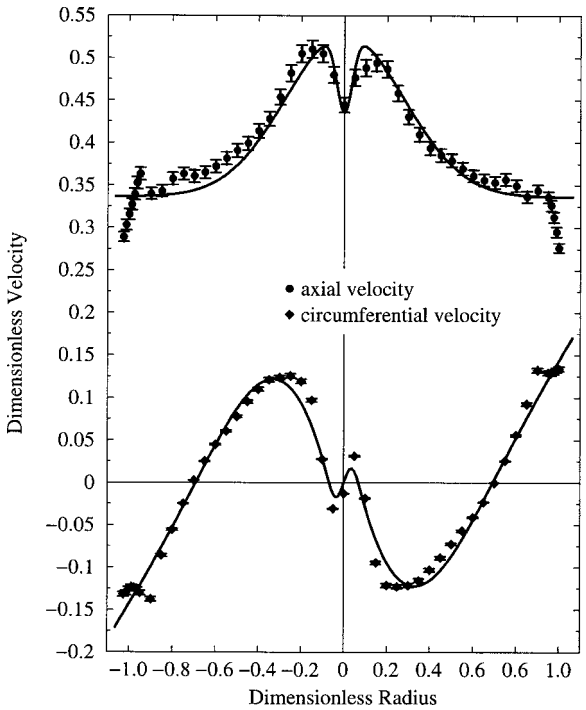

Fig. 14 Axial and circumferential velocity profiles at discharge φ=0.410

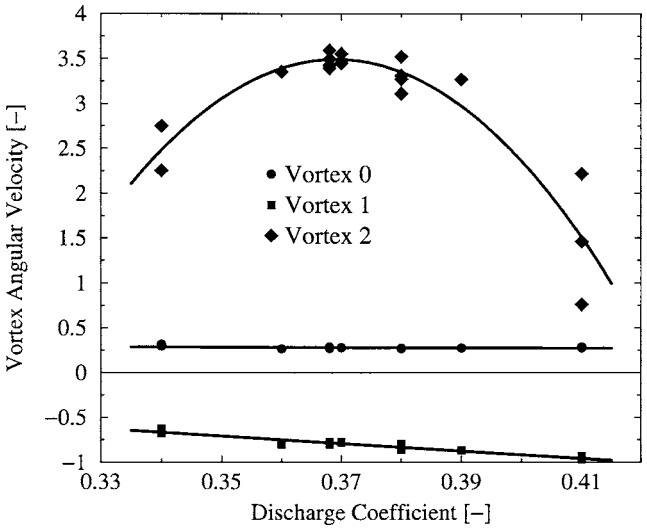

Fig. 15 Characteristic angular velocities Ω_0, Ω_1, and Ω_2 versus discharge coefficient φ

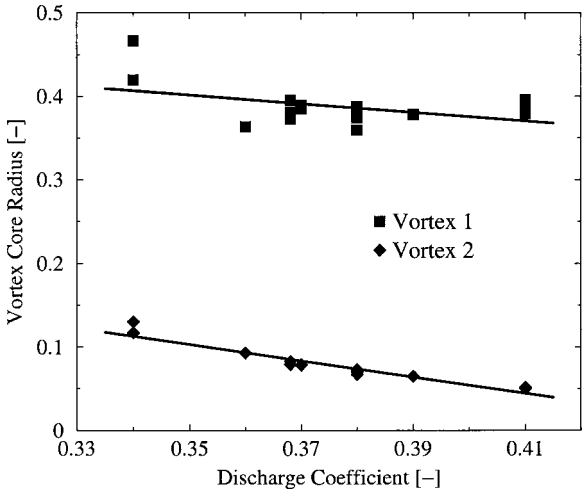

Fig. 17 Vortex core radii R_1 and R_2 versus discharge coefficient φ

[21] flow models to full 3D laminar [10] or turbulent [22] numerical simulation. However, it is useful to first examine the swirling flow at the draft tube inlet before performing an analysis of the flow in the straight cone or even in the whole 3D geometry. Such results may be quite useful if there is a correlation (even qualitative) with the overall draft tube behavior over a certain range of discharge variation.

If we restrict for now our analysis only for the runner outlet section, several simplifications must be admitted, and the results must be interpreted accordingly. We consider a steady mean flow with axial and circumferential velocity profiles derived from experimental data in Sec. 3. An inviscid incompressible fluid is considered, since our swirling flow representation does not account for the boundary layer near the wall.

The cylindrical flow assumption may not seem appropriate for the flow in the draft tube cone shown in Fig. 2, since it is known that the diverging pipe geometry precipitates the formation of breakdown by creating an adverse pressure gradient along the vortex axis. Shtern and Hussain [23] show that the nonparallel character of jets strongly affects their stability. Flow deceleration significantly enhances the shear-layer instability for both swirl-free and swirling jets. Buntine and Saffman [24] study a diverging flow using the steady axisymmetric Euler flow model. They show

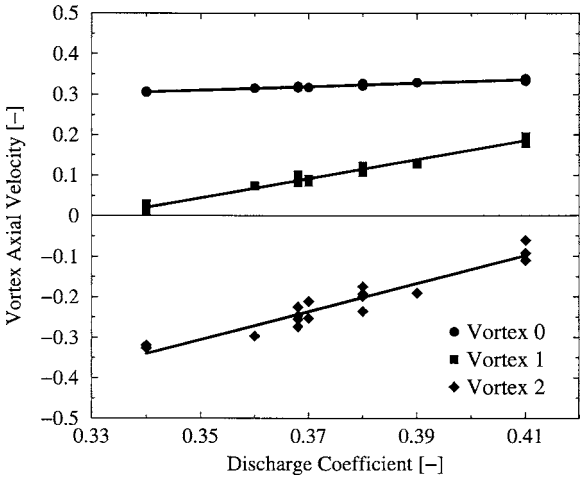

Fig. 16 Characteristic axial velocities U_0, U_1, and U_2 versus discharge coefficient φ

that solutions fail to exist or, alternatively, that flow ceases to be unidirectional, so that the breakdown can be inferred, when a parameter measuring the relative magnitude of rotation and axial flow exceeds critical values depending upon geometry and inlet profiles. However, for slightly diverging duct of angles less than 2°, Tsai [25] shows that the flow can be considered locally parallel for the flow stability analysis. This parallel flow assumption is not quite restrictive even for the 8.5° cone angle considered in this study. The diffusion process takes place only close to the wall, leading to a thin 3D boundary layer, as it can be seen from the measured velocity distribution (Figs. 4 and 5). Therefore, by neglecting the retarding influence of the wall, we can assume that the bulk flow is parallel. As far as the mean flow is concerned, the radial velocity is one order of magnitude smaller than the axial velocity since $v/u < \tan 8.5° \approx 0.15$.

Within these assumptions, the mathematical model to be considered here corresponds to the theory of finite transitions between frictionless cylindrical flows originally developed by Benjamin [11]. The equation of continuity for axisymmetric incompressible flows is automatically satisfied by introducing the streamfunction $\psi(z,r)$ such that the axial and radial velocity components can be written as

$$u = \frac{1}{r}\frac{\partial \psi}{\partial r} \quad \text{and} \quad v = -\frac{1}{r}\frac{\partial \psi}{\partial z}. \tag{13}$$

When applied to a circuit around a particular stream-surface ψ =const Kelvin's theorem shows rw to be a constant. Thus in general $rw \equiv K(\psi)$, where K is a function of ψ alone. Also, on a streamsurface the total specific energy $H = p/\rho + (u^2+v^2+w^2)/2$ is constant by Bernoulli's theorem, thus H is a function of ψ alone. The momentum equation for the steady, axisymmetric swirling flow becomes

$$\frac{1}{r^2}\left(\frac{\partial^2 \psi}{\partial z^2} + \frac{\partial^2 \psi}{\partial r^2} - \frac{1}{r}\frac{\partial \psi}{\partial r}\right) = H'(\psi) - \frac{K(\psi)K'(\psi)}{r^2}, \tag{14}$$

which is known in literature as the Long-Squire or Bragg-Hawthorne equation. Goldshtik and Hussain [14] noted that, in fact, Eq. (14) was derived much earlier by Meissel (in 1873). The prime denotes differentiation with respect to ψ. By introducing the new variable $y = r^2/2$ Eq. (14) can be rewritten as

$$\frac{\partial^2 \psi}{\partial y^2} + \frac{1}{2y}\frac{\partial^2 \psi}{\partial z^2} = H'(\psi) - \frac{K(\psi)K'(\psi)}{2y}. \tag{15}$$

If we substitute $Y_1 = R_1^2/2$ and $Y_2 = R_2^2/2$ the axial velocity profile (9*b*) can be written as

Table 2 Swirling flow structure

	Vortex 0	Vortex 1	Vortex 2
Circumferential velocity	rigid body rotation	counter-rotating	co-rotating
Axial velocity	constant	co-flowing	counter-flowing
Vortex core radius	—	$\sim 0.4R_0$	$\sim 0.1R_0$

$$u(y) = U_0 + U_1 \exp(-y/Y_1) + U_2 \exp(-y/Y_2). \tag{16}$$

Since from (13) $u = \partial\psi/\partial y$, the streamfunction for the above velocity profile is

$$\psi(y) = U_0 y + U_1 Y_1[1 - \exp(-y/Y_1)] + U_2 Y_2[1 - \exp(-y/Y_2)], \tag{17}$$

where without loss of generality we have considered $\psi = 0$ on the symmetry axis.

The discharge coefficient φ from Eq. (10) can be rewritten as

$$\varphi = 2U_0 Y_0 + 2U_1 Y_1[1 - \exp(-Y_0/Y_1)] + 2U_2 Y_2[1 - \exp(-Y_0/Y_2)], \tag{18}$$

where $Y_0 = R_0^2/2$. As a result, at the wall we have $\psi_{\text{wall}} \equiv \psi(Y0) = \varphi/2$.

For a mean flow with negligible radial velocity, the right-hand side in Eq. (15) is simply du/dy,

$$H'(\psi) - \frac{K(\psi)K'(\psi)}{2y} := \psi \xrightarrow{\text{Eq. 17}} y \to -\frac{U_1}{Y_1}\exp\left(-\frac{y}{Y_1}\right) - \frac{U_2}{Y_2}\exp\left(-\frac{y}{Y_2}\right).$$

The map $\Psi \to y$ has to be computed numerically, for example using the Newton iterative method,

$$y^{(m+1)} = y^{(m)} + \frac{\Psi - \psi(y^{(m)})}{u(y^{(m)})}, \quad \text{with initial guess } y^{(0)} = Y_0 \frac{\Psi}{\varphi/2},$$

where m denotes the iteration index. Note that due to the nonlinearity of this map, the solution of Eq. (15) with boundary conditions $\psi(0) = 0$ and $\psi(Y_0) = \varphi/2$ may be *nonunique*. To investigate this feature let us consider the streamfunction in (15) of the form

$$\psi(z,r) = \Psi(y) + \varepsilon\tilde{\psi}(y)\exp(i\kappa z), \tag{19}$$

where $\Psi(y)$ is the base flow given by (17), $\tilde{\psi}(y)$ is a perturbation of the base flow (Fig. 18), and κ is the axial wave number of this perturbation.

Introducing (19) in Eq. (15) one obtains the linearized equation

$$\frac{d^2\tilde{\psi}}{dy^2} - \left(H''(\Psi) - \frac{K'^2(\Psi) + K(\Psi)K''(\Psi)}{2y}\right)\tilde{\psi} = \frac{\kappa^2}{2y}\tilde{\psi}. \tag{20a}$$

Of course, in order to preserve the flow rate the perturbation must satisfy homogeneous boundary conditions

$$\tilde{\psi}(0) = \tilde{\psi}(Y_0) = 0. \tag{20b}$$

Equations (20) define a generalized eigenvalue problem. The eigenvalues κ^2 can be computed numerically once the problem is discretized. The expression inside square brackets on the left-hand side can be easily evaluated once an analytical swirl representation is available:

$$C(y) \equiv H''(\Psi) - \frac{K'^2(\Psi) + K(\Psi)K''(\Psi)}{2y} = \frac{1}{u}\frac{d^2u}{dy^2} - \frac{K}{2y^2u^2}\frac{dK}{dy}. \tag{21}$$

If we consider a grid $y_0 = 0, y_1, \ldots, y_1, \ldots, y_N, y_{N+1} = Y_0$ and a piecewise linear approximation of the solution $\tilde{\psi}(y) \approx \Sigma_j \tilde{\psi}_j N_j(y)$, the finite element discretization of problem (20) can be written in matrix form as

$$\mathbf{A}\tilde{\boldsymbol{\psi}} = \kappa^2 \mathbf{B}\tilde{\boldsymbol{\psi}}, \tag{22a}$$

where $\tilde{\boldsymbol{\psi}}$ is the nodal values vector, and

$$A_{ij} = -\int \frac{dN_i(y)}{dy}\frac{dN_j(y)}{dy}dy - \int N_i(y)C(y)N_j(y)dy,$$
$$B_{ij} = \int \frac{N_i(y)N_j(y)}{2y}dy \tag{22b}$$

are $N \times N$ tridiagonal symmetric matrices. Obviously the matrix entries in (22*b*) are evaluated only for the N interior nodes, due to the homogeneous Dirichlet conditions (20*b*). The GVCSP procedure from the International Math and Statistics Libraries (IMSL) [26] is used here to compute all of the eigenvalues and eigenvectors of the generalized real symmetric eigenvalue problem (22*a*), with **B** symmetric and positive definite.

Let us summarize now the swirling flow model according to the synoptic Fig. 18. Once the analytical representation for axial and circumferential velocity components has been established, the mean flow streamfunction can be computed. A streamtube Ψ = const may be subject to axisymmetric perturbations $\varepsilon\tilde{\psi}$, which are the eigenfunctions of problem (20). Such a perturbation can be

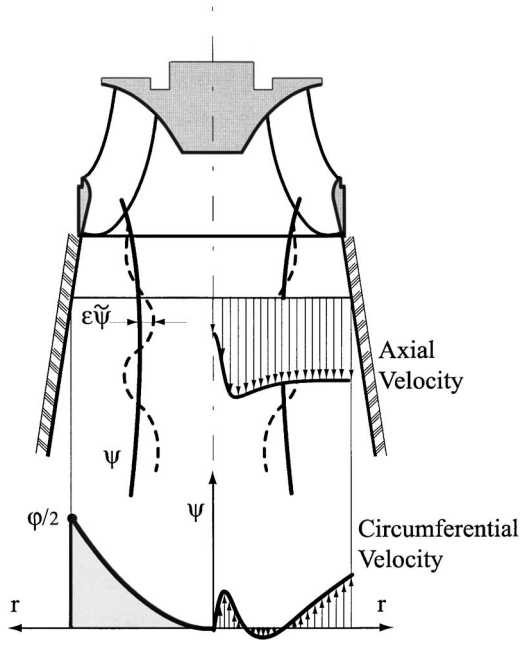

Fig. 18 Synoptic view of the model for swirling flow downstream of a Francis turbine runner

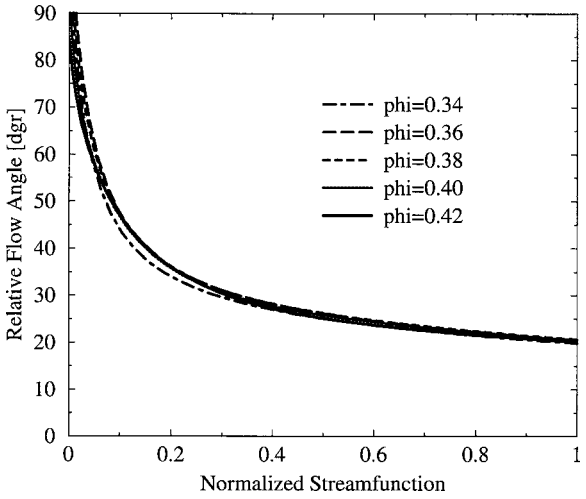

Fig. 19 Relative flow angle on streamtubes

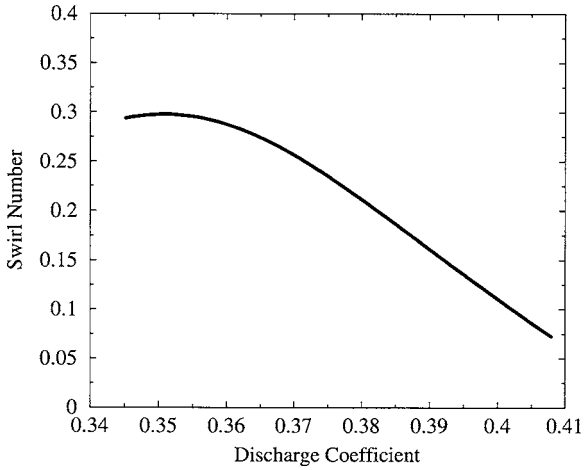

Fig. 20 The swirlnumber *S* from (23*a*) versus the discharge coefficient φ

sustained or not depending on the sign of the corresponding eigenvalue κ^2, according to the analysis to be presented in the next section.

5 Analysis of the Swirling Flow

An important property of the swirling flows downstream a constant pitch hydraulic turbine runner is that the relative flow angle depends only on the blade exit angle provided that the flow remains attached. This is certainly the case for a turbine runner operating in the neighborhood of the best efficiency point, therefore we can expect that the relative flow angle remains practically independent for the operating points of interest in this study. Moreover, due to negligible retarding forces, the global moment of momentum of the flow at the runner outlet should remain constant in the cone. Therefore, the relative flow angle (8) should depend only on the streamtube, i.e., on the normalized streamfunction $\psi/(\varphi/2)$ (Fig. 19). In other words, the relative flow angle on the survey section at runner outlet is practically constant on a streamtube originating at the same radius on the blade trailing edge, being determined by the blade exit angle irrespective of the discharge. This shows the direct correlation between the runner blade design and the kinematics of the swirl on the draft tube inlet. Moreover, the significant changes in the circumferential and axial velocity profiles can be associated only with the streamtube's cross-section variation downstream the blade trailing edge, as the discharge is modified.

The above considerations on the relative flow angle (8) help us understand the striking feature that the flow rotates in some radius range in the opposite direction to that at smaller and larger radii. Since the relative flow angle remains constant on a streamtube, an increase in the dimensionless axial velocity u must be accompanied by an increase in the dimensionless relative circumferential velocity r-w. In consequence, as the axial flow accelerates, i.e., a jetlike axial velocity profile is developed when the discharge increases, the corresponding absolute circumferential velocity w becomes negative in order to increase r-w, thus keeping $u/(r\text{-}w)$ practically constant in Eq. (8).

A global quantitative description of the swirling flow is provided by the swirl number S defined as the axial flux of swirl momentum divided by the axial flux of axial momentum [[27], p. 2],

$$S = \frac{\int_0^{R_0} \rho u(rw) r dr}{R_0 \int_0^{R_0} (\rho u^2 + p - p_{R_0}) r dr}, \tag{23a}$$

where p_{R_0} is the pressure at the wall. The pressure term in (23*a*) can be evaluated using the equation of radial equilibrium,

$$\frac{\partial p}{\partial r} = \frac{\rho w^2}{r} \Rightarrow p - p_{R_0} = -\int_r^{R_0} \frac{\rho w^2}{r} dr. \tag{23b}$$

The swirl number computed for the swirling flow given by (9), with parameters from Figs. 15–17, is plotted versus the discharge coefficient in Fig. 20. One can see that for the investigated range of φ the swirl number decreases as the discharge increases, but nevertheless the variation is smooth.

More interesting and useful conclusions can be drawn from the analysis of eigenvalues κ^2 and the corresponding eigenvectors in (20). If $\kappa^2 < 0$, then κ is imaginary and the exponential factor in (19) will be $\exp(\pm|\kappa|z)$. As we move downstream the current section, $z > 0$, the only physically acceptable solution corresponds to $\exp(-|\kappa|z)$, showing an exponential damping of $\tilde{\psi}$. A swirl configuration for which all eigenvalues are negative is unable to sustain axisymmetric small-disturbance standing waves and it was termed *supercritical* by Benjamin [11]. On the other hand, if at least one eigenvalue κ^2 is positive, then the perturbation will take the form of a standing wave $\exp(\pm i\kappa z)$, and the corresponding flow is termed *subcritical*. All physical interpretations attempted for the distinction between supercritical and subcritical states were mainly focused at the vortex breakdown phenomena. Benjamin's original interpretation was that for a given distribution of $H(\psi)$ and $K(\psi)$ one possible state of flow is subcritical and the conjugate state is supercritical. A deduction of this theory is that, compared with their conjugates, supercritical flows possess a deficiency of total momentum defined as the integral of axial momentum flux plus pressure over a cross section. This property would imply that supercritical flows are liable to undergo spontaneous transitions to subcritical state. Later, this theory came under quite heavy criticism, mostly because of its lack of explaining the axial flow reversal associated with the vortex breakdown. For example, Hall [28] particularly disagrees with the hydraulic jump analogy. Leibovich [29] considers that the most serious weakness of Benjamin's theory is that there is no clear way to relate it to experiments which, at high Reynolds numbers, always have unsteady, non-axisymmetric wakes. A decade ago Keller [12]

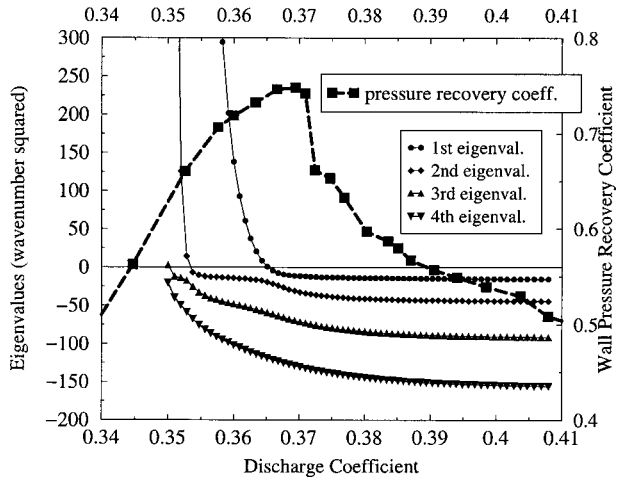

Fig. 21 The first four eigenvalues and the pressure recovery coefficient function of the discharge coefficient

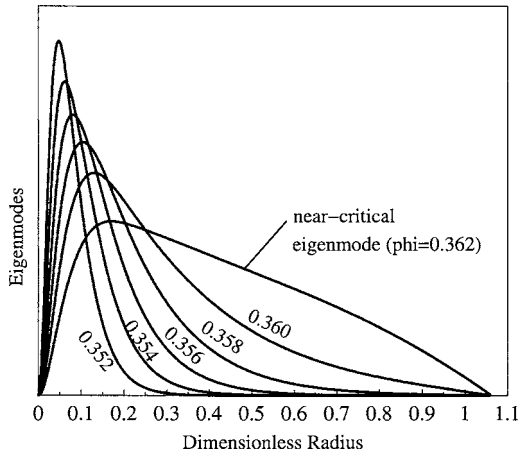

Fig. 22 Eigenmodes corresponding to the largest (positive) eigenvalue for subcritical swirling flows

pointed that various authors or even schools have conflicting views on the correct interpretation of the physics of vortex breakdown. Moreover, in his opinion, Benjamin's theory already contained most ideas for a successful theory of axisymmetric vortex breakdown but it was missing the definition of the total head circulation in regions with flow reversal, i.e., beyond the upstream interval of streamfunction values. The stagnation model emerged, where the total head is uniform and circulation vanishes in the domain of flow reversal, and was lately employed by Rusak et al. [30] to examine axisymmetric vortex breakdown in a finite length pipe. They present a comprehensive study of the Burgers vortex behavior, using both steady and unsteady axisymmetric inviscid flow models. Using essentially the same linearized eigenvalue problem, they determined the critical swirl level above which the base solution will evolve downstream to a solution that is a global (not local) minimizer of a certain functional. The flow in the pipe is computed explicitly, thus supporting the conclusions. However, no attempt has been made to directly correlate the computational results with any experimental data.

The approach we take in this paper is to examine the transition of the swirling flow downstream a Francis turbine runner from subcritical to supercritical as the discharge coefficient increases and to correlate the critical state with the experimentally observed sudden drop in the draft tube pressure recovery coefficient. A similar approach was advocated by Goldshtik and Hussain [14] who consider that vortex breakdown necessarily occurs when solution nonuniqueness is achieved by a continuous change in flow parameters. Moreover, we consider that valuable insight might be gained also by examining the eigenmodes $\tilde{\psi}$ corresponding to positive eigenvalues.

Let us examine first the main result of this paper, inferred from Fig. 21. For $\varphi > 0.365$, and correspondingly smaller swirl numbers, all eigenvalues from (20) are negative, thus the flow is supercritical and cannot sustain axisymmetric standing waves. However, for $\varphi < 0.365$ the largest eigenvalue becomes positive, followed by the next eigenvalues as φ decreases, and the flow is subcritical with standing waves described by the corresponding eigenvectors $\tilde{\psi}$. The critical state occurs according to our computations at $\varphi = 0.365$. This discharge value is quite close (only 1.3% smaller) to the value of $\varphi = 0.37$ where the sudden drop in draft tube pressure recovery coefficient is observed. It seems reasonable to assume that the critical state is directly related to this experimentally observed phenomenon, since by trying several draft tube geometries while keeping the same runner (and the swirling flow) the same behavior has been observed practically at the same discharge. While reaching the critical swirl configuration seems to be the cause, the actual physical mechanism by which the pressure recovery suffers an abrupt change cannot be inferred from the present analysis. Experimental [2] as well as numerical [3,4] investigations offer a comprehensive analysis of the Francis turbine draft tube flow.

Several eigenmodes $\tilde{\psi}(r)$ corresponding to the largest eigenvalue for subcritical flows are shown in Fig. 22. Since the eigenmodes are defined up to a multiplicative constant, it makes no sense to have marks on the vertical axis. One can easily see that as the discharge coefficient decreases the support of the eigenmode shrinks toward the axis neighborhood. It means that the induced velocity perturbations, for example their real part

$$\tilde{u} = \frac{d\tilde{\psi}}{dy}\cos(\kappa z) \quad \text{and} \quad \tilde{v} = \frac{\kappa\tilde{\psi}}{\sqrt{2y}}\sin(\kappa z),$$

are confined closer to the axis as φ decreases. Moreover, the relative amplitude of the perturbation increases since κ gets larger (leading to larger $\tilde{v}$) and also the slope at the origin increases (leading to larger $\tilde{u}$) on the axis. Although no vortex breakdown bubble is observed in the draft tube cone, the above velocity perturbations can be related to the axial velocity deficit reduction further downstream. This mechanism of reducing the "wakelike" axial velocity nonuniformity might be responsible for the improvement in the draft tube overall performance as the discharge gets smaller than the critical value. For even smaller discharge, more eigenmodes are successively present. For example, Fig. 23 presents the first two eigenmodes at $\varphi = 0.348$, corresponding to the two positive eigenvalues. While the first eigenmode is confined near the axis, the second one is not, but its behavior will follow the same pattern when further decreasing the discharge.

6 Conclusions

The present work started from the idea that the swirling flow configuration at the outlet of a Francis turbine runner has a major influence on the overall behavior of the flow downstream in the draft tube.

We have investigated experimentally the velocity axial and circumferential components at the runner outlet for 17 operating points within the turbine normal operating range. Then, a suitable analytical representation of the velocity profiles is developed, with the turbine discharge as an independent parameter. It is shown that the swirling flow in the survey section can be accurately represented using a superposition of three distinct vortices: a rigid body rotation motion, a counter-rotating and co-flowing Batchelor vortex with large core radius, and a co-rotating and counter-flowing Batchelor vortex with small vortex core. The eight parameters of

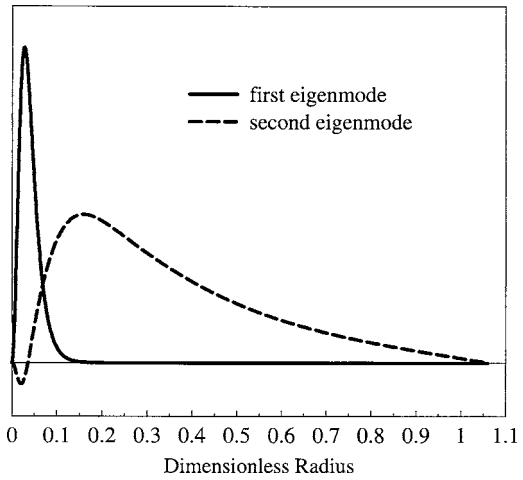

Fig. 23 First two eigenmodes for subcritical swirling flow at $\varphi=0.348$

this three-vortex system are determined by fitting the experimental data and are shown to vary smoothly (generally linear) with the discharge coefficient.

The flow at the runner outlet is then analyzed using the mathematical model for a steady, axisymmetric, and inviscid swirling flow. Following Benjamin's theory of finite transitions between frictionless cylindrical flows, we have performed an eigenvalue analysis of the linearized problem. It is shown that the swirl reaches a critical state at discharge $\varphi=0.365$. For larger discharge the flow ingested by the draft tube is supercritical, while at lower discharge it is subcritical. The critical state occurs quite close to the discharge $\varphi=0.370$ where a sudden variation in the draft tube pressure recovery, as well as in the overall turbine efficiency, is experimentally observed. For the particular turbine under investigation this discharge value happens to correspond to the best efficiency point, leading to a negative impact on the turbine regulation.

A qualitative correlation between the swirling flow at the draft tube inlet and the complex flow behavior further downstream may be inferred in conjunction with the Werlé-Legendre separation in the bend, discovered by Mauri et al. [15]. For subcritical swirling flow the sustained axisymmetric waves weaken the integrity of the vortex core, thus preventing the interaction with secondary flows in the draft tube bend. As the swirling flow reaches the critical state, and becomes supercritical as the discharge increases, the vortex core is no longer affected by axisymmetric perturbations, thus being able to trigger a global Werlé-Legendre separation that blocks the right channel of the draft tube and accelerates the flow in the other channel. The static pressure recovery is strongly affected, leading to an important loss in the overall machine efficiency.

Our analysis leads to the conclusion that when designing or optimizing turbine runners one should avoid reaching a critical state for the swirl at the runner outlet within the normal operating range.

Acknowledgment

The authors take this opportunity to thank our partners in the FLINDT Project Eureka No. 1625, Alstom Hydro, Electricité de France, GE Hydro, VA Tech Hydro, Voith-Siemens Hydro, PSEL (Funds for Projects and Studies of the Swiss Electric Utilities), and the CTI (Commission for Technology and Innovation), for their financial support. We also thank the staff of the Laboratory for Hydraulic Machines from the École Polytechnique Fédérale de Lausanne for their invaluable technical support. The first author would like to thank the École Polytechnique Fédérale de Lausanne, where he completed most of his contribution to this paper while a Visiting Professor in April 2003 and April–May 2004.

Nomenclature

A_{ref} = reference section area
H = Bernoulli's total head
K = circulation function
Q = turbine discharge
R_0 = survey section radius
R_{ref} = reference section radius
R_1, R_2 = vortex core radii
S = swirl number
U_0, U_1, U_2 = vortex characteristic axial velocities
p = pressure
r = radial coordinate
$u, \tilde{u}$ = axial velocity and its perturbation
$v, \tilde{v}$ = radial velocity and its perturbation
w = circumferential velocity
y = auxiliary variable
z = axial coordinate, aligned with the vertical machine axis
$\Omega_0, \Omega_1, \Omega_2$ = vortex characteristic angular velocities
β = relative flow angle
χ = draft tube wall pressure recovery coefficient
κ = wave number
ψ = streamfunction
φ = $Q/\omega R_{ref} A_{ref}$ discharge coefficient
ρ = density

References

[1] Escudier, M., 1987, "Confined Vortices in Flow Machinery," Annu. Rev. Fluid Mech., **19**, pp. 27–52.
[2] Avellan, F., 2000, "Flow Investigation in a Francis Draft Tube: the FLINDT Project," in *Proceedings of the 20th IAHR Symposium*, Charlotte, NC.
[3] Mauri, S., 2002, "Numerical Simulation and Flow Analysis of an Elbow Diffuser," Ph.D. thesis, École Politechnique Fédérale de Lausanne, Lausanne, Switzerland.
[4] Mauri, S., Kueny, J.-L., and Avellan, F., 2000, "Numerical Prediction of the Flow in a Turbine Draft Tube. Influence of the Boundary Conditions," FEDSM'00-11084, *Proceedings of the ASME 2000 Fluids Engineering Division Summer Meeting*, Boston, MA.
[5] Engström, T. F., 2003, "Simulation and Experiments of Turbulent Diffuser Flow With Hydropower Applications," Ph.D. thesis, Luleå University of Technology, Luleå, Sweden.
[6] Cervantes, M. J., 2003, "Effects of Boundary Conditions and Unsteadiness on Draft Tube Flow," Ph.D. thesis, Luleå University of Technology, Luleå, Sweden.
[7] Harvey, J. K., 1962, "Some Observations of the Vortex Breakdown Phenomenon," J. Fluid Mech., **14**, pp. 585–592.
[8] Faler, J. H., and Leibovich, S., 1977, "Disrupted States of Vortex Flow and Vortex Breakdown," Phys. Fluids, **20**(9), pp. 1385–1400.
[9] Mattner, T. W., Joubert, P. N., and Chong, M. S., 2002, "Vortical Flow. Part 1. Flow Through a Constant Diameter Pipe," J. Fluid Mech., **463**, pp. 259–291.
[10] Snyder, D. O., and Spall, R. E., 2000, "Numerical Simulation of Bubble-Type Vortex Breakdown Within a Tube-and-Vane Apparatus," Phys. Fluids, **12**(3), pp. 603–608.
[11] Benjamin, T. J., 1962, "Theory of the Vortex Breakdown Phenomenon," J. Fluid Mech., **14**, pp. 593–629.
[12] Keller, J. J., 1995, "On the Interpretation of Vortex Breakdown," Phys. Fluids, **7**(7), pp. 1695–1702.
[13] Leibovich, S., 1978, "The Structure of Vortex Breakdown," Annu. Rev. Fluid Mech., **10**, pp. 221–246.
[14] Goldshtik, M., and Hussain, F., 1998, "Analysis of Inviscid Vortex Breakdown in a Semi-infinite Pipe," Fluid Dyn. Res., **23**, pp. 189–234.
[15] Mauri, S., Kueny, J.-L., and Avellan, F., 2004, "Werlé-Legendre Separation in a Hydraulic Machine Draft Tube," ASME J. Fluids Eng., **126**, pp. 976–980.
[16] International Electrotechnical Commision, 1999, "Hydraulic Turbines, Storage Pumps and Pump-Turbines—Model Acceptance Tests," International Standard IEC 60193, 2nd ed.
[17] Ciocan, G. D., 1998, "Contribution à l'Analyse des Ecoulements 3D Complexes en Turbomachines," Ph.D. thesis, Institut National Polytechnique de Grenoble, Grenoble, France.
[18] Ciocan, G. D., Avellan, F., and Kueny, J.-L., 2000, "Optical Measurement Techniques for Experimental Analysis of Hydraulic Turbines Rotor-Stator Interaction," FEDSM2000-11056, *Proceedings of the ASME 2000 Fluids Engineering Division Summer Meeting*, Boston, MA.
[19] Batchelor, G. K., 1964, "Axial Flow in Trailing Line Vortices," J. Fluid Mech.,

20(4), pp. 645–658.
[20] Alekseenko, S. V., Kuibin, P. A., Okulov, V. L., and Shtork, S. I., 1999, "Helical Vortices in Swirl Flow," J. Fluid Mech., **382**, pp. 195–243.
[21] Wang, S., and Rusak, A., 1997, "The Dynamics of a Swirling Flow in a Pipe and Transition to Axisymmetric Vortex Breakdown," J. Fluid Mech., **340**, pp. 177–223.
[22] Lu, P., and Semião, V., 2003, "A New Second-Moment Closure Approach for Turbulent Swirling Confined Flow," Int. J. Numer. Methods Fluids, **41**, pp. 133–150.
[23] Shtern, V., and Hussain, F., 2003, "Effect of Deceleration on Jet Instability," J. Fluid Mech., **480**, pp. 283–309.
[24] Buntine, J. D., and Saffman, P. G., 1995, "Inviscid Swirling Flows and Vortex Breakdown," Proc. R. Soc. London, Ser. A, **449**, pp. 139–153.
[25] Tsai, C.-Y., 1980, "Examination of Group-Velocity Criterion for Breakdown of Vortex Flow in a Divergent Duct," Phys. Fluids, **23**(5), pp. 864–870.
[26] Visual Numerics, 2003, "IMSL Fortran Library User's Guide. Mathematical Functions in Fortran."
[27] Gupta, A. K., Lilley, D. G., and Syred, N., 1984, *Swirl Flows*, Abacus Press, Cambridge, MA.
[28] Hall, M. G., 1972, "Vortex Breakdown," Annu. Rev. Fluid Mech., **4**, pp. 195–218.
[29] Leibovich, S., 1984, "Vortex Stability and Breakdown: Survey and Extension," AIAA J., **22**(9), pp. 1192–1206.
[30] Rusak, Z., Wang, S., and Whiting, C. H., 1998, "The Evolution of a Perturbed Vortex in a Pipe to Axisymmetric Vortex Breakdown," J. Fluid Mech., **366**, pp. 211–237.

Journal of Fluids Engineering

Technical Briefs

Study on Hydrodynamic Torque of a Butterfly Valve

Ju Yeop Park[1]
e-mail: k385pjy@kins.re.kr
Regulatory Research Division,
Korea Institute of Nuclear Safety,
19 Guseong-dong, Yuseong-gu,
Daejeon, 305-338, Korea

Myung Kyoon Chung
Department of Mechanical Engineering,
Korea Advanced Institute of Science and Technology,
373-1 Guseong-dong, Yuseong-gu,
Daejeon, 305-701, Korea

Since knowledge on hydrodynamic torque of a butterfly valve is very important for butterfly valve design, its hydrodynamic torque is investigated theoretically. For this, a recently developed two-dimensional butterfly valve model is solved through the free-streamline theory with a newly devised iterative scheme and the resulting two-and three-dimensional torque coefficients are compared with previous theoretical results based on the conventional butterfly valve model and experiments. Comparison shows that the improvement due to the new butterfly valve model is marginal. That is, the three-dimensional torque coefficient is well represented by the new model. Otherwise, the two-dimensional torque coefficient is well predicted by the conventional model. In spite this fact, the present results can be used in further researches on butterfly valves because the improved butterfly valve model is mathematically correct and reflects physical reality more correctly than the conventional valve model. [DOI: 10.1115/1.2137348]

Keywords: butterfly valve, valve design, hydrodynamic torque

1 Introduction

The butterfly valve is widely used in various industrial applications for on-off and throttling services because it is easily closed or opened with relatively low pressure drop. In designing a butterfly valve, knowledge on its hydrodynamic torque is required for actuator sizing and structural design.

To the authors' best knowledge, a only theoretical study on hydrodynamic torque of the butterfly valve is given by Sarpkaya [1,2]. Based on a two-dimensional butterfly valve model, the flow field in the valve was solved by a free-streamline theory [3] with successive conformal transformations and contraction coefficients, force and torque coefficients were obtained. It is well known that the free-streamline theory is suited to analyze the plane irrotational flow field that includes free or bounded jets. Recently, Hassenpflug [4] suggested a new two-dimensional butterfly valve model that is more precise mathematically and physically than that of Sarpkaya [1,2]. The major difference between two models is an introduction of minimum velocity (see Fig. 1) that is located in the upper bounding wall to reflect four parameters in the hodograph plane [4]. Based on the new model, Hassenpflug [4] solved the problem with the free-streamline theory and found contraction coefficient but, unfortunately, the hydrodynamic torque of the butterfly valve was untouched. Since the hydrodynamic torque characteristic is an important parameter in designing a butterfly valve, in the present study, the hydrodynamic torque is investigated based on the improved valve model and the result is compared with that of Sarpkaya [2] and recent experiments [5,6].

2 Free-Streamline Theory

In order to determine the hydrodynamic torque that works on the two-dimensional butterfly valve, whole pressure distribution on a valve plate is required and this means that a complete flow field should be solved. Therefore, an application of the free-streamline theory is also made in the present study.

The free-streamline theory is composed of successive conformal transformations from a physical plane to a complex potential one. The unique feature of the theory is the introduction of a velocity plane, the hodograph. In the hodograph, an unknown free-streamline is transformed to a circular arc exactly and further conformal transformations can be done easily. In the present study, z (physical), w (hodograph), Λ (logarithmic hodograph), and t (Schwarz-Christoffel) planes are used. Equations (1)–(3) and Figs. 1–4 show corresponding transform functions and planes, respectively:

$$w = u - iv = qe^{-i\theta} \tag{1}$$

$$\Lambda = \ln \frac{w}{V_J} = \ln \frac{q}{V_J} - i\theta \tag{2}$$

$$\Lambda = M \int_0^t (t - t_{C_I})^{-1/2}(t - t_{D_I})^{-1/2}(t - t_E)^1(t - t_{D_{II}})^{-1/2}(t - t_{C_{II}})^{-1/2} dt + N \tag{3}$$

where $w[\equiv dF(z)/dz]$ is complex velocity, $F(z)[\equiv \phi(x,y) + i\psi(x,y)]$ is complex potential with velocity potential $\phi(x,y)$ and stream function $\psi(x,y)$, $z(\equiv x+iy)$ is a complex number, $i(\equiv\sqrt{-1})$ is an imaginary number, u and v are velocity components in the x and y directions, respectively, $q(\equiv\sqrt{u^2+v^2})$ is magnitude of velocity, $\theta[\equiv\tan^{-1}(v/u)]$ is an angle, and V_J is a jet velocity between wall boundary and free-streamline. M and N are con-

[1]Author to whom all correspondence should be addressed.

Contributed by the Fluids Engineering Division of ASME for publication in the JOURNAL OF FLUIDS ENGINEERING. Manuscript received July 26, 2005; final manuscript received August 10, 2005. Review conducted by Joseph Katz.

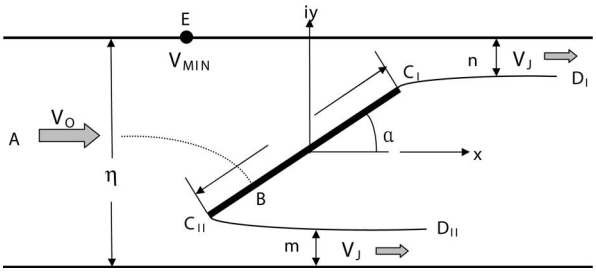

Fig. 1 Two-dimensional butterfly valve model (*z* plane)

stants of the Schwarz-Christoffel transformation and $t_{C_I}, t_{D_I}, \ldots$ are parameters of the Schwarz-Christoffel transformation.

The complex potential F in the t plane is easily deduced by noting that a source of strength $2\eta V_o$ and sinks of strength $2nV_J$ and $2mV_J$ are located at points t_A, t_{D_I}, and $t_{D_{II}}$, respectively. It is given by

$$F(t) = \frac{2\eta V_o}{2\pi}\ln(t-t_A) - \frac{2nV_J}{2\pi}\ln(t-t_{D_I}) - \frac{2mV_J}{2\pi}\ln(t-t_{D_{II}})$$

$$= \frac{V_J\eta}{2\pi}(1-\sin\alpha)[(C_{c1}+C_{c2})\ln(t-t_A) - C_{c1}\ln(t-t_{D_I}) - C_{c2}\ln(t-t_{D_{II}})] \quad (4)$$

where V_o is an inlet velocity of channel, η is a plate length and channel width, n and m are thickness of upper and lower jets, C_{c1} and C_{c2} are upper and lower contraction coefficients, and α is a valve closing angle. For Eq. (4), a continuity of mass and definition of contraction coefficients are used:

$$\eta V_o = nV_J + mV_J \quad (5)$$

$$C_{c1} \equiv \frac{2n}{\eta - \eta\sin\alpha} \quad \text{and} \quad C_{c2} \equiv \frac{2m}{\eta - \eta\sin\alpha} \quad (6)$$

Finally, an implicit solution can be determined as

$$z(t) = -\frac{\eta}{2\pi}(1-\sin\alpha)\int e^{-\Lambda}\left(\frac{C_{c1}}{t-t_{D_I}} + \frac{C_{c2}}{t-t_{D_{II}}} - \frac{C_{c1}+C_{c2}}{t-t_A}\right)dt + \text{const} \quad (7)$$

where

$$\frac{dz}{dF} = \frac{1}{V_J}e^{-\Lambda}$$

and

$$\frac{dF}{dt} = \frac{V_J\eta}{2\pi}(1-\sin\alpha)\left(\frac{C_{c1}+C_{c2}}{t-t_A} - \frac{C_{c1}}{t-t_{D_I}} - \frac{C_{c2}}{t-t_{D_{II}}}\right)$$

have been used.

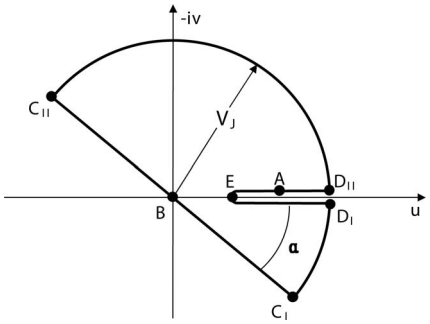

Fig. 2 Hodograph (*w* plane)

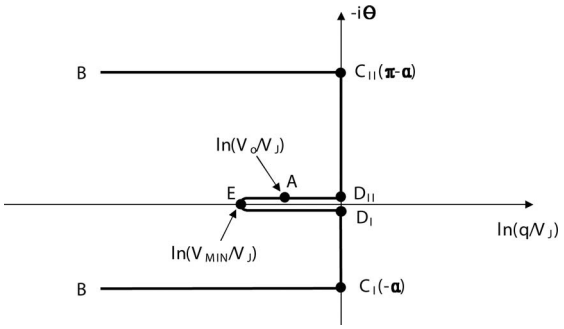

Fig. 3 Logarithmic hodograph (Λ plane)

3 Solution Procedure

Although the two-dimensional butterfly valve model is solved conceptually in the previous section, this is not the case. One should determine proper C_{c1}, C_{c2}, and Schwarz-Christoffel parameters such as t_{C_I}, $t_{D_{II}}$, and $t_{C_{II}}$ including complex constants M and N to complete the solution. In the present study, determination of corresponding parameters is done numerically through the following iterative procedure.

- Step 1. Assume V_J/V_{MIN} to fix a configuration of transformed region in the Λ plane.
- Step 2. Solve Schwarz-Christoffel parameter problem. Parameters such as t_{C_I}, $t_{D_{II}}$, and $t_{C_{II}}$ including M and N are solved by numerical algorithm of Chung, et al. [7]. Values of t_{D_I}, t_E, and t_B are fixed as 0, 1, and $\pm\infty$, respectively. Table 1 shows the calculated Schwarz-Christoffel parameters for various closing angles. Note that closing angles of 0 and 90 deg cases are excluded in the calculation.
- Step 3. Assume t_A value and find V_o/V_J and $C_{c1}+C_{c2}$ associated with t_A. Schwarz-Christoffel transformation determined in Step 2 is used for finding V_o/V_J since $\Lambda(t_A) = \ln(V_o/V_J)$. $C_{c1}+C_{c2}$ is determined as

$$C_{c1}+C_{c2} = \frac{2}{(1-\sin\alpha)}\frac{V_o}{V_J}. \quad (8)$$

- Step 4. Determine C_{c1} and C_{c2}, respectively, by the following equations (see Appendix A).

$$C_{c1} = \frac{1 - \frac{1}{\pi}\int_{t_{C_I}}^{t_{D_I}} e^{-\Lambda_R}\sin\Lambda_I\left(\frac{1}{t-t_{D_{II}}} - \frac{1}{t-t_A}\right)dt(C_{c1}+C_{c2})}{1 + \frac{1}{\pi}\int_{t_{C_I}}^{t_{D_I}} e^{-\Lambda_R}\sin\Lambda_I\left(\frac{1}{t-t_{D_I}} - \frac{1}{t-t_{D_{II}}}\right)dt} \quad (9)$$

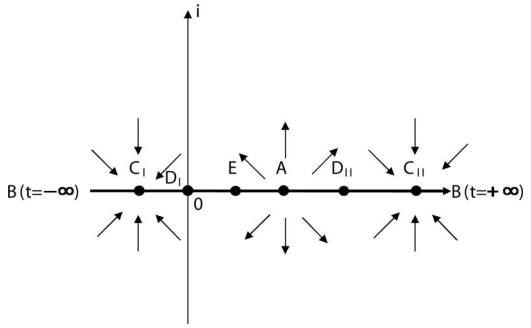

Fig. 4 Schwarz-Christoffel transformation (*t* plane)

Table 1 Parameters of Schwarz-Christoffel transform

α	t_{C_I}	$t_{D_{II}}$	$t_{C_{II}}$	M	N
0	…	…	…	…	…
5	−0.00257906512251	5.16772774261455	251.37036829504729	−1.00000000021639	0.00000000000000
10	−0.00268265764988	5.06471845671051	64.12536160056500	−1.00000000000000	0.00000000000000
15	−0.00274481375813	4.92286680162222	29.32203997791210	−1.00000000000000	0.00000000000000
20	−0.00276261168564	4.74812305914738	17.10017335921508	−1.00000000000000	0.00000000000000
25	−0.00272843500847	4.54770620137642	11.42548158028952	−1.00000000000000	0.00000000000000
30	−0.00263713925367	4.32850438304937	8.33504784312660	−1.00000000000000	0.00000000000000
35	−0.00248528120954	4.09709918892896	6.46838537135951	−1.00000000000000	0.00000000000000
40	−0.00227229233408	3.85956841452090	5.25594457556547	−1.00000000000000	0.00000000000000
45	−0.00200257474524	3.62133137548344	4.42489100810807	−1.00000000000000	0.00000000000000
50	−0.00168654216178	3.38716391998115	3.83086788553041	−1.00000000000000	0.00000000000000
55	−0.00134123768751	3.16121003062576	3.39133383630574	−1.00000000000000	0.00000000000000
60	−0.00098982880739	2.94697152569338	3.05599796072864	−1.00000000000000	0.00000000000000
65	−0.00065987892850	2.74723758023603	2.79257688221188	−1.00000000000000	0.00000000000000
70	−0.00037973471009760	2.56396916883108543	2.57950814874032676	−1.00000000000000	0.00000000000000
75	−0.00017305181135684	2.39816032527879861	2.40208354604927172	−1.00000000000000	0.00000000000000
80	−0.00005127533678435	2.24974515396132983	2.25031897642927925	−0.99999999999998	0.00000000000000
85	−0.00000518578360261	2.11763826731841664	2.11766164626554610	−1.00000000000000	0.00000000000000
90	…	…	…	…	…

$$C_{c2} = \frac{1 - \frac{1}{\pi}\int_{t_{D_{II}}}^{t_{C_{II}}} e^{-\Lambda_R}\sin\Lambda_I\left(\frac{1}{t-t_{D_I}} - \frac{1}{t-t_A}\right)dt(C_{c1}+C_{c2})}{1 - \frac{1}{\pi}\int_{t_{D_{II}}}^{t_{C_{II}}} e^{-\Lambda_R}\sin\Lambda_I\left(\frac{1}{t-t_{D_I}} - \frac{1}{t-t_{D_{II}}}\right)dt} \tag{10}$$

where Λ_R is a real part and Λ_I is an imaginary part of Λ. $C_{c1}+C_{c2}$ determined in Step 3 is used here.

- Step 5. Compare $C_{c1}+C_{c2}$ determined in step 3 with $C_{c1}+C_{c2}$ obtained in step 4. If the difference between these two values is within a predetermined error bound, proceed to next step. Otherwise, go to step 3 again and try another t_A value.
- Step 6. Calculate t_A from $t_{D_{II}}$, C_{c1}, and C_{c2} which were determined at steps 2 and 4, respectively. A relation among them is given as follows (see Appendix B):

$$t_A = \frac{C_{c2}t_{D_{II}}}{C_{c1}+C_{c2}}. \tag{11}$$

- Step 7. Compare t_A determined in step 6 with t_A assumed in step 3. If the difference between these two values is within a predetermined error bound, proceed to next step. Otherwise, go to step 1 again and try another V_J/V_{MIN} value.
- Step 8. Determine l_u and l_d with variables obtained in the previous steps (see Appendix B) and verify $\eta = l_u + l_d$ to check solution quality.

$$l_u = \frac{\eta(1-\sin\alpha)}{2\pi\sin\alpha}\int_{-\infty}^{t_{C_I}} e^{-\Lambda_R}\sin\Lambda_I\left(\frac{C_{c1}}{t-t_{D_I}} + \frac{C_{c2}}{t-t_{D_{II}}} - \frac{C_{c1}+C_{c2}}{t-t_A}\right)dt \tag{12}$$

$$l_d = \frac{\eta(1-\sin\alpha)}{2\pi\sin\alpha}\int_{t_{C_{II}}}^{+\infty} e^{-\Lambda_R}\sin\Lambda_I\left(\frac{C_{c1}}{t-t_{D_I}} + \frac{C_{c2}}{t-t_{D_{II}}} - \frac{C_{c1}+C_{c2}}{t-t_A}\right)dt \tag{13}$$

where l_u is a length from a stagnation point B to C_I and l_d is from B to C_{II}.

Table 2 shows determined parameters of the two-dimensional butterfly valve model for various closing angles. One can note that the present calculation agrees well with that of Hassenpflug [4].

Table 2 Parameters of the two-dimensional butterfly valve

α	V_J/V_{MIN}	V_J/V_o	C_{c1}	C_{c2}	C_{c1} [4]	C_{c2} [4]	l_u/η	l_d/η	$(l_u+l_d)/\eta$	l_d/η [4]
0	1.0000	1.0000	1.0000	1.0000	1.0000	1.0000	1.0000	0.0000	1.0000	0.0000
5	1.1946	1.1699	0.9630	0.9098	0.9630	0.9098	0.9999	0.00008347	1.0000	0.000083
10	1.4242	1.3721	0.9287	0.8352	0.9286	0.8352	0.9988	0.001115	0.9999	0.00112
15	1.6973	1.6157	0.8968	0.7733	…	…	0.9952	0.004743	0.9999	…
20	2.0251	1.9126	0.8672	0.7220	0.8672	0.7220	0.9873	0.01260	0.9999	0.0126
25	2.4234	2.2798	0.8396	0.6797	…	…	0.9740	0.02588	0.9999	…
30	2.9151	2.7410	0.8140	0.6453	0.8140	0.6453	0.9548	0.04514	0.9999	0.0452
35	3.5338	3.3310	0.7901	0.6180	…	…	0.9296	0.07036	0.9999	…
40	4.3314	4.1025	0.7678	0.5970	0.7678	0.5970	0.8989	0.1010	0.9999	0.1010
45	5.3903	5.1389	0.7469	0.5818	0.7469	0.5818	0.8638	0.1361	0.9999	0.1362
50	6.8485	6.5786	0.7275	0.5720	0.7275	0.5720	0.8252	0.1748	1.0000	0.1748
55	8.9496	8.6653	0.7093	0.5670	…	…	0.7842	0.2157	0.9999	…
60	12.1577	11.8632	0.6922	0.5661	0.6922	0.5661	0.7421	0.2578	0.9999	0.2578
65	17.4454	17.1445	0.6763	0.5688	…	…	0.6997	0.3002	0.9999	…
70	27.1434	26.8393	0.6614	0.5742	0.6614	0.5742	0.6578	0.3422	1.0000	0.3422
75	48.0565	47.7515	0.6475	0.5817	…	…	0.6168	0.3831	0.9999	…
80	107.7647	107.4600	0.6345	0.5905	0.6345	0.5905	0.5770	0.4230	1.0000	0.4230
85	430.1348	429.8307	0.6224	0.6004	0.6224	0.6002	0.5380	0.4618	0.9998	0.4617
90	∞	∞	0.6110	0.6110	0.6110	0.6110	0.5000	0.5000	1.0000	0.5000

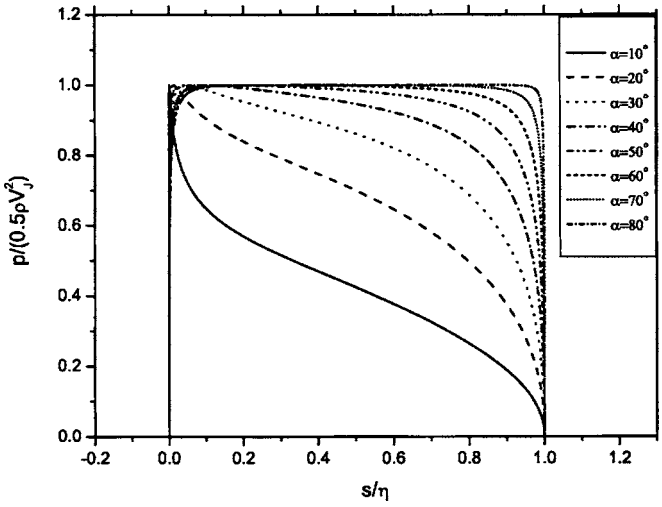

Fig. 5 Pressure distributions at various closing angles

Table 3 Moment arm, torque, and torce coefficients

α	η_c	T_c	F_c(numerical)	F_c(analytical)
0	0.00000	0.00000	0.00000	0.00000
5	−0.13887	0.016802	0.12096	0.12098
10	−0.11904	0.025210	0.21179	0.21177
15	−0.10088	0.028299	0.28051	0.28052
20	−0.084411	0.028096	0.33285	0.33284
25	−0.069561	0.025934	0.37284	0.37283
30	−0.056292	0.022711	0.40344	0.40344
35	−0.044575	0.019028	0.42689	0.42689
40	−0.034382	0.015296	0.44487	0.44487
45	−0.025688	0.011783	0.45869	0.45869
50	−0.018452	0.0086606	0.46935	0.46935
55	−0.012619	0.0060274	0.47764	0.47764
60	−0.0080984	0.0039206	0.48412	0.48412
65	−0.0047713	0.0023342	0.48921	0.48921
70	−0.0024865	0.0012263	0.49318	0.49318
75	−0.0010690	0.00053041	0.49618	0.49618
80	−0.00032247	0.00016069	0.49831	0.49831
85	−0.000030083	0.000015029	0.49957	0.49958
90	0.00000	0.00000	0.50000	0.50000

4 Torque Coefficient

To calculate the hydrodynamic torque of the two-dimensional butterfly valve, a pressure distribution on the plate should be obtained first. Application of the Bernoulli equation to lower plate segment $\overline{BC_{II}}$ gives

$$\frac{p}{\rho}+\frac{1}{2}q^2=\text{const}=\frac{1}{2}V_J^2. \tag{14}$$

Rearranging,

$$\frac{p}{1/2\rho V_J^2}=1-\left(\frac{q}{V_J}\right)^2. \tag{15}$$

Since $q/V_J=\exp[\Lambda_R(t)]$, determination of $\Lambda_R(t)$ spanning t from $t=t_{C_{II}}$ to $+\infty$ gives a pressure distribution on the lower plate segment. For the upper segment, a similar procedure should be followed. Figure 5 shows pressure distributions on the plate at various representative valve closing angles. By using the pressure distribution, a moment arm η_c with respect to the valve plate center for a specific closing angle is computed as

$$\eta_c=\frac{\int_0^\eta p(s)(s-1/2\,\eta)ds}{\int_0^\eta p(s)ds} \tag{16}$$

where s is a coordinate along the plate length and a numerical integration is performed by Simpson's one-third rule [8]. Finally, a hydrodynamic torque coefficient T_c of the two-dimensional butterfly valve is obtained by [2]

$$T_c\equiv\frac{T}{\rho\delta\eta^2V_J^2}=\frac{1}{2\sin\alpha}\left(1-\frac{V_o}{V_J}\right)^2\eta_c \tag{17}$$

where T is the hydrodynamic torque, ρ is the density of fluid, and δ is the unit depth of plate. To verify the accuracy of numerical integration, force coefficient F_c determined by numerical integration of the pressure and the analytical method are compared. F_c is given by [2]

$$F_c\equiv\frac{F}{\rho V_J^2\eta\delta}=\int_0^\eta\frac{p(s)}{\rho V_J^2}\frac{ds}{\eta}=\frac{1}{2\sin\alpha}\left(1-\frac{V_o}{V_J}\right)^2 \tag{18}$$

where F is the force on the valve plate. Table 3 shows calculation results of moment arm, torque, and force coefficients of Hassenpflug's two-dimensional butterfly valve model at various closing angles. Through comparison of F_c (numerical) with F_c (analytical), one can evaluate the accuracy of the present numerical integration.

5 Discussion

The two-dimensional torque coefficient of the butterfly valve determined by Hassenpflug's [4] model is compared with that of Sarpkaya [2] in Fig. 6. Experimental data obtained by Sarpkaya [2] are also included in the figure. It shows that although the overall tendency of torque coefficient with respect to the closing angle is similar in two models, the torque coefficient based on the Hassenpflug model is deviates more from the experiment than that of Sarpkaya. This is interesting because Hassenpflug's model is mathematically more precise than Sarpkaya's and is believed to reflect physical reality more closely [4]. Actually, as mentioned by Hassenpflug [4], Sarpkaya's model itself cannot give a unique stagnation point on the valve plate and, to resolve this anomaly, Sarpkaya applied the uniqueness of stagnation point in solving the problem.

Present results are also compared to the three-dimensional butterfly valve experiments [5,6]. For this, the two-dimensional torque coefficient T_c should be transformed to the three-

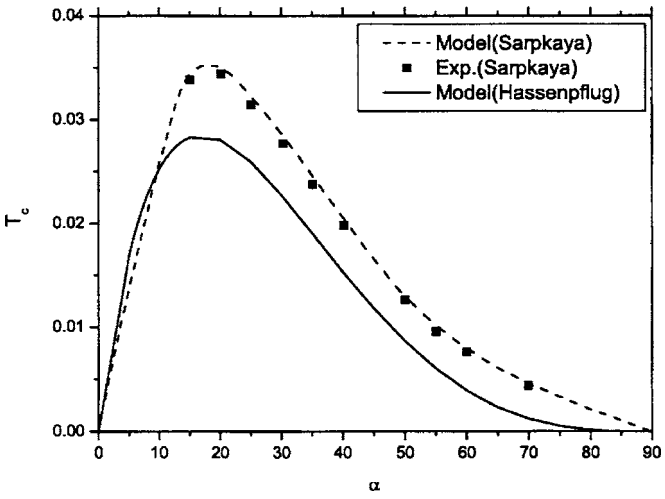

Fig. 6 Two-dimensional torque coefficient, T_c

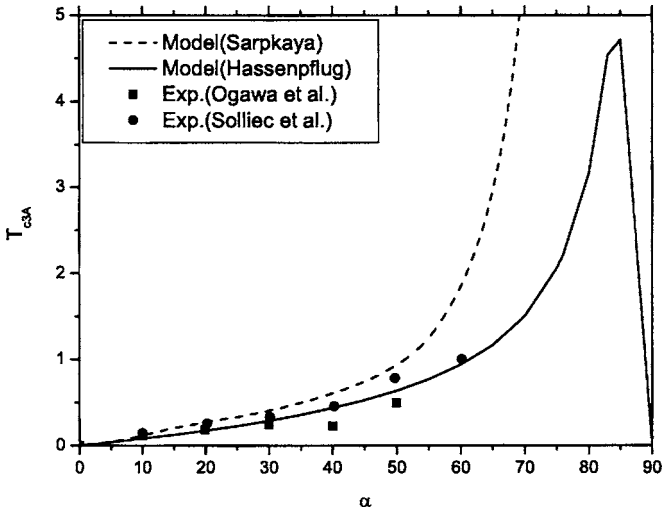

Fig. 7 Three-dimensional torque coefficient, T_{c3A}

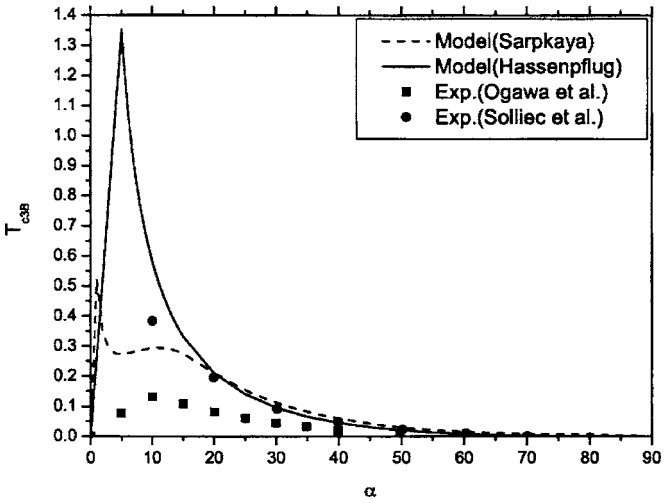

Fig. 8 Three-dimensional torque coefficient, T_{c3B}

dimensional counterpart. Sarpkaya [2] suggested a three-dimensional torque coefficient of butterfly valve T_{c3} as

$$T_{c3} \equiv \frac{T}{\rho D^3 V_J^2} \tag{19}$$

and showed that it is related to the two-dimensional torque coefficient as

$$T_{c3} = \frac{8}{3\pi} T_c. \tag{20}$$

T_{c3} suggested by Sarpkaya [2] is easily linked to two kinds of widely used three-dimensional torque coefficients as follows:

$$T_{c3A} = 2T_{c3}\left(\frac{V_J}{V_o}\right)^2 \tag{21}$$

$$T_{c3B} = 2T_{c3}\frac{1}{(1 - V_o/V_J)^2} \tag{22}$$

where

$$T_{c3A} \equiv \frac{T}{1/2\rho D^3 V_o^2} \quad \text{and} \quad T_{c3B} \equiv \frac{T}{D^3 \Delta P_{\text{Loss}}}$$

are torque coefficients normalized by dynamic pressure and static pressure drop, respectively [6], and ΔP_{Loss} is a pressure loss across the valve. In deriving Eq. (22), $\Delta P_{\text{Loss}} \equiv 1/2\rho K V_o^2$ with $K = (V_J/V_o - 1)^2$ is used [2]. Here, K is the loss coefficient of the butterfly valve. Figures 7 and 8 compare the two different calculations of T_{c3A} and T_{c3B} with experimental data. Unlike T_c, T_{c3A} based on Hassenpflug's model is better compared with experiments than Sarpkaya's model. For T_{c3B} case, both model predictions are not so good as the T_{c3A} case. But, here again, Hassenpflug's model gives a better fit for Solliec and Danbon's [6] experiment. Noting that the pressure loss is included in the definition of T_{c3B} and T_{c3B} is more likely to be influenced by an accuracy of pressure measurement across the valve, experimental uncertainty may be a source of such discrepancy.

As shown before, the two- and three-dimensional torque coefficients based on the Hassenpflug model did not show a great improvement over the two- and three-dimensional torque coefficients based on Sarpkaya's. In spite of this fact, the present result can be used as a cornerstone in developing any further research on butterfly valves because the present result is obtained by a more improved butterfly valve model.

Appendix A: Derivation of C_{c1} and C_{c2}

The implicit solution of the two-dimensional butterfly valve is given by Eq. (7) as

$$z(t) = -\frac{\eta}{2\pi}(1 - \sin\alpha)\int e^{-\Lambda}\left(\frac{C_{c1}}{t - t_{D_I}} + \frac{C_{c2}}{t - t_{D_{II}}} - \frac{C_{c1} + C_{c2}}{t - t_A}\right)dt + \text{const.} \tag{A1}$$

Then, it follows that

$$z(t_{D_I}) - z(t_{C_I}) = -\frac{\eta}{2\pi}(1 - \sin\alpha)\int_{t_{C_I}}^{t_{D_I}} e^{-\Lambda}\left(\frac{C_{c1}}{t - t_{D_I}} + \frac{C_{c2}}{t - t_{D_{II}}} - \frac{C_{c1} + C_{c2}}{t - t_A}\right)dt. \tag{A2}$$

Let $z(t_{D_I}) - z(t_{C_I}) = x + iy$ and $\Lambda = \Lambda_R + i\Lambda_I$. Then y becomes

$$y = \frac{\eta}{2\pi}(1 - \sin\alpha)\int_{t_{C_I}}^{t_{D_I}} e^{-\Lambda_R}\sin\Lambda_I\left(\frac{C_{c1}}{t - t_{D_I}} + \frac{C_{c2}}{t - t_{D_{II}}} - \frac{C_{c1} + C_{c2}}{t - t_A}\right)dt. \tag{A3}$$

C_{c1} is given by

$$C_{c1} = \frac{2n}{\eta - \eta\sin\alpha} \tag{A4}$$

where n is a normal distance from upper wall to upper streamline that is given by

$$n = \tfrac{1}{2}\eta(1 - \sin\alpha) - y, \tag{A5}$$

From Eqs. (A3)–(A5), it follows that

$$C_{c1} = 1 - \frac{1}{\pi}\int_{t_{C_I}}^{t_{D_I}} e^{-\Lambda_R}\sin\Lambda_I\left(\frac{C_{c1}}{t - t_{D_I}} + \frac{C_{c2}}{t - t_{D_{II}}} - \frac{C_{c1} + C_{c2}}{t - t_A}\right)dt. \tag{A6}$$

Finally, applying $C_{c2} = Y - C_{c1}$ to Eq. (A6) and rearranging it with respect to C_{c1} gives

$$C_{c1} = \frac{1 - \frac{1}{\pi}\int_{t_{C_I}}^{t_{D_I}} e^{-\Lambda_R}\sin\Lambda_I\left(\frac{1}{t-t_{D_{II}}} - -\frac{1}{t-t_A}\right)dtY}{1 + \frac{1}{\pi}\int_{t_{C_I}}^{t_{D_I}} e^{-\Lambda_R}\sin\Lambda_I\left(\frac{1}{t-t_{D_I}} - \frac{1}{t-t_{D_{II}}}\right)dt} \tag{A7}$$

where $Y \equiv C_{c1} + C_{c2}$.

For C_{c2}, a similar procedure reproduces Eq. (10).

Appendix B: Derivation of l_d and a Relationship Among t_A, $t_{D_{II}}$, C_{c1}, and C_{c2}

To seek a relationship among t_A, $t_{D_{II}}$, C_{c1}, and C_{c2}, one considers an exact equation for the plate lower length l_d first. It is determined as follows:

$$z(+\infty) - z(t_{C_{II}}) = -\frac{\eta}{2\pi}(1-\sin\alpha)\int_{t_{C_{II}}}^{+\infty} e^{-\Lambda}\left(\frac{C_{c1}}{t-t_{D_I}} + \frac{C_{c2}}{t-t_{D_{II}}} - \frac{C_{c1}+C_{c2}}{t-t_A}\right)dt. \tag{B1}$$

Let $z(+\infty) - z(t_{C_{II}}) = x + iy$ and $\Lambda = \Lambda_R + i\Lambda_I$. Then, y becomes

$$y = \frac{\eta}{2\pi}(1-\sin\alpha)\int_{t_{C_{II}}}^{+\infty} e^{-\Lambda_R}\sin\Lambda_I\left(\frac{C_{c1}}{t-t_{D_I}} + \frac{C_{c2}}{t-t_{D_{II}}} - \frac{C_{c1}+C_{c2}}{t-t_A}\right)dt \tag{B2}$$

and finally $l_d (= y/\sin\alpha)$ is given by

$$l_d = \frac{\eta}{2\pi}\frac{(1-\sin\alpha)}{\sin\alpha}\int_{t_{C_{II}}}^{+\infty} e^{-\Lambda_R}\sin\Lambda_I\left(\frac{C_{c1}}{t-t_{D_I}} + \frac{C_{c2}}{t-t_{D_{II}}} - \frac{C_{c1}+C_{c2}}{t-t_A}\right)dt. \tag{B3}$$

Through a similar procedure, one can also determine l_u. Now, determine the functional form of integrand of Eq. (B3) as $t \to +\infty$. For this, $\Lambda(t)$ should be considered first. $\Lambda(t)$ is given by

$$\Lambda(t) = -\int_0^t \frac{(t-t_E)}{\sqrt{(t-t_{C_I})(t-t_{D_I})(t-t_{D_{II}})(t-t_{C_{II}})}}dt. \tag{B4}$$

For large $t (t > t_I \gg t_{C_{II}} > 0)$, Eq. (B4) is rewritten as

$$\begin{aligned}\Lambda(t) &= -\int_0^{t_I} \frac{(t-t_E)}{\sqrt{(t-t_{C_I})(t-t_{D_I})(t-t_{D_{II}})(t-t_{C_{II}})}}dt \\ &\quad - \int_{t_I}^{t} \frac{(t-t_E)}{\sqrt{(t-t_{C_I})(t-t_{D_I})(t-t_{D_{II}})(t-t_{C_{II}})}}dt \\ &\approx (\pi-\alpha)i - \int_{C_{II}}^{t_I} \frac{(t-t_E)}{\sqrt{(t-t_{C_I})(t-t_{D_I})(t-t_{D_{II}})(t-t_{C_{II}})}} \\ &\quad \times dt - \ln(t) + \ln(t_I)\end{aligned} \tag{B5}$$

where $\Lambda(t_{C_{II}}) = (\pi-\alpha)i$ is used. Since $\Lambda(t) = \Lambda_R(t) + (\pi-\alpha)i$ for $t > t_I \gg t_{C_{II}}$, it follows that

$$\Lambda_R(t) = -\ln(t) + \beta(t_I) \tag{B6}$$

$$\Lambda_I(t) = \pi - \alpha \tag{B7}$$

where $\beta(t_I)$ is given by

$$\beta(t_I) \equiv \ln(t_I) - \int_{C_{II}}^{t_I} \frac{(t-t_E)}{\sqrt{(t-t_{C_I})(t-t_{D_I})(t-t_{D_{II}})(t-t_{C_{II}})}}dt.$$

Application of Eqs. (B6) and (B7) to the integrand of Eq. (B3) yields

$$\begin{aligned}\text{integrand} &= e^{\ln(t)}e^{-\beta(t_I)}\sin(\pi-\alpha)\left(\frac{C_{c1}}{t-t_{D_I}} + \frac{C_{c2}}{t-t_{D_{II}}} - \frac{(C_{c1}+C_{c2})}{t-t_A}\right) \\ &= e^{-\beta(t_I)}\sin(\alpha)\left[\frac{C_{c1}t_{D_I} + C_{c2}t_{D_{II}} - (C_{c1}+C_{c2})t_A}{t} + O\left(\frac{1}{t^2}\right)\right]\end{aligned} \tag{B8}$$

for $t \to +\infty$. For existence of Eq. (B3), the above integrand should more rapidly decay than $1/t$ as $t \to +\infty$. Therefore, the leading order term of Eq. (B8) should be zero. That is,

$$C_{c1}t_{D_I} + C_{c2}t_{D_{II}} - (C_{c1}+C_{c2})t_A = 0 \tag{B9}$$

This gives the relation among t_A, $t_{D_{II}}$, C_{c1}, and C_{c2} as follows:

$$t_A = \frac{C_{c2}t_{D_{II}}}{C_{c1}+C_{c2}} \tag{B10}$$

where $t_{D_I} = 0$.

References

[1] Sarpkaya, T., 1959, "Oblique Impact of a Bounded Stream on a Plane Lamina," J. Franklin Inst., **267**(3), pp. 229–242.

[2] Sarpkaya, T., 1961, "Torque and Cavitation Characteristics of Butterfly Valves," ASME J. Appl. Mech., **28**(4), pp. 511–518.

[3] Robertson, J. M., 1965, *Hydrodynamics in Theory and Application*, Prentice-Hall, Englewood Cliffs, NJ, Chap. 11.

[4] Hassenpflug, W. C., 1998, "Free-Streamlines," Comput. Math. Appl., **36**(1), pp. 69–129.

[5] Ogawa, K., and Kimura, T., 1995, "Hydrodynamic Characteristics of a Butterfly Valve-Prediction of Torque Characteristics," ISA Trans., **34**(4), pp. 327–333.

[6] Solliec, C., and Danbon, F., 1999, "Aerodynamic Torque Acting on a Butterfly Valve. Comparison and Choice of a Torque Coefficient," ASME J. Fluids Eng., **121**(4), pp. 914–917.

[7] Chuang, J. M., Gui, Q. Y., and Hsiung, C. C., 1993, "Numerical Computation of Schwarz-Christoffel Transformation for Simply Connected Unbounded Domain," Comput. Methods Appl. Mech. Eng., **105**(1), pp. 93–109.

[8] James, M. L., Smith, G. M., and Wolford, J. C., 1985, *Applied Numerical Methods for Digital Computation*, Harper & Row, New York, Chap. 5.

Inherently Linear Annular-Duct-Type Laminar Flowmeter

Janusz Wojtkowiak
e-mail: janusz.wojtkowiak@put.poznan.pl

Czeslaw O. Popiel[1]
e-mail: popiel@put.poznan.pl

Poznań University of Technology,
Institute of Environmental Engineering,
Piotrowo 3a, 60-965 Poznań, Poland

Introduction

A concept of the laminar flowmeter is based on the well-known relationship between laminar flow rate of fluid Q through a measuring element of length L and pressure drop ΔP. Usually the measuring element is a capillary tube, capillary tube bundle, parallel plate bundle, or concentric annular duct (Fig. 1).

The pressure drop in the measuring element ("long duct") consists of two components:

$$\Delta P = \frac{C\rho\nu L}{2AD_h^2}Q + \frac{K_\infty \rho}{2A^2}Q^2 \tag{1}$$

where: C is a constant (depends on a duct cross-section shape), A is the duct cross-sectional area, D_h is the hydraulic diameter of the duct, K_∞ is the incremental pressure drop number in a fully developed flow region (depends both on the duct cross-section shape and on the inflow conditions), L is the distance between the flowmeter pressure taps, ρ is fluid density, and ν is fluid kinematic viscosity.

The first component on the right-hand side of Eq. (1) is the pressure drop in the fully developed flow. The second one describes some additional pressure drop due to momentum change and accumulated increment in wall shear between developing flow and developed flow [1]. It is seen that the relationship between produced differential pressure ΔP and flow rate Q is not linear. As a result, in the majority of commercial laminar flowmeters, to obtain precise Q values software corrections are required. In some of the commercial "laminar flow elements" the entrance effect is ignored as a relatively low one. In order to eliminate the necessity of reading corrections and to achieve inherent linearity the second term of Eq. (1) must be removed. It can be done by locating the first pressure tap P_1 at the beginning of the fully developed flow region. As the entrance length L_e increases with the Reynolds number [$\mathrm{Re}=D_hQ/(A\nu)$], the distance between the duct entrance and the pressure tap P_1 should not be shorter than the entrance length for the maximum flow rate, i.e., for the laminar-turbulent transition Reynolds number.

The main aim of this work was to determine the design recommendation for the inherently linear laminar annular-duct flowmeter. The pressure distribution along the annular duct was measured. The entrance lengths for various inlet conditions and Reynolds numbers were investigated.

Theoretical Background

A solution of the continuity and momentum equations for the steady-state laminar fully developed flow of the Newtonian fluid in a concentric annulus provides us with the formula for the C constant in Eq. (1):

$$C = \frac{64(D-d)^2(D^2-d^2)}{D^4-d^4-(D^2-d^2)^2/\ln(D/d)} \tag{2}$$

where (see Fig. 2) d is the cylinder diameter and D is the tube internal diameter.

For a narrow annular duct we have $\lim_{d\to D} C=96$, which is the well-known value for parallel plates. One may examine that for $D/d<1.2$ the ratio $C_{FLAT}/C_{ANNULAR}<1.000\,55$. It means that the flow rate, even in a relatively "wide" annulus, can be calculated from an equation valid for the developed flow between parallel plates. If the first pressure tap of our flowmeter is located behind the entrance length L_e, the second component of the right-hand side of Eq. (1) will not exist. In this case the flow rate Q can be calculated using the simple linear relationship between Q and ΔP:

$$Q = \frac{2AD_h^2}{C\rho\nu L}\Delta P \tag{3}$$

in which $C=96$ (for $D/d<1.2$), $D_h=D-d$, and $A=\pi(D^2-d^2)/4$. As Eq. (3) is valid for a laminar flow and for a flowmeter having correctly located pressure tap P_1 it is very important to check the Reynolds number and the hydrodynamic entrance length L_e limit values.

Experimental Setup

The experimental flowmeter test section is shown in Fig. 2. Air of precisely controlled temperature ($23\pm0.2\,^\circ$C) and of known barometric pressure was used as a working fluid. An annular duct was formed between 215 mm long circular cylinders (stainless steel) of diameter $d=28.000\pm0.005$ mm and inner surface of calibrated thick-walled tube (polymethylmatacrylate) of diameter $D=30.23\pm0.01$ mm. Both the cylinder and tube surfaces were polished and their diameters were precisely measured at 23 °C. Two stainless steel turning covers and a special holding system were used to obtain rigid and concentric cylinder-tube connection. As a result, the obtained eccentricity was less than 0.1 mm. The inlet edge of the cylinder was rounded with the radius of about $R=0.3$ mm. Two test sections were investigated. The first one was equipped with a short (14 mm) upstream chamber receiving air

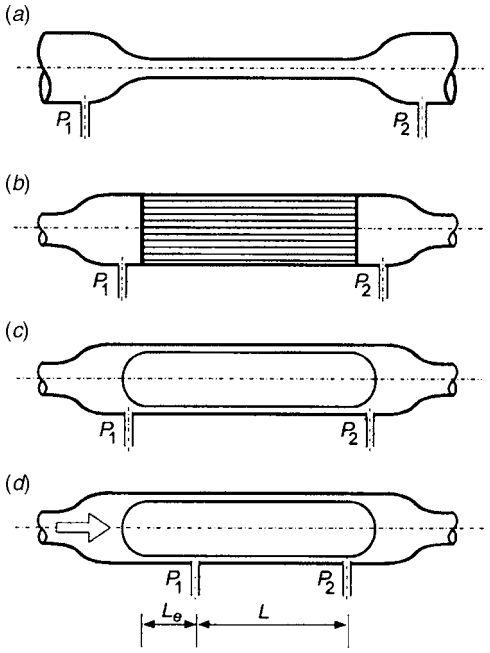

Fig. 1 Laminar flowmeters: (*a*) capillary tube, (*b*) capillary tube or parallel plate bundles, (*c*) concentric annular duct, and (*d*) concentric annular duct inherently linear

[1]Corresponding author.

Contributed by the Fluids Engineering Division of ASME for publication in the JOURNAL OF FLUIDS ENGINEERING. Manuscript received May 6, 2004; final manuscript received September 1, 2005. Review conducted by Joseph Katz.

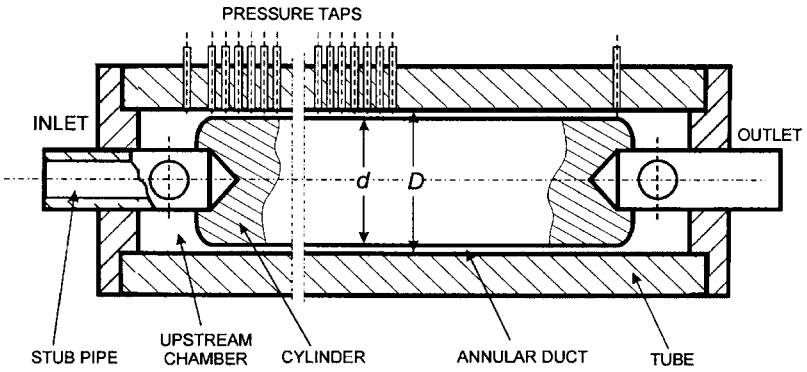

Fig. 2 Test section (not in scale)

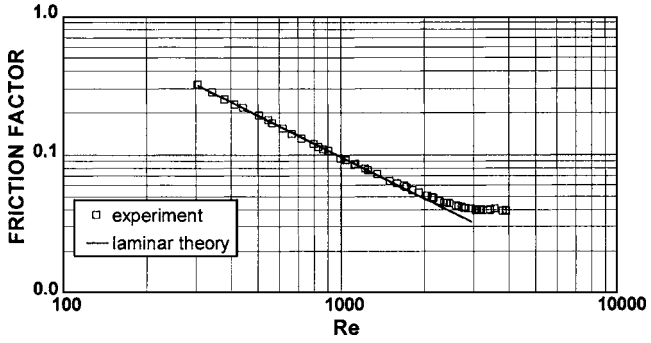

Fig. 3 Friction factor vs. Reynolds number (for the fully developed region)

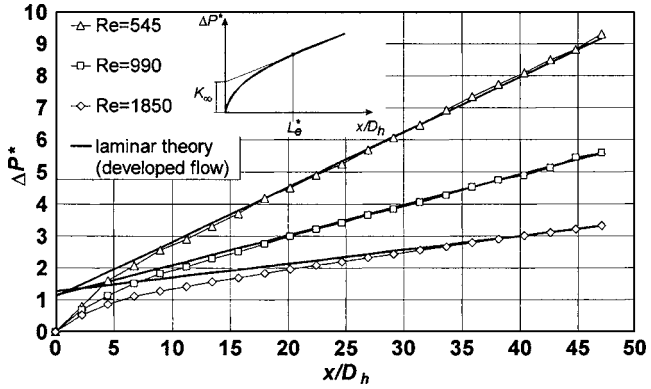

Fig. 4 Exemplary pressure drop distribution along the duct

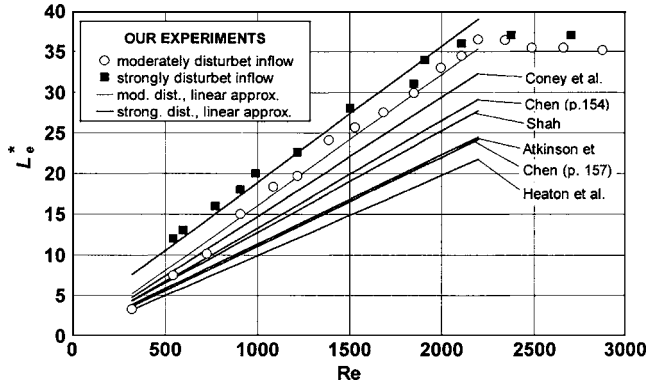

Fig. 5 Hydrodynamic entrance length (literature data: undisturbed inflow; our experimental data: disturbed inflow)

from the stub pipe 15 mm in diameter through four orifices each 8 mm in diameter. The air entering the gap was strongly disturbed (Fig. 2). The second one (not shown here) had a $3.3D$ long upstream chamber (tube of diameter D without the stub pipe) producing moderately disturbed inflow conditions. The tube of the test section was equipped with a set of 23 pressure taps having 0.7 mm diameter. Distances between adjoining taps were 5 mm. The first pressure tap was located precisely at the gap inlet.

Pressure drop ΔP was measured with the electric micromanometer, and flow rate Q was measured with the calibrated laboratory rotary gasmeter. Uncertainty evaluation of the final results was performed in accordance with a 95% confidence interval to satisfy ISO document [2]. Uncertainty of the pressure difference measurement ΔP was estimated to be ±2% for low and ±1% for moderate and high flow rates. Uncertainty of the volume flow rate measurement Q was about ±1.5% for low, ±1% for moderate, and ±0.5% for high flow rates. In the region of $\mathrm{Re}<1000$ the uncertainties of Re and L_e were estimated to be ±3.5% and ±5.5%, respectively. For $\mathrm{Re}>1000$ they were ±2.5% and ±4.5%.

Results and Discussion

As the diameter ratio is $D/d=1.0796<1.2$ we may neglect the curvature effect and treat the annular duct as the parallel plates [$C=96$ in Eq. (3)].

Limit Value of the Reynolds Number. In Fig. 3 the experimental data of the friction factor in the fully developed region for a strongly disturbed inflow condition versus Reynolds number are shown. It is seen that below the Reynolds number of $\mathrm{Re}\approx 1900$ our experimental data agree very well with the laminar theory for the parallel plate flow. This Reynolds number is considerably lower (probably due to strong inflow disturbances) than the results of Beavers et al. [3] who determined the laminar-turbulent transition Reynolds number within the range from 2200 to 3400.

Hydrodynamic Entrance Length. A definition of the hydrodynamic entrance length L_e proposed by Sparrow and Lin [4] was used, i.e., the length L_e required to achieve the local incremental pressure drop number as about 98% of the incremental pressure drop number in the fully developed region K_∞.

In Fig. 4 the dimensionless pressure drop distribution $\Delta P^*=(P_{x=0}-P_x)/P_d$ along the duct for various Reynolds numbers and a graphic representation of the dimensionless entrance length $L_e^*=L_e/D_h$ as well as the value of K_∞ are shown [where $P_d=0.5\rho(Q/A)^2$, x is distance from the duct entrance]. The available data concerning the hydrodynamic entrance length for the flow between parallel plates (Table 1) and the measured entrance length for strongly and moderately disturbed inlet flows are presented in Fig. 5. The experimental relationship $L_e^*=f(\mathrm{Re})$ seems to be linear and typical for laminar duct flow. Sudden change in the slope of the experimentally obtained entrance length at $\mathrm{Re}=2200$ is attrib-

Table 1 Hydrodynamic entrance length in laminar flow between parallel plates (literature data and experimental results)

Author(s)	L_e^*	Remarks
Chen [5] (p. 154)	$\frac{0.395}{0.02\,\mathrm{Re}+1}+0.01325\,\mathrm{Re}$	Integral momentum method
Chen [5] (p. 157)	$\frac{0.315}{0.0175\,\mathrm{Re}+1}+0.011\,\mathrm{Re}$	Finite differential method
Shah [6]	$0.25+0.0125\,\mathrm{Re}$	Correlation for straight duct of arbitrary but constant cross section
Atkinson et al. [7]	$0.3125+0.011\,\mathrm{Re}$	Theory: linear combination of creeping flow and boundary layer solution for uniform entrance velocity profile
Heaton et al. [8]	$0.0099\,\mathrm{Re}$	Based on the data tabulated by Shah and London [1]
Coney and El-Shaarawi [9]	$0.0147\,\mathrm{Re}$	Based on the data tabulated by Shah and London [1]
This paper	$0.0161\,\mathrm{Re}$	Moderately disturbed inflow
This paper	$2.11+0.0168\,\mathrm{Re}$	Strongly disturbed inflow

uted to laminar-turbulent transition. Higher values of L_e^* are observed for the disturbed inflow conditions. In this case the flow is likely not only in the course of developing flow but also in the process of damping of the large inlet disturbances. Moreover, some elongation of the entrance length is plausibly attributed to the flow separation from the cylinder edge and to the "vena contracta" phenomenon. As a result the measured pressure drop entrance length is larger than the theoretical values obtained for undisturbed inflow conditions (Table 1). As it is seen in Fig. 5 the dimensionless entrance length L_e^* at the Reynolds number $\mathrm{Re}=1900$ is about 32 for the moderately disturbed inlet flow and about 35 for strongly disturbed inlet flow. The last value is the recommended distance from the duct inlet to the place in which the first flowmeter pressure tap should be located.

Concluding Remarks

The inherently linear annular-duct-type laminar flowmeter [Fig. 1(*d*)] was investigated with air. To achieve the inherent linearity a proper location of the upstream pressure tap ($L_e^* \geqslant 35$) and the Reynolds number below $\mathrm{Re} \leqslant 1900$ are required. The flow characteristics of the flowmeter can be obtained theoretically using Eq. (3) for $D/d < 1.2$ and neither calibration nor software reading correction are necessary. This device can be relatively easily designed and produced in any laboratory workshop.

References

[1] Shah, R. K., and London, A. L., 1978, Supplement 1: "Laminar Flow Forced Convection in Ducts," *Advances in Heat Transfer*, Academic Press, New York, pp. 41–42, 168–169, 287–289.

[2] *Guide to the Expression of Uncertainty in Measurements*, 1993, ISO/IEC/OIML/BIPM, Int. Organization for Standardization (ISO), Switzerland (1st ed.).

[3] Beavers, G. S., Sparrow, E. M., and Magnuson, R. A., 1970, "Experiments on the Breakdown of Laminar Flow in a Parallel-Plate Channel," Int. J. Heat Mass Transfer, **13**, pp. 809–815.

[4] Sparrow, E. M., and Lin, S. H., 1964, "The Developing Laminar Flow and Pressure Drop in the Entrance Region of Annular Ducts," J. Basic Eng., **86**, pp. 827–834.

[5] Chen, R.-Y., 1973, "Flow in the Entrance Region at Low Reynolds Number," ASME Trans. J. Fluids Eng., **95**, pp. 153–158.

[6] Shah, R. K., 1978, "A Correlation for Laminar Hydrodynamic Entry Length Solutions for Circular and Noncircular Ducts," ASME Trans. J. Fluids Eng., **100**, pp. 177–179.

[7] Atkinson, B., Brockleband, M. P., Card, C. H., and Smith, J. M., 1969, "Low Reynolds Number Developing Flows," AIChE J., **15**, pp. 548–553.

[8] Heaton, H. S., Reynolds, W. C., and Kays, W. M., 1961, "Heat Transfer in Annular Passages. Simultaneous Development of Velocity and Temperature Fields in Laminar Flow," Int. J. Heat Mass Transfer, **7**, pp. 763–781.

[9] Coney, J. E. R., and El-Shaarawi, M. A. I., 1975, "Developing Laminar Radial Velocity Profiles and Pressure Drop in the Entrance Region of Concentric Annuli," Nucl. Sci. Eng., **57**, pp. 169–174.

Optimal Molar Gas Composition of Selected Gas Mixtures With Helium that Maximize Turbulent Free Convection Along Vertical Plates

Antonio Campo[1]
Department of Mechanical Engineering,
The University of Vermont,
Burlington, VT 05405
e-mail: acampo@cems.uvm.edu

Salah Chikh
Département de Génie Mécanique,
USTHB,
B.P. 32, El Alia,
Bab Ezzoaur 16111, Algeria

Shyam S. Sablani
Department of Bioresource
and Agricultural Engineering,
Sultan Qaboos University,
Al-Khod PC 123, Muscat, Oman

With the goal of intensifying turbulent free convection from heated vertical plates to cold gases, five binary gas mixtures are examined in this technical note. Helium (He) is chosen as the principal gas while xenon (Xe), nitrogen (N_2)*, oxygen* (O_2)*, carbon dioxide* (CO_2)*, and methane* (CH_4) *are the companion gases. From thermal physics, the thermophysical properties affecting turbulent free convection of binary gas mixtures are the viscosity* μ_{mix}*, the thermal conductivity* λ_{mix}*, the density* ρ_{mix}*, and the heat capacity at constant pressure* $C_{p,\text{mix}}$*. Invoking the similarity variable transformation, the system of two nonlinear differential equations is solved numerically by the shooting method and a fourth-order Runge-Kutta-Fehlberg algorithm. From the numerical temperature fields, the allied mean convection coefficients* $\bar{h}_{\text{mix}}/B$ *changing with the molar gas composition w in the w domain [0, 1] are plotted in congruous diagrams for the five binary gas mixtures under study.* [DOI: 10.1115/1.2137349]

Keywords: vertical plate, turbulent free convection, binary gas mixtures, maximum mean convection coefficient

1 Introduction

If a vertical plate is long enough, the free convection boundary layer at some point will undergo a transition from laminar to turbulent. The change may begin at a relatively low Grashof number around $\text{Gr}_x = 10^7$, where a viscous instability occurs that amplifies any disturbances to the laminar free convection boundary layer. The amplified waves travel along the vertical plate, growing in the way up until they turn large to trigger bursts of turbulence, which then cascade in the downstream region into full turbulent free convection boundary layer flow. The theory of free convection instability is discussed at length in a review paper by Gebhart [1]. A literature search reveals that the most notable theoretical predictions of turbulent free convection of air along a vertical plate have been done by Eckert and Jackson [2], Bailey [3], Kato et al. [4], Noto and Matsumoto [5], Mason and Seban [6], and Henkes and Hoogendoorn [7].

The present technical note explores the attributes of selected binary gas mixtures (instead of air) for the cooling of heated vertical plates with turbulent free convection. We employed helium (He) as the primary gas and carbon dioxide (CO_2), methane (CH_4), nitrogen (N_2), oxygen (O_2), and xenon (Xe) as the secondary gases to form five binary gas mixtures. Using the similarity variable method, the system of Navier-Stokes and energy equations for turbulent Grashof numbers $\text{Gr}_x > 10^9$ is transformed into a system of two nonlinear differential equations. The shooting method with an efficient fourth-order Runge-Kutta-Fehlberg algorithm is utilized to solve the system of nonlinear differential equations. Using the Matlab software, an interactive solution scheme is implemented in which successive calculation sweeps of the turbulent free convection boundary layers are performed to obtain the turbulent velocity and temperature fields of the binary gas mixtures. The computed temperature fields for each binary gas mixture are post-processed and presented in terms of the allied mean convection coefficient $\bar{h}_{\text{mix}}/B$ varying with the molar gas composition w of in the proper w domain [0, 1].

2 Model Equations

Based on the boundary layer approximations, the system of mass, momentum, and energy equations for turbulent free convection of a Boussinesqian gas along a heated vertical plate is [1]

$$\frac{\partial u}{\partial x} + \frac{\partial v}{\partial y} = 0 \tag{1}$$

$$u\frac{\partial u}{\partial x} + v\frac{\partial u}{\partial y} = \frac{\partial}{\partial y}\left[(\nu + \varepsilon_M)\frac{\partial u}{\partial y}\right] + g\beta(T - T_\infty) \tag{2}$$

$$u\frac{\partial T}{\partial x} + v\frac{\partial T}{\partial y} = \frac{\partial}{\partial y}\left[(\alpha + \varepsilon_H)\frac{\partial T}{\partial y}\right] \tag{3}$$

The boundary conditions for no-slip velocity and prescribed wall temperature are

$$\text{at } y = 0: \quad u = v = 0, \quad T = T_w \tag{4}$$

$$\text{as } y \to \infty: \quad u \to 0, \quad T \to T_\infty \tag{5}$$

Using the standard stream function $\psi(x, y)$

$$u = \frac{\partial \psi}{\partial y}, \quad v = -\frac{\partial \psi}{\partial x} \tag{6}$$

Noto and Matsumoto [5] implemented the similarity variable method for air. The dimensionless similarity variable ξ, the dimensionless stream function f, and the dimensionless temperature θ are expressed as

$$\xi = \frac{y}{x}\sqrt{\frac{u_{fc}x}{\nu}}, \quad f(x,\xi) = \frac{\psi}{\sqrt{u_{fc}x\nu}}, \quad \theta(x,\xi) = \frac{T - T_\infty}{T_w - T_\infty} \tag{7}$$

where u_{fc} is the so-called equivalent free convection velocity

$$u_{fc} = \sqrt{g\beta(T_w - T_\infty)x} \tag{8}$$

With this background, the system of partial differential equations (1)–(3) is transformed into the following pair of nonlinear ordinary differential equations

$$\left(1 + \frac{\varepsilon_M}{\nu}\right)\frac{\partial^3 f}{\partial \xi^3} + \left[\frac{3}{4}f + \frac{\partial}{\partial \xi}\left(\frac{\varepsilon_M}{\nu}\right)\right]\frac{\partial^2 f}{\partial \xi^2} - \frac{1}{2}\left(\frac{\partial f}{\partial \xi}\right)^2 + \theta = 0 \tag{9}$$

[1]Corresponding author.

Contributed by the Fluids Engineering Division of ASME for publication in the JOURNAL OF FLUIDS ENGINEERING. Manuscript received May 18, 2004; final manuscript received July 13, 2005. Assoc. Editor: Malcolm J. Andrews.

$$\left(\frac{1}{\mathrm{Pr}}+\frac{1}{\mathrm{Pr}_T}\frac{\varepsilon_M}{\nu}\right)\frac{\partial^2\theta}{\partial\xi^2}+\left[\frac{3}{4}f+\frac{1}{\mathrm{Pr}_T}\frac{\partial}{\partial\xi}\left(\frac{\varepsilon_M}{\nu}\right)\right]\frac{\partial\theta}{\partial\xi}=0 \tag{10}$$

which incorporates the local similarity concept that $\partial f/\partial x = \partial\theta/\partial x = 0$. Similarly, the boundary conditions in Eqs. (4) and (5) are rewritten as

$$\text{at } \eta=0: \quad f=\frac{\partial f}{\partial\eta}=0, \quad \theta=1 \tag{11a}$$

$$\text{as } \eta\to\infty: \quad \frac{\partial f}{\partial\eta}\to 0, \quad \theta\to 0 \tag{11b}$$

To integrate Eqs. (9)–(11), additional information about (a) the eddy viscosity of momentum ε_M, (b) the Prandtl number Pr, and (c) the turbulent Prandtl number Pr_T is required. For ε_M, Kato et al. [4] recommended the eddy viscosity profile

$$\frac{\varepsilon_M}{\nu}=0.4y^+\{1-\exp[-0.0017(y^+)^2]\} \tag{12}$$

The Prandtl numbers of the binary gas mixtures, $\mathrm{Pr}_{\mathrm{mix}}(w)$, have to be calculated beforehand. In this context, the molar gas composition w_i of a binary gas mixture is defined as the mass fraction of the gas i:

$$w_i=\frac{x_iM_i}{M_{\mathrm{mix}}}, \quad i=1,2 \tag{13}$$

where x_i is the mole fraction of the gas i, M_i is the molar mass of the gas i, and $M_{\mathrm{mix}}=x_1M_1+x_2M_2$ is the molar mass of the binary gas mixture [8]. For low Prandtl number fluids ($\mathrm{Pr}\ll 1$), like metallic liquids and binary gas mixtures, a Prandtl number effect on the turbulent Prandtl number Pr_T is observable [9]. The correlation equation that fits the available experimental data is

$$\frac{1}{\mathrm{Pr}_T}=\frac{1}{2\mathrm{Pr}_{T,\infty}}+C\mathrm{Pr}\frac{\varepsilon_M}{\alpha}\sqrt{\frac{1}{2\mathrm{Pr}_{T,\infty}}}-\left(C\mathrm{Pr}\frac{\varepsilon_M}{\alpha}\right)^2 \times\left[1-\exp\left(-\frac{1}{C\mathrm{Pr}(\varepsilon_M/\alpha)\sqrt{\mathrm{Pr}_{T,\infty}}}\right)\right] \tag{14}$$

where $\mathrm{Pr}_{T,\infty}$ is the value of Pr_T far away from the plate and C is an experimental constant.

3 Computational Procedure

The numerical solution procedure consists of four sequential steps. First, for a given binary gas mixture, values of the molar gas composition w are chosen in the proper domain [0, 1]. Second, the thermophysical properties η_{mix}, λ_{mix}, ρ_{mix}, and $C_{p,\mathrm{mix}}$ for the binary gas mixture are evaluated at the film temperature $T_f=(T_s+T_\infty)/2$. The formulas recommended in the physicochemistry literature are found in [10]. Third, knowing the imposed temperature difference T_w-T_∞, a fixed location of the axial coordinate x establishes the local Grashof number Gr_x. Fourth, the system of two nonlinear differential equations (9) and (10) is solved numerically in the ξ direction by the shooting method with a fourth-order Runge-Kutta-Fehlberg algorithm [11]. The convergence criterion was set at 10^{-6}. Using the Matlab software, an interactive solution scheme is implemented in which successive calculation sweeps of the turbulent free convection boundary layers are performed to obtain the turbulent velocity and temperature fields of the binary gas mixtures.

4 Numerical Results

Let $q_w(x)$ be the local wall heat flux at the vertical plate, which may be obtained from the numerical temperature field $T(x,y)$ as

$$q_w(x)=-\lambda(w)\frac{\partial T(x,0)}{\partial y}=-\lambda(w)\frac{(T_w-T_\infty)}{x}\sqrt{\frac{u_{fc}x}{\nu(w)}}[-\theta'(0)] \tag{15}$$

Alternatively, from Newton's equation of cooling,

$$q_w(x)=h(x,w)(T_w-T_\infty) \tag{16}$$

where $h(x,w)$ is the local convection coefficient. Combining Eqs. (15) and (16), the explicit expression for $h(x,w)$ turns out to be

$$h(x,w)=-\lambda(w)\frac{\sqrt{u_{fc}}}{\sqrt{x}}\sqrt{\frac{\rho(w)}{\eta(w)}}[-\theta'(0)] \tag{17}$$

Here, the dimensionless wall temperature gradient $\theta'(0)$ is a function of the Prandtl number $\mathrm{Pr}_{\mathrm{mix}}(w)$ for the specific binary gas mixtures.

Next, the mean convection coefficient $\bar{h}(w)$ is computed from its definition:

$$\bar{h}(w)=\frac{1}{L}\int_0^L h(x,w)dx \tag{18}$$

Owing that air is a commonly used fluid in cooling applications, air seems to be the logical fluid choice to validate the numerical turbulent velocity and temperature fields of the binary gas mixtures. In this context, a remarkable agreement exists between the numerical mean Nusselt number $\bar{\mathrm{Nu}}_L$ and the experimentally measured $\bar{\mathrm{Nu}}_L$ obtained by Warner and Arpaci [12] for air ($\mathrm{Pr}=0.71$) spreading over a large Rayleigh number subinterval $\mathrm{Ra}_x<10^{12}$.

It is instructive to contrast the turbulent free convection characteristics of the five binary gas mixtures: He–Xe, He–N_2, He–O_2, He–CO_2, and He–CH_4 against those of standard air at the same film temperature for $\mathrm{Gr}_x>10^9$ (the baseline case). The figure format adopted illustrates the magnitude of the allied convection coefficient $\bar{h}_{\mathrm{mix}}/B$ on the ordinate and the molar gas composition w on the abscissa. The constant B is a function of the gravity acceleration g, the vertical plate length L, and the temperature difference T_s-T_∞, because the thermal expansion coefficient $\beta=1/T_\infty$. Notice that the grouping of these quantities is unrelated to the thermo-physical properties of the binary gas mixtures. This facilitates the reinterpretation of the ratio $\bar{h}_{\mathrm{mix}}/B$ as an allied mean convection coefficient of the binary gas mixtures. In addition, the figure includes a horizontal line, indicative of the allied convection coefficient for air, $\bar{h}_a/B$, the so-called baseline case.

The allied mean convection coefficients for air and He are $\bar{h}_a/B=37.5$ and $\bar{h}_{\mathrm{He}}/B=55$, respectively. It may be seen in Fig. 1 that a remarkable maximum allied mean convection coefficient $\bar{h}_{\mathrm{mix,max}}/B=85$ is furnished by the He–Xe gas mixture at an optimal molar gas composition of $w_{\mathrm{opt}}=0.93$. Relative to air, the heat transfer enhancement $(\bar{h}_{\mathrm{mix,max}}-\bar{h}_a)/\bar{h}_a$ delivered by the He–Xe gas mixture is of the order of 127%. It may also be seen that the He–Xe gas mixture outperforms the pure He gas by a margin of 55%. The trio of He–CH_4, He–O_2, and He–N_2 gas mixtures does not attain a maximum for the allied mean convection coefficient $\bar{h}_{\mathrm{mix}}/B$ in the w domain [0, 1]. The other gas mixture He–CO_2 furnishes an imperceptible maximum for the allied mean convection coefficient $\bar{h}_{\mathrm{mix}}/B$. Besides, it may be realized that the comparison between pure CO_2 and air is meaningless because their four thermophysical properties are very similar.

5 Conclusions

For turbulent free convection along a heated vertical plate, it has been demonstrated that the allied mean convection coefficient $\bar{h}_{\mathrm{mix}}/B$ for He-based binary gas mixtures increases with incre-

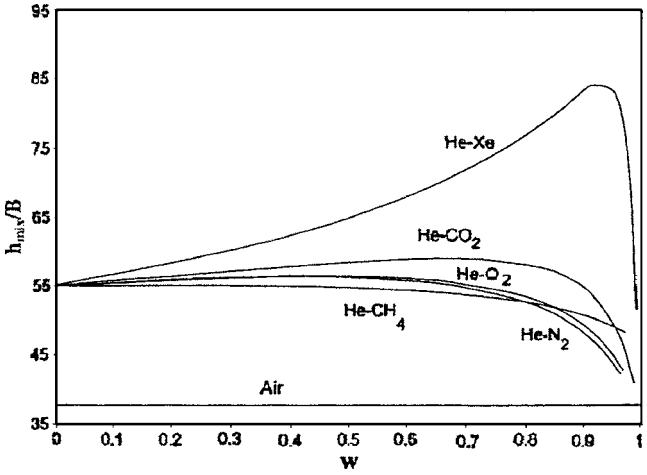

Fig. 1 Variation of the allied mean convection coefficient $\bar{h}_{mix}/B$ with the molar gas composition w for the five binary gas mixtures at a film temperature of 300 K

ments of the molar mass difference between the primary He gas and the secondary gases Xe, N_2, O_2, CO_2, and He–CH_4. For a case study described by a film temperature of 300 K, the He–Xe gas mixture emerged as the better gas candidate among the group of five binary gas mixtures tested. Based on the encouraging results, it is expected that the outcome of this paper will serve as a "*proof-of-concept*" for engineering analysis, design, and optimization.

Nomenclature

C_p = heat capacity at constant pressure $Jm^{-3}\,K^{-1}$
f = dimensionless stream function ψ in Eq. (7)
g = acceleration of gravity, ms^{-2}
Gr_x = local Grashof number, $g\beta(T_w-T_\infty)x^3/\nu^2$
Gr_L = Grashof number, $g\beta(T_w-T_\infty)L^3/\nu^2$
h = local convection coefficient, $Wm^{-2}\,K^{-1}$
$\bar{h}$ = mean convection coefficient, $Wm^{-2}\,K^{-1}$
L = length of vertical plate, m
Nu_x = local Nusselt number, hx/λ
$\bar{Nu}_L$ = mean Nusselt number, $\bar{h}L/\lambda$
Pr = Prandtl number, $\mu C_p/\lambda\rho$
Pr_T = turbulent Prandtl number, $\varepsilon_M\varepsilon_H$
q_w = local wall heat flux, Wm^{-2}
Ra_x = local Rayleigh number, Gr_xPr
Ra_L = Rayleigh number, Gr_LPr
T = temperature, K
T_w = wall temperature, K
T_∞ = free-stream temperature, K
u, v = axial and transversal velocity, ms^{-1}
u_{fc} = equivalent free convection velocity in Eq. (8), ms^{-1}
x, y = axial and transversal coordinates, m
y^+ = wall transversal coordinate, $(y/\nu)\sqrt{\tau_{w,x}/\rho}$
w = molar gas composition of binary gas mixture
w_{opt} = optimal molar gas composition of binary gas mixture

Greek Letters

α = thermal diffusivity, $m^2\,s^{-1}$
β = coefficient of thermal expansion, K^{-1}
ε_H = eddy diffusivity of heat $m^2\,s^{-1}$
ε_M = eddy viscosity of momentum, $m^2\,s^{-1}$
λ = thermal conductivity, $Wm^{-1}\,K^{-1}$
μ = viscosity, μPa s
ν = kinematic viscosity, $m^2\,s^{-1}$
θ = dimensionless T, Eq. (7)
ρ = density, $kg\,m^{-3}$
τ_w = wall shear stress, Nm^{-2}
ξ = dimensionless y, Eq. (7)
$\psi(x,y)$ = stream function, $u=\partial\psi/\partial y$, $v=-\partial\psi/\partial x$, $m^2\,s^{-1}$

Subscripts

a = air
max = maximum
mix = mixture of binary gases
x = axial location
w = wall

References

[1] Gebhart, B., 1969, "External Natural Convection Flows," Appl. Mech. Rev., **22**, pp. 691–730.
[2] Eckert, E. R. G., and Jackson, T. W., 1951, "Analysis of Turbulent Free-Convection Boundary Layer on a Flat Plate," NACA Tech. Report 1015.
[3] Bailey, F. J., 1955, "The Integral Method Applied to the Turbulent Free-Convection Boundary Layer," Proc. Inst. Mech. Eng., **169**, pp. 361–368.
[4] Kato, H., Nishiwaki, N., and Hirata, M., 1968, "On the Turbulent Heat Transfer by Free Convection From a Vertical Plate," Int. J. Heat Mass Transfer, **11**, pp. 1117–1125.
[5] Noto, K., and Matsumoto, R., 1975, "Turbulent Heat Transfer by Natural Convection Along an Isothermal Vertical Flat Surface," ASME J. Heat Transfer, **98**, pp. 621–624.
[6] Mason, H. B., and Seban, R. A., 1974, "Numerical Predictions for Turbulent Free Convection From Vertical Surfaces," Int. J. Heat Mass Transfer, **17**, pp. 1329–1336.
[7] Henkes, R. A., and Hoogendoorn, C. J., 1989, "Comparison of Turbulence Models for the Natural Convection Boundary Layer Along a Heated Vertical Plate," Int. J. Heat Mass Transfer, **32**, pp. 157–169.
[8] Polling, B. E., Prausnitz, J. M., and O'Connell, J. P., 2001, *The Properties of Gases and Liquids*, McGraw-Hill, New York, A.5–A.19.
[9] Kays, W., and Crawford, M., 1993, *Convective Heat and Mass Transfer*, McGraw-Hill, New York.
[10] Campo, A., and Papari, M. M., 2005, "Intensification of Turbulent Free Heat Transport in Various Configurations With Selected Binary Mixtures of Gases Taking the Weight of Air as a Constraint," Int. Commun. Heat Mass Transfer, **32**, pp. 1287–1306.
[11] Bradshaw, P., Cebeci, T., and Whitelaw, J. H., 1981, *Engineering Calculation Methods for Turbulent Flows*, Academic, San Diego, CA.
[12] Warner, Y., and Arpaci, V. S., 1968, "An Experimental Investigation of Turbulent Natural Convection in Air at Low Pressure Along a Vertical Heated Flat Plate," Int. J. Heat Mass Transfer, **11**, pp. 397–406.

Journal of Fluids Engineering

Memoriam

In Memoriam

This special section of JFE is dedicated to Dr. Sankaraiyer Gopalakrishnan who unexpectedly passed away recently. Gopal, as we affectionately called him, served the Fluids Engineering Division and ASME with great distinction over many years in various capacities. We appreciate his commitment and service even more considering Gopal's responsibilities as Vice President of Flowserve Corporation in California. He was an uplifting force in moving the Division forward. His wise counsel and guidance will be missed by all who grew accustomed to his presence at the meetings of the Division. He was a dignified gentleman, a deeply caring human being, and a dear friend. Our deepest sympathies are with his family. We miss him and we wish him well in his journey beyond.

Dennis Siginer
Associate Editor

Joseph Katz
Technical Editor

Journal of Fluids Engineering

Errata

Erratum: "Two-phase Flow in Jet Pumps for Different Liquids" [Journal of Fluids Engineering, 2005, 127(5), pp. 1038–1042]

S. Mikhail, Hesham A. M. Abdou, and Mohsen Abou-Ellail

The name of the third author was omitted from the paper:

Mohsen Abou-Ellail
Ph.D.
Mechanical Power Engineering, Cairo University,
Cairo, Egypt

Erratum: "Numerical Simulation of Two-Phase Flow in Injection Nozzles: Interaction of Cavitation and External Jet Formation" [Journal of Fluids Engineering, 2003, 125(6), pp. 963–969]

Weixing Yuan and Günter H. Schnerr

The sign "–" at the right side of Eq. (16) is missing. It should read "= –".

The first line of the text in the second column on p. 965, should read "water" not "meter".

